Pavel Matousek
Michael D. Morris
Editors

BIOLOGICAL AND MEDICAL PHYSICS, BIOMEDICAL ENGINEERING

Emerging Raman Applications and Techniques in Biomedical and Pharmaceutical Fields

Springer

BIOLOGICAL AND MEDICAL PHYSICS, BIOMEDICAL ENGINEERING

BIOLOGICAL AND MEDICAL PHYSICS, BIOMEDICAL ENGINEERING

The fields of biological and medical physics and biomedical engineering are broad, multidisciplinary and dynamic. They lie at the crossroads of frontier research in physics, biology, chemistry, and medicine. The Biological and Medical Physics, Biomedical Engineering Series is intended to be comprehensive, covering a broad range of topics important to the study of the physical, chemical and biological sciences. Its goal is to provide scientists and engineers with textbooks, monographs, and reference works to address the growing need for information.

Books in the series emphasize established and emergent areas of science including molecular, membrane, and mathematical biophysics; photosynthetic energy harvesting and conversion; information processing; physical principles of genetics; sensory communications; automata networks, neural networks, and cellular automata. Equally important will be coverage of applied aspects of biological and medical physics and biomedical engineering such as molecular electronic components and devices, biosensors, medicine, imaging, physical principles of renewable energy production, advanced prostheses, and environmental control and engineering.

Pavel Matousek
Michael D. Morris
(Editors)

Emerging Raman Applications and Techniques in Biomedical and Pharmaceutical Fields

With 182 Figures

Springer

Editors
Prof. Pavel Matousek
Central Laser Facility
Science & Technology
Facilities Council
Rutherford Appleton Laboratory
Oxfordshire OX11 0QX
United Kingdom
pavel.matousek@stfc.ac.uk

Prof. Michael D. Morris
University of Michigan
Dept. Chemistry
Ann Arbor MI 48109–1055
USA
mdmorris@umich.edu

ISSN 1618-7210
ISBN 978-3-642-02648-5 e-ISBN 978-3-642-02649-2
DOI 10.1007/978-3-642-02649-2
Springer Heidelberg Dordrecht London New York

Library of Congress Control Number: 2009938669

Cover design: Integra Software Services Pvt. Ltd., Pondicherry

Printed on acid-free paper

Springer is part of Springer Science+Business Media (www.springer.com)

Preface

In recent years, Raman spectroscopy has undergone a major transformation from a specialist laboratory technique to a practical analytical tool. This change was driven on several parallel fronts by dramatic advances in laser instrumentation, detectors, spectrometers, and optical filter technology. This resulted in the advent of a new generation of compact and robust Raman instruments with improved sensitivity and flexibility. These devices could be operated for the first time by non-specialists outside the laboratory environment. Indeed, Raman spectroscopy is now found in the chemical and pharmaceutical industries for process control and has very recently been introduced into hospitals. Handheld instruments are used in forensic and other security applications and battery-operated versions for field use are found in environmental and geological studies.

Simultaneously, major advances have been seen in the development of powerful processing methods, some driven by the progress of related spectroscopic methods such as NIR absorption spectroscopy. Numerous chemometric packages are available for advanced analysis of data. These do not require specialist user knowledge (although caution is required in interpreting results) and provide further enhanced sensitivity and capability to the Raman technique.

In this book we focus on two such major fields, biomedical and pharmaceutical. The book is aimed at life sciences and pharmaceutical readerships. Accordingly, the chapter authors emphasize explanatory material with practical implications rather than focusing on mathematical detail. The basics are explained in a way to give access to newcomers. The focus is on emerging applications of Raman spectroscopy in the concerned areas and the individual chapters emphasize the latest developments in these fields.

The first part of the book is devoted to Raman techniques and methods while the second part describes applications pertinent to biomedical and

pharmaceutical areas. The chapters are representative of activity in these focus areas. Of necessity, many interesting topics could not be included.

We hope you enjoy the reading!

Ann Arbor & Oxfordshire — *Michael D. Morris*
August 2009 — *Pavel Matousek*

Contents

*Chapter contact author

List of Contributors

Laurence D. Barron
Department of Chemistry, University of Glasgow, Glasgow G12 8QQ, UK
laurence@chem.gla.ac.uk

Andrew J. Berger*
The Institute of Optics, 405 Goergen Hall, University of Rochester, Rochester, NY 14627, USA
andrew.berger@rochester.edu

Rohit Bhargava*
Department of Bioengineering, Micro and Nanotechnology Laboratory, National Center for Supercomputing Applications and Beckman Institute for Advanced Science and Technology, University of Illinois at Urbana-Champaign, Urbana, IL 61801, USA
rxb@illinois.edu

Ewan W. Blanch*
Manchester Interdisciplinary Biocentre, Faculty of Life Sciences, University of Manchester, 131 Princess Street, Manchester M1 7DN, U.K.
E.Blanch@manchester.ac.uk

Valerian Ciobotă
Institut für Physikalische Chemie, Friedrich-Schiller-Universität Jena, Helmholtzweg 4, D-07743 Jena, Germany
Valerian.ciobota@uni-jena.de

Dana Cialla
Institut für Physikalische Chemie, Friedrich-Schiller-Universität Jena, Helmholtzweg 4, D-07743 Jena, Germany
dana.cialla@uni-jena.de

Don Clark*
Materials Science and Oral Products Centre of Emphasis, Pfizer Global R&D, Sandwich CT13 9NJ, UK
don.a.clark@pfizer.com

Mike Claybourn
Pharmaceutical & Analytical Development, AstraZeneca R&D, Macclesfield, UK
Mike.Claybourn@astrazeneca.com

Igor V. Ermakov
Department of Physics, University of Utah, Salt Lake City, Utah 84112, USA
ermakov@physics.utah.edu

Francis W.L. Esmonde-White
Department of Chemistry, University of Michigan, Ann Arbor, MI 48109, USA
few@umich.edu

Carol R. Flach
Department of Chemistry, Newark College, Rutgers University, 73 Warren Street, Newark, NJ 17102, USA
flach@andromeda.rutgers.edu

Staffan Folestad
Pharmaceutical & Analytical Development, AstraZeneca R&D Mölndal, Sweden
staffan.folestad@astrazeneca.com

Werner Gellermann*
Department of Physics, University of Utah, 115 S 1400 East RM 201, Salt Lake City, UT 84112, USA
werner@physics.utah.edu

Michaela Harz
Institut für Physikalische Chemie, Friedrich-Schiller-Universität Jena, Helmholtzweg 4, D-07743 Jena, Germany
michaela.harz@uni-jena.de

Mark Hewko
National Research Council Canada, Institute for Biodiagnostics, 435 Ellice Ave., Winnipeg, Manitoba, Canada, R3B 1Y6
Mark.Hewko@nrc.chrc.gc.ca

Gavin Jell
Department of Materials and Institute of Biomedical Engineering, Imperial College London SW7 2AZ, UK
g.jell@medsch.ucl.ac.uk

Jonas Johansson*
Pharmaceutical & Analytical Development, AstraZeneca R&D Mölndal, Sweden
Jonas.Johansson@astrazeneca.com

Virginia Joseph
Department of Chemistry, Humboldt University, Brook-Taylor-Str. 2, 12489 Berlin, Germany and BAM Federal Institute for Materials Research and Testing Richard-Willstätter-Str. 11, 12489 Berlin, Germany
virginia.joseph@bam.de

Catherine A. Kendall
Biophotonics Research Unit, Gloucestershire Hospitals NHS Foundation Trust, Great Western Road, Gloucester, GL1 3NN, UK

Janina Kneipp*
Department of Chemistry, Humboldt University, Brook-Taylor-Str. 2, 12489 Berlin, Germany and BAM Federal Institute for Materials Research and Testing, Richard-Willstätter-Str. 11, 12489 Berlin, Germany
janina.kneipp@chemie.hu-berlin.de

Fred LaPlant*
3M Corporate Research Analytical Laboratory, Saint Paul, MN 55105, USA
flaplant@mmm.com

Neil A. Macleod
Central Laser Facility, Science and Technology Facilities Council, Rutherford Appleton Laboratory, Harwell Science and Innovation Campus, Didcot, Oxfordshire OX11 0QX, UK
neil.macleod@stfc.ac.uk

Pavel Matousek*
Central Laser Facility, Science and Technology Facilities Council, Rutherford Appleton Laboratory, Harwell Science and Innovation Campus, Didcot, Oxfordshire OX11 0QX, UK
Pavel.Matousek@stfc.ac.uk

Richard Mendelsohn*
Department of Chemistry, Newark College, Rutgers University, 73 Warren Street, Newark, NJ 17102, USA
mendelso@andromeda.rutgers.edu

Michael D. Morris*
Department of Chemistry, University of Michigan, Ann Arbor, MI 48109, USA
mdmorris@umich.edu

Ulrich Panne
Department of Chemistry, Humboldt University, Brook-Taylor-Str. 2, 12489 Berlin, Germany and BAM Federal Institute for Materials Research and Testing, Richard-Willstätter-Str. 11, 12489 Berlin, Germany
ulrich.panne@bam.de

Giuseppe Pezzotti*
Full Professor & Leader, Ceramic Physics Laboratory, Department of Materials Science and Engineering Kyoto Institute of Technology, Sakyo-ku, Matsugasaki, 606-8585 Kyoto, Japan

Director, Research Institute for Nanoscience (RIN), Kyoto Institute of Technology (KIT), Sakyo-ku, Matsugasaki, 606-8585 Kyoto, Japan

Adjunct Professor, Orthopaedic Research Center, Department of Orthopaedics, Loma Linda University, 11406 Loma Linda Drive, Suite 606, Loma Linda, California 92354

Invited Professor, The Center for Advanced Medical, Engineering and Informatics, Osaka University, Yamadaoka, Suita, 565-0871 Osaka, Japan
pezzotti@kit.ac.jp

Lin-P'ing Choo-Smith*
National Research Council Canada, Institute for Biodiagnostics, 435 Ellice Ave., Winnipeg, Manitoba, Canada, R3B 1Y6
Lin-Ping.Choo-Smith@nrc-cnrc.gc.ca

Jürgen Popp*
Institut für Physikalische Chemie, Friedrich-Schiller-Universität Jena, Helmholtzweg 4, D-07743 Jena, Germany

Institut für Photonische Technologien e.V., Albert-Einstein-Straße 9, D-07745 Jena, Germany
juergen.popp@uni-jena.de

Rohith K. Reddy
Department of Bioengineering, Micro and Nanotechnology Laboratory, National Center for Supercomputing Applications and Beckman Institute for Advanced Science and Technology, University of Illinois at Urbana-Champaign, Urbana, IL 61801, USA
rohith.k@gmail.com

Caroline Rodger
Pharmaceutical and Analytical Research and Development (PARD) AstraZeneca, Macclesfield, UK
carolinerodger2002@yahoo.co.uk

Petra Rösch
Institut für Physikalische Chemie, Friedrich-Schiller-Universität Jena, Helmholtzweg 4, D-07743 Jena, Germany
Petra.Roesch@uni-jena.de

Franziska Schulte
Department of Chemistry, Humboldt University, Brook-Taylor-Str. 2, 12489 Berlin, Germany and BAM Federal Institute for Materials Research and Testing, Richard-Willstätter-Str. 11, 12489 Berlin, Germany
franziska.schulte@bam.de

Mohsen Sharifzadeh
Department of Physics, University of Utah, Salt Lake City, Utah 84112, USA
mohsen@physics.utah.edu

Michael G. Sowa
National Research Council Canada, Institute for Biodiagnostics, 435 Ellice Ave., Winnipeg, Manitoba, Canada, R3B 1Y6
Michael.Sowa@nrc-cnrc.gc.ca

Molly M. Stevens*
Department of Materials and Institute of Biomedical Engineering, Imperial College London, SW7 2AZ, UK
m.stevens@imperial.ac.uk

Stephan Stöckel
Institut für Physikalische Chemie, Friedrich-Schiller-Universität, Jena, Helmholtzweg 4, Jena D-07743, Germany
Stephan.Stoeckel@uni-jena.de

Nicholas Stone*
Biophotonics Research Unit, Gloucestershire Hospitals NHS Foundation Trust, Great Western Road, Gloucester, GL1 3NN, UK
n.stone@medical-research-centre.com

Robin Swain
Department of Materials and Institute of Biomedical Engineering, Imperial College London SW7 2AZ, UK
robin.j.swain@ic.ac.uk

Andreas Volkmer*
3. Physikalisches Institut, Universität Stuttgart, Pfaffenwaldring 57, Stuttgart 70550, Germany
a.volkmer@physik.uni-stuttgart.de

Guojin Zhang
Department of Chemistry, Newark College, Rutgers University, 73 Warren Street, Newark, NJ 17102, USA
gzhang12@its.jnj.com

* Chapter contact author

1

Lasers, Spectrographs, and Detectors

Fred LaPlant

Abstract The introduction of Raman spectroscopy into new fields has been driven largely by advances in the underlying technology. While the spectrometer is still comprised of a light source, a wavelength selector, and a detector, the improvement in functionality of each of these components has had dramatic impacts on areas where Raman was once thought impractical, if not impossible. In addition, esoteric techniques once confined to academic spectroscopy labs are now finding wide application.

This chapter will briefly describe the basic function of a Raman spectrometer, while focusing on the enabling advances in spectrometer components including capability, flexibility, ease of use, and cost. Traditional laser sources have become commodity items with air cooling, smaller forms, and lower cost in a variety of wavelengths. Likewise, availability of high-power, tunable, and pulsed laser systems have facilitated the use of higher-order techniques such as UV-resonance Raman and CARS. The spectrograph form can be selected based on application, from traditional dispersive, to FT, to liquid crystal tunable filter, etc. Introduction of the Raman signal to the spectrometer using fiber optics has seen similar advances, such as SORS and other fiber bundle techniques. Detectors have become more sensitive, with lower noise, better detection at longer wavelengths, and faster operation. Many of these advances have resulted in miniaturization of the Raman system, so that systems once requiring an entire lab bench can now be handheld. Applications where these advances have made significant impact will be highlighted.

1.1 Introduction

The evolution of Raman spectroscopy from a spectroscopic novelty, to a complementary technique in niche applications, to an analytical powerhouse, has closely paralleled the advancement of enabling technologies. While a simple block diagram of the components of a Raman spectrometer shown in Figure 1.1 would still be comparable to the very early instruments built by C.V. Raman [1], the improvement in functionality of each component has dramatically increased the impact of Raman spectroscopy in areas where it was

once thought impractical, if not impossible to perform. In addition, esoteric techniques once confined to academic spectroscopy labs are now finding wide application.

The principal difference in the current stage of Raman evolution, as exemplified by this book, is its breadth of application. From the earliest use of mercury arc lamps and photographic plates to replace sunlight and the human eye, to the introduction of the laser, to the rapid spread of multichannel detectors, each technological advance represented a quantum leap in the capacity of the Raman system to perform a wide range of useful experiments. But as befits a maturing technology, the most impressive advances are now occurring in specific disciplines, where the enabling technologies of the past allow new technologies to be specialized and optimized for individual applications.

This chapter will briefly describe the Raman effect and the basic function of a Raman spectrometer, while focusing on the advances in spectrometer components including capability, flexibility, ease of use, and cost that have enabled the emergence of new biomedical and pharmaceutical applications. Traditional laser sources have become commodity items with air cooling, smaller forms, and lower cost in a variety of wavelengths. Likewise, availability of high power, tunable, and pulsed laser systems have facilitated the use of techniques such as UV-resonance Raman and CARS (coherent anti-Stokes Raman spectroscopy). The spectrograph form can be selected based on application, from traditional dispersive, to FT, to liquid crystal tunable filter, etc. Detectors have become more sensitive, with lower noise, wider wavelength range, and faster operation. These advances, coupled with improved laser line rejection, have produced miniaturized spectrometers suitable for measurements in the harshest environments. Presentation of the sample to the spectrometer has seen similar advances: Raman imaging can be performed rapidly or over large areas; the use of fiber optics such as SORS (spatially offset Raman spectroscopy) and other fiber bundle techniques has enabled greater sampling flexibility; SERS (surface-enhanced Raman spectroscopy) has shown the potential for greatly enhanced sensitivity and specificity. This chapter will describe the available instrumental components that can be enlisted for the applications that will be described in detail in upcoming chapters.

1.2 Raman Spectroscopy: Background

A variety of other excellent texts are available for in-depth review of the fundamentals of Raman spectroscopy, including core technologies and applications [2, 3]. This is intended as a very brief, non-rigorous overview for non-spectroscopists who may be unfamiliar with the principles of Raman, its strengths, and practical limitations. For discussion of the experimental details of variant techniques such as ROA (Raman optical activity) or SERS, the reader is directed to the appropriate chapters in this text.

The Raman effect is conceptually simple: a photon can interact with a molecule in a material and can be scattered. This scattered photon almost always has the same energy/wavelength that it had before interacting with the molecule. This is referred to as Rayleigh (elastic) scattering. Very rarely a photon will either lose energy by exciting a vibration of the molecule or gain energy by causing return to the ground state of a vibration that has been thermally excited. These effects are Stokes or anti-Stokes scattering, respectively. The energy lost or gained is the vibrational energy of the vibrational mode. The Raman spectrum is produced by measuring the light shifted to lower frequencies (longer wavelengths) and to higher frequencies (shorter wavelengths) corresponding to each of the vibrational modes of the molecule. Because at thermal equilibrium there are always more molecules in the ground vibrational state than in an excited vibrational state the intensity of Stokes photons, those shifted to the red with respect to the exciting photon is much greater than the intensity of anti-Stokes photons. The Stokes spectrum is almost always the one used in a typical Raman measurement.

The absolute wavelength of the observed Raman spectrum is always relative to the exciting photon. Since lasers are the only practical light source for Raman excitation, the selection of the laser wavelength sets the wavelength region at which the Raman spectrum will be observed. The x-axis of the Raman spectrum is typically expressed as frequency in reciprocal centimeters (cm^{-1}), which can be referred to as relative wave numbers or Raman shift. Use of these units facilitates comparison to mid-IR spectra which use the same units. However, in the mid-IR, wave numbers refer to the absolute energy of the vibrational mode, whereas in Raman spectroscopy the frequency refers to the relative difference in energy from the laser frequency – hence the use of the term Raman shift. The Raman spectrum is almost never displayed in wavelength, since this would vary with the laser wavelength chosen and make comparison of spectra impossible.

For any vibrational mode, the relative intensities of Stokes and anti-Stokes scattering depend only on the temperature. Measurement of this ratio can be used for temperature measurement, although this application is not commonly encountered in pharmaceutical or biomedical applications. Raman scattering based on rotational transitions in the gas phase and low energy (near-infrared) electronic transitions in condensed phases can also be observed. These forms of Raman scattering are sometimes used by physical chemists. However, as a practical matter, to most scientists, Raman spectroscopy means and will continue to mean vibrational Raman spectroscopy.

Every molecule has a Raman spectrum; although not all vibrational modes are Raman active, any molecule of sufficient complexity will probably exhibit a usable Raman signature. The probability of a molecular bond producing a Raman photon (known as the Raman cross section) is associated with how polarizable the bond is. For instance, a phenyl ring, with a large π cloud of electrons is highly polarizable, and has a strong Raman response; an OH bond, which is less polarizable, has a weak response. This is significantly different from infrared absorption, where the important parameter is dipole moment;

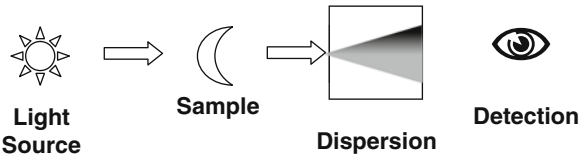

Fig. 1.1. Simplified components of a Raman spectrometer

the phenyl ring would have a weak response, while the OH would be very strong. However, in both infrared and Raman spectra, the exact frequency and intensity of a given vibrational band will be effected by interactions with the other vibrational modes present in the molecule. This means that the spectrum for a given molecule is effectively a fingerprint of that molecule. This is recognized in the US Pharmacopeia in that either the mid-IR or Raman spectrum can be used as conclusive identification of a pure substance. This also has the important implication in that Raman spectroscopy can be used to determine specific molecules that may be markers for disease states, biothreats, or environmental contaminants.

The Raman effect has also been broadly applied to online and bench-top quantitative applications, such as determination of pharmaceutical materials and process monitoring [4–6], in vivo clinical measurements [7], biological materials [8, 9], to name only a few. Because the absolute Raman response is difficult to measure accurately (sample presentation and delivered laser power can vary), these measurements are almost always calculated as a percentage with respect to the response from an internal standard. This standard is typically part of the sample matrix; in a drug product, the standard may be an excipient; in a biological sample, it is commonly water.

This is represented graphically in Fig. 1.1. These spectra are from a calibration set consisting of differing levels of ethanol in decanol ranging from 0 to 10%. As described above, the spectra-to-spectra overall intensity varies significantly. A wide variety of approaches can be taken to normalize the spectra, suppress background interference, and enhance selectivity and accuracy. Quantitative methods for Raman spectroscopy using univariate and multivariate methods are treated extensively elsewhere [10]. In this example, a second derivative was applied to the spectra, which removes baseline variation and enhances band resolution, followed by a univariate intensity calibration. Although limit of quantitation will vary widely depending on the analyte and matrix, the results shown in Fig. 1.2 (quantitation in the ∼1% by weight range) are typical.

Although both Raman and IR can be used to determine molecular identity or quantify the presence of an analyte, there are critical differences in the way that they can be applied. The extremely strong absorption of OH in the mid-IR makes any measurement difficult in the presence of water – a ubiquitous material in most biological samples. Subtle spectral differences that may be apparent in the Raman spectrum tend to be obscured by the overwhelming water absorption. This is shown in Fig. 1.3 for a solution of lactose in water;

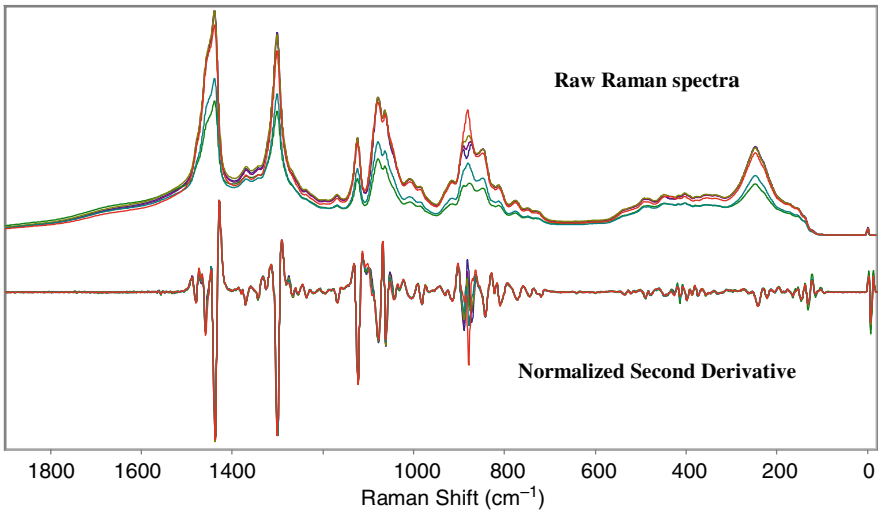

Fig. 1.2. Comparison of raw and second derivative spectra for EtOH in decanol

while the water contributes only weakly to the Raman signal, with most of the spectral features due to lactose. In general, the strength of the absorptions in the mid-IR also limits its optical flexibility; because almost all of the light is absorbed within the top few microns of the sample, only the surface (or a very thin section) of a sample can be measured. The capacity of the Raman probe laser to penetrate into a sample and generate signal – through a glass vial, through layers of water, through layers of tissue, or through any nominally transparent material – is a significant advantage. This advantage is possible only because the interaction of the laser with the intervening material is weak – as is the resulting Raman signal.

The likelihood of a Raman photon being generated is dependent on a variety of factors, but is generally on the order of one out of a million incident photons. The most directly controllable variable is the frequency of excitation. Within a first approximation, the intensity of the Raman signal is proportional to $1/(\lambda)^4$, where λ is the wavelength of the exciting photon. This approximation assumes that the excitation is nonresonant; in the case where a resonance exists, the signal can be orders of magnitude larger, and this relationship does not hold. This wavelength dependence means that as the photon wavelength becomes longer (shifted toward the red), the intensity of the Raman signal decreases rapidly. In order to maximize the Raman signal, it would appear that the highest energy photon (or bluest laser) would be the most desirable. However, fluorescence is a competing process that can be millions of times more efficient than the Raman effect. The transitions giving rise to fluorescence are more probable in the blue region of the spectrum, so that increases in Raman signal at shorter excitation wavelengths are typically more than offset by increases in background fluorescence. Due to this inequal-

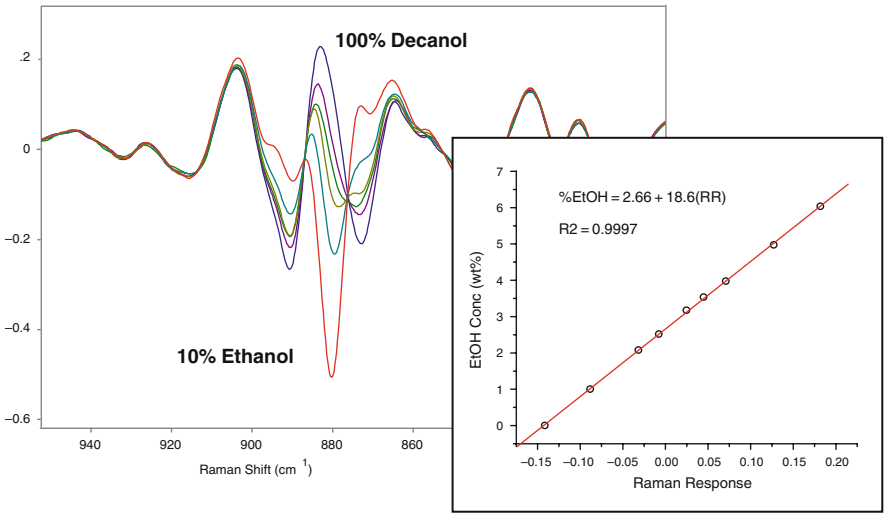

Fig. 1.3. Second derivative response for EtOH in decanol and calibration results

ity in signal strength, even trace quantities of fluorescent materials can mask the presence of a high-concentration analyte. Fluorescence can be minimized by exciting at longer wavelengths, so that wavelength selection is a balance between maximizing signal strength and minimizing interference.

The critical factor affecting every aspect of the Raman spectroscopy system is the weakness of the Raman effect: there are simply very few Raman photons generated. All of the technical hallmarks of the modern Raman system, including lasers as an excitation source, high efficiency collection geometries, high-throughput spectrometers with strong rejection of the laser wavelength, and low noise, high-sensitivity detectors are all a result of the necessity to absolutely maximize the sensitivity and selectivity of the Raman response.

1.3 Lasers

The laser is very much the ideal light source for generation of Raman scattered photons. The light output from a laser is typically a single wavelength (monochromatic) or a very narrow wavelength band. Because the width of an observed Raman band is a convolution of the natural linewidth of the vibrational band with the laser linewidth, a broad frequency excitation source will yield a spectrum with broad, poorly resolved Raman bands. Other practical benefits include efficient rejection of Rayleigh scattered photons (enabling very low-frequency measurements) and high excitation intensity. Characteristically low beam divergence enables optimization of a variety of sampling parameters. The laser can be focused to the diffraction-limited spot size (smallest

effective spot diameter approximately equal to the laser wavelength) for high photon flux at the measurement zone. This is the principle behind Raman microscopy, where sample spectra can be obtained with very high spatial resolution. This also allows facile and efficient coupling to fiber optics, which in turn generates a variety of flexibility advantages that will be discussed further in the next section. These advantages ensured that mercury arc lamps were abandoned rapidly and universally soon after the introduction of the laser [11].

Advances in laser technology, coupled with improvements in the supporting components, now enable a wide variety of lasers to be used. By far the most common laser used in the modern Raman spectrometer is the diode laser operating at 785 nm. Diode lasers lack some of the advantages of gas lasers, such as inherent wavelength stability and beam profile, although these differences are minimized in modern diode laser designs by using active temperature stabilization, dispersive intra- or extra-cavity optical elements, and beam-shaping optics. However, there are multiple practical advantages that drive the use of diode lasers in Raman applications. Although fluorescence may not be totally eliminated at 785 nm, it is significantly depressed. As shown in Fig. 1.4, the intensity of the Raman signal will be about a factor of 5 lower for a 785 nm diode vs. the Ar-ion 514 nm line. However, the absorption of most fluorescent materials drops off rapidly over this region, so that samples that would generate sufficient fluorescent photons to saturate the detector with 514 nm or 632 nm excitation are often very easily measured at 785 nm. Another factor is that the most common silicon-based detectors have a maximum detection efficiency in the region of 800–1000 nm, which coincides with the region in which the majority of the Raman signal of interest is generated (although the quantum efficiency falls of rapidly past 1000 nm, and the response to the CH region of the spectrum at 3000 cm^{-1} is diminished). The depth of penetration of NIR light into biological tissue (many millimeters or more) can also be a significant advantage over visible excitation when trying to detect or visualize subsurface materials.

There are several strategies to cope with samples that still exhibit unacceptable fluorescence at 785 nm. The obvious direction would be to make the excitation even redder; for example, some modern systems also operate at 830 nm to take advantage of further reduction of fluorescence of biological tissues. More commonly, the solid-state Nd:YAG laser operating at the 1064 nm fundamental is used in conjunction with a Fourier transform spectrometer (this will be discussed in more detail in Section 1.5). At this wavelength, fluorescence from all but the most intractable samples (e.g., charred materials, heavy petroleum distillates) is negligible. However, the Raman signal is again diminished by a factor of about 3.5 from excitation at 785 nm. To compensate, the laser power is typically increased accordingly, where 10–100 mW lasers are common in the visible, 1–2 W lasers are the norm at 1064 nm. A variety of sample protection schemes, such as sample spinning or wiggling, have been implemented to prevent burning in these systems.

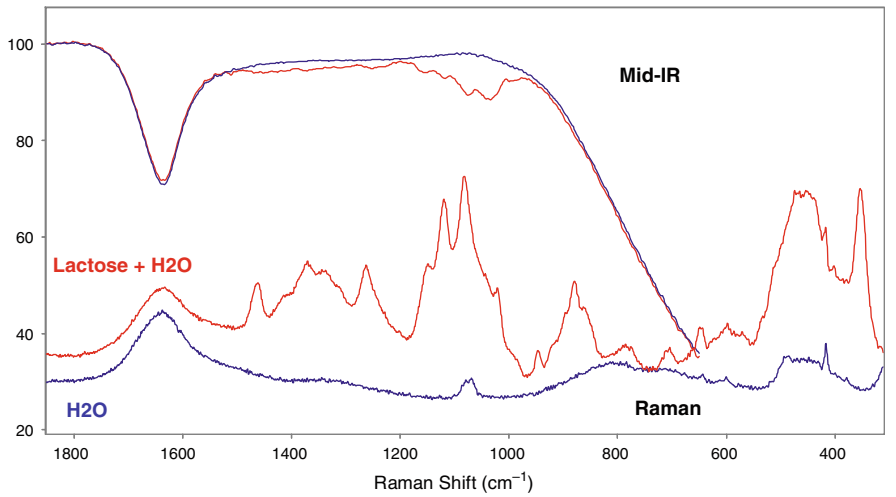

Fig. 1.4. Comparison of Raman and mid-IR spectra of lactose in water

The other option for reducing fluorescence contribution in the spectrum is to move the excitation deep into the UV (typically below 250 nm). Although the absorption (and subsequent fluorescence) will be much more intense, the absorption and fluorescence spectra are offset in wavelength (known as the Stokes shift) such that a spectral gap is present between the excitation laser wavelength and the onset of the fluorescence emission (typically at 280 nm). The Raman spectrum can be measured in this spectral window with no fluorescence interference. This technique is also appealing in that by moving toward the blue, the normal Raman signal is greatly enhanced. However, there are practical limitations that make the general use of UV Raman difficult. First, most samples (and biological samples in particular) absorb UV so strongly that sample burning/damage is of critical concern [12]. The laser power must often be reduced to an extent that completely offsets the gains made in the λ^4 factor. Absorption also operates to decrease the resulting signal; self-absorption of the Raman signal by the sample can cause signal nonuniformity, as well as severely limiting the depth into which the sample can be probed. Measuring in liquids, which is quite trivial at longer wavelengths, can be difficult because of absorption of both laser and signal. Other factors such as the expense and low throughput of the optical train, potential degradation of optics by solarization, and poor detector response, also make the technique compare less favorably to long-wavelength Raman systems than might be predicted. There are several laser options in this wavelength region: the quadrupled Nd:YAG at 266 nm is completely solid state, although this leaves only a narrow spectral window in which to measure the Raman signal; HeAg and NeCu are gas lasers operating below 250 nm, but both have lifetime and other issues that make them less than ideal; UV diode sources currently do

not have satisfactory optical specifications for Raman applications, although the technology is advancing rapidly.

Although the limitations of UV Raman for 'normal' samples are severe, where the excitation of the laser overlaps with an absorption band of the molecule, a huge enhancement of the Raman signal can occur, referred to as the resonance Raman effect [13]. These absorptions may occur in the visible region (such as hemoglobin at 550–600 nm [14]); however, they are ubiquitous in the UV, and enable sensitive, highly selective probing of the physical state of molecules [15]. This has proven especially useful in the elucidation of macromolecular structure; however, because it is important to be able tune the excitation wavelength to make full use of the power of this technique, tunable OPO or multiwavelength doubled Kr/Ar ion lasers are typically used, which are both large and costly [16]. The spectra are also currently difficult to interpret, with limited numbers of reference spectra. Although this is an important emerging technology, the cost and complexity of the equipment will likely prohibit its wide emergence outside the academic lab in the near future.

One further scheme for reducing fluorescence in Raman spectroscopy should be noted here, which is temporal filtering. The Raman signal is generated instantaneously after interaction with a photon, while fluorescence is delayed by several nanoseconds. If a very short pulse laser is used to generate the Raman signal, and an appropriately fast gated detector is used, the Raman signal can be obtained before the fluorescence signal has appeared [17]. This is a temporal corollary to the spectral window leveraged in deep UV Raman. Such systems have been demonstrated with good success on a variety of highly fluorescent samples. However, these systems are costly and complicated compared to widely available commercial systems; they also exhibit lower spectral and spatial resolution, coupled with lower tolerance of scattering samples [18]. Advances in pulsed laser technology and detection will almost certainly improve the attractiveness of these systems. However, currently the cost of the system coupled with the relatively small number of critical samples that cannot be measured using other techniques limits this technique's widespread applicability.

This highlights the importance of size and cost of the laser devices in emerging applications. Many of the measurements described in this book were shown to be possible by studies occurring as early as the 1970s (e.g., teeth [19], connective tissue [20], and ocular tissues [21]); the principle differentiating factor between these proof-of-principle studies and the potentially transformative technologies described in this book is the size and complexity of the Raman system, of which the laser makes up a large proportion. Diode lasers may be two orders of magnitude smaller than their gas laser counterparts from 20 years ago. Because many of the innovations applied to Raman instrumentation are technologies borrowed from the broader industrial market, the commoditization of laser diodes has also driven down the cost of Raman lasers. Solid-state diode pumped lasers, as well as stand-alone laser diodes can now be manufactured inexpensively with a wide range of output wavelengths

[22]. This combination of dramatic cost and size reduction has resulted in broad impact on Raman instrumentation. Raman microscopes, for example, often now have multiple excitation lasers integrated into the microscope body with little or no increase in the instrument footprint. There are a variety of handheld Raman systems that can operate for many hours on battery packs intended for handheld cameras. Instruments can be taken into the clinic for in vivo measurements, or integrated into the manufacturing process on the factory floor. This flexibility also allows facile choice of laser wavelength for specific measurements; for instance, fluorescence from the heme complex can be minimized by exciting at ∼830 nm rather than at 785 nm [23]. Laser wavelength can also be selected for resonant enhancement of specific vibrational bands, or to maximize the enhancement from different SERS substrates. The expense, availability, and cumbersome nature of the laser are no longer limiting factors in Raman spectroscopy; rather, selection of the laser is a key factor in optimizing the results for a given application.

1.4 Sample Presentation

Although the other components of the Raman spectrometer are always highlighted as the most technically important, many important innovations have been applied to optimizing and amplifying the signal by improving how the sample interfaces between the excitation laser and the spectrometer. In Fig. 1.1, this component would be represented by the arrow connecting the light source with the sample, and the sample with the dispersion element. Because different variations will be treated in detail in upcoming chapters on

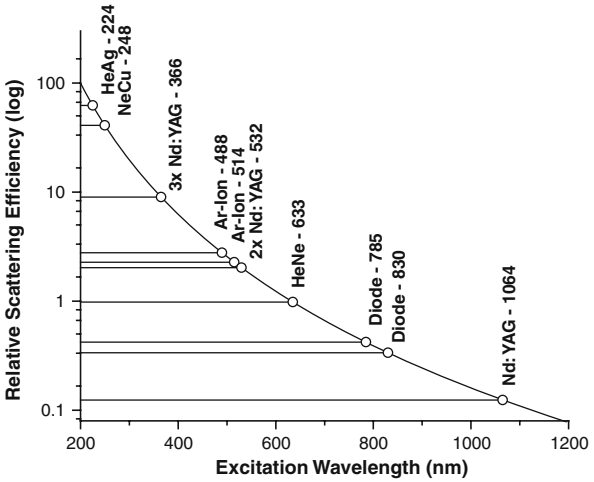

Fig. 1.5. Correlation of laser wavelength with scattering intensity

fiber probes, SORS, PhAT, etc., this section will only highlight these technologies and their relation with the other components.

As discussed previously, the relative weakness of the Raman effect has always required that the Raman spectrophotometer be as efficient as possible at generating, collecting, and detecting the scattered Raman photons. Because the entrance to the spectrograph was a slit, and the slit needed to be as narrow as possible to maintain spectral resolution, the focus of the laser on the sample also had to be as small as possible (since the focus of the laser was imaged onto the spectrometer slit). Because the Raman signal ideally scatters uniformly in every direction, the signal photon flux drops off rapidly with distance from the sample, and the collection optics needed a low f-number set as close to the sample as possible for efficient signal collection. This made the presentation of the sample to the Raman system extremely inflexible; if the sample could not be adapted to the constraints of the spectrometer, the experiment could not be performed. In addition, because both the laser and the signal photons were open beam, they needed to be steered by multiple lenses and mirrors to keep the system properly aligned. This has some advantages; for instance, maintaining the laser's Gaussian beam profile yields the smallest focal spot at the sample (important for high spatial resolution in confocal microscopy), and reflective optics may be the only way to transmit very high peak powers. However, maintaining stable geometry between the laser and spectrometer is difficult; even minor thermal variations can cause significant changes in the angle at which the signal enters the spectrometer, shifting the apparent wavelength and making accurate calibration challenging.

The introduction of fiber optics to transmit the excitation laser to the sample and the signal to the spectrometer yielded the double benefit of both improved geometric stability and sampling flexibility. Although there are a variety of specialty fiber constructions for transmitting in the mid-IR, preserving polarization state, narrow wavelength transmission window, etc., the most common type of optical fibers are comprised of a silica core surrounded by a material of higher index of refraction; this material may be either another doped silica or a polymer. The difference in the refractive index of the two materials will set the critical angle at which light will be transmitted down the length of the fiber, expressed as a numerical aperture (NA). Coupled with the diameter of the core, this will set the allowable modes that can propagate through the fiber. The effective result of increased numerical aperture is that the angle at which light can be accepted from the sample increases. Typical NA values will be between 0.12 and 0.22, although specialty fibers may have NAs as high as 0.40 or higher. The important issue is that for whatever fiber chosen, the NA is a critical parameter in the construction of the entire Raman system. The laser launch conditions, the focusing and collection optics in the fiber probe, and the spectrometer f-number must all take the fiber NA into account to maximize signal throughput.

A multitude of different probes with varying fiber orientation have been proposed [24] although most are essentially similar to the first fairly simple

design consisting of a central fiber carrying the excitation beam surrounded by a circle of collection fibers; these collection fibers could then be realigned along the slit of the spectrometer to maximize light input while still retaining optical resolution [25]. By being able to physically connect these fibers to the spectrometer, most of the beam pointing inconsistencies of the open-path systems have been eliminated. Numerous probes are commercially available for in situ monitoring based on this or similar designs, which essentially replicate the original open-beam collection strategy of a tightly focused excitation spot with only minimal depth of field and working distance from the tip of the probe. Optics is also now typically integrated into the fiber probe to filter out the laser line and any Raman signal arising from the silica in the fiber. Although glass is not a very strong Raman scatterer, because the path length through the fiber is long compared to the measurement volume, and much of the signal generated in the fiber will be internally reflected along with the laser, the resulting laser output at the sensor end of the fiber can be significantly contaminated with contributions from silica Raman bands. These are easily removed using a notch filter; however, this means that most integrated fiber probes are dedicated to a single laser wavelength.

The short working distance, high NA sampling configuration is ideal for measuring liquids or powders, where the presentation of the sample to the probe is fixed and consistent. However, it fails for solid samples that cannot be brought close to the probe, have uneven surfaces, or whose position cannot be controlled accurately. It should be noted that many of the biomedical and pharmaceutical applications in this book would fall into this category.

Subsequent increases in the size of the collection bundle have improved collection efficiency, allowing increased laser spot size, longer working distance, and increased depth of field [26]; this increased depth of field allowed contributions from subsurface scattering to be collected, which previously would have been spatially rejected. Although it was known that scattering occurred within the sample, no concerted attempt to capture this light was made, since the emphasis had always been on collecting signal very efficiently from a very tightly focused beam. These probes have been instrumental in enabling online solids measurement in pharmaceutical applications such as content uniformity of tablets [27], polymorph quantitation [28], and mixing homogeneity [29]. The natural development of this large-bundle collection strategy was to then parse the contribution of the signal at the edge of the bundle from that at the center; this led to the determination that sample depth-profiling in a scattering sample could be performed with a single bundle measurement, a technique now known as SORS (spatially offset Raman spectroscopy; see Chapter 3) [30]. All of these fiber techniques have been instrumental in enabling many of the in vivo and in situ studies described elsewhere in this text.

1.5 Spectrometers

Although there are a variety of wavelength selection methods available, the vast majority of Raman instruments utilize either dispersive or Fourier transform spectrometers. These are shown schematically in Fig. 1.6. The high throughput and spectral resolution obtainable from these instruments make them obvious choices for Raman spectroscopy; however, each has specific strengths and drawbacks which make them more suitable in specific applications.

The primary function of the dispersive monochromator is to spatially separate photons of different energy coming from the sample. The degree of separation (dispersion) is a function of groove spacing in the grating; the narrower the groove spacing, the higher the dispersion and the narrower the spectral window observed. Coupled with dispersion is the resolution of the instrument, which is how finely a narrow spectral feature can be observed. While this is also a function of the grating dispersion, the input and output apertures are limiting factors. While traditional monochromators used adjustable slits as apertures, many modern dispersive instruments no longer have true slits but use the input fiber optic diameter as the input aperture, and the pixel size on the CCD camera as the effective output aperture. This effectively fixes the limiting resolution of the instrument. Since most liquids and solids have relatively broad natural linewidths, systems designed for routine applications typically have a resolution of a few wave numbers.

Historically, the second most important function of the Raman spectrometer was to reject scattered laser radiation. Because the laser scatter from the sample can be many millions of times more intense than the signal and cannot be rejected spatially, the power of the spectrometer to efficiently and

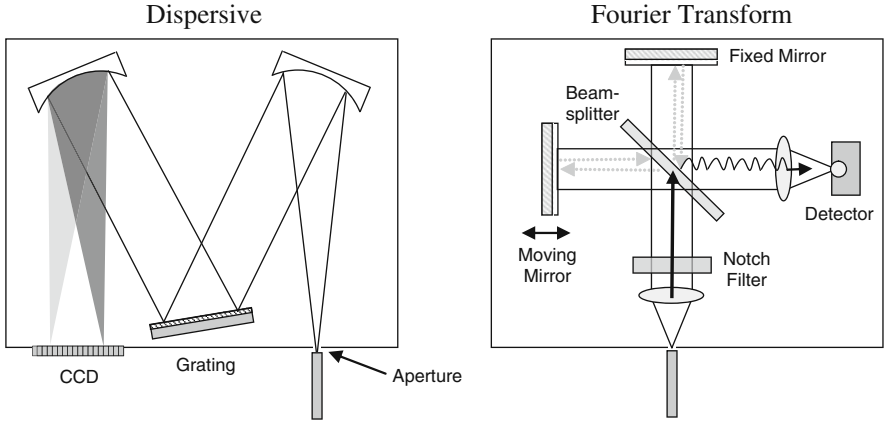

Fig. 1.6. Comparison of dispersive (Czerny-Turner) and FT (Michelson interferometer) spectrometers

completely separate this light from the signal was critical. The traditional dispersive solution to this problem was the use of a multi-stage monochromator. Large double or triple monochromators provide high spectral resolution and excellent rejection; spectra can be measured as near as $10\,\mathrm{cm}^{-1}$ from the laser line. The introduction of the holographic notch filter in the early 1990s provided a small, efficient method of selectively rejecting the laser photons before they entered the spectrometer. This enabled the used of (relatively) crude single monochromators like that shown in Fig. 1.6, and paved the way for the current generation of handheld instruments employing very minimal dispersive elements. Holographic notch filters were used because the dielectric stack filters available at the time had poor throughput; significant advances in filter manufacturing technology now produce dielectric stack long-pass edge or notch filters with >90% transmission efficiency, allowing signal to be collected as close as $50–100\,\mathrm{cm}^{-1}$ from the laser line, as well as operating well into the UV Raman range.

Although single monochromators with external laser filters are the only dispersive systems in common use, double and triple monochromators still have utility in some specialty applications [31]. Very low-frequency features arising from phonon modes such as Brillouin scattering, or rotational modes, are still best observed using this technique, since filters do not cut off efficiently enough to operate this close to the laser wavelength. For some resonance experiments where a tunable laser excitation source is used, it may also be impractical to use a fixed filter to reject the laser line, and wavelength selectibility and laser rejection become more critical than throughput.

Monochromator design has also seen significant advances, especially with respect to improved gratings. Because many of the emerging applications are associated with chemical imaging of the sample rather than single-point measurements, imaging spectrographs have been designed specifically to generate a flat-field output at the detector plane. Traditional gratings generate significant optical aberration including curvature of the input image and nonplanar focus at the detector. Aberration corrected holographic transmission gratings or nonplanar reflection gratings have largely eliminated these effects (imaging will be discussed at greater length at the end of this chapter). Reflective diffraction gratings have also improved to the point that they are approaching the efficiency of transmissive holographic gratings, which may be as high as 90% throughput at peak efficiency [32]. Significant flexibility in the footprint of the resulting spectrometer is possible through careful grating selection. A wide variety of miniature, fully integrated spectrometers are now commercially available as stand-alone units or as components integrated into systems by OEMs. Echelle spectrometers are also available, which parse the different regions of the spectrum such that they can be measured simultaneously in a stack on the detector, allowing rapid measurement of spectra at high spectral dispersion and wide wavelength spectrum in the coverage.

Fourier transform spectrometers measure the entire spectrum simultaneously in the form of an interferogram, rather than dispersing the spectrum

into separate wavelengths [33, 34]. As shown in Fig. 1.6, the interferogram is generated by changing the path length of the signal by varying the position of the moving mirror. This position is monitored very accurately using the interference fringes from the HeNe reference laser. The detected signal is then transformed into frequency, and a spectrum generated that is essentially equivalent to the dispersive response. The limiting resolution of the FT instrument is the distance that the moving mirror travels; even a fairly modest mirror movement of a few centimeters can give tenths of a wave number resolution. Because the full spectrum is contained in the interferogram, a wide spectral window can be obtained at high resolution. The spectrum also has inherent wavelength accuracy, since the spectrum is internally calibrated by the reference laser. Multivariate models can be more reliably applied to FT data, and the data between instruments will be much more consistent. More importantly, FT-Raman can work more efficiently using a long-wavelength 1064 nm excitation laser, which effectively eliminates fluorescence. This can be important advantage when working with biological samples, although typical FT-Raman laser powers can be well above the damage threshold for many samples [35].

Unfortunately, Fourier Transform instrumentation has been overshadowed to some extent by the advances made in dispersive technology. This is in no small part due to the ability of dispersive manufacturers to leverage advances in the rapidly evolving optoelectronics market, while FT-Raman depends heavily on already mature FT-IR platforms. Although better detectors and laser rejection filters have improved the noise characteristics of the system, the fundamental throughput advantage that made FT a universally adopted approach in the mid-IR was never sufficiently compelling to engender a similar dominance in Raman, principally because of the availability of low-noise CCD detectors in the visible. The almost total suppression of background fluorescence is a great advantage; however, the recent introduction of low-noise multichannel detectors for the near-IR region (950–1650 nm) has enabled the development of dispersive systems operating with higher efficiency with 1064 nm excitation. In spite of FT-Raman's intrinsic advantages, it is unclear how well it will compete with the small, cheaper, more sensitive, flexibly configured, and all-solid-state dispersive instruments as an enabling technology driving the emerging applications described in this book.

Another wavelength selection mechanism of note is electronically tunable bandpass filter. There are two commercially available technologies, the acousto-optic tunable filter (AOTF) and the liquid crystal tunable filter (LCTF). Each uses different underlying mechanisms. The AOTF uses an acoustic wave generated in an optically clear crystal to change the angle of the input beam based on wavelength (essentially a variable transmission grating) [36], while the LCTF uses oriented liquid crystals to selectively retard the beam, causing destructive interference for all wavelengths except the desired passband (referred to as a Lyot filter) [37]. There are a variety of other practical differences which impact the implementation of each technology; for

instance, the speed of switching is much greater with the AOTF, although there are significant input beam geometry restrictions; the LCTF has lower throughput, but has few spatial input restrictions. LCTF units typically have larger apertures with more uniform wavelength response across the aperture area which have made them the unit of choice for imaging applications [38], although AOTF units have been used for imaging as well [39]. Despite these differences, the ability of the user to either scan between selected wavelengths or randomly access individual wavelengths is similar, so that they can be grouped together for the purposes of this discussion.

There are several advantages to a tunable filter system. First, it is unnecessary to have a multichannel detector (for single-point measurements), since only one wavelength is being selected at a time. The size of the detector is also much more flexible, since spectral resolution of the system is not a function of the detector and input aperture as it is in a classical monochromotor, but rather limited only by the functional characteristics of the filter. Second, since focusing and dispersive elements are minimized the spectrometer could be made very small. Third, the entire spectrum does not need to be obtained; the random access nature of the filter allows only the spectral features required for a measurement to be made. This can be a significant advantage for routine measurements.

Small, robust instruments have been produced based on this technology [40, 41], and applications in biomedical, biothreat detection, and pharmaceutical analysis have been shown, especially for imaging [42]. However, there are various disadvantages that have limited their widespread use. The effective throughput of the tunable filters is not as high as for grating-based systems; each is sensitive to input polarization, which is not always easy to control. Because the Raman effect is comparatively weak, it is crucial that every component has the highest throughput possible. The spectral resolution of either of these systems is not as good as that of a traditional system. Hence tunable filters have had better success in applications in near-IR and fluorescence spectrometers, where the measurement is typically less signal-limited, and where the spectral features are broad. New generations of materials will no doubt exhibit improved performance, as increases in throughput [43] and application to deep UV wavelengths [44] have been presented. Further advances and decreased cost will be necessary before tunable filters will likely compete favorably with competing technologies for general use.

1.6 Detectors

The charge-coupled device was first used in Raman spectroscopic applications in the late 1980s [45, 46], followed rapidly by the introduction of holographic notch filters [47]. This combination, coupled with the visibility of FT-Raman instruments introduced at around the same time, helped drive the growth of Raman outside the academic lab. Although the throughput advantage of

measuring the entire spectrum simultaneously had been clearly understood, the early multichannel detectors (typically a photodiode array coupled to an image intensifier) exhibited poor signal-to-noise compared to photomultiplier tubes (PMT). The CCD was able to combine the low-light sensitivity of the PMT with the durability and multiplex advantage of the PDA. As with diode lasers, the spectroscopy community has benefited from detector technology developments made in other fields with low-light applications – specifically astronomy, where the CCD was first applied for stellar imaging, and the military – as well as general advances in silicon device manufacturing.

The operation of the CCD has been reviewed at length and in great detail elsewhere [48, 49], and only the basic operation will be discussed here to enable discussion of more recent advances. Each element (or pixel) of the detector array is a photoactive capacitor that will collect and hold charge based on the number of photons that strike it. Although a wide variety of chip architectures are possible, the general scheme shown in Fig. 1.7 is the typical CCD readout method. CCDs operate by shifting the charge accumulated in each pixel simultaneously to the adjacent pixel elements until they reach the 'bottom' shift register, where they are read out individually. The histogram representation of a spectrum in Fig. 1.8 highlights the function of the CCD in generating intensity data; each pixel is a specific resolution element at a given wavelength, and a variable quantity of photons. A number of key performance parameters can be inferred from this form of operation, such as how much noise is associated with each detector element, how much noise is generated during shifting/reading, the efficiency of the array in detecting individual photons, and how fast the detector can be read out.

Noise associated with the detector elements themselves (dark or thermal noise) can be reduced by decreasing the temperature, typically from −20 to −70°C; although cooling to liquid nitrogen temperatures essentially eliminates dark noise, it is typically impractical for applications outside of the laboratory. The theoretical value for relative signal-to-noise reduction is a factor of 2 improvement for every 6.3°C reduction in temperature, although this can be

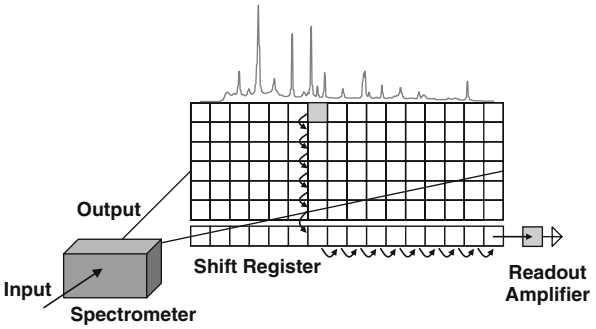

Fig. 1.7. Schematic of CCD readout

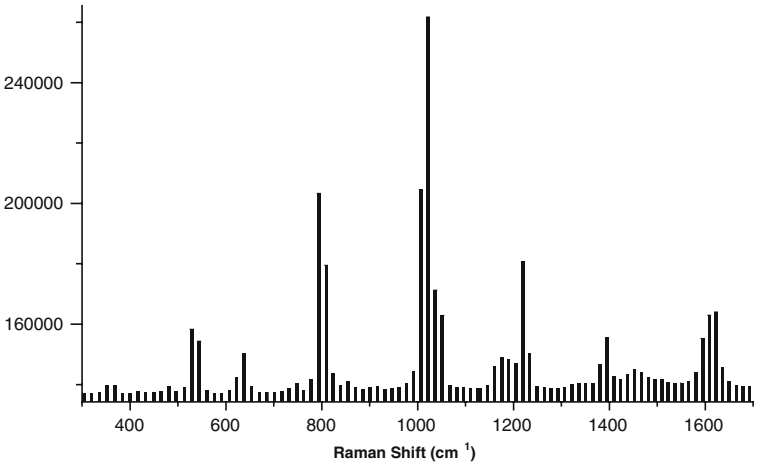

Fig. 1.8. Spectral output of CCD represented as histogram

somewhat variable depending on the quality of the CCD. The absolute S/N level, on the other hand, is very dependent on chip material quality and construction. In practice, the target temperature for many spectroscopic CCDs is around $-40°$C, although modern multistage Peltier cooling systems can now routinely cool CCDs down to $-80°$C. The other principal noise source is the noise induced in measuring the pixel charge, referred to as read noise. Although many CCDs read each pixel destructively (that is, the current from the pixel can only be read once), it is possible to implement measuring techniques that read the charge multiple times, minimizing the read noise contribution. Speed and duty cycle can be improved by adding parallel registers to the chip; although since the efficiency of the detector is a function of the photoactive area of the chip, addition of non-active areas will reduce the number of detected photons. Micro-lenses have been used to direct light to the active regions of the chip to improve efficiency for these kinds of devices.

There are a wide variety of variables on this basic theme that have been used to enhance the operation of the CCD; since many techniques now exist to minimize noise sources, most of the important current contributions are focused on maximizing the signal through higher quantum efficiency of the detector, or amplifying the signal while keeping the read noise constant. Back-thinning is one commonly used technique where the light enters what would normally be the back side of the chip. Illuminating from the back increases the effective photoactive area of the pixels since much of the front surface of the chip is obscured by the transfer electronics. The efficiency of a detector with similar material construction can be improved from 40% for a front-illuminated chip to 80% for a back-thinned model. The detector can also be made from specially doped silicon (referred to as deep depleted) that enhances the sensitivity toward the red end of the spectrum. Although chip architecture

limitations make a deep-depleted back-thinned CCD more susceptible to dark noise (requiring extra cooling), the increase in sensitivity for 785 nm excitation systems can be as much as a factor of 5–8 over a standard front-illumination system.

Further enhancement of the signal can be obtained using an EMCCD (electron multiplying CCD) [50]. The operation of the EMCCD is analogous to an avalanche photodiode in that the signal from each pixel is amplified by multiple avalanche gain events. The construction of the EMCCD is the same as a 'regular' CCD (with options for similar back-thinned deep-depleted configurations), but with an added avalanche gain register between the shift register and the amplifier. This gain register may be comprised of several hundred elements, each at a potential of ∼50 V which has the effect of amplifying the signal from each pixel proportionate to the number of photoelectrons present. Because the gain in the signal before reading the pixel electron is large, while the number of counts due to read noise is constant (and small), the contribution of read noise to the signal becomes negligible. Naturally, dark electrons are also amplified, so EMCCDs require significant cooling – −100°C is not uncommon – to make full use of their gain advantage. The advantages of the high gain are most fully realized for very low light level measurements, and single photon counting measurements can be performed using this detector. However, the principal advantage of the EM approach is that the CCD can be read very rapidly, typically on the order of milliseconds; other techniques to maximize gain and minimize read noise tend to slow down the operation of the chip significantly. This advantage is important for high-duty cycle applications such as imaging [51].

For very high speed applications, where gating on the nanosecond timescale is important [52, 53], intensified CCDs (ICCD) are also available. The ICCD is a CCD coupled to an image intensifier; this is a similar scheme to that used in the days before CCDs, when photodiode detectors were coupled with image intensifiers to overcome their noise limitations. The image intensifier is essentially a multichannel photomultiplier tube. The Raman photon hits the photocathode, and the resulting photoelectrons are accelerated through a micro-channel plate (MCP). The MCP consists of multiple fine tubes, each at high potential. The electrons passing through the tube cause an electron cascade, just like a PMT; the resulting electrons impinge on a phosphor screen and are converted back into photons for the CCD to detect. The resulting system is complicated, expensive, and has a limited lifetime. However, the image intensifier can be gated very rapidly; by changing the potential on the photocathode with respect to the MCP, the image intensifier becomes a shutter, blocking all light from reaching the phosphor screen. While the CCD itself is still limited by how fast the data can be polled off the chip to the readout amplifier, the very fast shutter allows discrimination of very fast events. In addition, the selection of appropriate photocathode material allows detection of deep UV photons using a silicon detector.

A similar approach has recently been introduced that uses an InGaAs detector as a photocathode, but with electron bombardment as the gain mechanism [54]. The detector is specifically designed to have high sensitivity/quantum efficiency in the NIR between 950 and 1650 nm where FT-Raman instruments classically operate, but with some gating capacity since a cathode intensifier is used. Although the Raman signal will be very weak in this region, amplification of the signal coupled with the multiplex advantage and signal gating may prove a useful addition for sensitive, highly fluorescent materials such as biological samples.

It should also be noted that although a great majority of Raman spectrometers are equipped with multichannel detectors, the single channel detector still has a variety of applications which resist replacement by the now common CCD. Various applications have been discussed above for which multichannel detectors have no advantage, such as AOTF spectrometers. Where very fast time gating is required and simultaneous wavelength measurement does not offer an advantage (many CARS imaging applications, for example), PMTs are a viable option, offering high sensitivity, single photon detection, and relatively low cost (in spite of their sensitivity to high light loads and the need for high-voltage power supplies). Avalanche photodiodes, when operated under the appropriate conditions, may also offer many of the same speed and gain advantages of the PMT, although typically with a much smaller active area [55].

1.7 Imaging and Microscopy Systems

The system components described above can be combined into a wide array of sampling configurations suitable for measurements as diverse as characterization of the effluent emitted from oceanic vents, to identification of explosives at a standoff of tens of meters, to determining the provenance of historical works of art. One of the areas of greatest Raman activity is in microscopy and microscopic imaging; this will be described briefly here as an example of how the various components are integrated into a complete system.

The schematic presentations in Fig. 1.9 represent three common configurations for Raman microscope signal collection [56] with dispersion elements implied but not shown for clarity. One of the principle advantages of Raman spectroscopy is the ability to make measurements on regions as small as the laser focus. Although the laser may be focused to a diffraction limited spot, the system will likely accept signal from other areas as well; at the very least on-axis light that is above or below the nominal focal position can be accepted, but depending on the system configuration and the degree of diffuse scattering from the sample, variety of off-axis light may be accepted as well. The slit (or fiber probe) will act as a first stage of spatial rejection; insertion of a pinhole in the optical train will further reject out-of-focus signal, as well as spurious light from other sources. As the input to the spectrometer is a

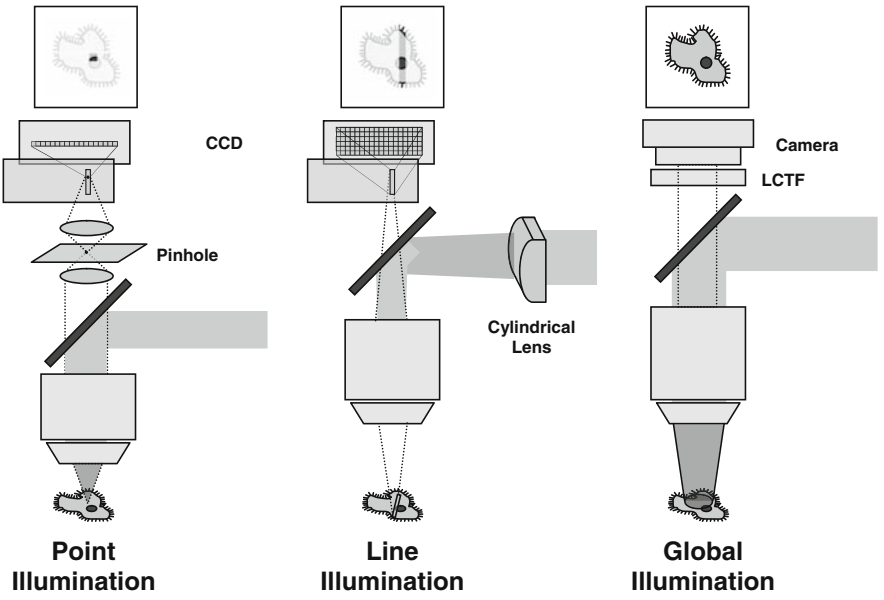

Fig. 1.9. Different microscope illumination configurations

single spot, the spectral image dispersed onto the CCD is also a spot; there is no spatial information, and most of the CCD area is left unused. An image of the sample, if such a thing is desired, can be obtained by rastering the sample under the laser focus, moving from point to point on the sample until the desired area has been mapped out. Much has been made of the limitations and potential pitfalls of this technique [57], although it has a long history of being used to good effect in a wide variety of applications.

While the point-by-point mapping strategy will certainly work, the signal throughput is very low – and lower than necessary, since only a small fraction of the CCD is used during any spectral acquisition. By focusing the laser to a line rather than a spot, the resulting image can be focused on the slit, and subsequently imaged on the CCD. The x-direction on the CCD is still frequency, while the y-axis is spatial variation in the sample. Alternately this configuration could employ various geometries of laser focus at the sample; since the fibers at the sample can be arranged in any configuration, with subsequent fiber rearrangement into a line at the slit, any configuration at the sample could be used as long as the fiber position can be decoded after collection of the image spectrum. This highlights the necessity for an aberration corrected imaging spectrometer/grating. If the image of the slit is distorted, the spectral features and the image can be convolved with one another, and the resulting image will be impossible to resolve. The throughput of the spectrometer is now greater than the increased fill factor of the CCD. Unfortunately the spatial rejection is also compromised somewhat, since a pinhole spatial filter

cannot be used, although this effect is generally minimal. As with the confocal imaging, the sample must be rastered in order to build up spectral data for the areas of interest.

The third configuration illuminates the sample globally, using an LCTF as the wavelength discrimination mechanism. A snapshot of the entire sample is obtained at a given wavelength; the spectrum is built up one wavelength at a time, rather than moving the sample and obtaining one position at a time. The throughput on such a system could be very high, especially if only a few wavelengths are required for spectral identification purposes. However, as the illumination pattern increases, the spatial rejection decreases. With removal of the slit, there is no spatial rejection mechanism at all. For reasonable images in a system such as this, either the sample needs to be very thin, or completely opaque. Any subsurface contributions or scattering from photon migration within the sample will contribute randomly to the collected signal, smearing the resulting image. In addition, thermal problems are more likely with wide-field illumination. Although the flux may be higher in a point system (consider 50 mW in a 1 μm diameter spot vs. 2 W in a 2 mm spot) heat transport becomes an issue. While a spot (or a line) can dissipate heat into the sample in three dimensions, the globally illuminated sample can only dissipate heat in one dimension into the depth of the sample. This makes it much more difficult for the sample to remove the excess heat [58].

1.8 Conclusion

Raman spectroscopy has suffered as the ugly, expensive, and finicky stepsister of mid-IR spectroscopy for many years. The principal factor holding it back from broader acceptance was the difficulty and expense of performing the experiments. It is instructive to note that almost every technological breakthrough was borrowed from another scientific discipline: the laser, gratings, and spectrometers from physics, Fourier transform and the CCD detector from the astronomers, and fiber optics from telecommunications (holographic notch filters may be a notable exception). But now that Raman instrumentation has proved its ability to sustain multiple practical applications, the emerging applications described in this book will now no doubt drive the development of new technologies and new Raman capabilities currently impossible to imagine.

References

1. C.V. Raman, K.S. Krishnan, Nature **121**, 501 (1928)
2. *Handbook of Raman Spectroscopy*, ed. by I. Lewis, H.G.M. Edwards (Dekker, New York, 2001)
3. M. Pelletier, *Analytical Applications of Raman Spectroscopy* (Blackwell, Oxford, 1999)

4. D.S. Hausman, R.T. Cambron, A. Sakr, Int. J. Pharm. **298**, 80 (2005)
5. G. Fevotte, Chem. Eng. Res. Des. **85**, 906 (2007)
6. C.J. Strachan, T. Rades, K.C. Gordon, J Rantanen, J. Pharm. Pharmacol. **59**, 179 (2007)
7. S.W.E. Van de Poll, D.J.M. Delsingl, J.W. Jukema, H.M.G. Princen, L.M. Havekes, G.J. Puppels, A. Van der Laarse, Appl. Spec. Atheroscler. **164**, 65 (2002)
8. R.M. Jarvis, E.W. Blanch, A.P. Alexander, J. Screen, R. Goodacre, Analyst **132**, 1053 (2007)
9. P.R. Carey, J. Dong, Biochemistry **43**, 8885 (2004)
10. M.J. Pelletier, Appl. Spec. **57**, 20A (2003)
11. S.P.S. Porto, D.L. Wood, J. Opt. Soc. Am. **52**, 251 (1962)
12. A. Jirasek, H.G. Schulze, C. Hughesman, A.L. Creagh, C.A. Haynes, M.W. Blades, R.F.B. Turner, J. Raman Spectrosc. **37**, 1368 (2006)
13. E.V. Efremov, F. Ariese, C. Gooijer, Anal. Chim. Acta. **606**, 119 (2008)
14. T.C. Strekas, T.G. Spiro, J. Raman. Spectrosc. **1**, 387 (1973)
15. A.V. Mikhonin, S.A. Asher, J. Am. Chem. Soc. **128**, 13879 (2006)
16. A. Willitsford, C.T. Chadwick, H. Hallen, C.R. Philbrick, Proc. SPIE **6950**(69500A) (2008)
17. P.P. Yaney, J. Raman Spectrosc. **5**, 219 (1976)
18. N. Everall, T. Hahn, P. Matousek, A.W. Parker, M. Towrie, Appl. Spectrosc. **55**, 1701 (2001)
19. W.P. Rippon, J.L. Koenig, A. Walton, Agri. Food Chem. **19**, 692 (1971)
20. B.G. Freshour, J.L. Koenig, Biopolymers **14**, 379 (1975)
21. R. Farrell, R. McCauley, J. Opt. Soc. Am. **66**, 342 (1976)
22. B. Mroziewicz, Opto-Electron. Rev., **16**, 347 (2008)
23. J.F. Brennan, Y. Wang, R.R. Dasari, M.S. Feld, Appl. Spectrosc. **51**, 201 (1997)
24. P.J. Hendra, G. Ellis, J. Raman Spectrosc., **19**, 413 (1988)
25. S.D. Schwab, R.L. McCreery, Anal. Chem. **56**, 2199 (1984)
26. K.F. Schrum, Seung Hyeon Ko, D. Ben-Amotz, Appl. Spectrosc. **50**, 1150 (1996)
27. H. Wikström, S. Romero-Torres, S. Wongweragiat, J.A. Stuart Williams, E.R. Grant, L.S. Taylor, Appl. Spectrosc. **60**, 672 (2006)
28. J. Rantanen, H. Wikström, F.E. Rhea, L.S. Taylor, Appl. Spectrosc. **59**, 942 (2005)
29. F. LaPlant, X. Zhang, Am. Pharm. Rev. **8**, 88 (2005)
30. P. Matousek, I.P. Clark, E.R.C. Draper, M.D. Morris, A.E. Goodship, N. Everall, M. Towrie, W.F. Finney, A.W. Parker, Appl. Spectrosc. **59**, 393 (2005)
31. V. Deckert, C. Fickert, D. Gernet, P. Vogt, T. Michelis, W. Kiefer, Appl. Spec. **49**, 149 (1995)
32. S.C. Barden, J.A. Arns, W.S. Colburn, J.B. Williams, SPIE Conf. **4485** (2001)
33. D.B. Chase, J. Am. Chem. Soc. **108**, 7485 (1986)
34. C.J.H. Brenan, I.W. Hunter, Appl. Spec. **49**, 1067 (1995)
35. N.A. Marigheto, E.K. Kemsley, J. Potter, P.S. Belton, R.H. Wilson, Spectrochim. Acta A **52**, 1571 (1996)
36. L. Bei, G.I. Dennis, H.M. Miller, T.W. Spaine, J.W. Carnahan, Prog. Quant. Electron. **28**, 67 (2004)
37. P.J. Miller, Metrologia **28**, 145 (1991)
38. H.R. Morris, C.C. Hoyt, P.J. Treado, Appl. Spectrosc. **48**, 857 (1994)

39. S.R. Goldstein, L.H. Kidder, T.M. Herne, I.W. Levin, E.N. Lewis, J. Microsc. **184**, 35 (1996)
40. N. Gupta, R. Dahmani, Spectrochim. Acta A **56**, 1453 (2000)
41. K. Chen, M.E. Martin, T. Vo-Dinh, Proc. SPIE, **5993**(599307) (2005)
42. F. Yan, T. Vo-Dinh, Sens. Actuators B **121**, 66 (2007)
43. X. Wang, T.C. Voigt, P.J. Bos, M.P. Nelson, P.J. Treado, Prog. Biomed. Opt. Imag. – Proc. SPIE **6378**(637808) (2006)
44. N.S. Prasad, Int. J. High Speed Electron. Syst. **17**, 857 (2007)
45. C.A. Murray, S.B. Dierker, J.D. Legrange, N.E. Schlotter, Chem. Phys. Lett. **137**, 453 (1987)
46. J.M. Williamson, R.J. Bowling, R.L. McCreery, Appl. Spec. **43**, 372 (1989)
47. M. Carrabba, K. Spencer, C. Rich, D. Rauh, Appl. Spec. **44**, 1558 (1990)
48. J.M. Harnly, R.E. Fields, Appl. Spectrosc. **51**, 334A (1997)
49. J. Janesick, Scientific charge-coupled devices. SPIE Press **PM83** (2001)
50. A. O'Grady, Prog.Biomed. Opt. Imag. – Proc. SPIE, **6093**(60930S) (2006)
51. T. Dieing, O. Hollricher, Vib. Spectrosc. **48**, 22 (2008)
52. J.C. Carter, J. Scaffidi, S. Burnett, B. Vasser, S.K. Sharma, S.M. Angel, Spectrochim. Actat A **61**, 2288 (2005)
53. E.V. Efremov, J.B. Buijs, C. Gooijer, F. Ariese, Appl. Spec. **61**, 571 (2007)
54. M.A. Greenwood, Photonics Spectra **41**, 33 (2007)
55. D. Renker, Nucl. Instrum. Methods Phys. Res., Sect. A **567**, 48 (2006)
56. S. Schlucker, M.D. Schaeberle, S.W. Huffman, I.W. Levin, Anal. Chem. **75**, 4312 (2003)
57. N. Everall, Appl. Spec. **62**, 591 (2008)
58. D. Zhang, J.D. Hanna, Y. Jiang, D. Ben-Amotz, Appl. Spec. **55**, 61 (2001)

2

Fiber-Optic Raman Probes for Biomedical and Pharmaceutical Applications

Hidetoshi Sato, Hideyuki Shinzawa, and Yuichi Komachi

Abstract This chapter reviews the development of optical fiber probe Raman systems and their applications in life science and pharmaceutical studies. Especially, it is focused on miniaturized Raman probes which open new era in the spectroscopy of the life forms. The chapter also introduces the important optical properties of conventional optical fibers to use for Raman probes, as well as new types of optical fiber and devices, such as hollow optical fibers and photonic crystal fibers.

2.1 Introduction

The recent evolution of Raman spectroscopy makes its practical clinical application more realistic. Especially important has been development of high-performance devices and spectral analysis methods, especially chemometrics. Many researchers have reported that they have succeeded in identifying strains and species of bacteria, in monitoring cell cycles and proliferation, and the diagnosis of cancerous tissues using in vitro Raman spectroscopy and chemometrics analysis [1–13]. Drug-resistant strains of bacteria have only small differences in their genes compared to wild types, but Raman spectroscopy has been able to detect the differences [1, 5, 7, 8]. The remarkable results of research in this field encourages us to believe that it may be possible to use Raman spectroscopy to diagnose cancers and other diseases that are induced by small gene alterations. If it is possible to obtain high-quality Raman spectra of the diseased tissue in vivo, it may be possible to diagnose the disease in internal organs. A narrow fiber-optic Raman probe is an attractive tool for this purpose [14–41]. It allows us to reach a lesion in a human subject and obtain information about the diseased tissues directly.

By inserting the Raman probe into the channel of various endoscopes, we can access the inside of the stomach, the large and small intestines, the bronchus, and portions of the pancreatic and bile ducts. If it is used with a laparoscope, the accessible areas expand to the liver and the outer walls of the digestive organs. If the probe is narrow enough to insert in hypodermic

needle, it can be inserted into other body parts. If the probe has a large enough focal depth to obtain information through a blood vessel wall, it may be able to reach inside organs located deep within the body, such as the pancreas and brain. At present, many of the techniques discussed above are still only proposals, but they are expected to be realized in the near future.

There is an increasing need for minimally invasive and highly accurate techniques for diagnosis confirmation. Noninvasive cancer screening technologies, such as positron-emission tomography (PET), X-ray computed tomography (CT), and magnetic resonance imaging (MRI) have become more and more sensitive and are capable of detecting small cancerous lesions, and so are increasingly commonly used in clinics. These techniques can detect "suspicious" tissues. It may be possible to reach a diagnosis from the obtained image of advanced and large cancerous tissues, but it is difficult for small suspicious tissues. Generally, for patients with positive results, a doctor performs a biopsy to confirm the diagnosis and decide on a treatment plan. This biopsy includes resections of the suspicious tissue, and the process becomes more invasive if the tissue is located in a body part that is inaccessible with an endoscope. Hence, an optical biopsy using a miniaturized Raman probe provide feasible alternative or further support for confirming a diagnosis. This is the case, not only for cancer but also for other diseases such as atherosclerosis.

2.2 Optical Properties of Fibers and Devices

There are generally two types of fiber-optic Raman probe. One is a probe with a confocal type head, as shown in Fig. 2.1A. Although it is rather large in size, various types of optical filter can be used because there is enough room to arrange filters and lenses for effectively removing the Raman scatter and fluorescence generated in the optical fiber. The other type is a miniaturized fiber-optic probe, in which the filters and lenses are directly mounted on the end of the optical fiber, as shown in Fig. 2.1B. In order to reduce the size, the head structure must be quite simple. The following section describes the properties of optical fibers and other devices to construct the latter type of fiber-optic Raman probe.

2.2.1 Glass and Fused Silica Optical Fibers

Since there are many different optical fibers that are commercially available, it is impossible to cover all of them in this chapter. Therefore, this section will describe the optical properties of glass and fused silica fibers that can be used as for miniaturized fiber-optic Raman probes. A major difficulty in developing a sensitive fiber-optic Raman probe is to suppress the fiber spectral background (FSB) generated in the optical fibers themselves [14–30]. This background is orders of magnitude larger than the Raman signal from the tissues to be measured. The FSB consists of Raman scattered light and fluorescence generated

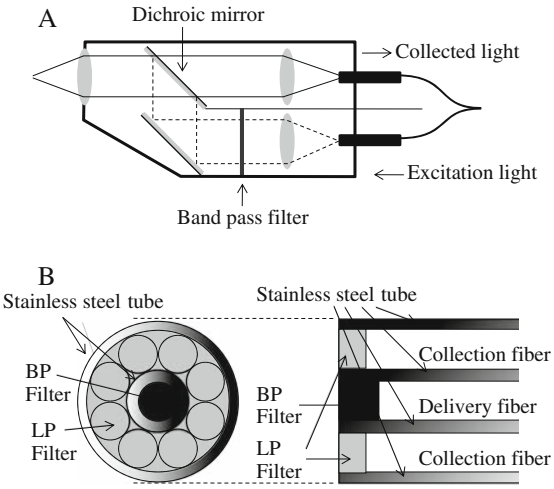

Fig. 2.1. Schematic representations of the confocal type Raman probe (**A**) and the miniaturized Raman probe (**B**)

by the core material in the fiber. The Raman scattered light and fluorescence generated by the glass optics, such as the lens, filter, and mirror, are usually negligible, but they are high in the fiber, because the incident excitation light and generated FSB light are not able to get out of the fiber except at either end.

Table 2.1 shows the efficiencies for the generation of FSB (R_b) for various optical fibers, together with information about their manufacturer, product number, core, cladding and outer diameters, numerical aperture (NA), and material [28]. Data for some other optical fibers have been added to the table [28].

The value of R_b in each optical fiber is defined as follows:

$$R_\mathrm{b} = I_\mathrm{f} I_\mathrm{l}^{-1} \tag{2.1}$$

where I_f is the peak intensity of the strongest silica Raman band (near $430\,\mathrm{cm}^{-1}$) in the FSB spectra and I_l is the intensity of the laser power transmitted by the fiber. I_f and I_l were measured with the same spectrometer under the same conditions, except for the ND filters, which were used to reduce the laser power for measurement by the Raman spectrometer. The data were obtained at an excitation wavelength of 720 nm. No major difference was observed in using a wavelength of 785 nm.

The table suggests that there is considerable variation in R_b. GeO_2-doped fused silica fibers generally have a large NA and a high R_b. R_b generally increases with an increase in the diameter of the fiber core and the NA of the fiber. The FSB intensities for various optical fibers earlier reported by Ma and Li [15] are inconsistent with our results, as these authors found that FSB

Table 2.1. R_b value and specifications of various optical fibers (modified from [8], with permission)

Manufacturer	Product number	$R_b/10^{-8}$	NA	Core diameter (µm)	Clad diameter (µm)	Total diameter (µm)	Notes (material)
Newport	F-SE	0.25	0.11	6	125	245	Single mode
	F-MLD	1.83	0.29	100	140	250	Graded index
	F-MTC	1.66	0.22	365	400	730	Pure silica
	F-MBB	2.97	0.37	200	230	500	Polymer clad
	F-MCB-T	1.53	0.22	100	110	140	Polymer clad
Sumitomo	SF-112	1.01	0.20	114	125	155	Pure silica
	SF-180	1.82	0.20	182	200	240	Pure silica
	F-MS03	1.09	0.20	300	330	650	Pure silica
	F-MKH03	3.93	0.35	300	330	650	GeO_2 doped
Mitsubishi	ST47AS	0.55	0.19	47	67	117	Pure silica
	ST-300UV	0.89	0.19	300	320	330	Pure silica
	STFH200A-S	0.73	0.19	200	225	300	Pure silica
	STFH230D	0.93	0.22	230	250	300	Pure silica
	E-190	5.35	0.32	190	200	217	GeO_2 doped
Polymicro Technology	FIP050070085	1.13	0.22	50	70	85	Ultra-low OH
	FIP100110125	1.01	0.22	100	140	170	Ultra-low OH
	FIP200220240	1.37	0.22	200	220	240	Ultra-low OH
	FIP400440480	1.23	0.22	400	440	480	Ultra-low OH

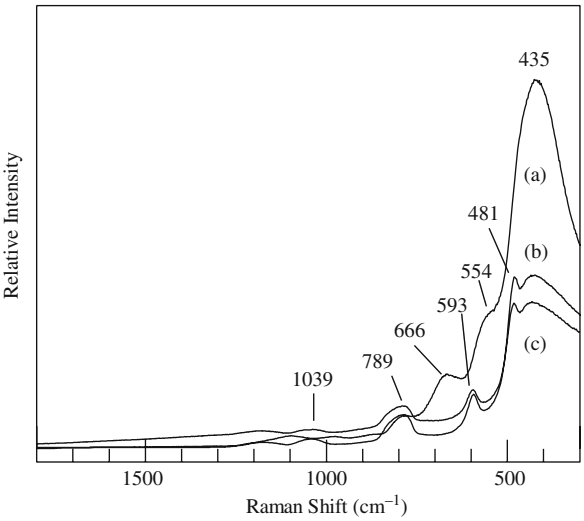

Fig. 2.2. FSB spectra of GeO_2-doped fused silica (**a**), low-OH fused silica **(b)**, and normal fused silica **(c)** fibers measured with 785 nm excitation (modified from [8])

increased with a decrease in core diameter. The FSB intensity was estimated in a different way, as they measured the laser transmission power and Raman background intensity separately.

Figure 2.2 depicts the typical FSB spectra for GeO_2-doped fused silica (E-190, Mitsubishi; a), low-OH fused silica (FIP200220240, Polymicro Technology; b), and normal fused silica (SF-180, Sumitomo; c) fibers. The bands at 1039, 789, 593, 481, and 435 cm^{-1} are assignable to silica. The FSB value of the pure silica fiber was slightly higher than that of the low-OH silica fiber at low wave numbers, but not above 500 cm^{-1} [28]. Since it is difficult to remove the FSB where it overlaps with sample Raman spectrum, the use of pure silica fiber is recommended. It is well known that pure silica fiber has a weak absorption band above 700 nm due to the OH group in the fiber. The maximum loss is only about 1% per meter, and is negligible for laboratory or clinical use, where fiber lengths rarely exceed designing a few meters. The user should be aware that there is a strong wavelength dependence to FSB, and the values of Table 2.1 may not be useful at much lower or higher excitation wavelengths. Therefore, researchers who want to fabricate a miniaturized Raman probe must take into account the excitation wavelength to be used.

Polymer clad fibers, plastic fibers, and multicomponent glass fibers are inappropriate Raman probes because these materials generate intense Raman scattered light and fluorescence. Although the core material is fused silica for some of these fibers, the light penetrates into the cladding material and the generated FSB is propagated in the fiber. The FSB spectra of graded-index fibers closely resemble that of GeO_2-doped fused silica fibers. Single-mode

fibers have a small R_b value and a small NA. They may be used as the delivery fiber for the excitation light. However, the core diameter of a single mode fiber is too small for efficient collection of Raman scattered light.

2.2.2 Other Optical Fibers

A hollow optical fiber (HOF) is a totally different type of optical fiber [42–46]. Figure 2.3A shows the structure of an HOF. An HOF is made of a glass tube with an inner coating of silver and a dielectric film, which enhances reflectivity. Matsuura et al. reported that the root mean square surface roughness of the silver film was 12 nm in their fabricated HOF [44].

The HOF was originally developed for delivery of high-power laser pulses and for optical pulse compression. In conventional silica glass fibers, the nonlinearity of the glass material causes a self-focusing effect at high laser power, resulting in severe damage to the fiber. The HOF propagates the laser light inside of an air core, which prevents the damage [45]. Since the light is transferred in the HOF by reflection, the transmission efficiency of the HOF depends on the reflectivity of the metal at the wavelength of the propagating light. A silver-coated HOF can operate at wavelengths from the mid-visible to the infrared and an aluminum-coated one operated between the deep ultraviolet through the visible [42, 44].

The HOF generates remarkably little FSB. Figure 2.3B depicts the FSB spectrum of a miniaturized Raman probe using an HOF. The spectrum is very flat and there are no silica bands, of course. The band at 1560 cm^{-1}, with the small side bands, is the stretching mode and associated rotational modes of O_2. It can be easily removed by replacing the air with argon or nitrogen. Raman band of nitrogen is near 2330 cm^{-1}, where few biologicals or pharmaceuticals have vibrations. The increase in the baseline toward low wave number is probably fluorescence emitted by the polyimide outer protective coat of the HOF and is comparable in intensity to the O_2 Raman band. This Raman probe has a sapphire ball lens at its distal end, from which small bands at 746, 637, 410, and 370 cm^{-1} are generated. It is easy to remove

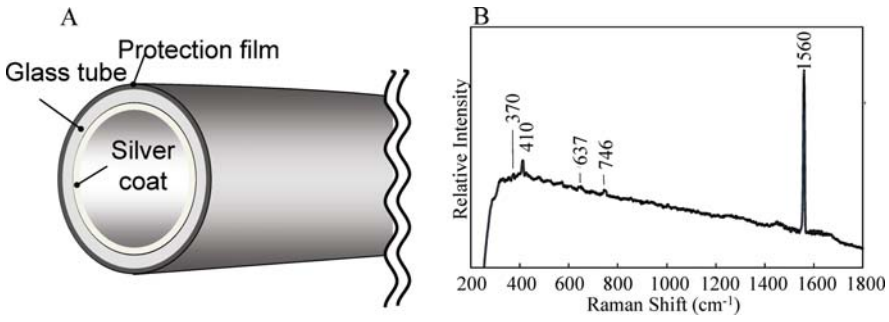

Fig. 2.3. Structure of the HOF (**A**) and FSB spectrum of the HOF (**B**) measured with a 785 nm excitation wavelength, 30 mW laser power, and 10 s exposure

the contributions of these bands by subtraction, because the intensities of these bands are similar or smaller than those of the Raman bands of general biological tissues. The HOF for Raman probe is commercially available from Doko Engineering LLC (2-15-31-510 Nagamachi-Minami, Sendai 982-0012, Japan; http://do-ko.jp/).

A photonic crystal fiber is made by stacking solid silica rods and/or hollow capillary tubes in a close-packed hexagonal pattern to make a preform, which is then drawn on a fiber pulling tower [47–51]. Konorov et al. have used a hollow-core photonic crystal fiber as the delivery fiber in a fiber-optic Raman probe [52]. They found that the fiber generated almost no Raman background. In this report, the FSB was measured in a transparent sample, ethanol. However, this transparent sample may not have been adequate for evaluating the FSB intensity, because any FSB generated in the delivery fiber passes through the sample and would not be seen by the collection fibers. Currently available photonic crystal fibers have rather narrow transmission spectral windows and small core diameters. Therefore, they are not suitable for use as collection fibers.

2.2.3 Filters

There are several kinds of filters that can be used in a miniaturized Raman probe. An interference filter has high performance in the sharpness of cutoff and optical density of blocking. An important criterion is the toughness of their filter coating. The most useful type is the so-called "hard coat" filter, which has a coating made of multilayered inorganic dielectric materials deposited by ion-beam sputtering onto a substrate surface. Since the coating is attached firmly to the substrate, it is relatively easy to avoid chipping and cracking the coating when the substrate is processed. It is more difficult to process "soft coat" and "semi-hard coat" filters.

Figure 2.4A shows the transmission spectra of a band-pass (BP) filter (Semrock, Inc., NY) measured at incidence angles of 0–15°. The cutoff wavelength of the interference filter shifts to shorter wavelengths with an increase in the incidence angle. The same shift to shorter angles is observed for long-pass filters, as shown in Fig. 2.4B. For the miniaturized Raman probes, filters are directly mounted on the fiber, as shown in Fig. 2.1B. The maximum angle of the incident light in an optical fiber with an NA of 0.2 is 11.5°. This suggests that the use of a fiber with a large NA may give poor performance at low wave numbers, because the angle of the filter is small. Finally, absorbing glass filters are not suitable for probe mounting, because the absorbing metal ions in the glass fluorescence intensely.

It is inadvisable to mount two or more filters close together in the light path to increase their blocking power. In a miniaturized optical system, the optical densities of the filters will not necessarily add. If the filters are parallel and positioned closely together in parallel uncollimated light be reflected at the second filter will be reflected again at the first. After several reflection

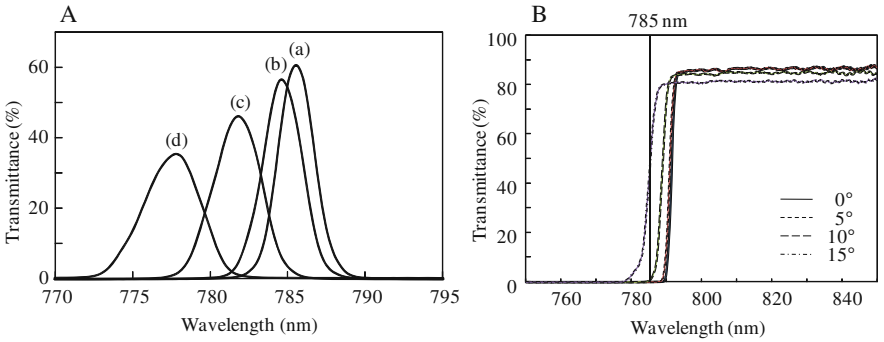

Fig. 2.4. Transmission spectra of the BP filter (**A**) and LP filter (**B**) measured at 0° (i), 5° (ii), 10° (iii), and 15° (iv) of incident angle

cycles, the transmission angle increases to the point where some of the light will pass through the second filter. Hence, attention must be paid to the stray light reflected by the filters when multiple filters are present in a small area.

2.2.4 Spectrometer Systems

The Raman scattered light collected by the fiber-optic probe is directed into the coupling stage, where it is collimated by a lens, L_a, and filtered, then focused on the slit of the Raman spectrometer by a second lens, L_b. To optimize the system efficiency, the optical property of the Raman spectrometer must be taken into consideration. Here, let us consider how to develop a high-throughput fiber-optic probe Raman system. It is presumed that one would like to simultaneously measure the spectral range from 0 to 2000 cm^{-1} with a spectral resolution of 10 cm^{-1}. We can also assume that the f/number of the Raman spectrometer will be 2.4 and the number of pixels and the size of 1 pixel will be 1024 and 25 μm in the lateral direction. In this case, the spectral range for a single pixel is about 2 cm^{-1} and a spectral spread of 10 cm^{-1} covers 5 pixels, which corresponds to a width of 125 μm on the CCD chip. Therefore, the slit width of the spectrometer must be 125 μm or smaller. Many workers use 100 μm slits which are usually available. Now, we assume again that an optical fiber with an NA of 0.2 will be employed for the collection fiber. To catch all of the light coming out of a fiber with an NA of 0.2, the f/number of the lens, L_a, collimating the light must be smaller than 2.45. The spectrometer governs the f/number of the lens, L_b, focusing the light into the slit to be 2.0. Therefore, to gather all of the light into the spectrometer, the core diameter of the fiber should be 128 ($= 102 \times 2.45/2.4$) μm or smaller. In fact, the power density across the fiber is Gaussian. Even if the image of the fiber is a little too large, not much light will be lost. Although this is a very rough estimation, it illustrates the need to take the entire Raman system into consideration in developing a high-throughput fiber-optic probe Raman system.

2.3 Miniaturized Raman Probes

Much effort has gone into determining ways to miniaturize fiber-optic Raman probes for biomedical applications [14–33]. Most of the development has been for probes designed for diagnosis of cancers and arteriosclerosis. Mahadevan-Jansen et al. developed a fiber-optic probe equipped with band-pass and notch filters and measured normal and pre-cancerous cervical tissues in vivo [21]. They reported that some silica signals obscure tissue Raman bands below $900\,\mathrm{cm}^{-1}$. Their probe was 12 mm in diameter. Motz et al. developed a Raman probe with a 2 mm diameter equipped with filters and a ball lens following their optical design strategy to optimize collection efficiency and minimize noise [26]. Figure 2.5 depicts the head design of their Raman probe. Their probe's performance was tested through simulations and experiments with tissue models and several in vitro tissue types. Buschman et al. reported the potential of Raman spectroscopy in the determination of the molecular composition of an artery wall in vivo using a Raman fiber probe [24]. They demonstrated the use of forward-viewing and side-viewing Raman fiber probes with diameters of about 2.5 mm on lamb and sheep in vivo. Our laboratory has developed two kinds of fiber-optic Raman probes. One is made of bundled

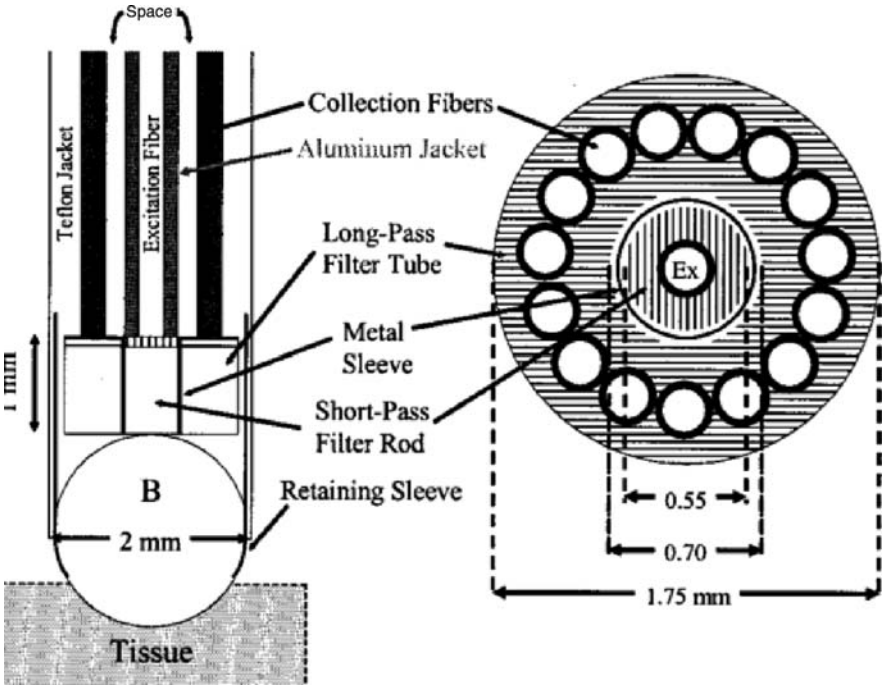

Fig. 2.5. Head structures of the miniaturized fiber-optic Raman probes developed by Motz et al. (modified from [29])

fibers and has a diameter of 600 µm [28]. The other is made of HOF with a ball lens and has a diameter of 640 µm [37].

The narrowest diameter fiber-optic Raman probes are single optical fiber, which were employed by Santos et al., Koljenović et al., and Nijssen et al. for high wave number $\left(> 2800\,\mathrm{cm}^{-1}\right)$ spectroscopy [39–41]. Although the probes are limited to collection of scatter from CH, NH and OH were used successfully in identifying basal cell carcinoma tissue with high accuracy. The FSB intensity in the high wave number region is much smaller than that in the fingerprint region because there is no silica Raman scatter and if the fiber is chosen carefully, little. Simple designs become possible. The simplest consists of a single unfiltered optical fiber that delivers the excitation light to the sample and serves to collect the Raman scatted light. Santos et al. tested different fiber core cladding and coating materials [39]. They recommended low-OH silica core–silica clad fibers with an acrylate coating and a black nylon jacket for minimal Raman scatter and fluorescence. With this fiber the background is flat [39]. In addition, the fluorescence of the sample is weaker because the high wave number region corresponds to the long wavelength region, in which molecules usually do not emit fluorescence.

Only a few types of vibrations can be observed in the high wave number region. Bands appearing between 2800 and 3000 cm^{-1} are the symmetric and asymmetric stretching modes of the CH_2 and CH_3 groups [38]. A broadband near 3300 cm^{-1} is due to the NH stretching mode of protein and other amides. A broad feature near 3400 cm^{-1} is the OH stretching mode of water. Diseased tissue can be detected by high wave number Raman spectroscopy if it has molecular compositional and structural changes that alter the frequencies of these vibrational modes.

2.3.1 Development of the Miniaturized Fiber-Optic Raman Probe

In Sect. 2.2 the optical properties of the fiber, filters, and spectrometers were described and their interrelated properties explained. In this section the optical design considerations for Raman probe made of bundled fibers will be discussed. The need to suppress FSB from the fibers and the need to couple the fibers properly to the spectrograph are largely the same as in the probes employing single fibers. For measurements in the fingerprint wave number region, it is necessary to suppress the FSB generated in the optical fibers used for delivery of the excitation light and those used for the collection of the scattered light [26]. To suppress the FSB, a BP filter is attached at the distal end of the fiber delivering the excitation light and an LP filter is attached at the distal end of the fiber used to collect the Raman scattered light to block the strong Rayleigh scattered light.

We developed a micro-Raman probe (MRP) with a total diameter of 600 µm to use with an intravascular endoscope [28]. To develop this MRP, it was important to consider the following three parameters when selecting the optical fiber: (1) R_b, (2) NA, and (3) core diameter. The first parameter

depends on the excitation wavelength to be used. It may be found in Table 2.1 and Fig. 2.2 for a fiber with an excitation wavelength of 720 nm. The second criterion must be considered by balancing two inconsistent principles. An optical fiber with a large NA is preferable in terms of its efficiency in collecting Raman scattered light. However, a fiber with a small NA is preferred in terms of its efficiency at cutting off the FSB, because the interference filter attached to the optical fiber operates to reject light with a large divergence or entrance angle, as discussed in Sects. 2.2–2.3. The shift in the transmission spectra of a BP filter, as shown in Fig. 2.4B indicates that the FRB light in the Stokes Raman shift region does not penetrate the BP filter and so does not interfere in the Stokes Raman measurement. Attaching a BP filter directly to the fiber may reduce the effective NA of the fiber, resulting in a reduction in the excitation power. The problem is more serious for an LP filter. The blue-shift of the transmission edge allows penetration of the Rayleigh scattered light. This problem depends on the performance and tolerance of the filters, and the probe designer should carefully check these. This problem occurs only with miniaturized probes where filters are directly mounted on the fibers. With large probes, as shown in Fig. 2.1A, as the problem does not usually arise because the fiber output is usually collimated and the filter is placed in the collimated zone. Finally, the third parameter governs the size and structure of the probe head, and the method of mounting filters.

In our earlier study, a pure fused silica optical fiber, SF-112UV (Sumitomo Co. Ltd., Japan), was chosen to serve as both delivery and collection fibers. The fiber has a core diameter of 114 μm, a total diameter of 125 μm, and an NA value of 0.20 [28]. Table 2.1 shows fibers with smaller R_b values, and they would have been satisfactory, but we were also concerned about cost and continuing availability. There was no problem with using this fiber for both 720 and 785 nm excitation wavelengths.

It was necessary to develop a technique to mount the BP and LP filters on the probe head. The detailed process to cut and polish the filters is described in the previous paper [28]. The BP filter is glued inside the tube and mounted at the end of the delivery fiber with an epoxy adhesive. There is no adhesive agent placed between the BP filter and the delivery fiber to avoid damage from the strong pulsed laser light. No damage was observed with the propagation of laser light with an average power of 40 mW (22 μJ/pulse at 1.8 kHz). The damage threshold for the adhesive agent placed between the BP filter and the delivery filter was lower than 10 mW (5.5 μJ/pulse at 1.8 kHz). The stainless-steel tube serves as a shield to prevent optical cross talk between the delivery and collection fibers at the distal end of the probe. The mounting design mentioned above is that optimized for the pulsed laser light. However, it has the disadvantages of energy loss and inefficient heat transfer. The curves in Fig. 2.6 plot the temperature increase in the BP filter head fixed in two different ways, the method described above (a) and a method where the head is adhered directly to the fiber (b). It suggests that the latter design is better for the cw-laser, which has considerably lower peak power than the pulsed laser.

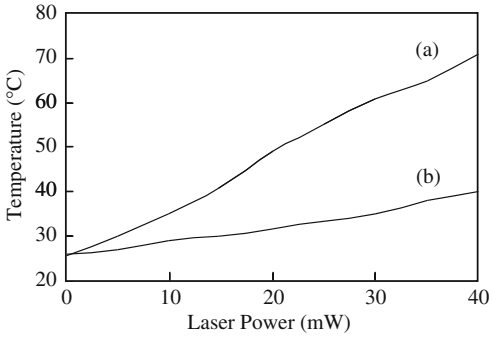

Fig. 2.6. Temperature change of the delivery fiber head with the BP filter glued at the side (**a**) and at the face (**b**)

The actual temperature increase is more moderate because the BP filter head is covered with the collection fiber, another metal tube, and the protection coat. We also tried to deposit a dielectric coating directly on the distal end of the optical fiber. Several dozen fibers were held separately in a holder that was inserted into the deposition chamber and the filter was deposited with the usual process. In this experiment, the filter was successfully deposited on the end face of the fibers, but its properties were not constant. This seems to be ascribable to a localized thermal irregularity in the deposition chamber, which affected the temperature of the end face of the individual fibers. The low quality of the deposited filter at the circumference of the fiber end was also a problem. It seems that the layer structure of the filter membrane at the edge of the fiber end face was in disorder and this portion got into the core part. The thickness of the cladding was only 5.5 μm in our fiber. It may be possible to avoid this problem by employing a thicker fiber.

2.3.2 Hollow Fiber Raman Probes

We developed a different type of miniaturized Raman probe using a hollow optical fiber (HOF) [34–38]. Transmission of a laser through the HOF generates no Raman scattering or fluorescence. Thus, an HOF Raman probe does not require a complex filter system at the distal end of the probe. A single HOF can be used bi-directionally, i.e., for sending the excitation light and for collecting the Raman scattered light [34]. However, the low NA, which causes low collection efficiency, is the major disadvantage of an HOF Raman probe [34, 37]. Addition of a ball lens to the distal end of the HOF Raman probe (BHRP; Fig. 2.7) resulted in a promising design for a miniaturized Raman probe [35, 37]. The probe is made of a single HOF that transmits both excitation and collected light. The HOF (core diameter: 320 μm, outer

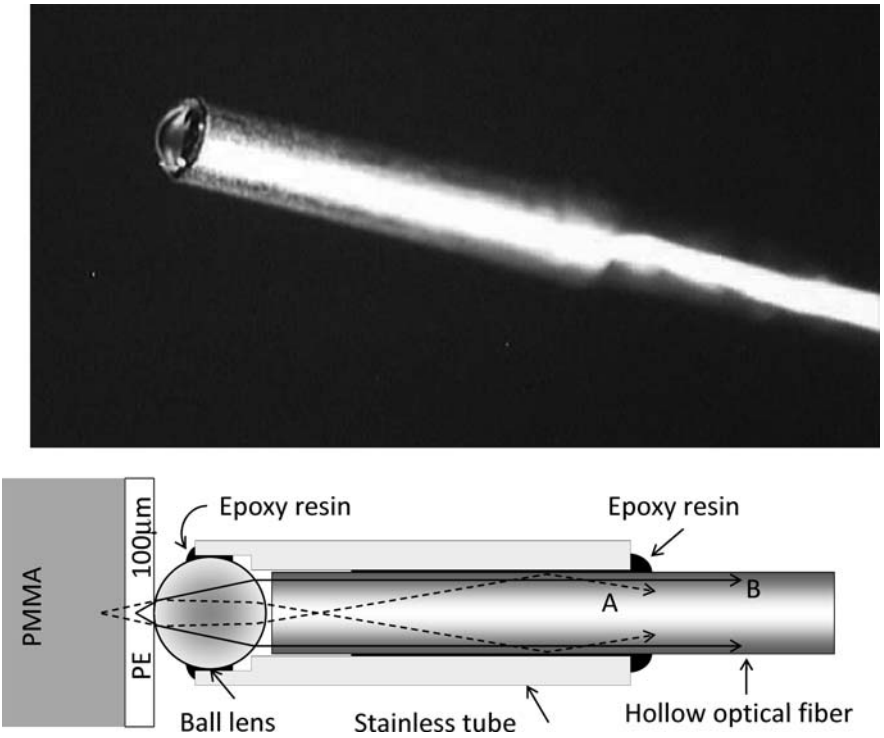

Fig. 2.7. Photograph and structure of the BHRP head (modified from [37], with permission)

diameter: 435 μm, and length: 1.5 m) was fabricated by coating a thin silver film on the inner surface of a flexible glass capillary tube [42, 43]. The ball lens was mounted on an Al sheath and sealed with an epoxy resin to prevent water leakage. Then, the sheath was glued to the distal end of the HOF. A fiber chuck was attached to the other end of the HOF to attach to the fiber coupling stage [37]. The total diameter of the probe head was 640 μm.

An advantage of the BHRP is that it is possible to control the working distance (WD) by selecting materials with different refractive indices and/or varying the diameter of the ball lens [37]. Since the spatial resolution of the BHRP is limited by the spherical aberration of the ball lens and the NA of the HOF, as described in Fig. 2.8, it is difficult to improve the axial resolution by modifying the optical configuration. If it is necessary to further improve the axial resolution, chemometric analysis may be used. Yamamoto et al. succeeded in obtaining a virtual axial resolution of approximately 10 μm by using the BHRP and partial least square regression (PLSR) analysis [36].

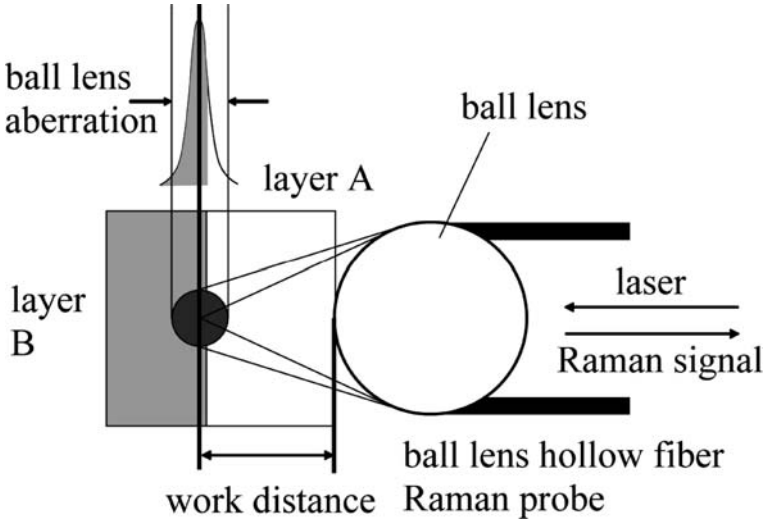

Fig. 2.8. Aberration of the BHRP (modified from [36], with permission)

2.4 Applications of Miniaturized Raman Probes

Miniaturized Raman probes are potentially powerful tools for in situ diagnoses deep inside the human body, if used inside a catheter or in combination with an endoscope. Since a Raman probe is usually used with other techniques, such as endoscopy and ultrasound imaging, it may be regarded as an assist device. Therefore, Raman probes must be designed to fit the system with which they will be used.

Mahadevan-Jansen et al. measured in vivo Raman spectra of cervical precancerous tissues using a filtered fiber-optic Raman probe under the guidance of a colposcope [21]. The diameter of their Raman system was 12 mm. The excitation wavelength and power were 789 nm and 15 mW at the sample, and the exposure time was 90 s. The reported spectra contained silica and tissue Raman signals but it was possible to analyze the Raman bands, which were not hidden by the silica bands. Shim et al. successfully applied a miniaturized fiber-optic Raman probe to obtain in situ Raman spectra of a human esophagus, stomach, and colon [23]. The Raman probe, which had a 2 mm diameter, could pass through the accessory channel of a standard gastrointestinal endoscope. The excitation wavelength and incident power were 785 nm and 100 mW at the sample, and the exposure time was 5 s. The measured spectra were free from the silica bands near 800 and 1040 cm^{-1}, demonstrating the importance of FSB filtration.

Molckovsky et al. succeeded in differentiating adenomatous from hyperplastic polyps during a gastrointestinal endoscopy [25]. Figure 2.9 shows the in vivo Raman spectra of adenomatous compared with hyperplastic polyps.

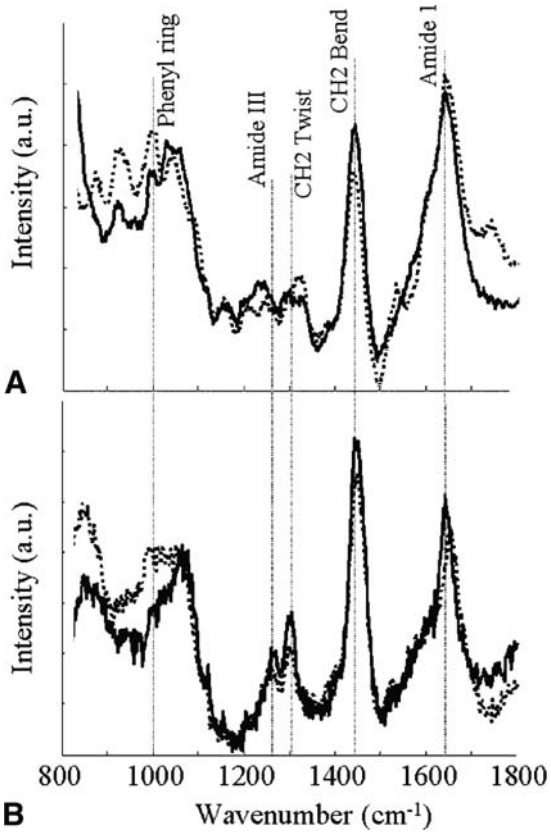

Fig. 2.9. A Average Raman spectra of hyperplastic ($n = 20$; *solid line*) and adenomatous ($n = 34$; *broken line*) colon polyps collected ex vivo (power = 200 mW; 30-s collection time). **B** Average Raman spectra of hyperplastic ($n = 9$; *solid line*) and adenomatous ($n = 10$; *broken line*) colon polyps collected in vivo (power = 100 mW; 5-s collection time). The spectra have been intensity corrected, wavelength calibrated, and fluorescence background subtracted (modified from [25], with permission)

They employed principal components analysis (PCA) and linear discriminant analysis (LDA) to distinguish the two types of polyps. The spectra (Fig. 2.9) have bands at similar wave numbers and their features are similar, making it difficult for the untrained eye to distinguish between them. The application illustrates the importance of multivariate analysis in clinical applications of Raman spectroscopy. It is often the case that there are only small differences between normal and diseased tissues.

Motz et al. developed a clinical Raman system and applied it to the diagnosis of atherosclerosis and to provide margin assessment during surgery [29]. The excitation wavelength and incident power were 830 nm and $\sim$ 100 mW,

and the collection time was 1 second. In their system the measurement, data analysis, and diagnosis were integrated to allow real-time in vivo disease diagnosis.

Buschman et al. demonstrated in vivo Raman measurements in live lambs and sheep using forward-viewing and side-viewing Raman probes with a 2.5 mm diameter [24]. The excitation wavelength and incident power were 830 nm and $\sim$ 100 mW at the tissue, and the exposure time was 10–30 s. Their experiments were performed during catheterization. After catheterization, the probe was guided to the site of the investigation under fluoroscopy. The in vivo-collected aorta spectra were a simple summation of the aortic wall and blood signals.

We developed a self-guided intravascular catheter equipped with a forward-viewing endoscope and side-viewing miniaturized Raman probe [30]. The total diameter of the catheter was 2 mm. With a water flow arterial model, it was shown that the side-viewing window of the Raman probe could make gentle contact with the arterial wall by inflating the balloon incorporated into the head, as shown in Fig 2.10. Following the suggestions of clinicians, we also tested the viability of using the catheter for non-contact measurement in blood vessels. The Raman spectra of a phantom target made of cholesteryl oleate, calcium carbonate, calcium hydroxyapatite, and fluorescent powder were successfully obtained in whole blood at a distance of up to 0.4 mm away from the target, using 15 mW at 785 nm and an exposure time of 1–2 s [30].

Small, portable Raman systems that can be used in the clinic are very important. It is often difficult to obtain ethics committee permission to remove human specimens from the clinic. The system should be small and tough, and it must be enough sensitive to detect the weak Raman spectra of biological tissues. We recommend to check carefully the toughness of Raman spectrometer, CCD detector, and laser as well as performance, before purchasing. It is warm and humid in the clinic. The system should be air cooled and does not emit radio wave not to affect clinical instruments.

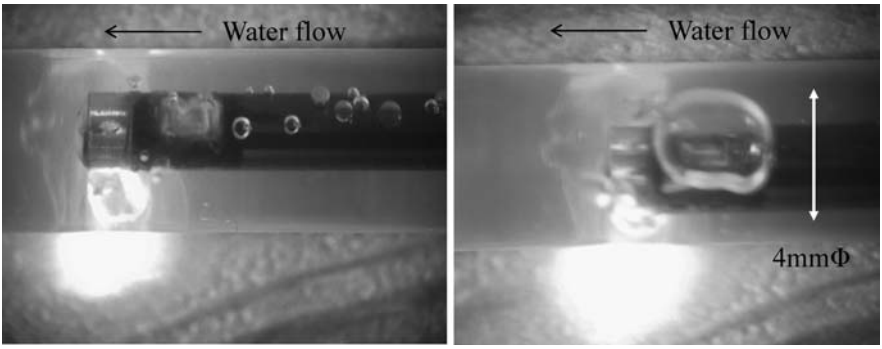

Fig. 2.10. Head of the self-guided intravascular catheter (modified from [30]

2.4.1 Animal Model Studies

A Raman spectroscopy-based optical biopsy system for small animal models was developed by our group. Its in vivo use in rat stomach under the guidance of an endoscope was reported by Hattori et al. [32]. The total diameter of the endoscope was 2.5 mm. With 785 nm 80 mW at the probe head the exposure time needed to obtain the stomach wall spectra was 50 s. Figure 2.11 shows that the Raman spectrum of the live rat stomach measured with the MRP (a) was different from that measured by the BHRP (b). The spectrum measured by the MRP includes contributions from adipose tissue, which does not exist at the stomach wall surface, suggesting that the MRP picks up information from the deep subsurface tissues. In contrast, the spectrum measured by the BHRP is very weak and shows major contributions only from protein, which suggests that the BHRP picks up information only from the surface mucosa tissue. Light microscopy of a cross section of the stomach wall revealed that there was a mucosa layer at the surface and a muscle layer with adipose tissue lay beneath the mucosa. This result suggests that subsurface information can be obtained selectively in a totally noninvasive manner by using these two fiber-optic Raman probes. For observation of much deeper tissues, the miniaturized Raman probe may be inserted directly into a body part to reach the lesion. The BHRP can be inserted into a 20 G biopsy needle. It may be feasible to utilize the Raman probe to guide biopsy needle to the tissue of high malignancy as part of a diagnostic procedure.

The spectra of the brains of live mice and rats in the fingerprint and high wave number regions were measured with excitation wavelengths of 785 and 720 nm, respectively [38]. These two excitation wavelengths were selected to avoid the low sensitivity of the CCD detector in the long wavelength region.

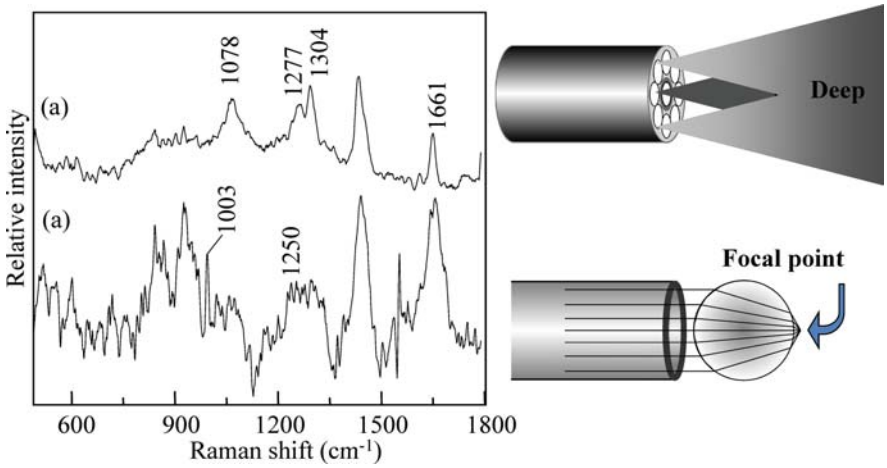

Fig. 2.11. Raman spectra of the live rat stomach wall measured by MRP (**a**) and BHRP (**b**)

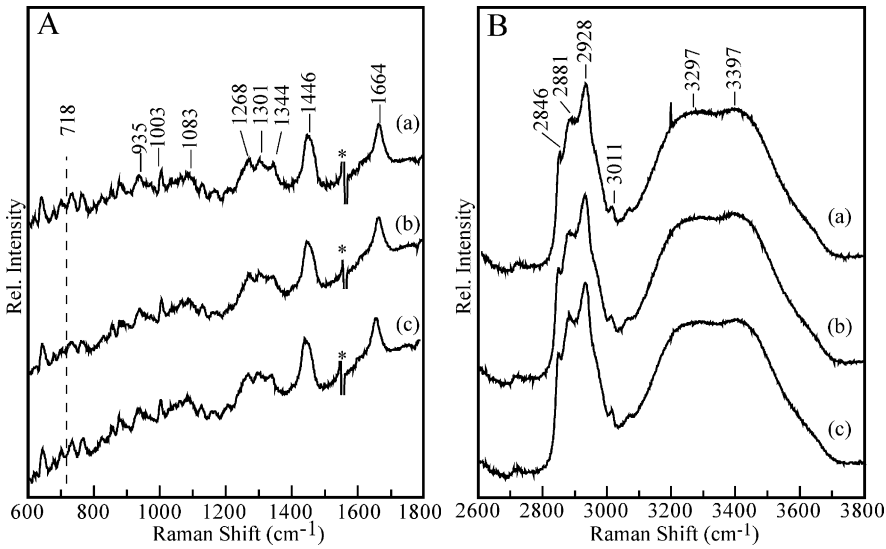

Fig. 2.12. Raman spectra of the mice brain in finger-print region (**A**) and high wave number region (**B**), measured under anesthesia (a), under inhalation of diethyl ether (b), and after killing (c) (modified from [38])

Dual wavelength measurement with the BHRP was straightforward, because it does not have filters. The skulls of the mice and rats were exposed and small holes were drilled at the frontal cortex and olfactory lobes in order to insert the BHRP. Since the probe has a high spatial resolution and was kept in contact with the tissue surface during the experiment, the spectral changes at exactly the same point on the brain could be compared.

Figure 2.12 shows the Raman spectra of a mouse brain under anesthesia (a), under the inhalation of diethyl ether (b), and after euthanasia (c). No alteration was observed in the fingerprint region, suggesting that the molecular composition of the general materials, such as the protein and lipid species, did not change by the inhalation of diethyl ether or killing the animal. In contrast, changes were observed in the high wave number region, suggesting that the water concentration and its cluster conformation changed. The study of the brain in live animals could provide new insights into the mechanisms of the effect of small molecules, such as diethyl ether, chloroform, and ethanol that cause unconsciousness in animals [38].

2.5 Conclusion

There is no doubt that Raman spectroscopy is already a powerful tool in basic and translational medical research. However, there is still room for development of new devices to facilitate practical applications. The fiber-optic Raman

probe will be necessary for many of these applications. The dream applications described in Sect. 2.1 seem to be closer than ever. In this chapter, we have devoted space to development of miniaturized Raman probes and discussed the hurdles to be overcome and the solutions that have been proposed in the literature. Improved instrumentation and new applications are appearing at an ever-increasing rate. We hope that introduction to this field will enable the user to delve into the details in the references and to contribute to further advances.

Acknowledgments

We would like to express our sincere gratitude to Prof. Yukihiro Ozaki (Kwansei Gakuin Univ.), Prof. Yuji Matsuura (Tohoku Univ.), Prof. Toru Shimosegawa (Tohoku Univ.), Prof. Masakazu Toi (Kyoto Univ.), and Dr. Hideo Tashiro (RIKEN) for the fruitful discussions and technical support. We also feel grateful to Mr. Gen'ichi Kanai (Machida Endoscope Co. Ltd.), Mr. Nobuo Ura (Soma Opt. Co. Ltd.), and Dr. Koji Masutani (Micro Science Co. Ltd.) for their cooperation in the development and technical support.

References

1. K. Maquelin, L.-P. Choo-Smith, H.P. Endtz, H.A. Bruining, G.J. Puppels, J. Clin. Microbiol. **40**, 594 (2002)
2. I. Notingher, A. Bisson, E. Bishop, W.L. Randle, J.M.P. Polak, L.L. Hench, Anal. Chem. **76**, 3185 (2004)
3. C.M. Krishna, G.D. Sockalingum, G. Kegelaer, S. Rubin, V.B. Kartha, M. Manfait, Vib. Spectrosc. **38**, 95 (2005)
4. K.W. Short, S. Carpenter, J.P. Freyer, J.R. Mourant, J. Biophys. **88**, 4274 (2005)
5. C.M. Krishna, G. Kegelaer, I. ADT, S. Rubin, V.B. Kartha, M. Manfait, G.D. Sockalingum, Biopolymers **82**, 462 (2006)
6. S. Rehman, Z. Movasaghi, A.T. Tucker, S.P. Joel, J.A. Darr, A.V. Ruban, I.U. Rehman, J. Raman Spectrosc. **38**, 1345 (2007)
7. J. Popp, M. Krause, M.K. Harz, M. Schmitt, P. Roesch, Proc. SPIE, **6853A-09** (2008).
8. G.J. Puppels, D. Willemse-Erix, M. Scholtes, J.W. Jachtenberg, T.C. Bakker-Shut, A. van Belkum, K. Maquelin, Proc. SPIE, **6853A-48** (2008)
9. J. Kneipp, T.B. Schut, M. Kliffen, M. Menke-Pluijmers, G. Puppels, Vib. Spectrosc. **32**, 67 (2003)
10. M.V.P. Chowdary, K.K. Kumar, J. Kurien, S. Mathew, C.M. Krishna, Biopolymer **83**, 556 (2006)
11. R.A. Bitar, H.S. Martinho, C.J. Tierra-Criollo, L.N.Z. Raamalho, M.M. Netto, A.A. Martin, J. Biomed. Opt. **11**, 054001-1 (2006)
12. P. Matousek, N. Stone, J. Biomed. Opt. **12** (2007)
13. B. Bronzek-Pluska, I. Placek, K. Kurczewski, Z. Morawiec, M. Tazbir, H. Abramczyk, J. Mol. Liq. **141**, 145 (2008)

14. K.P.J. Williams, J. Raman Spectrosc. **21**, 147 (1989)
15. J. Ma, Y.S. Li, Appl. Opt. **35**, 2527 (1996)
16. I.R. Lewis, P.R. Griffiths, Appl. Spectrosc. **50**, 12A (1996)
17. T.F. Cooney, H.T. Skinner, S.M. Angel, Appl. Spectrosc. **50**, 836 (1996)
18. T.F. Cooney, H.T. Skinner, S.M. Angel, Appl. Spectrosc. **50**, 849 (1996)
19. V. Benoit, M.C. Yappert, Anal. Chem. **68**, 2255 (1996)
20. M.G. Shim, B.C. Wilson, J. Raman Spectrosc. **28**, 131 (1997)
21. A. Mahadevan-Jansen, M.F. Mitchell, N. Ramanujam, A. Malpica, S. Thomsen, U. Utzinger, R. Richards-Kortum, Photochem. Photobiol. **68**, 427 (1998)
22. M.G. Shim, B.C. Wilson, E. Marple, M. Wach, Appl. Spectrosc. **53**, 619 (1999)
23. M.G. Shim, L.M.W.K. Song, N.E. Marcon, B.C. Wilson, Photochem. Photobiol. **72**, 146 (2000)
24. H.P. Buschman, E.T. Marple, M.L. Wach, B. Bennett, T.C. Bakker Schut, H.A Bruining, A.V. Bruschke, A. van der Laarse, G.J. Puppels, Anal. Chem. **72**, 3771 (2000)
25. A. Molckovsky, L.M. Wong Kee Song, M.G. Shim, N.E. Marcon, B.C. Wilson, Gastrointest. Endosc. **57**, 396 (2003)
26. J.T. Motz, M. Hunter, L.H. Galindo, J.A. Gardecki, J.R. Kramer, R.R. Dasar, M.S. Feld, Appl. Opt. **43**, 542 (2004)
27. T.D. Wang, J. van Dam, Clin. Gastroenterol. Hepatol. **2**, 744 (2004)
28. Y. Komachi, H. Sato, K. Aizawa, H. Tashiro, Appl. Opt. **44**, 4722 (2005)
29. J.T. Motz, S.J. Gandhi, O.R. Scepanovic, A.S. Haka, J.R. Kramer, R.R. Dasari, M.S. Feld, J. Biomed. Opt. **10**, 031113-1 (2005)
30. Y. Komachi, H. Sato, H. Tashiro, Appl. Opt. **45**, 7938 (2006)
31. Y. Oshima, Y. Komachi, C. Furihata, H. Tashiro, H. Sato, Appl. Spectrosc. **60**, 964 (2006)
32. Y. Hattori, Y. Komachi, T. Asakura, T. Shimosegawa, G. Kanai, H. Tashiro, H. Sato, Appl. Spectrosc. **61**, 579 (2007)
33. M.A. Short, S. Lam, A. McWilliams, J. Zhao, H. Lui. H. Zeng, Opt. Lett. **33**, 711 (2008)
34. Y. Komachi, H. Sato, Y. Matsuura, M. Miyagi, H. Tashiro, Opt. Lett. **30**, 2942 (2005)
35. Y. Matsuura, S. Kino, E. Yokoyama, T. Katagiri, H. Sato, H. Tashiro, IEEE J. Sel. Top. Quantum Electron. **13**, 1704 (2007)
36. Y.S. Yamamoto, Y. Oshima, H. Shinzawa, T. Katagiri, Y. Matsuura, Y. Ozaki, H. Sato, Anal. Chim. Acta. **619**, 8–13 (2008)
37. T. Katagiri, Y.S. Yamamoto, Y. Ozaki, Y. Matsuura, H. Sato, Appl. Spectrosc. **63**, 103–107 (2009)
38. H. Sato, Y.S. Yamamoto, A. Maruyama, T. Katagiri, Y. Matsuura, Y. Ozaki, Vib. Spectrosc. **50**, 125–130 (2009)
39. L.F. Santos, R. Wolthuis, S. Koljenovic, R.M. Almeida, G.J. Puppels, Anal. Chem. **77**, 6747 (2005)
40. S. Koljenović, T.C. Bakker Schut, R. Wolthuis, A.J.P.E. Vincent, G. Hendriks-Hagevi, L. Santos, J.M. Kros, G.J. Puppels, Anal. Chem. **79**, 557 (2007)
41. A. Nijssen, K. Maquelin, L.F. Santos, P.J. Caspers, T.C. Bakker Schut, M.H.A. Neunmann, G.J. Puppels, J. Biomed. Opt. **12**, 034004-1 (2007)
42. Y. Matsuura, M. Miyagi, Opt. Lett. **23**, 1226 (1998)
43. H. Jelínková, J. Šulc, P. Černý, Y.W. Shi, Y. Matsuura, M. Miyagi, Opt. Lett. **24**, 957 (1999)

44. Y. Matsuura, G. Takada, T. Yamamoto, Y.W. Shi, M. Miyagi, Appl. Opt. **41**, 442 (2002)
45. Y. Matsuura, M. Miyagi, K. Shihoyama, M. Kawachi, J. Appl. Phys. **91**, 887 (2002)
46. M. Mohebbi, R. Fedosejevs, V. Gopal, J.A. Harrington, Appl. Opt. **41**, 7031 (2002)
47. P. Rigby, Nature **396**, 415 (1998)
48. B. Temeikuran, S.D. Hart, G. Benoit, J.D. Joannopoulos, Y. Fink, Nature **420**, 650 (2002)
49. C.M. Smith, N. Venkataraman, M.T. Gallagher, D. Müller, J.A. West, N.F. Borrelli, D.C. Allan, K.W. Koch, Nature **424**, 657 (2003)
50. J.C. Knight, Nature **424**, 847 (2003)
51. F. Benabid, F. Cony, J.C. Knight, T.A. Birks, P.StJ. Rusell, Nature **434**, 488 (2005)
52. S.O. Konorov, C.J. Addison, H.G. Schulze, R.F.B. Turner, M.W. Blades, Opt. Lett. **31**, 1911 (2006)

3

Characterisation of Deep Layers of Tissue and Powders: Spatially Offset Raman and Transmission Raman Spectroscopy

Neil A. Macleod, Michael D. Morris and Pavel Matousek

Abstract This chapter reviews emerging techniques for deep, non-invasive Raman spectroscopy of diffusely scattering media. As generic analytical tools, these methods pave the way for a host of new applications including non-invasive disease diagnosis, chemical identification and characterisation of pharmaceutical products.

3.1 Introduction

A number of biomedical and pharmaceutical applications require a highly chemically specific analytical method capable of non-invasive interrogation of deeply buried regions of turbid samples. Examples include the non-invasive diagnosis of bone disease and subsurface cancers, process and quality control applications in the pharmaceutical industry, detection of concealed explosives and illicit drugs and the identification of counterfeit drugs through packaging.

Raman spectroscopy holds particular promise in this area due to its high chemical specificity (far exceeding that of near-infrared absorption (NIR) spectroscopy) combined with the ability to probe hydrated samples. The relative weakness of the Raman effect and its sensitivity to fluorescence emission, which can potentially swamp the weaker Raman signals, can be managed, to some degree, using near-infrared excitation to minimise or eliminate excitation into photo-emissive electronic states [1]. A more formidable problem stems from the excessive sensitivity towards surface layers of complex, multilayered, diffusely scattering samples (e.g. biological tissue or pharmaceutical formulations). This bias and the resulting lack of accessible depth is a consequence of the backscattering geometry commonly used in most spectrometers; in the case of biological tissue, confocal Raman spectroscopy is capable of probing to a depth of typically only a few hundred micrometers.

3.2 Propagation of Light in Diffusely Scattering Media

The principal barrier preventing conventional optical analytical methods from interrogating deep layers of tissue or powders is the diffuse nature of the medium. The high level of random scattering prevents the collection of the optical images required, for example, by confocal Raman microscopy. Photon propagation in such media, in the absence of significant absorption, is governed principally by diffuse scattering [2], a process analogous to diffusion of molecules in solution. Figure 3.1 depicts the three main components identified in the propagation of light through such media: ballistic, snake and diffuse [2]. The ballistic component is the part of light not scattered by the medium; its intensity decreases exponentially with depth. Upon propagation through a turbid medium this component gradually converts to the snake component which in turn converts to the diffuse component. The snake component is defined as the component that is only weakly deviated from its original direction by a small number of events which are each biased towards scattering in the forward direction. This component also undergoes an exponential decay but with a substantially higher penetration depth than that of the ballistic component. The straight (or semi-straight) pathways of both components form an ideal basis for imaging such media.

In contrast, light which undergoes a large number of scattering events and whose direction is randomised (the diffuse component) cannot be used for imaging in conventional instruments. However, this disadvantage is more than compensated by the greatly enhanced penetration depth (several *centimetres* in biological tissue for near-infrared radiation) which forms the basis for recent developments in the Raman spectroscopy of deeply buried sublayers. Exploitation of the diffuse component of light allows the retrieval of Raman signatures of deeply buried layers within turbid media using a variety of related techniques. These methods (which share a number of characteristics with more established techniques including NIR absorption tomography

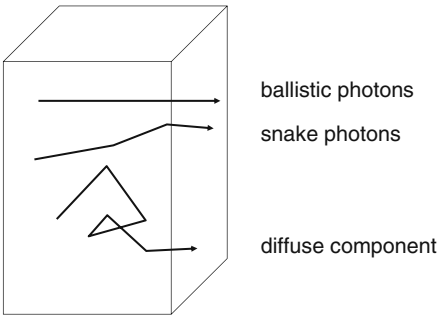

Fig. 3.1. Three main light components within turbid media

[2–4] and fluorescence spectroscopy [5–8]) are described in this chapter and highlighted with a diverse set of applications.

The foundation for the development of these techniques is built on investigations into photon migration processes [2, 9]. Subsequent, detailed examination by Everall et al. [10, 11] demonstrated that the inelastically scattered (Raman) component decays substantially more slowly than its elastically scattered counterpart (i.e. the laser light) due to the regeneration of the Raman signal from the laser component. Discrimination between diffusely scattered photons and the ballistic and snake components is achieved by gating the detector in the temporal or spatial domain.

3.3 Deep Probing Raman Techniques

In practical terms, diffuse scattering in a conventional backscattering Raman spectrometer results in the overwhelming dominance of the signal from surface layers over the considerably weaker subsurface layer signals. This bias is a consequence of the dilution of deep layer Raman signals due to their large lateral diffusion upon propagation to and from deep layers of the sample. In contrast, the surface-generated Raman photons are more tightly confined to the vicinity of the laser deposition area and hence are much more effectively collected.

3.3.1 Ultrafast Raman Signal Gating

The interfering surface Raman signal can be effectively suppressed using impulsive excitation and fast (picosecond) temporal gating of the backscattered Raman signal. The viability of this concept with Raman spectroscopy was first demonstrated by Wu et al. [9] using photon counting detection which allowed non-invasive imaging of a buried object. The recovery of the full Raman spectrum of a deeply buried layer in a turbid sample was demonstrated using a Kerr gating approach by Matousek et al. [12] on a two-layer powder sample. This work combined pioneering research into Raman photon migration by Everall et al. [10, 11] and Morris et al. [13] with fluorescence rejection methods developed by Matousek et al. [14–16]. A more extensive description of these methods and underlying principles can be found in [17].

3.3.2 SORS

The time-resolved Raman approach proved effective in isolating the Raman spectra of deep layers; however, the complexity of the instrumentation required and the high peak intensities associated with short-pulse lasers precluded its wider use. These problems were addressed by utilising the spatial

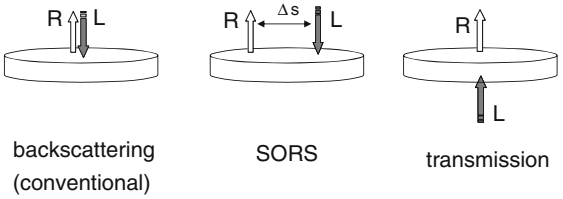

Fig. 3.2. Raman spectroscopy modalities: Conventional backscattering Raman, SORS and Raman transmission geometries. R, Raman light; L, laser beam

(rather than the temporal) properties of diffusely scattered photons. Spatially offset Raman spectroscopy (SORS) [18, 19] utilises continuous wave diode lasers to acquire Raman spectra from regions spatially offset (by a distance Δs) on the sample surface from the laser beam interaction point (see Fig. 3.2). Raman spectra observed at different spatial offsets contain *different relative contributions* from surface and subsurface layers due to the wider spread of photons emerging from the surface which have penetrated deeper layers of the sample. The lateral offset also effectively discriminates against photons propagating sideways within the surface layer due to the effective loss of such photons at the air-to-sample interface – a loss mechanism that is closed to photons propagating through deeper layers. A data set of spectra recorded over a range of spatial offsets can be analysed (to produce pure spectra of each layer or to construct calibration models) by a variety of multivariate, statistical techniques. In general terms such separation can be achieved for a multilayer stratified system using multivariate techniques [18, 20], such as band target entropy minimisation (BTEM) [21–25]. In the case of a two-layer sample, a simple scaled subtraction of SORS spectra acquired at two different spatial offsets is sufficient for the complete separation of the signals between the two layers [18]. The SORS method was first demonstrated on a stratified powder sample [18] and subsequently in numerous applications including, for example, non-invasive Raman spectroscopy of bones [20], pharmaceutical applications [26] and security screening [27].

An additional benefit of SORS is the suppression of surface-generated fluorescence which has an identical spatial (but not temporal) distribution to the Raman signal of the surface layer. This feature is particularly beneficial in situations where intense surface-layer fluorescence masks the underlying Raman signal; examples include melanin-induced fluorescence in biological tissue in vivo and intensely coloured capsules or coated tablets in pharmaceutical applications.

The SORS concept was first demonstrated (see Fig. 3.3a) on a two-layer sample composed of a 1 mm thick PMMA powder layer on top of a *trans*-stilbene powder sublayer [18]. The Raman spectra obtained at different spatial offsets are illustrated in Fig. 3.4. The conventional Raman spectrum is that obtained with zero spatial offset. The introduction of a non-zero spatial offset led to a more rapid decrease of the surface-generated Raman signal (PMMA)

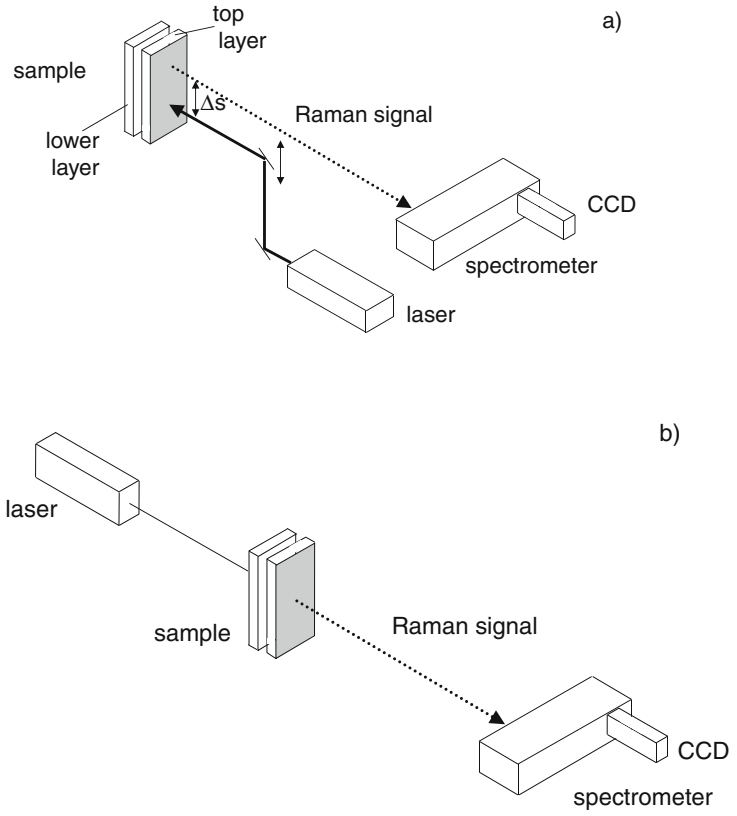

Fig. 3.3. Basic implementations of the **(a)** SORS and **(b)** transmission Raman concepts

than that exhibited by the sublayer component (*trans*-stilbene). For a spatial offset of 2 mm, the surface-to-subsurface relative Raman intensity was diminished by an order of magnitude [18].

A simple variant of SORS compatible with commercial Raman instruments was demonstrated by Eliasson et al. [28]. This approach exploits the variation in the relative contribution of surface and subsurface layers to the overall Raman signal upon defocusing of the collection optics. Raman spectra acquired under different focusing conditions generate a data set analogous to that produced using different spatial offsets. Although less effective than the SORS method, the concept is useful for less challenging samples and provides a cost-effective stepping stone for researchers in possession of a conventional Raman instrument initiating research in the area of deep Raman spectroscopy.

The fibre-optic-based collection scheme developed for conventional Raman spectroscopy [29] is equally valid for SORS. In the original concept, the collection fibres (arranged in a disk pattern) were re-organised onto the spectrograph slit into a linear pattern matching the geometry of the spectrograph

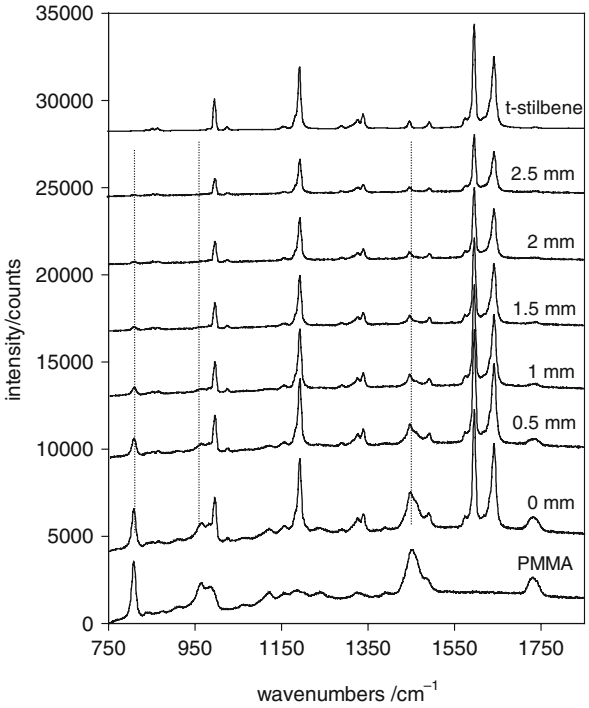

Fig. 3.4. A set of SORS spectra collected from a two-layer system consisting of 1 mm thick layer of PMMA made of 20 µm diameter spheres followed by a 2 mm layer of *trans*-stilbene powder measured using 514 nm as the probe wavelength. The spectra are shown for different spatial offsets. The *top* and *bottom spectra* are those of the individual layers obtained in separate measurements. The spectra are offset for clarity. The acquisition time was 100 s for each spectrum and the average laser power 12 mW (reprinted with permission from [18]. Copyright (2005) The Society for Applied Spectroscopy)

detection system [18, 19, 30–32]. Similar probes have also found use in fluorescence tomography [5–8]. In the case of SORS, the collection fibres can be arranged into an annular (ring) geometry (see Fig. 3.5) to maximise collection efficiency at a particular offset. With this arrangement the spatial offset is defined as the radius of the ring.

3.3.3 Inverse SORS

The fixed nature of the collection fibres in a conventional SORS experiment limits the range of spatial offsets available. An alternative approach (inverse SORS) swaps the laser and collection fibre geometries; Raman light is collected through a group of fibres (arranged in a disc shape) contained within the centre of a probed area defined by a ring-shaped laser beam (see Fig. 3.5).

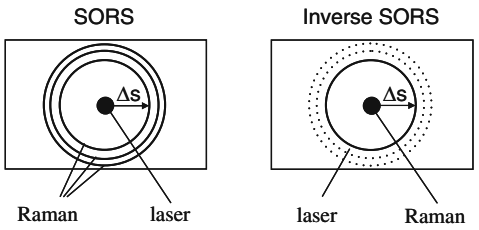

Fig. 3.5. Schematic diagram of conventional SORS and inverse SORS concepts showing Raman collection and laser beam delivery geometries (reprinted with permission from [34]. Copyright (2006) The Society for Applied Spectroscopy)

The required beam shape is typically generated using a conical lens (axicon) [33] where the radius of the ring (and hence the spatial offset) is altered, over a wide and user-selectable range, either by adjusting the distance of the axicon from the sample [34] or by varying the magnification of a telescope located between sample and axicon [35, 36]. The laser radiation is coupled into the sample through a substantially larger area relative to conventional SORS. This is particularly beneficial in situations where strict illumination intensity limits are enforced; for example, in the use of laser radiation in potentially explosive environments or in illumination of human skin in vivo. Additional benefits include a reduced sensitivity to imaging imperfections in the spectrograph and detector and the ability to tailor the radius of the ring, and hence the spatial offset, to match the size and shape of each sample. This is not possible with conventional ring SORS probes where the ring radii are fixed in the probe head. The inverse SORS concept was developed independently by Matousek [34] and Schulmerich et al. [35, 36].

3.3.4 Subsurface Mapping and Tomography

Subsurface Raman imaging can be accomplished, but with spatial resolution ultimately limited by photon diffusion. The principles are largely the same as in fluorescence and absorption imaging [37]. In practice the resolution is often limited by the number and distribution of excitation sources and is perhaps more appropriately labeled Raman mapping. Subsurface Raman mapping was first demonstrated by Schulmerich et al. [31] using global illumination and fibre-by-fibre display of the collected Raman scatter. It was soon realised that better contrast and deeper penetration could be obtained by an inverse SORS illumination scheme, which suffered less from surface weighting than the global illumination method [20]. Proof of principle was demonstrated with polymer block test systems, as shown in Fig. 3.6.

Diffuse Raman tomography has been demonstrated, with reconstruction of low-definition three-dimensional maps of phantoms and of canine bone tissue [38, 39]. Spatial priors (i.e. independent information on the location and

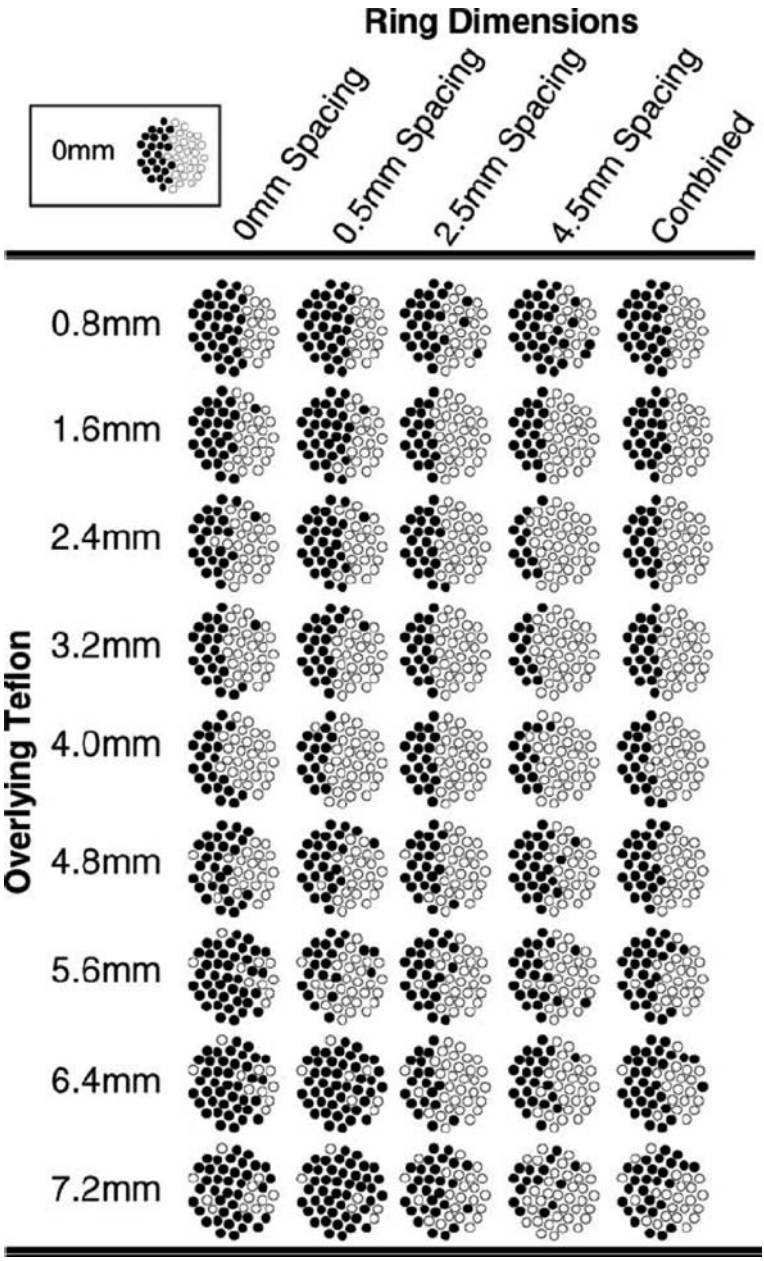

Fig. 3.6. Fibre maps of the subsurface interface between polyethylene (*filled circles*) and Delrin (*open circles*) at different ring/disk spacings (reprinted with permission from [20]. Copyright (2007) Society for Applied Spectroscopy)

topography of the imaged components) were not used, resulting in some position inaccuracy. While diffuse Raman tomography with spatial priors has not yet been achieved, the closely related image-guided Raman spectroscopy [40] has been performed [41]. In this technique, spatial priors are used to define the volume in which the average Raman spectrum of a specimen is painted. With this method a contrast of 145:1 over background was obtained for a canine bone specimen. Contrast of 460:1 for a Teflon sphere embedded in an agarose/intralipid phantom was reported, suggesting that very high contrast may be obtainable in tissue specimens as well.

3.3.5 Transmission Raman

A perhaps surprising property is the depth (up to several centimetres) to which diffusely scattered Raman photons are capable of migrating in turbid media. In consequence, for relatively small samples (e.g. pharmaceutical capsules or tablets), the penetration depth actually exceeds the physical dimensions of the sample. This simple observation has led to the renaissance of transmission Raman spectroscopy, which is particularly suitable for the determination of the *bulk* content of turbid samples. This concept can be considered as an extreme version of SORS in which the laser beam impacts on one side of the sample and the Raman signal is collected from the opposite side (see Figs. 3.2 and 3.3b). Although the transmission Raman technique was demonstrated in the early days of Raman spectroscopy [42], its benefits for the non-invasive probing of the bulk content of biological tissue and pharmaceutical samples have not been recognised or exploited. These include the removal of the subsampling problem [43, 44] (an inability to sense deeper layers in thick turbid samples, e.g. pharmaceutical tablets) and the effective suppression of surface-generated Raman and fluorescence signals (e.g. melanin in skin tissue or intensely coloured pharmaceutical capsules) [45].

Until recently, subsampling presented a major limitation on the use of conventional Raman spectroscopy in identifying and quantifying the bulk content of pharmaceutical tablets and capsules; frequently such samples are highly heterogeneous and can have localised domains of a size comparable to the laser spot size which give rise to Raman signals which are not indicative of the bulk content and skew the results of any predictive or quantitative model applied to the data set [43]. To overcome these limitations, for example, elaborate schemes for rotating pharmaceutical tablets in front of a conventional backscattering Raman spectrometer have been developed. These issues are neatly side-stepped by transmission Raman.

The absence of the subsampling problem in transmission Raman was demonstrated experimentally and computationally by Matousek and Parker [43]. The results of Monte Carlo simulations are shown in Fig. 3.7; re-location of a thin 'impurity' layer from the sample surface to a depth of 3 mm within a typical tablet medium diminishes its conventional backscattering Raman signal by four orders of magnitude. In practical situations, such signal levels are

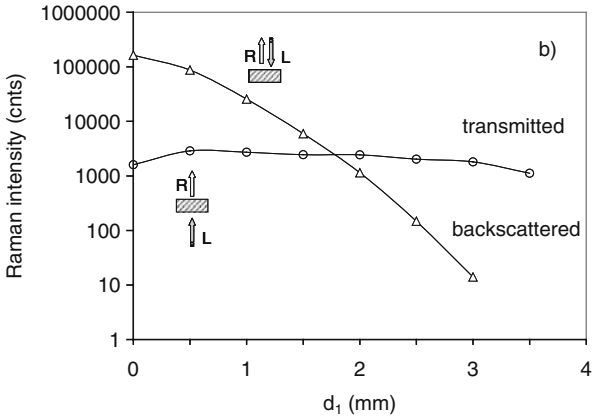

Fig. 3.7. Theoretical plot of Raman intensities for the backscattering and transmission geometries versus depth (d_1) of the inter-layer (impurity) within a pharmaceutical tablet-like medium. The dependencies are the results of Monte Carlo simulations (reprinted with permission from [43]. Copyright (2006) The Society for Applied Spectroscopy)

typically overwhelmed by the surface Raman signal. In contrast, the transmission geometry yields a Raman signal level unperturbed (to within +/–50% accuracy) by the depth of the impurity layer. Experimentally, similar results were found using a paracetamol tablet with a simulated impurity layer of *trans*-stilbene powder placed either in front or behind the tablet relative to the incoming laser beam [43].

Conventional Raman spectroscopy (plagued by the subsampling problem) yielded only the Raman signature of the surface layer in both possible orientations of the sample with no trace of the sublayer signal even after numerical subtraction of the dominant surface signal. In contrast, the transmission geometry provided a Raman spectrum comprising a mixture of signals from the tablet and the 'impurity'; the similarity of the spectra in both sample orientations is expected from a technique that does not suffer from subsampling.

3.3.6 Signal-Enhancing 'Unidirectional' Mirror

The intrinsically low intensity of Raman scattering strongly influences both the sensitivity and penetration depth of SORS and its variants. Dominant noise components (photon shot noise or thermal/dark count [1]) can be minimised relative to signal by increasing absolute signal levels. In many Raman systems, collection optics, laser power and other relevant parameters are usually maximised for optimum performance of the system; current detectors (CCD devices), for example, have detection efficiencies approaching 100%. Typically, acquisition time provides the only straightforward means available

to further improve sensitivity in a given application. In practical terms, the additional time required may not be available. Recently Matousek [46] reported a new approach to enhance signal in Raman spectroscopy using dielectric mirrors. This is achieved by limiting the large photon loss which occurs within the immediate vicinity of the laser illumination zone; this dominant loss mechanism leads to severely reduced Raman signals, in particular in transmission Raman. The technique is straightforward to implement and applicable to both Raman spectroscopy (conventional, SORS and transmission) and fluorescence measurements [47].

The enhancement is facilitated by a multilayer dielectric optical element placed on the sample surface within the laser illumination zone. The method is based on the angular dependence of dielectric filters on impacting photon direction, which exhibit a spectral profile shifted to shorter wavelengths with increasing angle of incidence. This property is used to facilitate a 'unidirectional' mirror (photon diode) through which a semi-collimated laser beam passes from one side at normal incidence while, at the other side, laser photons emerging from the sample at angles *away from normal incidence* are reflected back into the sample (see Fig. 3.8).

This leads to a substantial increase in the coupling of laser radiation into the sample with a corresponding boost to the overall Raman signal. In practical terms, the method requires that the sample surface is not excessively curved as dielectric filters are typically only readily available as flat optical elements, although this is not a fundamental obstacle.

Although conventional mirrors have long been used to redirect transmitted laser light back into the sample as a way of increasing the intensity of Raman signal [48] and to reduce photon loss *near* the laser radiation coupling zone [49] such elements do not prevent photon loss at what is often the most critical area, the delivery zone of laser radiation into the sample. This loss becomes more marked in applications where safety or other limits prevent the laser radiation from being concentrated onto a small area. Examples include the illumination of human skin or applications in explosive powder environments in the pharmaceutical industry. The solution presented here is fully compatible with the defocused laser beams used in such conditions.

Figure 3.9 shows the results of a feasibility study performed in the transmission Raman geometry on a standard paracetamol tablet with and without the 'unidirectional' mirror (3.2 nm bandwidth dielectric band-pass filter centred at 830 nm at normal incidence). *Raman signal in transmission mode was enhanced using this method by an order of magnitude.* The measurement was carried out using a compact spectrometer equipped with a detector array cooled to moderate levels (–15°C). Under such conditions the spectral noise was dominated by the detector dark count (thermal noise) [1] and the Raman spectrum signal-to-noise improvement was linearly proportional to the enhancement factor (i.e. it improved by a factor of 10). Achievement of the same signal-to-noise ratio would require an increase in the acquisition time of a factor of 100 (signal to noise improves as the square root of the acqui-

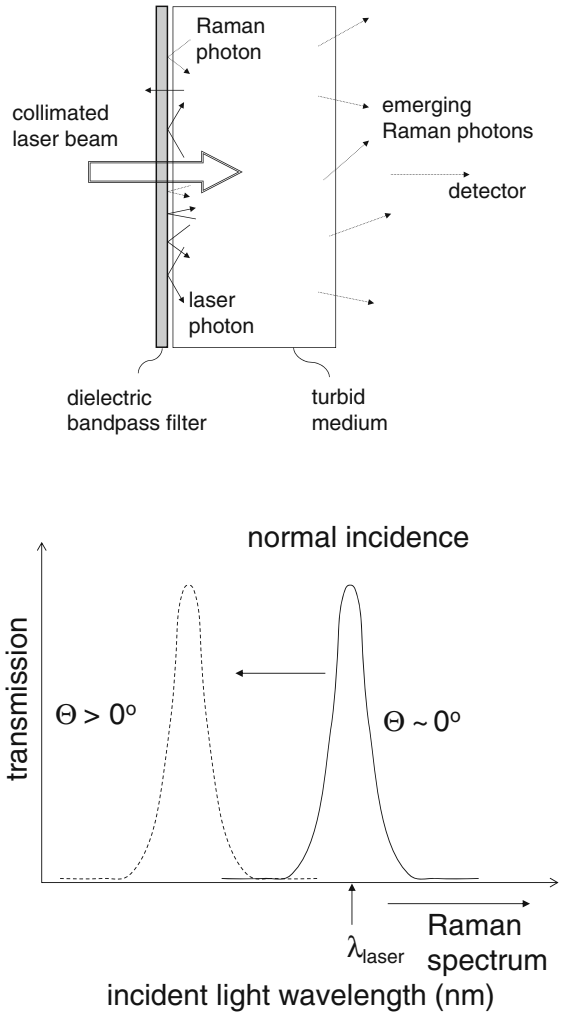

Fig. 3.8. Dielectric band-pass filter used for the enhancement of signals in transmission Raman spectroscopy and a schematic illustration of the shift of the design wavelength with the angle of photon incidence

sition time [1]). For a more efficiently cooled detector (–80 to –100°C), the signal to noise is typically dominated by the photon shot noise of the Raman (and fluorescence background) signal and the signal-to-noise ratio improves with the square root of the enhancement factor [1]. Such substantial enhancements would be difficult, if not impossible, to obtain through technological improvements in the collection optics and detection electronics. The method was found to be particularly effective with pharmaceutical tablets; lower enhancement factors were observed for biological tissue. This is believed to be

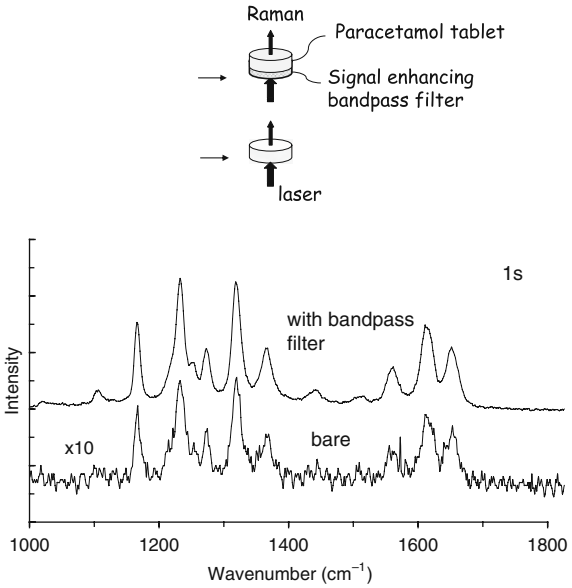

Fig. 3.9. Enhancement of transmission Raman signal using a standard dielectric band-pass filter (BF) placed within the laser beam into the proximity of sample. The Raman spectra are those of a standard paracetamol tablet measured with (with band-pass filter) and without (bare) the filter. The spectra are offset for clarity. The acquisition times were 1 s in both cases with a laser power of 250 mW (827 nm). The spectra were detected with an Ocean Optics spectrograph equipped with a detector array cooled to –15°C

due to higher photon absorption in tissue and the differences in sample and collection geometries in relation to the scattering mean free path length.

3.4 Applications

3.4.1 Biomedical Applications

Probing of Bones Through Skin for Disease Diagnosis

As discussed in [Chap. 14] there is considerable benefit to be obtained from applying Raman spectroscopy to the analysis of bone matrices. The ability to perform such interrogation quickly, safely and, most importantly, non-invasively through soft overlying tissue opens a host of new potential applications including the diagnosis of brittle bone disease and osteoporosis [13, 51, 52]. Building on the pioneering work of Morris et al. [13, 50] in this area, both the temporal and spatial Raman approaches have been applied successfully. The first non-invasive study of bone matrix was reported by Draper

et al. [51] who (using Kerr gating) successfully detected the spectral signature of *osteogenesis imperfecta* (brittle bone disease) in mouse limbs through 1 mm of overlying soft tissue. The presence of the condition was apparent from differences in relative band intensities between the organic (collagen) and mineral (phosphate) components. This represented a major milestone, although instrumental complexity and the excessively high laser intensities (two to three orders of magnitude above the legal limits for skin illumination) precluded an extension to human subjects.

These issues were subsequently addressed with the advent of SORS, which only requires continuous wave laser beams with substantially lower intensities. The first use of SORS in the area of non-invasive spectroscopy of bones was reported by Schulmerich et al. [30] who obtained Raman spectra of bone from depths of several millimetres in animal and human cadavers using multivariate curve resolution (band-targeted entropy minimisation (BTEM)). The subsequent use of a ring illumination geometry (equivalent to inverse SORS) by Schulmerich et al. [35] permitted further increases in the quality of Raman spectra and penetration depth. The team succeeded in determining the ratio of the intensities of the phosphate $\left(958\,\mathrm{cm}^{-1}\right)$ and carbonate $\left(1070\,\mathrm{cm}^{-1}\right)$ bands of chicken tibia (a potential indicator of the presence of osteoporosis [52]), through 4 mm of overlying soft tissue to within an accuracy of 8%. Typical Raman spectra obtained in these experiments are shown in Fig. 3.10.

This group has developed methodology for in vivo subsurface spectroscopy of anaesthised mice and other small animals [53]. In this study of 32 animals, they demonstrated that there is no statistically significant difference between measurements made in vivo and on the exposed cortical bone of the femur after killing of the animals. Because of the small size of the mouse, alignment of the probe over the bone is critical for obtaining accurate results. It is expected that it may be easier to do in vivo measurements in larger animals because of the greater ease of positioning multifibre probes.

Parallel research by Matousek et al. [32] demonstrated the feasibility of obtaining the Raman spectra of bones from humans in vivo. Although the Raman spectra were of limited quality with some overlying tissue signals present, the experiment demonstrated that the key spectral features of human bone could be measured transcutaneously in vivo under safe illumination conditions. The measurements were performed with a laser power of only 2 mW, approximately an order of magnitude *below* the safe level for skin illumination in the near infrared. In these measurements a ring fibre probe with 0 and 3 mm spatial offsets was used; scaled subtraction of the spectra obtained at the two offsets produced an estimate for the spectrum of the underlying bone. The measurements were performed on the thumb distal phalanx bone of volunteers through 2 mm of overlying soft tissue. For further details of the research in this area the reader is referred to [Chap. 14].

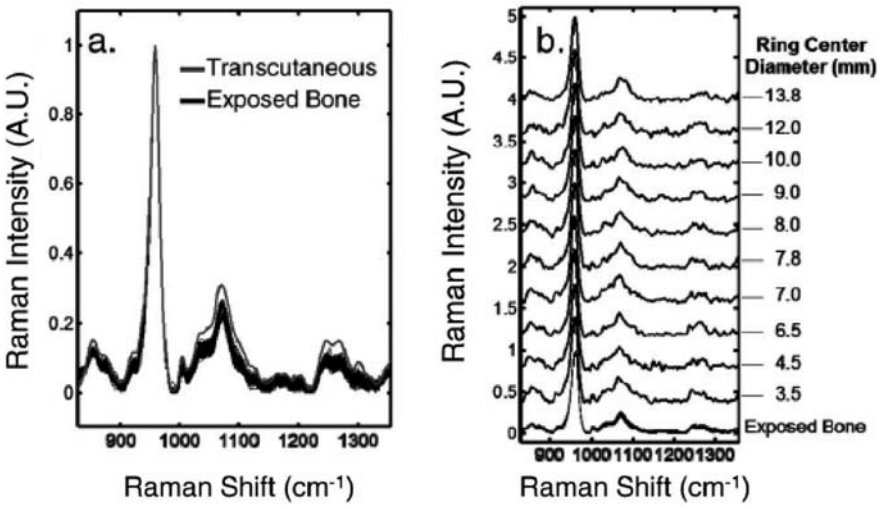

Fig. 3.10. Transcutaneous Raman spectra of dog tibia positioned at the medial side of the left tibia at the diaphysis, with 2 mm of overlying tissue. **a** Averaged ($n = 500$) transcutaneous spectra (*grey*) and exposed bone ($n = 100$) spectra (*black*). **b** Recovered bone spectrum at ring/disk spacings between 3.5 and 13.8 mm (reprinted with permission from [20]. Copyright (2007) Society for Applied Spectroscopy)

Non-invasive Cancer Detection

As discussed in [Chap. 13], SORS and transmission Raman are applicable to the non-invasive detection of the chemical composition of calcifications within breast tissue. Their detection, with the high chemical specificity inherent to Raman spectroscopy, opens the prospect of non-invasive identification of associated malignant and benign lesions, thus providing additional diagnostic power to more established techniques (such as X-ray mammography) which are blind to chemical composition. The current protocol following detection of suspect calcifications by X-ray mammography is a needle biopsy, which in most cases (70–90%) results in the detection of a benign lesion. The potential for the non-invasive characterisation of the chemical make up of calcifications buried deep within tissue was conceptually demonstrated by Baker et al. [54], Stone et al. [55] and Matousek et al. [56] using Kerr-gated Raman, SORS and transmission Raman on chicken breast tissue phantoms. The penetration depths achieved were 0.9, 8.7 and 16 mm, respectively.

The research in this area builds on the earlier work of Haka et al. [57] who found that excised calcifications can be classified into two groups using Raman spectroscopy: type I – calcium oxalate dihydrate (cod) and type II – calcium hydroxyapatite (hap). Calcium oxalate crystals are mainly found in benign ductal cysts while calcium hydroxyapatite is found in both carcinoma and in benign breast tissue; the chemical specificity of Raman spectroscopy identifies

significant spectral differences between the calcifications found in benign and malignant lesions. For details of the research in this area the reader is referred to [Chap. 13].

3.4.2 Pharmaceutical Applications

Forensic Applications

An area where SORS has proved to be particularly useful is the authentication of pharmaceutical products through non-invasive chemical analysis of the content of opaque plastic bottles and other types of packaging. The method offers a unique potential to inspect and chemically identify products throughout the entire supply chain in a non-invasive and non-destructive manner. The need for such inspection has heightened in recent years with the increase of counterfeit products on the market [58]. The targeted drugs in the developed world often include lifestyle drugs and drugs for chronic diseases. More seriously, in Africa and Asia, it is the essential life-saving medicines, such as anti-infective drugs, which are plagued by this growing problem [59, 60].

Raman techniques offer an attractive alternative to current methods (principally NIR spectroscopy) in which subtle spectral differences in composition are often hard to detect and chemometric tools are routinely required for data interpretation. In addition, NIR cannot be deployed non-invasively in many cases because of the interference and absorption of NIR signal by common packaging materials. Although conventional Raman spectroscopy has been used [61], in many instances, and in particular with darkly coloured coatings or capsules, or opaque packaging, the Raman signal of the active pharmaceutical ingredient (API) can be heavily polluted (or totally masked) by fluorescence and Raman signals originating from the coating, capsule [45] or blister pack itself. These interfering signals reduce the sensitivity of the technique and often preclude the observation of the API and other ingredients altogether.

Recently Eliasson and Matousek [26, 62] demonstrated that SORS can provide a chemical signature of the internal content of opaque plastic containers. This is demonstrated in Fig. 3.11 for aspirin tablets held inside an opaque (white) plastic pharmaceutical bottle (1.3 mm thick). The conventional Raman signal is overwhelmed by the Raman component originating from the container wall and is consequently ineffective in determining the contents of the bottle. In contrast, the SORS method using a scaled subtraction of two SORS spectra measured at different spatial offsets yields a clean Raman spectrum of the tablets inside the bottle. SORS has also been used in the detection of counterfeit anti-malarial tablets by Ricci et al. [63]; the chemical specificity of Raman spectroscopy readily distinguished between genuine and fake tablets and identified the content of the counterfeit tablets.

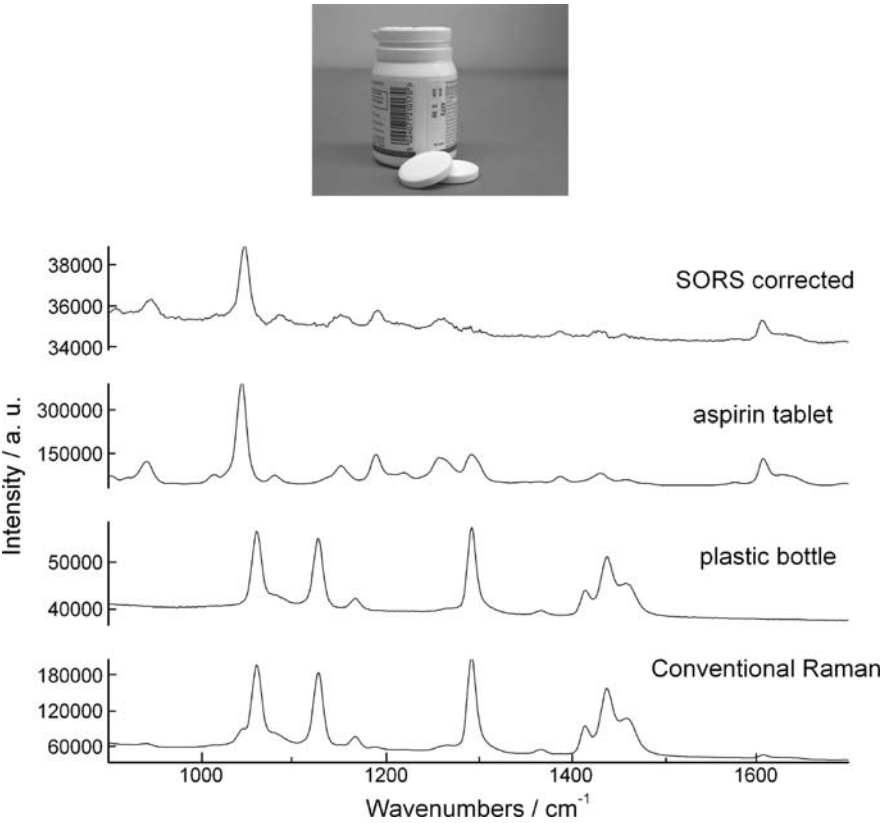

Fig. 3.11. Non-invasive Raman spectra of aspirin tablets measured through a white, diffusely scattering 1.3 mm thick plastic container. Conventional Raman and the scaled and subtracted SORS data are shown together with the reference Raman spectra of aspirin and the plastic container. The conventional Raman spectrum is dominated by the Raman signal of the container masking the Raman signal of the aspirin contents. The acquisition time was 1 s and the laser beam power 250 mW (N.A. Macleod, P. Matousek, Emerging non-invasive Raman methods in process control and forensic applications, Pharm. Res. **25**, 2205 (2008). Copyright (2008) Springer)

Quality Control of Pharmaceutical Products

In a number of process analytical technology (PAT) applications in the pharmaceutical industry it is desirable to monitor rapidly and non-invasively the bulk content of drugs with high chemical specificity. Although NIR absorption spectroscopy has been used widely in this area its comparatively low chemical specificity places limits on its usefulness. As noted earlier, transmission Raman is particularly well suited for this application since it removes the key obstacle of conventional Raman, the subsampling problem [43]. Matousek and

Parker et al. [45] also demonstrated that the transmission Raman geometry can also dramatically reduce the fluorescence background originating from capsule shells, permitting more sensitive spectroscopic interrogation of the bulk capsule content. This also applies to coated tablets where fluorescence originating from the coating is suppressed.

The ability of the transmission Raman approach to determine not only the chemical signature of the internal make-up of pharmaceutical tablets and capsules but also to *quantify* the content was recently demonstrated experimentally by Johansson et al. [64] using 20 test tablets (3.3 mm thick) prepared in a laboratory environment. The active pharmaceutical ingredient (API) was quantified (using partial least squares regression analysis) with a relative root mean square error of 2.2%. The study was also performed in a conventional backscattering Raman geometry which yielded a lower relative accuracy of 2.9% under the same experimental conditions due to a strong subsampling effect. This was confirmed by the analysis of an outlier spectrum using the backscattering mode that exhibited a clear deviation from the expected intensity profile for the API and excipients for the given concentration and was explained as an inhomogeneity present in the probed area. No such outlier was found in the corresponding data collected in the transmission geometry which samples the entire bulk content of the tablet and effectively averages

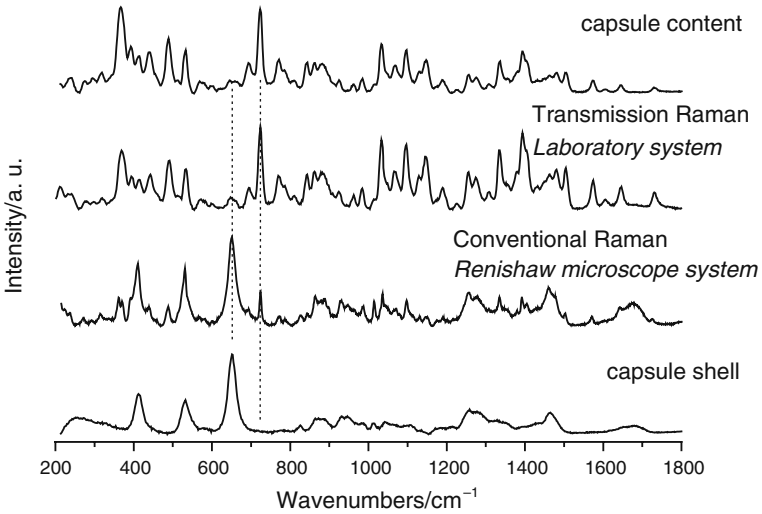

Fig. 3.12. Non-invasive Raman spectra of pharmaceutical capsules. The spectra were obtained using a laboratory instrument configured in the transmission Raman geometry and a standard commercial Raman microscope (Renishaw) in conventional backscattering geometry. The Raman spectra of an empty capsule shell (lowest trace) and the capsule content itself (*top trace*, the capsule content was transferred into an optical cell) are shown for comparison. The *dashed lines* indicate the principal Raman bands of the capsule and of the API (this figure was published in [65], Copyright Elsevier (2008))

any heterogeneities. A parallel study on pharmaceutical capsules yielded a relative accuracy of 3.6%. The study also indicated that the transmission Raman mode requires a linear calibration model relative to conventional backscattering Raman and was capable of providing an accurate model based on only two or three calibration spectra.

In parallel research, the feasibility of quantifying the content of real production line type samples prepared in a laboratory environment was demonstrated by Eliasson et al. [65]. This study used 150 capsules and established the feasibility of quantifying the active pharmaceutical ingredient to within a few percent relative error in the transmission Raman mode through capsules containing a high level of TiO_2. The intense interfering signals of the capsules precluded accurate analysis by other techniques including conven-

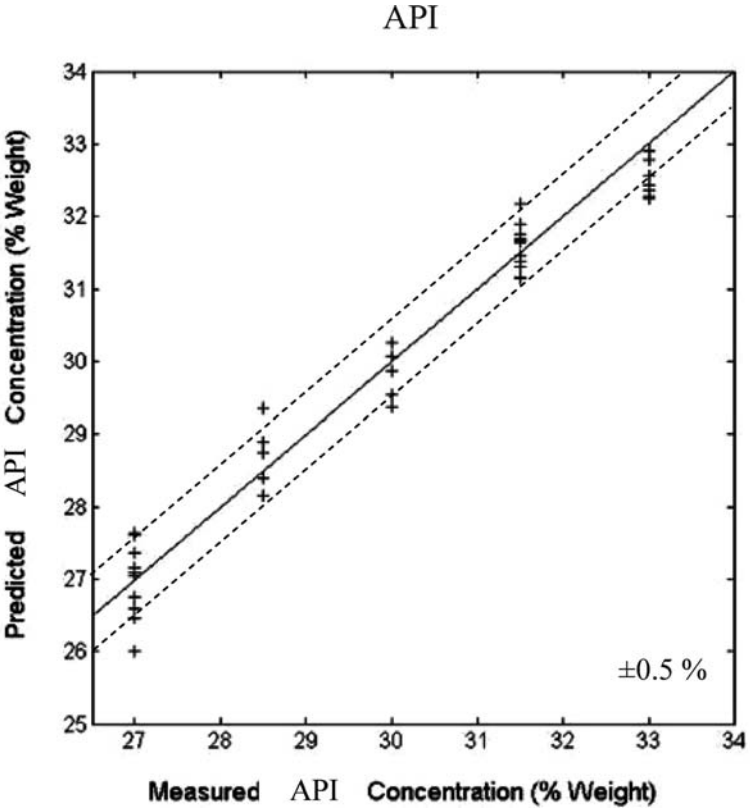

Fig. 3.13. Partial least-squares (PLS) calibration of the API data set (5 s accumulation time). Spectra were baseline corrected, normalised to unit length and mean centred. The data set was randomly split into a calibration set (two-thirds) and a prediction set (one-third); obvious outliers from the PCA analysis were excluded from the analysis. The graph shows predicted versus measured API concentration of the prediction set. The *straight line* represents the 45° diagonal (this figure was published in [65], Copyright Elsevier (2008))

tional Raman and NIR absorption. The adoption of the transmission concept led to the suppression of the interfering Raman capsule signal by a factor of 33 (see Fig. 3.12) permitting accurate quantification of the API with a relative root mean square error of 1.2% with 5 s acquisition time (see Fig. 3.13). The reduction of the acquisition time to 1 s yielded a still acceptable level of accuracy with the relative root mean square error increasing to 1.8%.

These feasibility studies indicate that the transmission geometry is particularly well suited for the non-invasive probing of pharmaceutical tablets and capsules. The ability to use defocused beams with transmission Raman spectroscopy also makes it possible to increase laser power without risking sample damage, thus further decreasing the exposure times required or improving the spectral quality. The large illumination and collection areas also dramatically reduce requirements for the alignment of the sample in front of the instrument. Further reduction of the acquisition times with tablets can also be accomplished using a 'unidirectional' mirror, which so far has not been used in any quantification studies.

3.5 Conclusions

The non-invasive Raman spectroscopic techniques for deep probing of turbid media highlighted in this chapter promise to impact on many analytical areas. The combination of the established advantages of Raman spectroscopy with the ability to probe deeply hidden layers holds great promise across a variety of fields. Several new exciting potential applications are already emerging on the horizon including the diagnosis of bone disease and breast cancer, quality control and authentication of pharmaceutical products and the detection of powder and liquid explosives and illicit drugs through packaging. The scope and diversity of these applications is a direct result of the flexibility and straightforward adaptability of the basic concept to specific conditions and problems.

Acknowledgements

The authors wish to thank Dr Darren Andrews and Dr Tim Bestwick of CLIK Knowledge Transfer and Dr Charlotte Eliasson, Professor Anthony Parker and Professor Mike Dunne of the Science and Technology Facilities Council for their support of this work. The EPSRC is also gratefully acknowledged for their support (grant EP/D037662/1).

References

1. M.J. Pelletier, *Analytical Applications of Raman Spectroscopy* (Blackwell Science, Oxford, 1999)

2. B.B. Das, F. Liu, R.R. Alfano, Rep. Prog. Phys. **60**, 227 (1997)
3. J.C. Hebden, A. Gibson, R. Yusof, N. Everdell, E.M.C. Hillman, D.T. Delpy, S.R. Arridge, T. Austin, J.H. Meek, J.S. Wyatt, Phys. Med. Biol. **47**, 4155 (2002)
4. H. Koizumi, Y. Yamashita, A. Maki, T. Yamamoto, Y. Ito, H. Itagaki, R. Kennan, J. Biomed. Opt. **4**, 403 (1999)
5. T.J. Pfefer, K.T. Schomacker, M.N. Ediger, N.S. Nishioka, Appl. Opt. **41**, 4712 (2002)
6. N. Ghosh, S.K. Majumder, H.S. Patel, P.K. Gupta, Opt. Lett. **30**, 162 (2005)
7. L. Quan, N. Ramanujam, Opt. Lett. **27**, 104 (2002)
8. S.C. Gebhart, S.K. Majumder, A. Mahadevan-Jansen, Appl. Opt. **46**, 1343 (2007)
9. J. Wu, Y. Wang, L. Perelman, I. Itzkan, R. Dasari, M.S. Feld, Appl. Opt. **34**, 3425 (1995)
10. N. Everall, T. Hahn, P. Matousek, A.W. Parker, M. Towrie, Appl. Spectrosc. **55**, 1701 (2001)
11. N. Everall, T. Hahn, P. Matousek, A.W. Parker, M. Towrie, Appl. Spectrosc. **58**, 591 (2004)
12. P. Matousek, N. Everall, M. Towrie, A.W. Parker, Appl. Spectrosc. **59**, 200 (2005)
13. M.D. Morris, P. Matousek, M. Towrie, A.W. Parker, A.E. Goodship, E.R.C. Draper, J. Biomed. Opt. **10**, 014014 (2005)
14. P. Matousek, M. Towrie, A. Stanley, A.W. Parker, Appl. Spectrosc. **53**, 1485 (1999)
15. P. Matousek, M. Towrie, C. Ma, W.M. Kwok, D. Phillips, W.T. Toner, A.W. Parker, J. Raman Spectrosc. **32**, 983 (2001)
16. P. Matousek, M. Towrie, A.W. Parker, J. Raman Spectrosc. **33**, 238 (2002)
17. P. Matousek, Chem. Soc. Rev. **36**, 1292 (2007)
18. P. Matousek, I.P. Clark, E.R.C. Draper, M.D. Morris, A.E. Goodship, N. Everall, M. Towrie, W.F. Finney, A.W. Parker, Appl. Spectrosc. **59**, 393 (2005)
19. P. Matousek, M.D. Morris, N. Everall, I.P. Clark, M. Towrie, E. Draper, A. Goodship, A.W. Parker, Appl. Spectrosc. **59**, 1485 (2005)
20. M.V. Schulmerich, K.A. Dooley, T.M. Vanasse, S.A. Goldstein, M.D. Morris, Appl. Spectrosc. **61**, 671 (2007)
21. E. Widjaja, C.Z. Li, M. Garland, Organometallics **21**, 1991 (2002)
22. W. Chew, E. Widjaja, M. Garland, Organometallics **21**, 1982 (2002)
23. C.Z. Li, E. Widjaja, M. Garland, J. Catal. **213**, 126 (2003)
24. E. Widjaja, C.Z. Li, W. Chew, M. Garland, Anal. Chem. **75**, 4499 (2003)
25. E. Widjaja, N.J. Crane, T.C. Chen, M.D. Morris, M.A. Ignelzi, B.R. McCreadie, Appl. Spectrosc. **57**, 1353 (2003)
26. C. Eliasson, P. Matousek, Anal. Chem. **79**, 1696 (2007)
27. C. Eliasson, N.A. Macleod, P. Matousek, Anal. Chem. **79**, 8185 (2007)
28. C. Eliasson, M. Claybourn, P. Matousek, Appl. Spectrosc. **61**, 1123 (2007)
29. J.Y. Ma, D. Ben-Amotz, Appl. Spectrosc. **51**, 1845 (1997)
30. M.V. Schulmerich, W.F. Finney, V. Popescu, M.D. Morris, T.M. Vanasse, S.A. Goldstein, Transcutaneous Raman spectroscopy of bone tissue using a non-confocal fiber optic array probe, in *Biomedical Vibrational Spectroscopy III: Advances in Research and Industry*, ed. by A. Mahadevan-Jansen, W.H. Petrich. Proceedings of SPIE, vol. 6093 (2006), article number 60930O

31. M.V. Schulmerich, W.F. Finney, R.A. Fredricks, M.D. Morris, Appl. Spectrosc. **60**, 109 (2006)
32. P. Matousek, E.R.C. Draper, A.E. Goodship, I.P. Clark, K.L. Ronayne, A.W. Parker, Appl. Spectrosc. **60**, 758 (2006)
33. B. Depret, P. Verkerk, D. Hennequin, Opt. Commun. **211**, 31 (2002)
34. P. Matousek, Appl. Spectrosc. **60**, 1341 (2006)
35. M.V. Schulmerich, K.A. Dooley, M.D. Morris, T.M. Vanasse, S.A. Goldstein, J. Biomed. Opt. **11**, 060502 (2006)
36. M.V. Schulmerich, M.D. Morris, T.M. Vanasse, S.A. Goldstein, Transcutaneous Raman spectroscopy of bone global sampling and ring/disk fiber optic probes, in *Advanced Biomedical and Clinical Diagnostic Systems V*, ed. by T. Vo-Dinh, W.S. Grundfest, D.A. Benaron, G.E. Cohn, R. Raghavachari. Proceedings of SPIE, vol. 6430 (2007), article number 643009
37. A.H. Hielscher, Curr. Opin. Biotech. **16**, 79 (2005)
38. M.V. Schulmerich, J.H. Cole, K.A. Dooley, M.D. Morris, J.M. Kreider, S.A. Goldstein, S. Srinivasan, B.W. Pogue, J. Biomed. Opt. **13**, 020506 (2008)
39. M.V. Schulmerich, S. Srinivasan, J. Kreider, J.H. Cole, K.A. Dooley, S.A. Goldstein, B.W. Pogue, M.D. Morris, Raman tomography of tissue phantoms and bone tissue. Paper presented at Biomedical Optical Spectroscopy, San Jose, CA, USA, SPIE, 2008
40. C.M. Carpenter, B.W. Pogue, S. Jiang, H. Dehghani, X. Wang, K.D. Paulsen, W.A. Wells, J. Forero, C. Kogel, J.B. Weaver, S.P. Poplack, P.A. Kaufman, Opt. Lett. **32**, 933 (2007)
41. S. Srinivasan, M. Schulmerich, J.H. Cole, K.A. Dooley, J.M. Kreider, B.W. Pogue, M.D. Morris, S.A. Goldstein, Opt. Express **16**, 12190 (2008)
42. B. Schrader, G. Bergmann, Z. Anal. Chem. **225**, 230 (1967)
43. P. Matousek, A.W. Parker, Appl. Spectrosc. **60**, 1353 (2006)
44. J. Johansson, S. Pettersson, S. Folestad, J. Pharm. Biomed. Anal. **39**, 510 (2005)
45. P. Matousek, A.W. Parker, J. Raman Spectrosc. **38**, 563 (2007)
46. P. Matousek, Appl. Spectrosc. **61**, 845 (2007)
47. K. Buckley, A. Goodship, N.A. Macleod, A.W. Parker, P. Matousek, Anal. Chem. **80**, 6006 (2008)
48. D.A. Long, *Raman Spectroscopy* (McGraw-Hill, New York, 1977)
49. J.C. Henderson, Q. Su, R. Grobe, Laser Phys. **14**, 515 (2004)
50. A. Carden and M.D. Morris, J. Biomed. Opt. **5**, 259 (2000)
51. E.R.C. Draper, M.D. Morris, N.P. Camacho, P. Matousek, M. Towrie, A.W. Parker, A.E. Goodship, J. Bone Miner. Res. **20**, 1968 (2005) and references therein
52. B.R. McCreadie, M.D. Morris, T. Chen, D.S. Rao, W.F. Finney, E. Widjaja, S.A. Goldstein, Bone **39**, 1190 (2006)
53. M.V. Schulmerich, J.H. Cole, J.M. Kreider, F. Esmonde-White, K.A. Dooley, S.A. Goldstein, M.D. Morris, Appl. Spectrosc. **63**, 286 (2009)
54. R. Baker, P. Matousek, K.L. Ronayne, A.W. Parker, K.Rogers, N. Stone, Analyst **132**, 48 (2007)
55. N. Stone, R. Baker, K. Rogers, A.W. Parker, P. Matousek, Analyst **132**, 899 (2007)
56. P. Matousek, N. Stone, J. Biomed. Opt. **12**, (2007) 024008
57. S. Haka, K.E. Shafer-Peltier, M. Fitzmaurice, J. Crowe, R.R. Dasari, M.S. Feld, Cancer Res. **62**, 5375 (2002)

58. R. Cockburn, P.N. Newton, E.K. Agyarko, D. Akunyili, N.J. White, PLoS Med. **4**, 1553 (2007)
59. P. Aldhous, Nature **434**, 132 (2005)
60. P.N. Newton, M.D. Green, F.M. Fernández, N.P.J. Day, N.J. White, Lancet Infect. Dis. **6**, 602 (2006)
61. M.R. Witkowski, Am. Pharm. Rev. **8**, 56 (2005)
62. C. Eliasson, P. Matousek, Laser Focus World **43**, 123 (2007)
63. C. Ricci, C. Eliasson, N.A. Macleod, P. Newton, P. Matousek, S.G. Kazarian, Anal. Bioanal. Chem. **389**, 1525 (2007)
64. J. Johansson, A. Sparen, O. Svensson, S. Folestad, M. Claybourn, Appl. Spectrosc. **61**, 1211 (2007)
65. C. Eliasson, N.A. Macleod, L. Jayes, F.C. Clarke, S. Hammond, M.R. Smith, P. Matousek, J. Pharm. Biomed. Anal. **47**, 221 (2008)

4

Applications of Raman and Surface-Enhanced Raman Scattering to the Analysis of Eukaryotic Samples

Franziska Schulte, Virginia Joseph, Ulrich Panne, and Janina Kneipp

Abstract In this chapter, we discuss Raman scattering and surface-enhanced Raman scattering (SERS) for the analysis of cellular samples of plant and animal origin which are several tens to hundreds of microns in size. As was shown in the past several years, the favorable properties of noble metal nanostructures can be used to generate SERS signals in very complex biological samples such as cells, and result in an improved sensitivity and spatial resolution. Pollen grains, the physiological containers that produce the male gametes of seed plants, consist of a few vegetative cells and one generative cell, surrounded by a biopolymer shell. Their chemical composition has been a subject of research of plant physiologists, biochemists [1, 2], and lately even materials scientists [3, 4] for various reasons. In spite of a multitude of applied analytical approaches it could not be elucidated in its entirety yet. Animal cells from cell cultures have been a subject of intense studies due to their application in virtually all fields of biomedical research, ranging from studies of basic biological mechanisms to models for pharmaceutical and diagnostic research. Many aspects of all kinds of cellular processes including signalling, transport, and gene regulation have been elucidated, but many more facts about cell biology will need to be understood in order to efficiently address issues such as cancer, viral infection or genetic disorder. Using the information from spectroscopic methods, in particular combining normal Raman spectroscopy and SERS may open up new perspectives on cellular biochemistry. New sensitive Raman-based tools are being developed for the biochemical analysis of cellular processes [5–8].

4.1 Surface-Enhanced Raman Scattering and its Applications to Bioanalytical Chemistry

As demonstrated by numerous papers, including the chapters of this and other books, Raman spectroscopy has long been used for the analysis of biological samples. In the inelastic Raman scattering process, photons from a laser source interact with the molecular vibrations of a sample, yielding scattered photons with a changed energy. The energy difference corresponds to the energy of the molecular vibration the photons interacted with. The resulting spectra

provide superimposed vibrational information on structure, composition and interactions from all classes of molecules in the samples. Thereby, information obtained in Raman spectra of biological samples such as cells or pollen or other tissues naturally integrates the genomic, proteomic and metabolic status of the sample. Other kinds of complex biological materials that have been studied by Raman spectroscopy include prokaryotes, fungi, animal cells and foodstuffs [9–16].

Raman scattering is a very weak effect, with typical Raman cross-sections being 10^{-30}–$10^{-26}\,\mathrm{cm}^2$ per molecule. As described in a large body of literature, in surface-enhanced Raman scattering (SERS), we observe an increase in Raman cross-section from molecules that are in close proximity to a noble metal nanostructure [17–20]. Cross-sections in SERS can be on the order of $10^{-16}\,\mathrm{cm}^2$ per molecule and higher, and hence become comparable to typical cross-sections of fluorophores [21]. The favourable optical properties of noble metal nanostructures, based on their surface plasmon polaritons, provide the key effect for the observation of SERS. The so-called electromagnetic field enhancement, the major contributor to the enhancement observed in SERS, is brought about by resonances of the optical fields (excitation and Raman scattering field) with surface plasmons of gold or silver nanostructures. The plasmon resonance condition for silver and gold is fulfilled in the visible and near infrared wavelength range, and therefore nanostructures of these metals are particularly suited for SERS experiments excited with light of such frequencies. Since the plasmon resonance covers a relatively wide frequency range compared to the frequency shift between excitation and Raman scattered light, both excitation and scattering fields can be in resonance with the surface plasmons of the metal nanostructures. In such a case, the SERS intensity enhancement scales approximately to the fourth power of the enhancement of the local optical fields. In addition to the electromagnetic field enhancement, the so-called chemical or electronic enhancement takes place, which yields an increase in Raman cross-section $\left(\sigma^{\mathrm{R}}{}_{\mathrm{ads}}\right)$ due to the electronic interaction of the analyte molecule with the metal surface. Several mechanisms have been proposed for this chemical enhancement [17, 20, 22]. Expression 1 summarizes the two different enhancement contributions:

$$P_{\mathrm{SERS}}(\nu_{\mathrm{S}}) \propto N \cdot I(\nu_{\mathrm{L}}) \cdot \left|A(\nu_{\mathrm{L}})\right|^2 \cdot \left|A(\nu_{\mathrm{S}})\right|^2 \cdot \sigma^{\mathrm{R}}_{\mathrm{ads}},$$

with N being the number of molecules involved in the Raman process, I the laser intensity, $A\,(\nu_{\mathrm{L}})$ and $A\,(\nu_{\mathrm{S}})$ enhancements of the excitation and the scattering field and $\sigma^{\mathrm{R}}{}_{\mathrm{ads}}$ the Raman cross-section of the adsorbed molecule.

Since its observation more than three decades ago by VanDuyne and Jeanmaire as well as Albrecht and Creighton [23, 24], SERS has been gaining popularity in analytical and physical chemistry and very recently also in the biomedical field [25–28]. The potential of SERS in bioanalytics lie in the combination of sensitivity that can be achieved [29–31] with the structural information that is generated in Raman spectroscopy as a vibrational method. In addition to the increased sensitivity, SERS offers the opportunity

of probing very small volumes, owing to the fact that the SERS signal comes from the immediate vicinity of a metal nanostructure whose size and shape dictate the range of the electromagnetic field enhancement. Individual metal nanostructures or their aggregates can act as tiny probes that can be brought to the analyte of interest or be arranged in space. The concept of a SERS label, where 'reporter' molecules with a specific SERS signature are attached to metal nanostructures [25, 32, 33], is generally accepted and already being commercialized. SERS labels provide significant advantages over fluorescence labels in particular because of their higher stability and their multiplexing capability. The latter results from the fingerprint nature of a Raman spectrum compared to broad and relatively unspecific fluorescence bands of conventional optical labels. If resonant enhancement of the reporter is used in addition to SERS, SERRS labels can provide a higher sensitivity than fluorescence and enable quantitative detection of analytes; for a summary see e.g. [34].

SERS can provide new vibrational spectroscopic perspectives on biological and physiological processes. This is true literally in a topological sense when SERS spectra are obtained from a specific location within a cell or complex biomatrix, but also since SERS provides selectivity regarding which compounds in a heterogeneous mixture have access to the SERS substrate and can be detected. The spectra of the biological samples themselves, rather than those of label molecules, are of great interest in many bioanalytical applications of SERS. Not only the characterization and identification of bacteria [27, 35–38], but also the sensitive detection of their spores [39] can be achieved by SERS. With tip-enhanced Raman spectroscopy (TERS), where a silver-coated AFM tip serves as substrate for SERS [40], membranes of individual bacterial cells can be studied [41]. SERS-active nanoparticles assembled on surfaces form efficient sensors for important metabolites, such as glucose and lactate, also through additional selectivity implemented through self-assembled monolayers (SAMs) [42, 43].

In this chapter, we will discuss the SERS signals from two different types of eukaryotic cells. SERS in cells from cell cultures will be discussed regarding the ability to detect intrinsic cellular molecules of physiological importance. Emphasis of this chapter will be put on a second type of eukaryotic system, the water-soluble cellular fraction of pollen grains. As will be explained, SERS on the cells from pollen grains gives us additional information to the normal Raman information we use to study pollen biochemistry and will enable sensitive detection for fast allergy warning.

4.2 Raman Spectroscopy of Pollen

4.2.1 Questions and Motivation

It has become clear that pollen grains, owing to their biological function, consist of a broad variety of molecules. These range from an extremely stable

biopolymer of largely unknown composition and structure, the sporopollenin of their outer layer, to flavonoid and carotenoid pigments, lignin, pectin and the constituents of the cells in the pollen interior, namely proteins, lipids, carbohydrates and nucleic acids [1, 2, 4, 44]. Many phenomena related to pollen are not well understood yet, among them the composition of the aforementioned sporopollenin capsules and the local distribution of molecules. To date, approaches to pollen chemical characterization involve purification, the latter implying possible modification or extraction of selected pollen constituents (allergens, carotenoids and lipids) [45, 46].

Different from identification of other biological entities, e.g. in bacterial typing, current pollen identification procedures do not rely on molecular parameters, but mainly on morphological information obtained through optical or electron microscopies. Morphological information from light microscopy and image analysis is also the basis of current allergy warning systems. In the light of the urgent need for more efficient pollen identification and early warning systems due to an increased prevalence of pollen allergies [47], a fast identification method based on objective chemical information is sought.

The first Raman spectroscopic work on whole pollen was carried out in resonance with electronic transitions in molecules mainly from the pollen exine layer by Manoharan et al. [48]. Non-resonant Raman spectroscopy has been proposed for studies of pollen for several years, but was based on feasibility studies on the few freeze-dried pollen species that are commercially available [49–51]. Some of these spectra in the literature were excited at very high laser powers of several watts and discussed very high fluorescence backgrounds [49, 50], even at NIR excitation [51]. The idea of using vibrational spectroscopic methods for discrimination between pollen from different plant species, similar to classification approaches for microorganisms, cells and tissue types is not new. However, it must have been hampered by methodological problems, in particular the fluorescence background. We could show that fresh pollen samples, which are of particular relevance to the development of actual on-line pollen detection methods, exhibit only low levels of fluorescence and enable acquisition of high-quality Raman spectra [52]. A study on IR spectra of dried pollen from different plants (trees, shrubs and grasses) demonstrated separation of different species within the *Citrus* genus [53]. In this case, however, sample preparation (preparation of KBr pellets) was relatively complicated. The few other vibrational studies of pollen conducted so far investigated the spectra of different species that were also members of different genera, different families and oftentimes even different orders of plants [48, 49, 51, 53]. In a study using surface-enhanced Raman scattering (SERS) on four species, which concluded that pollen of the same two plant families have similar SERS spectra [54], the pollen did not only belong to different plant families, but also to different orders, classes and even divisions in the plant kingdom.

All these studies left the question open whether distinction between Raman spectra down to species level can really be achieved (within the same genus). To find an answer to this question, we have included in our sample set a

number of species that belong to the same genus, the taxonomic rank next to the species level and a number of genera that belong to the same families. Species of the same genus are assumed to have a common ancestor species and are therefore closely related.

As we will describe in the following, individual fresh pollen grains and their morphological constituents can be characterized and also classified in situ without prior preparation. In the method presented here, the classification of pollen is based on their biochemical fingerprint revealed in their Raman spectrum. Raman spectroscopy is non-destructive and can be carried out with single pollen grains or their fragments.

4.2.2 Mapping Pollen Biochemistry

With a spectrometer coupled to a microscope, it is possible to collect Raman spectra from individual pollen grains. Examples of spectra from fresh pollen are shown in Fig. 4.1. The most prominent bands in the spectra are labelled in the figure, their tentative assignments are given in Table 4.1. As can be seen there, the pollen spectra consist of superimposed signals from a variety of biomolecules, such as nucleic acids, lipids and proteins. Considering the diameter of the pollen grains as microscopic objects of 15–60 microns and millimetre penetration depth of the excitation laser in the pollen material, we can assume to probe the outer pollen wall (exine) together with the cellulose-rich intine layer beneath and the cellular pollen interior. In accordance with this, we detect the spectral signatures of nucleotide bases, aromatic amino acids in protein side chains, lipid molecules, the nucleic acid and protein amide backbones, pigments, sugars and their polymers (compare Table 4.1).

To elucidate the contribution of the different histological structures to the average Raman spectral signatures from intact pollen grains, we conducted spatially resolved measurements on sections of rye pollen grains. Such mapping experiments can help separation of predominant spectral contributions from different substructures.

Rye pollen was purchased from Sigma, mounted for cryo-sectioning in a drop of Jung Tissue Freezing Medium (Leica Microsystems, Germany) and snap-frozen. After equilibration to –20°C, cryo-sections were cut at a thickness of 10 µm using a cryostat (Leica, Germany). The sections were thaw-mounted onto polished CaF_2 crystals for Raman mapping experiments.

The measurements were performed using a LabRam HR800 Raman setup (Horiba Jobin Yvon, Bensheim, Germany). A BX41 microscope (Olympus, Hamburg, Deutschland) with a 100× objective coupled to the 800 mm focal length spectrograph. To reject the Rayleigh scattered light, notch filters were used. The spectrometer was equipped with a nitrogen-cooled CCD (1024×256 pixels, Horiba). Using the computer-controlled x,y-stage of the Raman microscope, the sections of the pollen grains were raster-scanned. In this way, a Raman spectrum was obtained in each of the sampling positions of a predefined grid. Chemical imaging was done using CytoSpec (CytoSpec Inc.,

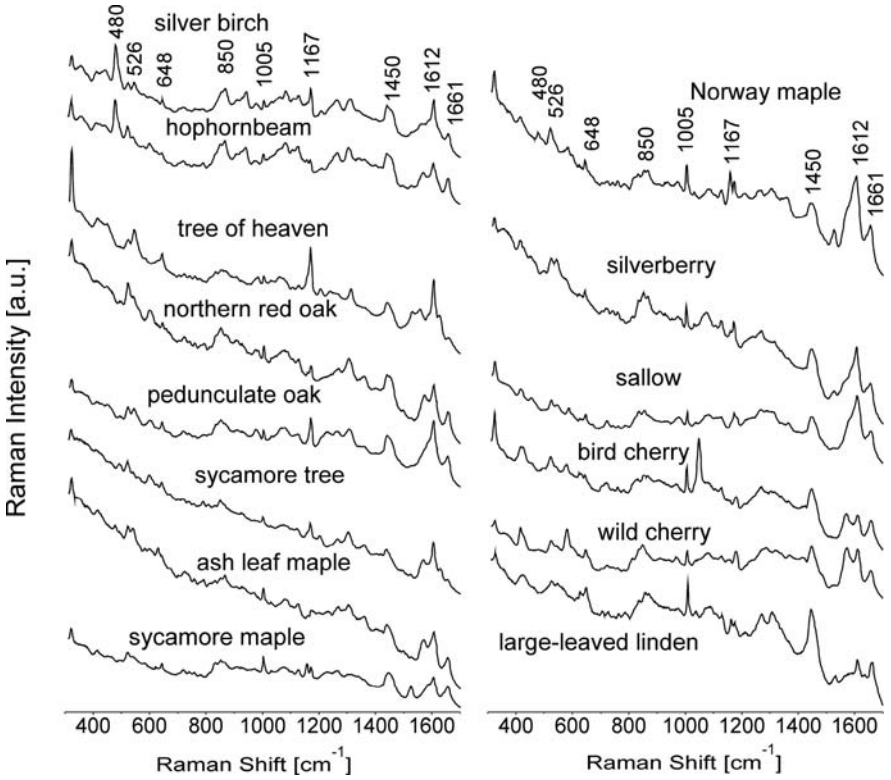

Fig. 4.1. Raman spectra of pollen. The Raman spectra were excited with a wavelength of 785 nm, laser power 18 mW (irradiance $1.8 \times 10^6\,\mathrm{W/cm^2}$), accumulation time was 10 s. The spectra are averages from 5 to 10 individual pollen grains from different samples (compare also Fig. 4.3)

Boston, USA). For the plots of the intensities as a function of spatial coordinate, after baseline correction, the areas under the respective bands were calculated. Figure 4.2 shows results of four examples of mapping experiments.

The plots of the intensities of selected characteristic bands as a function of lateral position (so-called chemical maps) provide information on the amount of the respective molecules or molecular groups in the different morphological structures (Fig. 4.2). The band at $784\,\mathrm{cm^{-1}}$ can be assigned to out-of-plane deformation vibrational modes of the nucleobases cytosine, thymine and uracil and serves as an indicator for the presence of nucleic acids. At $483\,\mathrm{cm^{-1}}$, a C–C–C deformation of carbohydrate polymers such as starch or pectin is present in some of the spectra. To study the distribution of protein compounds, we analysed characteristic signals of the amino acid phenylalanine ($1002\,\mathrm{cm^{-1}}$ ring breathe) as well as of the protein amide I band $\left(1651\,\mathrm{cm^{-1}}\right)$ that is brought about by vibrations of the protein backbones. The maximum of the phenylalanine signal co-localizes with a maximum in protein content

Table 4.1. Raman frequencies observed in spectra of whole pollen and their tentative assignments based on [70, 104–106] to the classes of molecules and/or vibrational modes (compare Figs. 4.1 and 4.5)

Raman shift (cm^{-1})	Tentative assignment
1661	U, C, G, C=O stretch
1650	Protein backbone, Amide I
1608	Phe, Tyr, Trp
1585	Proteins : Phe, Tyr
1573	G, A
1522	Carotenoid ν_1
1445	Lipids, proteins, $\delta(CH_2,\ CH_3)$
1360	Trp: indole ring
1279	Carotenoid ν_5
1268	Protein backbone: Amide III
1198	Tyr, Phe
1189	Carotenoid ν_2
1177	Nucleotides: base ν(CN)
1156	Carotenoid ν_3, C-H stretch, C-C stretch
1030	Proteins, Phe
1010	Carotenoid ν_6, C=C (ring breathe)
1012	Proteins, Trp
1004	Phe, proteins, C=C (ring breathe)
968	Carotenoid
850/830	Tyr, proteins, δ(CCH) aliphatic
784	C, T, U:δ(o-o-p)
780	ν(O–P–O) diester
717	Proteins: Met C–S stretch
643	Tyr
620	Phe, proteins (ring)
521	Cysteine disulfide bond, S–S-stretch
480	Pectin, δ(C–C–C) skeletal vibrations

Abbreviations: ν, stretching; δ, deformation; o-o-p, out-of-plane; Tyr, tyrosine; Phe, phenylalanine; Trp, tryptophan; Met, methionine; Cys, cysteine; A, adenine; T, thymine; C, cytosine; G, guanine

(compare examples in Fig. 4.2). A characteristic vibration, namely the $\nu_1/2\nu_{16a}$ Fermi doublet at 850/830 cm^{-1} [55], dominates some of the spectra of the pollen sections, and identifies *para*-disubstituted benzene rings. Its maximum signals localize to the pollen capsule, and no overlap is found with the protein signals in the pollen interior. Therefore, it can be inferred that the signal does not stem from the tyrosine side chains of proteins. The signal may be caused by non-protein tyrosine-containing structures, but also by other phenolic compounds, which have been discussed to be building blocks of the exine [56]. Raman signals that can be assigned to a deformation mode of CH_2 groups of aliphatic carbon chains at 1448 cm^{-1} are found in different regions of the

pollen grain. Consistent with the fact that such molecules are contained both in the phospholipids of cellular, nuclear and other membranes, but also in so far unidentified aliphatic compounds in the pollen exine, the CH_2 deformation intensity is high not only in the pollen capsule but also in some cellular regions (Fig. 4.2).

A major advantage of Raman spectroscopy in the chemical characterization of pollen is its applicability in situ. The pollen grains in this study were investigated without prior purification or extraction procedures, which has been the case in most other investigations on pollen composition so far [45, 46, 57, 58]. Using Raman microspectroscopy on sections of snap-frozen samples, the chemical composition and very likely also their ultrastructure remain unaltered, and the co-localization of individual components could be studied in the context of pollen micromorphology, simultaneously in very short

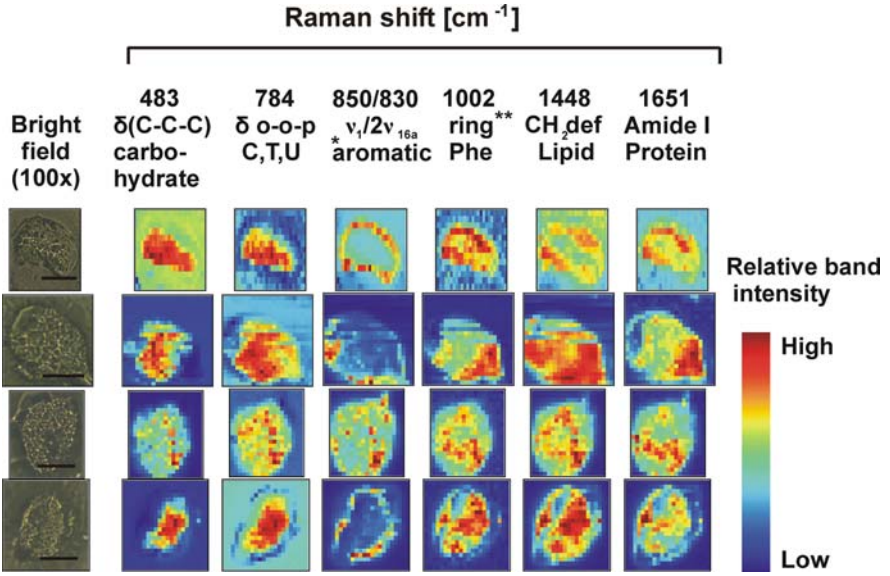

Fig. 4.2. Chemical maps of selected molecular groups in sections of rye pollen grains (four examples). The maps were constructed by plotting the intensities of the respective band as a function of lateral position. For comparison, a photomicrograph (bright field, 100×) is displayed (leftmost column). Scale bars: 20 µm. Abbreviations: ν, stretching; δ, deformation; o-o-p, out-of-plane; Phe, phenylalanine; A, adenine; T, thymine; C, cytosine. * represents the Fermi doublet at 850/830 cm^{-1} which is characteristic for *para*-disubstituted benzene rings. ** represents the band at 1002 cm^{-1} which is due to a breathing mode of the Phe ring. The diameter of the sampled spots was ∼1 µm, step width was 2 µm in each direction, except in one measurement (first row) where it was 1.5 µm in x direction and 3 µm in y direction. At each position in the predefined grid a Raman spectrum was measured using an excitation of 785 nm, 18 mW laser power and an acquisition time of 10 s. Reprinted with permission from [52]

times (several seconds per spectrum). The distribution of different molecular groups in the various structures of the pollen grains is not homogeneous. As illustrated by the example in Fig. 4.2, the observed localization of molecular compounds in the investigated rye pollen sections is in good agreement with cytochemistry. As expected, the area of the sporopollenin capsule can be easily recognized in spatially resolved measurements due to intense signals from, e.g. aromatic and aliphatic compounds. In the cells, the regions of the nuclei (DNA bands) and of carbohydrate reservoirs can be identified. Knowing about the spectral contributions from different parts of the pollen may help to develop methods not only for classification of whole pollen as shown here but also for pollen fragments in bioaerosols. The ability to obtain molecular information from pollen structures in situ is of significance to pollen research, considering that so far both protoplast and sporopollenin capsules have only been studied after purification by more or less harsh methods [57, 58].

4.2.3 Towards Raman-Based Allergy Warning Systems

Current pollen detection and warning systems are based solely on morphological information. Pollen samples are deposited from the air, pretreated, and then analysed microscopically. The method works well, but it can be slow. Our research is directed towards the development of a fast automated on-line detection of pollen species based on Raman spectral fingerprints. The Raman spectra are treated as patterns that can be recognized by identification algorithms, which are more objective and less time-consuming than mere visual inspection.

Pollen was collected during the flowering season of each respective tree species. The pollen samples were snap-frozen in liquid nitrogen and stored at –20°C. We considered snap-freezing as the method of choice if a sample is to be studied unaltered. Morphological structures are fully preserved due to prevention of ice crystal formation, and also the majority of important biological molecules including sensitive species such as RNA should be preserved. The pollen grains were snap-frozen within very short times upon removal from their flowers. About 45 min prior to the Raman experiments, the samples were thawed in a desiccator on CaF_2 slides to avoid accumulation of condensing water and possible hydration. Raman spectra were acquired over the range 350 cm^{-1}–1900 cm^{-1} using an integration time of 10 s per spectrum with 785 nm excitation (18 mW at a spot diameter of ~1 µm, corresponding to $\sim 1.8 \times 10^6$ W/cm^2 irradiance) after irradiation with laser light from a HeNe laser (633 nm, $\sim 1 \times 10^6$ W/cm^2 irradiance).

To test whether the full spectral patterns can be used like fingerprints for an overall chemical classification without decomposing the information, we conducted classification studies on whole pollen spectra (corresponding to the examples shown in Fig. 4.1a).

To base classification and possible identification upon the whole chemical information contained in the pollen, we used a multivariate method. For an

evaluation of overall variance between different pollens and to obtain an unbiased perspective on possible chemical differences, we aim at a classification method that does not require pre-selection of chemical parameters or weighing of input information. As a consequence, we chose to use hierarchical cluster analysis (HCA) as an unsupervised method.

Prior to analysis, the Raman shift axes of the spectra were calibrated using the Raman spectrum of 4-acetamidophenol. Pretreatment of the raw spectra, such as vector normalization and calculation of derivatives were done using Matlab (The Mathworks, Inc.) or OPUS (Bruker) software. OPUS NT software (Bruker, Ettlingen, Germany) was used to perform the HCA. The first derivatives of the spectra were used over the range from $380\,\mathrm{cm}^{-1}$ to $1700\,\mathrm{cm}^{-1}$. To calculate the distance matrix, Euclidean distances were used and for clustering, Ward's algorithm was applied [59].

We applied HCA to a spectral data set containing 91 spectra from different samples of 15 tree species using almost the full spectrum $\left(380\text{–}1700\,\mathrm{cm}^{-1}\right)$ (Fig. 4.3). The descriptions of the samples are listed in Table 4.2. The resulting dendrogram reveals formation of three large clusters (see Fig. 4.3). Except for the case of the different oak species and <4% other misclassifications, the spectra of the different samples of each respective species form individual groups within these larger clusters (Fig. 4.3). This result is in accordance with the assumption that the variation between different specimens of a particular species is smaller than the variation between species and permits us to conclude that most of the pollen samples of the different species studied here can be distinguished based on their Raman spectra. The average spectra of each of the species were displayed in Fig. 4.1.

As evidenced by the dendrogram in Fig. 4.3, separation down to species level is superimposed by a high similarity within genera. Examples for a high chemical similarity within the same genus are the spectra obtained from two species of *Prunus*, Bird Cherry and Wild Cherry. They form a distinct group, as do also two *Acer* species, Norway Maple and Sycamore Maple (see Fig. 4.3). However, the pollen spectra from a third species of *Acer*, the Ash-leaf Maple (or Maple Ash), resemble those of oak and sycamore tree pollen rather than the other *Acer* species. The tree is native to North America, different from the other two *Acer* species, which are natives to Europe and Asia.

In good agreement with the order of the systematic taxa, the next level of similarity revealed by HCA is that of plant families, as illustrated by the examples of the Birch and of the Soapberry families (Betulaceae and Sapindaceae). Silver birch (genus *Betula*) and Hophornbeam (genus *Ostrya*) are members of the Birch family (Betulaceae), and their spectra form one of the three main data clusters. Sycamore Maple, Norway Maple and Horse-chestnut are all members of the Soapberry family (Sapindaceae), and are also contained in one group.

When classifying biological samples by analytical methods, usually the question arises about individual variation vs. variation between groups of individuals. To take into account such variation between individuals, each of

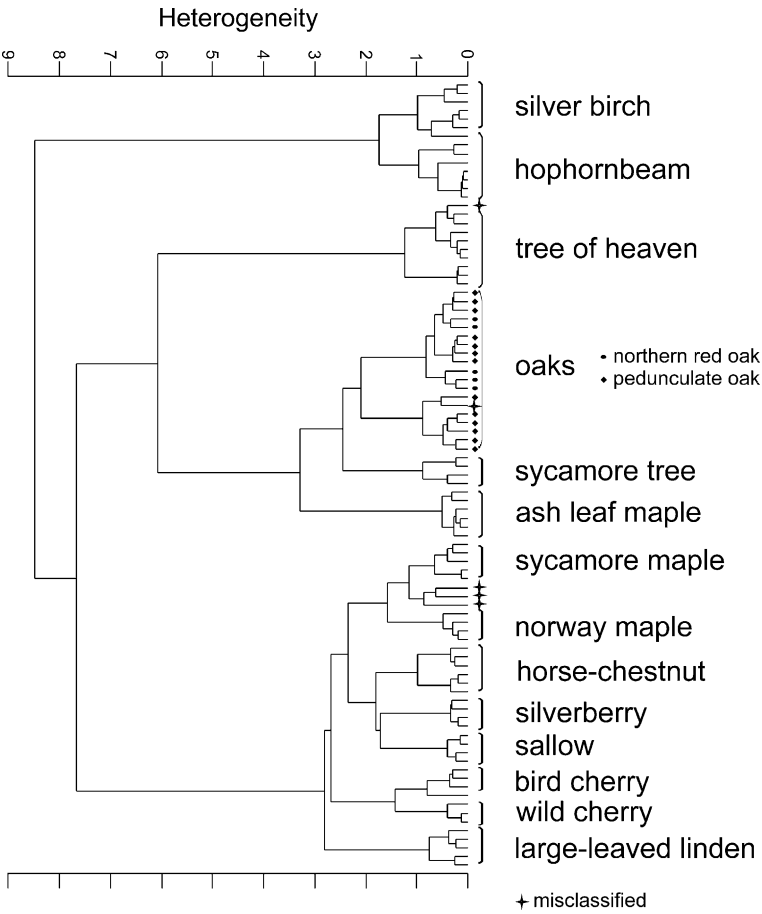

Fig. 4.3. Dendrogram resulting from cluster analysis containing 91 spectra from 15 tree species (see also Table 4.2). Cluster analysis was done on first derivatives over the spectral range 380 cm^{-1} to 1700 cm^{-1}). The distance matrix was calculated using Euclidean distance and Ward's algorithm was applied for clustering. Spectra were measured after decomposition of carotenoid molecules with 633 nm irradiation. For example, spectra of each species are shown in Fig. 4.1. Reprinted with permission from [52]

the measurements was performed with 5–10 samples in different experiments. Variation of spectral signatures is also brought about by structural heterogeneity. Considering that pollen grains are spheroid objects of several (sometimes tens of) microns in size with heterogeneous surfaces, the exact position of the excitation laser focus with respect to surface microstucture can influence the background and intensities. Furthermore, the micromorphology of the pollen surface, e.g. different thicknesses of the exine layer, protrusions or complete absence at the pollen apertures, represents a certain amount of morphological

Table 4.2. Tree species analysed in this study

Species name		Family	No. of samples
Salix caprea	(Sallow)	Salicaceae	5
Betula pendula	(Silver Birch)	Betulaceae	7
Ostrya carpinifolia	(Hophornbeam)	Betulaceae	8
Acer negundo	(Ash Leaf Maple)	Sapindaceae	6
Acer platanoides	(Norway Maple)	Sapindaceae	5
Acer pseudoplatanus	(Sycamore Maple)	Sapindaceae	5
Aesculus hippocastanum	(Horse Chestnut)	Sapindaceae	6
Platanus acerifolia	(Sycamore Tree)	Platanaceae	4
Prunus avium	(Wild Cherry)	Rosaceae	4
Prunus padus	(Bird Cherry)	Rosaceae	4
Quercus robur	(Pedunculate Oak)	Fagaceae	13
Quercus rubra	(Northern Red Oak)	Fagaceae	5
Tilia platyphyllus	(Large-leaved Linden)	Malvaceae	5
Ailanthus altissima	(Tree of heaven)	Simaroubaceae	9
Elaeagnus angustifolia	(Silverberry)	Elaeagnaceae	5

heterogeneity a spectrum-based pollen classification procedure has to withstand. The cluster analysis results show that such intra-species differences due to variability and microscale heterogeneity are smaller than inter-species variation (compare Fig. 4.3).

The results presented here yield an answer to the question posed at the beginning of this section: Species that belong to the same genus and of genera that belong to the same families can be distinguished from one another based on a chemical fingerprint. However, for the oak genus, no distinction can be made between the spectra from the species Pedunculate Oak (*Quercus robur*) and Northern Red Oak (*Quercus rubra*) in HCA. This indicates that the molecular differences between pollens of these two species may be too small to be detected with HCA as unsupervised method sensu stricto, i.e. using the whole spectral range in a completely unsupervised similarity test. Molecular differences between species may be so small that they only reflect in a few selected spectral alterations localized in short spectral ranges. This observation is in good agreement with other studies that demonstrated spectral classification to species level or even below, e.g. between different strains of one bacterial species [60–62]. In most studies, HCA-based classification is restricted to the use of certain spectral ranges or their weighted combination, or for supervised classification [61, 62]. In this light, the HCA result obtained on full-range pollen spectra is surprising, since the whole spectral range, that is, of all classes of molecules is variable to a high extent and can be used for discrimination between most of the species investigated here. The poor spectral discrimination of pollen of the different oak species is in good agreement with the fact that inter-specific hybridization is very common among oaks and occurs much more frequently than in other plant species [63, 64].

Hybridization has retained oaks a model taxon for species concepts that rely on ecological criteria rather than on reproductive isolation [65]. The high similarity in chemical constitution of different oak pollens, which is verified by a very similar biochemical fingerprint in our Raman experiments, can be interpreted as part of the very weak barriers to being pollinated by another (oak) species.

Raman spectra of pollen are fingerprints of their particular biochemical composition. Therefore, they reflect part of the phenotype of a plant. To summarize the discussion of the spectral classification result in the context of phylogenetic groups investigated here, the similarities and dissimilarities observed in the Raman spectra of the pollen are in accordance with concepts of systematics and speciation. These are the processes of reproductive or mating isolation (which is sensible, considering that pollen are critical parts of mating systems), but also, as was observed here for the case of the Maple genus, ecological and geographical criteria. It remains to be investigated whether the latter separation represents environmental or evolutionary effects.

4.2.4 Influence of Resonant Raman Signals from Carotenoid Molecules

From the cluster analyses we learn that the biochemical origins of the species-specific fingerprints lie in all classes of molecules contained in the pollen grains. However, the content in certain molecular constituents can interfere with the meaningful classification of a sample. Initially, we noticed very intense contributions from carotenoids in the Raman spectra of pollen from some species. They led to a classification of the spectra according to carotenoid content in multivariate analyses (Fig. 4.4). Carotenoids have been reported to be commonly involved in pollen pigmentation, mainly contained in the exine layer, although early hypotheses that carotenoids and carotenoid esters polymerize to form the sporopollenin polymer itself [66] have proven false [1]. However, the outer pollen wall (exine) is an accumulation site for various pigments, and in a recent report, CARS imaging of an individual cherry pollen grain was based entirely on the ν_1 and ν_3 Raman modes of carotene [67].

It should be noted that our excitation wavelength of 785 nm is far away from the absorption maxima of typical carotenoid molecules [68, 69]. We conclude that the intense spectral contributions of the carotenoids are caused by both a relatively high carotenoid content in the pollen of particular species, as well as pre-resonant enhancement, yielding carotenoid intensities that are about one order of magnitude above those of the other bands, e.g. the relatively strong CH_2 deformation mode at 1445 cm^{-1} (Fig. 4.5, traces a, c and e). The observed pre-resonant Raman signals of carotenoids can be orders of magnitude stronger than the normal Raman signals of all other molecules in the pollen.

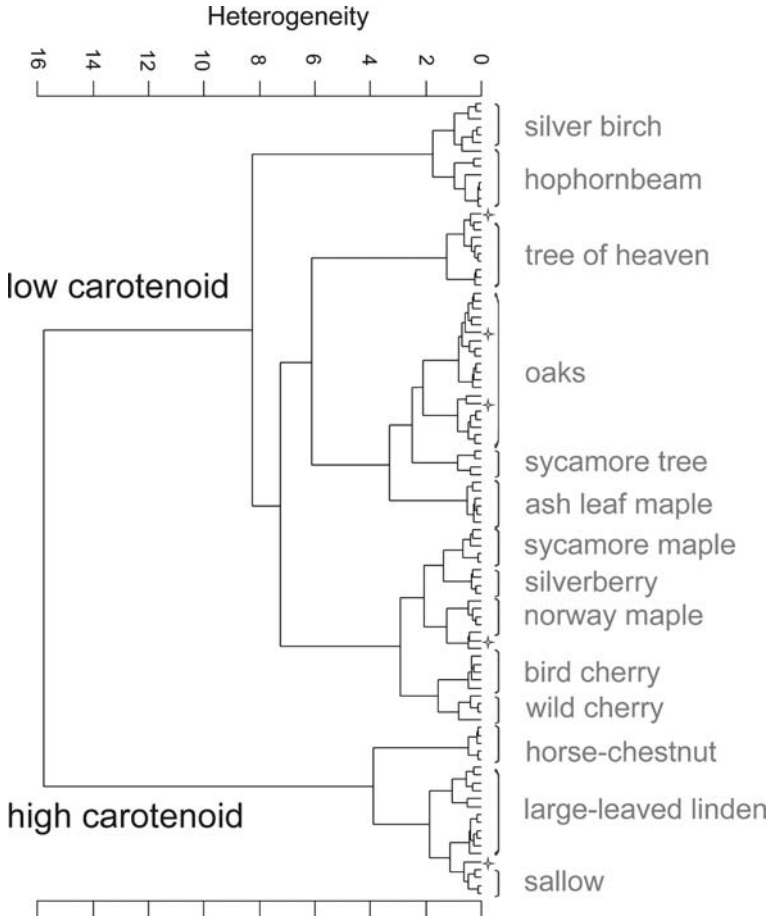

Fig. 4.4. Influence of carotenoid pre-resonant Raman contributions on cluster analysis result. The dendrogram was obtained using the same parameters as in the one displayed in Fig. 4.3. However, the spectra of the used data set were obtained without decomposing carotenoid before the Raman experiments. The species sallow, horse-chestnut and large-leaved linden form a distinct cluster due to the intense carotenoid contribution. The corresponding spectra are shown in Fig. 4.5 traces a, c and e. Reprinted with permission from [52]

In particular, the spectra of large-leaved linden, sallow and horse-chestnut are dominated by typical carotenoid features (compare spectra a, c and e of Fig. 4.5). These spectra display the characteristic combination of the intense carotenoid vibrations ν_1 $(\sim 1520\,\mathrm{cm}^{-1})$, ν_3 $(\sim 1160\,\mathrm{cm}^{-1})$ and ν_6 $(\sim 1006\,\mathrm{cm}^{-1})$ and also of the much weaker modes ν_2 $(\sim 1190\,\mathrm{cm}^{-1})$ and in some cases ν_5 $(\sim 1280\,\mathrm{cm}^{-1})$ [70, 71]. In the other investigated tree species, such intense carotenoid features were not detected and/or probably super-

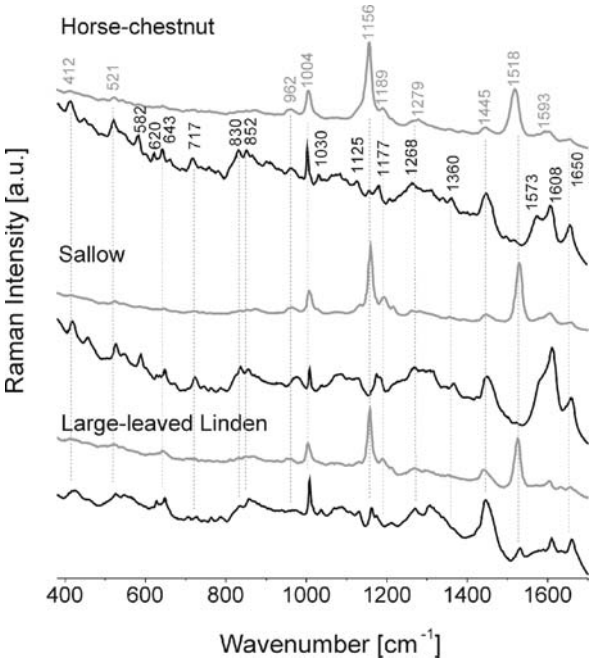

Fig. 4.5. Raman spectra of tree pollen that is rich in carotenoid. Spectra of pollen from horse-chestnut (a, b), sallow (c, d), large-leaved linden (e, f) before irradiation with laser light of 633 nm wavelength for photodestruction of carotenoids (traces a, c and e) and after 1 h photodestruction with 633 nm. All spectra were excited with 785 nm, 10 s accumulation time and laser power of 18 mW $\left(\sim 1.8 \times 10^6\,\mathrm{W/cm^2}\right)$

imposed with the contributions from other molecules. Originally, in HCA, the spectra of these species formed one large cluster, obviously due to their high resemblance with respect to the carotenoid spectral features (Fig. 4.4). Therefore, the strong carotenoid features have to be taken into account either prior to or post data acquisition. Interference from carotenoid pigments needs to be considered before automated pollen identification procedures can be established.

To enable the utilization of the full spectral range for classification also in carotenoid-rich species, we propose a method for photodestruction of carotenoid pigments in pollen using 633 nm light. In initial experiments that were conducted at 633 nm excitation, we observed that the bands ascribed to carotenoid molecules were not stable but diminished steadily, even at relatively low excitation intensities of 10 mW. Figure 4.6 displays spectra of horse-chestnut pollen excited with 633 nm as a function of exposure time to the laser. The irreversible decrease of the intensities of the typical carotenoid bands suggests the photodestruction of these molecules (see arrows in Fig. 4.6) [72–74]. With excitation at 785 nm, the spectra of the pollen remained unal-

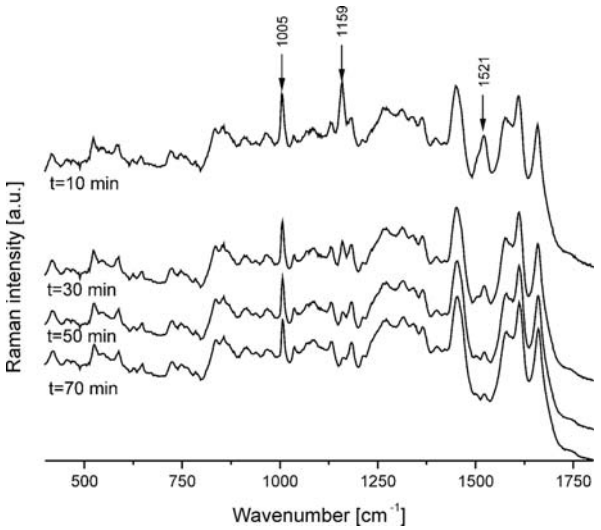

Fig. 4.6. Series of spectra of pollen from horse-chestnut, indicating the decomposition of carotenoids during irradiation with 63 nm laser light. The spectra were taken during the decomposition process at 20 min intervals at 10, 30, 50 and 70 min exposition time. Accumulation time was 10 s, excitation wavelength 633 nm, 10 mW laser power $(\sim 1 \times 10^6\,\mathrm{W/cm^2})$ on the sample. Reprinted with permission from [52]

tered, independent of exposure time (data not shown). For an illustration, the reader is again referred to Fig 4.3. The traces b, d and f of Fig. 4.5 show spectra from the same pollen species as in a, c and e after removal of the carotenoid components. After irradiation with 633 nm, the characteristic spectra of the pollen, with the superposition of all the different spectral contributions become clearly visible (Fig. 4.5 b, d and f).

As evidenced by these data, the impact of the carotenoid features on the classification results is remarkable. Photodestruction of the carotenoid components is an efficient alternative to omitting all spectral regions where carotenoid bands may superimpose other features; the latter being proposed, e.g. in studies on microorganisms [61]. The width of some of the carotenoid bands would force us to discard numerous important other spectral features hidden beneath the intense carotenoid signals.

4.3 Intrinsic Surface-Enhanced Raman Scattering from Pollen and Other Cellular Samples

4.3.1 SERS and Cells

SERS substrates for use in biosamples have to meet a number of requirements: They have to be close to the molecules to be probed, hence mobile

inside a biosystem, at the same time, they must enable targeting of specific substructures, e.g. cellular compartments. As has been demonstrated, several different methods in principle allow to accomplish precise positioning of a SERS substrate, such as the utilization of sharp probe tips and atomic force technique or the combination with electron microscopy [37, 40, 75, 76], but most of these approaches are difficult or impossible to carry out without complicated preparation. An alternative is the in situ synthesis of SERS-active substrate in the biosystem itself [35, 77]. In addition to being controllable with respect to topology, uptake and retention characteristics of the respective cell or biosystem, the material should be inert and if possible not influence its surroundings.

Utilization of SERS in live cell studies has been getting more and more attention in recent years. Most work conducted so far has been focusing on the detection of extracellular molecules in cells such as dye molecules introduced with silver particles [78–80] or of drugs adsorbed onto the cellular membrane [11, 81]. In these cases, high concentrations of the foreign molecules or silver particles or both were used and no SERS signal was detected from the cells themselves. The feasibility of measuring SERS spectra from live cells without any label molecules was first demonstrated with the cell line HT29 [82]. Since then, our efforts have been directed towards development of SERS into a method for systematic label-free studies of cells and tissues [83, 84], including the construction of SERS labels that can also deliver information on cellular chemistry [8, 85]. In a recent study, intrinsic SERS signals were reported from epithelial cells that were generated with intracellularly grown gold nanoparticles [77].

In a Raman experiment, live cells can be investigated directly in buffer or in the cell culture medium. During such measurements, Raman spectra can be collected from individual cells in an x–y raster scan point by point, similar to any other Raman mapping experiment. Excitation intensities can be as low as 10^4–$10^5\,\mathrm{W/cm^2}$, and by using near-infrared excitation, possible changes in the live cells due to laser illumination are avoided. As we saw in control experiments with cells incubated in medium without gold nanoparticles, the applied low excitation intensity and 1 s collection time per spectrum do not enable acquisition of normal Raman spectra from the cells. Only those spots where SERS-active nanostructures were introduced into the cellular system yield a SERS spectrum. Thereby, we selectively probe the immediate vicinity of the particles. We choose the locations to be probed by choosing the targets of the SERS substrates. This was illustrated for the case of the endosomal system of cultured cells, where the chemical composition of endosomes of different age in the process of endosomal maturation was shown to change over time [84]. When the endosomal SERS signatures obtained from different cell lines were compared, very different typical spectra were found. In particular, apart from spectra that were similar to those found in an epithelial cell line, a distinct spectral signature appeared in the spectra of a macrophage cell line (J774). Almost all bands in this spectrum were characteristic of adeno-

sine phosphate and show contributions from all constituents of this nucleotide (adenine, ribose and phosphate; see band assignments in Fig. 4.7 [86]). A comparison with data of pure adenosine monophosphate (AMP) and adenosine triphosphate (ATP) suggested a prevailing contribution from AMP, since triphosphate and diphosphate markers were absent. From this 'AMP/ATP fingerprint' we concluded that one can detect molecular species involved in the generation of a specific endosomal milieu: The key players in the acidification and pH regulation of endosomes include an ATP-dependent proton pump and a Na–K–ATPase [87, 88]. Furthermore, the endosome acidification profile can be modified by cyclic AMP [89].

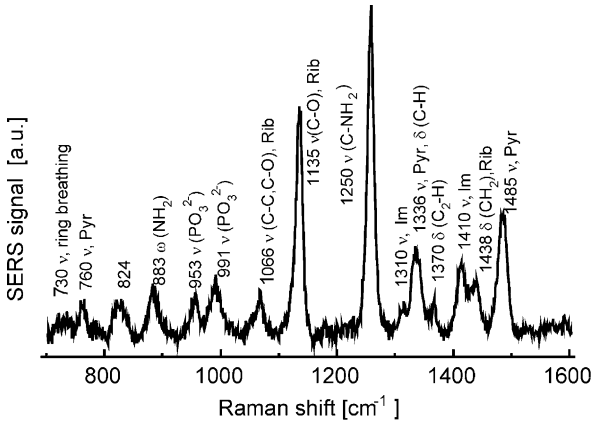

Fig. 4.7. SERS spectrum collected from endosomes in the cell line J774 after incubation with gold nanoparticles. It was identified as SERS spectrum of AMP and/or ATP. Band assignments are based on [86] are indicated. Excitation wavelength $<3 \times 10^5$ W/cm^2 at 785 nm, collection time 1 s. Abbreviations: cps, counts per second; ν, stretching mode; ω, wagging mode; δ, bending mode; Rib, ribose; Pyr, pyrimidine; Im, imidazol

In the following we will discuss SERS measurements of the pollen cellular fraction in more detail.

4.3.2 SERS from Pollen Cellular Fraction

Obtaining SERS spectra from pollen and in particular from the cellular interior is of interest as it may provide higher sensitivity for detection of pollen fragments in bioaerosols, and may also enable studies of allergologically relevant pollen molecular constituents. Sengupta et al. published SERS spectra from suspensions of cottonwood and redwood pollen as well as two types of grass and compared them with spectra from bacteria [54, 90]. The spectra were obtained from suspensions of pollen particles in silver colloids. As the amount of pollen used was not quantified in these experiments, it remains unclear

whether the spectra show characteristic SERS signatures or if they contain normal Raman contributions from soluble and insoluble pollen compounds. We have observed that strong normal Raman scattering signal of the pollen outer shell (exine), as well as pre-resonant excitation of carotenoid molecules can be of similar intensity as a SERS spectrum of pollen cells. Therefore it is important to ensure which part of the pollen is probed by SERS, either in spatially resolved experiments or following a separation of different constituents, and to design a proper control experiment.

For a SERS experiment, the water-soluble cellular fraction from pollen can be obtained as shown in the schematic in Fig. 4.8. About 0.2 mg of freeze-dried pollen, which correspond to a few hundred pollen grains, was suspended in 100 µl water and incubated at room temperature. When water is added to intact pollen, the cellular interior bearing the allergens, but also other proteins, carbohydrates, pigments and nucleic acids is released [91] and hence should be contained in the aqueous supernatant. About 2 µl of the supernatant, which should contain the amount of soluble content of a few individual pollen grains can then be added to 20 µl of a solution of gold nanoparticles. The gold nanoparticles were prepared as described by Lee and Meisel [92]. In the control experiments, the volume of the nanoparticle suspension is replaced by pure water.

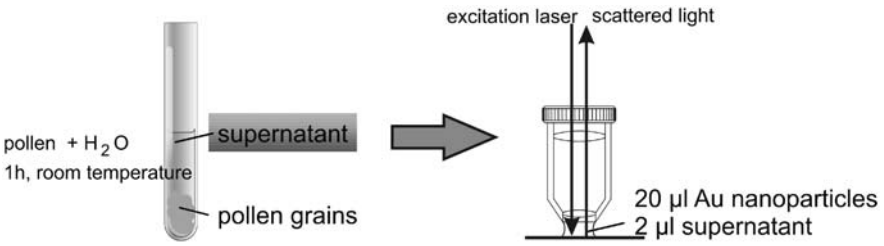

Fig. 4.8. Schematic of SERS experiment on pollen cellular fraction. Freeze-dried pollen was incubated with water, the supernatant was probed by SERS by adding a small amount to a solution of gold nanoparticles. The Raman experiments were carried out using a water immersion objective

In the Raman experiments, an excitation wavelength of 785 nm (intensity $1.8 \cdot 10^5$ W/cm^2) was used. The sample, i.e. a drop of Au nanoparticle suspension with soluble pollen content was placed under a (60×) water immersion objective. Raman spectra were recorded with 1 s acquisition time. The control preparations (pollen supernatant with water) did not yield any spectral features. A spectrum of rye pollen supernatant with Au nanoparticles is shown in Fig. 4.9, together with a normal Raman spectrum of a rye pollen grain. The difference in spectral information that can be obtained by both approaches is evident from a comparison of these two spectra. Although an estimate of an enhancement factor is not possible from this experiment, it is clear that

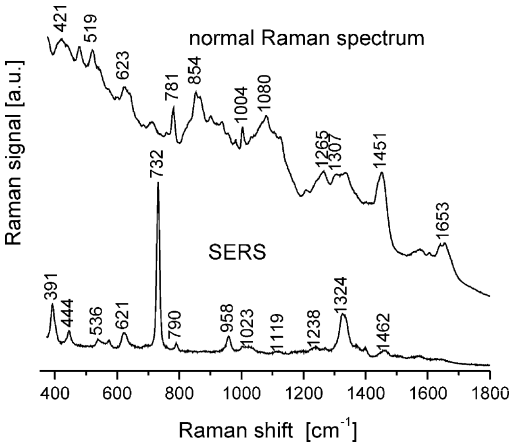

Fig. 4.9. Normal Raman spectrum (excitation intensity 1.8×10^6 W/cm^2, 10 s acquisition time) of intact rye pollen grain and SERS spectrum (excitation intensity 1.8×10^5 W/cm^2, 1 s acquisition time) of rye pollen supernatant excited at 785 nm

the SERS signals must be orders of magnitude higher than the bands in the normal Raman spectrum: The normal spectrum was acquired at 10 times the excitation intensity and 10 times the acquisition duration of the SERS spectrum, but with much higher concentration of molecules in the probed volume ('solid' intact pollen grain), rather than a small fraction of the interior of 2–3 pollen grains in the case of the SERS measurement (∼50 pl probed volume in a drop of 22 µl).

As evidenced by the spectra of Fig. 4.10, the SERS spectral information of the soluble fraction varies for the different species. The qualitative comparison of the spectra with assignments from existing work on purified compounds shows for the different samples varying contributions from nucleic acids (adenine, guanine, cytosine, thymine), several amino acids, such as valine, methionine, isoleucine, proline, cysteine, tryptophan, phenylalanine and histidine and also flavonoids (FAD, campherol, apigenine, quercetin and luteolin) [93–100]. Many of the observed spectral signatures have a known physiological basis: cysteine-rich proteins that are responsible for lipid transfer have been associated with the formation of the pollen exine, as have been aromatic amino acids such as phenylalanine and tyrosine [56]. Flavonoids have various functions in pollen physiology: They protect from harmful radiation and also from pathogenic attacks [44]. FAD is a key player in cellular respiration. Some vibrations can be assigned to isoquinoline (e.g. 625 cm^{-1}, 1368 cm^{-1}) [95] and indole (e.g. at 542 cm^{-1}) [101]. Both could hint at indole- and isoquinolin alkaloids, substances that have been isolated from roots and leaves of higher plants. Many of these alkaloids have antimicrobial and antimykotic activity [102, 103].

Currently, algorithms that allow a multivariate analysis of the SERS spectra are being developed in order to utilize SERS spectroscopic information also for pollen detection.

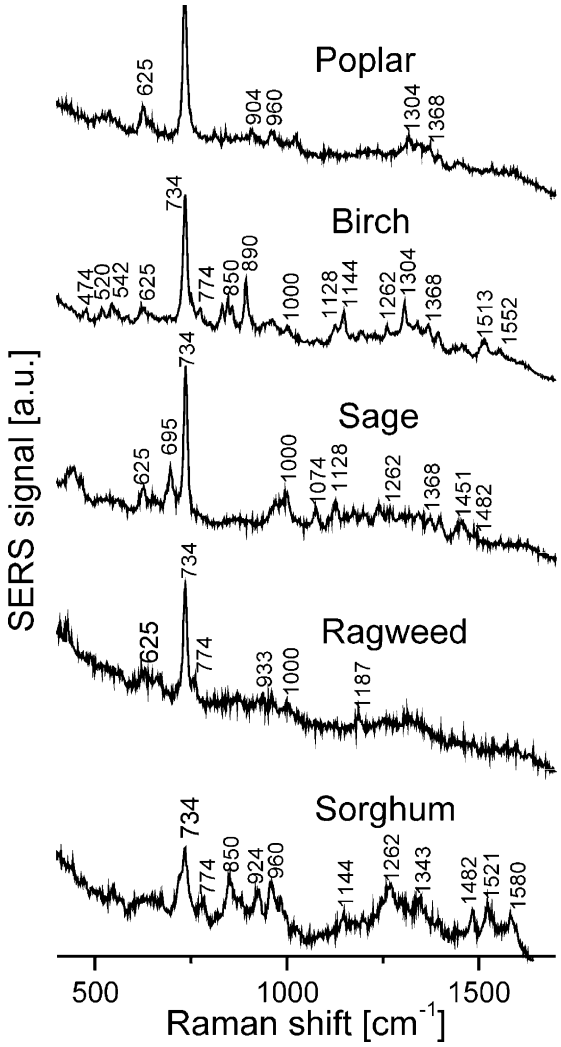

Fig. 4.10. SERS spectra of pollen cellular fraction from different species. Excitation wavelength 785 nm, intensity, 1.8×10^5 W/cm^2, acquisition time 1 s

4.4 Conclusions

With Raman microspectroscopy, an in situ chemical characterization and classification of cellular samples can be achieved. As demonstrated, it is possible to localize different spectral signals to specific morphological microstructures in individual pollen grains. Maps of important molecular constituents in cryosections of pollen grains could be constructed simultaneously and without purification or staining. The data permit conclusions about the relative levels and localization of aromatic amino acids along with aliphatic molecules, nucleic acids, protein and carbohydrate storage in different structures of the pollen. This combined analysis of different classes of molecular constituents in the unaltered material differs from previous purification-based approaches. Surface-enhanced Raman scattering (SERS) can significantly increase the sensitivity of Raman spectroscopic approaches for pollen characterization and allows a characterization of very small amounts of pollen cellular fraction, which is water soluble. This is of particular interest for studies of pollen allergens which are released by the pollen grains upon hydration, but also for the identification of very small amounts of pollen material in aerosols.

By using a Raman spectroscopic approach, we could prove the working hypothesis that the biochemical make-up of the pollen (as part of a recognition/mating system) is altered during formation of a new biological species and that the species-specific chemical similarities and dissimilarities indeed reflect in the Raman spectral fingerprint. Based on the chemical information, unsupervised multivariate analysis consisting of hierarchical clustering revealed in most cases chemical similarities between species that were indicative of both taxonomic relationship and mating behaviour. As illustrated by the data, the spectra of whole pollen can be used for their classification. Such an approach is very promising, considering its potential to be employed for automatic pollen detection and early warning.

Acknowledgements

We would like to thank the group of Dieter Naumann, Robert-Koch-Institut Berlin, for providing the cryostat and Peter Lasch, RKI and CytoSpec, Inc. for CytoSpec software. J.K. is grateful to Katrin Kneipp, Wellman Center for Photomedicine, Harvard Medical School, Boston, for providing Raman setups for SERS experiments in live cells. We gratefully acknowledge funding of this research by Deutsche Forschungsgemeinschaft (Grants DFG KN 557/9-1 and PA 716/9-1).

References

1. A.-K. Prahl et al., Zeitschrift für Naturforschung **40c**, 621 (1986)
2. C.J. Keijzer, New Phytol. **105**, 499 (1987)

3. G. Shaw, A. Yeadon, J. Chem. Soc. C **16** (1966)
4. V.N. Paunov, G. Mackenzie, S.D. Stoyanov, J. Mater. Chem. **17**, 609 (2007)
5. H.-J. van Manen et al., PNAS **102**, 10159 (2005)
6. H.J. Van Manen, C. Otto, Nano Lett. **7**, 1631 (2007)
7. B.R. Wood, B. Tait, D. McNaughton, Biochim. Biophys. Acta **1539**, 58 (2001)
8. J. Kneipp et al., J. Raman Spectrosc. (2008). doi: 10.1002/jrs.2060
9. T. Bakker Schut et al., Anal. Chem. **72**, 6010 (2000)
10. J.J. Baraga, M.S. Feld, R.P. Rava, Proc. Natl. Acad. Sci. U S A **89**, 3473 (1992)
11. G. Breuzard et al., Biochem. Biophys. Res. Commun. **329**, 64 (2005)
12. C.J. Frank et al., Anal. Chem. **66**, 319 (1994)
13. E.B. Hanlon et al., Phys. Med. Biol. **45**, R1 (2000)
14. D. Hutsebaut et al., Syst. Appl. Microbiol. **29**, 650 (2006)
15. K. Maquelin et al., Anal. Chem. **72**, 12 (2000)
16. G.J. Puppels et al., Nature **347**, 301 (1990)
17. A. Otto, in *Light Scattering in Solids IV. Electronic Scattering, Spin Effects, SERS and Morphic Effects*, ed. by M. Cardona, G. Guntherodt (Springer-Verlag, Berlin, 1984), p. 289
18. A. Campion, P. Kambhampati, Chem. Soc. Rev. **27**, 241 (1998)
19. M. Moskovits, Rev. Mod. Phys. **57**, 783 (1985)
20. B.N.J. Persson, Chem. Phys. Lett. **82**, 561 (1981)
21. K. Kneipp et al., Phys. Rev. Lett. **76**, 2444 (1996)
22. Z.H. Sun et al., J. Phys. Chem. C **112**, 6093 (2008)
23. D.L. Jeanmaire, R.P. Van Duyne, J. Electroanal. Chem. **84**, 1 (1977)
24. M.G. Albrecht, J.A. Creighton, J. Am. Chem. Soc. **99**, 5215 (1977)
25. T. Vo-Dinh, L.R. Allain, D.L. Stokes, J. Raman Spectrosc. **33**, 511 (2002)
26. C.R. Yonzon et al., Anal. Chem. **76**, 78 (2004)
27. L. Zeiri, S. Efrima, J. Raman Spectrosc. **36**, 667 (2005)
28. K. Kneipp et al., J. Phys. Condens. Matter **14**, R597 (2002)
29. K. Kneipp et al., Phys. Rev. E **57**, R6281 (1998)
30. H.X. Xu et al., Phys. Rev. Lett. **83**, 4357 (1999)
31. S. Habuchi et al., J. Am. Chem. Soc. **125**, 8446 (2003)
32. Y.W.C. Cao, R.C. Jin, C.A. Mirkin, Science **297**, 1536 (2002)
33. Y.C. Cao et al., J. Am. Chem. Soc. **125**, 14676 (2003)
34. D. Graham, K. Faulds, Chem. Soc. Rev. **37**, 1042 (2008)
35. S. Efrima, B.V. Bronk, J. Phys. Chem. B **102**, 5947 (1998)
36. L. Zeiri et al., Colloid Surf. A-Physicochem. Eng. Asp. **208**, 357 (2002)
37. R.M. Jarvis, A. Brooker, R. Goodacre, Anal. Chem. **76**, 5198 (2004)
38. R.M. Jarvis, R. Goodacre, Chem. Soc. Rev. **37**, 931 (2008)
39. X.Y. Zhang, N.C. Shah, R.P. Van Duyne, Vib. Spectrosc. **42**, 2 (2006)
40. R. Zenobi, V. Deckert, Angew. Chem.-Int. Ed. **39**, 1746 (2000)
41. C. Budich et al., J. Microsc. **229**, 533 (2008)
42. N.C. Shah et al., Anal. Chem. **79**, 6927 (2007)
43. O. Lyandres et al., Anal. Chem. **77**, 6134 (2005)
44. P. Piffanelli, J.H.E. Ross, D.J. Murphy, Sex. Plant Reprod. **11**, 65 (1998)
45. R.C. Lord et al., Spectrochim. Acta A-Mol. Biomol. Spectrosc. **41**, 199 (1985)
46. R.W. Scott, M.J. Strohl, Phytochemistry **1**, 189 (1962)
47. J. Ring, Curr. Opin. Immunol. **13**, 701 (2001)
48. R. Manoharan et al., Appl. Spectrosc. **45**, 307 (1991)

49. M.L. Laucks et al., J. Aerosol. Sci. **31**, 307 (2000)
50. A.R. Boyain-Goitia et al., Appl. Opt. **42**, 6119 (2003)
51. N.P. Ivleva, R. Niessner, U. Panne, Anal. Bioanal. Chem. **381**, 261 (2005)
52. F. Schulte et al., Anal. Chem. **80**, 9551 (2008)
53. C.S. Pappas et al., Appl. Spectrosc. **57**, 23 (2003)
54. A. Sengupta, M.L. Laucks, E.J. Davis, Appl. Spectrosc. **59**, 1016 (2005)
55. M.N. Siamwiza et al., Biochemistry **14**, 4870 (1975)
56. P.F. Vanbergen, M.E. Collinson, J.W. Deleeuw, Grana, **18** (1993)
57. E. Dominguez et al., Grana **37**, 93 (1998)
58. D. Southworth, Am. J. Bot. **61**, 36 (1974)
59. D.L. Massart, L. Kaufman, *The Interpretation of Analytical Chemical Data by the Use of Cluster Analysis* (Wiley, New York, 1983)
60. D. Naumann, D. Helm, H. Labischinski, Nature **351**, 81 (1991)
61. C. Kirschner et al., J. Clin. Microbiol. **39**, 1763 (2001)
62. K. Maquelin et al., J. Microbiol. Methods **51**, 255 (2002)
63. J.H. Williams, W.E. Friedman, M.L. Arnold, Proc. Natl. Acad. Sci. U S A **96**, 9201 (1999)
64. J.H. Williams, W.J. Boecklen, D.J. Howard, Heredity **87**, 680 (2001)
65. L. Van Valen, Taxon **25**, 233 (1976)
66. J. Brooks, G. Shaw, Nature **219**, 532 (1968)
67. H. Kano, H.O. Hamaguchi, Chem. Lett. **35**, 1124 (2006)
68. S. Sufrà et al., J. Raman Spectrosc. **6**, 267 (1977)
69. V.R. Salares et al., J. Phys. Chem. **80**, 1137 (1976)
70. M. Veronelli, G. Zerbi, R. Stradi, J. Raman Spectrosc. **26**, 683 (1995)
71. R.J. Weesie et al., Biospectroscopy **5**, 19 (1999)
72. A. Andreeva et al., Photochem. Photobiol. **83**, 1301 (2007)
73. J.W. Jung, S.K. Lee, J. Sci. Food Agric. **86**, 2296 (2006)
74. M.N. Merzlyak et al., Physiol. Plant. **104**, 661 (1998)
75. B. Pettinger et al., Phys. Rev. Lett. **92**, 96 (2004)
76. A. Rasmussen, V. Deckert, J. Raman Spectrosc. **37**, 311 (2006)
77. A. Shamsaie et al., JBO Lett. **12**, 020502 (2007)
78. M.B. Wabuyele et al., Rev. Sci. Instrum. **76** (2005)
79. C. Eliasson et al., Chemometr. Intell. Lab. Syst. **81**, 13 (2006)
80. C.E. Talley et al., Anal. Chem. **76**, 7064 (2004)
81. G. Breuzard et al., Biochem. Biophys. Res. Commun. **320**, 615 (2004)
82. K. Kneipp et al., Appl. Spectrosc. **56**, 150 (2002)
83. J. Kneipp, H. Kneipp, K. Kneipp, Proc. Natl. Acad. Sci. U S A **103**, 17149 (2006)
84. J. Kneipp et al., Nano Lett. **6**, 2225 (2006)
85. J. Kneipp et al., Anal. Chem. **77**, 2381 (2005)
86. S. Sanchez-cortes, J.V. Garcia Ramos, J. Mol. Struct. **274**, 33 (1992)
87. R.W. VanDyke, Am. J. Physiol. **265**, C901 (1993)
88. M. Grabe, G. Oster, J. Gen. Physiol. **117**, 329 (2001)
89. R.W. Van Dyke, Hepatology **32**, 1357 (2000)
90. A. Sengupta, N. Brar, E.J. Davis, J. Colloid Interface Sci. **309**, 36 (2007)
91. M. Grote et al., J. Allergy Clin. Immunol. **108**, 109 (2001)
92. P.C. Lee, D. Meisel, J. Phys. Chem. **86**, 3391 (1982)
93. B. Giese, D. McNaughton, J. Phys. Chem. B **106**, 101 (2002)
94. C. Otto et al., J. Phys. Chem. **92**, 1239 (1988)

95. M. Bolboaca, W. Kiefer, J. Popp, J. Raman Spectrosc. **33**, 207 (2002)
96. S. Stewart, P.M. Fredericks, Spectrochim. Acta A **55**, 1641 (1999)
97. R. Aroca, R. Bujalski, Vib. Spectrosc. **19**, 11 (1999)
98. Y. Zheng, P.R. Carey, B.A. Palfey, J. Raman Spectrosc. **35**, 521 (2004)
99. K. Sokolov et al., Appl. Spectrosc. **47**, 515 (1993)
100. Z. Jurasekova et al., J. Raman Spectrosc. **37**, 1239 (2006)
101. J. Bukowska, K. Jackowska, J. Electroanal. Chem. **322**, 347 (1992)
102. U. Abbasoglu et al., Arch. Pharm. **324**, 379 (1991)
103. J. Quetin-Leclercq et al., Planta Med. **61**, 475 (1995)
104. F.S. Parker, *Applications of Infrared, Raman, and Resonance Raman Spectroscopy in Biochemistry* (Plenum Press, New York, 1983)
105. W.L. Peticolas et al., J. Raman Spectrosc. **27**, 571 (1996)
106. E.W. Small, W.L. Peticolas, Biopolymers **10**, 69 (1971)

5

Raman Imaging and Raman Mapping

Francis W.L. Esmonde-White and Michael D. Morris

Abstract Raman spectroscopy can be used to non-destructively add image contrast in visualizing structures and dynamics in living systems and materials. Image contrast can be derived from any information contained in Raman spectra, including band intensities, positions and widths. Because these parameters are functions of the local physical and chemical environment of a constituent, the images can display these properties as well. This chapter discusses instrumentation for acquiring low definition Raman maps and high definitions Raman images in two and three dimensions. Experimental configurations and their advantages and drawbacks are described. Methods for enhancing resolution are discussed. Finally several examples these techniques are presented, with an emphasis on application areas not elsewhere discussed in the book.

5.1 Introduction

Raman spectroscopy can be used to construct images, whose contrast is based on any sample property directly or indirectly contained in the spectrum. In this chapter, instrumentation for Raman imaging is reviewed, along with selected recent developments. Methods for the analysis of Raman images are described in Chap. 8 and will not be repeated here. The two major uses of Raman imaging are for determining relative chemical composition and classification. Chemical composition is most commonly used to provide contrast for determining spatial distributions of chemical components (as shown in Figs. 5.3 and 5.4). The intensity at any pixel in the image is proportional to the amount of component at the point corresponding to that pixel. Similarly, the intensity ratio of two components can also be used to determine a relative composition. Some of the physical properties that influence the spectrum of a component can also be used to generate contrast. Important examples include lattice strain and component orientation. Further chemical and physical properties can be detected through parameters such as the center of gravity, area, and width of Raman bands.

The term Raman mapping is conventionally used when the number of pixels in the image is small, typically 100–1,000 pixels. Imaging is used when the number of pixels is large, typically 4,000–20,000. There is, however, no fixed boundary between a map and an image. As the discussion below shows, the most easily and inexpensively implemented technologies generally require impractically long measurement times for generation of an image.

5.2 Instrumentation for Raman Imaging

Since its development by Delhaye and Dhamelincourt in 1975 [1] the epi-illumination Raman microprobe has become one of the most important input systems in Raman spectroscopy and is the instrument around which most Raman imaging systems are constructed. Epi-illumination instruments are almost always constructed around research-grade commercially available fluorescence microscope frames, with input optics modified to accept an exciting laser and with output optics modified to direct backscattered Raman signal to a spectrograph.

The three general methods for constructing a Raman map proposed and demonstrated in 1975 remain in use today, but with vastly improved technology. They are point focusing and point-by-point scanning, line focusing and line-by-line scanning, and widefield (also called global) illumination and imaging detection.

5.2.1 Point-by-Point Mapping

In this method the laser is point focused, and the object under test is translated past the laser focus, or the focus is raster scanned across the object. Motor-driven x–y stages are the most commonly used devices for translating the object. While the stages available as accessories for research microscopes can be positioned with accuracy better than $\pm 1\,\mu$m and can be stepped in 0.1μm increments, they must be allowed to settle for about 0.5 s to achieve this accuracy [2]. The settling time can add significant time to the overall image acquisition time, when the integration time at each pixel is only a second or a few seconds. Despite the dead time problem, motor-driven stages remain popular with vendors and end users. An important reason is that the stages are useful both for microscopic mapping and for larger scale mapping, because the most common models are capable of 10–20 cm travel in each axis.

There are several scan methodologies that can reduce the dead time. One method is to use a faster translation stage. An x–y stage driven by piezoelectric translators is preferred, because these stages settle in 0.001 s or less. While they can be incremented in steps as small as 10–20 nm, most are flexure (one-piece) designs and can travel only a few millimeters in either direction. Alternatively, the laser beam itself can be scanned, as commonly done in confocal microscopy. Crossed galvanometer-driven mirrors have been used for this purpose, as have acousto-optic translators.

5.2.2 Line Scanning

Line scanning offers a more rapid image generation method. In this method the laser is focused on a line, usually with a cylinder lens. Because the lens focuses a Gaussian beam to a high aspect ratio, only the central portion of the beam is usable. This problem can be overcome with a Powell lens [3], which does focus the beam to a uniform intensity high aspect rectangle. In the most popular scanning configuration, the line-focused beam is stationary and the object is translated beneath it. Less commonly, a line-focused beam is scanned across a stationary object [4].

The reduction in total measurement time from point-by-point scanning is significant, because 100 or more spectra are obtained simultaneously. The measurement time to acquire these spectra may be a short as or only a little longer than the measurement time for a single spectrum with a point-focused laser. The reason is that total laser power can be much larger in the line-focused case. However, because each charge-coupled device (CCD) row contains the spectrum at 1 pixel, the detector must be read out pixel by pixel. To minimize detector noise CCDs are read out at low rates (16–50 kHz), so that 1–3 s is required to read the detector, depending on the number of pixels in the detector. This time can be reduced by synchronizing stage movement with readout of the bottom row of the detector, followed by shifting the remaining spectral image one row toward the readout register [5]. An alternative, at least for use with green lasers, is to use a fast-readout detector. The electron-multiplying CCD (EMCCD) has been used for this purpose [4, 6]. It can be read out at 1 MHz or faster. Because the avalanche gain mechanism of the EMCCD introduces very little excess noise, the amplification also allows reduced acquisition times for objects containing weak scatterers.

In line-scanning Raman imagers, the spectrograph entrance slit is often used as the spatial filter that enables confocal operation. However, the sectioning provided by a slit is less strong than the sectioning provided by the more common pinhole. Stronger sectioning can be obtained if the point spread function of the objective is deconvoluted pixel by pixel along the slit direction.

5.2.3 Global Illumination

A narrowband filter can be used for Raman imaging. The first successful modern instrumentation employed an interference filter, which could be tilted to vary the passband [7]. Subsequently, acousto-optic tunable filters (AOTF) [8] and liquid crystal tunable filters (LCTF) [9] were introduced into Raman imaging and provided electronic tunabililty. The tunable filter approach has proven most useful for measurement of isolated bands. If only a few frames are needed to define the band, global Raman imaging can be quite rapid. Where there are many overlapping bands or a non-linear background, many images must be taken at different Raman shifts, and the time advantage disappears.

It should be noted that the transmission of the acousto-optic filter is only about 50%, while the transmission of the liquid crystal filter is about 20–40%. By contrast, a dielectric filter passes 80–90% of the incident light. The differences arise because both the AOTF and LCTF operate on linearly polarized light. In most Raman microprobes, both polarization components of the Raman scatter are collected, even when the exciting laser is linearly polarized.

5.2.4 Raman Mapping

Most Raman maps are constructed point by point by rastering the specimen underneath a fixed microprobe. However Ma and Ben-Amotz [10] developed a global illumination probe in which a laser beam was defocused to cover the field of view of a tightly packed cylindrical bundle of 61 optical fibers (100 μm core/130 μm cladding). The fibers are arranged linearly at the entrance slit of a spectrograph. Mapping is rapid, because the light is defocused and the numerical aperture of optical fibers is relatively large.

More recently, we have shown that the global illumination configuration probe can be used for subsurface mapping [11]. The subsurface capability arises because each fiber views light arising from material directly below it, but also from material that is not directly below. In effect, individual fibers operate as spatially offset collection systems (see Chap. 3, SORS). However, global illumination is less effective for spatial offsetting than mapping fiber probes in which there is no physical overlap between illumination region and the field of view of the collection fibers [12]. A ring of laser light surrounding a circular collection bundle gives deeper penetration and better spatial resolution. Similar results are expected for other excitation/collection geometries.

5.2.5 Improving Resolution

Both the lateral and axial resolution of widefield microscopy images can be improved by digital deconvolution [13] of the microscope point spread function. The simple nearest-neighbors axial deblurring procedure developed for widefield light microscopy has been adapted for Raman imaging by Govil et al. [14]. In this technique three images are taken at small increments of axial position. The central image is deblurred by pixel-by-pixel subtraction of a fraction of the intensity, usually of about 40%, of both the upper and lower images. The technique requires no special software and is computationally rapid, but the resulting image is noisy.

A more sophisticated approach uses a stack of serial sections. Three-dimensional images in all forms of light microscopy are built up as serial sections. That is, the microscope (or other device) is focused at different depths through an object, and the resulting stack of images rendered as a three-dimensional object. This technique was introduced into Raman microscopy

by Govil et al., who used a widefield microscope and blind digital deconvolution of the microscope objective point spread function to improve both lateral and axial resolution [15]. Blind deconvolution starts with an approximate idealized point spread function and performs a constrained iterative deconvolution. Blind deconvolution has the advantage that it is not necessary to use an independently measured point spread function. However, three-dimensional Raman imaging has not found widespread use, because it is time consuming and is limited to specimens that are transparent or nearly transparent. Additionally, spherical aberration can degrade both axial and lateral resolution in confocal Raman imaging, particularly with the commonly used achromatic metallurgical microscope objectives [16]. If understood, many of these problems can be minimized by the use of objectives designed for depth penetration in transparent or slightly turbid materials.

Recently, a new approach to improving lateral resolution has been developed [17]. These investigators treat lateral super-resolution as an ill-posed inverse problem. They generate almost 50 Raman images of the same material, shifting each member laterally by a small amount (0.1–1 μm). Recovery of a single deblurred image requires regularization, i.e., adding additional constraining information to the data set so that only one solution is possible. This operation can be viewed as a type of deconvolution of the microscope lateral point spread function, analogous to the three-dimensional blind deconvolution method described above.

5.2.6 Near-Field Raman Imaging

Near-field Raman imaging with a scanned probe has been reported [18, 19]. However, the technique is painfully slow (5–10 h, even for strong scatterers) and it has found very little use. Acquisition time can be decreased by using a polystyrene bead as a very high numerical aperture immersion lens. Working at 532 nm, Kasim et al. used a 60×/1.2 immersion aperture as an optical tweezer to simultaneously position the bead and operate it as a high NA lens [20]. They obtained a spatial resolution of about 80 nm on doped silicon with a few minutes scan time (Fig. 5.1). However, because of the need for a relatively smooth surface and a very intense scatterer, this technique is not likely to find much application in biomedical or pharmaceutical applications [21, 22].

5.2.7 SERS and Tip-Enhanced Raman Imaging

Intracellular surface-enhanced Raman imaging has been reviewed by Chourpa and colleagues [23]. For intracellular measurements SERS provides a mechanism for enhancement of the signals from very small amounts of cell constituents, such as DNA, or pharmaceuticals. Typically colloidal silver or

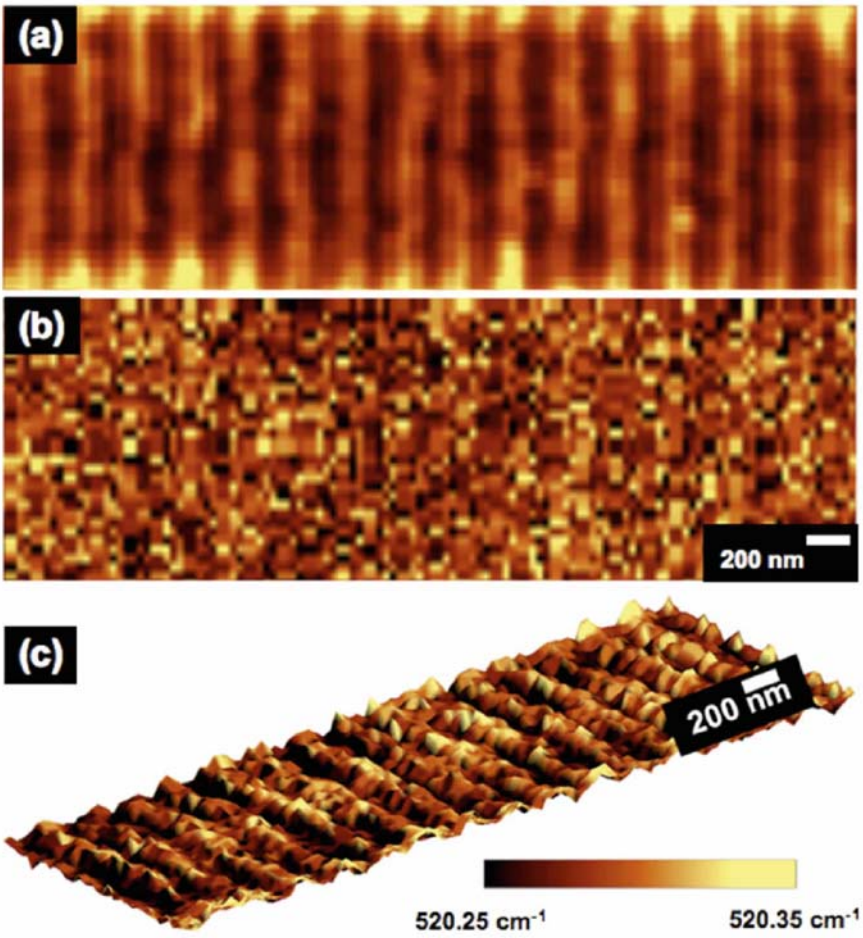

Fig. 5.1. **a** and **b** $4.0 \times 1.3\,\mu m^2$ near-field reflectance and confocal Raman images of periodic poly-Si lines on a patterned SiGe wafer with buried SiGe stressors obtained in about 6 min, respectively, generated from the Si–Si peak intensity. **c** Three-dimensional near-field Raman image from Si–Si peak position showing the spatial variation of relative strain in a selected region of the wafer (reprinted with permission from [20]. Copyright 2008 Optical Society of America)

gold is injected into the cell. However, electrodes deposited on the end of an optical fiber or metallic tip can also be used. If an AFM tip coated with gold or silver is used for scanning, the technique is usually called tip-enhanced Raman spectroscopy (TERS) [24]. TERS imaging is extraordinarily sensitive, but tip fabrication and operation remain difficult.

5.2.8 Raman Tomography

Raman tomography has recently been demonstrated using canine cortical bone as a test case [25]. An example of a reconstructed image is shown in Chap. 14. Transmission geometry was used to measure spectra through 13 projections. A reconstruction program previously developed for fluorescence tomography was employed to reconstruct the tomographic image. Because of multiple elastic scattering of light, this technique yields blurred images.

Diffuse tomography is an ill-posed inverse problem, where the light emerges is known but its sources are not known and more than one reconstruction is possible. The most accurate reconstruction requires spatial priors to define where the light should originate. Spatial priors are the three-dimensional coordinates that define shape and position of the Raman scattering (or fluorescing) object and must be found from independent measurements. The spatial priors are usually obtained from magnetic resonance images (MRI) or X-ray computed tomographic images (CT). In the absence of spatial priors, it is rarely possible to obtain an accurate shape and position. Spatial priors can also be used to paint a surprisingly high contrast and detailed spectroscopic image of a structure, provided that only one Raman component is found for that structure [26]. An example is shown in Fig. 5.2.

Best results are obtained when spatial variation is maximized. For that reason the recovered contrast is over 140:1 when the image reconstruction is based on transmission measurements, but only about 1.4:1 for contrast based on backscattered measurements. It is likely that even better results would be obtained in both image-guided Raman spectroscopy and Raman tomography if illumination and collection fibers were placed strategically around the specimen.

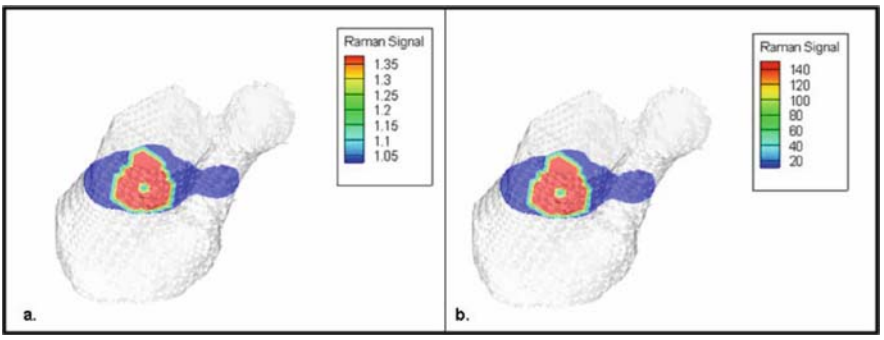

Fig. 5.2. Cross section of the reconstructed image-guided Raman spectroscopic estimates of bone distribution using (**a**) backscattered collection using a ring/disk fiber optic probe and (**b**) transmission measurements using a rectangular array of collection fibers. The contrast between the bone and background from skin and tendons was more than 100-fold greater in the transmission measurements used than in the backscattered measurements (reprinted with permission from [26]. Copyright 2008 Optical Society of America)

5.2.9 Thermal Damage

Thermal damage from a tightly focused laser beam limits the amount of power that can impinge on a sample, and therefore may determine the time required to collect a Raman spectrum. More power can be used if the light is distributed over a greater area on the specimen. An illumination geometry that distributes heat effectively and so reduces thermal damage is said to have a power distribution advantage [27]. Although there is still no consensus definition of this parameter, the thermal damage threshold can be measured experimentally for any material and the power distribution advantage can be defined relative to a standard condition, such as point focus of a laser of a specified wavelength. It is also possible to estimate for different illumination geometries the maximum power that can impinge on a sample without causing thermal damage.

Using classical heat transport theory, Zhang et al. have evaluated several illumination geometries for effective heat dissipation [28]. Under steady-state conditions, for a fixed illumination area and laser power the best geometries are as follows: array of spots $>$ line (high aspect rectangle) $>$ rectangle $\approx$ circle. These results are understandable because heat generated at a point can be conducted away in all directions in which the heat source does not extend. If global illumination is used, then except at the edges of the illuminated region, heat can be dissipated in only one dimension (axial), while for an array of spots heat can be dissipated in all three dimensions. What is surprising is how few points are required for an array of tightly focused spots to match the heat dissipation of a focused high aspect rectangle. If the total areas are equal, four spots have the same power distribution advantage as a rectangle of aspect ratio 35:1, while only nine spots are required to match the power distribution advantage of a rectangle of aspect ratio 120:1.

Laser excitation power is a limiting factor in the application of non-invasive in vivo Raman imaging and tomography. Several guidelines for laser exposure limits exist, including guidelines for safe use, as well as maximum permissible exposure limits for eye and skin. Organizations providing guidelines for laser exposure include the American National Standards Institute (ANSI), the Food and Drug Administration (FDA), the Occupational Health and Safety Administration in the United States (OSHA), and numerous other agencies worldwide. In addition to exposure limits, factors such as pigmentation and scarring will alter the risk associated with laser irradiation on skin. A variety of skin type classification systems exist which may help in guiding exposure based on skin pigmentation, including the Fitzpatrick and Roberts skin type classification systems.

5.3 Selected Applications

Several recent studies that illustrate the scope of Raman imaging to fields of study not otherwise covered in this volume are presented here.

5.3.1 Single Cell Imaging

By using line scanning and with 532 nm excitation wavelength to maximize the ratio of Raman scattering to background fluorescence, Hamada and co-workers have been able to obtain high-definition images of HeLa cells in 3 min or less [29]. The use of a high numerical aperture water-immersion objective (NA 1.2) in these experiments also contributed to rapid signal acquisition.

Figure 5.3 shows the progress of cytokinesis followed by time-lapse Raman imaging. Proteins exist at high concentrations in the chromosomes, so the

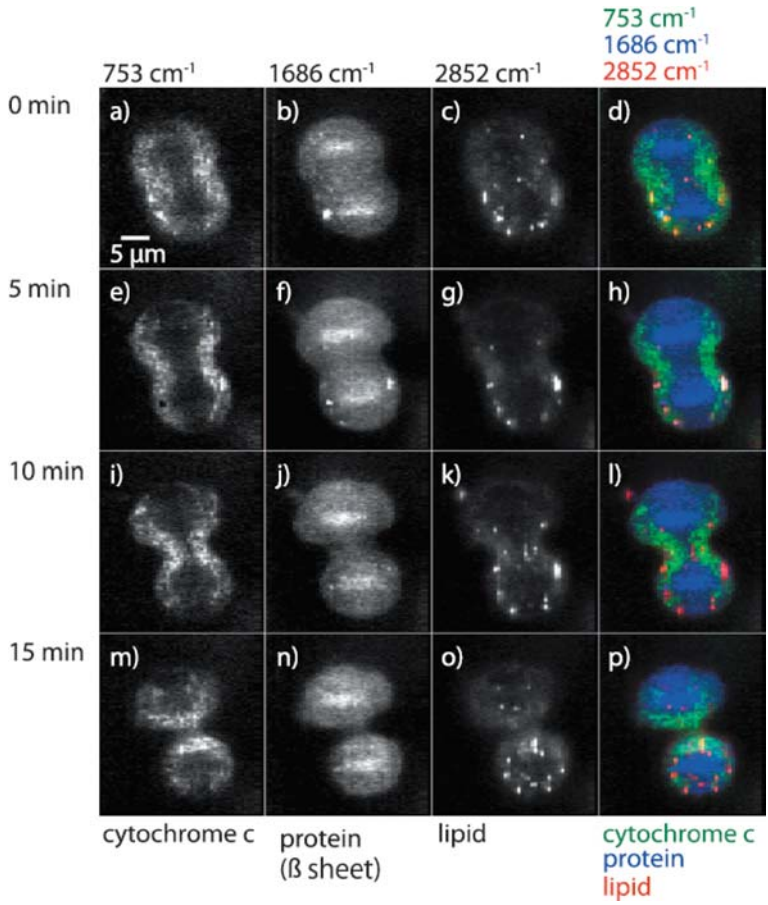

Fig. 5.3. Time-resolved Raman imaging of cytochrome *c*, protein, and lipid molecule distributions in a label-free HeLa cell during cytokinesis. The images were taken at 5-min intervals (frame rate of 185 s/image). Cytokinesis seen as the change in the distribution of proteins and a high concentration of cytochrome *c* is observed at positions near the contracting ring. The field of view is 161 × 48 pixels. The pixel size is not specified (reprinted with permission from [29])

progress of cell division can be followed by imaging the beta-sheet amide I signature at $1,686\,\mathrm{cm}^{-1}$. Cytochrome c $\left(753\,\mathrm{cm}^{-1}\right)$ is also concentrated near the nascent boundary of the two daughter cells and lipids $\left(2,852\,\mathrm{cm}^{-1}\right)$ at the cell walls. A short movie of the process can be viewed at the following web site. http://dx.doi.org/10.1117/1.2952192.1.

Incorporation and distribution of amino acids into cells can be followed by Raman mapping using deuterium-labeled amino acids in the growth media [30]. The advantage of this stable isotope technique is that it puts C–D stretches of the amino acids into the $2,100$–$2,300\,\mathrm{cm}^{-1}$ region, where there is no interference from other Raman bands. Distribution of incorporated phenylalanine-d_5 into a HeLa cell is shown in Fig. 5.4. As expected, structures such as nucleoli in the nucleus are regions of concentrated accumulation. The cell takes up either phenylalanine or phenylalanine-d_5 randomly, as shown by the uniform distribution of phenyl C–D/phenyl C–H stretch intensity across the cell. Because point-by-point mapping (dwell time 1 s) was used acquisition of the 900 pixel images (30×30 $0.47\,\mu\mathrm{m}$ steps, $15 \times 15\,\mu\mathrm{m}$ area) required 15 min, plus microscope stage and camera readout time.

5.3.2 Lung Tissue

Congenital cystic adenomatoid malformations (CCCMs) have been examined in four specimens taken from the lungs of infants who had undergone lung surgery [31]. There are several classes of CCCMs, all of which prevent formation of normal alveolar growth. From the specimens both FTIR images (64×64 pixels) and point-by-point Raman maps with definitions ranging between 42×46 and 80×80 pixels were obtained with spatial resolution similar to that for the FTIR images. Coarse resolution was deliberately used to allow examination of relatively large regions. Unsupervised cluster analysis was used to separate the specimens into groups. The combination of FTIR and Raman provided better results than either alone. FTIR is more sensitive to mucus (i.e., to polysaccharides) and lipids than Raman spectroscopy. However, identification of lipids by low wavenumber $\left(<1,000\,\mathrm{cm}^{-1}\right)$ is better performed by Raman spectroscopy. The combination of the two modalities provided better results than either alone. Of course, as discussed above, the time required for Raman mapping could be reduced from many hours to a few minutes with line scanning or the other modes discussed in earlier sections.

5.3.3 Cell and Small Animal Imaging with Surface-Enhanced Raman Spectroscopic (SERS) and Other Nanoparticle Tags

SERS is discussed in greater detail in Chap. 8. We discuss only two recent imaging applications. An advantage of SERS labels is that several different labels, and therefore several cell or tissue components, can be tracked simultaneously. In theory, SERS labeling should allow dozens or perhaps even hundreds of distinguishable labels to be used. SERS-active metallic particles

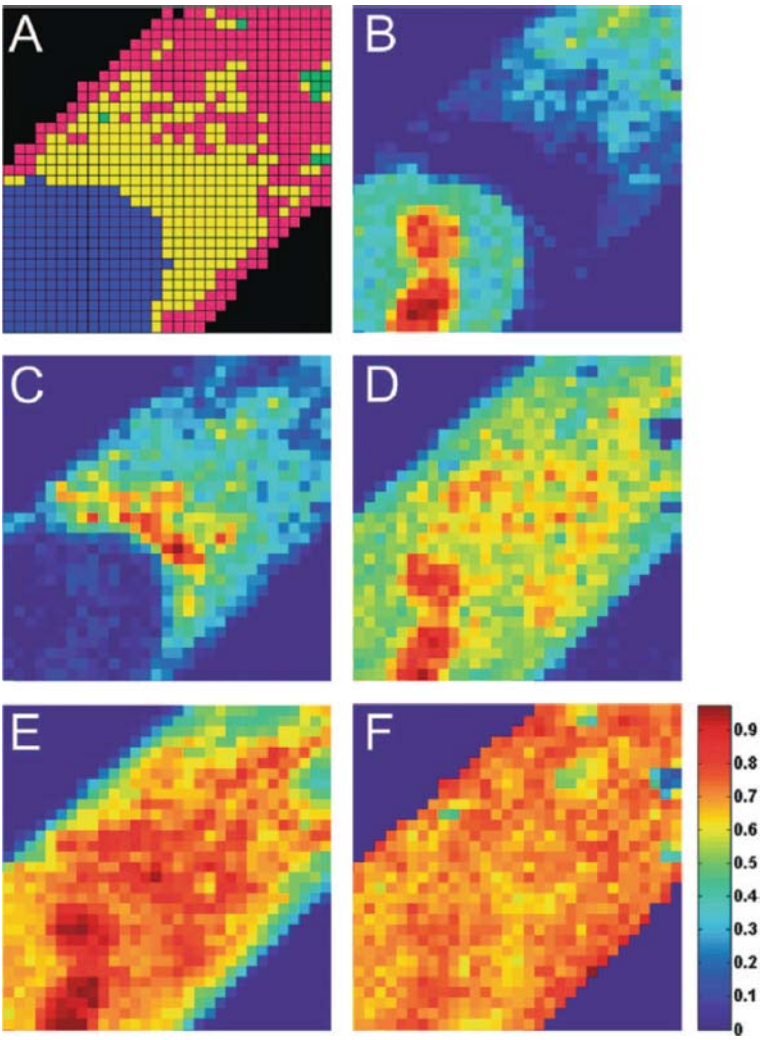

Fig. 5.4. Raman imaging of a HeLa cell incubated for 28 h with Phe-d5. (**A**) Hierarchical cluster analysis image with five clusters. Univariate images of (**B**) nucleotides $(770–790\,\mathrm{cm}^{-1})$, (**C**) phospholipids $(700–730\,\mathrm{cm}^{-1})$, **(D)** Phe-d5 $(950–965\,\mathrm{cm}^{-1})$, (**E**) Phe-h5 $(995–1,005\,\mathrm{cm}^{-1})$, and (**F**) Phe-d5/Phe-h5 ratios (950–965 cm^{-1} region divided by the 995–1, 005 cm^{-1} region). Image acquisition parameters: Exposure time 1 s/pixel, step size 0.47 µm/pixel, field of view $15 \times 15\,\mu\mathrm{m}^2$ (reprinted with permission from [30]. Copyright 2008 American Chemical Society)

tagged with both a molecule that has strong resonance-enhanced SERS and a selective binder such as an antibody can be used for imaging the antibody target. Recently such particles have been encased in a nanometer-thick fused silica shells to enhance stability and minimize toxicity. Commercial versions are available (Nanoplex, Oxonica Inc., Mountain View, CA).

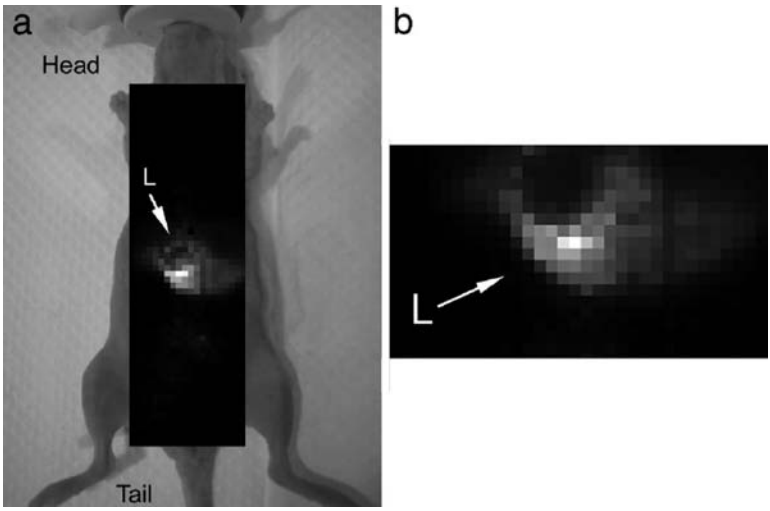

Fig. 5.5. SERS image of mouse liver. **a** Whole-body map (1-mm steps) of nude mouse 2 h after tail vein injection of SERS nanoparticles. Most SERS particles accumulate in the liver (L, *arrow*). **b** Higher resolution (750 µm steps) and higher definition map of liver (*arrow*) showing organ detail including differentiation of the two liver lobes (reprinted with permission from [33]. Copyright 2008 National Academy of Sciences, USA)

This SERS labeling approach has been used by Yu and co-workers for imaging apoptosis in cells and lung cancer tissue [32]. In most reported SERS imaging papers, the SERS nanoparticles have been prepared by the investigators themselves. Yu et al. were able to employ the commercially available SERS-active nanoparticles, and so have demonstrated that SERS imaging is now open to a much larger community of scientists than just SERS specialists.

A similar methodology has been extended by Keren et al. to non-invasive imaging of the mouse, using SERS nanoparticles that had accumulated in the liver [33]. An example is shown in Fig. 5.5. This group also demonstrated that single-walled carbon nanotubes, which have an intense Raman band at $1,593\,\mathrm{cm}^{-1}$, can be functionalized and used for non-invasive imaging.

5.3.4 Correlative Raman Spectroscopy and Optical Coherence Tomographic (OCT) Imaging

Several groups have used Raman spectroscopy in combination with OCT, which is a rapid, high spatial resolution technique. OCT is used to identify suspicious areas of tissue and single-point Raman spectroscopy is used to confirm presence or absence of disease. Application to dental caries is discussed in Chap. 15. A very recent development is an integrated Raman/OCT probe [34], which is shown in Fig. 5.6. Using biopsied breast tissue, the instrument

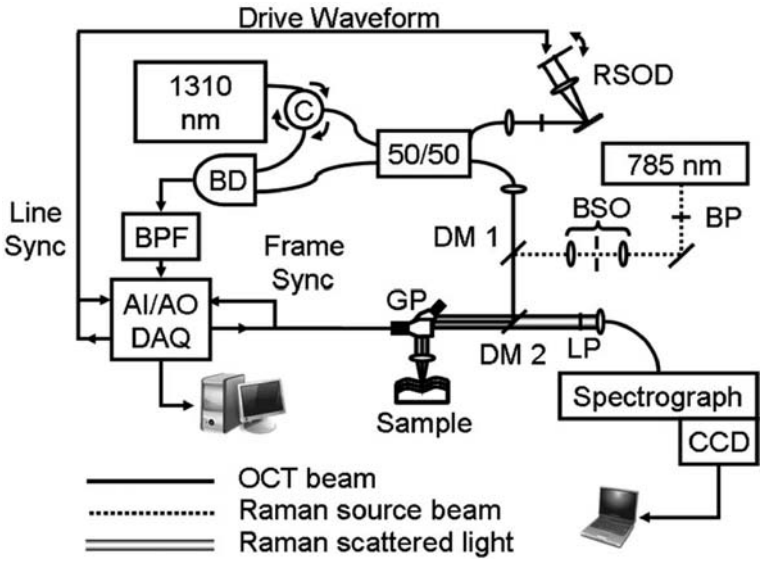

Fig. 5.6. A block diagram of an optical coherence tomography/Raman spectroscopy system: C, circulator; RSOD, rapid scanning optical delay; BP, 785 bandpass; BSO, beam shaping optics; DM1, dichroic mirror at 990 nm; DM2, dichroic mirror at 800–950 nm; LP, long pass at 808 nm; GP, galvanometer pair; BD, balanced detector; BPF, electronic band-pass filter; AI–AO DAQ, analog input–output data acquisition (reprinted with permission from [34]. Copyright 2008 Optical Society of America)

was shown to provide a Raman spectrum with cancer signatures (intense protein bands) in tumor tissue and a normal spectrum in unaffected tissue. Similar instrumentation could be almost certainly be developed for endoscopic applications of OCT.

5.4 Conclusions

Advancements in technology over the past decade have enabled the use of Raman imaging and Raman mapping in a wide variety of applications. In particular the developments of holographic gratings, robust lasers, and thermoelectric cooled CCDs have made Raman imaging accessible beyond specialist spectroscopy laboratories. In addition to broadening the application of existing Raman imaging methodologies, novel methodologies such as Raman tomography have become technically feasible. Raman imaging and Raman mapping have enabled visualization of patterns in complex heterogeneous systems using contrast arising from chemical and physical properties. The high spatial resolution of Raman imaging in the visible and near infrared has allowed detailed chemical mapping of sophisticated systems such as living cells, biological tissues, pharmaceutical tablets, and polymer films.

References

1. M. Delhaye, P. Dhamelincourt, J. Raman Spectrosc. **3**, 33 (1975)
2. S. Schlucker et al., Anal. Chem. **75**, 4312 (2003)
3. K.A. Christensen, M.D. Morris, Appl. Spectrosc. **52**, 1145 (1998)
4. K. Golcuk et al., Biochim. Biophys. Acta – Biomembr. **1758**, 868 (2006)
5. S. Bernard, O. Beyssac, K. Benzerara, Appl. Spectrosc. **62**, 1180 (2008)
6. K. Golcuk et al., in *Biomedical Vibrational Spectroscopy III: Advances in Research and Industry* (SPIE, San Jose 2006), p. 609314
7. D.N. Batchelder, C. Cheng, G.D. Pitt, Adv. Mater. **3**, 566 (1991)
8. E.N. Lewis, P.J. Treado, I.W. Levin, Appl. Spectrosc. **47**, 539 (1993)
9. H.R. Morris, C.C. Hoyt, P.J. Treado, Appl. Spectrosc. **48**, 857 (1994)
10. J. Ma, D. Ben-Amotz, Appl. Spectrosc. **51**, 1845 (1997)
11. M.V. Schulmerich et al., Appl. Spectrosc. **60**, 109 (2006)
12. M.V. Schulmerich et al., in *Advanced Biomedical and Clinical Diagnostic Systems V* (SPIE, San Jose 2007), p. 643009
13. J.R. Swedlow, in *Deconvolution of Images and Spectra*, ed. by P.A. Jansson (Academic Press, San Diego, 1997), p. 284
14. A. Govil et al., Appl. Spectrosc. **45**, 1604 (1991)
15. A. Govil, D.M. Pallister, M.D. Morris, Appl. Spectrosc. **47**, 75 (1993)
16. N.J. Everall, Appl. Spectrosc. **54**, 1515 (2000)
17. L. Duponchel et al., Anal. Chim. Acta. **607**, 168 (2008)
18. C.L. Jahncke, H.D. Hallen, M.A. Paesler, J. Raman Spectrosc. **27**, 579 (1996)
19. C.L. Jahncke, M.A. Paesler, H.D. Hallen, Appl. Phys. Lett. **67**, 2483 (1995)
20. J. Kasim et al., Opt. Express **16**, 7976 (2008)
21. N. Anderson et al., Nano Lett. **6**, 744 (2006)
22. M. Becker et al., Small **4**, 398 (2008)
23. I. Chourpa et al., Chem. Soc. Rev. **37**, 993 (2008)
24. E. Bailo, V. Deckert, Chem. Soc. Rev. **37**, 921 (2008)
25. M.V. Schulmerich et al., J. Biomed. Opt. **13**, 020506 (2008)
26. S. Srinivasan et al., Opt. Express **16**, 12190 (2008)
27. P.J. Treado, M.D. Morris, Anal. Chem. **61**, 723A (1989)
28. D. Zhang et al., Appl. Spectrosc. **55**, 61 (2001)
29. K. Hamada et al., J. Biomed. Opt. **13**, 044027 (2008)
30. H.-J. van Manen, A. Lenferink, C. Otto, Anal. Chem. **80**, 9576 (2008)
31. C. Krafft et al., Analyst **133**, 361 (2008)
32. K.N. Yu et al., Bioconjug. Chem. **18**, 1155 (2007)
33. S. Keren et al., Proc. Natl. Acad. Sci. **105**, 5844 (2008)
34. C.A. Patil et al., Opt. Lett. **33**, 1135 (2008)

6

Coherent Raman Scattering Microscopy

Andreas Volkmer

Abstract A series of advances over the past decade have made the combination of coherent Raman scattering (CRS) with optical microscopy a highly sensitive and chemically selective tool for the label-free and noninvasive analysis of chemical species or biological components inside a sub-femtoliter probe volume. By exploiting the coherent driving and detection of Raman modes in coherent anti-Stokes Raman scattering (CARS) and stimulated Raman scattering (SRS), CRS imaging allows the point-by-point chemical mapping of living cells and tissues in three dimensions and in real time, which is often difficult to attain by fluorescence and incoherent vibrational microscopy techniques. Beyond imaging, CRS microspectroscopy in the frequency- and time-domain provides fast access to the full wealth of the sample's spontaneous Raman response. In this review, we give an overview of the common fundamental aspects of CARS and SRS microscopy, their distinct image contrast mechanisms and microspectroscopy implementations, together with emerging biomedical applications.

6.1 Introduction

A subject of wide interest in the physical and life sciences is the noninvasive characterization of microscopic objects within a complex heterogeneous system through optical microscopy. In recent years, the emphasis has been on the development of microscopy techniques with the goal to achieve three-dimensional imaging with high spatial resolution, high sensitivity, and high chemical selectivity. In particular, fluorescence microscopy with three-dimensional sectioning capability by means of confocal detection [1] or multiphoton excitation [2] has become a powerful tool in biological research [3]. Chemical selectivity is provided by labeling with natural or artificial fluorescent probes [4, 5]. For chemical species or biological components that either do not fluoresce or cannot tolerate the toxicity associated with staining and the photobleaching of fluorophores [6], their intrinsic molecular vibrational properties can be used as contrast mechanisms. Infrared imaging [7] and spontaneous Raman imaging [8] are two prevalent methods in vibrational

microscopy. The former is limited to low spatial resolution due to the longer wavelength involved and by the vibrational absorption of the common solvent water. Spontaneous Raman scattering microscopy with laser excitation in the visible and near-infrared avoids this problem. However, it is often limited by the weak Raman scattering cross section that necessitates high laser powers and by the presence of auto-fluorescence background.

The signal-to-background limitations inherent to spontaneous Raman detection schemes can be circumvented by the use of a nonlinear process that significantly enhances the Raman scattering signal. As such, surface-enhanced Raman scattering has been demonstrated to provide single-molecule detection sensitivity [9, 10], but requires the molecular sample in the vicinity of surfaces of metal colloidal particles or substrates and often lacks the reproducibility of enhancement efficiency. In an alternative attempt, coherent Raman scattering (CRS) has been combined with optical microscopy. Because of its coherent nature, in which the molecular bonds oscillate in phase and interfere constructively, the CRS signal can be orders of magnitude more sensitive than spontaneous Raman scattering. Although it is not possible to detect a single vibrational mode at room temperature, it is feasible to detect a macromolecule with thousands of identical vibrational modes that interfere coherently. CRS microscopy has been shown to provide advantages for the vibrational imaging of biological samples for the following reasons [11–13]: (i) It does not require fluorescent probes. (ii) Since there is no population of electronically excited molecular states, photobleaching and damage to biological samples are suppressed. (iii) It is much more sensitive than spontaneous Raman microscopy, requiring only a moderate average power for excitation, which is tolerable by most biological samples. (iv) Being a nonlinear microscopy with signal generation confined to the focal volume, it exhibits three-dimensional sectioning capability similar to multi-photon-induced fluorescence microscopy. (v) The use of near-infrared excitation minimizes sample heating due to the lack of water absorption and provides a deep penetration depth for imaging through thick tissues or cells.

The most predominant realization of CRS microscopy to date is coherent anti-Stokes Raman scattering (CARS) microscopy [14, 11], which has emerged as a highly sensitive tool for label-free vibrational imaging and microspectroscopy in the life and material sciences [15–19]. Only recently, stimulated Raman scattering (SRS) has been used as a vibrational contrast for optical microscopy [20, 21, 12, 13, 22]. CARS and SRS microscopy can be readily combined with other nonlinear coherent optical processes that provide image contrast, such as second-harmonic generation (SHG) [23], sum-frequency generation (SFG) [24], and third-harmonic generation (THG) [25]. Among them, SFG generation provides vibrational contrast, but this technique is surface sensitive instead of bulk sensitive. Common to all techniques, ultrashort pulses of high peak powers and moderate average power are required for efficient signal generation. In combination with laser beam scanning, CRS microscopy has been demonstrated to provide high image acquisition rates

allowing the visualization of fast dynamical processes in living cells and tissue at video rates [26].

Beyond imaging, the combination of CRS microscopy with spectroscopic techniques has been used to obtain the full wealth of the chemical and the physical structure information of submicron-sized samples. In the frequency domain, multiplex CRS microspectroscopy allows the chemical identification of molecules on the basis of their characteristic Raman spectra and the extraction of their physical properties, e.g., their thermodynamic state. In the time domain, time-resolved CRS microscopy allows the recording of the localized Raman free induction decay occurring on the femtosecond and picosecond time scales. CRS correlation spectroscopy can probe three-dimensional diffusion dynamics with chemical selectivity.

This review is dedicated to the common underlying physical principles behind CARS and SRS microscopy, the comparison of their image contrast mechanisms and microspectroscopy implementations. We will discuss exemplary applications in biomedical areas with chosen illustrations taken from recent literature. This chapter is organized as follows: Section 6.2 starts out with a brief review of the fundamentals of CRS in general and the excitation pulse schemes providing high vibrational selectivity in particular. This identifies the analogies between CARS and SRS microscopy, while concurrently indicating their distinct image contrast mechanisms. Section 6.3 gives an overview of the general characteristics, the efforts for increasing the detection sensitivity, and biomedical applications of CARS imaging and microspectroscopies. Section 6.4 is dedicated to the principles behind and the applications of SRS imaging and microspectroscopy. A summary and a brief perspective conclude this review.

6.2 Fundamentals of Coherent Raman Scattering

6.2.1 Basic Theory

Coherent Raman scattering (CRS) is classically described as a parametric four-wave mixing process. For ease of experimental implementation, the arrangement most commonly used in microscopy is frequency-degenerate CRS requiring two synchronized laser fields at different frequencies, with at least one of them being tunable to adjust the desired Raman shift. Here, the pump and Stokes laser pulses with electromagnetic field amplitudes $\boldsymbol{E}_{\mathrm{p}}$ and $\boldsymbol{E}_{\mathrm{S}}$ at frequencies ω_{p} and ω_{S} ($\omega_{\mathrm{p}} > \omega_{\mathrm{S}}$), respectively, interact with the sample and induce a third-order nonlinear polarization not only at the frequencies of the input fields but also at their combination frequencies. As a result, a variety of distinct CRS processes concurrently occur. Among the different CRS detection schemes, coherent anti-Stokes Raman scattering (CARS), stimulated Raman gain (SRG), and stimulated Raman loss (SRL) have been successfully exploited to generate contrast in microscopy. The induced third-order polarizations are given by [27–29]

$$\boldsymbol{P}^{(3)}_{\mathrm{CARS}}(\omega_{\mathrm{AS}}) = 3\chi^{(3)}(-\omega_{\mathrm{AS}};\omega_{\mathrm{p}},\omega_{\mathrm{p}},-\omega_{\mathrm{S}})\,\boldsymbol{E}_{\mathrm{p}}(\omega_{\mathrm{p}})\,\boldsymbol{E}_{\mathrm{p}}(\omega_{\mathrm{p}})\,\boldsymbol{E}^{*}_{\mathrm{S}}(\omega_{\mathrm{S}}) \quad (6.1)$$

$$\boldsymbol{P}^{(3)}_{\mathrm{SRG}}(\omega_{\mathrm{S}}) = 6\chi^{(3)}(-\omega_{\mathrm{S}};\omega_{\mathrm{p}},-\omega_{\mathrm{p}},\omega_{\mathrm{S}})\,|\boldsymbol{E}_{\mathrm{p}}(\omega_{\mathrm{p}})|^{2}\,\boldsymbol{E}_{\mathrm{S}}(\omega_{\mathrm{S}}) \quad (6.2)$$

and

$$\boldsymbol{P}^{(3)}_{\mathrm{SRL}}(\omega_{\mathrm{p}}) = 6\chi^{(3)}(-\omega_{\mathrm{p}};\omega_{\mathrm{S}},\omega_{\mathrm{p}},-\omega_{\mathrm{S}})\,|\boldsymbol{E}_{\mathrm{S}}(\omega_{\mathrm{S}})|^{2}\,\boldsymbol{E}_{\mathrm{p}}(\omega_{\mathrm{p}}) \quad (6.3)$$

which act as sources of coherent radiation at the new CARS frequency $\omega_{\mathrm{AS}} = 2\omega_{\mathrm{p}} - \omega_{\mathrm{S}}$, at the Stokes frequency ω_{S}, and at the pump frequency ω_{p}. Pictorial descriptions of these processes are shown in the energy level diagrams of Fig. 6.1A. While the underlying physics is shared by all CRS processes, it is possible to selectively detect CARS, SRG, or SRL, which exhibit markedly different signal properties. In contrast to the detection of stimulated Raman scattering (SRS), which encompasses SRG and SRL, where the generated output field is in the same mode as one of the input fields, CARS detection benefits from the fact that the CARS output field is in a mode different from the input fields. The latter allows the selective detection of CARS through spectral filtering. This is schematically illustrated in Fig. 6.1B where the CARS power generated at the anti-Stokes frequency ω_{AS} is monitored, whereas in SRL and SRG the changes in the pump and Stokes power are examined, respectively.

The efficiency of the nonlinear interaction with the sample is expressed by the third-order nonlinear susceptibility of the form

$$\chi^{(3)} = \chi^{(3)\mathrm{nr}} + \chi^{(3)\mathrm{r}}. \quad (6.4)$$

The complex quantity, $\chi^{(3)\mathrm{r}} = \mathrm{Re}\left(\chi^{(3)\mathrm{r}}\right) + \mathrm{i}\,\mathrm{Im}\left(\chi^{(3)\mathrm{r}}\right)$, represents the nuclear response of the molecules. The induced polarization is resonantly enhanced when the Raman shift $\omega_{\mathrm{p}} - \omega_{\mathrm{S}}$ matches the frequency Ω_{r} of a Raman-active molecular vibration (Fig. 6.1A). Therefore, $\chi^{(3)\mathrm{r}}$ provides the intrinsic vibrational contrast mechanism in CRS-based microscopies. The nonresonant term $\chi^{(3)\mathrm{nr}}$ represents the electronic response of both the one-photon and the two-photon electronic transitions [30]. Typically, near-infrared laser pulses are used to prevent the effect of two-photon electronic resonances. With input laser pulse frequencies away from electronic resonances, $\chi^{(3)\mathrm{nr}}$ is independent of frequency and is a real quantity. It is important to realize that the nonresonant contribution to the total nonlinear polarization is simply a source for an unspecific background signal, which provides no chemical contrast in some of the CRS microscopies. While CARS detection can be significantly effected by the nonresonant contribution $\chi^{(3)\mathrm{nr}}$ [30], SRS detection is inherently insensitive to it [27, 29]. As will be discussed in detail in Sects. 6.3 and 6.4, this has major consequences for the image contrast mechanism of CARS and SRS microscopy, respectively.

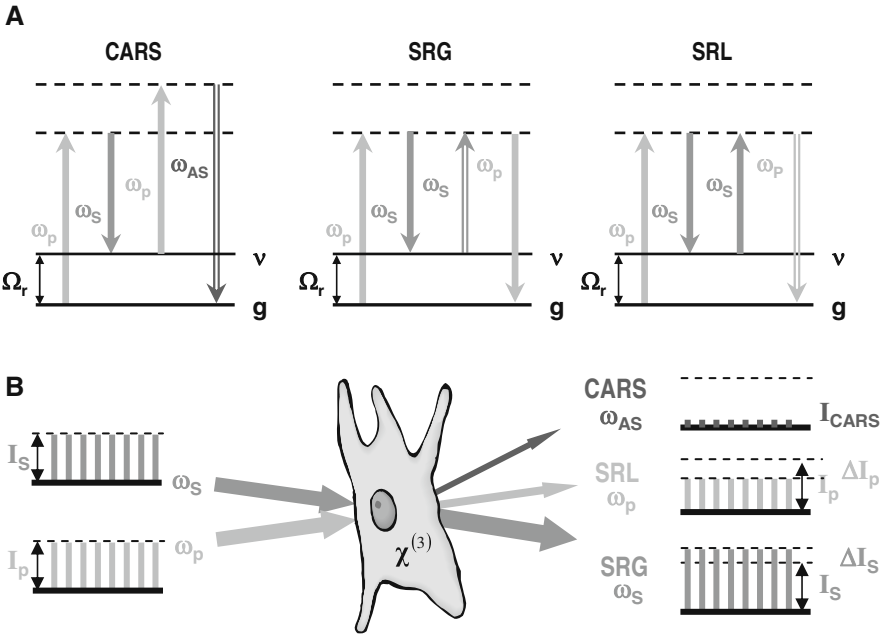

Fig. 6.1. A Energy level diagrams for the third-order nonlinear optical processes of coherent anti-Stokes Raman scattering (CARS), stimulated Raman gain (SRG), and stimulated Raman loss (SRL), in which pump and Stokes fields (solid arrows) at frequencies ω_{p} and ω_{S}, respectively, interact with a nonlinear Raman-active medium and generate a coherent radiation field (double-lined arrows). g and ν denote the electronic ground state and the vibrational state of a Raman mode with resonance frequency Ω_{r}, respectively. **B** Schematic illustration of CARS, SRL, and SRG occurring simultaneously in a nonlinear Raman-active medium described by $\chi^{(3)}$, e.g., a living cell. Under Raman resonance conditions, the pair of spatially and temporally overlapped pump and Stokes laser pulse trains generate a CARS signal I_{CARS} pulse train at a new frequency $\omega_{\mathrm{AS}} = 2\omega_{\mathrm{p}} - \omega_{\mathrm{S}}$. The Stokes pulse intensity I_{S} experiences a gain by ΔI_{S} and the pump pulse intensity I_{p} suffers a concomitant loss by ΔI_{p}. The detection of these signals provides vibrational contrast in CRS microscopy

6.2.2 Relation Between Coherent and Spontaneous Raman Scattering

If monochromatic and linearly polarized input fields are considered, the third-order susceptibility can be expressed by its tensor components, $\chi^{(3)}_{ijkl} = \chi^{(3)\mathrm{nr}}_{ijkl} + \sum_r \chi^{(3)\mathrm{r}}_{ijkl}$, which refer in their order of appearance to the Cartesian polarization components of the CRS, pump, probe, and Stokes fields in the four-wave mixing process [31]. In transparent and optically inactive media, where the input frequencies are away from any electronic transition frequencies, and only the molecular ground state is populated, the selection rules of both resonant coherent and spontaneous Raman scattering are identical

[32–35]. Accordingly, for a given Raman-active resonance r, the amplitudes of $\chi^{(3)\mathrm{r}}_{ijkl}$ can be expressed in terms of the isotropy and symmetric anisotropy invariants of the corresponding spontaneous Raman scattering tensor, α^2 and ${\gamma_\mathrm{s}}^2$, respectively. In the case of frequency-degenerate CRS considered here, the two relevant independent tensor components assume the following form [33, 34]:

$$\chi^{(3)\mathrm{r}}_{1111} = \frac{A_{\mathrm{r},1111}}{\delta_\mathrm{r} - \mathrm{i}\Gamma_\mathrm{r}} = CN\Gamma_\mathrm{r}\frac{\alpha^2 + \frac{4}{45}{\gamma_\mathrm{s}}^2}{\delta_\mathrm{r} - \mathrm{i}\Gamma_\mathrm{r}} \tag{6.5}$$

$$\chi^{(3)\mathrm{r}}_{1221} = \frac{A_{\mathrm{r},1221}}{\delta_\mathrm{r} - \mathrm{i}\Gamma_\mathrm{r}} = CN\Gamma_\mathrm{r}\frac{\frac{1}{15}{\gamma_\mathrm{s}}^2}{\delta_\mathrm{r} - \mathrm{i}\Gamma_\mathrm{r}}. \tag{6.6}$$

$\delta_\mathrm{r} = \Omega_\mathrm{r} - (\omega_\mathrm{p} - \omega_\mathrm{S})$ is the detuning from the Raman resonance at frequency Ω_r with a half width at half maximum (HWHM) of Γ_r. N is the number density of Raman-active scatterers and C is a proportionality constant.

The ratio between the susceptibility components, $\chi^{(3)}_{1221}$ / $\chi^{(3)}_{1111}$, defines the resonant and nonresonant nonlinear depolarization ratios:

$$\rho_\mathrm{r} = \frac{\chi^{(3)\mathrm{r}}_{1221}}{\chi^{(3)\mathrm{r}}_{1111}} = \frac{3{\gamma_\mathrm{s}}^2}{45\alpha^2 + 4{\gamma_\mathrm{s}}^2} \quad \text{and} \quad \rho_\mathrm{nr} = \frac{\chi^{(3)\mathrm{nr}}_{1221}}{\chi^{(3)\mathrm{nr}}_{1111}} = \frac{1}{3} \tag{6.7}$$

respectively. ρ_r is the direct CRS analogue for the spontaneous Raman depolarization ratio of the rth Raman mode, with values ranging between 0 for an isotropic and 0.75 for an anisotropic vibrational mode symmetry. In contrast, ρ_nr has no spontaneous Raman analogue. For the nonresonant background susceptibility tensor components, Kleinman's symmetry conjecture holds [36], $\chi^{(3)\mathrm{nr}}_{1111} = 3\chi^{(3)\mathrm{nr}}_{1221}$, and ρ_nr assumes the value of 1/3.

The spontaneous Raman spectrum is then described by the sum of the imaginary parts of the complex resonant susceptibility,

$$I_\mathrm{Raman} \propto \sum\nolimits_\mathrm{r} \mathrm{Im}\left(\chi^{(3)\mathrm{r}}\right) \tag{6.8}$$

which is linearly dependent on the number density of Raman-active scatterers.

6.2.3 Excitation Pulse Schemes with High Vibrational Selectivity

Because of the nonlinearity of CRS, conventional wisdom states that high input field peak amplitudes, which are readily provided by ultrashort laser pulses, are required to induce a strong nonlinear polarization (cf. (6.1)–(6.3)). The use of transform-limited femtosecond pulses, however, results in a broad distribution of Raman shifts, $\omega_\mathrm{p} - \omega_\mathrm{S}$, that by far exceeds the line width of a typical Raman resonance $\left(\sim 10\,\mathrm{cm}^{-1}\right)$ in condensed-phase samples at room temperatures. This is schematically depicted in Fig. 6.2A where the frequency–time dependences of a transform-limited pump and Stokes

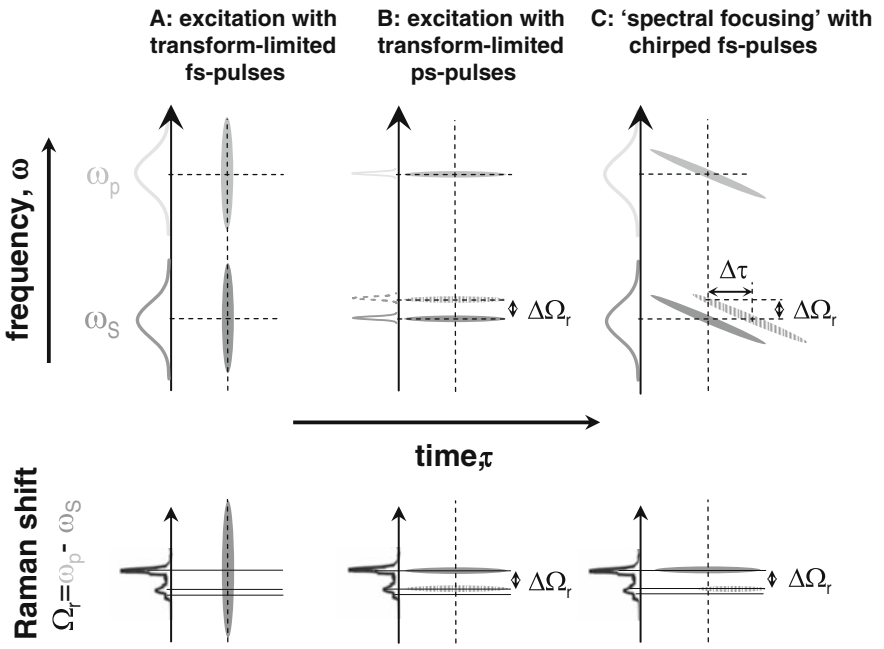

Fig. 6.2. Illustration of the frequency–time dependences of pump and Stokes pulses in three different CRS excitation pulse schemes and their corresponding spectral resolution of Raman shifts. **A** Using a pair of transform-limited femtosecond pulses of broad spectral and narrow temporal widths results in a broad bandwidth of Raman shifts that exceeds the line width of a single Raman resonance. **B** Using transform-limited picosecond pulses of broad temporal and narrow spectral width readily provides high spectral resolution matching the Raman resonance line width to be probed. Selection of a Raman resonance shifted by $\Delta\Omega_r$ is achieved by tuning the frequency of one of the laser beams by the same amount. **C** 'Spectral focusing' of a pair of identically linear chirped pump and Stokes femtosecond pulses results in a narrow *instantaneous* frequency difference in the CRS process, thus also providing narrow-bandwidth CRS excitation. Selection of a Raman resonance shifted by $\Delta\Omega_r$ is achieved by adjusting the time delay $\Delta\tau$ between the pulses. Shifted pulses in (**B**) and (**C**) are depicted hatched

femtosecond pulse and the consequential poor spectral CRS selectivity are illustrated. To achieve not only higher spectral resolution that allows the selective excitation of a particular vibrational resonance but also higher sensitivity in CRS detection, it is therefore desirable to use narrow-bandwidth excitation schemes.

As shown in Fig. 6.2B, this can be directly achieved by using transform-limited pump and Stokes pulses, of which the spectral bandwidth matches the Raman resonance line width to be probed [37]. The temporal width of the pulses is typically $\sim$5 ps, corresponding to a spectral width of $\sim$2.9 cm^{-1}. A frequency-resolved CRS spectrum is obtained by tuning the wavelength of

one of the laser beams. In an alternative approach, narrow-bandwith excitation in multi-photon processes can be achieved with chirped broad-bandwidth pulses [38–40]. Such an implementation of 'spectral focusing' in CARS [41–43] is illustrated in Fig. 6.2C, where both the pump and the Stokes femtosecond pulses are linearly chirped by the same amount in order to obtain a narrow *instantaneous* frequency difference in the CRS process at a given time delay between the pulses. This way, the entire bandwidth of both pulses is focused into a narrow spectral region, resulting in a higher spectral resolution (typically $\sim 3\,\mathrm{cm}^{-1}$). By scanning the time delay, the CRS spectrum is acquired. A yet different concept for high spectral resolution in CRS detection, as introduced by Silberberg and coworkers [44–46], is based on coherent control techniques. In contrast to standard two-beam CRS, the CRS signal is produced by an intrapulse four-wave mixing process of all the frequency components within the bandwidth of a single ultrashort laser pulse. By tailoring the spectral phase of the pulse via Fourier transform pulse shaping using a programmable liquid-crystal spatial light modulator (SLM), the interference of all quantum paths in the sample induced by various spectral components of the pulse is controlled. A periodic modulation of the spectral phase yields a selective excitation at a given Raman shift [44]. A spectrum is obtained by scanning the phase modulation periodicity. Here, the spectral resolution of the generated CRS signal is typically $\sim 5\,\mathrm{cm}^{-1}$, which is determined by the pixel size of the SLM [47].

Common to all narrow-bandwidth excitation schemes is sequential scanning of an experimental parameter in order to adjust the Raman shift in CRS detection. In order to obtain an entire CRS spectrum, this is not only time consuming but also prone to sources of noise induced by fluctuations in laser pulse parameters. As a consequence, dynamical changes in a CRS spectrum are difficult to follow. This problem can be circumvented by use of multiplex CRS spectroscopies [48, 49], which will be discussed in combination with CARS and SRS microscopy in Sects. 6.3 and 6.4, respectively.

6.3 Coherent Anti-Stokes Raman Scattering Microscopy

CARS was first reported in 1965 by Maker and Terhune [50] and has been extensively used as a spectroscopic tool for chemical analysis in the condensed and gas phases [28–30]. In 1982, Duncan et al. first demonstrated CARS microscopy using non-collinear pump and Stokes visible dye laser beams and a two-dimensional detector to record the anti-Stokes beam in the phase matching direction [14, 51]. The use of visible light resulted in a large two-photon enhanced nonresonant background signal. Zumbusch et al. [11] revived CARS microscopy in 1999 by using tightly focused collinearly propagating pump and Stokes near-infrared laser beams and CARS detection in the forward direction. This work demonstrated a significant reduction of the nonresonant background signal and established the above-listed advantages of CRS microscopy.

Variants of collinear CARS microscopy were also reported, including a BOXCARS geometry [52], wide-field CARS microscopy [53–55], CARS near-field scanning optical microscopy using a fiber probe [56] and a metal tip [57], and a proof-of-principle demonstration of CARS endoscopy [58]. In this review, we restrict our discussion to the collinear input beam geometry and CARS detection in the forward and backward directions (Fig. 6.3A), which became the configuration of choice in CARS microscopy exhibiting superior spatial resolution and image quality.

6.3.1 General Characteristics

In order to qualitatively describe the physical picture behind collinear CARS microscopy, we first make the simplifying assumption that the pump and Stokes beams are monochromatic plane waves with wave vectors $\boldsymbol{k}_{\mathrm{P}}$ and $\boldsymbol{k}_{\mathrm{S}}$, respectively, that collinearly co-propagate along the optical axis $\boldsymbol{z}$ through a sample slab of thickness L. For the detection of CARS, the nonlinear polarization $\boldsymbol{P}^{(3)}_{\mathrm{CARS}}(\omega_{\mathrm{AS}})$ (cf. (6.1)) induced in the slab is the source of an anti-Stokes emission with wave vector $\boldsymbol{k}_{\mathrm{AS}}$ that propagates in the forward ($\boldsymbol{k}_{\mathrm{AS}}$ along $\boldsymbol{z}$) and the backward ($\boldsymbol{k}_{\mathrm{AS}}$ along $-\boldsymbol{z}$) directions. The CARS intensity detected is then given by [28, 59]

$$I_{\mathrm{CARS}}(\omega_{\mathrm{AS}}) \propto \left|\chi^{(3)}(-\omega_{\mathrm{AS}};\omega_{\mathrm{p}},\omega_{\mathrm{p}},-\omega_{\mathrm{S}})\right|^2 I_{\mathrm{p}}^2(\omega_{\mathrm{p}})\, I_{\mathrm{S}}(\omega_{\mathrm{S}}) \left(\frac{\sin(|\Delta\boldsymbol{k}|\, L/2)}{|\Delta\boldsymbol{k}|\,/\,2}\right)^2 \tag{6.9}$$

where $I_{\mathrm{S}}(\omega_{\mathrm{S}}) \propto |\boldsymbol{E}_{\mathrm{S}}(\omega_{\mathrm{S}})|^2$ and $I_{\mathrm{p}}(\omega_{\mathrm{p}}) \propto |\boldsymbol{E}_{\mathrm{p}}(\omega_{\mathrm{p}})|^2$ are the undepleted Stokes and pump beam intensities, respectively, and $\Delta\boldsymbol{k} = \boldsymbol{k}_{\mathrm{AS}} - (2\boldsymbol{k}_{\mathrm{P}} - \boldsymbol{k}_{\mathrm{S}})$ is the wave vector phase mismatch. The quantity physically detected in CARS microscopy has thus the following properties: (i) The signal is proportional to the modulus square of the total nonlinear susceptibility $\chi^{(3)}$ (cf. (6.4)), thus being sensitive to the nonresonant background contribution $\chi^{(3)\mathrm{nr}}$ and, via (6.5) and (6.6), shows a square-dependence on the number density of Raman-active modes within the probe volume. (ii) The signal scales quadratically with the pump and linearly with the Stokes laser intensities. (iii) The CARS signal is a function of the extent of wave vector phase mismatch $|\Delta\boldsymbol{k}|$, and therefore depends on the propagation directions of the pump, Stokes, and CARS fields.

The Effect of Wave Vector Phase Mismatch

The phase matching condition is $|\Delta\boldsymbol{k}|\, L << \pi$, which means that for the generation of CARS the coherence length defined by $\pi/|\Delta\boldsymbol{k}|$ has to exceed the effective interaction length L. The latter is determined by the axial dimension of the nonlinear sample. Thus, the actual extent of $|\Delta\boldsymbol{k}|$ acts as a size filter for the scatterer of dimensions for which an efficient CARS signal is generated. When the slab thickness is smaller than the pump wavelength, i.e., $L \approx 0$, the

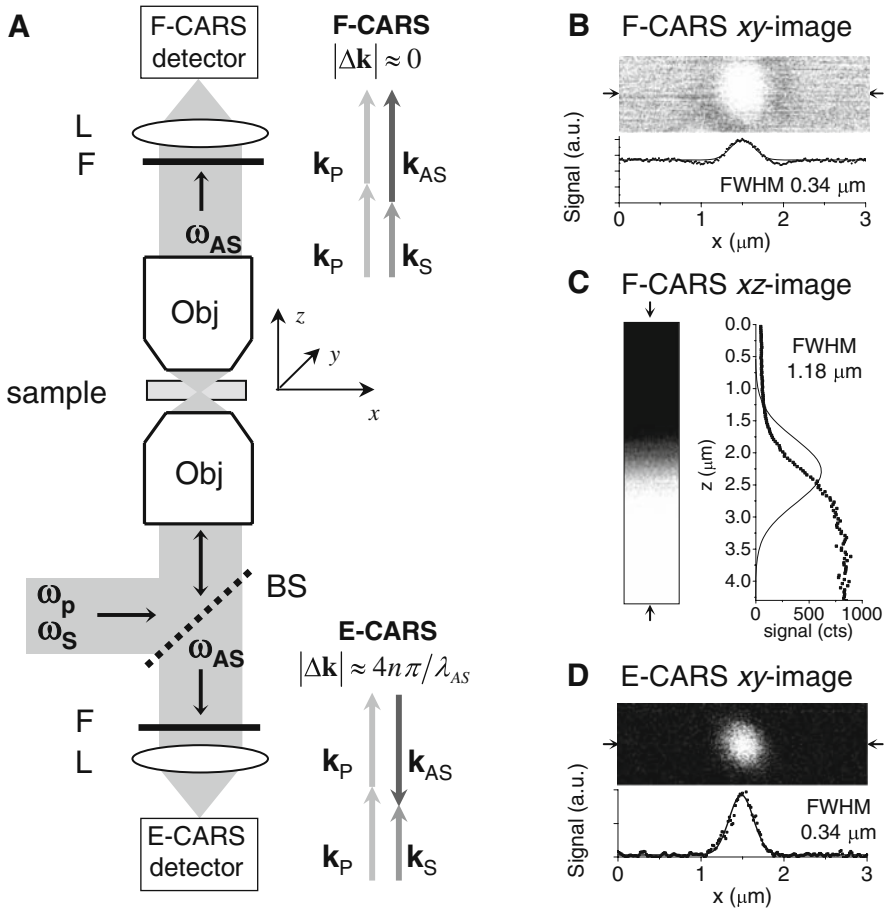

Fig. 6.3. A Schematic configuration of forward- and epi-detected CARS (F- and E-CARS) microscopy with collinear, co-propagating pump and Stokes beams. The corresponding wave vector mismatch and diagrams along the optical axis z are indicated (BS: dichroic beam splitter; Obj: objective lens; F: filter; L: lens). **B** and **D** F- and E-CARS x–y images of a 0.5-μm polystyrene sphere embedded in water, recorded at a Raman shift of 1595 cm^{-1} with pump- and Stokes wavelengths at 800 and 917 nm, respectively. The lateral intensity profiles along the lines indicated by the arrows reveal a typical lateral resolution of 340 nm (FWHM). **C** F-CARS x–z image of an interface between a cover glass and immersion oil, recorded with pump and Stokes pulses at 717 and 900 nm (Raman shift: 2840 cm^{-1}), respectively. The axial edge profile along z together with its smoothed first derivative (solid line) reveals a typical longitudinal resolution in CARS microscopy of 1.2 μm (FWHM)

phase matching condition is satisfied in both the forward and backward (epi) directions. Accordingly, the forward- and epi-detected CARS (F-CARS and E-CARS) are equal in intensity. As illustrated in Fig. 6.3A, the phase matching condition along $\boldsymbol{z}$ is always fulfilled for forward-detected CARS ($|\Delta \boldsymbol{k}| \approx 0$), whereas in the case of epi-detected CARS a large wave vector mismatch of $|\Delta \boldsymbol{k}| = 2\,|\boldsymbol{k}_{\mathrm{AS}}| \approx 4n\pi/\lambda_{\mathrm{AS}}$ is introduced [60], where n is the refractive index of the medium assumed to be independent of frequency. As a result, the F-CARS signal starts to overwhelm the E-CARS signal with increasing L because of the constructive interference in the forward direction and the destructive interference in the backward direction. For large L, which resembles the case of focusing into an isotropic bulk medium, the E-CARS intensity is significantly reduced as compared to the corresponding forward signal. Likewise, a large wave vector mismatch is established in a geometry with collinearly counter-propagating pump and Stokes beams, denoted counter-propagating CARS (C-CARS) (not shown), with a signal dependence on the interaction length similar to that of E-CARS [61, 16].

Nonlinear Susceptibility Contributions to the CARS Signal

For the understanding of CARS contrast mechanisms, it is essential to discuss in more detail the proportionality of the CARS intensity to the modulus square of the total nonlinear susceptibility in (6.9). Substituting (6.4) into (6.9) yields

$$I_{\mathrm{CARS}} \propto \left|\chi^{(3)\mathrm{nr}} + \chi^{(3)\mathrm{r}}\right|^2 = \left(\chi^{(3)\mathrm{nr}}\right)^2 + \left|\chi^{(3)\mathrm{r}}\right|^2 + 2\chi^{(3)\mathrm{nr}}\,\mathrm{Re}\left(\chi^{(3)\mathrm{r}}\right). \quad (6.10)$$

In their order of appearance the terms involved in this expression describe the nonresonant background CARS signal, the purely resonant CARS contributions, and the CARS contribution due to mixing of the nonresonant and the real part of the resonant Raman responses, respectively. Figure 6.4 displays the spectral response of each CARS signal component for an isolated Raman resonance in the presence of a nonresonant background contribution. Their sum yields the well-known CARS dispersive line shape where the peak frequency is red-shifted, an intensity minimum at the blue side of the resonance line appears, and a constant offset is introduced [30]. All these features are more pronounced the larger the relative intensity of the nonresonant contribution is in the sample. As a consequence, the often unknown relative intensity of the nonresonant contribution not only introduces a background to CARS image contrast and spectra, but also precludes their quantitative interpretation in terms of known spontaneous Raman spectra from the literature.

A full description of polarization-sensitive CARS signal generation that takes the polarization properties of the pump, Stokes, and CARS fields and the tensor character of the nonlinear susceptibility components (cf. (6.5)–(6.7)) into account can be found elsewhere [16].

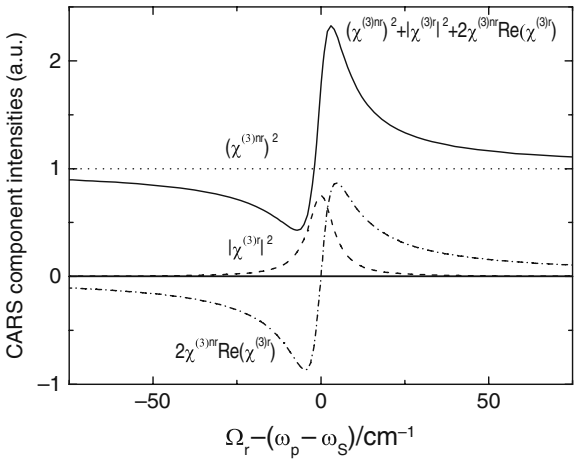

Fig. 6.4. Typical CARS spectral profile modeled for an isolated Lorentzian Raman line assuming (6.5) ($\Gamma_\mathrm{r} = 4.6\,\mathrm{cm}^{-1}$, $A_\mathrm{r} = 4\,\mathrm{cm}^{-1}$) and parallel-polarized input and CARS fields. According to (6.10), the total CARS spectrum (solid line) is composed of a constant nonresonant background $\left(\boldsymbol{\chi}^{(3)\mathrm{nr}}\right)^2$, a resonant contribution $\left|\boldsymbol{\chi}^{(3)\mathrm{r}}\right|^2$, and a heterodyne mixing term of dispersive character, $2\boldsymbol{\chi}^{(3)\mathrm{nr}}\mathrm{Re}\left(\boldsymbol{\chi}^{(3)\mathrm{r}}\right)$

6.3.2 Increasing the Detection Sensitivity

In condensed-phase CARS, the effects of the nonresonant susceptibility $\chi^{(3)\mathrm{nr}}$ are most profound when a sample with weak Raman modes is embedded in a nonlinear medium. The nonresonant background of the latter can be easily comparable to or larger than the resonant contribution from the sample of interest. This is a situation commonly encountered in biological applications of CARS microscopy. Depending on the experimental situation, the CARS detection sensitivity to weak resonances can then be restricted either by the nonresonant background or by the photon shot-noise [62]. To maximize either the relative or the absolute CARS intensity, nonresonant background suppression schemes [44, 60, 61, 63, 64] and optical heterodyne detection (OHD) techniques [65–67] have been developed during recent years.

Suppression of Nonresonant Background

It is important to realize that, unlike in fluorescence detection, CARS detection is not background free. Nonresonant background signals, which provide no vibrational contrast, and the solvent water that has strong resonant signals of broad spectral width often overwhelm the CARS signal from small objects and limit the sensitivity. During recent years, various methods have been developed that permit efficient suppression of nonresonant background

signal in CARS microscopy. These include epi detection [37, 60], counter-propagating CARS [61], polarization-sensitive detection [63], pulse-sequenced detection [64], and the implementation of coherent control techniques [44]. Common to all these techniques is that the suppression of nonresonant background is accompanied by a significant reduction of the absolute strength of the Raman-resonant CARS signal resulting in a modest detection sensitivity for very weak resonances and/or low sample concentrations.

Optical Heterodyne-Detected CARS

Background-free CARS microscopy without any loss of resonant signal strength can be achieved through phase-controlled OHD schemes. In OHD-CARS, the measured signal is the interference of a weak resonance CARS field with an intense reference field at the anti-Stokes frequency. The latter acts as a so-called local oscillator (LO) field. As Oudar et al. [68] have pointed out, OHD-CARS allows the recovery of both the real and imaginary parts of the Raman-resonant susceptibility. Furthermore, it allows a significant enhancement of the CARS detection sensitivity through amplification of the Raman-resonant signal.

Weak Raman-resonant CARS, i.e., when $\left|\chi^{(3)\mathrm{r}}\right| << \chi^{(3)\mathrm{nr}}$, can be amplified by interference with the intense nonresonant CARS that acts as an intrinsic local oscillator field created within the same sample. For weak resonances, the second term in (6.10) becomes negligible and the nonresonant background and the heterodyne mixing term then dominate the total CARS intensity. As a result, the amplified CARS signal is proportional to the real part of the resonant susceptibility and falls off linearly with the number density of Raman scatterers. Such an intrinsic OHD-CARS effect has been exploited in CARS microscopy for high-sensitivity imaging [69] and microspectroscopy [70], where shot-noise limited detection sensitivity has been achieved.

In methods based on nonlinear interferometry, originally proposed by Chang et al. [71], the CARS field generated by the sample is heterodyne mixed with a well-controlled and stable local oscillator field that is created in an external nonresonant CARS bulk medium [66] or that is provided by an additional laser reference beam at the anti-Stokes frequency from a cascading phase preserving chain [67]. Because both the CARS field from the sample and the LO field are phase and frequency locked, nonresonant background suppression is achieved by the addition of the sample CARS field with a reference field of opposite phase [72, 73]. The potential of CARS interferometry for nonresonant background suppression in CARS microscopy has been demonstrated using detection in the time domain [65, 74] as well as in the frequency domain [75, 67].

Recently, Silberberg and coworkers have introduced a different approach for active phase control in CARS [44–47]. By tailoring the spectral phase of a single ultrashort laser pulse, phase-sensitive detection of the resonant signal has been demonstrated where the strong nonresonant CARS background of

the same species is used as the local oscillator [45]. Background-free CARS spectroscopy has been achieved by use of both spectral phase and polarization pulse shaping [46].

6.3.3 Contrast Mechanisms in Forward and Epi Detection

In the actual experiment, pump and Stokes beams are not monochromatic plane waves but rather have Gaussian intensity profiles and are tightly focused onto the sample by a high numerical aperture (N.A.) objective lens (cf. Fig. 6.3A). Here, the above plane wave approximation is strict only for the CARS radiation along the optical axis $\boldsymbol{z}$. However, the physical picture described above remains the same. Unlike in fluorescence or spontaneous Raman microscopy, the contrast mechanism in CARS microscopy is governed by the coherent sum of both the resonant and nonresonant CARS radiations of the sample and/or the solvent (cf. (6.10)). An amount of theoretical work was published [52, 76, 60, 77, 61, 78–80], which takes the distinct features of signal generation in CARS microscopy into account, such as (i) the tightly focused excitation beams [76, 60, 77, 61], (ii) the wave vector mismatch in the different geometries [60, 61], and (iii) a heterogeneous sample of Raman scatterers of arbitrary shape and size embedded in a nonlinear medium, i.e., the solvent [61].

Here, we provide a qualitative description of the CARS contrast mechanism in the F- and E-CARS geometries by considering a submicron sphere and hemisphere object with $\chi^{(3)}_{\mathrm{obj}}$ located in the center of the focus and embedded in an isotropic nonresonant medium, i.e., $\chi^{(3)}_{\mathrm{solv}} = \chi^{(3)\mathrm{nr}}_{\mathrm{solv}} \neq 0$ [61]. This is illustrated in Fig. 6.5, where the CARS radiation fields generated by the object and the solvent are symbolized by filled and white arrows, respectively. The above-described F-CARS signal dependence on the object dimension results in a poor imaging contrast when the object volume is much smaller than the focal excitation volume. A weak F-CARS signal from an object is then either superimposed on a large bulk solvent F-CARS background when $\chi^{(3)}_{\mathrm{obj}} > \chi^{(3)\mathrm{nr}}_{\mathrm{solv}}$ or it can cause a negative image contrast by depleting the background signal when $\chi^{(3)}_{\mathrm{obj}} < \chi^{(3)\mathrm{nr}}_{\mathrm{solv}}$. The coherent sum of the resonant susceptibility component of the object ($\chi^{(3)\mathrm{r}}_{\mathrm{obj}}$) and the nonresonant background component predominantly of the solvent ($\chi^{(3)\mathrm{nr}}_{\mathrm{solv}}$) yields an expression for the total F-CARS intensity that has the form of (6.10). In the common case where $\left|\chi^{(3)\mathrm{r}}_{\mathrm{obj}}\right| << \chi^{(3)\mathrm{nr}}_{\mathrm{solv}}$, the intense nonresonant signal can act as a local oscillator in such a heterodyne detection scheme and can be used for resonant signal enhancement [70] (for an example, see Fig. 6.9).

On the contrary, a way to image small objects embedded in a nonresonant solvent with high contrast is provided by the epi-detection geometry [60]. Because the E-CARS signal intensity from an isotropic bulk medium is negligible the signal from the microscopic object with an effective

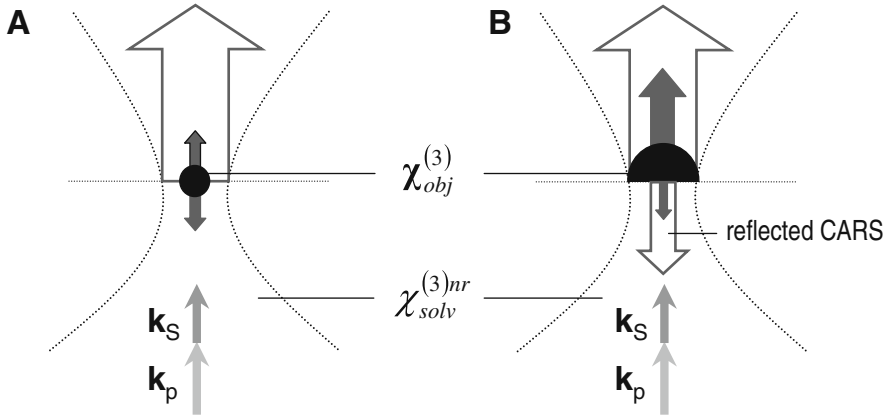

Fig. 6.5. Illustration of the F- and E-CARS contrast generation mechanisms for (**A**) a sphere and (**B**) a hemisphere object placed in a nonlinear solvent medium at the origin of tightly focused excitation beams. Filled and white arrows denote the CARS radiation fields created in the submicron-sized object with $\chi^{(3)}_{\mathrm{obj}}$ and the surrounding solvent with $\chi^{(3)\mathrm{nr}}_{\mathrm{solv}}$, respectively

susceptibility of $\chi^{(3)}_{\mathrm{obj}} - \chi^{(3)\mathrm{nr}}_{\mathrm{solv}}$ provides the first contrast mechanism in E-CARS microscopy (Fig. 6.5A). Since the E-CARS image contrast is determined by $\left|\chi^{(3)}_{\mathrm{obj}} - \chi^{(3)\mathrm{nr}}_{\mathrm{solv}}\right|^2$, objects with $\chi^{(3)}_{\mathrm{obj}} < \chi^{(3)\mathrm{nr}}_{\mathrm{solv}}$ provide positive image contrast. The second contrast mechanism in E-CARS microscopy is provided by objects with an interface perpendicular to the optical axis [61], as shown for the hemisphere object in Fig. 6.5B. In contrast to the situation described for a sphere, the symmetry break of the focal plane caused by the boundary in $\chi^{(3)}$ of the semi-infinite object results in an inefficient cancellation of E-CARS signal. In addition, it should be noted that a refractive index mismatch between the sample and the solvent causes back-reflection of intense F-CARS from the solvent. In practice, if the input beams are not focused on the interface perpendicular to the optical axis, the back-reflected signal is defocused on the E-CARS detector and can be minimized by the use of confocal detection. For small scatterers, the back-reflected solvent signal is negligible compared to the epi-scattering signal from the object. If back-reflection of strong nonresonant forward-scattered signal from bulk solvent occurs, it can amplify the weak resonant signal from the object propagating in the epi direction via heterodyne mixing [69]. Note that while E-CARS microscopy can efficiently reject nonresonant background contributions from a bulk sample (e.g., the solvent) it cannot discriminate the intrinsic nonresonant background of an object itself. Consequently, the spectral selectivity is poor when the nonresonant contribution of the object exceeds its resonant contribution, i.e., $\chi^{(3)\mathrm{nr}}_{\mathrm{obj}} - \chi^{(3)\mathrm{nr}}_{\mathrm{solv}} >> \chi^{(3)\mathrm{r}}_{\mathrm{obj}}$.

6.3.4 CARS Imaging

CARS microscopy has emerged as a highly sensitive analytical tool for vibrational bioimaging, predominantly, of lipids in membrane model systems [69, 81–84], live unstained cells [85–95, 43], and both ex vivo and in vivo tissues [26, 96–103, 43]. Examples of CARS imaging applications in the physical and material sciences include the study of fracture dynamics in drying silica nanoparticle suspensions [104], patterned polymeric photoresist film [105], drug molecules in a polymer matrix [106], and liquid crystals [107, 108].

Instrumentation and Experimental Characterization

In the most common realization of two-beam CARS imaging, mode-locked picosecond laser systems that operate at high repetition rates (∼100 MHz) and provide narrow bandwidth and tunable pump and Stokes pulses [37, 109–111] are used as excitation sources (cf. Fig. 6.2B). Alternatively, in the spectral focusing excitation scheme (cf. Fig. 6.2C), identically linear chirped pump and Stokes pulses of broad spectral width from a femtosecond laser system are employed [41–43]. As schematically shown in Fig. 6.3A, the pump and Stokes pulse trains are temporally overlapped and collinearly sent into an optical microscope. Tight focusing is accomplished with a high N.A. objective lens. The CARS signal is collected in the epi direction by the same objective lens (E-CARS [60]) or collected parfocally in the forward direction by using a second lens (F-CARS [11]). Because of the high directionality of the F-CARS radiation, the collection with a condenser lens has been demonstrated to be sufficient [112, 85]. For polarization-sensitive CARS detection [63, 61], the setup is combined with polarization control of the input and CARS beams (not shown). From the practical point of view, E-CARS detection obviates the need for a second microscope objective lens and thus leaves above space for sample manipulation. It is readily implemented with a standard epi-fluorescence microscope setup. The collected CARS radiation is spectrally filtered against the pump and Stokes frequencies and confocally detected by the use of either single-photon counting or analog detection techniques. To obtain images, either the sample is scanned with respect to the fixed laser beams or the laser beams are scanned with respect to the fixed sample. For applications where the emphasis is on high image acquisition rates rather than detection sensitivity, laser galvo scanning together with analog photo-multiplier detection is used [85]. Real-time image acquisition at video rates has been demonstrated [26]. For applications where a high detection sensitivity is required, sample scanning in combination with single-photon detection is the method of choice [69]. In sample scanning, however, the image acquisition rate is often limited by the piezo-driven sample stage. In order to avoid photodamage to the sample while still maintaining high

excitation pulse peak powers, it is therefore beneficial to reduce the repetition rate of both the pump and Stokes pulses by one to two orders of magnitude [37].

Typically, polystyrene spheres of well-defined diameter immersed in water are used to characterize the imaging properties in CRS microscopies. Figure 6.3B and D shows F- and E-CARS images, respectively, of an individual 0.5-μm sphere recorded under identical experimental conditions. The F-CARS image exhibits a poor contrast because bulk water gives rise to a large background signal. Moreover, two dips about the bead are observed in the lateral intensity profile. This phenomenon is attributed to the coherent mixing between the F-CARS of the sample and that of the surrounding water. The comparison of this F-CARS image with the E-CARS image in Fig. 6.3D clearly demonstrates the efficient rejection of bulk solvent signal, a concomitant lack of coherent imaging effects, and an increase of sensitivity for submicron-sized objects in E-CARS microscopy. Typically, a full width at half maximum (FWHM) of $<$400 nm is observed in the lateral intensity profiles across the spheres, which is smaller than the sphere diameter. Note that, unlike fluorescence microscopy, the lateral CARS intensity FWHM of a sphere cannot be determined by the convolution of its diameter with the point spread function of the excitation/detection profile. Figure 6.3C displays the F-CARS image in the x–z plane from an interface between glass- and refractive index-matched immersion oil. The first derivative of the measured intensity profile along the z axis results in a typical longitudinal resolution in CARS imaging of $\sim$1.2 μm (FWHM).

Biomedical Applications

One of the key advantages of CARS imaging is the noninvasive and nondestructive chemical mapping of live cells and tissues in three dimensions without staining. While many stains are impossible to apply in vivo, the vibrations of the intrinsic biomolecules can be used for CARS contrast. Moreover, it has been experimentally demonstrated that under the excitation conditions typically applied in in vivo CARS imaging perturbations to the sample are minimized, if not negligible [85, 87, 89]. Among the different vibrational modes, most CARS bioimaging applications take advantage of the strong signal from the CH_2 stretching vibration (2845 cm^{-1}) of intrinsic lipids.

Vibrational imaging of living cells has been applied for studying intracellular lipid droplet organelles [86, 89, 90, 113, 114] (cf. Fig. 6.10A), monitoring receptor-mediated endocytosis [92], analyzing mouse embryonic stem cells [93], and measuring adipocyte populations by microfluidic CARS cytometry [94]. By taking advantage of the deep penetration depth offered by CARS microscopy with near-infrared laser pulses, CARS tissue imaging has been demonstrated to complement other label-free optical techniques, such as autofluorescence that is limited to a few chemical species and optical tomography, second harmonic generation (SHG), and third harmonic generation (THG)

that often do not offer chemical contrast. Applications of CARS tissue imaging with subcellular resolution include the study of in vivo mouse skin [26], axonal myelin in both ex vivo and in vivo spinal nerve tissues [96, 87, 97, 101], lipid storage in a living *Caenorhabditis elegans* nematode [98], brain tissue structures [99], arterial tissues [100, 43], collagen sheaths around internal organs and muscles [102], liver tissue [103], and the localization of metal oxide nanoparticles in fish grill lamellae [115]. In the following, we first discuss an exemplary demonstration of the full potential of CARS imaging in live tissue and then describe an example of multimodal CARS microscopy in a spectral focusing implementation that allows simultaneous imaging of three endogenous nonlinear signals.

Cheng and coworkers [96, 97, 116, 117] have demonstrated real-time CARS imaging of neuronal myelin under physiological conditions. Myelin sheaths that surround axons in the central nervous system are formed of wrapped cell membranes. The high density of CH_2 groups in myelin leads to a strong and directional CARS signal at $2840\,\mathrm{cm}^{-1}$ that allows overcoming the sensitivity limitations of Raman microscopy and thus facilitates high-speed imaging of live spinal tissues. Figure 6.6A shows a CARS image of normal myelin sheath when focused into the equatorial plane of axons. Efficient CARS generation is observed when the linearly polarized pump and Stokes laser beams are in the direction parallel to the vertical orientation of axons, whereas horizontally polarized beams show weak CARS contrast. This photoselection effect [69] reveals the preferential vertical alignment of the symmetry axis of the CH_2 groups in the equatorial plane of the myelin (Fig. 6.6C). The ratio between the two polarization-resolved CARS image pixel intensities allows the determination of the degree of ordering of the myelin lipids. The image in Fig. 6.6B exemplifies the ability to monitor chemically induced degradation and disorders of myelin in spinal tissues [116]. Extensive myelin swelling characterized by a decrease in CARS contrast was observed after incubation of the sample with lysophosphatidylcholine (Lyso-PtdCho). Furthermore, the comparison with the polarization-resolved images of normal myelin sheath reveals a lack of a pronounced photoselection effect, indicating an increased disorder of lipid orientations upon myelin swelling. As this experiment demonstrates, CARS imaging facilitates the real-time characterization of the molecular distribution and the orientation of lipids in live spinal tissues under physiological conditions. It therefore offers the opportunity to study pathological pathways in neurological diseases.

The chemical specificity of CARS microscopy is readily combined with other nonlinear optical image contrast mechanisms, such as two-photon fluorescence (TPF), SHG, and THG, resulting in a multimodal CARS microscopy [88, 118, 117, 43]. In multimodal nonlinear optical imaging, TPF, SHG, and THG signals all benefit from the use of femtosecond laser pulses of high peak intensities, whereas the contrast and chemical selectivity of CARS benefits from the use of picosecond (narrow-bandwidth) pulses (see discussion in Sect. 6.2.3). As demonstrated by Pegoraro et al. [43], this apparent

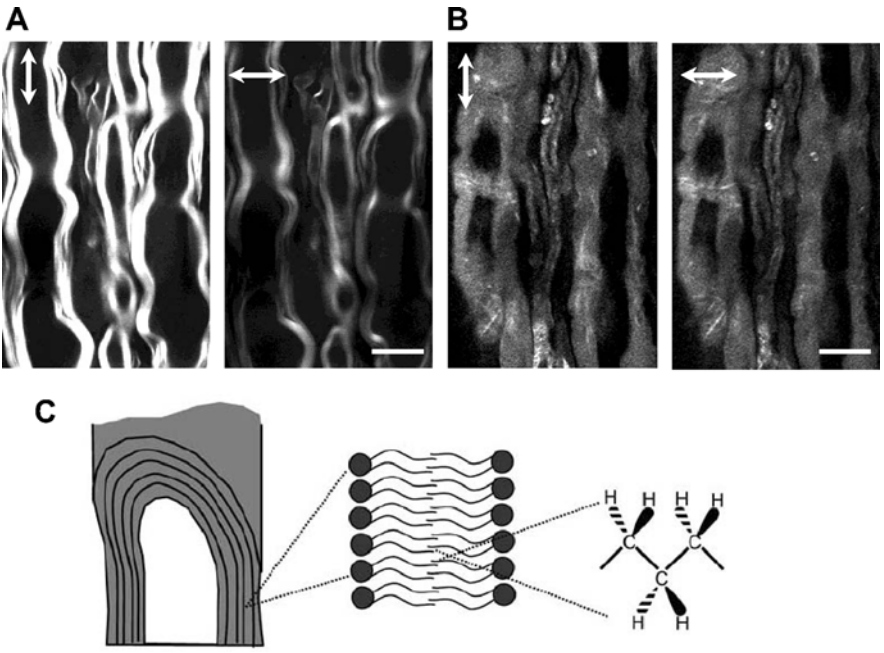

Fig. 6.6. Characterization of lyso-PtdCho-induced myelin swelling by CARS imaging. Parallel and linear polarized pump and Stokes laser beams were focused into the equatorial plane of axons. CARS images of normal (**A**) and swollen (**B**) myelin sheath that wrap parallel axons recorded with vertical (↕) and horizontal (↔) excitation polarization at a Raman shift of 2840 cm^{-1}. **C** The symmetry axis of the CH_2 groups in the equatorial plane of the myelin is parallel to the vertical direction. The images in (**B**) were acquired after injecting 2 µL of 10 mg/mL lyso-PtdCho into the tissue. Note the decrease of CARS intensity and the significantly reduced photoselection effect in the swollen region. All images were acquired at 1.13 s/frame (Scale bar: 10 µm) (Image courtesy of Ji-Xin Cheng [96, 97, 116])

discrepancy in multimodal CARS imaging can be elegantly resolved by implementing a spectral focusing scheme (cf. Fig. 6.2C). By using a single pair of femtosecond pump and Stokes pulses and controlling their degree of linear chirp, one can choose to optimize contrast in CARS imaging or enhance signals in TPF, SHG, and THG imaging. Figure 6.7 shows a measurement of a plaque cross section of an atherosclerotic arterial sample from a rabbit aorta, demonstrating the capability of using this spectral focusing implementation for the simultaneous imaging of three endogenous nonlinear signals: The CARS image visualizes the C-H stretching vibrations at a Raman shift of ∼2850 cm^{-1} from lipids (Fig. 6.7A). The TPF image shows the smooth muscle elastin fiber network, indicating that it is broken into short segments (Fig. 6.7B). And, the SHG image reveals the distribution of collagen (Fig. 6.7C). As this example demonstrates, one can routinely balance the resolution in CARS imaging

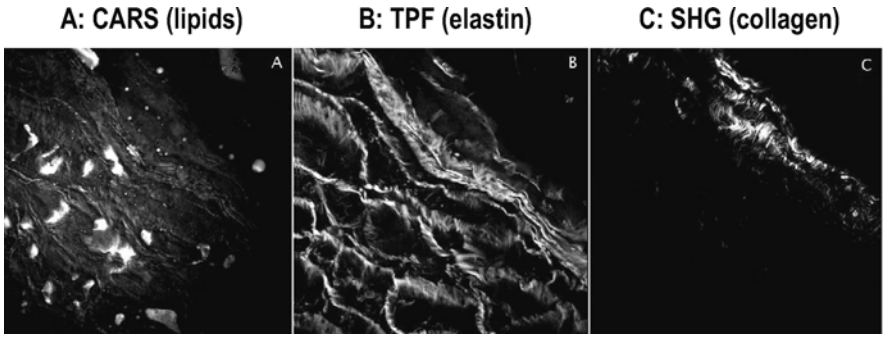

Fig. 6.7. Spectral focusing implementation of multimodal CARS imaging of rabbit aorta. A plaque cross section from a rabbit with an advanced atherosclerosis condition was imaged for (**A**) C–H stretching vibrations of lipids with CARS at a Raman shift of $\sim$2850 cm^{-1}, (**B**) the elastin fiber network with two-photon induced fluorescence (TPF), and (**C**) collagen with second harmonic generation (SHG). All three signals are endogenous to the sample and were detected simultaneously. CARS and SHG were collected in the forward direction whereas TPF was collected in the epi direction. The image size is $100 \times 100\,\mu\mathrm{m}$ ($512 \times 512\,\mathrm{pixel}^2$). Pixel dwell times were about 6 µs (Image courtesy of Adrian F. Pegoraro, Andrew Ridsdale, Douglas J. Moffatt, and Albert Stolow (Steacie Institute for Molecular Sciences, National Research Council of Canada, Ottawa), and Alex C.T. Ko and Michael G. Sowa (Institute for Biodiagnostics, National Research Council of Canada, Winnipeg) [43]))

versus signal from other nonlinear optical processes for a given sample when using the versatility of chirped femtosecond pulses that are readily provided by highly stable femtosecond laser sources.

6.3.5 CARS Microspectroscopies

Beyond imaging, CARS microscopy offers the possibility for spatially resolved vibrational spectroscopy [16], providing a wealth of chemical and physical structure information of molecular specimens inside a sub-femtoliter probe volume. As such, multiplex CARS microspectroscopy allows the chemical identification of molecules on the basis of their characteristic Raman spectra and the extraction of their physical properties, e.g., their thermodynamic state. In the time domain, time-resolved CARS microscopy allows recording of ultrafast Raman free induction decays (RFIDs). CARS correlation spectroscopy can probe three-dimensional diffusion dynamics with chemical selectivity. We next discuss the basic principles and exemplifying applications of the different CARS microspectroscopies.

Multiplex CARS Microspectroscopy

The principal concept of multiplex CARS spectroscopy, which was first demonstrated by Akhmanov et al. [48], is illustrated in Fig. 6.8A. In multiplex CARS,

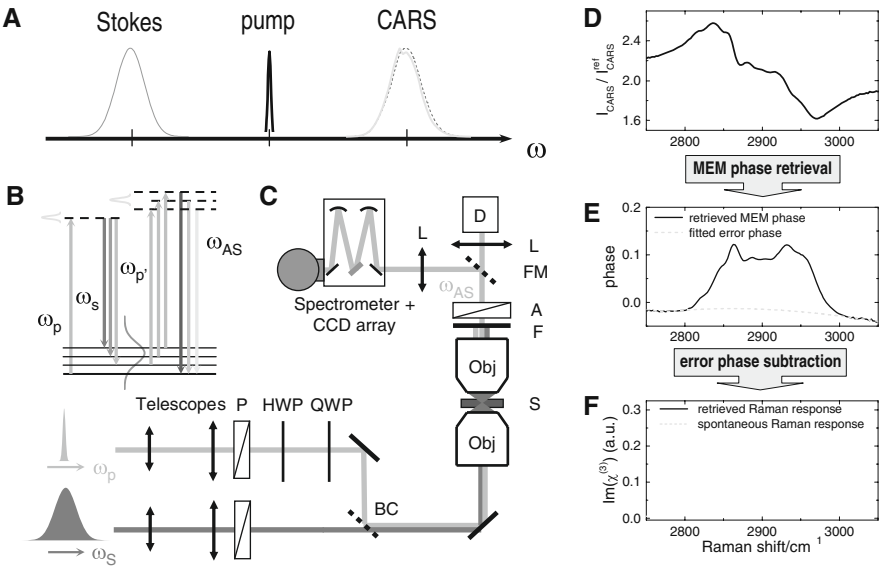

Fig. 6.8. A Principle of frequency-multiplexed CARS microspectroscopy: A narrow-bandwidth pump pulse determines the inherent spectral resolution, while a broad-bandwidth Stokes pulse allows simultaneous detection over a wide range of Raman shifts. The multiplex CARS spectra shown originate from a 70 mM solution of cholesterol in CCl_4 (solid line) and the nonresonant background of coverglass (dashed line) at a Raman shift centered at 2900 cm^{-1}. **B** Energy level diagram for a multiplex CARS process. **C** Schematic of the multiplex CARS microscope (P: polarizer; HWP/QWP: half/quarter-wave plate; BC: dichroic beam combiner; Obj: objective lens; F: filter; A: analyzer; FM: flip mirror; L: lens; D: detector; S: sample). **D** Measured normalized CARS spectrum of the cholesterol solution. **E** Maximum entropy method (MEM) phase spectrum (solid line) retrieved from (**D**) and the error background phase (dashed line) determined by a polynomial fit to those spectral regions without vibrational resonances. **F** Retrieved Raman response (solid line) calculated from the spectra shown in (**E**), directly reproducing the independently measured spontaneous Raman response (dashed line) of the same cholesterol sample

a narrow-bandwidth pump pulse and a broad-bandwidth Stokes pulse are used to simultaneously excite multiple Raman resonance frequencies. As a result, CARS radiation over a wide range of Raman shifts is generated. The corresponding energy level diagram is shown in Fig. 6.8B. The bandwidth of the pump pulse determines the inherent spectral resolution of the measurement, while that of the Stokes pulse determines the spectral width of the generated CARS spectrum. The observed multiplex CARS is thus captured in a single-shot measurement that is insensitive to fluctuations in the excitation and is approximated by the product of the weak dispersive CARS spectral profile of the sample (cf. Fig. 6.4) and the Stokes pulse intensity spectrum. Using a transform-limited femtosecond Stokes and a picosecond pump pulse, this is

exemplified in Fig. 6.8A for a CARS spectrum of cholesterol dissolved in CCl_4 in the high wavenumber region.

The combination of multiplex CARS spectroscopy with microscopy was first reported by Otto et al. [119]. Multiplex CARS microspectroscopy has been implemented with picosecond pump and transform-limited femtosecond Stokes pulses [120, 121] or with broadband Stokes continuum pulses generated in a nonlinear optical fiber [122–130]. Alternatively, coherent control schemes have been demonstrated for multiplex CARS microscopy [45, 47, 131–133, 126, 134]. Figure 6.8C shows a schematic of a standard two-beam multiplex CARS microscope that uses the collinear F-CARS geometry depicted in Fig. 6.3A. In contrast to imaging applications where the spectrally integrated CARS signal is measured, detection of the parfocally collected CARS signal is performed by the use of an imaging spectrometer equipped with a detector array (e.g., CCD camera). Hyperspectral CARS imaging then consists of recording a CARS spectrum for each submicron voxel. Due to the signal enhancement in CARS, spectrum acquisition times are typically in the order of milliseconds rather than seconds when compared to those used in spontaneous Raman scattering microscopy, which allow for rapid generation of hyperspectral images [120, 123, 124, 135].

The spectral analysis is carried out on the normalized CARS spectrum, $I_{\mathrm{CARS}} \,/\, I^{\mathrm{ref}}_{\mathrm{CARS}}$, where the normalization with a nonresonant reference CARS spectrum measured under identical experimental conditions eliminates the proportionality constants and laser pulse amplitudes involved in the absolute CARS intensity spectrum (cf. (6.9)). In order to extract the linear Raman response that is encoded in the normalized CARS spectrum, as exemplary shown in Fig. 6.8D for the cholesterol solution, its spectral analysis requires the retrieval of the hidden phase and amplitude of the total $\chi^{(3)}$ (cf. (6.4)). Different approaches have been pursued: (i) Least-squares fitting a spontaneous Raman model spectrum consisting of a superposition of Raman lines to the normalized CARS spectrum allows the extraction of line shape parameters and of the magnitude of the nonresonant background contribution. This method is applicable for the analysis of samples of known Raman response [70, 120, 121, 136]. (ii) In contrast, the use of the maximum entropy method (MEM) allows the phase retrieval from the normalized CARS power spectrum without any a priori information regarding the Raman resonances of the sample [137, 138]. As shown for the case of cholesterol, this method is particularly advantageous for the analysis of CARS spectra from samples with congested Raman spectra, where the interferences between overlapping resonances and with nonresonant background make the former approach very challenging, if not impossible (see Fig. 6.8D). The MEM procedure yields a phase spectrum that consists of a sample-specific resonant phase and a contribution that is independent of vibrational resonances, denoted 'error phase' (Fig. 6.8E). The latter represents an unspecific background phase and is determined from a polynomial fit of the retrieved phase spectrum in those regions where there are no vibrational resonances. After subtraction of the error phase, the imag-

inary part of the third-order nonlinear susceptibility is calculated, $\mathrm{Im}\left(\chi^{(3)}\right)$. As shown in Fig. 6.8F, the retrieved Raman response of cholesterol is identical with its independently measured spontaneous Raman spectrum, as predicted by (6.8). MEM has emerged as the method of choice for the quantitative analysis of CARS spectra [138–141].

Multiplex CARS microspectroscopy, in conjunction with appropriate spectral analysis tools, was successfully applied to the study of phospholipid bilayer model systems [120, 121, 142, 70, 143], lipids within cells [144, 127, 145–147, 141], a single pollen grain [148], a single bacterial endophore [140], a molecular J-aggregate microcrystal [149], silicon components on a wafer [130], separated phases in polymer blends [123, 135], and concentration profiles in a microreactor [150].

As an example, we first discuss an experiment by Wurpel et al. [70] who studied the chemical and physical structure of a planar-supported phospholipid mono- and bilayer on a glass/water interface in the C–D stretch vibration region. Figure 6.9 shows the normalized multiplex CARS spectra together with the spontaneous Raman spectrum of a deuterated bilayer formed by *d*62−DPPC (1,2-Dipalmitoyl-D62-*sn*-Glycero-3-Phosphocholine) and an asymmetric bilayer where one leaflet is replaced by a monolayer of DOPC (1,2-Dioleoyl-*sn*-Glycero-3-Phosphocholine). Since the spectral signature of C–D stretch vibrations is in a distinct window of the Raman spectrum (2000–2300 cm^{-1}), the deuterated leaflet of the asymmetric bilayer can be imaged despite the insufficient axial resolution of the microscope. The analysis of

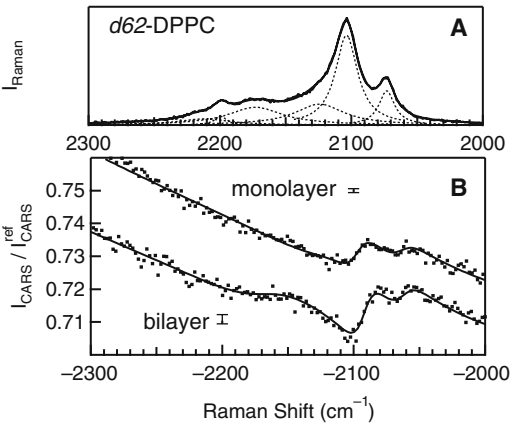

Fig. 6.9. A Spontaneous Raman spectrum of *d*62-DPPC lipids and its decomposition into Lorentzian line profiles. **B** Normalized multiplex CARS spectra (dots) of a planar-supported bilayer and monolayer formed by *d*62-DPPC on a glass–water interface for parallel-polarized input beams, together with the fit using the center frequency and line width parameters extracted from the decomposition analysis in **(A)** (solid line). The spectrum exposure time was 0.64 s. Error bars indicate the shot-noise standard deviation (Copyright © American Chemical Society [70])

the CARS spectra in Fig. 6.9B yields a twofold increase of the peak intensity for the ν_s (CD_2) signal of the bilayer when compared to that of the monolayer. This result directly confirms the linear signal dependence on solute concentration, as is expected in heterodyne-detected multiplex CARS microscopy. Here, the intense nonresonant F-CARS from the glass substrate acts as the local oscillator field amplifying the weak resonant CARS of the lipids. This example demonstrates that even at the level of a single lipid monolayer the main Raman features can readily be detected by multiplex CARS microspectroscopy with a shot-noise limited sensitivity. Next, we provide an example for in vivo intracellular CARS microspectroscopy. Figure 6.10A shows the image of a living NIH 3T3-L1 fibroblast cell obtained by integrating the CARS signal over the spectral region where C–H stretch vibrations reside. The subcellular distribution of constituents with high densities of lipids is visualized. Besides intracellular lipid droplet (LD) organelles of very high contrast, the membrane envelope of the nucleus is visible. Different image locations of interest were selected for subsequent CARS microspectroscopy. Figure 6.10B

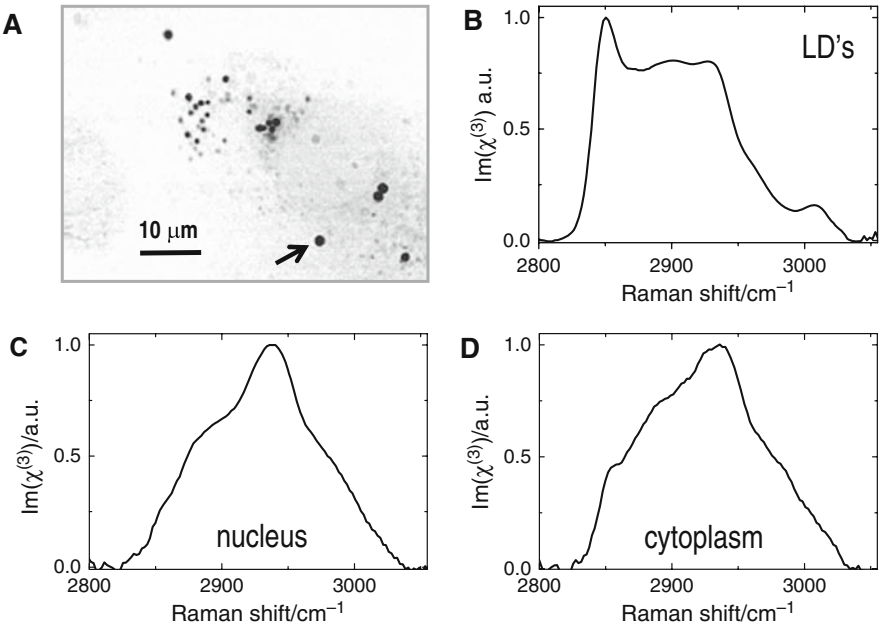

Fig. 6.10. In vivo multiplex CARS microspectroscopy of a NIH 3T3-L1 fibroblast cell in the high-wavenumber region where C–H stretch vibrations reside. **A** CARS image revealing the intracellular distribution of constituents with high densities of lipids, such as the membrane envelope of the nucleus and intracellular lipid droplet (LD) organelles. Typical MEM-reconstructed Raman spectra taken for **(B)** a single LD organelle that is indicated by the arrow in **A**, (**C**) the nucleus, and (**D**) the cytoplasm. The spectrum exposure time was 0.3 s

displays a MEM-reconstructed Raman spectrum of a single LD organelle that is indicated by an arrow in the image of Fig. 6.10A. Its spectrum exhibits an intense symmetrical CH_2 stretch resonance at $2845\,\mathrm{cm}^{-1}$, a vibrational resonance at $\sim 3020\,\mathrm{cm}^{-1}$ that is related to $=\mathrm{C}-\mathrm{H}$ bond vibrations indicative of acyl-chain unsaturation, and an otherwise featureless spectral response suggesting a liquid thermodynamic state of the lipids inside the organelle. The spectral differences among the different LD organelles are very small, indicating a remarkable homogeneity of chemical compositions of LDs throughout the living cell. Figure 6.10C and D show typical retrieved Raman responses when focused inside the nucleus and the cytoplasm, respectively, which are dominated by proteins with a characteristic Raman band at $\sim 2930\,\mathrm{cm}^{-1}$.

As these examples illustrate, in vivo CARS microspectroscopy with shot-noise limited detection sensitivity allows the noninvasive quantification of densities, chemical composition, and physical state of molecular species inside biological systems ranging from a single lipid monolayer to a complex living cell.

Time-Resolved CARS Microspectroscopy

While in the frequency domain all the spectroscopic information regarding vibrational frequencies and relaxation processes is obtained from the positions and widths of the Raman resonances, in the time domain this information is obtained from coherent oscillations and the decay of the time-dependent CARS signal, respectively. In principle, time- and frequency-domain experiments are related to each other by Fourier transform and carry the same information. However, in contrast to the driven motion of molecular vibrations in frequency-multiplexed CARS detection, time-resolved CARS allows recording the Raman free induction decay (RFID) with the decay time T_2, i.e., the free evolution of the molecular system is observed. While the nonresonant contribution dephases instantaneously, the resonant contribution of RFID decays within hundreds of femtoseconds in the condensed phase. Time-resolved CARS with femtosecond excitation, therefore, allows the separation of nonresonant and vibrationally resonant signals [151].

The implementation of time-resolved CARS for microspectroscopy and its application for vibrational imaging based on RFID was first demonstrated by Volkmer et al. [64] using three incident pulses that are much shorter than the relevant material time scale. Here, a pair of temporally overlapped pump and Stokes femtosecond pulses was used to impulsively polarize the molecular vibrations in the sample. Impulsive excitation with a single ultrashort pulse is also possible provided that the spectral bandwidth of the pulse exceeds the Raman shift of the molecular vibration of interest [152]. The relaxation of the induced third-order nonlinear polarization is then probed by scattering of another pulse at a certain delay time, τ. A measurement of the RFID consists of the CARS signal collected at a series of delay times.

Figure 6.11A displays an RFID measurement when focused into a 1-μm polystyrene bead embedded in water and tuned to a Raman shift centered

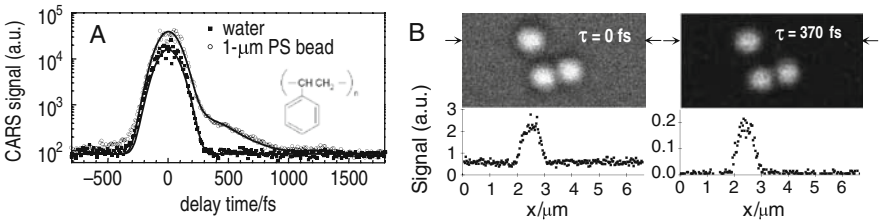

Fig. 6.11. Temporally and spatially resolved CARS signal from a 1-μm polystyrene sphere embedded in water at a Raman shift centered at 3054 cm^{-1} where aromatic C–H stretching vibrations reside. **A** Measured and simulated decay curves when focused on the bead and into bulk water. **B** RFID images and the lateral intensity profiles along the lines indicated by the arrows at time 0 and $\tau \approx 370$ fs, demonstrating the complete removal of nonresonant background contributions from both the object and the solvent to the image contrast at $\tau \approx 370$ fs (Adapted from [64])

at the aromatic C–H stretching vibrations of polystyrene. Due to the broad spectral width of the input fields, a coherent superposition of all vibrational modes whose frequencies reside within the broad bandwidth of Raman shifts is prepared. The observed RFID curve exhibits an initial fast decay of the instrumental response function, followed by a single exponential decay with a time constant of about ∼390 fs, which is superimposed with a coherent oscillation (quantum beat) that recurs at $\tau \approx 1280$ fs. Figure 6.11B displays ultrafast vibrational images of the same polystyrene bead at zero time delay and at $\tau = 370$ fs. Comparison of the two images clearly reveals that the time-delayed detection is capable of completely removing the nonresonant background contributions of both the object and the solvent. Consequently, the signal-to-background ratio increases by more than an order of magnitude. In this way, the vibrational contrast in the time-delayed image arises exclusively from the Raman resonant modes.

In conclusion, although the increased propensity for photodamage by femtosecond pulses and the requirement for an additional delayed laser pulse can be disadvantageous, time-resolved CARS microspectroscopy not only provides a means for efficient and complete nonresonant background suppression but also offers the prospect for monitoring ultrafast processes of molecular species inside a sub-femtoliter sample volume [64, 152–154].

CARS Correlation Spectroscopy

Dynamic processes at thermodynamic equilibrium that occur within a time range from sub-microseconds to seconds can be probed without the imposition of a transient disturbance by optical intensity fluctuation spectroscopy. As such, dynamic light scattering (DLS) [155] measures the fluctuation of quasi-elastic scattering intensity, and fluorescence correlation spectroscopy (FCS) [156–158] measures concentration fluctuations of specific fluorescent molecules

and photophysical processes of the fluorophore itself [159]. Correlation spectroscopy that measures the fluctuation of Raman scattering intensity, thus providing vibrational selectivity, was reported by Schrof and coworkers using confocal spontaneous Raman microscopy [160] and by Eggeling et al. [161] using surface-enhanced resonance Raman scattering microscopy. The limitations inherent to the latter two methods can be circumvented by CARS correlation spectroscopy (CARS-CS) [162, 163].

CARS-CS represents a novel type of CRS spectroscopy that is a direct consequence of the spatial compartmentation provided by CARS microscopy. With a probe volume that can be much smaller than the average volume of particle occupancy given by the reciprocal particle concentration, CARS-CS can monitor the number fluctuation of Raman-active particles caused by Brownian diffusion. The CARS signal is typically investigated by means of photon counting that registers distinct photon arrival times and is analyzed in terms of its photon number trajectory. As an example, Fig. 6.12A shows spontaneous stochastic CARS signal fluctuations about its equilibrium mean value originating from freely diffusing 110-nm polystyrene spheres in water. The CARS intensity changes as particles move in and out of the probe focal volume. To achieve a high fluctuation contrast in CARS-CS, it is vital to efficiently suppress any nonresonant CARS from surrounding solvent and/or auto-fluorescence background because these signals are stationary and show no vibrational selectivity. The photon number trajectory is analyzed in the

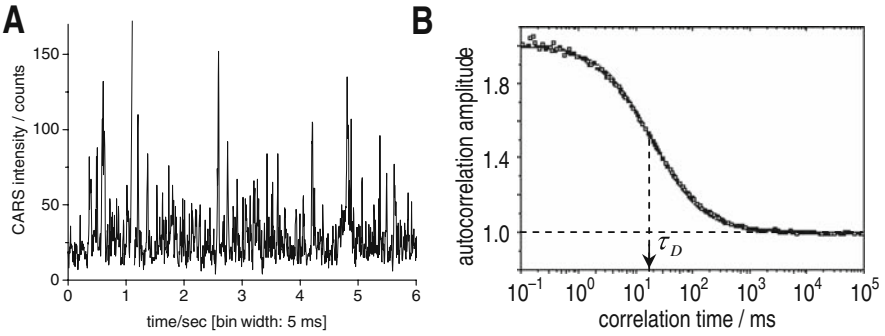

Fig. 6.12. A Typical CARS signal trajectory revealing the particle number fluctuations of 110-nm polystyrene spheres undergoing free Brownian diffusion in water. The epi-detected CARS contrast arises from the breathing vibration of the benzene rings at $\sim$1003 cm^{-1}. **B** Measured CARS intensity autocorrelation function for an aqueous suspension of 200-nm polystyrene spheres at a Raman shift of 3050 cm^{-1} where aromatic C–H stretch vibrations reside. The corresponding translational diffusion time, τ_{D}, of 20 ms is indicated. (Panel **B** courtesy of Andreas Zumbusch, adapted from [162])

time domain by computing the normalized intensity autocorrelation function (ACF), shown in Fig. 6.12B [162].

In analogy to FCS theory [164, 165], Xie and coworkers [163] have developed a theory of CARS-CS for Poisson-distributed particle concentration fluctuations, which also takes the effect of wave vector mismatch for the different CARS detection geometries into account. For sub-wavelength particles undergoing free Brownian diffusion, two regimes of average particle number densities, $\langle N \rangle$, can be distinguished [163]: (i) At $\langle N \rangle << 1$, the autocorrelation model functions for F- and E-CARS-CS are identical, reflecting the symmetry in the forward and backward directions of the CARS radiation field. Except for the introduction of a squared excitation Gaussian amplitude profile [166], the ACF of CARS-CS resembles the mathematical form of that for conventional FCS [167–169], reflecting the similar isotropic radiation patterns of CARS and fluorescence. (ii) At $\langle N \rangle \geq 1$, the coherent sum of CARS fields from many scatterers causes additional contributions to the CARS-CS ACF, and the expression becomes dependent on the CARS detection geometry. While in the forward detection scheme the ACF amplitude will vanish for $\langle N \rangle >> 1$ (like in FCS), the large wave vector mismatch in the epi-detected CARS signal results in a high initial amplitude of the epi-detected ACF that is independent of $\langle N \rangle$ and decays exponentially with correlation time. Unlike FCS, which relies on very low particle concentrations, epi-detected CARS-CS is thus sensitive to the detection of scatterers at high concentrations and may therefore be advantageous in the study of cluster and aggregate dynamics.

CARS-CS experiments have been reported in the low-concentration limit ($\langle N \rangle << 1$) on freely diffusing submicron-sized polymer spheres of different chemical compositions using both the E-CARS [162, 163] and the polarization-resolved CARS [163] detection scheme for efficient nonresonant background suppression. These experiments have unambiguously demonstrated the vibrational selectivity of CARS-CS, the dependence of its ACF amplitude on the particle concentration, $\langle N \rangle$, the dependence of lateral diffusion time, τ_D, on the sphere size, and the influence of the microviscosity on its Brownian motion.

The additional advantage of CARS-CS over DLS and FCS is the spectral selectivity for individual chemical components in their native state, where fluorescent labeling is not desired. This may not only allow mapping of 3D diffusion coefficients, for example inside life cells, but also offer a method to monitor the specific interaction of individual components within complex systems, e.g., aggregation processes of different chemical species. Another prospect is the implementation of CARS cross-correlation spectroscopy that may allow the investigation of correlated fluctuations between two different species. These could be two distinct Raman spectral features of one and the same compound, or a specific intrinsic Raman band and an emission of a more sensitive fluorescence label [160].

6.4 Stimulated Raman Scattering Microscopy

When a pump and a Stokes laser beam coincide on the sample and their difference frequency matches a particular molecular vibrational frequency, then SRS appears in the form of a gain of the Stokes pulse intensity and a loss of the pump pulse intensity, as first observed by Woodbury and Ng in 1962 [170] and by Jones and Stoicheff in 1964 [171], respectively (see Fig. 6.1). SRS has long been recognized as a highly sensitive spectroscopic tool for chemical analyses in the condensed and gas phases [172, 173, 29, 174]. For example, a shot-noise limited SRS spectrum of a single molecular monolayer was demonstrated by Heritage and Allara in 1980 [175]. In this section, we discuss the fundamental properties and applications of SRS microscopy, as was first successfully demonstrated by Nandakumar et al. [20] and subsequently reported by several research teams [21, 12, 13, 22].

6.4.1 General Characteristics

SRS is quantum mechanically described as a two-photon stimulated process where one pump photon at ω_p is annihilated (stimulated Raman loss: SRL) and one Stokes photon at ω_S is created (stimulated Raman gain: SRG) while the Raman medium makes a transition from the initial electronic ground state to the final vibrationally excited state [28] (Fig. 6.1A). In analogy to the theoretical depiction of CARS microscopy [60, 61], here we consider SRS classically as a parametric four-wave mixing process. To derive the characteristic properties of the quantity detected in SRS microscopy, we assume that the pump and Stokes beams are monochromatic plane waves collinearly propagating through an isotropic Raman-active slab sample of thickness L. For the detection of SRL, the nonlinear polarization $\boldsymbol{P}^{(3)}_\mathrm{SRL}(\omega_\mathrm{p})$ (cf. (6.3)) induced in the slab is the source of a coherent output field $\boldsymbol{E}_\mathrm{SRL}(\omega_\mathrm{p}, L)$ that is in the same mode as the input pump field $\boldsymbol{E}_\mathrm{p}(\omega_\mathrm{p})$. Thus, the total intensity at the detector is reminiscent of an optical heterodyne mixing signal where the pump field acts as an intrinsic local oscillator field automatically injected along with the generated output field [29]. Compared to OHD-CARS microscopy, no additional external local oscillator field is required. Furthermore, because $\boldsymbol{E}_\mathrm{SRL}(\omega_\mathrm{p}, L)$ is in phase with $\boldsymbol{E}_\mathrm{p}(\omega_\mathrm{p})$ the phase matching condition is automatically fulfilled. Consequently, the quantity physically detected in the SRL experiment is then a change of the optical pump intensity, which in the weak signal limit ($\boldsymbol{E}_\mathrm{SRL}(\omega_\mathrm{p}, L) << \boldsymbol{E}_\mathrm{p}(\omega_\mathrm{p})$) is given by [27]

$$\Delta I^\mathrm{SRL}_\mathrm{p}(\omega_\mathrm{p}) \propto -\mathrm{Im}\left[\chi^{(3)}(-\omega_\mathrm{p}; \omega_\mathrm{S}, \omega_\mathrm{p}, -\omega_\mathrm{S})\right] I_\mathrm{p}(\omega_\mathrm{p})\, I_\mathrm{S}(\omega_\mathrm{S})\, L. \tag{6.11}$$

The analogous expression describing the quantity detected in the SRG experiment is given by

$$\Delta I^\mathrm{SRG}_\mathrm{S}(\omega_\mathrm{S}) \propto -\mathrm{Im}\left[\chi^{(3)}(-\omega_\mathrm{S}; \omega_\mathrm{p}, -\omega_\mathrm{p}, \omega_\mathrm{S})\right] I_\mathrm{p}(\omega_\mathrm{p})\, I_\mathrm{S}(\omega_\mathrm{S})\, L. \tag{6.12}$$

Because in SRL $\mathrm{Im}\left[\chi^{(3)}\left(-\omega_\mathrm{p};\omega_\mathrm{S},\omega_\mathrm{p},-\omega_\mathrm{S}\right)\right] \geq 0$, (6.11) describes a pump intensity attenuation. In SRG $\mathrm{Im}\left[\chi^{(3)}\left(-\omega_\mathrm{S};\omega_\mathrm{p},-\omega_\mathrm{p},\omega_\mathrm{S}\right)\right] = -\mathrm{Im}\left[\chi^{(3)}\left(-\omega_\mathrm{p};\right.\right.$ $\left.\left.\omega_\mathrm{S},\omega_\mathrm{p},-\omega_\mathrm{S}\right)\right] \leq 0$ [28]. Thus, (6.12) describes an increase in Stokes intensity, the Raman gain.

SRS microscopy provides advantages for the vibrational imaging of biological samples for the following reasons [13]: (i) The signal is linearly proportional to the imaginary part of $\chi^{(3)}$, thus being directly proportional to the corresponding spontaneous Raman cross section, to the line shape, and via (6.5) and (6.6) to the number density of Raman-active modes within the focal volume. (ii) The signal scales linearly with the pump and the Stokes input laser intensities, I_p and I_S. (iii) The signal is inherently insensitive to real nonresonant background contributions, which is especially important for bioimaging applications where water represents the predominant source of nonresonant background signal in the sample. In addition, because the phase matching condition is automatically fulfilled, unlike CARS image contrast, the SRS contrast is insensitive to the microscope's detection geometry and the dimension of the microscopic scatterer. In combination with the general benefits common to all CRS microscopy techniques, as listed in Sect. 6.1, these properties make SRS microscopy an attractive alternative to spontaneous Raman scattering microscopy.

6.4.2 SRS Imaging

Instrumentation and Experimental Characterization

To implement SRS microscopy for vibrational imaging applications, the CARS microscope setup shown in Fig. 6.3A has to be somewhat modified [12, 13]. Briefly, pump and Stokes laser pulse trains consisting of near-transform-limited pulses with temporal widths of 2–5 ps at a repetition rate of ∼80 MHz are typically used. The wavelength difference between the two laser beams is tuned to match the desired Raman shift. Unlike CARS detection, SRL (SRG) detection requires the amplitude modulation of the Stokes (pump) pulse train intensity at radio frequencies (MHz) where laser noise is negligible in conjunction with phase-sensitive lock-in detection of the pump (Stokes) pulses, which are modulated due to SRL (SRG). This directly provides the quantity described by (6.11) and (6.12). Images are collected either by raster scanning the sample relative to the fixed laser beams [13] or by laser scanning the collinear pump and Stokes beams over a fixed sample [12]. The characteristic properties of SRS microscopy, as expressed by (6.11) and (6.12), are experimentally demonstrated by imaging a layer of 2.4-μm diameter polystyrene spheres surrounded by water. Figure 6.13A shows an SRL image recorded at the Raman shift of the aliphatic $\nu_\mathrm{as}\,(\mathrm{CH_2})$ resonance of polystyrene. The image contrast completely vanishes when the pump and Stokes pulses are not spatially or temporally overlapped. Since SRS detection is free of nonlinear

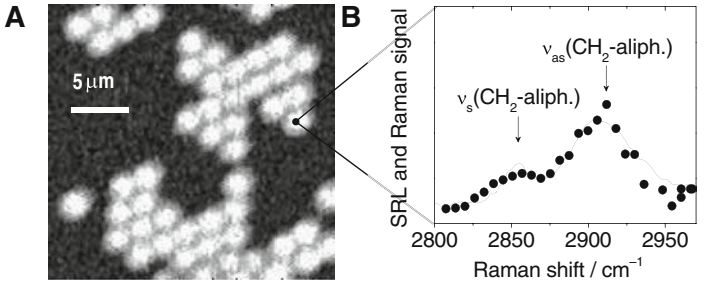

Fig. 6.13. A Stimulated Raman loss (SRL) imaging of self-assembled 2.4-μm polystyrene beads in water recorded at a Raman shift of $2904\,\mathrm{cm}^{-1}$. **B** Measured SRL spectrum (filled circles) when focused on a single bead. Both the aliphatic symmetric $\nu_\mathrm{s}\,(\mathrm{CH_2})$ and antisymmetric $\nu_\mathrm{as}\,(\mathrm{CH_2})$ Raman modes of polystyrene at $2853\,\mathrm{cm}^{-1}$ and $2912\,\mathrm{cm}^{-1}$, respectively, are resolved, directly reproducing the spontaneous Raman spectrum (solid line) of bulk polystyrene (Adapted from Nandakumar et al. [13].)

nonresonant background, no signal from water is detected. When focused on a single bead, linear proportionality to both the pump and Stokes average laser powers is observed. Figure 6.13B displays the spectral dependence of the SRL signal on the Raman shift from a single bead within the range where CH– stretching vibrations reside. The observed SRL spectrum reproduces the corresponding spontaneous Raman spectrum measured for bulk polystyrene. All observations combine to verify that the information content obtained by SRS and by spontaneous Raman scattering is identical. Consequently, the recorded image pixel intensity in Fig. 6.13A can now be readily interpreted as the number density of $\nu_\mathrm{as}\,(\mathrm{CH_2})$ Raman modes of polystyrene inside the probe volume.

Biomedical Applications

The potential of SRS imaging as a label-free and noninvasive tool in biological and biomedical research has been demonstrated in visualizing distributions of lipids in living cells [12, 13, 22]. As such, Freudiger et al. [12] followed the uptake of polyunsaturated omega-3 fatty acids by living human lung cancer cells through SRL imaging in the high-wavenumber Raman shift region. Nandakumar et al. [13] applied SRL imaging at a Raman shift C=C stretching vibrations to map the subcellular distribution of lipid droplet organelles in unstained differentiated human leukemia cells that are rich in unsaturated lipids. Ozeki et al. [22] demonstrated the three-dimensional visualization of the cell wall and the nucleus in an unstained tobacco BY-2 cell based on the SRS contrast of the CH– stretching modes. Examples for SRS tissue imaging without staining include the visualization of lipid-rich myelin sheaths surrounding

axons in a ∼1-mm-thick slice of mouse brain, which clearly reveals individual neurons, and the imaging of lipid-rich structures that make up the stratum corneum, the sebaceous gland, and the subcutaneous fat layer in skin tissue at increasing depths [12].

Xie and coworkers [12] also applied SRS imaging for monitoring the penetration pathway for the topically applied drug diffusion enhancer dimethyl sulfoxide (DMSO) into mouse skin tissue. DMSO is hydrophilic and hence penetrates the skin via the protein phase, avoiding lipid structures such as adipocytes. This is evident from Fig. 6.14 that shows a dual-frequency SRS image tuned into both the characteristic vibration of DMSO at $670\,\mathrm{cm}^{-1}$ and the CH_2 vibration of typical adipocytes at $2845\,\mathrm{cm}^{-1}$ at a depth of $\sim 65\,\mu\mathrm{m}$ into the skin. As this experiment demonstrates, SRS imaging facilitates the spectroscopic identification of a small drug molecule based on its characteristic spontaneous Raman response and monitoring its delivery through the epidermis in three dimensions while maintaining a drug's efficacy and diffusion characteristics.

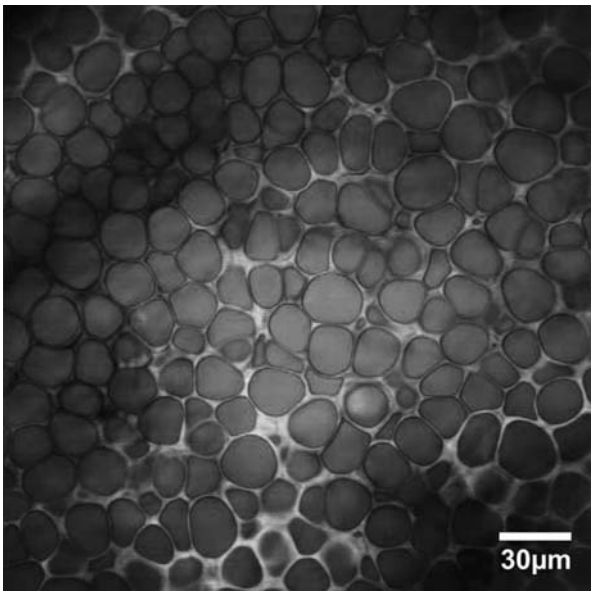

Fig. 6.14. Label-free chemical imaging of the penetration pathways for the topically applied drug diffusion enhancer dimethyl sulfoxide (DMSO) into mouse skin tissue: Dual-frequency SRS imaging tuned into the characteristic vibration of DMSO at $670\,\mathrm{cm}^{-1}$ (bright gray regions) and the CH_2 vibration of lipid-rich adipocytes at $2845\,\mathrm{cm}^{-1}$ (dark gray regions) at a depth of $\sim 65\,\mu\mathrm{m}$ into the tissue. DMSO is hydrophilic and hence avoids lipid structures such as adipocytes (Image courtesy of Brian Saar, Chris Freudiger, and Wei Min [12])

6.4.3 SRS Microspectroscopy

Like CARS microscopy, SRS microscopy also offers the possibility for spatially resolved vibrational spectroscopy in the frequency and time domain and for Raman correlation spectroscopy. In the frequency domain, an SRS spectrum is recorded over a wide range of Raman shifts, whereas in the time domain the SRS signal decay occurring on the femto- and picosecond time scales due to vibrational dephasing processes is monitored. SRS correlation spectroscopy can monitor the SRS signal fluctuation due to diffusion and transport of the microscopic scatterer through the focal volume on time scales of micro- to milliseconds. Among these SRS microspectroscopies, the feasibility of combining frequency-multiplexed SRS spectroscopy and optical microscopy has been experimentally demonstrated to date [21].

Analogous to the principal concept of multiplex CARS microspectroscopy (cf. Sect. 6.3.5), in multiplex SRS detection a pair of a broad-bandwidth pulse, eg., white-light femtosecond pulse, and a narrow-bandwidth picosecond pulse that determine the spectral width of the SRS spectrum and its inherent spectral resolution, respectively, is used to simultaneously excite multiple Raman resonances in the sample. Due to SRS, modulations appear in the spectrum of the transmitted broad-bandwidth pulse, which are read out using a photodiode array detector. Unlike SRS imaging, it is difficult to integrate phase-sensitive lock-in detection with a multiplex detector in order to directly retrieve the Raman spectrum from these modulations. Instead, two consecutive spectra, i.e., one with the narrow-bandwidth picosecond beam present and one with that beam blocked, are recorded. Their ratio allows the computation of the linear Raman spectrum that can readily be interpreted in a quantitative manner [49]. Unlike the spectral analysis of a multiplex CARS spectrum, no retrieval of hidden phase information is required to obtain the spontaneous Raman response in multiplex SRS microspectroscopy.

In a proof-of-principle experiment, Ploetz et al. [21] demonstrated multiplex SRL microspectroscopy of polystyrene spheres dispersed in water. Figure 6.15A shows Raman spectra that are calculated from SRL spectra recorded when focused on and next to an individual 20-μm bead. Raster scanning the sample in the focal plane while recording SRL spectra results in a data set of Raman spectra, from which Raman images for a particular Raman resonance can be reconstructed. This is shown in Fig. 6.15B, which displays density maps of the ring breathing mode at $1003\,\mathrm{cm}^{-1}$, the aliphatic C–H stretching mode at $2904\,\mathrm{cm}^{-1}$, and the aromatic C–H stretching modes of the benzene ring at $3066\,\mathrm{cm}^{-1}$ of polystyrene beads. In this demonstration, however, the SRS detection sensitivity is more than three orders of magnitude lower than that typically achieved in CARS/SRS imaging, and the spectrum acquisition time per image pixel is more than two orders of magnitude longer than typically used in CARS microspectroscopy (cf. Sect. 6.3.5.). To facilitate fast multiplex SRS microspectroscopy of biological samples at

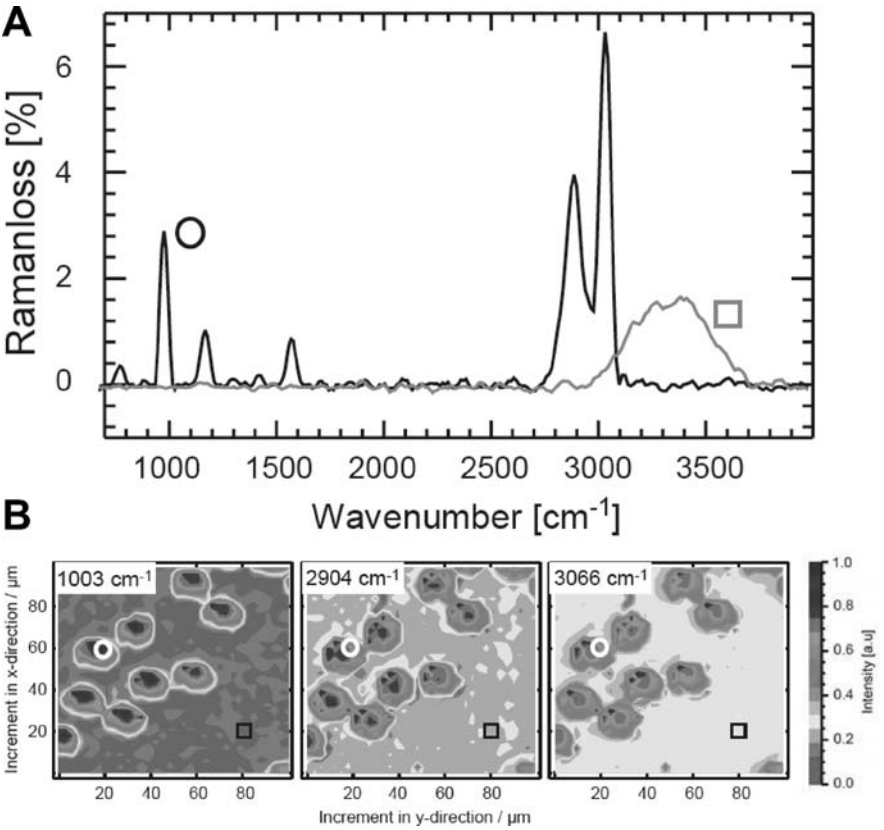

Fig. 6.15. Multiplex stimulated Raman loss microspectroscopy of 20-µm polystyrene beads dispersed in water. **A** Raman spectra retrieved from SRL spectra of an individual bead and of bulk water at locations indicated by circles and squares, respectively, in the images. **B** Reconstructed Raman images of the beads representing the density maps of three characteristic Raman resonances at $1003\,\mathrm{cm}^{-1}$, $2904\,\mathrm{cm}^{-1}$, and $3066\,\mathrm{cm}^{-1}$ of polystyrene (Courtesy of Evelyn Ploetz et al., after [21])

significantly reduced laser pulse energies, future technological improvements and optimization of the SRL detection sensitivity are required.

6.5 Conclusions and Perspectives

A series of advances over the past decade have made CRS microscopy a highly sensitive tool for label-free imaging and vibrational microspectroscopy that is capable of real-time, non-perturbative studies of complex biological samples based on molecular Raman spectroscopy. In particular, biomedical applications where fluorescent labeling of small molecules represents a severe pertur-

bation of the sample and where conventional Raman microscopy requires a long averaging time and high laser powers will benefit from the use of CRS imaging. For example, in vivo CRS microscopy opens exciting possibilities to study chemical processes inside a living cell or organism in real time. It thus has the potential to overcome many limitations of conventional cell biology techniques for the detection, identification, and quantification of the chemical composition of intracellular components and organelles, which are often destructive by nature, possess imperfect specificity, and can even perturb the cellular biology under investigation. Furthermore, multimodal CRS microscopy that readily combines the chemical specificity of CRS with other nonlinear optical image contrast mechanisms, such as TPF, SHG, and, THG, allows tissue diagnostics based on a variety of simultaneously imaged endogenous signals.

For a particular biomedical application of CRS microscopy, the best choice whether to use CARS or SRS detection depends on the optimal balance between the pros and cons of each technique regarding its detection sensitivity, image acquisition time, and interpretability of image contrast and spectrum. In the following, we provide a critical discussion of the advantages and disadvantages of both complementary detection techniques:

Since CARS microscopy benefits from the fact that the signal can be selectively detected through spectral filtering against the pump and Stokes beams, it allows video-rate chemical mapping and fast hyperspectral CARS imaging with acquisition times only limited by signal strength. Because the CARS signal scales quadratically with the number density of vibrational modes inside the probe volume, samples with a high density of chemical bonds, e.g., lipids, are best studied by CARS contrast. CARS microscopy is then capable of monitoring dynamic processes in real time. On the other hand, the modulus square dependence of the CARS signal on the total third-order susceptibility causes distorted Raman line shapes and limits the detection sensitivity due to unavoidable nonresonant background contributions. Moreover, the CARS signal scales as the square of the spontaneous Raman scattering signal and as a cube of laser power. Consequently, weak Raman resonances and low densities of scatterers are not easily detected. In addition, the need to fulfil the phase matching condition in CARS results in a signal that is dependent on both the dimension of the microscopic scatterer and the microscope's geometry for the propagation directions of the input and output fields. In consequence, unlike in fluorescence and spontaneous Raman microscopy, both CARS images and spectra cannot readily be interpreted in a quantitative manner. The efficient suppression of nonresonant background signal or OHD-CARS schemes have to be implemented to significantly simplify image interpretation. An alternative approach to quantify the CARS image contrast is based on the separation of individual susceptibility components by means of multiplex CARS microspectroscopy in combination with spectral phase retrieval using MEM.

The detection of stimulated Raman scattering (SRS) has the major advantage that it inherently avoids these problems. A readily interpretable chemical

image contrast and Raman spectrum is obtained with SRS microscopy. Being insensitive to electronic nonresonant background nonlinearities, linearly proportional to the spontaneous Raman response of the sample, and to each of the input laser intensities, the SRS image contrast is proportional to the number density of Raman-active modes inside the focal overlap volume. Combined with a detection sensitivity exceeding that of CARS, the use of SRS microscopy is thus particularly attractive for the study of weak Raman resonances and/or low densities of scatterers and whenever a quantitative interpretation of the obtained chemical map is essential. The main disadvantage of SRS microscopy results from the fact that SRS detection requires amplitude modulation of one of the input laser beams and phase-sensitive lock-in detection. Consequently, acquisition times in both SRS imaging and microspectroscopy are limited to the reciprocal modulation frequency. To facilitate SRS imaging at video rates, the future technological development of suitable laser sources and the optimization of the SRL detection sensitivity are required. Similarly, fast hyperspectral SRS imaging has to await the implementation of multiplex lock-in detection with a photodiode array detector.

When compared to fluorescence-based microscopies, a major drawback of CRS microscopy is its limited detection sensitivity. While confocal fluorescence microscopy exhibits single-molecule sensitivity, CRS relies on the coherent enhancement of thousands of Raman modes contributing to a detectable signal. Therefore, research on further increasing the sensitivity of CRS detection will continue. In addition, further instrumental and methodological developments can be anticipated in the future: For example, the proliferation of CARS and SRS microscopy into the life sciences' laboratory and hospital will certainly profit from the availability of cost-efficient and compact excitation sources optimized for CRS microscopy, such as fiber-based laser sources. Adaptive optics will help to extent the penetration depth in CRS tissue imaging applications [176]. And, CRS detection in combination with microendoscopy may emerge as a noninvasive surgical probe for tumor detection [58].

Acknowledgments

I would like to extent a special thanks to my former colleagues X. Sunney Xie, Gary R. Holtom, Ji-Xin Cheng, and Lewis D. Book at Harvard University where the work on CARS microscopy described in this review had its origin. In equal measure, I wish to acknowledge my former and past group members Nandakumar Patincharath, Alexander Kovalev, Adam Muschielok, Stephan Busch, and Gregor Hehl at the University of Stuttgart for their essential contributions to the depicted work on in vivo CARS microspectroscopy and SRS imaging. Financial and infrastructural support from the Emmy-Noether program of the Deutsche Forschungsgemeinschaft (DFG: VO 825/1-2, 1-3, 1-4), from the European Commission's Seventh Framework program under grant

agreement N° HEALTH-F5-2008-200820 (CARS EXPLORER), from the 3. Physikalisches Institut, and the University of Stuttgart is gratefully acknowledged.

References

1. T. Wilson, C. Sheppard, *Theory and Practice of Scanning Optical Microscopy* (Academic Press, Orlando, 1984)
2. W. Denk, J.H. Strickler, W.W. Webb, Science **248**, 73 (1990)
3. *Handbook of Biological Confocal Microscopy*, ed. by J.B. Pawley (Plenum, New York, 1995)
4. R.P. Haugland, *Handbook of Fluorescent Probes and Research Chemicals*, 6th edn. (Molecular Probes, Eugene, 1996)
5. R.Y. Tsien, A. Miyawaki, Science **280**, 1954 (1998)
6. J. Hoyland, in *Fluorescent and Luminescent Probes for Biological Activity*, ed. by W.T. Mason (Academic Press, San Diego, 1999), p. 108
7. H.J. Humecki, in *Practical Spectroscopy*, vol. 19, ed. by J.E.G. Brame (Marcel Dekker, New York, 1995)
8. G. Turrell, J. Corset, *Raman Microscopy Development and Applications* (Academic Press, San Diego, 1996)
9. S. Nie, S.R. Emory, Science **275**, 1102–1106 (1997)
10. K. Kneipp, Y. Wang, H. Kneipp, L.T. Perelman, I. Itzkan, R.R. Dasari, M.S. Feld, Phys. Rev. Lett. **78**, 1667–1670 (1997)
11. A. Zumbusch, G.R. Holtom, X.S. Xie, Phys. Rev. Lett. **82**, 4142 (1999)
12. C.W. Freudiger, W. Min, B.G. Saar, S. Lu, G.R. Holtom, C. He, J.C. Tsai, J.X. Kang, X.S. Xie, Science **322**, 1857–1861 (2008)
13. P. Nandakumar, A. Kovalev, A. Volkmer, New J. Phys. **11**, 033026 (2009)
14. M.D. Duncan, J. Reintjes, T.J. Manuccia, Opt. Lett. **7**, 350 (1982)
15. J.X. Cheng, X.S. Xie, J. Phys. Chem. B **108**, 827–840 (2004)
16. A. Volkmer, J. Phys. D: Appl. Phys. **38**, R59–R81 (2005)
17. J.X. Cheng, Appl. Spectrosc. **61**, 197A–208A (2007)
18. M. Müller, A. Zumbusch, ChemPhysChem **8**, 2156–2170 (2007)
19. C.L. Evans, X.S. Xie, Annu. Rev. Anal. Chem. **1**, 883–909 (2008)
20. P. Nandakumar, A. Kovalev, A. Volkmer. Paper presented at the 17th international conference on laser spectroscopy (ICOLS'05), T54, Aviemore, 19–24 June 2005, and the 8th European/French Israeli symposium on nonlinear and quantum optics (FRISNO-8), Ein Bokek, 20–25 February 2005 (http://www.weizmann.ac.il/conferences/frisno8/program.html)
21. E. Ploetz, S. Laimgruber, S. Berner, W. Zinth, P. Gilch, Appl. Phys. B **87**, 389–393 (2007)
22. Y. Ozeki, F. Dake, S. Kajiyama, K. Fukui, K. Itoh, Opt. Express **17**, 3651–3658 (2009)
23. J.N. Gannaway, C.J.R. Sheppard, Opt. Quantum Electron. **10**, 435–439 (1978)
24. M. Florsheimer, C. Brillert, H. Fuchs, Langmuir **15**, 5437–5439 (1999)
25. Y. Barad, H. Eisenberg, M. Horowitz, Y. Silberberg, Appl. Phys. Lett. **70**, 922–924 (1997)

26. C.L. Evans, E.O. Potma, M. Puoris'haag, D. Côté, C.P. Lin, X.S. Xie, Proc. Natl. Acad. Sci. U S A **102**, 16807–16812 (2005)
27. G.L. Eesley, *Coherent Raman spectroscopy* (Pergamon Press, Oxford, 1981)
28. Y.R. Shen, *The Principles of Nonlinear Optics* (Wiley, New York, 1984)
29. M.D. Levenson, S.S. Kano, *Introduction to Nonlinear Laser Spectroscopy* (Academic Press, San Diego, 1988)
30. S. Maeda, T. Kamisuki, Y. Adachi, in *Advances in Non-linear Spectroscopy*, ed. by R.J.H. Clark, R.E. Hester (Wiley, New York, 1988), p. 253
31. P.N. Butcher, D. Cotter, *The Elements of Nonlinear Optics* (Cambridge University Press, Cambridge, 1990)
32. S.A. Akhmanov, N.I. Koroteev, Sov. Phys. Usp. **20**, 899 (1977)
33. M.A. Yuratich, D.C. Hanna, Mol. Phys. **33**, 671–682 (1977)
34. R. Igarashi, Y. Adachi, S. Maeda, J. Chem. Phys. **72**, 4308–4314 (1980)
35. D. Lee, A.C. Albrecht, in *Advances in Infrared and Raman Spectroscopy*, vol. 12, ed. by R.J.H. Clark, R.E. Hester (Wiley Heyden, London, 1985), pp. 179–213
36. D.A. Kleinman, Phys. Rev. **126**, 1977–1979 (1962)
37. J.X. Cheng, A. Volkmer, L.D. Book, X.S. Xie, J. Phys. Chem. B **105**, 1277–1280 (2001)
38. B. Broers, L.D. Noordam, H.B.v.L.v.d. Heuvell, Phys. Rev. A **46**, 2749–2756 (1992)
39. E.T.J. Nibbering, D.A. Wiersma, K. Duppen, Phys. Rev. Lett. **68**, 514–517 (1992)
40. A.M. Zheltikov, A.N. Naumov, Quantum Electron. **30**, 606–610 (2000)
41. T. Hellerer, A.M.K. Enejder, A. Zumbusch, Appl. Phys. Lett. **85**, 25–27 (2004)
42. I. Rocha-Mendoza, W. Langbein, P. Borri, Appl. Phys. Lett. **93**, 201103 (2008)
43. A.F. Pegoraro, A. Ridsdale, D.J. Moffatt, Y. Jia, J.P. Pezacki, A. Stolow, Opt. Express **17**, 2984–2996 (2009)
44. N. Dudovich, D. Oron, Y. Silberberg, Nature **418**, 512–514 (2002)
45. D. Oron, N. Dudovich, Y. Silberberg, Phys. Rev. Lett. **89**, 273001 (2002)
46. D. Oron, N. Dudovich, Y. Silberberg, Phys. Rev. Lett. **90**, 213902 (2003)
47. N. Dudovich, D. Oron, Y. Silberberg, J. Chem. Phys. **118**, 9208–9215 (2003)
48. S.A. Akhmanov, N.I. Koroteev, A.I. Kholodnykh, J. Raman Spectrosc. **2**, 239–248 (1974)
49. D.W. McCamant, P. Kukura, R.A. Mathies, Appl. Spectrosc. **57**, 1317–1323 (2003)
50. P.D. Maker, R.W. Terhune, Phys. Rev. **137**, A801 (1965)
51. M.D. Duncan, Opt. Commun. **50**, 307–312 (1984)
52. M. Müller, J. Squier, C.A.d. Lange, G.J. Brakenhoff, J. Microsc. **197**, 150–158 (2000)
53. C. Heinrich, S. Bernet, M. Ritsch-Marte, Appl. Phys. Lett. **84**, 816–818 (2004)
54. I. Toytman, K. Cohn, T. Smith, D. Simanovskii, D. Palanker, Opt. Lett. **32**, 1941–1943 (2007)
55. C. Heinrich, A. Hofer, S. Bernet, M. Ritsch-Marte, New J. Phys. **10**, 023029 (2008)
56. R.D. Schaller, J.C. Johnson, K.R. Wilson, L.F. Lee, L.H. Haber, R.J. Saykally, J. Chem. Phys. B **106**, 5143–5154 (2002)
57. T. Ichimura, N. Hayazawa, M. Hashimoto, Y. Inouye, S. Kawata, Phys. Rev. Lett. **92**, 220801 (2004)

58. F. Legare, C.L. Evans, F. Ganikhanov, X.S. Xie, Opt. Express **14**, 4427–4432 (2006)
59. S. Mukamel, *Principles of Nonlinear Optical Spectroscopy* (Oxford University Press, Oxford, 1995).
60. A. Volkmer, J.X. Cheng, X.S. Xie, Phys. Rev. Lett. **87**, 023901 (2001)
61. J.X. Cheng, A. Volkmer, X.S. Xie, J. Opt. Soc. Am. B **19**, 1363–1375 (2002)
62. P. Hall, B. Selinger, Z. Phys. Chem.-Int. J. Res. Phys. Chem. Chem. Phys. **141**, 77–89 (1984)
63. J.X. Cheng, L.D. Book, X.S. Xie, Opt. Lett. **26**, 1341–1343 (2001)
64. A. Volkmer, L.D. Book, X.S. Xie, Appl. Phys. Lett. **80**, 1505–1507 (2002)
65. D.L. Marks, S.A. Boppart, Phys Rev. Lett. **92**, 123905 (2004)
66. E.O. Potma, C.L. Evans, X.S. Xie, Opt. Lett. **31**, 241–243 (2006)
67. M. Jurna, J.P. Korterik, C. Otto, H.L. Offerhaus, Opt. Express **15**, 15207–15213 (2007)
68. J.L. Oudar, R.W. Smith, Y.R. Shen, Appl. Phys. Lett. **34**, 758–760 (1979)
69. E.O. Potma, X.S. Xie, J. Raman Spectrosc. **34**, 642–650 (2003)
70. G.W.H. Wurpel, J.M. Schins, M. Müller, J. Phys. Chem. B **108**, 3400–3403 (2004)
71. R.K. Chang, J. Ducuing, N. Bloembergen, Phys. Rev. Lett. **15**, 6–8 (1965)
72. Y. Yacoby, R. Fitzgibbon, B. Lax, J. Appl. Phys. **51**, 3072–3077 (1980)
73. G. Marowsky, G. Luepke, Appl. Phys. B **51**, 49–51 (1990)
74. C. Vinegoni, J.S. Bredfeldt, D.L. Marks, S.A. Boppart, Opt. Express **12**, 331–341 (2004)
75. C.L. Evans, E.O. Potma, X.S. Xie, Opt. Lett. **29**, 2923–2925 (2004)
76. E.O. Potma, W.P.d. Boeij, D.A. Wiersma, J. Opt. Soc. Am. B **17**, 1678–1684 (2000)
77. M. Hashimoto, T. Araki, J. Opt. Soc. Am. A **18**, 771–776 (2001)
78. D. Gachet, N. Sandeau, H. Rigneault, J. Eur. Opt. Soc. **1**, 06013 (2006)
79. D. Gachet, F. Billard, H. Rigneault, J. Opt. Soc. Am. B **25**, 1655–1666 (2008)
80. M. Marrocco, J. Phys. Chem. A **112**, 13458–13462 (2008)
81. J.X. Cheng, S. Pautot, D.A. Weitz, S.X. Xie, Proc. Natl. Acad. Sci. **100**, 9826–9830 (2003)
82. E.O. Potma, X.S. Xie, ChemPhysChem. **6**, 77–79 (2005)
83. L. Li, H. Wang, J.X. Cheng, Biophys. J. **89**, 3480–3490 (2005)
84. L. Li, J.X. Cheng, Biochemistry **45**, 11819–11826 (2006)
85. J.X. Cheng, Y.K. Jia, G. Zheng, X.S. Xie, Biophys. J. **83**, 502–509 (2002)
86. X. Nan, J.X. Cheng, X.S. Xie, J. Lipid Res. **44**, 2202–2208 (2003)
87. Y. Fu, H. Wang, R. Shi, J.X. Cheng, Opt. Express **14**, 3942–3951 (2006)
88. X. Nan, A.M. Tonary, A. Stolow, X.S. Xie, J.P. Pezacki, ChemBioChem. **7**, 1895–1897 (2006)
89. X. Nan, E.O. Potma, X.S. Xie, Biophys. J. **91**, 728–735 (2006)
90. X.S. Xie, J. Yu, W.Y. Yang, Science **312**, 228–230 (2006)
91. B. Rakic, S.M. Sagan, M. Noestheden, S. Belanger, X. Nan, C.L. Evans, X.S. Xie, J.P. Pezacki, Chem. Biol. **13**, 1–8 (2006)
92. L. Tong, Y. Lu, R.J. Lee, J.X. Cheng, J. Phys. Chem. B **111**, 9980–9985 (2007)
93. S.O. Konorov, C.H. Glover, J.M. Piret, J. Bryan, H.G. Schulze, M.W. Blades, R.B. Turner, Anal. Chem. **79**, 7221–7225 (2007)
94. H. Wang, N. Bao, T.T. Le, C. Lu, J.X. Cheng, Opt. Express **16**, 5782–5789 (2008)

95. S. Murugkar, C.L. Evans, X.S. Xie, H. Anis, J. Microsc. **233**, 244–250 (2009)
96. H. Wang, Y. Fu, P. Zickmund, R. Shi, J.X. Cheng, Biophys. J. **89**, 581–591 (2005)
97. T.B. Huff, J.X. Cheng, J. Microsc. **225**, 175–182 (2006)
98. T. Hellerer, C. Axäng, C. Brackmann, P. Hillertz, M. Pilon, A.M.K. Enejder, Proc. Natl. Acad. Sci. U S A **104**, 14658–14663 (2007)
99. C.L. Evans, X. Xu, S. Kesari, X.S. Xie, S.T.C. Wong, G.S. Young, Opt. Express **15**, 12076–12087 (2007)
100. S. Ly, G. McNerney, S. Fore, J. Chan, T. Huser, Opt. Express **15**, 16839–16851 (2007)
101. I. Veilleux, J.A. Spencer, D.P. Biss, D. Cote, C.P. Lin, IEEE J. Sel. Top. Quantum Electron. **14**, 10–18 (2008)
102. C.P. Pfeffer, B.R. Olsen, F. Ganikhanov, F. Légaré, J. Struct. Biol. **164**, 140–145 (2008)
103. Y.M. Wu, H.C. Chen, W.T. Chang, J.W. Jhan, H.L. Lin, I. Liau, Anal. Chem. **81**, 1496–1504 (2009)
104. E.R. Dufresne, E.I. Corwin, N.A. Greenblatt, J. Ashmore, D.Y. Wang, A.D. Dinsmore, J.X. Cheng, X.S. Xie, J.W. Hutchinson, D.A. Weitz, Phys. Rev. Lett. **91**, 224501 (2003)
105. E.O. Potma, X.S. Xie, L. Muntean, J. Preusser, D. Jones, J. Ye, S.R. Leone, W.D. Hinsberg, W. Schade, J. Phys. Chem. B. **108**, 1296–1301 (2004)
106. E. Kang, H. Wang, K. Kwon, J. Robinson, K. Park, J.X. Cheng, Anal. Chem. **78**, 8036–8043 (2006)
107. A.V. Kachynski, A.N. Kuzmin, P.N. Prasad, Appl. Phys. Lett. **91**, 151905 (2007)
108. B.G. Saar, H.S. Park, X.S. Xie, O.D. Lavrentovich, Opt. Express **15**, 13585–13596 (2007)
109. E.O. Potma, D.J. Jones, J.X. Cheng, X.S. Xie, J. Ye, Opt. Lett. **27**, 1168–1170 (2002)
110. F. Ganikhanov, S. Carrasco, X.S. Xie, M. Katz, W. Seitz, D. Kopf, Opt. Lett. **31**, 1292–1294 (2006)
111. M. Jurna, J.P. Korterik, H.L. Offerhaus, C. Otto, Appl. Phys. Lett. **89**, 251116 (2006)
112. G.R. Holtom, B.D. Thrall, B.Y. Chin, H.S. Wiley, S.D. Colson, Traffic **2**, 781–788 (2001)
113. I.W. Schie, T. Weeks, G.P. McNerney, S. Fore, J.K. Sampson, S. Wachsmann-Hogiu, J.C. Rutledge, T. Huser, Opt. Express **16**, 2168–2175 (2008)
114. C. Heinrich, A. Hofer, A. Ritsch, C. Ciardi, S. Bernet, M. Ritsch-Marte, Opt. Express **16**, 2699–2708 (2008)
115. J. Moger, B.D. Johnston, C.R. Tyler, Opt. Express **16**, 3408–3419 (2008)
116. Y. Fu, H. Wang, T.B. Huff, R. Shi, J.X. Cheng, J. Neurosci. Res. **85**, 2870–2881 (2007)
117. T.B. Huff, H. Wang, J.X. Cheng, IEEE J. Sel. Top. Quantum Electron. **14**, 4–9 (2008)
118. T.T. Le, I.M. Langohr, M.J. Locker, M. Sturek, J.X. Cheng, J. Biomed. Opt. **12**, 054007 (2007)
119. C. Otto, A. Voroshilov, S.G. Kruglik, J. Greve, J. Raman Spectrosc. **32**, 495–501 (2001)
120. M. Müller, J.M. Schins, J. Phys. Chem. B **106**, 3715–3723 (2002)

121. J.X. Cheng, A. Volkmer, L.D. Book, X.S. Xie, J. Phys. Chem. B **106**, 8493–8498 (2002)
122. H.N. Paulsen, K.M. Hilligsoe, J. Thogersen, S.R. Keiding, J.J. Larsen, Opt. Lett. **28**, 1123–1125 (2003)
123. T.W. Kee, M.T. Cicerone, Opt. Lett. **29**, 2701–2703 (2004)
124. H. Kano, H. Hamaguchi, Appl. Phys. Lett. **86**, 121113 (2005)
125. G.I. Petrov, V.V. Yakovlev, Opt. Express **13**, 1299–1306 (2005)
126. B. von Vacano, W. Wohlleben, M. Motzkus, Opt. Lett. **31**, 413–415 (2006)
127. H. Kano, H. Hamaguchi, Opt. Express **14**, 2798–2804 (2006)
128. T.W. Kee, H. Zhao, M.T. Cicerone, Opt. Express **14**, 3631–3640 (2006)
129. E.R. Andresen, S.R. Keiding, E.O. Potma, Opt. Express **14**, 7246–7251 (2006)
130. V.P. Mitrokhin, A.B. Fedotov, A.A. Ivanov, M.V. Alfimov, A.M. Zheltikov, Opt. Lett. **32**, 3471–3473 (2007)
131. K.P. Knutsen, J.C. Johnson, A.E. Miller, P.B. Petersen, R.J. Saykally, Chem. Phys. Lett. **387**, 436–441 (2004)
132. S.H. Lim, A.G. Caster, S.R. Leone, Phys. Rev. A **72**, 041803(R) (2005)
133. B. von Vacano, T. Buckup, M. Motzkus, Opt. Lett. **31**, 2495–2497 (2006)
134. B.C. Chen, S.H. Lim, J. Phys. Chem. B **112**, 3653–3661 (2008)
135. B. von Vacano, L. Meyer, M. Motzkus, J. Raman Spectrosc. **38**, 916–926 (2007)
136. H.A. Rinia, M. Bonn, M. Müller, J. Phys. Chem. B **110**, 4472–4479 (2006)
137. E.M. Vartiainen, J. Opt. Soc. Am. B **9**, 1209–1214 (1992)
138. E.M. Vartiainen, H.A. Rinia, M. Müller, M. Bonn, Opt. Express **14**, 3622–3630 (2006)
139. H.A. Rinia, M. Bonn, M. Müller, E.M. Vartiainen, ChemPhysChem. **8**, 279–287 (2007)
140. G.I. Petrov, R. Arora, V.V. Yakovlev, X. Wang, A.V. Sokolov, M.O. Scully, Proc. Natl. Acad. Sci. U S A **104**, 7776–7779 (2007)
141. H.A. Rinia, K.N.J. Burger, M. Bonn, M. Müller, Biophys. J. **95**, 4908–4914 (2008)
142. G.W.H. Wurpel, J.M. Schins, M. Müller, Opt. Lett. **27**, 1093–1095 (2002)
143. G.W.H. Wurpel, M. Müller, Chem. Phys. Lett. **425**, 336–341 (2006)
144. H. Kano, H. Hamaguchi, Opt. Express **13**, 1322–1327 (2005)
145. H. Kano, H. Hamaguchi, Jpn. J. Appl. Phys. **46**, 6875–6877 (2007)
146. H. Kano, H. Hamaguchi, Anal. Chem. **79**, 8967–8973 (2007)
147. H. Kano, J. Raman Spectrosc. **39**, 1649–1652 (2008)
148. H. Kano, H. Hamaguchi, Chem. Lett. **35**, 1124–1125 (2006)
149. H. Kano, H. Hamaguchi, Vibr. Spectrosc. **42**, 135–139 (2006)
150. D. Schafer, J.A. Squier, J. van Maarseveen, D. Bonn, M. Bonn, M. Müller, J. Am. Chem. Soc. **130**, 11592–11593 (2008)
151. F.M. Kamga, M.G. Sceats, Opt. Lett. **5**, 126–128 (1980)
152. J.P. Ogilvie, E. Beaurepaire, A. Alexandrou, M. Joffre, Opt. Lett. **31**, 480–482 (2006)
153. K. Shi, P. Li, Z. Liua, Appl. Phys. Lett. **90**, 141116 (2007)
154. Y.Y. Lee, M.T. Cicerone, Appl. Phys. Lett. **92**, 041108 (2008)
155. B.J. Berne, R. Pecora, *Dynamic Light Scattering* (Wiley, New York, 1976)
156. D. Magde, E.L. Elson, W.W. Webb, Phys. Rev. Lett. **29**, 705–708 (1972)
157. D. Magde, E.L. Elson, W.W. Webb, Biopolymers **13**, 29–61 (1974)
158. M. Ehrenberg, R. Rigler, Chem. Phys. **4**, 390–401 (1974)
159. J. Widengren, U. Mets, R. Rigler, J. Phys. Chem. **99**, 13368–13379 (1995)

160. W. Schrof, J.F. Klingler, S. Rozouvan, D. Horn, Phys. Rev. E **57**, R2523–R2526 (1998)
161. C. Eggeling, J. Schaffer, C.A.M. Seidel, J. Korte, G. Brehm, S. Schneider, W. Schrof, J. Phys. Chem. A **105**, 3673–3679 (2001)
162. T. Hellerer, A. Schiller, G. Jung, A. Zumbusch, ChemPhysChem. **7**, 630–633 (2002)
163. J.X. Cheng, E.O. Potma, S.X. Xie, J. Phys. Chem. A. **106**, 8561–8568 (2002)
164. A.G. Palmer, N.L. Thompson, Biophys. J. **51**, 339–343 (1987)
165. A.G. Palmer, N.L. Thompson, Biophys. J. **52**, 257–270 (1987)
166. P. Schwille, U. Haupts, S. Maiti, W.W. Webb, Biophys. J. **77**, 2251–2265 (1999)
167. S.R. Aragón, R. Pecora, J. Chem. Phys. **64**, 1791–1803 (1976)
168. R. Rigler, J. Widengren, in *Bioscience*, ed. by B. Klinge, C. Owman (Lund University Press, Lund, 1990), pp. 180–183
169. M. Eigen, R. Rigler, Proc. Natl. Acad. Sci. U S A **91**, 5740–5747 (1994)
170. E.J. Woodbury, W.K. Ng, Proc. Inst. Radio Eng. **50**, 2367 (1962)
171. W.J. Jones, B.P. Stoicheff, Phys. Rev. Lett. **13**, 657 (1964)
172. A. Owyoung, E.D. Jones, Opt. Lett. **1**, 152–154 (1977)
173. B.F. Levine, C.G. Bethea, Appl. Phys. Lett. **36**, 245–247 (1980)
174. P. Kukura, D.W. McCamant, R.A. Mathies, Annu. Rev. Phys. Chem. **58**, 461–488 (2007)
175. J.P. Heritage, D.L. Allara, Chem. Phys. Lett. **74**, 507–509 (1980)
176. A.J. Wright, S.P. Poland, J.M. Girkin, C.W. Freudiger, C.L. Evans, X.S. Xie, Opt. Express **15**, 18209–18219 (2007)

7

Raman Optical Activity of Biological Molecules

Ewan W. Blanch and Laurence D. Barron

Abstract Now an incisive probe of biomolecular structure, Raman optical activity (ROA) measures a small difference in Raman scattering from chiral molecules in right- and left-circularly polarized light. As ROA spectra measure vibrational optical activity, they contain highly informative band structures sensitive to the secondary and tertiary structures of proteins, nucleic acids, viruses and carbohydrates as well as the absolute configurations of small molecules. In this review we present a survey of recent studies on biomolecular structure and dynamics using ROA and also a discussion of future applications of this powerful new technique in biomedical research.

7.1 Introduction

There is currently much interest in developing new tools for studying the structure and behaviour of biological molecules. Particularly useful in this respect is Raman optical activity (ROA), which measures vibrational optical activity as a small difference in the intensity of Raman scattering from chiral molecules in right- and left-circularly polarized incident light or, equivalently, a small circularly polarized component in the scattered light, as shown in Fig. 7.1. First predicted in 1969 by Atkins and Barron [1] and observed experimentally in 1972 by Barron, Bogaard and Buckingham [2], ROA spectroscopy was, until recently, restricted to a handful of laboratories around the world as it is a weak effect which requires great care in its measurement. Nevertheless, the great value of ROA's sensitivity to the stereochemistry of both chemical and biological molecules was illustrated in numerous studies, particularly from the Glasgow laboratory [3–5]. As a result of the success of these studies, in which both the range of samples and the types of structural information obtainable were expanded, a commercial spectrometer was made available in 2003 which has led to the current surge in the growth of ROA. As many of the researchers now using ROA are particularly interested in studying biological molecules, we hope that this review will be a useful reference describing past and recent work in this field from our laboratories. Many chemical species, from

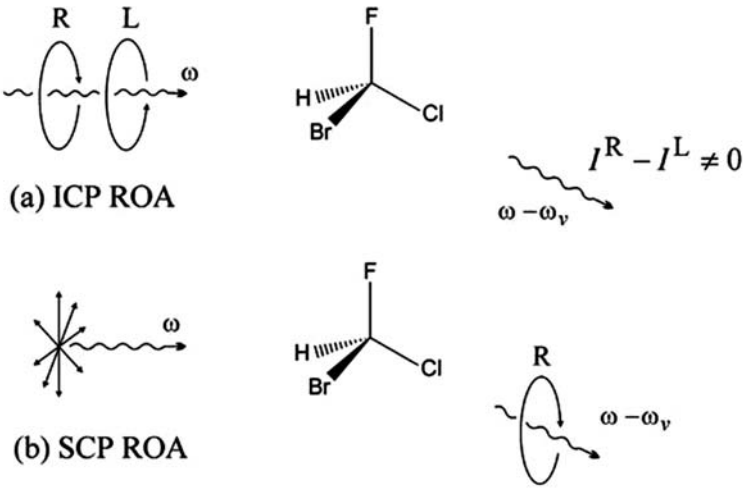

Fig. 7.1. Two equivalent ROA experiments involving Stokes vibrational Raman scattering at angular frequency $\omega - \omega_v$ in incident light of angular frequency ω far from resonance. **a** The ICP ROA experiment measures $I^{\mathrm{R}} - I^{\mathrm{L}}$, where I^{R} and I^{L} are the scattered intensities (shown here as unpolarized) in right- and left-circularly polarized incident light, respectively. **b** The SCP ROA experiment measures $I_{\mathrm{R}} - I_{\mathrm{L}}$, where I_{R} and I_{L} are the intensities of the right- and left-circularly polarized components, respectively, of the scattered light using incident light of fixed polarization (shown here as unpolarized)

pharmaceutical compounds to chiral reagents and novel chiral materials, are also suitable for ROA studies, for such purposes as determination of absolute stereochemistry or enantiomeric purity, but these will not be surveyed here. For reviews of such applications of ROA we direct the reader to a number of excellent earlier reviews and primary references [6–11].

7.2 Theory

7.2.1 ROA Observables

In 1969, Atkins and Barron discovered the fundamental scattering mechanism responsible for ROA in which interference between the light waves scattered via the molecular polarizability and optical activity tensors of a molecule yields a dependence of the scattered intensity on the degree of circular polarization of the incident light and to a circular component in the scattered light [1]. A more definitive version of the theory was presented 2 years later by Barron and Buckingham [12] which introduced as an appropriate experimental observable the dimensionless circular intensity difference (CID), defined as

$$\Delta = \left(I^{\mathrm{R}} - I^{\mathrm{L}}\right) / \left(I^{\mathrm{R}} + I^{\mathrm{L}}\right) \tag{7.1}$$

where I^{R} and I^{L} are the scattered intensities in right- and left-circularly polarized incident light, respectively. In terms of the electric dipole–electric dipole molecular polarizability tensor $\alpha_{\alpha\beta}$ and the electric dipole–magnetic dipole and electric dipole–electric quadrupole optical activity tensors $G'_{\alpha\beta}$ and $A_{\alpha\beta\gamma}$ [13, 14], the CIDs for *forward* (0°) and *backward* (180°) scattering from an isotropic sample for incident transparent wavelengths much greater than the molecular dimensions are expressed as [13]

$$\Delta\left(0^{\circ}\right)=\frac{4\left[45\alpha G'+\beta\left(G'\right)^{2}-\beta\left(A\right)^{2}\right]}{c\left[45\alpha^{2}+7\beta\left(\alpha\right)^{2}\right]}, \tag{7.2a}$$

$$\Delta\left(180^{\circ}\right)=\frac{24\left[\beta\left(G'\right)^{2}+\frac{1}{3}\beta\left(A\right)^{2}\right]}{c\left[45\alpha^{2}+7\beta\left(\alpha\right)^{2}\right]} \tag{7.2b}$$

where the isotropic invariants are defined as

$$\alpha=\tfrac{1}{3}\alpha_{\alpha\alpha}\quad G'=\tfrac{1}{3}G'_{\alpha\alpha}, \tag{7.3}$$

and the anisotropic invariants as

$$\beta\left(\alpha\right)^{2}=\tfrac{1}{2}\left(3\alpha_{\alpha\beta}\alpha_{\alpha\beta}-\alpha_{\alpha\alpha}\alpha_{\beta\beta}\right), \tag{7.4a}$$

$$\beta\left(G'\right)^{2}=\tfrac{1}{2}\left(3\alpha_{\alpha\beta}G'_{\alpha\beta}-\alpha_{\alpha\alpha}G'_{\beta\beta}\right), \tag{7.4b}$$

$$\beta\left(A\right)^{2}=\tfrac{1}{2}\omega\alpha_{\alpha\beta}\varepsilon_{\alpha\gamma\delta}A_{\gamma\delta\beta} \tag{7.4c}$$

These equations use Cartesian tensor notation in which a repeated Greek suffix denotes summation over the three components, and where $\varepsilon_{\alpha\beta\gamma}$ is the third-rank antisymmetric unit tensor. For a molecule composed entirely of idealized axially symmetric bonds, for which $\beta\left(G'\right)^{2}=\beta(A)^{2}$ and $\alpha G'=0$ [13, 15], a simple bond polarizability theory shows that ROA is generated exclusively by *anisotropic* scattering, and the CID expressions then reduce to [13]

$$\Delta\left(0^{\circ}\right)=0, \tag{7.5a}$$

$$\Delta\left(180^{\circ}\right)=\frac{32\beta\left(G'\right)^{2}}{c\left[45\alpha^{2}+7\beta\left(\alpha\right)^{2}\right]}. \tag{7.5b}$$

Therefore, in contrast to the case of conventional Raman scattering intensities, which are the same in the forward and backward directions, within the bond polarizability approximation ROA intensity is not spatially symmetric but is maximized in backscattering and zero in forward scattering. This finding shows that backscattering boosts the ROA signal relative to the background Raman intensity and so is the best experimental strategy for most ROA studies of biomolecules in aqueous solution [16, 17].

ROA is also manifest as a small circularly polarized component in the scattered beam using incident light with a fixed polarization state (including unpolarized) [1, 13, 18–20]. Within the far-from-resonance approximation, this circular component (SCP ROA) is measured as $(I_R - I_L) / (I_R + I_L)$, where I_R and I_L represent the intensities of the right- and left-circularly polarized components, respectively, of the scattered light, provides equivalent information and identical spectra to the CID measurement (ICP ROA). Other ROA measurement strategies are possible and are described elsewhere [18, 21, 22].

These results apply specifically to Rayleigh, or elastic, scattering. For Raman, or inelastic, scattering the same basic CID expressions apply but with the molecular property tensors replaced by corresponding vibrational Raman transition tensors between the initial and final vibrational states n_v and m_v. In this way $\alpha_{\alpha\beta}$'s are replaced by $\langle m_v | \, \alpha_{\alpha\beta}(Q) \, | n_v \rangle$, where $\alpha_{\alpha\beta}(Q)$'s are effective polarizability and optical activity operators that depend parametrically on the normal vibrational coordinates Q such that, within the Placzek polarizability theory of the Raman effect [23], ROA intensity depends on products such as $(\partial\alpha_{\alpha\beta} / \partial Q)_0 \left(\partial G'_{\alpha\beta} / \partial Q\right)_0$ and $(\partial\alpha_{\alpha\beta} / \partial Q)_0 \, \varepsilon_{\alpha\gamma\delta} \, (\partial A_{\gamma\delta\beta} / \partial Q)_0$.

7.2.2 Enhanced Sensitivity of ROA to Structure and Dynamics of Chiral Biomolecules

The normal vibrational modes of biopolymers are highly complex, containing contributions from local vibrational coordinates within both the backbone and the side chains, whether they are amino acids in proteins, bases in nucleic acids or sugars in polysaccharides. ROA is able to cut through the complexity of the corresponding vibrational spectra since the largest signals are often associated with vibrational modes that sample the most rigid and chiral parts of the structure. These modes are usually located within the backbone and often give rise to ROA band patterns characteristic of the backbone conformation. This situation contrasts with the parent conventional Raman spectra of biomolecules, which are typically dominated by bands arising from the side chains which often obscure the backbone bands (Fig. 7.2).

As the time scale of the Raman scattering event ($\sim 3.3 \times 10^{-14}$ s for a vibration with a Stokes wave number shift of $\sim 1000\,\mathrm{cm}^{-1}$ excited in the visible) is much shorter than that of the fastest conformational fluctuations, an ROA spectrum is a superposition of 'snapshot' spectra from all the distinct conformations present in a sample at equilibrium. Since ROA observables depend on absolute chirality, there is a cancellation of contributions from enantiomeric structures arising as a mobile structure explores the range of accessible conformations. Therefore, ROA exhibits an enhanced sensitivity to the dynamic aspects of biomolecular structure. In contrast, conventional Raman band intensities are 'blind' to chirality and so are generally additive and therefore less sensitive to conformational mobility. Ultraviolet circular dichroism (UVCD) also demonstrates an enhanced sensitivity to the dynamics of chiral structures;

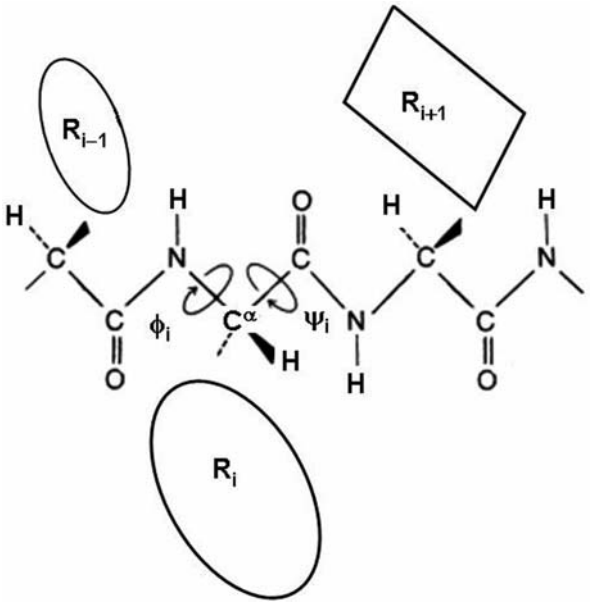

Fig. 7.2. Cartoon representation of the polypeptide backbone of a protein, illustrating the Ramachandran ϕ, ψ angles and the amino acid side chains R_i

however, the sensitivity of UVCD is less than that for ROA due to its dependence on electronic rather than vibrational transitions.

7.3 Instrumentation

As discussed above, a backscattering geometry is essential for the routine measurement of ROA spectra of biomolecules. Backscattering ROA spectra may be acquired using both the ICP and SCP measurement strategies, although the designs of the corresponding instruments are completely different. A backscattering ICP measurement strategy was utilized in Glasgow for many years and provided a large number of biomolecular ROA spectra. A detailed description of the optical layout of the Glasgow backscattering ICP ROA instrument can be found elsewhere [24]. Typical laser power at the sample is ∼700 mW and sample concentrations of proteins, carbohydrates and nucleic acids are ∼30–100 mg/ml while those of intact viruses are ∼5–30 mg/ml. Under these conditions ROA spectra over the range ∼600–1700 cm^{-1} are typically obtained in ∼5–24 h for proteins and nucleic acids and ∼1–4 days for intact viruses.

A completely new design of ROA instrument with significant advantages inherent to the SCP strategy has recently been developed by Hug [19, 25]. This strategy cancels out the flicker noise arising from dust particles and

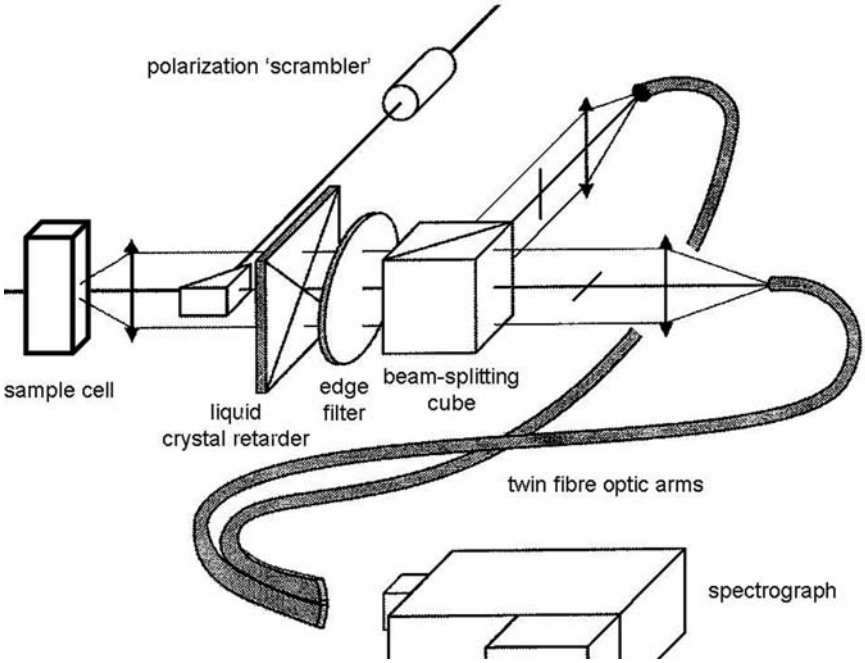

Fig. 7.3. Optical layout of the scattered circular polarization (SCP) BioTools Chiral*Raman* backscattering ROA instrument. Adapted from [25]

density fluctuations in the sample, laser power fluctuations, etc., resulting in greatly superior signal-to-noise characteristics. The basic design is illustrated in Fig. 7.3, which corresponds to Hug's original implementation of the SCP strategy [25]. A commercial instrument based on this new design that also incorporates a sophisticated artifact suppression protocol, based on a 'virtual enantiomers' approach which greatly facilitates the routine acquisition of reliable ROA spectra [26] is now available (the Chiral*Raman* spectrometer from BioTools, Inc.).

7.4 Sensitivity of ROA to Protein Structure

The majority of ROA studies on biomolecules have been reported for proteins and we present here an overview of protein ROA spectra. Vibrations of the peptide backbone are generally associated with three main regions of the Raman spectrum [27, 28]. The backbone skeletal stretch region $\sim$870–1150 cm^{-1} originates in C_α–C, C_α–C_β and C_α–N stretch coordinates; the extended amide III region $\sim$1230–1340 cm^{-1} arises from mainly the in-phase combination of the N–H in-plane deformation with the C_α–N stretch along with, as is now recognized, mixing between the N–H and C_α–H deformations [29–31]; and the amide I region $\sim$1630–1700 cm^{-1} originates in the C=O stretch. In protein ROA spectra, the extended amide III region is of particular importance as coupling between the N–H and C_α–H deformations is sensitive

to geometry, which results in a rich and informative band structure. Amide II vibrations, which occur in the region ∼1510–1570 cm^{-1} and are assigned to the out-of-phase combination of the in-plane N–H deformation with the C–N stretch, can also be more prominent and informative in ROA spectra than in the corresponding conventional Raman spectra [32]. As discussed above, side-chain vibrations generate many characteristic Raman bands [27, 28, 33] but are typically less prominent in ROA spectra due to some conformational freedom averaging out the net chirality in certain situations. Despite this, some side-chain vibrations give rise to useful ROA signals as will be discussed later.

Homopolypeptides provide useful secondary structural models for spectroscopic studies on proteins and the ROA spectra of poly(L-lysine) in the three most important conformers are shown in Fig. 7.4. Poly(L-lysine) at alkaline pH

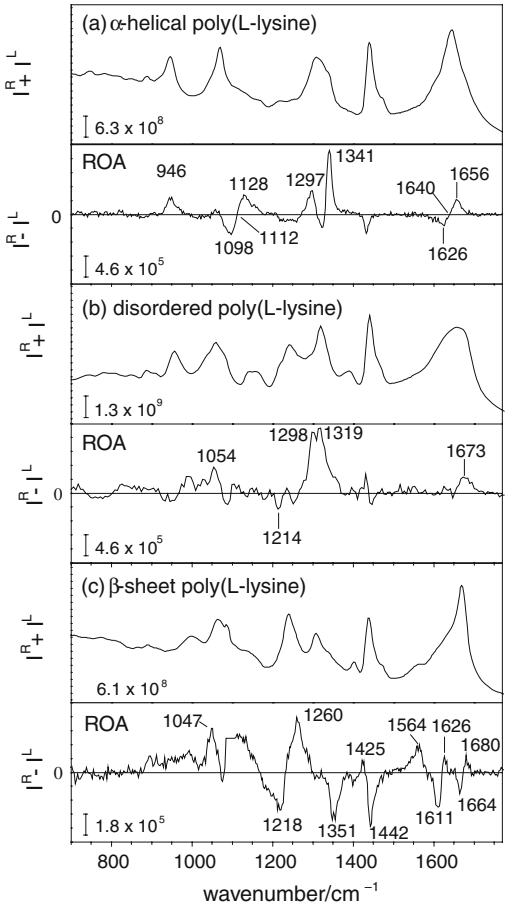

Fig. 7.4. Backscattered Raman $\left(I^{\mathrm{R}} + I^{\mathrm{L}}\right)$ and ROA $\left(I^{\mathrm{R}} - I^{\mathrm{L}}\right)$ spectra of poly (L-lysine) in (**a**) α-helical, (**b**) disordered and (**c**) β-sheet conformations

has neutral side chains and so adopts an α-helical conformation stabilized both by internal hydrogen bonds and by hydrogen bonds to the solvent; whereas poly(L-lysine) at neutral and acidic pH has charged side chains that repel each other, which leads to a disordered structure [34]. Heating of α-helical polylysine leads to adoption of a β-sheet conformation. The backscattered ICP Raman (top) and ROA (bottom) spectra of these samples are shown in Fig. 7.4a–c, respectively [3, 4, 35]. There are obvious differences between the Raman spectra for the α-helical, disordered and β-sheet conformations of poly(L-lysine) but it is clear that the differences between the corresponding ROA spectra are far more significant, particularly in the fingerprint amide III region, indicating the enhanced sensitivity of ROA spectra to secondary structure.

7.4.1 ROA Signatures of α-Helix

The ROA spectra of hen lysozyme [3, 35] and bovine β-lactoglobulin [3] are shown in Fig. 7.5. These spectra contain marker bands for the secondary structural motifs discussed above showing that this information is retained

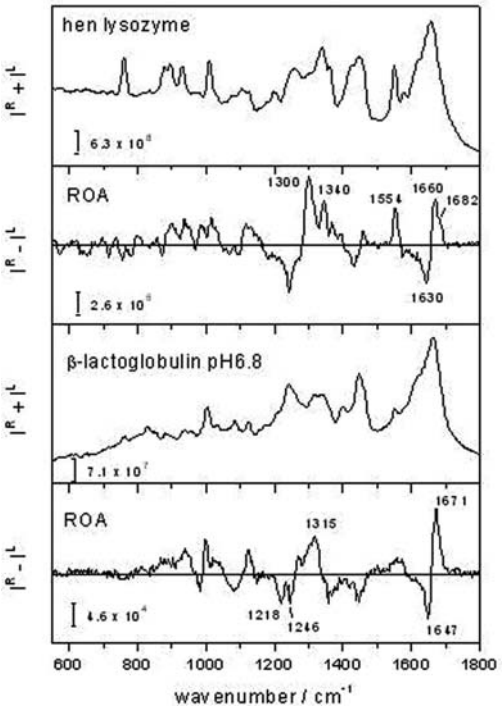

Fig. 7.5. Backscattered ICP Raman $\left(I^{\mathrm{R}} + I^{\mathrm{L}}\right)$ and ROA $\left(I^{\mathrm{R}} - I^{\mathrm{L}}\right)$ spectra of (**a**) hen lysozyme and (**b**) bovine β-lactoglobulin

in protein ROA spectra. In addition, these spectra also contain many bands from the loops and turns located between secondary structural motifs that are important for determining tertiary structure plus discrete bands from some side chains that can serve as reporters of protein secondary and tertiary structure. The sensitivity of protein ROA spectra to these details of structure is apparent in these spectra. For example, the ROA spectra of hen lysozyme are dominated by two positive bands in the amide III region at $\sim$1300 and 1340 cm^{-1} both arising from α-helix, but with these two bands reporting on different aspects of α-helix. The positive $\sim$1340 cm^{-1} band disappears immediately when the protein, or peptide or virus, is dissolved in D_2O. This indicates that N–deformations make a significant contribution to the generation of this ROA band as the corresponding N–D deformations contribute to normal modes several hundred wave numbers lower; and that, in proteins and viruses, the corresponding sequences are exposed to solvent and not buried in hydrophobic regions where amide protons can take far longer to exchange. Although the positive α-helix ROA band at $\sim$1300 cm^{-1} also changes in D_2O, again suggesting some contribution from N–H deformations, in proteins containing a large amount of α-helix in a protected hydrophobic environment much of its intensity is often retained. The positive $\sim$1300 and 1340 cm^{-1} ROA bands have, therefore, been assigned to non-hydrated and hydrated forms of α-helix, respectively [3, 36].

This interpretation is supported by studies of water molecules in high-resolution protein X-ray crystal structures [37–40]. For example, Blundell et al. [37] found that water induces distortions and curvature in α-helices, with average Ramachandran ϕ, ψ angles of $-59°$, $-44°$ with $n = 3.55$ residues per turn for α-helices in hydrophobic environments, and ϕ, ψ angles of $-66°$, $-41°$ with $n = 3.62$ for α-helices in hydrophilic environments. Sundaralingam and Sekharudu [40] later identified three types of hydrogen bonding interactions between water molecules and the peptide backbone. In *external* hydration, the $C{=}O_i$ group already engaged in intrachain helix hydrogen bonding to NH_{i+4} forms a hydrogen bond with an external water molecule. In *three centred* hydration, the amide group forms a hydrogen bond with the carbonyl group as well as water molecules and hence participates in a bifurcated or three-centred hydrogen bond. In *water inserted* hydration, the water molecule inserts itself between the $C{=}O_i$ and NH_{i+4} groups, replacing the $i \rightarrow i+4$ α-helix hydrogen bond with a hydrogen-bonded bridge. Such water inserted hydration of α-helices in protein crystal structures gives rise to a range of conformations including 3_{10}-helical elements (equivalent to type III turns) and type I turns containing $i \rightarrow i+3$ hydrogen bonds stabilized by the inserted water molecule and extended β-strands. Since these hydrated structures occupy contiguous regions of the Ramachandran surface, such hydrated structures may represent intermediates in the helix–coil transition pathway and so provide insight into the role of the aqueous medium in promoting helix (un)folding [40].

External backbone hydration is more common than the other two types and may be especially relevant to aqueous solution studies as it is typical

of interactions between water molecules and the hydrophilic side of amphipathic α-helix, which has a distinct hydrophobic side protected from water and a distinct exposed hydrophilic side each with slightly different Ramachandran ϕ, ψ angles on the two sides [37–39]. This leads to the characteristic bending of amphipathic α-helix indicating that ROA spectral features can be used to monitor helix topology, though the situation can be complicated by other factors such as solvation of the hydrophobic side and side-chain interactions with the backbone. ESR studies have identified a new more open conformation of the α-helix, the experimental data being consistent with a model having ϕ, ψ angles of $-70°$,$-45°$ and $n = 3.8$–3.9 [41, 42]. Computer modelling found that this more open geometry leaves the intramolecular hydrogen bonding network intact but changes the O=C–N angle resulting in a splaying of the backbone amide carbonyls away from the helix axis and into the aqueous solution. This more open structure may even be preferred in aqueous solution as it allows hydrogen bonding of the amide carbonyls with water molecules similar to the external hydration observed in X-ray crystal structures.

In the amide I region there is a distinctive negative/positive couplet from ∼1630 to 1660 cm^{-1} characteristic of α-helix, apparently in either hydrated or nonhydrated form. There are also a number of weaker positive bands in the backbone skeletal stretch region from ∼950 to 1000 cm^{-1}.

7.4.2 ROA Signatures of β-Sheet

Compared to α-helical structures, β-sheets display a far more diverse range of structures as the number and lengths of component strands as well as environment can influence the topology. Although marker bands have been reported for different β-sheet types in conventional infrared and Raman spectra and in UVCD and VCD, it is usually difficult to differentiate between the different structural types of β-sheet found in proteins using these other spectroscopies. This is in part due to overlap of the characteristic β-sheet bands with other structural marker bands for these other techniques. However, ROA spectra from β-sheets tend to be better resolved and more distinct. As for conventional Raman and IR, the amide I region in ROA spectra generates characteristic features for β-sheet as already shown for poly(L-lysine). In Fig. 7.5b, the ROA amide I couplet is dominant for β-lactoglobulin, as one would expect, but appears as a shoulder at ∼1682 $^{-1}$ for hen lysozyme as only 6.2% of the protein is in the form of β-sheet and there is overlap with large bands from α-helix and disordered structure. This situation is similar to that routinely occurring in protein Raman and IR spectroscopies, where band deconvolution is typically required to differentiate between overlapped amide I bands. An advantage of ROA is the presence of marker bands in other spectral regions, as shown by those in the amide III region and the amide I couplet from 1647 to 1671 cm^{-1} clearly dominating the ROA spectrum of β-lactoglobulin. Even when β-sheet is not a dominant structural feature such as for hen lysozyme,

where only a small three-stranded sheet is formed by 6.2% of the sequence, the negative ROA band at $\sim$1240 cm^{-1} in the spectrum of hen lysozyme is able to clearly monitor its presence. Conventional Raman and IR spectra of β-sheet proteins also contain bands in the amide III region but they are typically too weak or obscured by other bands for diagnostic use. The backbone skeletal stretch region from $\sim$1000 to 1100 cm^{-1} also contains β-sheet ROA marker bands as observed for both β-lactoglobulin and hen lysozyme. Therefore, the sensitivity of ROA to the manner in which a vibrational mode interacts with the local chirality gives rise to marker bands, such as those for β-sheet, that are difficult to observe in other spectroscopies, thus opening up a wider and more informative spectral window.

As with α-helix, other signature bands exist within the ROA spectrum that are diagnostic of β-sheet [3]. The characteristic amide I couplet is again negative at lower wave number and positive at higher wave number, though it appears 20–30 cm^{-1} higher than for α-helix. This is sufficient to differentiate between the two structural motifs, as is evident in the hen lysozyme spectrum. The corresponding backbone skeletal stretch marker bands for β-sheet appear in the region $\sim$1000–1050 cm^{-1}.

7.4.3 ROA Signatures of Disordered Structure

It is now obvious that disordered structure, from wholly natively unfolded proteins to flexible loops between structured domains, plays a critical role in the behaviour and function of many proteins. Such flexible regions have proven difficult to resolve at atomic resolution and various optical spectroscopies have proven useful in characterizing and studying disordered sequences. Protein unfolding is also closely related to the phenomenon of protein misfolding,which is critical to the formation of fibrils by some proteins. The large number and complexity of disordered protein structures are indicated by the DisProt Database [43] (http://www.disprot.org) and it is thought that unfolded proteins, or proteins with long unfolded sequences, may comprise at least 25% of all proteins so far discovered [44]. NMR studies are able to recognize the presence of disordered structure but the flexibility of these sequences and the slow relaxation times of NMR (on the order of milliseconds) reduce the sensitivity of these measurements compared to those on folded proteins. ROA, in common with other Raman techniques, operates on a much faster timescale allowing a 'snapshot' of the whole ensemble of inter-converting conformers to be taken. The sensitivity of ROA also generates a more information-rich spectrum for disordered proteins than other Raman techniques [45–49], allowing the complexity of disordered structures such as polyproline II helix to be characterized.

7.5 Glycoproteins

Though there have been few studies performed on glycoproteins so far, these indicate that intact glycoproteins provide high-quality ROA spectra with clear

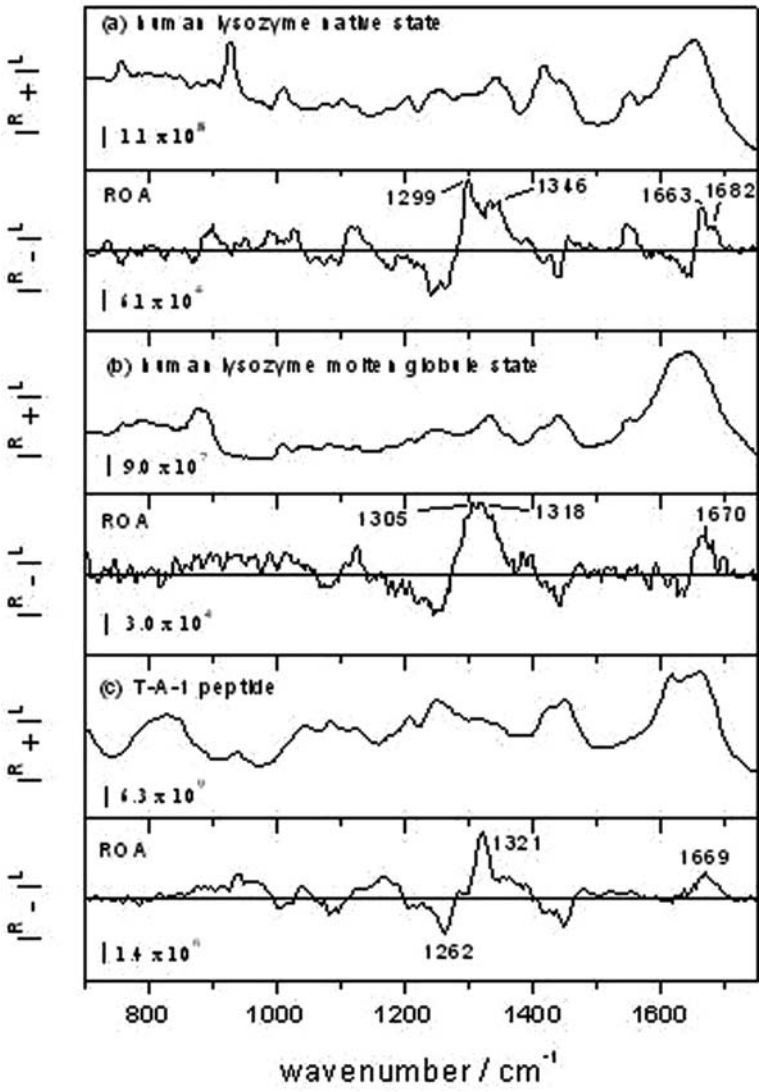

Fig. 7.6. Figure 7.6. Backscattered ICP Raman (IR + IL) and ROA (IR - IL) spectra of (a) human lysozyme in the native state, (b) human lysozyme in the low pH molten globule state, and (c) the T-A-1 peptide from wheat glutenin. Adapted from references 45 and 46

bands originating from both the polypeptide and carbohydrate components [3]. Glycoproteins perform a wide range of roles in biology but their structures are difficult to study using most techniques, creating a good opportunity for ROA to demonstrate its usefulness in structural biology.

Carbohydrates in aqueous solution themselves have been shown to be highly favourable samples for ROA and they generate rich and informative band structures over a wide range of the Raman spectrum [3]. The ROA

spectra of monosaccharides display bands that are sensitive to sugar ring conformation, the relative disposition of hydroxyl groups around the ring, the absolute configuration and orientation (axial or equatorial) of groups attached to the anomeric carbon and the exocyclic CH_2OH conformation. ROA spectra of di- and oligosaccharides also display bands that are sensitive to the conformation of the C–O–C glycosidic linkage, while the spectra of polysaccharides provide information as to whether the structure is disordered or has extended order.

As an example, we present in Fig. 7.7 the ROA spectrum of AGP [49], a much-studied glycoprotein whose exact biological function is unknown [50]. So far no X-ray crystal or NMR structure has been reported for AGP, but spectroscopic studies in combination with homology modelling of the polypeptide component have provided insight into the structure [51]. The polypeptide moiety is based on a single chain composed of 183 amino acids with two disulphide bridges. The carbohydrate content makes up 45% of the molecular weight of AGP and contains five or six highly sialyated oligosaccharide chains, N-glycosylated to asparagine residues. The polypeptide chain is thought to adopt a lipocalin-type fold based on an eight-stranded antiparallel β-sheet closed back on itself to form a continuously hydrogen-bonded barrel with strands linked by β-hairpins and a long loop [51]. The lipocalin fold is also found in β-lactoglobulin, whose ROA spectrum is shown in Fig. 7.5b. Those ROA bands for AGP thought to originate from the carbohydrate component are marked with an asterisk in Fig. 7.7, and many of the unmarked ROA bands of AGP are similar to those observed for β-lactoglobulin, indicating that their folds are similar.

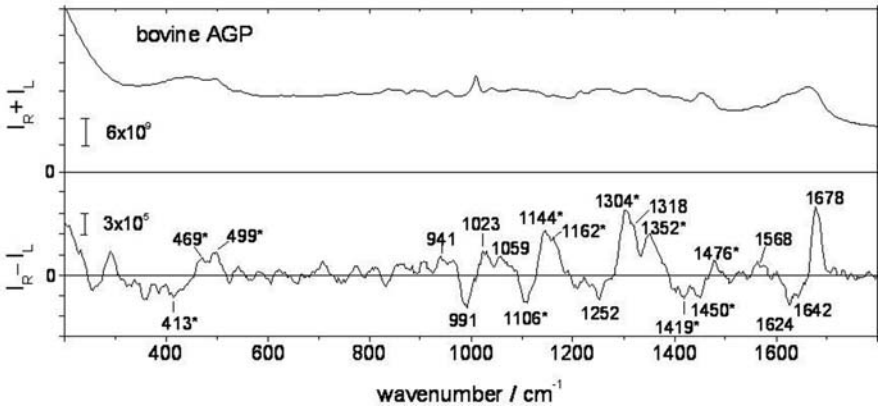

Fig. 7.7. Backscattered SCP Raman ($I_R + I_L$) and ROA ($I_R - I_L$) spectra of bovine α_1-acid glycoprotein (AGP). The AGP ROA bands thought to originate mainly in the carbohydrate component are marked with an asterisk

7.6 ROA Signatures from Side Chains

Though there are few prominent bands reported from side chains in protein ROA spectra, they can be remarkably informative. In particular, bands in the range ∼1400–1480 cm^{-1} originate in CH_2 and CH_3 side-chain deformations and also in tryptophan vibrations; bands in the range ∼1545–1560 cm^{-1} originate in tryptophan W3 mode vibrations; and some bands in the range ∼1600–1630 cm^{-1} originate in vibrations of aromatic side chains, especially tyrosine [3]. In addition, the ring breathing mode of the aromatic ring in phenylalanine, which often generates a strong band in the conventional Raman spectra of proteins at ∼1000 cm^{-1} [28] may be associated with ROA bands observed in this region in some proteins: examples are seen in the ROA spectra of bovine β-lactoglobulin in Fig. 7.5b and bovine AGP in Fig. 7.7. To date, the W3 mode vibrations have been most widely utilized. It has long been known that the magnitude of the angle $\chi^{2,1}$ may be deduced from the position of the parent W3 Raman band of the indole ring [27, 52]. Due to the sensitivity of ROA to chirality, the absolute stereochemistry of the tryptophan conformation, both the sign and magnitude of the torsion angle $\chi^{2,1}$ around the bond connecting the indole ring to the C_β atom, may be obtained from the corresponding ∼1545–1560 cm^{-1} tryptophan ROA band [27]. A recent computational study has verified the sensitivity of this ROA band to tryptophan stereochemistry [53]. This level of structural detail is usually only obtainable from high-resolution X-ray protein crystal structures. The W3 ROA band may also be used as a probe of conformational heterogeneity among tryptophans in disordered protein sequences since cancellation of ROA contributions with opposite signs will result in a loss of ROA intensity. The ROA signature from tryptophans is therefore similar in this respect to those of near UVCD bands from aromatic side chains, which disappear when tertiary structure is lost on denaturation [54]. The two techniques thus provide complementary views on unfolding as ROA probes the intrinsic skeletal chirality of the tryptophan side chain while UVCD probes the chirality in the general environment of the chromophore.

7.7 Studies on Ribonucleic Acids

Similarly to proteins, ribonucleic acids (RNAs) also adopt a wide range of secondary and tertiary structures that can be identified from their characteristic features in both Raman and ROA spectra. The relatively few ROA spectra so far reported for RNAs indicate a similar level of sensitivity to structure and dynamics as has been found for proteins, and that they are sensitive to three different sources of chirality in nucleic acids: the chiral base-stacking arrangement of intrinsically achiral base rings, the chiral disposition of the base and sugar rings with respect to the C–N glycosidic link and the inherent chirality associated with the asymmetric centres of the sugar rings. Initial studies

were conducted on pyrimidine nucleosides [55] and polyribonucleotides [56–58] but functional RNA molecules are also highly suited to ROA measurements, particularly as RNA secondary structure motifs are often stable in isolation, unlike those of proteins.

In Fig. 7.8 we present Raman and ROA spectra of three RNA secondary structural motifs and a functional RNA [59]. In the bottom two panels, Raman and ROA spectra are shown for a 37 nucleotide RNA fragment from Domain I of the encephalomyocarditis virus (EMCV) internal ribosome entry site (IRES) RNA, which guides internal, non-cap dependent, initiation of EMCV protein translation. The upper two and middle two panels show the spectra for a GNRA tetraloop with stem in comparison with those of the same parent structure with either a U·C base mismatch or a pyrimidine-rich asymmetric bulge (called Hairpin, Mismatch and Bulge RNA constructs by the authors). The GNRA tetraloop, mismatch and bulge are common RNA secondary structural motifs and are all present in the 37 nucleotide EMCV

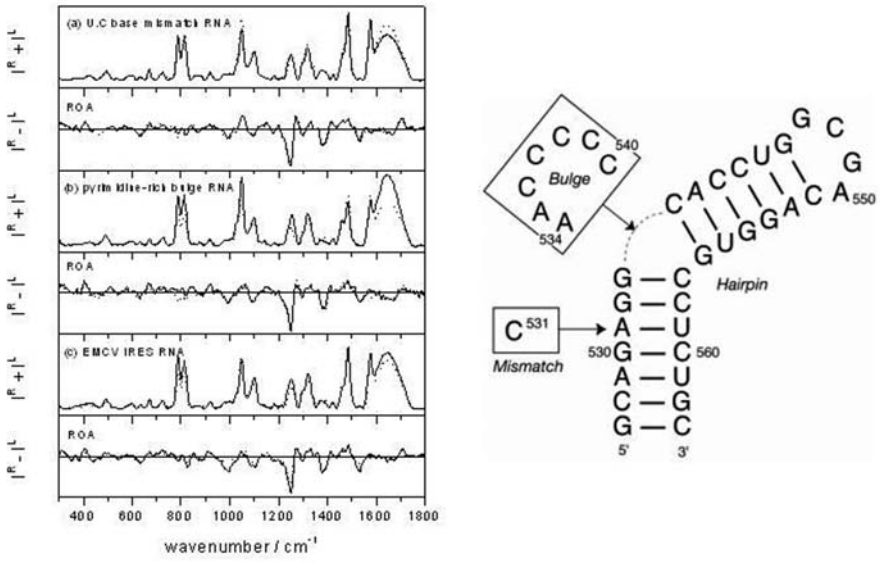

Fig. 7.8. Backscattered SCP Raman ($I_R + I_L$) and ROA ($I_R - I_L$) spectra of a short polyribonucleotide forming a GNRA hairpin (*dashed line*) in comparison with those of (**a**) a U·C base mismatch (*solid line*), (**b**) a pyrimidine-rich asymmetric bulge (*solid line*) and (**c**) a 37 nucleotide RNA fragment from Domain I of the encephalomyocarditis virus (EMCV) internal ribosome entry site (IRES) RNA (*solid line*) [59]. The structures of the RNA constructs and the 37 nucleotide EMCV IRES RNA are shown right. The U C mismatch and pyrimidine-rich bulge RNAs were generated by the addition of the single structural motif of interest (boxed sequences), the U C mismatch base pair and pyrimidine-rich asymmetric bulge, respectively, to the GNRA hairpin RNA. The EMCV RNA contains both of these motifs and all four RNAs contain the GNRA tetraloop

fragment. The structures of these three RNA motifs and that of the 37 nucleotide fragment are also shown in the figure. The ROA spectra for these RNA constructs show only small differences in comparison to the ROA spectrum of the common GNRA hairpin, which is unsurprising as the hairpin dominates each construct, but are still sufficient to identify differences in local conformations of the phosphodiester backbone.

For example, both Raman and ROA bands observed for RNAs from ∼950 to 1150 cm^{-1} are generally thought to be associated with the sugar–phosphate backbone. A negative–positive–negative triplet at ∼994, 1049 and 1086 cm^{-1} has been reported for a number of nucleic acids and is associated with the C3′-endo ribose sugar pucker present in A-form double helix [56, 60]. This triplet appears to be highly sensitive to not only A-type helix content but also to the conformational mobility of the individual ribose sugars which increases within the region of the mismatch [59]. In contrast, the introduction of the pyrimidine bulge decreases the intensity of this triplet, again monitoring a difference in sugar pucker conformations, but in this case the decrease in intensity is also probably due to a decrease in A-form helical content for the bulge RNA. This triplet is most intense for the EMCV RNA suggesting that the presence of both motifs in a sequence produces a cooperative effect, resulting in a structure with more constrained C3′-endo sugar pucker conformation than in sequences containing only one of these two motifs. Such cooperative effects on local RNA structure are not unexpected as the mismatched base pair in EMCV RNA is located only three residues away from the pyrimidine-rich bulge. From ∼1648 to 1704 cm^{-1}, the broad negative–positive ROA couplet also appears to be indicative of A-type helix although other structural factors may affect this feature. As the number of RNA spectra reported for nucleic acids increases in the future we are confident that much new structural information will be revealed.

7.8 Studies on Viruses

As with conventional Raman spectroscopy, there is no size limitation to ROA so that studies can be performed on the largest macromolecules such as intact viruses. The first virus ROA spectra were reported for filamentous bacteriophages [60–62]. These studies greatly assisted in the identification of ROA bands associated with unhydrated and hydrated α-helix, already discussed, as both types are present in significant proportions in the helical coat proteins in the intact bacteriophages. Subsequent studies showed that ROA spectra can provide fingerprints of the structures of proteins in the viral capsid, allowing similarities or differences between viruses to be quickly determined [35, 60, 62, 63]. There is obvious interest in the use of ROA for simultaneously investigating the structures of both the protein and nucleic acid components of intact viruses, paralleling previous Raman studies of viruses. There is considerable potential for the use of both Raman and ROA in structural virology

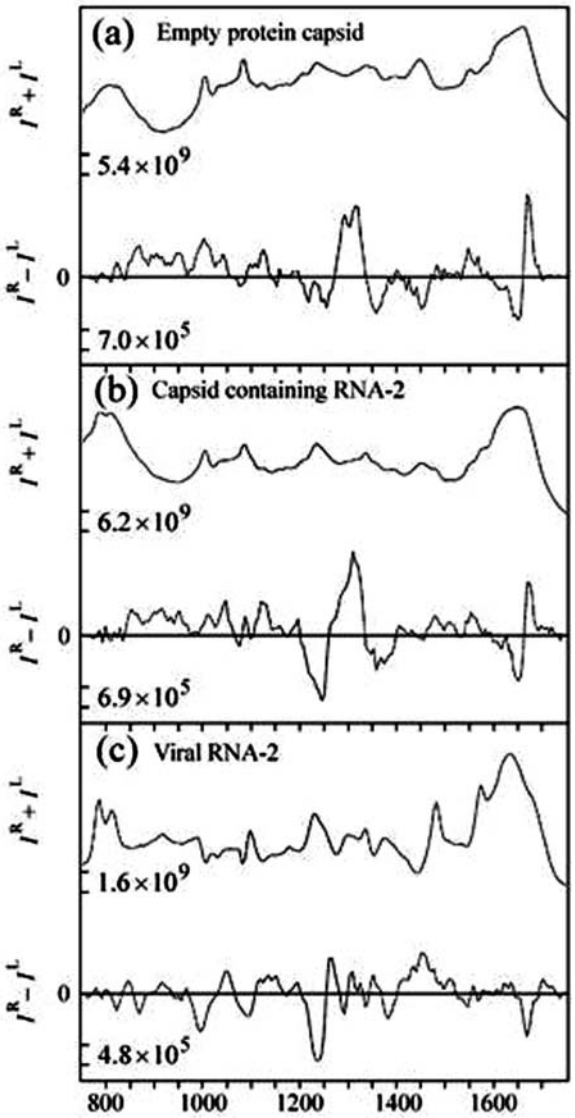

Fig. 7.9. Backscattered ICP Raman $\left(I^{\mathrm{R}}+I^{\mathrm{L}}\right)$ and ROA $\left(I^{\mathrm{R}}-I^{\mathrm{L}}\right)$ spectra measured for (**a**) the empty cowpea mosaic virus (CPMV) protein capsid (top pair), (**b**) the intact capsid containing RNA-2 (middle pair), and (**c**) the difference spectra obtained by subtracting the top from the middle spectra to reveal the spectra of the viral RNA-2 (bottom pair)

due to the recognized difficulties of characterizing intact viruses, particularly the encapsidated nucleic acid, using X-ray diffraction and NMR. As an illustration of one strategy for characterizing both the protein capsid and the encapsidated nucleic acid of a virus using ROA, we present in Fig. 7.9 results for cowpea mosaic virus (CPMV) [60].

CPMV is the type member of the comovirus group of plant viruses and is a bipartite virus with the genome consisting of two different RNA molecules (RNA-1 and RNA-2) separately encapsidated in identical icosahedral capsids. The structure of the protein capsid is known to be constructed from 60 copies of an asymmetric unit made up of three different protein domains each of which supports a 'jelly-roll β-sandwich' fold [64–66]. However, the structures of RNA-1 and RNA-2 were not resolved. Preparations of CPMV can be separated into empty protein capsids, capsids containing RNA-1 and capsids containing RNA-2. The top panel of Fig. 7.9 shows the Raman and ROA spectra of the empty protein capsid, with the spectral band patterns being characteristic of the jelly-roll β-sandwich fold of the capsid proteins. The middle panel shows the spectra of the capsid containing RNA-2, with bands from the nucleic acid now evident as well as those from the protein. Though not shown here, the Raman and ROA spectra for the capsid with RNA-1 were very similar. The bottom panel shows the spectra obtained by subtracting the top from the middle spectra, leading to Raman and ROA spectra for the encapsidated RNA-2 plus any changes in protein bands due to protein–RNA interactions [59]. The difference ROA spectrum is very similar to those of synthetic and natural RNA molecules and therefore probably originates mainly in the viral RNA: the details reflect the single-stranded A-type helical conformation of the encapsidated RNA-2, which was not previously known. The ROA spectrum of RNA-1 was extracted using the same procedure and was found to be very similar to that of RNA-2, despite having a quite different length and base sequence. This suggests that both RNAs take up the same 'default' conformation within the capsid, possibly because the protein–nucleic acid interactions in this particular virus are very weak.

7.9 Developments in Computational Spectral Analysis

It is likely that many of the most exciting advances in ROA over the next few years will be in computational approaches. In particular, the implementation of basis functions and computational procedures for modelling ROA spectra in both the GAUSSIAN and DALTON suites has recently provided several new insights into ROA spectra–structure relationships [67–71]. However, we will not review such computational modelling work here but summarize the application of chemometric tools for analysing measured ROA spectra.

7.9.1 Principal Component Analysis (PCA)

Pattern recognition methods have been widely used to better understand many types of vibrational spectra of biological systems and biomolecules, and principal component analysis (PCA) [72] was first implemented for ROA in order to conduct an initial representation of the structural relationships among polypeptide and protein states based on their ROA spectra [35]. In this example, the set of 78 ROA spectra for proteins and polypeptides were first normalized by scaling to the sum of the squared spectral intensities. Figure 7.10 shows a plot of the two most significant basis functions, which together account for ∼50% of the total variance of the data, with the positions of samples being colour-coded with respect to the seven different structural types listed in the figure, which provide a useful initial classification of tertiary structure. Since α-helix and β-sheet contents of proteins tend to be inversely

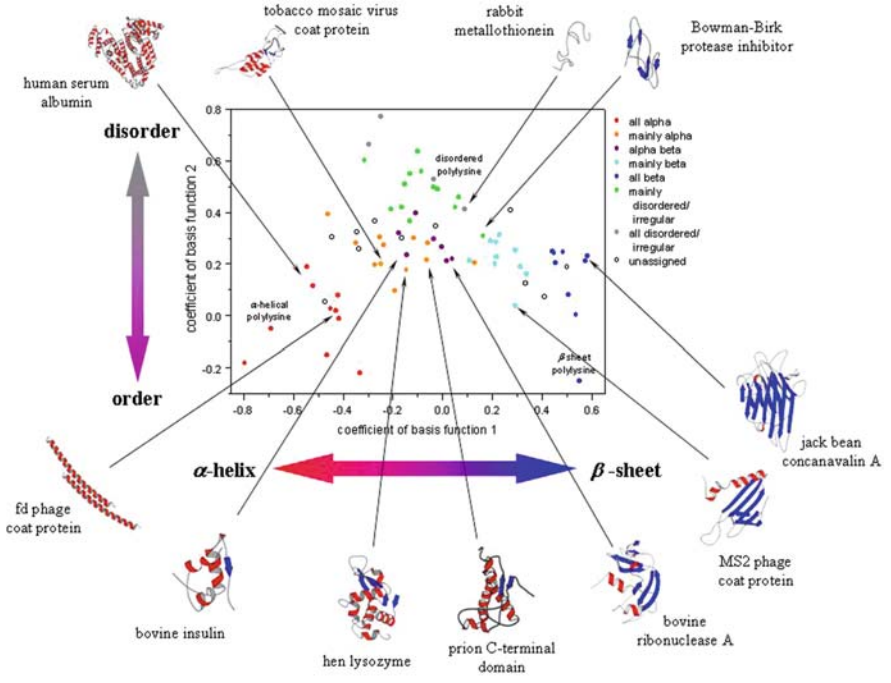

Fig. 7.10. Plot of the PCA coefficients for the two most important basis functions for a set of 78 polypeptide, protein and virus ROA spectra. Definitions of the structural types analysed are: all alpha, > ∼60% α-helix with little other secondary structure; mainly alpha, > ∼35% α-helix and a small amount of β-sheet (∼5–15%); alpha beta, similar significant amounts of α-helix and β-sheet; mainly beta, > ∼35% β-sheet and a small amount of α-helix (∼5–15%); all beta, > ∼45% β-sheet with little other secondary structure; mainly disordered/irregular, little secondary structure; all disordered/irregular, no secondary structure

correlated (the larger the amount of one the smaller the amount of the other), the coefficients associated with α-helix and β-sheet have opposite signs, here being negative for α-helix and positive for β-sheet in the first basis function. The coefficients for the second basis function reflect the amount of disordered (principally PPII) structure, large positive coefficients being associated with disordered polypeptides and proteins. It is obvious that the spectra separate into clusters corresponding to different types of structure, with increasing α-helix content to the left, increasing β-sheet content to the right, and increasing disordered or unfolded structure from bottom to top. The positions of example proteins are indicated.

7.9.2 Nonlinear Mapping (NLM) Analysis

Like PCA, nonlinear mapping (NLM) is a form of data clustering technique visualized in a low dimensionality plot, but NLM better conveys the relationships between data points rather than just the gross overall variance, thus providing a truer representation of similarities and differences [73]. The advantage of NLM over PCA is that it conveys the relationships between data points rather than just the gross overall variance, thus providing a truer representation of similarities and differences between the spectra. In brief, the NLM method minimizes the following function:

$$S = \sum_{i} \sum_{<j} w_{ij} \left(d_{ij} - \widehat{d}_{ij} \right)^2 \tag{7.6}$$

where d_{ij} and $\widehat{d}_{ij}$ are the inter-point (i.e. inter-spectra) distances in the full multidimensional space and the reduced dimensionality space, respectively, and w_{ij} is a weighting factor dependent upon the specific type of multidimensional scaling or nonlinear mapping undertaken. Examples of 2D NLM plots constructed from protein ROA spectra, displaying clustering of data based on the structural class of each protein, can be found elsewhere [47] and NLM has been shown [74] to be especially valuable in dealing with the elusive problem of structural propensities in different types of unfolded protein. We anticipate that further ROA studies on disordered proteins coupled with machine learning tools such as NLM and PCA will lead to a better characterization of their structural complexities.

7.9.3 2D Correlation Analysis

Generalized two-dimensional correlation (2DCOS) analysis is based on a cross-correlation analysis of spectra as a function of two independent wave number positions, thereby spreading the spectra over an additional dimension, and is a useful approach to studying structural changes in biological and chemical species. The 2D technique is applicable to any external perturbation, such as

temperature, pH and reagent concentration [75]. Two-dimensional correlation generates two plots, called the synchronous and asynchronous, which may be conveniently displayed in the form of contour maps [76], facilitating the detailed analysis of sequential spectral changes associated with the perturbation influence. Recently, Blanch and coworkers have developed 2DCOS ROA for the investigation of conformational transitions in polypeptides and proteins [77–81]. An example is shown in Fig. 7.11, where ROA spectra collected for the unfolding of α-helix in polyglutamic acid [82] show two stages of changes in the transition, one occurring from pH 4.75–5.05 and the other from pH

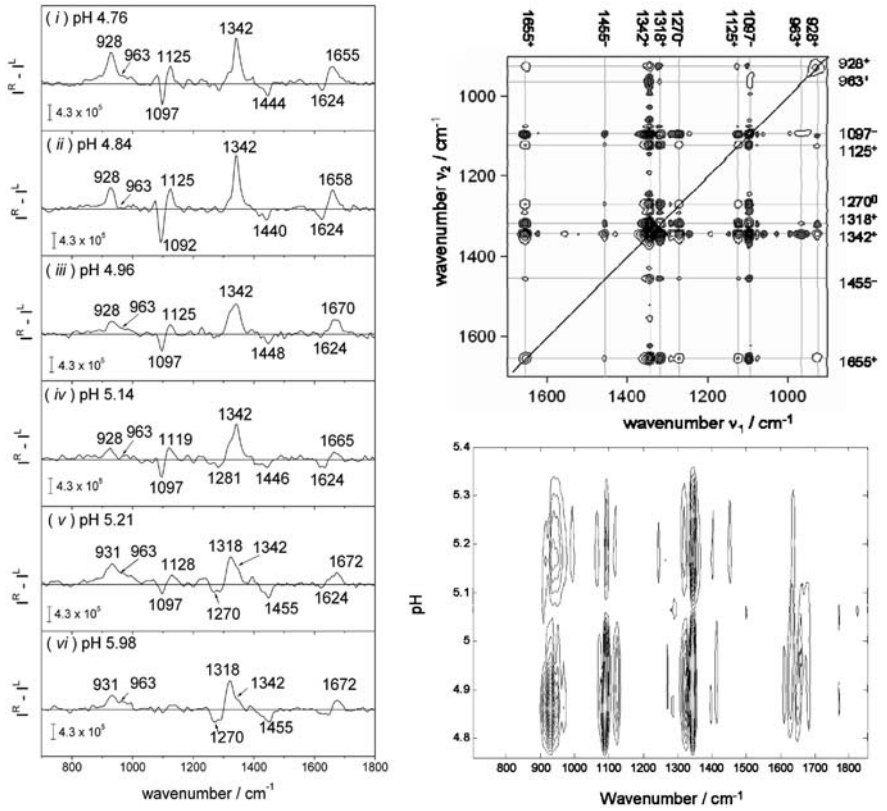

Fig. 7.11. A 2DCOS ROA moving window analysis. Backscattered ICP ROA $\left(I^{\mathrm{R}} - I^{\mathrm{L}}\right)$ spectra of poly(L-glutamic acid) at pHs over the range 4.76 (α-helical) – 5.98 (disordered) are shown *left*. *Top right* is the 2D synchronous plot showing changes in these ROA spectra with positive correlations (bands changing in the same direction) being represented as unshaded contours and negative correlations (bands changing in opposite directions) shown as shaded contours. The moving window analysis of these data is presented *bottom right* and monitors the two distinct phases of spectral change occurring during helix unfolding

5.05–5.35 reflecting differences in helical stability between the central region of helix and the relatively destabilized residues at the N- and C-termini [3, 83].

7.10 Conclusion

One of the most important tasks in biology for the foreseeable future will be the structural characterization of the wide range of biological molecules now being identified. While conventional, and particularly atomic resolution, methods will continue to be exploited for this purpose, ROA has an important role to play. Although the application of ROA to biological molecules has been pursued until recently in only a few laboratories, considerable success has already been achieved in providing new and detailed structural information on not only proteins but also RNA, viruses and glycoproteins. As shown in this review, the level of information contained within these spectra varies from fingerprints unique to sample identity, to qualitative or quantitative measures of structural competition, to a precise probe of tryptophan indole ring orientation. As new researchers take ROA forward into other areas of structural biology, with these future advances being made more likely by further developments in instrumentation or machine learning, we anticipate that ROA will demonstrate even greater versatility and insight for the analysis of the structure and behaviour of most, or even all, types of biological molecules.

Acknowledgements

We would like to recognize the important contributions to this work of Dr Lutz Hecht at the University of Glasgow and the many postdoctoral researchers and postgraduate students at Glasgow and Manchester. In addition, L.D.B. thanks both EPSRC and BBSRC for continued support over many years and E.W.B. thanks EPSRC, RSC and the Wellcome Trust for their support for his lab.

References

1. P.W. Atkins, L.D. Barron, Mol. Phys. **16**, 453 (1969)
2. L.D. Barron, M.P. Bogaard, A.D. Buckingham, J. Am. Chem. Soc. **95**, 603 (1973)
3. L.D. Barron, L. Hecht, E.W. Blanch, A.F. Bell, Prog. Biophys. Mol. Biol. **73**, 1 (2000)
4. L.D. Barron, E.W. Blanch, L. Hecht, Adv. Protein Chem. **62**, 51 (2002)
5. E.W. Blanch, L. Hecht, L.D. Barron, Methods **29**, 196 (2003)
6. L. Hecht, A.L. Phillips, L.D. Barron, J. Raman Spectrosc. **26**, 727 (1995)
7. K.M. Spencer, R.B. Edwards, R.D. Rauh, M.M. Carruba, Anal. Chem. **66**, 1269 (1994)
8. K.M. Spencer, R.B. Edmonds, R.D. Rauh, Appl. Spectrosc. **50**, 681 (1996)

9. J. Costante, L. Hecht, P.L. Polavarapu, A. Collet, L.D. Barron, Angew. Chem. Int. Ed. Engl. **36**, 885 (1997)
10. P.L. Polavarapu, *Vibrational Spectra: Principles and Applications with Emphasis on Optical Activity* (Elsevier, Amsterdam, 1998)
11. J. Haesler, L. Schindelholz, E. Riguet, C.G. Bochet, W. Hug, Nature **446**, 526 (2007)
12. L.D. Barron, A.D. Buckingham, Mol. Phys. **20**, 1111 (1971)
13. L.D. Barron, *Molecular Light Scattering and Optical Activity*, 2nd edn. (Cambridge University Press, Cambridge, 2004)
14. L.D. Barron, A.D. Buckingham, J. Am. Chem. Soc. **96**, 4769 (1974)
15. A.D. Buckingham, Adv. Chem. Phys. **12**, 107 (1967)
16. L. Hecht, L.D. Barron, W. Hug, Chem. Phys. Lett. **158**, 341 (1989)
17. L. Hecht, L.D. Barron, Appl. Spectrosc. **44**, 483 (1990)
18. L.A. Nafie, Annu. Rev. Phys. Chem. **48**, 357 (1997)
19. W. Hug, in *Handbook of Vibrational Spectroscopy*, vol. 1, ed. by J.M. Chalmers, P.R. Griffiths (Wiley, Chichester, 2002), p. 745
20. L.D. Barron, A.D. Buckingham, Annu. Rev. Phys. Chem. **26**, 381 (1975)
21. L.A. Nafie, T.B. Freedman, Chem. Phys. Lett. **154**, 260 (1989)
22. L.D. Barron, L. Hecht, E.W. Blanch, Mol. Phys. **102**, 731 (2004)
23. D.A. Long, *The Raman Effect* (Wiley, Chichester, 2002)
24. L. Hecht, L.D. Barron, E.W. Blanch, A.F. Bell, L.A. Day, J. Raman Spectrosc. **30**, 815 (1999)
25. W. Hug, G. Hangartner, J. Raman Spectrosc. **30**, 841 (1999)
26. W. Hug, Appl. Spectrosc. **57**, 1 (2003)
27. T. Miura, G.J. Thomas Jr., Subcellular biochemistry. in *Proteins: Structure, Function and Engineering*, vol. 24, ed. by B.B. Biswas, S. Roy (Plenum Press, New York, 1995), p. 55
28. A.T. Tu, Adv. Spectrosc. **13**, 47 (1986)
29. M. Diem, *Modern Vibrational Spectroscopy* (Wiley, New York, 1993)
30. R. Schweitzer-Stenner, J. Raman Spectrosc. **32**, 711 (2001)
31. R. Schweitzer-Stenner, F. Eker, Q. Huang, K. Griebenow, P.A. Mroz, P.M. Kozlowski, J. Phys. Chem. B, **106**, 4294 (2002)
32. P.R. Carey, *Biochemical Applications of Raman and Resonance Raman Spectroscopies* (Academic Press, New York, 1982)
33. S.A. Overman, G.J. Thomas Jr., Biochemistry **38**, 4018 (1999)
34. P.R. Bergethon, *The Physical Basis of Biochemistry* (Springer-Verlag, New York, 1998)
35. L.D. Barron, E.W. Blanch, I.H. McColl, C.D. Syme, L. Hecht, K. Nielsen, Spectroscopy **17**, 101 (2003)
36. I.H. McColl, E.W. Blanch, L. Hecht, L.D. Barron, J. Am. Chem. Soc. **126**, 8181 (2004)
37. T.L. Blundell, D. Barlow, N. Borakoti, J.M. Thornton, Nature **306**, 281 (1983)
38. D.J. Barlow, J.M. Thornton, J. Mol. Biol. **201**, 601 (1998)
39. R. Parthasarathy, S. Chaturvedi, K. Go, Prog. Biophys. Mol. Biol. **64**, 1 (1995).
40. S. Sundaralingam, Y.C. Sekharudu, Science **244**, 1333 (1989)
41. P. Hanson, D.J. Anderson, G. Martinez, G.L. Millhauser, F. Formaggio, M. Crisma, C. Toniolo, C. Vita, Mol. Phys. **95**, 957 (1998)
42. K.A. Bolin, G.L. Millhauser, Acc. Chem. Res. **32**, 1027 (1999)

43. M. Sickmeier, J.A. Hamilton, T. LeGall, V. Vacic, M.S. Cortese, A. Tantos, B. Szabo, P. Tompa, J. Chen, V.N. Uversky, Z. Obradovic, A.K. Dunker, 2006, Nucleic Acids Res. **35**(Database issue), D786-93 (2007) Epub 2006 Dec 1
44. P. Romero, Z. Obradovic, X. Li, E.C. Garner, C.J. Brown, A.K. Dunker, Proteins: Struct. Funct. Genetics **42**, 38 (2001)
45. E.W. Blanch, L.A. Morozova-Roche, D.A.E. Cochran, A.J. Doig, L. Hecht, L.D. Barron, J. Mol. Biol. **301**, 553 (2000)
46. E.W. Blanch, D.D. Kasarda, L. Hecht, K. Nielsen, L.D. Barron, Biochemistry **42**, 5665 (2003)
47. F.J. Zhu, J. Kapitan, G.E. Tranter, P.D.A. Pudney, N.W. Isaacs, L. Hecht, L.D. Barron, Proteins – Struct. Funct. Bioinform. **70**, 823 (2008)
48. C.D. Syme, E.W. Blanch, C. Holt, R. Jakes, M. Goedert, L. Hecht, L.D. Barron, Eur. J. Biochem. **269**, 148 (2002)
49. L.D. Barron, F. Zhu, L. Hecht, N.W. Isaacs, *Structure and Behaviour of Proteins from Raman Optical Activity*, ed. by V. Uversky, E. Permyakov (Nova Science Publishers Inc., New York, 2008), p. 27
50. T. Fournier, N. Medjoubi-N, D. Porquet, Biochim. Biophys. Acta **1482**, 157 (2000)
51. V. Kopecký Jr., R. Ettrich, K. Hofbauerová, V. Baumruk, Biochem. Biophys. Res. Commun. **300**, 41 (2003)
52. G.J. Thomas Jr., Annu. Rev. Biophys. Biomol. Struct. **28**, 1 (1999)
53. C.R. Jacob, S. Luber, M. Reiher, Chem. Phys. Chem. **9**, 2177 (2008)
54. R.W. Woody, A.K. Dunker, *Circular Dichroism and the Conformational Analysis of Biomolecules*, ed. by G.D. Fasman (Plenum Press, New York, 1996), p.109
55. A.F. Bell, L. Hecht, L.D. Barron, J. Chem. Soc. Faraday Trans. **93**, 553 (1997)
56. A.F. Bell, L. Hecht, L.D. Barron, J. Am. Chem. Soc. **119**, 6006 (1997)
57. A.F. Bell, L. Hecht, L.D. Barron, Biospectroscopy **4**, 107 (1998)
58. A.F. Bell, L. Hecht, L.D. Barron, J. Raman Spectrosc. **30**, 651 (1999)
59. A.J. Hobro, M. Rouhi, E.W. Blanch, G.L. Conn, Nucleic Acids Res. **35**, 1169 (2007)
60. E.W. Blanch, L. Hecht, C.D. Syme, V. Volpetti, G.P. Lomonossoff, K. Nielsen, L.D. Barron, J. Gen. Virol. **83**, 2593 (2002)
61. E.W. Blanch, A.F. Bell, L. Hecht, L.A. Day, L.D. Barron, J. Mol. Biol. **290**, 1 (1999)
62. E.W. Blanch, L. Hecht, L.A. Day, D.M. Pederson, L.D. Barron, J. Am. Chem. Soc. **123**, 4863 (2001)
63. E.W. Blanch, D.J. Robinson, L. Hecht, C.D. Syme, K. Nielsen, L.D. Barron, J. Gen. Virol. **83**, 241 (2002)
64. G.P. Lomonossoff, J.E. Johnson, Prog. Biophys. Mol. Biol. **55**, 107 (1991)
65. T. Lin, Z. Chen, R. Usha, C.V. Stauffacher, J.-B. Dai, T. Schmidt, J.E. Johnson, Virology, **265**, 20 (1999)
66. T. Lin, A.J. Clark, Z. Chen, M. Shanks, J.-B. Dai, Y. Li, T. Schmidt, P. Oxelfelt, G.P. Lomonossoff, J.E. Johnson, J. Virol. **74**, 493 (2000)
67. K.J. Jalkanen, R.M. Nieminen, M. Knapp-Mohammady, S. Suhai, Int. J. Quantum Chem. **92**, 239 (2003)
68. M. Pecul, E. Larnparska, C. Cappelli, L. Frediani, K. Ruud, J. Phys. Chem. A **110**, 2807 (2006)

69. N.A. Macleod, C. Johannessen, L. Hecht, L.D. Barron, J.P. Simons, Int. J. Mass Spectrom. **253**, 193 (2006)
70. E. Lamparska, V. Liegeios, O. Quinet, B. Champagne, Chem. Phys. Chem. **7**, 2366 (2006)
71. C. Herrmann, K. Ruud, V. Reiher, Chem. Phys. **343**, 200 (2008)
72. E.R. Malinowski, in *Factor Analysis in Chemistry*, 3rd edn. (Wiley, New York, 2002)
73. W.J. Krzanowski, *Principles of Multivariate Analysis, A User's Perspective* (Oxford University Press, Oxford, 1998)
74. F.J. Zhu, G.E. Tranter, N.W. Isaacs, L. Hecht, L.D. Barron, J. Mol. Biol. **363**, 19 (2006)
75. I. Noda, Appl. Spectrosc. **47**, 1329 (1993)
76. I. Noda, Y. Ozaki, *Two-Dimensional Correlation Spectroscopy* (Wiley, Chichester, 2004)
77. L.A. Ashton, L.D. Barron, B. Czarnik-Matusewicz, L. Hecht, J. Hyde, E.W. Blanch, Mol. Phys. **104**, 1429 (2006)
78. B. Czarnik-Matusewicz, L.A. Ashton, E.W. Blanch, J. Mol. Struct. **799**, 61 (2006)
79. L.A. Ashton, B. Czarnik-Matusewicz, E.W. Blanch, J. Mol. Struct. **799**, 253 (2006)
80. L.A. Ashton, E.W. Blanch, Appl. Spectrosc. **62**, 469 (2008).
81. L.A. Ashton, A.J. Hobro, G.L. Conn, M. Rouhi, E.W. Blanch, J. Mol. Struct. **883**, 187 (2008)
82. L.A. Ashton, L.D. Barron, L. Hecht, J. Hyde, E.W. Blanch, Analyst **132**, 468 (2007)
83. S.T. Thomas, V.V. Loladze, G.I. Makhatadze, Proc. Natl. Acad. Sci. U S A **98**, 10670 (2001)

8

Chemometric Methods for Biomedical Raman Spectroscopy and Imaging

Rohith K. Reddy and Rohit Bhargava

Abstract The vibrational spectrum is a quantitative measure of a sample's molecular composition. Hence, classical chemometric methods, especially regression-based, have focused on exact mapping between identity and sample composition. While this approach works well for molecular identifications and scientific investigations, problems of biomedical interest often involve complex mixtures of stochastically varying compositions and complex spatial distributions of molecules contributing to the recorded signals. Hence, the challenge often is not to predict the identity of materials but to determine chemical markers that help rapidly detect species (e.g. impurities, conformations, strains of bacteria) in large areas or indicate changes in function in complex tissue (e.g. cancer or tissue engineering). Hence, the rate of data analysis has to be rapid, has to be robust with respect to stochastic variance and the provided information is usually related to biomedical context and not to molecular compositions. The emergence of imaging techniques and clinical applications are spurring growth in this area. In this chapter, we discuss chemometric methods that are useful in this milieu. We first review methods for data pre-processing with a focus on the key challenges facing a spectroscopist. Next, we survey some of the well known, widely used pattern classification techniques under the framework of *supervised* and *unsupervised* classification. We discuss the applicability, advantages and drawbacks of each of these techniques and help the reader not only gain useful insights into the techniques themselves but also acquire an understating of the underlying ideas and principles. We conclude by providing examples of the coupled use of chemometric and statistical tools to develop robust classification protocols for prostate and breast tissue pathology. We specifically focus on the critical factors and pitfalls at each step in converting spectral data sets into hi-fidelity images useful for decision making.

8.1 Introduction

Spectroscopic data can broadly be used to understand molecular structure, to relate function to molecular content, and to understand evolution of structure and properties with both time and/or stimulus [1]. Generalizing these activities, one can summarize that much effort in biomedical spectroscopy is

related to categorizing substances into classes that reflect function. With the emergence of large-scale data recording (including imaging), high-throughput experimental designs, and increasing computational power, this categorization is increasingly being conducted using automated numerical algorithms. The richness and availability of myriad data allow vibrational spectroscopists to both use methods from and actively contribute to the development of chemometrics [2]. The primary focus here is on describing the general methods a practicing spectroscopist may use for biomedical data processing and their relative merits. We also present an illustrative case study from our laboratories to emphasize an integrated approach to designing experiments, recording data, obtaining results, and verifying their statistical validity.

Chemometrics relates chemical measurements of a material to its functional state using mathematical and statistical methods. Hence, in our view, it encompasses the domain of using numerical methods to improve data quality (both the signal-to-noise ratio and resolution), classification of information from the data (both supervised and unsupervised methods), and the appropriate display of information (both visualization of information content and its statistical validity). For problems especially focused on classification, the first category of methods is usually termed as pre-processing while the last is usually termed as post-processing. In this chapter, we organize the method descriptions within these broad sub-sections. Due to limited space, we do not provide many details of methods but will point to key references. We also do not discuss aspects of data acquisition physics, for example, for tomography or nonlinear spectroscopy that are needed to obtain the data. Last, since the data handling methods for IR and Raman spectroscopy are rather similar, we provide examples from either domain without significant distinction.

The vibrational spectrum is a quantitative measure of a sample's molecular composition. Hence, classical chemometric methods, especially regression based, have focused on exact mapping between identity and sample composition. Typically, these methods include a training (calibration) step and a prediction (validation) step in which exact compositions of molecules are known and predicted. Fundamentally, the methods involve some form of regression [3] for identity mapping with different optimization conditions and constraints, using optimized spectral sections [4, 5]. The basic process in classical chemometrics [6] is illustrated in Fig. 8.1. Consider that measurements are performed on a sample. The "sample" may be a protein, tablet, person, or some other extract. Many data may be expressed for the sample, including identity (class) of the sample, concentrations, or spectra. The measured quantities are generally termed as variables. When $\boldsymbol{K}$ variables are measured for $\boldsymbol{S}$ samples, the resulting data can be reconstituted in terms of a matrix of size $\boldsymbol{S} \times \boldsymbol{K}$ (Fig. 8.1). The fundamental focus of classical chemometrics approaches is to decompose the matrix into significantly smaller matrices of size $\boldsymbol{S} \times \boldsymbol{M}$ and $\boldsymbol{M} \times \boldsymbol{K}$ that contain all relevant information about the sample as well as a matrix $\boldsymbol{S} \times \boldsymbol{K}$ that is predominantly noise. The principal rationale is that the

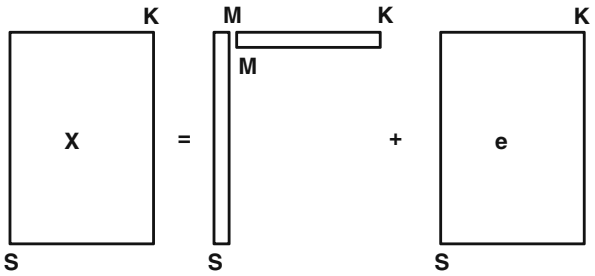

Fig. 8.1. A key idea in chemometrics is to record $\boldsymbol{K}$ variables (including spectral data) for $\boldsymbol{S}$ samples to form a matrix $\boldsymbol{S} \times \boldsymbol{K}$. The critical characteristics of both the samples and the spectral data can then be understood using a smaller set of matrices $\boldsymbol{S} \times \boldsymbol{M}$ and $\boldsymbol{M} \times \boldsymbol{K}$ while the unmodeled residual remains available for analysis as the matrix $\boldsymbol{e}$. While the reduced matrices provide insight into the system or process, residual data can be used to understand errors or limitations of the model

recorded data are repeated measures of a small set of sample characteristics. The small set defines almost entirely the sample as well as its characteristic spectral properties.

A number of excellent references are available for classical techniques, including those by Kowalski et al. [7, 8], Kramer [9], Brereton [10], compilations [11, 12], and series of periodic reviews [13]. There are two somewhat related problems in chemometrics that are relevant to spectral data. The first is to predict molecular identifications in mixtures from a spectrum and the second is to predict a class or label for a spectrum. While regression techniques work well for molecular identifications, problems of biomedical interest often involve stochastically varying compositions and spatial distributions of

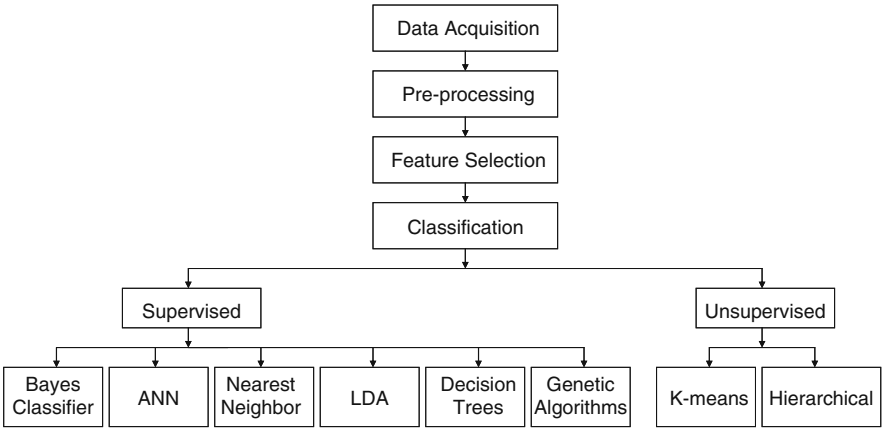

Fig. 8.2. Overview of data processing steps and classification methods discussed in this chapter

molecules contributing to the recorded signals. Hence, the challenge often is not to predict the composition but to determine chemical markers that help rapidly detect species (e.g., impurities, conformations, strains of bacteria) in large areas or indicate changes in function in complex materials (e.g., cancer or tissue engineering). Hence, the provided information must be usually related to biomedical context and not to molecular compositions. Pattern recognition methods are more useful in this context. Hence, we focus the classification portion of the review on these methods (Fig. 8.2). The emergence of imaging techniques, process biotechnology, and potential clinical applications are especially spurring growth in this area.

8.2 Pre-processing Methods

Pre-processing methods are used to remove spectral contributions that are not related to the material under study (prevent confounding artifacts in the analysis), to enhance the signal such that analysis is facilitated, or to understand the extent of analysis required by examining the problem. The end goal in all cases is to enable extraction of information in a consistent and accurate manner by follow-up methods. While we will underscore the integrative nature of data extraction later as well, the influence of pre-processing methods on the quality of information obtained [14] cannot be over-emphasized. A number of examples have been reported in the literature examining the effects of pre-processing methods on the classification of samples, for example, in [15].

8.2.1 Baseline Correction

Baseline correction is generally needed to remove signals arising from fluorescence. While a straightforward approach is to manually determine the "best" subtraction using an expert spectroscopist, confounding effects can result in the routine use of this approach [16]. Further, the large volume of data in many experiments makes this approach less attractive; the objective and automated features offered by numerical methods are more suited. The common approach is to fit a polynomial curve to a large segment of the spectrum and simply subtract the smooth curve from the combined Raman and fluorescence data. Subtracting a likely background from the recorded data can be accomplished using many algorithms. A methodology for comparison of baseline correction methods has been reported [17] and, in this study, the method proposed by Lieber and Mahadevan-Jansen [18] was proposed to be superior. Classification results obtained by the compared methods were the same; however, the superior correction method preserved spectral features better. While more complicated schemes and somewhat better performance can be achieved by other algorithms [19], a balance must be struck by the practitioner between the accuracy, speed, and simplicity of the specific approach used.

It is worth noting that there are several elegant hardware methods for fluorescence background suppression. A simple strategy is to simply move to longer excitation wavelengths [20]. The drawbacks include weaker scattering and the need for higher laser powers. Nevertheless, low absorption in the near-IR wavelength regime (the so-called optical window in tissue) may make this strategy a particularly useful one for non-destructive biomedical analysis. Another approach, due to Chase and Hirschfeld, is to use Fourier transform Raman spectroscopy [21, 22]. The obvious need for an interferometer-based spectrometer is somewhat palatable due to spectroscopists' familiarity with and success of FT-IR spectroscopy in the mid-IR regime. Unfortunately, unlike mid-IR spectroscopy that is dominated by detection noise, shot noise of the excitation laser limits a dramatic multiplexing advantage in FT-Raman spectroscopy [23] and measures can be adopted for overcoming disadvantages due to limited dynamic range [24].

Both old [25] and new ideas [26] have become practical due to advances in hardware [27], algorithms, and computing power. Two interesting examples are illustrative of the potential at either the excitation (source) or detection end. While one relies on fast gating for temporal rejection during detection, the other major one relies on shifted wavelength Raman excitation [28]. Raman spectra that are a millionfold lower intensity than the fluorescence signal can be recovered. While the former relies on hardware-based gating, the latter method makes use of a multimode laser. The physics of the process can additionally be realized and gate adjusted as per need in the former while cheaper, lower power lasers can be used in the latter. Software reconstruction is needed to account for Raman shift correspondence and efficient rejection of the background in the latter. The assumption is that fluorescence is little changed while Raman lines are shifted with changing frequency. A combined method is indeed possible [29] and was shown to improve the signal-to-noise ratio (SNR) by an order of magnitude. Both hardware and software methods (more likely) will be increasingly incorporated in commercial instruments and their combination with chemometric methods [30] will become more prevalent.

8.2.2 Spike Removal

Charge coupled devices (CCDs) are now commonly used to record the exceptionally low level of light available from the Raman scattering process. The efficacy of these detectors may be sometimes limited by infrequent events that are not part of the experiment. Spikes in recorded data, sometimes termed "spike noise," are generated by cosmic rays or γ- and α-rays emitted from materials around the detector chip. Each quantum of such high-energy rays usually generates thousands of electrons when incident on the detector, while a single visible/NIR photon produces less than one electron on the average. Though, ordinarily, the probability of a cosmic event is small, the use of larger CCDs with increased integration times (especially for imaging biological tissue) can

lead to a significant portion of the data set being affected by spikes [31]. The same effects are observed in atomic emission spectroscopy and analogous effects, though of different origin, are seen in FT-IR imaging [32].

The challenge is to devise efficient methods to eliminate spike noise without compromising spectral information. In the first approach, simple filters or transform techniques may be used. A common approach is to use median filtering in which neighboring spectral elements are used to smooth the data. There is most certainly a loss of spectral resolution and less than exceptionally sharp spikes may not be well filtered. In another implementation, successively acquired spectra (commonly used for averaging in FT-IR) were median filtered prior to averaging [32] to preserve spectral fidelity. For analogous recording of Raman spectra, a benefit may be obtained by increasing the gain of the detector but reducing the integration time, followed by collecting repeated observations. The strategy has not been reported for Raman data. In Raman spectroscopic images, neighborhood median filtering has been shown to be effective for 3×3 pixel box sizes, thereby limiting the trade-off between spatial smoothing and spectral recovery [33]. A summation approach was used in comparing successively acquired spectra from the same material and shown to be superior to median filtering [34]. More complex methods may be used and can be effective in preserving both spectral fidelity and reducing a temporal/spatial trade-off [35]. These methods are essentially likelihood estimators with various boundary conditions. While they are generally applicable, they are especially effective for use on known (bounded) spectral sets. Since a number of biological materials have reasonably well understood and consistent spectra that need to be repeatedly measured, likelihood algorithms can be very useful. For example, if the bandwidths of the sample are relatively large, a simple cut-off value for width helps identify spikes that can then be averaged out [36]. In general, the quality of spectral data retained must be balanced by the complexity of the algorithm and the time required for application, especially for large data sets. In the usual case, however, the overhead for this process is likely minimal and, since data acquisition times are often long, spike removal may well be incorporated into the data acquisition process in real time.

8.2.3 De-noising

Since the Raman effect is weak, acquisition of high-quality data in a short time is difficult. The problem is especially compounded in imaging data sets where large numbers of spectra have to be recorded and time is at a premium. Yet, analytical problems often require high SNR data for sophisticated analysis, especially for samples from small volumes. Numerical methods for noise rejection are useful in aiding the acquisition of such data. Fundamentally, the process of noise rejection involves recognizing some property of noise that is distinct from that of the signal, transforming the data such that the characteristic measures of the property are highlighted, suppressing the noise-related

property values and inverse transforming the data to recover high SNR data. The transformation may involve simple smoothing (since signals are generally concentrated in lower frequencies while noise is spread across the spectrum), determining correlations using point-wise [37] or multivariate means or statistical reconstruction [38]. Wavelet transforms [39] (see Sect. 6.2.6 too) have been used to suppress noise frequencies and, hence, provide high SNR data. The quantity of available data often dictates the optimal method. The use of multivariate covariance method is especially interesting when large numbers of spectra are available and can be especially powerful for spectroscopic imaging data. Briefly, the approach consists of an eigenvalue decomposition of the data using a forward transform, for example, a principal components analysis (PCA) [40]. After selecting eigenimages with sufficient SNR, the selected data are inverse transformed to reconstruct the original data set with lower noise content.

A method based on a modified principal components analysis was proposed by Green et al. and termed the minimum noise fraction (MNF) [41]. Adopted from the remote sensing community [42], the method has been used for IR spectroscopic imaging [43–45]. Normalizing the signal to the noise content in the images was then used to order eigenimages in decreasing order of SNR. A modified version [46] of this transform was shown to improve image fidelity and achieve better noise reduction than PCA. An example is shown in Fig. 8.3 in which data from a single pixel of an imaging data set are shown simulated

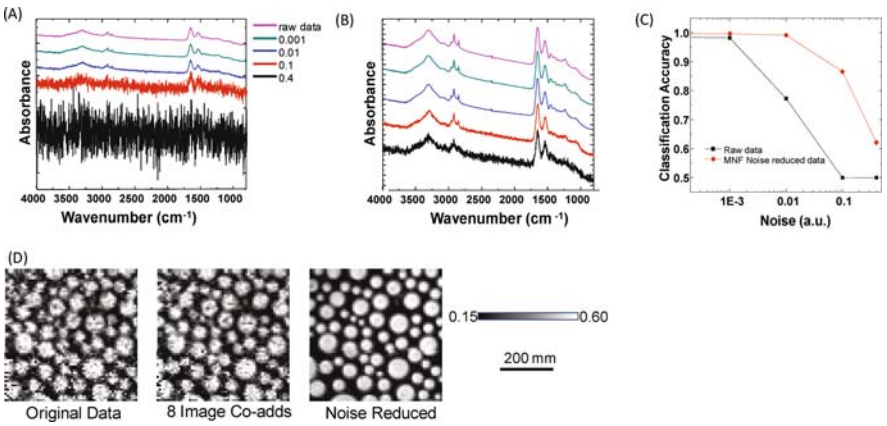

Fig. 8.3. **A** Acquired high SNR data and simulated noisy spectra (peak-to-peak noise = 0.001, 0.01, 0.1, and 0.4 a.u.), showing the degradation in data quality. Spectra are offset for clarity. **B** Spectra after noise reduction demonstrate the dramatic gains possible by chemometric methods. **C** Noise reduction was implemented to classify breast tissue and application of noise rejection allowed the same quality of classification (accuracy) to be recovered at higher noise levels. **D** In another example, image fidelity (here the nitrile stretching vibrational mode at $2227\,\mathrm{cm}^{-1}$) is much enhanced as a result of spectral noise rejection **A** and **C** are reproduced from Reddy and Bhargava, Submitted [165]. **D** is reproduced from [43]

with increasing noise levels. Upon de-noising, significant recovery of spectral detail can be observed. The spectral detail can be used to improve both the appearance of an image and the quality of information extracted from the image.

Transform techniques for noise reduction utilize the property that noise is uncorrelated whereas spectra (signals) have a higher degree of correlation. Hence, in the transform domain, the signal becomes largely confined to a few eigenvalues whereas the noise is spread across all. It is the relative proportion of the signal and noise which forms a criterion for inclusion of specific factors in the inverse transform. Inclusion of too many factors will not allow for significant noise rejection, while inclusion of too few would result in loss of fine spectral features or small variances in the data set. Hence, identifying eigenvalues corresponding to high signal content is an important step in the noise reduction process but is often performed manually. An automated method has recently been suggested that uses spatial correspondence between eigenimages and structure of the sample as an objective measure of inclusion of any eigenimage for inverse transformation. In all cases, it must be recognized that there is some element of filtering in the process and usually causes both a loss of signal detail (which may not have been recoverable ordinarily, though) and a consequent smoothing of the spectral profile. For imaging cases, as noted in the example above, a smoothing in the spatial domain may be tolerated and traded off against spectral smoothing. The practitioner must be aware, however, that the best option for accurate quantitative analysis is to simply acquire higher SNR data, if needed. The results from a de-noising procedure must be validated rigorously, if the method is to be routinely employed. As an interesting note, methods to estimate noise are also proposed [47].

8.2.4 Super-Resolution

The trade-off between data acquisition time, spectral quality, spatial resolution, and coverage is usually a consideration in acquisition of data. As seen for the de-noising case, chemometric techniques can help overcome certain hardware trade-off limits for SNR of data. An exciting avenue for overcoming resolution vs. coverage trade-off, similarly, has been described using motion-based super-resolution techniques [48]. The method acquires several low-resolution images of the same sample in order to retrieve a higher resolution chemical image. Briefly, the idea is that each low-resolution image is a result of a specific geometric transformation, a linear space-invariant blurring, and uniform rational decimating performed on the ideal high-resolution image. In this case, the authors used a linear translation as the geometric transformation but added Gaussian noise in the decimated images to simulate the effects of measurement noise. The authors stress the use of more low-resolution images than the minimum needed using, for example, regularization methods to both pose the problem in a tractable form and suppress noise. Hence, it is difficult to

quantify the time gained by the procedure as well as to decide on parameters a priori, as the algorithm would likely have to obtain both from the data quality and resolution enhancement. Another key step in the approach is the use of an iterative scheme to estimate the likely structure, which involves a careful selection of constraints on the solution (e.g., smoothness or positivity of values).

An interesting observation reported was that the reconstruction was not especially sensitive to the instrument's point spread function. Hence, a detailed knowledge of the optics of the instrument is not required for super-resolution. Further, in principle, smoothing and noise rejection could be achieved in the inversion process (though this idea was not reported in the chapter). As with other inverse problems (e.g., filtered backprojection in computed tomography) the choice of an appropriate filter may be made to minimize the effects of noise and actually reconstruct both a high-resolution and low-noise image set from constituent low-resolution, noisy data sets. Finally, caution must be exercised in that results of both high-resolution and low-noise reconstructions are dependent on the algorithm and do result in a loss of data. The results are a best estimate of the actual structure/data quality under the constraints of the algorithms employed. When used appropriately, though, both chemometric approaches help improve the trade-offs that a spectroscopist must consider in the design and conduct of experiments.

8.2.5 Eigenvector-Based Multivariate Analysis

Spectral data are highly redundant (many vibrational modes of the same molecules) and sparse (large spectral segments with no informative features). Hence, before a full-scale chemometric treatment of the data is undertaken, it is very instructive to understand the structure and variance in recorded spectra. Hence, eigenvector-based analyses of spectra are common and a primary technique is principal components analysis (PCA). PCA is a linear transformation of the data into a new coordinate system (axes) such that the largest variance lies on the first axis and decreases thereafter for each successive axis. PCA can also be considered to be a view of the data set with an aim to explain all deviations from an average spectral property. Data are typically mean centered prior to the transformation and the mean spectrum is used a base comparator. The transformation to a new coordinate set is performed via matrix multiplication as

$$\boldsymbol{Y} = \boldsymbol{V}^{\mathrm{T}}\boldsymbol{X} \tag{8.1}$$

where $\boldsymbol{X}$ is the same data matrix shown in Fig. 8.1 and $\boldsymbol{Y}$ is the new data matrix after rotation. The specific axes along which the data are rotated are found by solving an eigenvalue equation and it can be shown that a rotation matrix ($\boldsymbol{V}^{T}$) always exists. The weights assigned to different axes are representative of the spectral characteristics of separate sub-groups that may

be obtained via a classification based on variance. The vector of weights (often termed, loadings) can also be used as a surrogate for a difference spectrum from the mean. In sum, these two properties are exceptionally useful in assigning a group of spectra into sub-groups (classes) whose biochemical distinctions may be explained by the spectra of the weight vectors. Hence, PCA is often used to classify a group of spectra into similar classes and just a few principal components can segment observations meaningfully. This approach has been used numerous times to classify Raman spectra; representative examples from tissue, cellular, microbiological, pharmaceutical, polymeric, and other scientific domains demonstrate the wide popularity of the approach.

PCA is performed without any prior information about the spectra under consideration and can be shown to be related to rigorous least-squares regression approach. Hence, it is both easy to implement, is robust [49], and is based on strong fundamentals due to the linearly additive properties of vibrational spectra. There is a large database of applications, significant understanding of the other pre-processing steps required, extensive theoretical work and tutorials to aid the practitioner [50]. There are some drawbacks as well. Matrix multiplications can be computationally expensive and, especially for large data sets encountered in imaging, may have practical limitations due to computer memory. From a scientific perspective, further, different biochemical components do not always correspond to variance groupings. Large differences in spectral content or group sizes could potentially confound the realization of true biochemical classes in the data. The inherent complexity of the data is the same as that of spectra – it is transformed into a much more tractable form for understanding. Spectroscopists are typically interested in spectral characteristics, for example, band heights, ratios, shifts position, and width of the bands. Most of these features are nonlinear and linear transform techniques such as PCA would not be effective in capturing such information. Hence, nonlinear PCA methods [51] have been reported but are not widely adopted yet by the spectroscopy community. There is some sensitivity to pre-processing methods and contamination in the samples could lead to confounding results as well. Hence, caution must be exercised in the use of the method for further classification and the practitioner must always refer back to the weight vectors to ensure the biochemical validity of the insight obtained.

The reader may be surprised to find PCA discussed as a pre-processing method in this chapter. It is here, however, that we feel is its greatest utility. Pre-processing often is a discovery phase and exploratory analysis of data [52] often guides the development of a protocol for the routine information extraction. The insight provided by PCA is invaluable in that regard. For purposes of classification, we are less enthused about the use of PCA to recognize classes on a routine basis, for example, in the classification of benign and malignant tissue. The potential for failing to readily identify confounding artifacts (from sample contamination, instrumental artifacts, or correlated noise) and the in-

ability to use prior information about the sample are two drawbacks added to those mentioned above. In controlled systems, however, for example where a small class of pure materials or limited numbers of constituents without chance of significant contamination are available, PCA is exceptionally useful for classification and identification. Several recent examples are available from studies on protein optical activity [53], recognition of atherosclerotic plaques [54], polymer mixtures [55], fiber types [56], narcotics [57], chemical histology [58], cellular transformations [59–61]. Finally, our logic for assigning PCA to the pre-processing stage is the emergence of many sophisticated classification studies that do not employ simple spectral measures but employ PCA loadings and vectors as inputs for more sophisticated classification techniques discussed in the next sections [62–65].

PCA is also a powerful adjunct to classical regression techniques [66]. One major drawback of multivariate linear regression (MLR) techniques is their sensitivity to collinear data [67], which is sometimes masked by noise. Hence, approaches like step-wise linear regression have been suggested to discard variables. An alternative is to employ PCA and conduct regression on components that are, by definition, orthogonal. Further, principal components regression (PCR) is less sensitive to measurement noise. The blind nature of variance, however, does not guarantee that the first m selected features are indeed most relevant to the scientific question. Hence, all components need to be extracted and evaluated in the prediction model. Partial least-squares regression [67, 68] (PLSR) and related formulations [69–71] can be used to address this drawback [72]. The algorithm extracts components that are relevant to both dependent and independent variables in the regression in decreasing order of relevance. Hence, an incrementally larger model can be compared to a smaller model to choose the more useful one. Implicit in these strategies is the fact that the correlated signal in the first few components is akin to signal averaging spectra in the data set. Hence, noise reduction is implicit in PCA-based regression. Other classification schemes will have to explicitly use larger spectral features or, for example, constrained regularization methods [73] to be comparable. Similarly, other algorithms can be used to eliminate sample variances due to preparation and process artifacts [74], but PCA-based methods retain the noise reduction benefits from all data points very well. A major consequence of this property and orthogonality is that classifications are often highly accurate and facile, contributing to the popularity of PCA-based methods [75]. Similarly, PCA-based discriminant analysis has been used to obtain highly accurate classifications that are at least as good as more sophisticated, nonlinear methods [76].

8.2.6 High-Performance Algorithms

While we have discussed pre-processing steps in a sequential manner, newer approaches are capable of integrating all the steps into single transformation approaches. For example, applications of wavelet transforms [77] can

potentially alter the routine treatment of data by combining several steps. A single transform [78, 79] can act to determine dimensionality of the data, compress manyfold the data size for analysis and storage, eliminate background effects, remove spikes [80], de-noise [81], and perform classification [82]. Extensive application of the method has been reported for spectral analyses [83]. An attractive feature of the approach, in addition its universal applicability and utility, is the capability to examine data at different levels of granularity [84]. The selection of a specific component allows for the examination of fine or coarse structure in the data – both spectral and spatial. The drawbacks discussed for PCA above also remain for wavelet transforms.

8.2.7 Dimensionality Reduction

Spectra have significant regions of redundant information, spectral regions that may not be useful in classification or regions that have no spectral information content. Hence, a subset of recorded spectral regions is useful and the process of finding this subset is termed as dimensionality reduction. The first approach is to employ a completely objective and automated technique. For example, regression techniques can be used to determine which indices are most effective at explaining the relationship between recorded data and the predicted result. Yet another means are factor-based approaches (e.g., PCA) since most of the important information is captured in a few components. A third approach may be to use expert algorithms (e.g., genetic algorithms) that integrate well with the data analysis. A comparison of various approaches is available against newer ideas [85, 86]. Last, a completely manual approach, in which the spectroscopist examines spectra for important features, may be used [87]. In general, the more automated the method, the more comprehensively it can examine data. Similarly, when the data reduction method includes a human expert element, an enhanced understanding of the underlying biochemical knowledge can be obtained and prior knowledge can be incorporated.

8.2.8 Summary of Pre-processing Methods

Pre-processing methods are key to understanding the true scientific content of the data structure and are critical to enabling accurate, fast, and robust information extraction from the methods we will describe next. The purview of such methods has expanded from simple spectral corrections to sophisticated algorithms that assure and improve data quality, provide consistency for subsequent processing, and optimal retrieval and storage of data. We emphasize that these steps are crucial and necessarily integrative with the entire chain of designing experiments to analyzing results. Hence, the practitioner must exercise due care to use the methods carefully and understand implications of these operations on results obtained.

8.3 Classification Methods

Classification, or the division of data into groups, methods can be broadly of two types: supervised and unsupervised. The primary difference is that prior information about classes into which the data fall is known and representative samples from these classes are available for supervised methods. The supervised and unsupervised approaches loosely lend themselves into problems that have prior hypotheses and those in which discovery of the classes of data may be needed, respectively. The division is purely for organization purposes; in many applications, a combination of both methods can be very powerful. In general, biomedical data analysis will require multiple spectral features and will have stochastic variations. Hence, the field of statistical pattern recognition [88] is of primary importance and we use the term "recognition" with our learning and classification method descriptions below.

8.3.1 Supervised Recognition

Any method that incorporates information from known samples into the design of a classification protocol involves learning. In supervised learning, every sample in a representative data set belongs to a specific class. The size and scope of samples, conversely, must be such that they are representative of the population from which prediction samples will be drawn. This set of samples and spectra are termed a training set. The underlying premise of classification is usually to construct a protocol based on the training set that minimizes the chance of making an error with samples whose classes are to be found (validation set). Other approaches may be to minimize the cost of errors or maximize the detection of a specific class. It may also be important to consider important classifier characteristics, including robustness to noise, computational complexity, scaling with increasing data size, numbers of spectral features used, and speed of classification. The number of classes is usually determined from scientific considerations.

There are three steps to constructing a classification protocol for supervised recognition. First, appropriate pre-processing of the data is conducted. Second, a training set is utilized with an appropriate algorithm such that parameters of the classification function are obtained (training, learning, or calibration step). Third, quantitative measures of validation (accuracy or error) are obtained using an independent set for validation of the protocol. The parameters of the classification function and the results from the validation set can be used in conjunction to understand the scientific problem that is being studied. The problem can be stated for spectroscopy as follows: given a spectrum (or measures derived from the spectrum), $\boldsymbol{K}$, it must be assigned to one of n possible classes, C_i where $i = 1, 2, 3, \ldots, n$. Hence, a decision rule partitions the entire measurement space into n regions, D_i such that if any $\boldsymbol{K}$ lies in D_i, the sample belongs to class C_i. The boundaries between the regions are the decision boundaries (or surfaces) and the highest errors are usually in

observations close to these boundaries. To overcome classifications that may be ambiguous at these boundaries, the practitioner may choose to reject or withhold a decision. This option is known as the reject option and is simply another class. The goal of classification is to assign an unknown to a specific class using the decision boundaries developed from known samples (training). In this chapter, examples of the steps in classification are provided in the case study at the end of the chapter; we describe the algorithms to form decision boundaries next.

8.3.2 Bayes Classifier

Bayes classifier [89] is an elementary probabilistic method to obtain decision boundaries based on using Bayes' theorem. A decision rule based on probabilities is to assign $\boldsymbol{K}$ to class C_j if the probability of class C_j given the observation $\boldsymbol{K}$, $p(C_j|\boldsymbol{K})$ is greatest over all classes, i.e.,

$$p(C_j|\boldsymbol{K}) > p(C_i|\boldsymbol{K}), \qquad i = 1, 2, 3, \ldots, n, \quad i \neq j \tag{8.2}$$

The conditional probability of the observed $\boldsymbol{K}$ (a posteriori) in the validation set may be expressed in terms of the observed distributions of members of the training set as

$$p(C_i|\boldsymbol{K}) = \frac{p(\boldsymbol{K}|C_i)\, p(C_i)}{p(\boldsymbol{K})} \tag{8.3}$$

Hence, the decision rule can also be written as follows: If $p(\boldsymbol{K}|C_j)\, p(C_j) > p(\boldsymbol{K}|C_i)\, p(C_i)$, the sample whose spectral variables are given by $\boldsymbol{K}$ should be assigned to class C_j.

This is often termed the Bayes' rule for minimum error. An associated concept of likelihood ratio, l_{r}, to segment an observed profile into two classes (Fig. 8.4) is defined as follows:

$$l_{\mathrm{r}} = \frac{p(\boldsymbol{K}|C_1)}{p(\boldsymbol{K}|C_2)} > \frac{p(C_2)}{p(C_1)} \tag{8.4}$$

As can be seen from the equations, distribution of spectral profiles in each class and the distribution of the class itself are required. Hence, this technique is especially useful if we have a large training data set. The lack of rapid data acquisition in the past has precluded the use of this simple and fundamental method in Raman spectroscopy and its use is just emerging in IR spectroscopy. Estimation of the distributions of the training set may also be made using a likelihood estimator (e.g., Gaussian maximum likelihood approach is most common). A second interesting feature is that the procedure does not consider any relationship between the variables in $\boldsymbol{K}$. Thus, the powerful links between vibrational modes are utilized in a limited fashion. Last, this method explicitly grants probabilities of occurrence of different classes and this could be very useful in assessing the risk of being wrong or building more sophisticated cost models than minimum error discussed above.

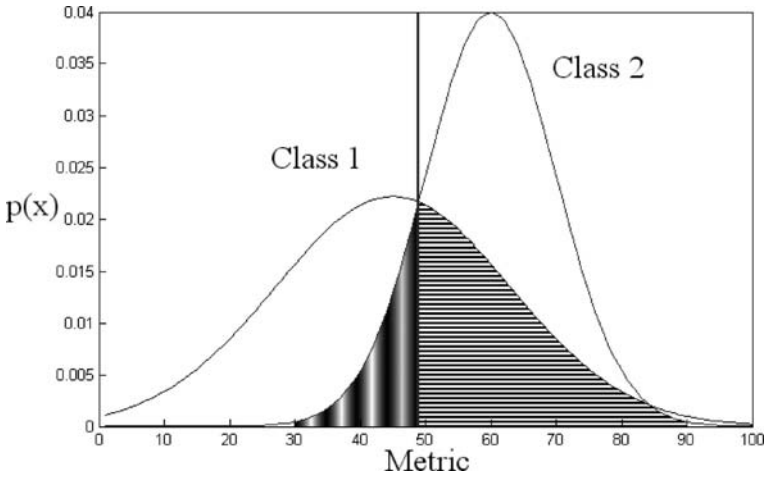

Fig. 8.4. A priori probability density functions (pdfs) of two classes and their resulting assignments after weighting them with their corresponding class probabilities. For a given feature value along the x-axis, the higher of the corresponding y-axis values decides the class for that value. Two types of errors are possible with this scheme, namely the misclassification of class 1 as class 2 (*horizontal stripes*) and the misclassification of class 2 as class 1 (*vertical stripes/shaded*). The colored regions indicate the relative probabilities of such errors. Errors can be explicitly understood and the contribution of each feature to classification can be quantitatively measured

8.3.3 Artificial Neural Networks (ANN)

Neural network methods [90] are among the most well-known nonlinear classification techniques. They involve a "layer" of input nodes and a layer of output nodes along with one or more "hidden" layers of elements called neurons (Fig. 8.5). Each neuron sums input from points in different layers and changes its output to these inputs in a nonlinear fashion. The major advantage of artificial neural network (ANN) methods is that they are general: they can handle problems with large numbers of parameters and classify objects well, even when distributions in the N-dimensional parameter space are very complex. ANNs are good at capturing information and recognizing patterns, especially in modeling human pattern observation and recognition capabilities (i.e., repetitive tasks). The nonlinear nature of the classifier makes it exceptionally powerful and there are few problems that the classifier will not address to high accuracy. ANNs have been extensively employed in Raman spectroscopy and imaging. Representative examples include bacterial identification [91, 92], histopathology of skin [93, 94] and vessels [95], aqueous humor glucose [96], plant materials [97], and for fundamental peak assignments [98].

A major criticism of ANNs is that features that were critical to decision making are not explicitly available. Consequently, it is difficult to determine

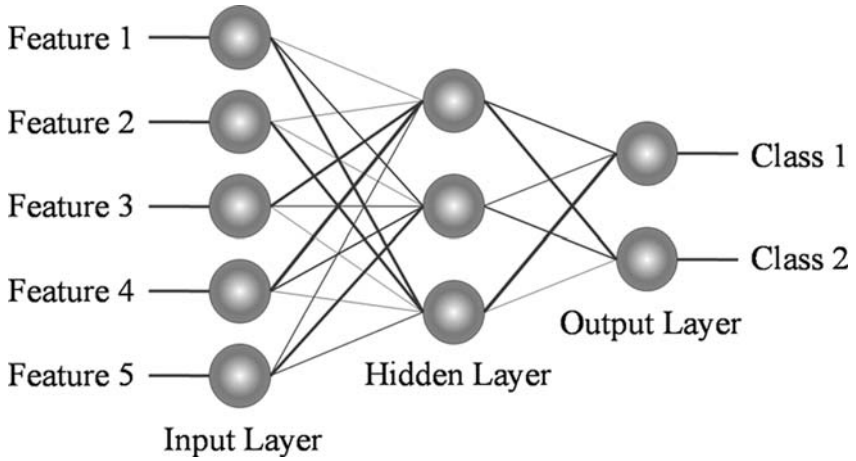

Fig. 8.5. Schematic diagram of neural network architecture. The hidden and output layer nodes perform nonlinear operations on their inputs. Some of the common nonlinear operations include computing hyperbolic tangents, step functions, and sigmoid functions. During training, features corresponding to different objects from the training set are presented as inputs and the (known) object class for each training object is forced to be the result of the output layer. The lines connecting different layers are associated weights. The process of learning (training) involves computing these weights using a set of fixed values at the input and output layers. During testing, features corresponding to an unknown object are presented at the input and the weights from training are used to propagate the inputs through the hidden layer all the way to the output. The output layer finally settles at a set of values corresponding to a final classification result

which spectral features are being used for classification and which are worthless. The classifier operates much like a "black box"; hence, their validation must be exceedingly rigorous. Another common problem is that of over- and under-training. Over-training, in which the training set is predicted well but the validation set is not because of modeling peculiarities or noise in the training set, is easily possible with the high dimensionality of data commonly encountered and appropriate dimensionality reduction much be implemented [99]. Hence, training results may be excellent but validation often falls short. On the other hand, if the network is not trained enough it is possible that the classification may not achieve its true potential. Unfortunately, there is no general optimal framework for choosing the amount of training required. The algorithms implementing ANNs usually involve an error-correction technique [100] to optimize the network. Consequently, there is a possibility of the optimization reaching only a local optimal point (minima) and it may not be easy to know if the solution is optimal. A practical disadvantage is that ANNs may be slow if they are too complicated, especially in the training phase but may also be slow in the application phase.

The ideas behind neural networks are essentially that of nonlinear transformations to provide segmentation. Other methods are based on similar ideas, including support vector machines (SVM) in which classification is accomplished by constructing a high-dimensional hyperplane that optimally separates the data into categories. SVM models can sometimes be related to neural networks, e.g., a sigmoid kernel function is equivalent to a two-layer, perceptron neural network. The method is illustrated in Fig. 8.6. The accuracy of SVM is largely determined by the selection of parameters to define the hyperplane. The simplest way to divide two groups is with a straight line, flat plane, or an N-dimensional hyperplane. If the points are separated by a nonlinear region, rather than fitting nonlinear curves to the data, SVM uses a kernel function to map the data into a space where a simple hyperplane can be used. For separation of more than two categories, one-against-all or one-against-one approaches may be used. SVMs are very powerful in that they can find generalized transformations but are susceptible to over-training, especially when the numbers of spectra are small compared to the dimensionality of the data. Classifications using Raman spectral data and SVM have been reported for bacteria in a set of studies reported by the Popp group [101–103], colon histopathology [104], and yeast classification [105]. SVM has

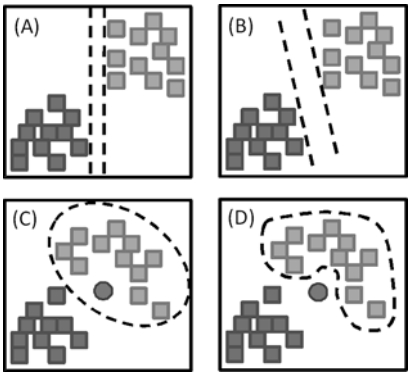

Fig. 8.6. A An example of a two-class system (denoted by *light and dark squares*) in which the data can be separated. SVM analysis is used to achieve a one-dimensional hyperplane (here, a line) that separates the data into two classes. The plane (here, line) is drawn such that separation is achieved by the segmentation line lying between the *two dashed lines*. **B** The second aspect is to increase the distance between the dashed lines by optimization (here, rotation angle) such that the distance between the hyperplane and the data points is highest. The distance between the dashed lines is called the margin. The vectors (points) that constrain the width of the margin are the support vectors. **C** Nonlinear kernels may be useful in segmenting complex distributions but there is some danger of over-fitting. The *circle at the center* in (**C**) and (**D**) becomes critical to definition of the kernel if it is encountered during training. One possible approach to minimize such errors is to build successively complex models and evaluate results

been compared to other techniques in at least two publications using Raman spectra. The key finding was that SVM was superior to other methods, especially when nonlinear temperature effects were observed [106].

8.3.4 Linear Discriminant Analysis (LDA)

Linear discriminant analysis (LDA) is also a probabilistic classifier in the mold of Bayes algorithms but can be related closely to both regression and PCA techniques. A discriminant function is simply a function of the observed vector of variables ($\boldsymbol{K}$) that leads to a classification rule. The likelihood ratio (above), for example, is an optimal discriminant for the two-class case. Hence, the classification rule can be stated as

$$h(\boldsymbol{K}) \begin{cases} > m \Rightarrow \boldsymbol{K} \in C_1 \\ < m \Rightarrow \boldsymbol{K} \in C_2 \end{cases} \tag{8.5}$$

where m is a constant. Discriminant functions are not unique as any monotonic function, g, can be found such that $g(\boldsymbol{K}) = f(h(\boldsymbol{K})) > m'$ becomes the new discriminant function. The primary distinction between the discriminant function approach and simple Bayes classifiers is that the form of the discriminant function is specified explicitly and is not imposed by the underlying distribution. The choice of discriminant function can be made either by using prior knowledge or by using a specific function whose parameters are adjusted by a training procedure. The linear discriminant function (in which g is a linear combination of $\boldsymbol{K}_i$) ranges from a least complex function that is clearly related to Bayes rule on one hand to a multi-parameter nonlinear functions that can resemble a multilayer perceptron. LDA is also similar to PCA in the sense of a transform, but it actively tries to separate data into classes. The linear discriminant analysis (LDA) is specified as

$$g(\boldsymbol{K}) = \boldsymbol{w}^{\mathrm{T}}\boldsymbol{K} + \boldsymbol{w}_0 \tag{8.6}$$

where $\boldsymbol{w}$ is the vector of weights and $\boldsymbol{w}_0$ a vector of thresholds. For the $\boldsymbol{S} \times \boldsymbol{K}$ matrix of known classes (from Fig. 8.1), the LDA process makes several simplifying assumptions, chiefly assumptions of normal distributions for the class densities and equal covariance matrices. Another variant is Fisher's discriminant analysis, which maximizes the distance between the means of the two classes while minimizing the variance within each class using a projection of the high-dimensional data (can also be termed, the signal-to-interference maximization).

The wide latitude available to the practitioner and its relative ease of implementation have made discriminant analysis and, especially, LDA a useful data analysis technique for spectroscopic data. Initial reports document carefully the steps and caveats in implementation [107] and substantial acceptance of the methodology exists in the spectroscopy community due to these early

successes. Discriminant analysis has been used to analyze Raman spectra extensively in histopathology by Stone et al. [108, 109], Hench et al. [110], and Puppels et al. [111, 112], in cervical [113], stomach [114] and colon tissue [115], in human serum [116] and tears [117], foodstuffs [118, 119], in atherosclerosis [120], for tissue engineering [121], animal models [122] of disease [123–125], cellular activity [126] and animal products [127, 128]. A major common threat in the applications is extensive pre-processing [129], a data reduction step (often PCA) and frequent use of an exploratory unsupervised step [130], as illustrated in [131]. A number of authors have presented augmented algorithms based on the LDA [132] and the application of these methods remains a focus area, especially in spectroscopic analysis of disease.

8.3.5 Nearest-Neighbor Classifier

A simple classifier is based on a nearest-neighbor approach (Fig. 8.7) [133]. In this method, the closest sample from the training set to the sample being classified is found using a scalar distance using the vector $\boldsymbol{K}$. The object being classified is assigned the same class as the class of the training object so found. Nearest-neighbor methods have the advantage that they are easy to implement. They provide remarkably accurate results if the features are chosen carefully (and if they are weighted carefully in the computation of the distance). Clearly, the similarity of vectors is based on the spectral feature subset that is considered. In the absence of other tools or for rapid analysis of data, nearest-neighbor methods are exceptionally useful. When representative spectra that are clearly distinct are encountered, these methods provide a useful classification protocol. For a small number of classes and small training sets, the methods work very well. A number of methods have been proposed to calculate the distance between spectra or clusters of spectra, including mean, median, and ensemble based to deal with noise and outliers.

There are also disadvantages of the nearest-neighbor methods. First, they (like neural networks) do not simplify the distribution of objects in parameter

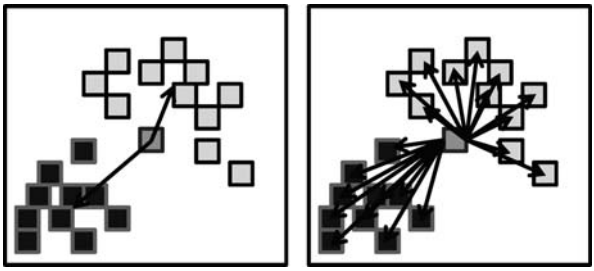

Fig. 8.7. Nearest-neighbor decisions involve the use of distance calculations between the vectors of an unknown (*gray point at the center*) and moments of training data (*left*) with labels (*black and light gray*) or more detailed calculations, for example, average distance to all points (*right*)

space to a comprehensible set of parameters. Instead, the training set is retained in its entirety as a description of the object distribution. Thinning methods can be used on the training set, but the result still does not usually constitute a compact description of the object distribution. The method is also rather slow if the training set has many examples. The most serious shortcoming of nearest-neighbor methods is that they are sensitive to the presence of irrelevant parameters. Adding parameters that have random values for all objects (so that it does not separate the classes) can cause these methods to fail. Outliers are not easy to analyze and errors are likely to occur at decision boundaries. Simple algorithms do not ensure optimality of classification. It could be especially useful as a starting point for further optimization based on better modeling of data. Simply put, it is "rough but quick" [134].

8.3.6 Decision Trees

Decision trees [135] can be used to identify and segment spectra when discriminating rules are known or desired (Fig. 8.8). A binary tree consists of nodes in which a single parameter is used as a discriminant. After a series of nodes are traversed, leaf nodes of the tree are encountered in which all the objects are labeled as belonging to a particular class. Decision trees can be axis parallel or oblique. Axis-parallel trees are called so because they correspond to

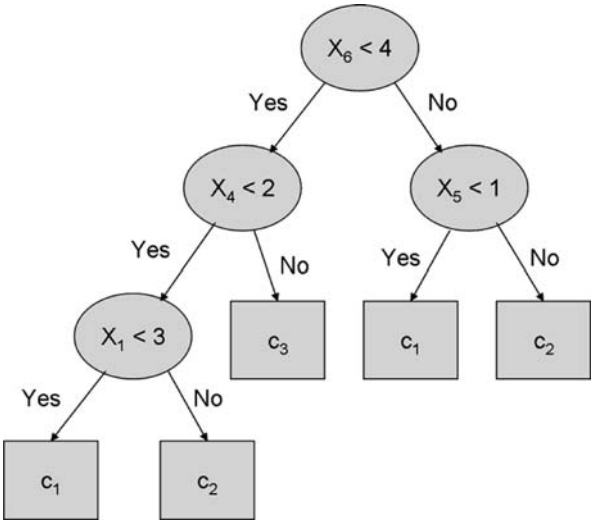

Fig. 8.8. Schematic of a simple decision tree in which the vector of conditions is used to partition data into one of the classes, c_i. The question at every node concerns a particular property or element of the input vector $\boldsymbol{X}$. Successive nodes are visited until a terminal or leaf node is reached where the object is finally classified. Note that different conditional questions can have different number of branches and also that many leaf nodes can have the same class

partitioning the parameter space with a set of hyperplanes that are parallel to all of the feature axes except for the one being tested. Oblique decision trees attempt to overcome the disadvantage of axis-parallel trees by allowing the hyperplanes at each node of the tree to have any orientation in parameter space. Axis-parallel decision trees are usually much faster in the construction (training) phase than neural network methods, and they also tend to be faster during the application phase. Their disadvantage is that they are not as flexible at modeling parameter space distributions having complex distributions as either neural networks or nearest-neighbor methods. Many steps may be required and axis-parallel trees tend to be rather elaborate, with many nodes, for realistic problems. Decision trees are especially useful when problems can be broken down into small segments, each of which is a simple decision. However, not all problems can be posed as those involving a binary tree. The use of decision trees in Raman spectroscopic analysis has been limited. While their use in parameter optimization has been reported [136], classification approaches have not really made use of either the learning or classification ability of these methods. Part of the reason is that they are computationally expensive if large numbers of nodes are used. Other limitations include the lack of interactions between nodes, essentially limiting the analysis to successive univariate comparisons. The transparency and clear dependence on spectral features, however, are important attributes that may help explain the rationale for decisions. Hierarchical organizations of decision trees or groups of trees (decision forests) [137] are likely to be useful tools in spectroscopy but are currently under-utilized.

8.3.7 Genetic Algorithms (GA)

Genetic algorithms [138] are adaptive (heuristic) search algorithm based on the evolutionary ideas of natural selection and genetics. The concept of GAs is designed to simulate processes in natural system necessary for evolution, specifically those that follow the principles of survival of the fittest. As such, they represent an intelligent exploitation of a random search within a defined search space to solve a problem. GAs involve four basic steps: initialization, selection, reproduction, and termination. The initialization step provides the starting point for exploration and is usually chosen randomly. In the selection stage, changes are made to the decision rules and in the reproduction stage, only those rules that improve classification are retained. This process is repeated until a predefined condition or until all the data points have been utilized in building the set of rules. These rules are later used in classification of unknown data. One benefit of GAs is that they can be implemented in parallel and can have large computational advantages, especially when a cluster of parallel processors are available. They are especially elegant if the problem naturally renders itself to a process of gradual change that could be tracked over time, perturbation, or space. A caveat in GAs is the need for careful estimation of each parameter of the algorithm. Some parameters

depend on the problem at hand and optimality of final result is not always guaranteed, but GA-based methods have been proposed to be superior to regression approaches [139]. In this sense, they are similar to ANNs. However, GAs give explicit information about important and unimportant features as feature selection is integrated into the method [140]. Goodacre et al. [141–144] have pioneered the use of GAs for spectroscopic analyses and their group and others have reported numerous applications [145, 146].

8.3.8 Unsupervised Learning

In unsupervised classification there is no explicit knowledge of the categories to which the data belong. The system forms clusters or natural groupings of input data. "Natural" here is defined explicitly or implicitly in the clustering system itself. It must be noted that, for a given data set and categories, different clustering algorithms could lead to different clusters. Hence, clustering is best used as a visualization and discovery tool whose results must be carefully examined and validated. In contrast to supervised methods in which an initial knowledge of the data is required, a secondary source of knowledge is required to validate results in unsupervised methods.

8.3.9 k-Means Clustering

k-Means clustering (Fig. 8.9) [147, 148] is one of the simplest unsupervised learning algorithms that aggregate the observed data into classes or clusters fixed a priori. The main idea is to define k centroids, one for each cluster, that act as aggregating markers for data. The next step is to take each data point and associate it with the nearest centroid. When no point is pending, the first step is completed and an early grouping is done. At this point we need to re-calculate k new centroids as barycenters of the clusters resulting from the previous step. After k new centroids, a new association is obtained between the same data set points and the nearest new centroid. As a result of this loop, k centroids change their location step by step until no further changes are observed. The data can now be understood in terms of centroids. k-Means is also a good exploratory tool when data form natural groups. It usually converges rapidly and is easy to implement. The number of classes (k) must be known or a reasonable guess must be possible to evaluate a small number of models. The initial points, however, can be very important to final outcome and may give rise to misleading clusters when there are no natural clusters. The choice of spectral information used is also critical and extensive preprocessing is often required, including dimensionality reduction. There is also the possibility of getting stuck in an infinite loop and implementations counter this possibility with a termination condition. Data would usually require a second examination before reaching conclusions. The ease of implementation and rapid application is especially suited to imaging applications in which classes can be easily visualized using different colors and unnatural clusters can

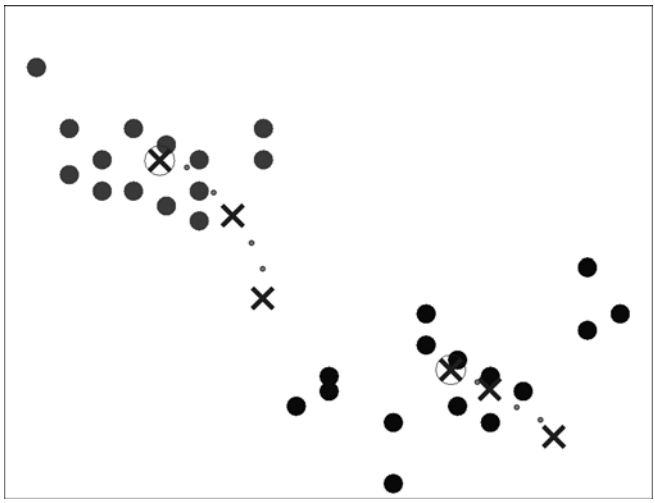

Fig. 8.9. Example of two-class k-means clustering. Only the first two dimensions are represented. After starting at random initial points, the centroids (marked by x) are re-calculated in every iteration along with the association of each data point with its nearest centroid. The iteration stops when there is no further change in centroid positions or associations

be readily observed. Hence, many Raman spectroscopic imaging applications have utilized k-means clustering for both preliminary and final visualization [149, 150].

8.3.10 Hierarchical Clustering Analysis (HCA)

Hierarchical clustering [151] does not involve the partitioning of data into clusters in a single step. Instead, a series of partitions or fusions take place such that a single cluster of M objects is successively organized into a different number of groups. The smallest group consists of each sample and the largest is the entire data set. Visualization of the data grouping can be accomplished at any intermediate step. Hierarchical clustering could broadly be divided into *agglomerative* methods and *divisive* methods. In agglomerative methods, every step involves the *fusion* of objects into successively smaller number of groups. We start from M groups of objects each belonging to a unique group and end when the entire data are in one group. Divisive methods involve the successive *separation* of objects into finer groupings at every stage. In this case, we start from a single group of M objects and end when each cluster contains a single object. The partitioning of fusion of groups is based on a measure of similarity (*distance*) of the objects to one another. In agglomerative hierarchical clustering, for example, at every step, we connect or fuse two clusters that have the smallest distance between them. The distance between the newly formed cluster and all the other clusters is computed

at every stage and the new fusion is chosen based on the new set of distances. By optimally choosing fusions at every stage, a unique tree of connections is obtained that is termed a dendrogram (Fig. 8.10). The major benefit of hierarchical organization is that groups can be visualized at different levels, no prior knowledge or estimate of the groups is needed and spectral features of each group can also be deduced. It is an excellent method for exploratory analysis and is highly recommended when a hypothesis needs to be developed for the set of observations. Hence, HCA is a very powerful method that has been used for visualizing spectral data in a variety of applications, including drugs [152] and human tissue [153]. Segmentation of bacterial and microbial material has proven to be exceptionally successful using this technique [154–158]. Its use in imaging [159] is especially attractive as clusters at various levels of detail show not only the natural chemical similarity in images but also provide an estimate of the heterogeneity. Combined HCA and conventional pattern recognition methods can be used to understand and develop robust protocols for data sets.

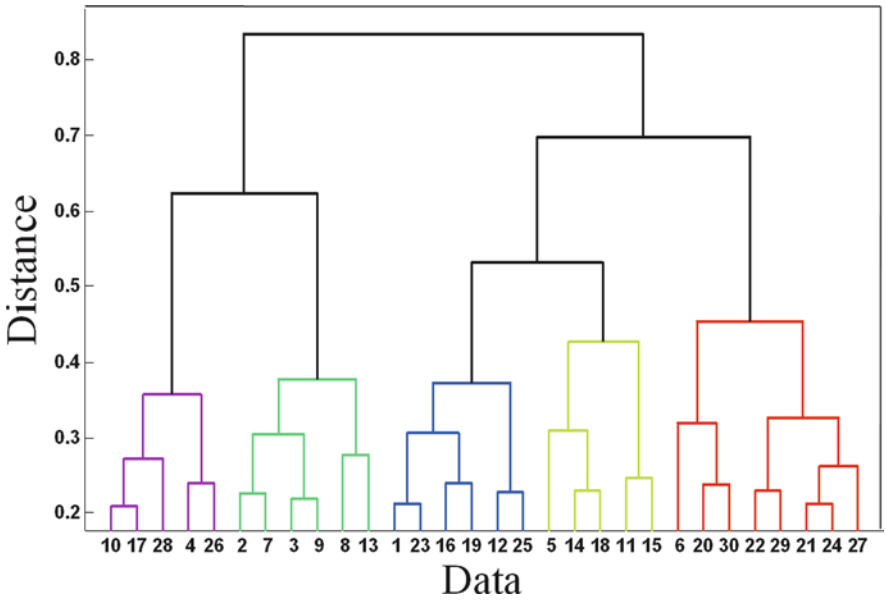

Fig. 8.10. Example of a dendrogram. The horizontal axis corresponds to data points (sample number) and the vertical axis shows (a measure of) distance between clusters. Points or clusters with the smallest distance between them (i.e., with a high degree of similarity) are merged first at the bottom, followed by clusters that are further apart as we move up the dendrogram. If necessary, the number of classes (5 here, for example) can be chosen by drawing an (imaginary) horizontal line at a chosen *distance* (0.5 here in the example) and assigning all vertical connecting lines as belonging to separate clusters

8.4 Data Representation and Result Visualization

Visualization of results, their statistical validity, and analysis of results are becoming increasingly important. Several techniques are available to represent data and compact representations are increasingly being made by images. The ease of visualization, however, must always be tempered with the need to present data completely and in an accurate manner. In particular, two areas are of relevant important. The first is two-dimensional spectral representation to better understand spectral structure while the second is more useful for imaging.

8.4.1 Two-Dimensional Correlation Analysis

Two-dimensional data analysis [160, 161] is a very powerful technique that examines correlated changes in spectra with changes in any other measurement of sample perturbation. The elegance of the method demonstrated in earlier studies has been extensively augmented by finer details on application and numerous examples. The primary advantage of two-dimensional correlation analysis lies in the extension of data examination "space" to a second domain. Subtle changes that may not be easily discernable in spectra and even weak spectral effects may be easily enhanced and understood in the context of molecular spectra [162].

8.4.2 Morphologic–Spectroscopic Data Representation

While correlations between clusters and groups of spectra can be easily visualized in the form of images, spectroscopic imaging data are becoming increasingly prevalent. Spectral–spatial associations are both easy to visualize and can be compactly represented in imaging format using a number of techniques for evaluating, representing, and enhancing images from spectroscopic imaging data [163].

8.5 Case Study: Classification of Prostate Tissue

In this section, we present the development of an automated protocol for prostate tissue histology [164] from infrared spectroscopic imaging data as an example of the techniques described (Fig. 8.11). The data is three dimensional with x–$y-$axes representing the image plane and the z-axis representing the spectral dimension. After data acquisition, two important pre-processing steps, namely baseline correction and de-noising, are performed. Since the entire data set is derived from human tissue samples, the spectra have similar characteristics and, therefore, a manually chosen set of pre-defined wave number could be used as the reference points for baseline correction. It is

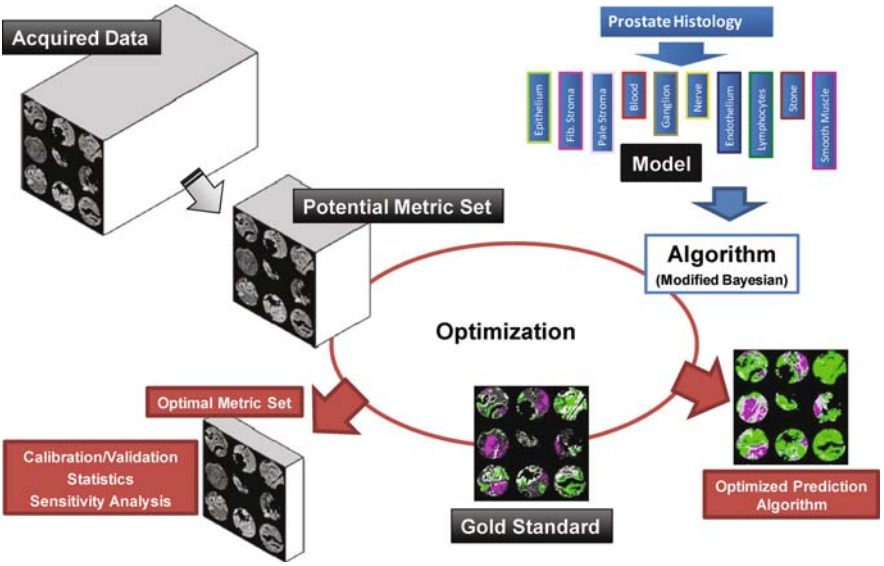

Fig. 8.11. The classifier development process. Clinical knowledge provides us with a set of classes for supervised classification (*top, right*). Large numbers of spectra from large sample numbers are reduced to a set of potentially useful features (*top, left*) or metrics. A modified Bayesian algorithm operates on the metrics to provide predictions that are compared to a gold standard. The end result of the training and validation process is an optimized algorithm, metric set, calibration and validation statistics, and sensitivity analysis of the data

important to ensure that all spectra are subjected to the same procedure and that the same reference points are used in all cases. De-noising is performed by computation of minimum noise fraction (MNF) transform, selection of a subset of eigenimages corresponding to low-noise data followed by an inverse MNF transformation [165]. Feature selection for dimensionality reduction is then carried out. Here, feature selection in prostate tissues is guided by our knowledge of biologically significant spectral characteristics reported in literature as well as through empirical observations. Newer methods have used model molecular biology experiments to inform the selection process. We term potentially significant features of the data as "metrics." These features may be spatial, spectral, or reflective of both. Spectral metrics could include spectral peak heights, center of gravity of peaks, area under a peak, ratios of two peaks, and position of peaks as determined by an expert spectroscopist. Spatial metrics could include the diameter of features, regularity of acinar structures, or geometrical patterns. Combination features could be extraction of basal-to-apical ratio using spectral features. It should be noted that defining a large number of metrics (i.e., defining a few more metrics than necessary) is not a problem and it is not necessary for us to know the significance of

every metric that is defined. Using the correct classification procedure would prevent over-fitting later.

Defining metrics achieves two important goals. First, relevant information is retained in a small number of measures relative to the number of points in a spectrum (dimensionality reduction). Second, information captured by metrics is spectroscopically/morphologically significant and, therefore, provides a framework to interpret results of subsequent classifications. Choosing metrics with this prior scientific knowledge allows for maximal leveraging of our knowledge base. At the same time, however, it does not preclude discovery of new features as those could easily be included and determined to be significant or not. Many of the classification techniques are based on linear transformations and metrics are a very good way of including spectroscopically significant nonlinear information (ratios of peaks, center of gravity of peaks, peak positions, etc.) that is otherwise difficult to incorporate. While it may appear that the superset of metrics is better attained via computer algorithms, we argue that the same algorithms are actually written by expert spectroscopists. Hence, the manual nature of examination proposed here has all the benefits of detecting features. It is variable, however, depending on the practitioner. Hence, thorough and meticulous efforts must be undertaken – which are time consuming. As an example, metrics for the prostate study reported here were developed over the period of a year.

After pre-processing, the various tissue classes in the data are identified by comparing it with a gold standard (hematoxylin and eosin-stained tissue analyzed by an expert pathologist). Regions corresponding to different classes are marked and spectral data are extracted from these regions. The entire data set consists of two independent parts, namely the *training* set and the *testing* set. The training set is used to extract information and learn characteristics of the metric data as it relates to the pre-defined classes. The testing set is used to quantify the accuracy of the classifier and provides the platform for validation. Among the various classification techniques that could be used, a Bayesian classifier was selected because of the comprehensive nature of available data and histologic categories or classes that are defined by clinical practice. Since the number of data points that we have is large (>1 million), estimating pdfs of different classes become facile. Therefore a Bayesian classifier is a good choice.

The results demonstrate a high degree of correlation between the gold standard and predicted data (Fig. 8.12). Evaluation of the quality of prediction can be performed by examining the images or, more rigorously, using receiver operating curve (ROC) analysis. The last step is to verify that the accuracy obtained is sufficient for use in the clinic. It could be argued that choosing the correct metrics is more important than the *specific* classification technique used. If the metrics have inherent differences (high variance and high separability), the use of different classification techniques would bring out these differences; however, no classification algorithm would work for a

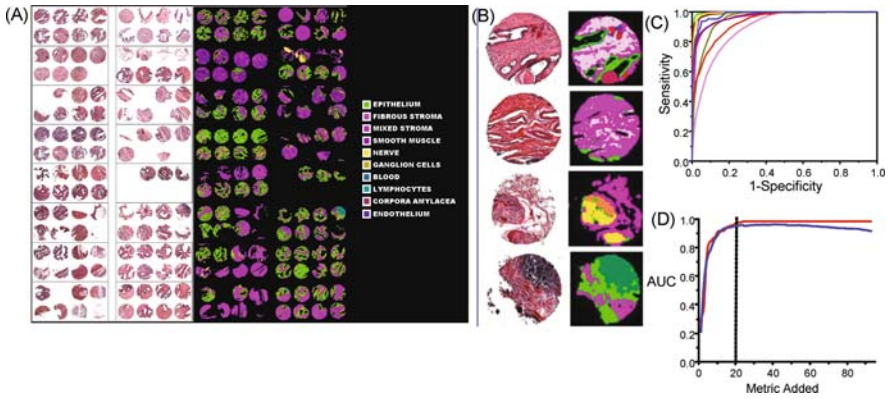

Fig. 8.12. **A** Conventional H&E stained images and their classified counterpart (*right*) can be compared pixel by pixel for accuracy. **B** Selected regions showing correspondence between H&E and class images. **C** Accuracy is best assessed by ROC curves shown for individual classes with colors as per legend in (**A**). **D** The number of spectral features and classification accuracy for training data (*red*) and validation data (*blue*) show that high accuracy is possible. The effects of over-training with a feature set larger than ∼45 can be seen

broad range of data if there are no inherent differences in the spectral metrics that are chosen. As an example, we have demonstrated equal classification accuracy using GA [166]. After a protocol is developed the metrics are available for interpretation. Based on the selection of parameters, the algorithm is now fully automated.

8.6 Conclusion

Multivariate techniques are very powerful in extracting information both amenable and hidden from human examination. Appropriate understanding of the system can provide excellent results with a single univariate analysis as with more complicated multivariate schemes [167]. In our experience, classification techniques for vibrational spectroscopy often provide the same accuracy in prediction due to the richness of the spectral data [168], especially when large numbers of measurements are available. Data pre-processing is critical and may influence the evaluation of one type of protocol against another [169] and the use of modified experimental conditions has been suggested in other examples to improve results [170]. Given the large dimensionality of the data and, often, large data sets, integrated feature selection [171, 172] becomes very critical. The specific classification technique used is largely dictated by the quantity and known characteristics of the data as well as the desired level of insight into the classification process. A major influence, further, is the selection of features to include in the process. Hence, we have strongly

emphasized the pre-processing portion of this chapter. We are (somewhat biased) of the view that a biochemical understanding of the problem should be both the starting point and ultimate validation of chemometric methods. Hence, optimal feature selection must include some element of prior knowledge and part of objective evaluation. In summary, the science must be integrated with the strategy for data processing, classification, and analysis of results for a synergistic combination of spectroscopy and chemometrics.

References

1. M.J. Pelletier, Appl. Spectrosc. **57**(1), 20A–42A (2003)
2. R. Kramer, *Chemometric Techniques for Quantitative Analysis* (Marcel Dekker, New York, 1998)
3. D.M. Haaland, E.V. Thomas, Anal. Chem. **60**(11), 1193–1202 (1988) and 1202–1208 (1998)
4. A. De Juan, R. Tauler, Anal. Chim. Acta **500**(1–2), 195–210 (2003)
5. J.J. Andrew, T.M. Hancewicz, Appl. Spectrosc. **52** (6), 797–807 (1998)
6. P. Geladi, Spectrochim. Acta B **58**(5), 767 –782 (2003)
7. B.R. Kowalski, *Chemometrics: Theory and Applications* (ACS, Washington DC, 1977)
8. M.A. Sharaf, D.L. Illman, B.R. Kowalski, *Chemometrics* (Wiley, New York, 1986)
9. R. Kramer, *Chemometric Techniques for Quantitative Analysis* (Marcel Dekker, New York, 1998)
10. R.G. Brereton, *Applied Chemometrics for Scientists* (Wiley , New York, 2007)
11. S.J. Haswell, *Practical Guide to Chemometrics* (Marcel Dekker, New York, 1992)
12. P. Gemperline, Taylor, Francis, *Practical Guide to Chemometrics*, 2nd edn. (CRC Press, Boca Raton, 2006)
13. B. Lavine, J. Workman, Anal. Chem. **80**(12), 4519–4531 (2008)
14. N.K. Afseth, V.H. Segtnan, J.P. Wold, Appl. Spectrosc. **60** (12), 1358–1367 (2006)
15. P. Heraud, B.R. Wood, J. Beardall, D. McNaughton, J. Chemometr. **20**(5), 193–197 (2006)
16. A. Jirasek, G. Schulze, M.M.L. Yu, M.W. Blades, R.F.B. Turner, Appl. Spectrosc. **58**(12), 1488–1499 (2004)
17. M.N. Leger, A.G. Ryder, Appl. Spectrosc. **60**(2), 182–193 (2006)
18. C.A. Lieber, A. Mahadevan-Jansen, Appl. Spectrosc. **57**(11), 1363–1367 (2003)
19. A. O'Grady, A.C. Dennis, D. Denvir, J.J. McGarvey, S.E.J. Bell, Anal. Chem. **73**(9), 2058–2065 (2001)
20. M. Fujiwara, H. Hamaguchi, M. Tasumi, Appl. Spectrosc. **40**(2), 137–139 (1986)
21. T. Hirschfeld, B. Chase, Appl. Spectrosc. **40**(2), 133–137 (1986)
22. D.B. Chase, J. Am. Chem. Soc. **108**(24), 7485–7488 (1986)
23. D.N. Waters, Appl. Spectrosc. **41**(4), 539–709 (1987)
24. S. Fendel, R. Freis, B. Schrader, J. Mol. Struct. **410–411**, 531–534 (1997)
25. P.P. Yaney, J. Opt. Soc. Am. **62**(11), 1297–1303 (1972)

26. S.-Y. Lee, D. Zhang, D.W. McCamant, P. Kukura, R.A. Mathies, J. Chem. Phys. **121**(8), 3632–3642 (2004)
27. D.W. McCamant, P. Kukura, R.A. Mathies, Appl. Spectrosc. **57**(11), 1317–1323 (2003)
28. A.P. Shreve, N.J. Cherepy, R.A. Mathies, Appl. Spectrosc. **46**, 707–711 (1992)
29. P. Matousek, M. Towrie, A.W. Parker, J. Raman Spectrosc. **33**(4), 238–242 (2002)
30. S.H. Mosier-Boss, S.H. Lieberman, R. Newbery, Appl. Spectrosc. **49**, 630–638 (1995)
31. W. Hill, D. Rogalla, Anal. Chem. **64**(21), 2575–2579 (1992)
32. R. Bhargava, I.W. Levin, Anal. Chem. **74**, 1429–1435 (2002)
33. C.J. Behrend, C.P. Tarnowski, M.D. Morris, Appl. Spectrosc. **56**(11), 1458–1461 (2002)
34. H.Takeuchi, S. Hashimoto, I. Harada, Appl. Spectrosc. **47**, 129 (1993)
35. D. Zhang, K.N. Jallad, D. Ben-Amotz, Appl. Spectrosc. **55**(11), 1523–1531 (2001) and D. Zhang, D. Ben-Amotz, Appl. Spectrosc. **56**(1), 91–98 (2002)
36. Y. Katsumoto, Y. Ozaki, Appl. Spectrosc. **57**(3), 317–322 (2003)
37. H.G. Schulze, L.S. Greek, C.J. Barbosa, M.W. Blades, R.F.B. Turner, Appl. Spectrosc. **52**(4), 621–625 (1998)
38. C. Craggs, K.P. Galloway, D.J. Gardiner, Appl. Spectrosc. **50**(1), 43–47 (1996)
39. M. Lang, H. Guo, J.E. Odegard, C.S. Burrus, R.O. Wells Jr., IEEE Signal Process. Lett. **3**(1), 10–12 (1996)
40. S. Sâsîć, D.A. Clark, J.C. Mitchell, M.J. Snowden, Analyst **129**(11), 1001–1007 (2004)
41. A.A. Green, M. Berman, P. Switzer, M. Craig, IEEE Trans. Geosci. Remote Sens. **26**, 65–74 (1988)
42. J. B. Lee, A. S. Woodyatt, M. Berman, IEEE Trans. Geosci. Remote Sens. **28**, 295–304 (1990)
43. R. Bhargava, S. Wang, J.L. Koenig, Appl. Spectrosc. **54**, 486–495 (2000)
44. M.J. Wabomba, Y. Sulub, G.W. Small, Appl. Spectrosc. **61**, 349–358 (2007)
45. R. Bhargava, S. Wang, J.L. Koenig, Appl. Spectrosc. **54**, 1690–1706 (2000)
46. J.Boardman, F. Kruse, Proc. ERIM Tenth Thematic Conf. Geological Remote Sensing (1994), pp. 407–418
47. H.G. Schulze, M.M.L. Yu, C.J. Addison, M.W. Blades, R.F.B. Turner, Appl. Spectrosc. **60**(7), 820 (2006)
48. L. Duponchela, P. Milanfarb, C. Ruckebuscha, J.P. Huvennea, Anal. Chim. Acta **607**(2), 168–175 (2008)
49. C.A. Hayden, M.D. Morris, Appl. Spectrosc. **50**(6), 708–714 (1996)
50. G.H. Dunteman, *Principal Components Analysis (Quantitative Applications in the Social Sciences)* (SAGE publications, Newbury park, 1989)
51. M.A. Kramer, AIChE J. **37**(2), 233–243 (1991)
52. P.J. De Groot, G.J. Postma, W.J. Melssen, L.M.C. Buydens, V. Deckert, R. Zenobi, Anal. Chim. Acta **446**(1–2), 71–83 (2001)
53. I.H. McColl, E.W. Blanch, A.C. Gill, A.G.O. Rhie, M.A. Ritchie, L. Hecht, K. Nielsen, L.D. Barron, J. Am. Chem. Soc. **125**(33), 10019–10026 (2003)
54. G. Deinum, D. Rodriguez, T.J. Römer, M. Fitzmaurice, J.R. Kramer, M.S. Feld, Appl. Spectrosc. **53**(8), 938–942 (1999)

55. M. Shimoyama, H. Maeda, K. Matsukawa, H. Inoue, T. Ninomiya, Y. Ozaki, Vib. Spectrosc. **14**(2), 253–259 (1997)
56. I.P. Keen, G.W. White, P.M. Fredericks, J. Forensic Sci. **43**(1), 82–89 (1998)
57. A.G. Ryder, J. Forensic Sci. **47**(2), 275–284 (2002)
58. C. Krafft, T. Knetschke, A. Siegner, R.H.W. Funk, R. Salzer, Vib. Spectrosc. **32**(1 SPEC.), 75–83 (2003)
59. J.W. Chan, D.S. Taylor, T. Zwerdling, S.M. Lane, K. Ihara, T. Huser, Biophys. J. **90**(2), 648–656 (2006)
60. C.M. Krishna, G. Kegelaer, I. Adt, S. Rubin, V.B. Kartha, M. Manfait, G.D. Sockalingum, Biopolymers **82**(5), 462–470 (2006)
61. I. Notingher, I. Bisson, A.E. Bishop, W.L. Randle, J.M.P. Polak, L.L. Hench, Anal. Chem. **76**(11), 3185–3193 (2004)
62. W.F. Pearman, A.W. Fountain III, Appl. Spectrosc. **60**(4), 356–365 (2006)
63. M. Veij, P. Vandenabeele, K.A. Hall, F.M. Fernandez, M.D. Green, N.J. White, A.M. Dondorp, P.N. Newton, L. Moens, J. Raman Spectrosc. **38**(2), 181 – 187 (2007)
64. A. Mahadevan-Jansen, M.F. Mitchell, N. Ramanujam, A. Malpica, S. Thomsen, U. Utzinger, R. Richards-Kortum, Photochem. Photobiol. **68**(1), 123–132 (1998)
65. R.M. Jarvis, A. Brooker, R. Goodacre, Faraday Discuss. **132**, 281–292 (2006)
66. F. Estienne, D.L. Massart, Anal Chim. Acta **450**(1–2), 123–129 (2001)
67. S. Wold, A. Ruhe, H. Wold, W.J. Dunn, SIAM J. Sci. Comput. **5**(3), 735–743 (1984)
68. P. Geladi, B.R. Kowalski, Anal. Chim. Acta, **185**(C), 1–17 (1986)
69. S. De Jong, Chemom. Intell. Lab. Syst. **18**(3), 251–253 (1993)
70. U. Kruger, Y. Zhou, X. Wang, D. Rooney, J. Thompson, J. Chemometr. **22**(1), 1–13 (2008)
71. There are several instances of, for example, newer algorithms (S.J. Qin, Comput. Chem. Eng. **22**(4–5), 503–514 (1998)) and comparisons of robustness (G.R. Phillips, E.M. Eyring, Anal. Chem. **55**(7), 1134–1138 (1983), I.S. Helland, Scand. J. Stat. **17**(2), 97–114 (1990)) among others.
72. P. Geladi, J. Chemometr. **2**(4), 231–246 (1988)
73. W.-C. Shih, K.L. Bechtel, M.S. Feld, Anal. Chem. **79**(1), 234–239 (2007)
74. K. Kachrimanis, D.E. Braun, U.J. Griesser, J. Pharm. Biomed. Anal. **43**(2), 407–412 (2007)
75. L. Zhang, M.J. Henson, S.S. Sekulic, Anal. Chim. Acta **545**(2), 262–278 (2005)
76. J.R. Beattie, S.E.J. Bell, C. Borggaard, A.M. Fearon, B.W. Moss, Lipids **42**(7), 679–685 (2007)
77. B.K. Alsberg, A.M. Woodward, D.B. Kell, An introduction to wavelet transforms for chemometricians: A time- frequency approach. Chemometr. Intell. Lab. Syst. **37**(2), 215–239 (1997). doi: 10.1016/S0169-7439(97)00029-4
78. U. Depczynski, K. Jetter, K. Molt, A. Niemöller, Chemometr. Intell. Lab. Syst. **39**(1), 19–27 (1997)
79. U. Depczynski, K. Jetter, K. Molt, A. Niemöller, Chemometr. Intell. Lab. Syst. **49**(2), 151–161 (1999)
80. F. Ehrentreich, L. Summchen, Anal. Chem. **73**(17), 4364–4373 (2001)
81. Y.-P. Wang, Y. Wang, P. Spencer, Appl. Spectrosc. **60**(7), 826–832 (2006)

82. B. Walczak, D.L. Massart, Chemometr. Intell. Lab. Syst. **36**(2), 81–94 (1997)
83. A.K.-M. Leung, F.-T. Chau, J.-B. Gao, A review on applications of wavelet transform techniques in chemical analysis: 1989–1997. Chemometr. Intell. Lab. Syst. **43**(1–2), 165–184 (1998). doi: 10.1016/S0169-7439(98)00080-X
84. B.R. Bakshi, J. Chemometr. **13**(3–4), 415–434 (1999)
85. S.C. Yusta, Different metaheuristic strategies to solve the feature selection problem. Pattern Recognit. Lett. **30**(5), 525–534 (2009)
86. A. Perera, T. Yamanaka, A. Gutieérrez-Gaélvez, B. Raman, R. Gutieérrez-Osuna, Sens. Actuators, B **116**(1–2), 17–22 (2006)
87. G. Srinivasan, R. Bhargava, Spectroscopy **22**, 40–51 (2007)
88. A.R. Webb, in *Statistical Pattern Recognition* (Wiley , Chichester, 2002)
89. J.O. Berger, *Statistical Decision Theory and Bayesian Analysis,* 2nd edn. (Springer-Verlag, New York, 1985)
90. R.O. Duda, P.E. Hart, D.G. Stork, *Pattern Classification.* 2nd edn. (Wiley, New York, 2001), p. 282–347
91. R. Goodacre, E.M. Timmins, R. Burton, N. Kaderbhai, A.M. Woodward, D.B. Kell, P.J. Rooney, Microbiology **144**(5), 1157–1170 (1998)
92. K. Maquelin, C. Kirschner, L.-P. Choo-Smith, N.A. Ngo-Thi, T. Van Vreeswijk, M. Stämmler, H.P. Endtz, H.A. Bruining, D. Naumann, G.J. Puppels, J. Clin. Microbiol. **41**(1), 324–329 (2003)
93. S. Sigurdsson, P.A. Philipsen, L.K. Hansen, J. Larsen, M. Gniadecka, H. Christian Wulf, IEEE Trans. Biomed. Eng. **51**(10), 1784–1793 (2004)
94. M. Gniadecka, P.A. Philipsen, S. Sigurdsson, et al., J. Invest. Dermatol. **122**(2), 443–449 (2004)
95. A.R. De Paula Jr., S. Sathaiah, Med. Eng. Phys. **27**(3), 237–244 (2005)
96. M.S. Borchert, M.C. Storrie-Lombardi, J.L. Lambert, Diabetes Technol. Ther. **1**(2), 145–151 (1999)
97. I.R. Lewis, N.W. Daniel Jr., N.C. Chaffin, P.R. Griffiths, Spectrochim. Acta A **50**(11), 1943–1958 (1994)
98. K. Judge, C.W. Brown, L. Hamel, Appl. Spectrosc. **62**(11), 1221–1225 (2008)
99. M. Defernez, E.K. Kemsley, Analyst **124**(11), 1675–1681 (1999)
100. B. Widrow, M.A. Lehr. Proc. IEEE **78**(9), 1415–1442 (1990)
101. P. Rösch, M. Harz, M. Schmitt, K.D. Peschke, O. Ronneberger, H. Burkhardt, H.W. Motzkus, M. Lankers, S. Hofer, H. Thiele, J. Popp, Appl. Environ. Microbiol. **71**(3), 1626–37 (2005)
102. M. Krause, P. Rösch, B. Radt, J. Popp, Anal. Chem. **80**(22), 8568–8575 (2008)
103. M. Harz, P. Rösch, K.-D. Peschke, O. Ronneberger, H. Burkhardt, J. Popp, Analyst **130**(11), 1543–1550 (2005)
104. E. Widjaja, W. Zheng, Z. Huang, Int. J. Oncol. **32**(3), 653–662 (2008)
105. P. Rösch, M. Harz, K.-D. Peschke, O. Ronneberger, H. Burkhardt, J. Popp, Biopolymers **82**(4), 312–316 (2006)
106. U. Thissen, M. Pepers, B. Uštün, W.J. Melssen, L.M.C. Buydens, Chemometr. Intell. Lab. Syst. **73**(2), 169–179 (2004)
107. T.C. Bakker Schut, R. Wolthuis, P.J. Caspers, G.J. Puppels, J. Raman Spectrosc. **33**(7), 580–585 (2002)
108. N. Stone, C. Kendall, N. Shepherd, P. Crow, H. Barr, J. Raman Spectrosc. **33**(7), 564–573 (2002)

109. P. Crow, B. Barrass, C. Kendall, M. Hart-Prieto, M. Wright, R. Persad, N. Stone, Brit. J. Cancer **92** (12), 2166–2170 (2005)
110. I. Notingher, G. Jell, P.L. Notingher, I. Bisson, O. Tsigkou, J.M. Polak, M.M. Stevens, L.L. Hench, J. Mol. Struct. **744–747**(SPEC. ISS.), 179–185 (2005)
111. S. Koljenovicé, L.-P. Choo-Smith, T.C.B. Schut, J.M. Kros, H.J. Van den Berge, G.J. Puppels, Lab. Invest. **82**(10), 1265–1277 (2002)
112. A. Nijssen, K. Maquelin, L.F. Santos, P.J. Caspers, T.C. Bakker Schut, J.C. den Hollander, M.H.A. Neumann, G.J. Puppels, Discriminating basal cell carcinoma from perilesional skin using high wave-number Raman spectroscopy, J. Biomed. Opt. **12**(3), article number 034004, 1–7 (May/June 2007)
113. F.M. Lyng, E.Ó Faoláin, J. Conroy, A.D. Meade, P. Knief, B. Duffy, M.B. Hunter, J.M. Byrne, P. Kelehan, H.J. Byrne, Exp. Mol. Pathol. **82**(2), 121–129 (2007)
114. S.K. Teh, W. Zheng, K.Y. Ho, M. Teh, K.G. Yeoh, Z. Huang, Br. J. Cancer **98**(2), 457–465 (2008)
115. A. Molckovsky, L.-M. Wong Kee Song, M.G. Shim, N.E. Marcon, B.C. Wilson, Gastrointest. Endosc. **57**(3), 396–402 (2003)
116. J.L. Pichardo-Molina, C. Frausto-Reyes, O. Barbosa-Garciéa, R. Huerta-Franco, J.L. Gonzaélez-Trujillo, C.A. Ramiérez-Alvarado, G. Gutieérrez-Juaérez, C. Medina-Gutieérrez, Laser. Med. Sci. **22**(4), 229–236 (2007)
117. J.M. Reyes-Goddard, N. Barr, H., Stone, Photodiagn. Photodyn. Ther. **5**(1), 42–49 (2008)
118. M.M. Paradkar, J. Irudayaraj, Food Chem. **76**(2), 231–239 (2002)
119. V. Baeten, P. Hourant, M.T. Morales, R. Aparicio, J. Agr. Food Chem. **46**(7), 2638–2646 (1998)
120. L. Silveira Jr., S. Sathaiah, R.A. Zngaro, M.T.T. Pacheco, M.C. Chavantes, C.A.G. Pasqualucci, Laser. Surg. Med. **30**(4), 290–297 (2002)
121. I. Notingher, G. Jell, U. Lohbauer, V. Salih, L.L. Hench, J. Cell. Biochem. **92**(6), 1180–1192 (2004)
122. C. Medina-Gutieérrez, C. Frausto-Reyes, J.L. Quintanar-Stephano, R. Sato-Berrué, Spectrochim. Acta, Part A **60**(10), 2269–2274 (2004)
123. J. G. Thakur, H. Dai, G. K. Serhatkulu, R. Naik, V. M. Naik, A. Cao, A. Pandya, G. W. Auner, R. Rabah, M. D. Klein, C. J. Freeman, Raman Spectrosc. **38**, 127–134 (2007)
124. R.E. Kast, G.K. Serhatkulu, A. Cao, A.K. Pandya, H. Dai, J.S. Thakur, V.M. Naik, R. Naik, M.D. Klein, G.W. Auner, Biopolymers **89**(3), 235 (2008)
125. K. Pandya, G. Serhatkulu, A. Cao, R. Kast, H. Dai, R. Rabah, J. Poulik, S. Banerjee, R. Naik, V. Adsay, G. Auner, M. Klein, J. Thakur, F. Sarkar, Pancreas **36**(2), e1–e8 (2008)
126. M.F. Escoriza, J.M. Vanbriesen, S. Stewart, J. Maier, Appl. Spectrosc. **61**(8), 812–823 (2007)
127. R.H. Brody, H.G.M. Edwards, A.M. Pollard, Anal. Chim. Acta **427**(2), 223–232 (2001)
128. H.G.M. Edwards, N.F. Nik Hassan, N. Arya, J. Raman Spectrosc. **37**(1–3), 353–360 (2006)
129. K. De Gussem, P. Vandenabeele, A. Verbeken, L. Moens, Anal. Bioanal. Chem. **387**(8), 2823–2832 (2007)
130. A. Taleb, J. Diamond, J.J. McGarvey, J.R. Beattie, C. Toland, P.W. Hamilton, J. Phys. Chem. B **110**(39), 19625–19631 (2006)

131. P. Vandenabeele, L. Moens, Analyst **128**(2), 187–193 (2003)
132. C.A. Lieber, S.K. Majumder, D. Billheimer, D.L. Ellis, A. Mahadevan-Jansen, J. Biomed. Opt. **13**(2), 024013 (2008)
133. Y. Cheng, IEEE Trans. Pattern Anal. Mach. Intell. **17**(8), 790–799 (1995)
134. T. Kanungo, D.M. Mount, N.S. Netanyahu, C.D. Piatko, R. Silverman, A.Y. Wu, IEEE Trans. Pattern Anal. Mach. Intell. **24**(7), 881–892 (2002)
135. J.R. Quinlan, Mach. Learn. **1**, 81–106 (1986)
136. S.-J. Baek, A. Park, S. Kang, Y. Won, J.Y. Kim, S.Y. Na, Lect. Notes Comput. Sci. (Part 2) **4492**, 1240–1247 (2007)
137. T.K. Ho, IEEE Trans. Pattern Anal. Mach. Intell. **20**(8), 832–844 (1998)
138. M. Mitchell, *An Introduction to Genetic Algorithms* (Bradford Books, Cambridge, 1999)
139. M.H. Hennessy, A.M. Kelley, Phys. Chem. Chem. Phys. **6**(6), 1085–1095 (2004)
140. D. Broadhurst, R. Goodacre, A. Jones, J.J. Rowland, D.B. Kell, Anal. Chim. Acta 348 (1–3), 71–86 (1997)
141. R.M. Jarvis, R. Goodacre, Bioinformatics **21**(7), 860–868 (2005)
142. R. Goodacre, Vib. Spectrosc. **32**(1 SPEC.), 33–45 (2003)
143. D.I. Ellis, R. Goodacre, Analyst **131**(8), 875–885 (2006)
144. D.I. Ellis, W.B. Dunn, J.L. Griffin, J.W. Allwood, R. Goodacre, Pharmacogenomics **8**(9), 1243–1266 (2007)
145. B.K. Lavine, C.E. Davidson, A.J. Moores, P.R. Griffiths, Appl. Spectrosc. **55**(8), 960–966 (2001)
146. E. Seli, D. Sakkas, R. Scott, S.C. Kwok, S.M. Rosendahl, D.H. Burns, Fertil.Steril. **88**(5), 1350–1357 (2007)
147. S.Z. Selim, M.A. Ismail, IEEE Trans. Pattern Anal. Mach. Intell. PAMI-**6**(1), 81–87 (1984)
148. A.K. Jain, R.C. Dubes, *Algorithms for Clustering Data* (Prentice Hall, New Jersey, 1988), p. 356
149. S. Koljenovicé, T.C. Bakker Schut, J.P. van Meerbeeck, A.P.W.M. Maat, S.A. Burgers, P.E. Zondervan, J.M. Kros, G.J. Puppels, J. Biomed. Opt. **9**(6), 1187–1197 (2004)
150. S.T. Nandagawali, J.S. Yerramshetty, O. Akkus, J. Biomed Mater. Res. A **82**(3), 611–617 (2007)
151. R. Xu, D. Wunsch, *Clustering* (IEEE Press Series on Computational Intelligence, Wiley, 2009)
152. M. de Veij, A. Deneckere, P. Vandenabeele, D. de Kaste, L. Moens, J. Pharm. Biomed. Anal. **46**(2), 303–309 (2008)
153. L. Chrit, C. Hadjur, S. Morel, G. Sockalingum, G. Lebourdon, F. Leroy, M. Manfait, J. Biomed. Opt. **10**(4), article number 044007, 1–11(July/August 2003)
154. P. Lasch, J. Kneipp, *Biomedical Vibrational Spectroscopy* (Wiley-Interscience, Hoboken, 2008)
155. K. Maquelin, C. Kirschner, L.-P. Choo-Smith, N. Van Den Braak, H.Ph. Endtz, D. Naumann, G.J. Puppels, J. Microbiol. Methods **51**(3), 255–271 (2002)
156. P. Daniel, P. Picart, L. Bendriaa, G. D. Sockalingum, I. Adt, Th. Charrier, M. J. Durand, F. Ergan, M. Manfait, G. Thouand, Spectrosc. Lett. **41**(1), 19–28 (2008)
157. R.A. Dluhy, S. Shanmukh, L. Jones, Y.-P. Zhao, J.D. Driskell, R.A. Tripp, Anal. BioAnal. Chem. **390**(6), 1551–1555 (2008)

158. I.S. Patel, W.R. Premasiri, D.T. Moir, L.D. Ziegler, J. Raman Spectrosc. **39**(11), 1660–1672 (2008)
159. B.W.D. De Jong, T.C.B. Schut, K. Maquelin, T. Van Der Kwast, C.H. Bangma, D.-J. Kok, G.J. Puppels, Anal. Chem. **78**(22), 7761–7769 (2006)
160. I. Noda, Appl. Spectrosc. **44**(4), 550–561 (1990)
161. I. Noda, J. Am. Chem. Soc. **111**(21), 8116–8118 (1989)
162. L. Ashton, B. Czarnik-Matusewicz, E.W. Blanch, J. Mol. Struct. **799**(1–3), 61–71 (2006)
163. R. Bhargava, S.-Q. Wang, J.L. Koenig, Appl. Spectrosc. **54**(11), 1690–1706 (2000)
164. D.C. Fernandez, R. Bhargava, S.M. Hewitt, I.W. Levin, Nat. Biotech. **23**(4), 469–474 (2005)
165. R.K Reddy, R. Bhargava, Anal. Chem. Submitted (2008) (Under Review)
166. X. Llora, A. Priya, R. Bhargava, Observer-invariant histopathology using genetics-based machine learning. Nat. Comput. **8**, 101–120 (2009)
167. O. Svensson, M. Josefson, F.W. Langkilde, Chemometr. Intell. Lab. Syst. **49**(1), 49–66 (1999)
168. C. Xie, J. Mace, M.A. Dinno, Y.Q. Li, W. Tang, R.J. Newton, P.J. Gemperline, Anal. Chem. **77**(14), 4390–4397 (2005)
169. H. Georg Schulze, L. Shane Greek, B.B. Gorzalka, A.V. Bree, M.W. Blades, R.F.B. Turner, J. Neurosci. Methods **56**(2), 155–167 (1995)
170. K. Gaus , P. Rösch, R. Petry, K.-D. Peschke, O. Ronneberger, H. Burkhardt, K. Baumann, J. Popp, Biopolymers **82**(4) 286–290 (2005)
171. M.J. McShane, B.D. Cameron, G.L. Coteé, M. Motamedi, C.H. Spiegelman, Anal. Chim. Acta **388**(3), 251–264 (1999)
172. R. Kohavi, G.H. John, Artif. Intell. **97**(1–2), 273–324 (1997)

9

Discovery and Formulation

Don Clark and Caroline Rodger

Abstract The uses of Raman spectroscopy in active pharmaceutical ingredient (API) discovery, development and release cover a wide variety of sample types and applications. However, the technique does not have a high prominence in the pharmaceutical industry despite being recognised by regulatory authorities as a suitable methodology for the analysis and release of pharmaceutical API and products. One reason is that other analytical techniques are well established and changing to Raman methods is cost prohibitive considering return on investments (ROI). In addition the technique is often regarded as being one for "experts" and not one for main stream applications. As a consequence Raman spectroscopy is frequently the 2nd or 3rd technique of choice for a specific application. However, due to its unique sampling attributes (e.g. micro and macro measurements direct from the sample, through glass, from well plates or in the presence of water) and selectivity, applications of this technology are found throughout the life cycles of pharmaceutical products. It can therefore be considered to be a spectroscopic common denominator. This chapter highlights a number of routine, specialised and niche Raman spectroscopy applications which have been used in the development of new medicines while detailing some of the limitations of these approaches.

9.1 Characterisation of Molecular Structure (Research/Discovery)

Within the pharmaceutical industry research and development refer to two distinct phases that may lead to approval of a new medicine. The research (or discovery) phase focuses on the design and synthesis of molecules that show biological activity in model systems and have desirable pharmacokinetic properties in the human body [1]. The development phase takes those new molecules to the marketplace and involves steps to ensure that the optimum compound form and formulation are selected for product efficacy and stability.

During the research phase the use of spectroscopy is focussed on the determination and confirmation of chemical structure. In this respect mass spectrometry (MS) and nuclear magnetic resonance spectroscopy (NMR) are the

primary techniques used. Vibrational spectroscopy is rarely used, and when it is, FT-IR is the first choice as it is most sensitive to functional groups that have a dipole moment. Raman spectroscopy can be used as a probe for functional groups with a magnetic moment; for example, the alkene (>C=C<) and cyano (–C≡N) groups have the strongest bands in a Raman spectrum, while those bands arising from nitro (–NO_2) and disulfide (–S–S–) are also particularly characteristic [2]. Although Raman spectroscopy can provide information on functional groups, its strength is in characterising the molecular backbone of a compound. In addition, the comprehensive interpretation of vibrational spectra is specialised and is becoming a dying skill. In fact the interpretation of a Raman spectrum is often performed just to confirm the presence of specific functional groups where assignment of IR spectra has proved difficult or ambiguous.

There are, however, some niche Raman applications in the early phases of drug discovery. Once the structure of a new molecule has been determined it is important to determine its absolute configuration if it has one or more chiral centres. This is usually performed by single crystal X-ray diffraction (SCXRD). However, if a molecule is difficult to crystallise or lacks a heavy atom or salt form this approach cannot be taken. In these cases Raman optical activity (ROA) or vibrational circular dichroism (VCD) may be used. In simple terms a difference spectrum is obtained after the sample is irradiated with left and right polarised laser light or IR radiation (see Chap. 7 and the review by Nafie [3] for more detailed descriptions). The absolute configuration is determined by matching the experimental ROA or VCD spectrum to one from a series of ab initio spectral calculations for each possible molecule conformation. In this aspect the ROA spectrum ab initio calculations are more complex than those required for VCD. Experimentally ROA has advantages over VCD as it covers a wider spectral range (1800–600 cm^{-1} vs. 1800–1500 cm^{-1}), has greater sensitivity and only has minor interferences from water bands [4, 5]. As a consequence ROA can be performed on samples in biologically relevant systems with far greater ease than VCD. The other key application for ROA/VCD is in the determination of enantiomeric excess (EE). As a unique ROA band is used for the determination, the %EE for any specific chiral compound can be measured from multi-component mixtures containing both chiral and achiral compounds. ROA has a sensitivity that can differentiate between 100:0 and 99:1 enantiomeric mixtures [6]. Despite these advantages, the use of VCD and ROA still remains limited within the pharmaceutical industry.

A critical aspect of identifying a potential pharmaceutical drug candidate is relating the biological activity of the material (potency) to the physical and chemical structures. This structure–activity relationship (SAR) is used as a primary tool to evaluate the activity potential of a particular chemical series to a specific disease target. This method of trending and evaluating performance helps to guide the discovery chemist in developing a series of potential compounds with greater potency and selectivity. Traditionally computational

chemistry coupled with X-ray crystallography and comparative molecular field analysis (CoMFA) has been used to establish quantitative structure–activity relationships (QSARs). However, limitations due to difficulties in accurately modelling molecular shape and charge have restricted its application.

Raman spectra can provide a complementary approach by providing a three-dimensional molecular descriptor as a starting point for SARs evaluation [7]. Trending of band frequencies and intensity can help establish structure–activity properties. There are many barriers for completing trending using the direct experimental approach. For example Raman analysis in the presence of proteins is difficult due to a number of factors including matrix effects, limited sensitivity, selectivity, spectral complexity and noise. Therefore a two-step approach has been adopted that uses the Raman frequency and intensity trends obtained from pure materials and correlating these to independent chemical/biological assays. Where these can be related to bioassay binding affinity values an insight into structural and electronic properties of the chemical series can be obtained. This information can be used to indicate molecular motifs that can enhance binding activity and hence improve the potency of the drug candidate. This information is a key to the drug discovery process. Pivonka has demonstrated the value of this approach by correlating Raman shifts to the binding activity of isoflavone, coumarin and benzoxazole within a human oestrogen receptor (ER-β) [8]. By identifying Raman spectral shifts, he concluded that bonding activity was strongly influenced by electron density of the pi-bonding system of the backbone scaffold for each series. By relating the physical electronic state of molecular subcomponents within a compound series involved in binding kinetics it was possible to identify and optimise binding activity and potency.

The unique potential of Raman has also been used to establish SARS using an acyclic amide series [9]. Raman spectra were collected directly from a naphthyl ring containing series of compounds, and trends in the band frequency shifts of the nitrile vibration were observed. It was determined that an increase in potency of this series could be correlated to a decrease in the nitrile frequency. This was related to inductive effects resulting from variant substitution on the naphthyl ring. Therefore the ring substitution enhanced the electron density of the naphthyl aromatic system, increasing potency. This type of information is critical for the discovery chemist and allows proactive targeted structural molecule development to optimise potency and deliver a compound suitable for commercialisation.

9.2 Selection and Characterisation of API Form (Development)

When a compound moves from discovery into development it is critical that the drug candidate's molecular properties are optimised in terms of bioavailability (solubility), stability, processability, hygroscopicity, etc. The compound

delivered from discovery is often a free base or acid. While satisfying mechanistic and efficacy criteria, these compounds often have issues with their chemical or physical properties that prevent commercialisation. Two important properties are chemical stability and solubility. Both can be improved through the formation of a suitable crystalline salt or co-crystal. The counter ion that will produce the ideal API form cannot be predicted, so it is found through extensive experimentation using salt screens. These are performed using solvents suitable for use in pharmaceutical manufacture to identify salts that have desired candidate drug properties [10]. The salt screens may be performed using sitting drop or well plates using counterions that have pharmaceutical precedence and have also been approved by the industry's regulatory authorities.

Testing of materials generated by these screens include optical polarised microscopy to determine crystallinity, thermal methods (i.e. differential scanning calorimetry (DSC) and thermogravimetric analysis (TGA)), powder X-ray diffraction (PXRD), dynamic vapour sorption (DVS) and vibrational spectroscopy. Raman spectroscopy is used to provide information on the physical form of the material as it offers specific advantages including (i) little or no sample preparation, (ii) rapid sample analysis, (iii) sensitivity to molecular geometry and (iv) small amounts of material required for analysis. As salt screens are performed using very small quantities of material, the output from any well may be only one tiny crystal. Although small, this may produce a lead to a commercialisable form of the compound. Analysis of this crystalline material is very challenging for bulk methods, such as PXRD and DSC, but can be performed much more easily using polarised light (PLM) and Raman microscopy. The PLM is used to identify crystalline materials, through their birefringence properties, which is followed by Raman analysis. This is performed easily as Raman microscopes can be configured with polarised light capability. Obviously manual measurement of salt screen plates is very time consuming due to the large number of wells and potentially crystals within them. However, the Raman microscopy analysis can be automated making Raman spectroscopy very attractive as a rapid analysis tool for salt selection studies [11–13]. The consequence of an automated approach is that large amounts of data are generated from which the different forms must be identified. Chemometric packages are now available that will assess the Raman data [14] or use multiple spectroscopic inputs [15] to identify those samples that contain unique crystalline forms or mixtures of materials. This allows the pharmaceutical development scientist to quickly identify key salts to progress in the development process.

The further selection of an API salt for a formulation is governed by a number of factors and is crucial to the successful launch of a new medicine. Ideally this salt is monomorphic and has no hydrate or solvate forms. In some cases, the amorphous salt form may be developed to improve solubility though this is often at the expense of stability. Frequently, API salts have

more than one crystalline form and the pharmaceutical development process requires that each form including the amorphous form is characterised using a variety of techniques [16]. Properties such as bioavailability, solubility and stability of the API in drug product are often directly related to the physiochemical properties of the polymorph(s) present [17]. In addition, different polymorphs often adopt different morphologies. These may display vastly different physical properties, including flowability and compaction, which may in turn influence the manufacturability of the drug product [18]. All of these factors have implications for the safety, efficacy and manufacturability of the drug product. Regulatory bodies therefore require polymorphic form to be closely monitored and controlled unless proof of form bio-equivalence can be demonstrated.

In recent years there has been increasingly more interest in determining the amorphous content of pharmaceutical materials. This is due to

a) regulatory requirements;
b) amorphous materials having a higher solubility (but lower stability) than crystalline forms. This may be particularly important for formulation delivery of API salts with low aqueous solubility;
c) crystalline disorder caused by processing (e.g. milling, micronisation). These amorphous surfaces can provide the sites for the formation of undesirable API polymorphic forms and are of great interest in inhaled products where the API particle size is in the order of 2–10 μm.

Raman spectroscopy has been used to assess the relative composition of crystalline and amorphous in bulk samples. The vibrational spectra of amorphous materials typically have fewer and broader bands than crystalline materials due to the molecular disorder. By building reference training sets with different crystalline to amorphous ratios, chemometric methods can be developed to determine the amorphous content of provided samples. However this does not truly reflect the types of samples of most interest. These chemometric models are based on mixtures that are comprised of either crystalline or amorphous particles. Of far more interest and significantly more challenging is the determination of amorphous material on particle surfaces and interfaces. Studies by Ward et al. [19] have started to address this issue using atomic force microscopy (AFM) and confocal Raman microscopy. Using D-sorbitol, a pharmaceutical excipient with four polymorphic forms and a relatively stable and easy to produce amorphous form, these techniques have been used to study different solid state phases on sample surfaces. After preparing discs of crystalline D-sorbitol a microthermal analyser was used to produce localised areas of amorphous material. Figure 9.1 shows the Raman spectra of the initial crystalline and subsequent amorphous D-sorbitol. The two forms can be distinguished from their Raman spectra, and band broadening is evident in the amorphous form. As the D-sorbitol changes from a crystalline to the amorphous phase the peak width at half height for the 878 cm^{-1} band

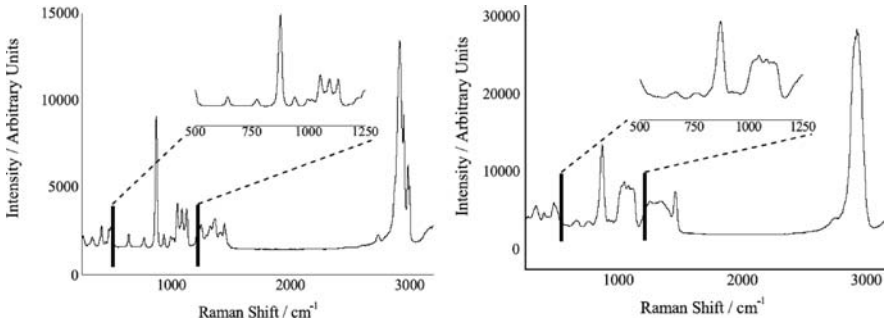

Fig. 9.1. Raman spectra of (*left*) crystalline D-sorbitol and (*right*) quench cooled glassy (amorphous) D-sorbitol. Reproduced from [19]

(attributed to the C-C-O stretch) changes from 15 to 34 cm^{-1}. This allowed the depth and distribution of the amorphous D-sorbitol through the crystalline bulk to be determined. This approach shows promise in providing a better understanding of batch-to-batch variations in crystallinity that lead to formulation and/or manufacturing problems which cannot be detected by bulk Raman methods.

Polymorph and amorphous form identification must be made in the solid state as all structural information is lost when employing wet chemistry methods. The solid state techniques most commonly employed by the pharmaceutical industry for polymorph characterisation are powder X-ray diffraction (PXRD), differential scanning calorimetry (DSC) and solid state NMR [18]. However, owing to its versatility, speed of analysis and minimal requirements for sample preparation, Raman spectroscopy is becoming a more commonly used tool for analysis and characterisation of pharmaceutical solids [20]. Of all the vibrational spectroscopies, Raman has the widest spectral range (4000–30 cm^{-1}). The lower frequency range covers those frequencies associated with crystal lattice vibrations and these can be particularly informative in discriminating between different crystalline and amorphous forms of a material [21]. However, subtle changes in the unit cell, for example in the position of an alkyl chain, are rarely discriminatory when using vibrational spectroscopic methods, so other methods are preferred in the identification of new forms. This is because FT-IR and Raman spectroscopy are both short-range probes obtaining information from chemical functional groups and structural fragments within a molecule, whereas X-ray diffraction methods are much longer range techniques which gather information on the whole molecule unit cell. Due to these considerations DSC and PXRD are the "gold standard" analytical methods for polymorph identification due to their better sensitivity to changes in the unit cell. Raman spectroscopy provides an important supportive role in the characterisation of API forms with spectra and peak tables being used as part of the patent applications for new materials.

9.3 Quantitative Raman Approaches in API Characterisation

A more challenging analysis is the quantitative analysis of polymorphic mixtures. Thermal techniques (e.g. thermogravimetric analysis (TGA) and DSC) and PXRD are commonly used to determine polymorphic form in drug substance with limits of detection as low as 1% w/w. However these techniques often lack sensitivity in the presence of excipients. PXRD typically has a limit of detection of approximately 5% w/w in formulated product and is unsuitable for samples containing large amounts of excipients [18]. Solid state NMR has a number of advantages. It can routinely determine polymorphic form with a limit of detection lower than 1% w/w in drug substance and it is suitable for use with formulated product. However, the sensitivity is greatly reduced in samples containing large amounts of excipients. This technique is expensive, requires specialist equipment and operators and significant sample preparation. It is also extremely time consuming with some bulk samples taking up to 24 h to analyse.

In this application, Raman spectroscopy is gaining acceptance as a powerful tool for pharmaceutical analysis and has a number of advantages over both FT-IR and non-spectroscopic techniques. Raman requires no sample handling or preparation and may be collected non-invasively from within a sealed container [20]. It is non-destructive, fast and can assess both drug substance and formulated product. In contrast to FT-IR, Raman spectra may be obtained in the presence of moisture [17] and the Raman spectra of most excipients are significantly less intense than that of the API, thus giving Raman an inherent selectivity for the API of interest [22]. As well as use in the qualitative determination of unknowns, proof of structure and confirmation of identity, Raman spectroscopy is being increasingly used quantitatively to measure API concentrations and determine compositions of polymorphic forms [17, 18, 20, 22–27]. Using modern chemometric approaches it is possible to build robust quantitative methods for polymorph or impurity identification using FT-Raman. Depending on the material and quality of standards prepared detection limits of below 2% can be readily achieved [28]. Similarly, spectral pre-processing techniques such as taking derivatives and orthogonal signal correction (OSC) have been successfully used to remove backgrounds and sampling variations [17, 29–31]. Unsupervised techniques such as principal component analysis (PCA) and supervised techniques such as partial least squares (PLS) have been used in combination with vibrational spectroscopy and have demonstrated an increased ability to achieve precise quantification in pharmaceutical systems [17].

Raman is not immune from experimental difficulties. One of the major problems associated with using Raman spectroscopy to analyse pharmaceutical products is fluorescence [32]. This arises from the emission of a photon during relaxation to the electronic ground state and may be caused by the drug itself, a low-level impurity, excipients in the formulated product or

introduced by manufacturing processes. In some instances fluorescence may be removed by photo-bleaching the sample (irradiating it with laser light prior to analysis) [33]. Fluorescence may also be significantly reduced or even removed by changing the excitation wavelength of the laser. The fluorescence emission of aromatic molecules generally occurs in the 300–700 nm region; therefore, fluorescence may often be removed by moving from a 633 nm to a 785 nm or 1064 nm excitation wavelength. The main disadvantage associated with moving to longer wavelength excitation is that the Raman intensity is inversely proportional to the fourth power of the laser wavelength [34]. The Raman signal therefore decreases rapidly with increasing wavelength [32]. When using FT-Raman spectroscopy (1064 nm lasers) the Raman signal strength is typically substantially lower due to both the wavelength dependence of Raman scattering cross section and often lower performance of FT-Raman systems compared with their dispersive counterparts typically used in the visible spectral range. Hence the laser power must be often dramatically increased in order to obtain good spectra. Thus, while fluorescence is rarely a problem when using FT-Raman, sample burning and sample heating are common. This is often overcome by using a spinning sample holder to disperse the laser energy [24, 26].

Other sources of error, particularly in quantitative Raman analysis, include laser self-absorption effects leading to attenuation of some spectral bands. Similarly diffuse reflectance of the laser light, which is dependent on the particle size of the formulation components, may increase or decrease the collection volume. However, normalisation techniques can be used to overcome some of these effects [35].

Another difficulty is sub-sampling [23]. It is difficult to measure a statistically representative amount of sample when the focus of the laser beam is a few tenths of a millimetre. This problem may be addressed by using a bulk or wide-area sampling probe, by rotating the sample or by translating the sample combined with multiple replicates [17]. Similarly, sample inhomogeneity can be a major source of error when using Raman spectroscopy to analyse mixtures. A number of different approaches have been used to ensure complete sample mixing including vibrating the samples and shaking the samples in a ball mill without the steel balls [27].

In summary, the analyst has a number of options in deciding which Raman method to use for their specific analysis. As a general rule of thumb FT-Raman spectroscopy should be used for bulk samples (ca. >1–10 mg sample). A dispersive Raman microscope system is generally the best option for individual particles or small areas of larger samples.

9.4 API Form Behaviour and Relationships

Having identified and characterised all known polymorphs, hydrates and solvates of an API it is important to determine the relationship between all known forms. Conversion of one form to another can be caused by common

processes such as milling/micronisation, wet granulation (particularly hydrate formation) and tabletting (form conversion via pressure changes). Similarly the most stable polymorphic form at room temperature may not be the most stable form at a different temperature. For these enantiotropic systems it is important to know under what conditions and how conversion takes place (e.g. kinetically or thermodynamically) as this may impact on how the formulated API is manufactured or stored. The relationships between forms and their thermodynamic stability can be represented in flowcharts and phase diagrams as illustrated in Fig. 9.2 for the monotropic solid state forms of prilocaine hydrochloride [36].

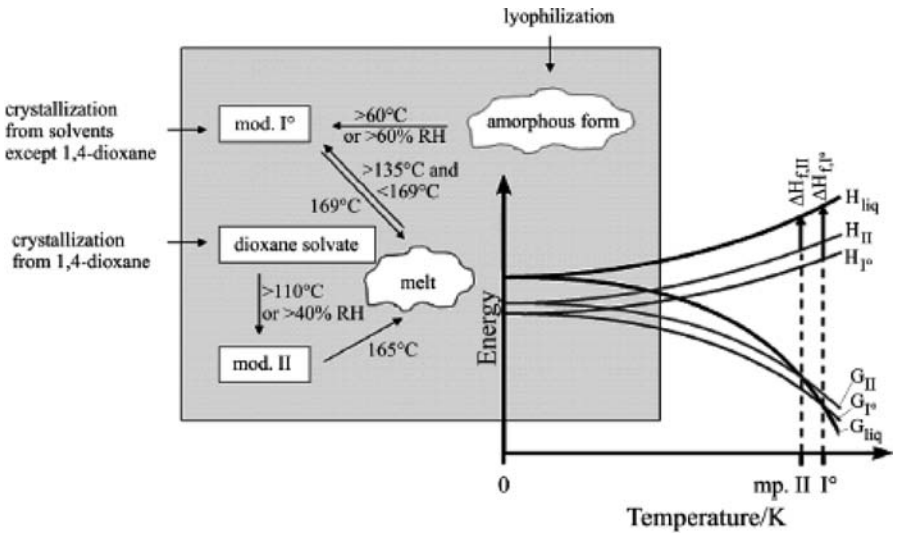

Fig. 9.2. Flowchart of prilocaine hydrochloride solid state forms and melt with transformation temperatures under ambient pressure conditions (*left*) and semi-schematic energy/temperature diagram of the polymorphs (*right*). Key: H, enthalpy; G, Gibbs free energy; ΔH_f, heat of fusion; Liq, liquid phase (melt). Reproduced from [36]

In the construction of these diagrams the use of Raman is limited and generally restricted to form identification. However, it is when Raman spectroscopy is coupled to other techniques that the information required to understand API forms and their behaviour is more fully realised. The combination of thermal analysis instrumentation with Raman systems has been particularly beneficial, and there has been a clear progression of purpose-built instrumentation to observe the relationship of material forms at non-ambient conditions. Szelagiewicz et al. [37] used a standard light microscope hot stage to observe and heat individual particles of paracetamol and record their Raman spectra at elevated temperatures. Using very little material (e.g. micrograms) this approach allowed new API forms to be produced at non-ambient conditions

and to be characterised via their Raman spectra. These data, when used in phase and flow diagrams, are valuable as they may flag processing conditions to avoid if process-induced transformations of API (or excipients) are to be avoided. In the paracetamol study, the amorphous form of the API was produced by melting and cooling the sample. Visual observations of the sample on reheating showed the sequential formation of spherolites, prisms and plates which were identified by their Raman spectra as paracetamol forms III, II and I, respectively. Although a morphology change can be observed visually, it is only when Raman spectra are obtained from each type of particles that positive identification of specific forms can be made. The study also demonstrated that Raman spectra are temperature sensitive and peaks can broaden and their positions may change by $>\pm 2\,\mathrm{cm}^{-1}$. This can be critical if identification of the polymorphic form is required as a shift of this magnitude would normally indicate a change in form as described by Mehrens et al. [38].

This approach can be used to study crystallisation or to vary both temperature and relative humidity to construct a "phase-like" diagram [39]. In the following example, the fate of the hydrate form of an API at non-ambient temperatures and %RH is followed [40]. Hydrates are notorious within the pharmaceutical industry as changing condition within manufacturing processes can form hydrates (e.g. with theophylline during the wet granulation) or produce anhydrous materials (e.g. during drying steps). As a consequence, development of API hydrates is discouraged so as to avoid possible process-induced transformations (PIT). The exception is when a hydrate has improved stability or solubility compared to the anhydrous API (e.g. for antibiotics erythromycin and cefixime) or has better processability properties (e.g. Paxil®).

Figure 9.3a shows that on increasing the temperature and decreasing the %RH the ingoing API monohydrate transforms to one of two anhydrous forms. Increasing the %RH leads to the formation of a pentahydrate or deliquescent state. From the "phase-like" diagram the monohydrate is stable over the lifetime of the experiment (which is several hours) and over a significant range of temperature and %RH conditions. Based on this information the API

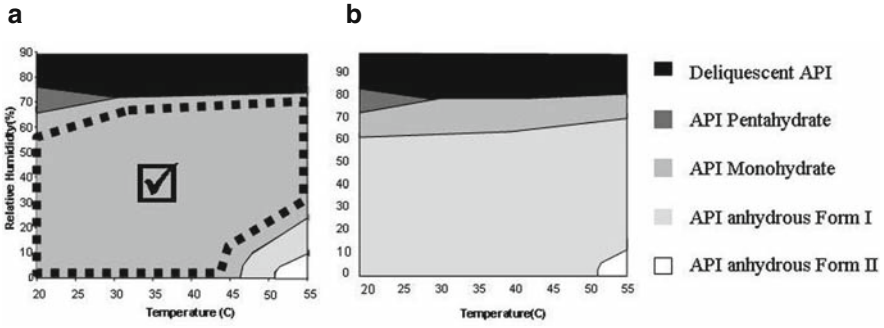

Fig. 9.3. (a) *Left*: Phase-like diagram starting with API monohydrate. **(b)** *Right*: Phase-like diagram starting with API anhydrous Form II

could be processed as the monohydrate with confidence that no conversion to another form would occur. Subsequent Raman mapping microscopy analysis of manufactured tablets detected only the API monohydrate form. It should be recognised that API form conversions can be both kinetically and thermodynamically driven, so that these experiments can only provide a guide as to the probable fate of any form under specific conditions. However it is valuable to know that should the monohydrate convert to an anhydrous form significantly higher %RHs are required to return to the monohydrate form as shown in Fig. 9.3b.

Although the variable temperature/humidity stage is very useful its drawback is that as a microscopy system only one particle can be measured at a time and individual particle behaviour may not be typical of the sample bulk. To overcome this, Raman probes have been applied to analytical instruments used for macrosamples. For example simultaneous in situ Raman–DSC instrumentation has been used to characterise and study the non-ambient temperature transformations of macrosamples of salmeterol xinafoate [41], while the coupling of a probe to a dynamic vapour sorption instrument (DVS) allows the thermogravimetric properties/hygroscopicity of a sample to be determined simultaneously with its characterisation by Raman spectroscopy [42]. One advantage of these types of experiments is that by using non-ambient conditions new metastable API forms, which are not formed at ambient conditions, may be observed. Using a combination of DSC and Raman spectroscopy, data have been obtained for acetaminophen form III that until now has not been characterised as a bulk material due to its unstable nature [43]. This approach allows thermal events and the associated phase transformations to be better identified and characterised.

Another reported bulk experiment followed the conversion of carbamazepine from form III to form I by FT-Raman spectroscopy using a modified variable temperature diffuse reflectance accessory [44]. The solid state transformation was observed over a range of temperatures (130–150°C) and concluded that there were multiple kinetic events operating simultaneously to produce form I, but were ultimately controlled by phase boundary kinetics. From these data the activation energy for the transformation was calculated and was consistent, if a little higher, with previous off-line X-ray diffraction measurements. The authors suggest that using a modification of the Raman equipment would allow in-process monitoring and control of the API polymorphic form during manufacture. In fact, since the United States Food and Drug Administration (FDA) provided guidance to the pharmaceutical industry on improving drug product quality through better process understanding a number of opportunities for Raman spectroscopy have been demonstrated [45–47]. These include monitoring

(i) the effect of water and chopper speed on API form during wet granulation;
(ii) formulations for blend uniformity at the tablet press feed frame immediately prior to compression;

(iii) API distribution in molten excipients;
(iv) the progress of tablet coating;
(v) API form in solvents and slurries including aqueous systems;
(vi) for future real-time product release.

All these applications have different instrumental configurations and in many cases the laser can be delivered to the analysis point via fibre optics. This provides an implementation challenge as laser exposure and eye safety are paramount concerns particularly in a manufacturing environment. Although mentioned briefly here Raman PAT applications are likely to be an area of significant growth over the coming years.

9.5 Formulation Development

It is in the development and support of formulated products that Raman spectroscopy probably has most to offer the life cycle of a pharmaceutically active molecule. Due to there being few limitations to sample presentation prior to analysis, Raman spectroscopy is particularly versatile and can be applied to both macro- and microsamples.

For formulated products an essential analysis is the assay for API content. This is usually performed by HPLC, but Raman spectroscopy can offer a quantitative analytical alternative. These applications have been extensively researched and reviewed by Strachan et al. [48] and provide over 30 literature references of where Raman spectroscopy has been used to determine the chemical content and physical form of API in solid dosage formulations. As no sample preparation is required the determination of multiple API forms (e.g. polymorphs, hydrates/solvates and amorphous content) provides a solid state analysis that is not possible by HPLC. However, as previously discussed sampling strategies must be employed to ensure the Raman measurement is representative of the whole sample. A potential solution is to sample the whole of a solid dosage form and not multiple regions of it. As presented in Chap. 3 the emerging technique of transmission Raman provides a method to do just this. With acquisition times in the order of seconds, this approach offers an alternative to HPLC and NIR analyses and is also applicable to tablet and capsule analysis in a PAT environment.

Having overcome sampling issues Raman spectroscopy has been successfully used to determine the API content of diclofenac, sulfasalazine, ciprofloxacin, aciclovir and provera tablets and suspensions [48]. The analytical result is determined using a variety of methods including univariate, multiple linear regression and partial least-squares methods. In all cases the Raman method was equivalent to the more common HPLC method, but provided a faster assay. On more than one occasion the analysis was performed without the need to remove the solid dosage form from the blister it was supplied in. An extension of this approach is to detect the low-level content of one polymorphic form in another within a tablet matrix. Using bulk sampling

methods, the reported limit of quantification (LOQ) for minor polymorphs is between 0.6 and 2%, though using Raman microscope systems this LOQ can be significantly reduced.

Raman microscopy provides an extremely convenient method of performing forensic-like examinations of individual particles (<10 μm) that have been isolated or are present in bulk matrices (e.g. tablets) as shown in the following example. On compression of a formulated blend (i.e. API and excipients) "off-white" areas were evident on the surface of the newly formed tablets. A representative Raman spectrum from one of these areas along with spectra from the API itself is shown in Fig. 9.4. What is immediately clear is that the "off-white" area (see Fig. 9.4c) has a highly fluorescent Raman spectrum and bears little similarity to the API's spectrum. Upon investigating the API's physical stability evidence concluded that the compound was pressure sensitive. The Raman spectrum of the compressed API is shown in Fig. 9.4b and from these collective data (Fig. 9.4a–c) it is clear that the API has undergone a process-induced transformation. Investigation of the tablets core by mapping the internal cross section indicated that the API form was preserved. From this we can conclude that (i) due to its physical and stability attributes this API form is not suitable for delivery as a compressed tablet and (ii) there are higher compression forces exerted at a tablet's surface compared to its core. This effect was subsequently confirmed using X-ray microtomography [49].

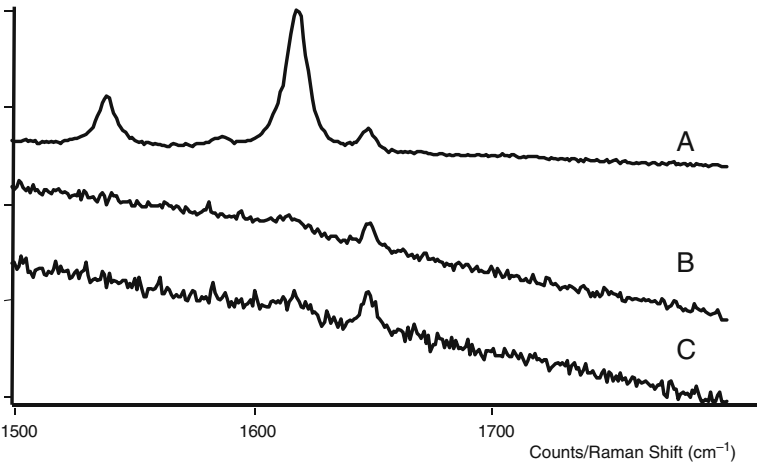

Fig. 9.4. (A) API spectrum; **(B)** API after compression; and **(C)** "off-white" area on tablet surface

This example can be classified as a forensic investigation. When Raman is used to identify unknown materials in formulations, the spectral analysis may be challenging when using Raman libraries as they do not have the compound diversity compared with spectral diversity of FT-IR libraries. In addition the

relative band intensities of a compound's Raman spectrum can change depending on the laser power and frequency particularly at high intensities and when using tightly focussed laser beams. This can lead to reduced confidence in any library search, due to the poorer correlation between the sample spectra and the reference library when different laser frequencies have been used for each spectrum. However the spectrum still contains valuable information from which the class of compound can be determined through spectral interpretation.

9.6 Raman Mapping and Imaging Applications

Raman mapping microscopy continues to make a significant impact on the development and understanding of solid dosage forms (e.g. tablet and capsule formulations). The instrumentation, methodologies and some applications have been previously presented (see Chap. 5 and other reviews [50, 51]). In general, the spatial resolution and spectral specificity of Raman microscopy allows the identity of individual particles ($<10\,\mu m$) to be determined. Automating these measurements leads to the production of Raman chemical images from sample surfaces, usually tablet cross sections. The Raman spectra and chemical images are used to assess the API form in the formulation, estimate domain/particle sizes and material distribution or association (at a microscopic scale) that is required for the desired product performance and blend homogeneity.

An early example of Raman mapping by Breitenbach et al. [52] showed that when crystalline ibuprofen is formulated in a hot melt extrudate the API changes to the amorphous form. Ibuprofen is a sparingly water-soluble compound, so this formulation provides a route to better bioavailability via the more soluble amorphous form. Using confocal Raman mapping the form of the API was determined at the time of manufacture and under stress conditions and was used to assess the stability of the amorphous form. These studies also showed that the API was homogeneously distributed throughout the formulation based on the relative band intensities of the amorphous API and a formulation excipient, polyvinylpyrrolidone (PVP).

This work unwittingly demonstrated an error inherent in many mapping experiments in that very few experiments on pharmaceutical formulations yield spectra of pure components at individual pixels in the chemical image. This observation may be at first surprising in that the Raman collection volume on a microscope system is regularly quoted as being ca. 1–2 μm^3, a size that is considerably smaller than the majority of API and excipient domains in a sample. This means that in this example either (i) the API and PVP become intimately mixed during the manufacturing process/method or that (ii) the Raman collection volume is significantly larger than first envisaged. The work by Everall [53, 54] showed that when using a confocal Raman microscope both depth and lateral laser penetration into the sample are at least an

order of magnitude greater than anticipated. Complementary studies [55] have shown that roughening sample surfaces reduces the laser penetration into the sample, but that the Raman collection volume is still larger than expected. Coupled with the fact that both the refractive index and the 3D shape of each material in a sample can affect the response in mapping experiments, there will always be a degree of uncertainty in the domain sizes indicated by Raman chemical images.

A further limitation of Raman mapping experiments is that the technique is inherently slow. Experiments can take many hours or even days to produce enough data to allow meaningful conclusions to be made. Several manufacturers now offer systems that make measurements at significantly faster sampling rates, but as yet there is no body of literature related to pharmaceutical samples to allow their effectiveness to be evaluated. Speed can also be obtained through Raman imaging, but as the laser is defocused the resultant chemical image is generally of poorer quality than that obtained via Raman mapping. Raman imaging generally works best with spatially resolved samples.

Coherent anti-Stokes Raman scattering (CARS) microscopy is an emerging technology. By tuning a pump laser and a Stokes laser to a Raman-active molecular vibration, molecular selectivity and faster measurement speed can be obtained. This approach has been used to track the phase segregation, crystallisation and dissolution of paclitaxel from biocompatible excipients and films providing kinetic data not achievable through standard Raman microscopy methods [56].

A complementary approach is that of FT-NIR mapping. With more relative energy being available from NIR sources and having a larger spot size, these instruments map considerably faster over a larger sample area than Raman systems though significantly sacrifice spectral and spatial resolution. This will be important when particle domains of $<10\,\mu m$ are being investigated. Similarly, NIR microscopy methods may forfeit sensitivity particularly for compounds present at low concentrations. It is clear that when a chemical image of a sample is required careful consideration must be given to what information is required and then in matching the appropriate technology to deliver the required data.

Irrespective of the method chosen, meaningful data can only be obtained if the appropriate level of signal to noise (S/N) is reached in the spectrum of each analyte. This has been achieved for Raman measurements through short data acquisition times ($<1\,s$) and application of mathematical approaches such as K-harmonic means clustering (KHMC), factor analysis [57] and principal component analysis (PCA) [58] to the data set. Ultimately the sample response to the excitation energy determines the speed that a measurement can be made.

Despite these limitations the ability to obtain information from tablets (and other solid dosage forms) about the location and form of excipients and API non-destructively using Raman mapping approaches is second to none.

Belu et al. [59] detail the use of confocal Raman microscopy as a tool to track the elution and location of rapamycin from poly(lactic-*co*-glycolic acid) coatings designed for use on medical devices (e.g. stents). Similarly Docoslis et al. [60] use Raman mapping to show how the form and crystal size of nimodipine changes on storage. This is particularly important when a change of form can affect the safety or efficacy of a product. Regulatory guidance requires, where such changes cannot be detected by a performance test (e.g. dissolution), monitoring should be employed where technically possible. This becomes a challenge when dealing with high potency API present in low concentrations. In the study of 0.5 mg Xanax^{TM} tablets, the API (0.4% w/w alprazolam) could not be detected by NIR but was visible using Raman microscopy and PCA [61]. Mapping experiments on a number of tablets showed good API homogeneity and distribution within each unit dose. Lower limits of detection were achieved by Henson and Zhang [62] who demonstrated a detection limit of 0.05%w/w for two minor polymorphs. The data were also able to show an increase of API domain size from 13 µm to 21–23 µm which represented a change of API processing between different tablet batches. These workers have subsequently extended this limit for polymorph detection to 0.01% w/w in a formulation where API conversion to one of three less desirable forms was potentially possible. The chemical images from LOD feasibility studies are shown in Fig. 9.5 and the model used to demonstrate that no undesired polymorphs were present in the formulated product.

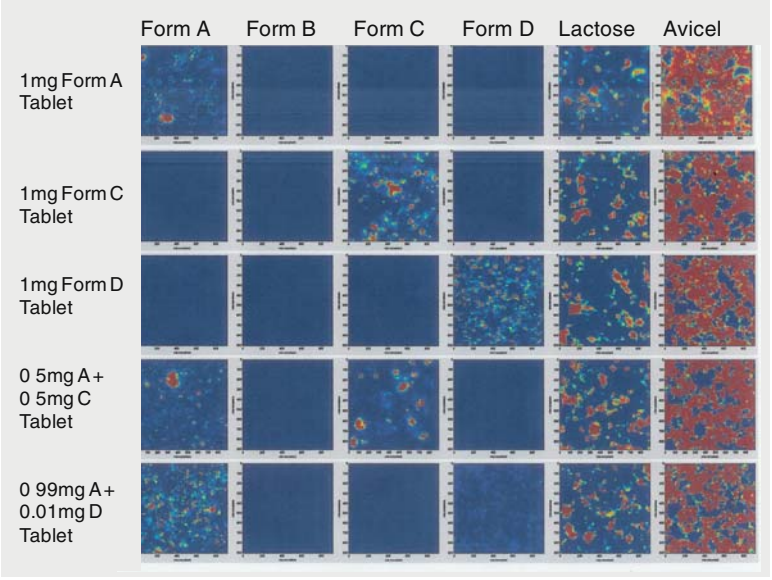

Fig. 9.5. Raman chemical images of tablet formulations with different API form compositions to demonstrate technique limit of detection of 0.01% w/w for form D

However, these limits of detection must be treated with caution. Where single particles (>1–2 μm in size) of a polymorph exist, a Raman spectrum can be obtained provided they can be located. For example, a common pharmaceutical excipient used to lubricate formulation blends is magnesium stearate. This is typically present at ca. 0.5–1.0% w/w, though formulations with a few %w/w content exist where the excipient is also used to control API dissolution rate. Magnesium stearate has a strong and characteristic Raman spectrum but is rarely detected in Raman chemical images. Although the excipient is present at nominally detectable levels, it is not observed because being a lubricant it is spread throughout the sample and as a result at any sample location it is below its Raman LOD (unless it fails to lubricate the sample and is present as a lump).

With such low detection levels being possible there is always a question of how much data should be collected to ensure all present materials are detected in a mapping experiment. Experimental optimisation and statistical approaches have been reported [63], but Šašić and Whitlock have specifically addressed this question for systems where the detection of API in formulations at concentrations of less than 1% is required [64]. Using probability and statistical theory a low-level component should be detectable making $5 \times 1/p$ measurements, where p represents the concentration of the targeted component ($p = 1$ for a pure component). Thus for API concentrations of 0.5 and 0.2% w/w, 1000 and 2500 measurements are required, respectively, to ensure detection at the 95% confidence limit. Of course, multiple experiments are required as insurance against failure. Probability theory indicates that between 20 and 60 experiments are required to ensure success, but in practice this number is significantly less as demonstrated by the experimental data produced to test the theoretical hypothesis. Another interesting feature of this work was that the mapping step size was >200 μm to ensure maximum coverage of the tablet surface. This stage shift is considerably larger than typical API particle sizes. Here the Raman microscope system was used as a convenient way of collecting many spectra automatically in the search for low-level components. However, any subsequently generated chemical image would be meaningless in terms of component domain sizes.

An emerging application for Raman chemical images is in the characterisation of inhaled products. The size of the API particles is critical for inhaled delivery. A particle >10 μm will not enter the lung; 2–5 μm particles are essential for reaching the deep lung, while a cough reflex will expel particles <1 μm. As a consequence particle size analysis of ingoing API and formulations is a key activity in the development and production of inhalation products. The use of impactors (e.g. Anderson cascade and new generation impactor (NGI)) provides a method for separating dispensed formulation into specific aerodynamic ranges that are linked to deposition profiles. These fractions can then be assessed visually by light and scanning electron microscopy methods while quantitative analysis is performed by HPLC. Laser diffraction methods are the primary tools used for dynamic particle size analysis. One drawback of

the particle counting and shape evaluation tools is that it is generally difficult if not impossible to confirm the identity of any individual particle. With a number of inhalation products being combination products (i.e. contain more than one active compound) discrimination between API particles becomes a tougher challenge. However, the nominal collection volume and specificity of Raman microscopy provides an elegant solution to this identification problem. This was first demonstrated with the Raman mapping of deposits on impactor plates from pressurised metred-dose inhalers (P-MDI) containing Ventide® [65]. Individual particles of each API present in the formulation (salbutamol and beclometasone dipropionate) were easily identified from their Raman spectra. From these data it was clearly demonstrated that neither API had changed form or degraded in the formulation suspension. In the presence of moisture, beclometasone dipropionate will convert to the monohydrate form, so this result also suggested there was no significant moisture ingress into the p-MDI canister. The Seretide®/Advair® formulation also contained two APIs: salmeterol xinafoate and fluticasone propionate. This formulation was believed to have better efficacy over the individual active compounds administered separately as the combination product allowed better co-deposition of the two APIs. To evaluate this hypothesis impactor plates from combined and separate API administrations were studied by Raman mapping [66]. The Raman spectra obtained confirmed each particle's identity and form, and the chemical images allowed identification of particles formed by API co-deposition. These images were then analysed for differences in API distributions using a statistical technique known as bootstrapping. The outcome was that significantly more co-deposition occurs from APIs delivered simultaneously from the same inhaler.

Although the use of Raman mapping has clear benefits to the analysis of inhaled product, the approach has a number of limitations. These include

(i) that the method cannot be used quantitatively as the thickness of each particle cannot be controlled or determined;
(ii) the method can be time consuming (a $128 \times 128\,\mu m$ area mapped with a $1\,\mu m$ step size with a 10 s data acquisition takes 48 h to complete);
(iii) a significant part of the experiment time is wasted due to spectra being acquired from blank areas of the impactor plate because the individual or co-deposited particles are spatially resolved.

This particular type of analysis is ideal for Raman imaging. As particles are spatially resolved there is no opportunity for spectral mixing from materials below them, a problem inherent in Raman imaging of heterogeneous mixtures (e.g. tablet formulations). Similarly, as all points in the field of view are analysed simultaneously there is no time wasted in the data acquisition from blank regions in the sampling area. This has been exploited by Doub et al. [67] in the analysis of Beconase AQ® nasal spray. Imaging areas at least a factor of 2 larger than the previously described mapping experiments, spectral acquisition took less than 3.5 h providing con-

siderably faster sample analysis. As this product is a nasal spray a different sample preparation technique was required compared to that for MDIs. In this case droplets from an actuated device were captured on an aluminium-coated microscope slide and allowed to dry. This resulted in particles of each formulation component being distributed across the slide. Using polarised bright-field reflectance microscopy crystalline materials were observed, which included API particles, through their birefringence. The individual API particles were then identified through the generation of a Raman chemical image at wavelengths specific to the active compound, beclometasone dipropionate (BDP). Using image analysis the maximum chord length of the API particles was determined and from those data a particle size distribution for the API was constructed. Naturally comparisons with traditional laser diffraction methods were made. There was not a clear correlation between the two approaches but these can be explained through the measurement approach (i.e. chord length (2D) vs. assumed spherical particle shape (3D)), sample aspect ratio and particle orientation produced by the sample preparation. An additional source of error was particle agglomeration.

Ultimately chemical images have the ability to show API adhering to other formulation excipients which is not possible by other sizing methods. Statistically, laser diffraction methods have less errors in the measurement as they measure millions of particle compared to the hundreds by Raman chemical imaging, but their lack of specificity means the whole sample is measured and not just the API. Ultimately the Raman method is still under development but provides the formulators of inhaled products an additional tool in understanding formulation properties and product.

Throughout the drug discovery and development process protection of intellectual property through patents is paramount. Raman is one tool in an arsenal of techniques used in this area because it can be used to probe both API and drug products (though it may not be the preferred method at any specific point through the drug development process). IP use of Raman spectroscopy in its most basic form is in the production of a peak table for the compound list peak frequencies and relative intensities. Where a compound exists in a number of forms, specific bands that are characteristic of each polymorph will be highlighted. For example, the patent application for lysine, arginine and ornithine salts of atorvastatin details unique Raman bands for each characterised amorphous and polymorphic forms of the new salts [68]. As no sample preparation is required to obtain a Raman spectrum, the possibility of a conversion of one polymorphic form to another is eliminated. As Raman bands are typically sharper than other vibrational spectroscopic methods, this offers greater opportunities for the detection and discrimination of low-level detection of a minor polymorphic form in a bulk API material. This is particularly important once a medicine reaches the marketplace, as the ability to detect all API forms is essential to ensure whether any patent infringement has occurred [47]. The following hypothetical example illustrates

this point. Figure 9.6 shows a Raman chemical image that was obtained from a bead formulation which contained an immediate release layer of API on the exterior surface of the bead and a controlled release (CR) layer of the API within the bead. The interesting feature of this image is that the CR layer comprises four different forms of the API. Investigation of the bead manufacturing process determined that these forms were produced under specific processing conditions. In addition, Raman microscopy's low detection levels provided a tool to track all API forms that may appear in the product. These data could be valuable in supporting and defending patent claims for both the product and the manufacturing process.

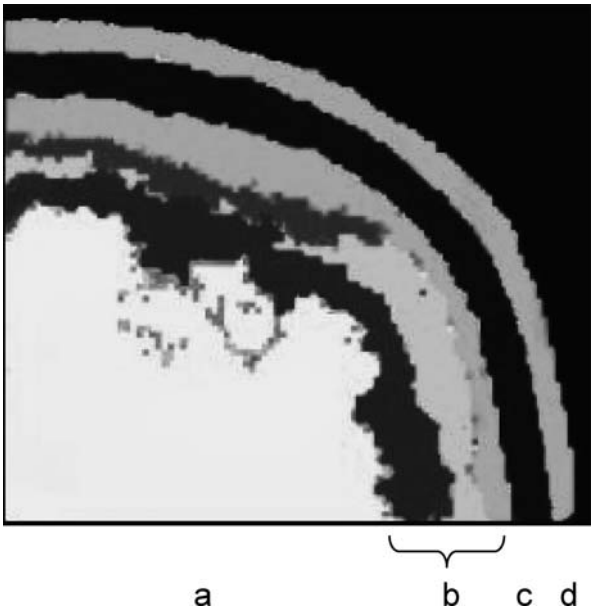

Fig. 9.6. Raman chemical image of a bead formulation. **(a)** Lactose core, **(b)** API (CR layer), **(c)** controlled release layer, and **(d)** API (IR layer)

9.7 API and Formulation Identification

Active pharmaceutical ingredients (API) can be identified using many different analytical approaches. A Raman spectroscopy method may not be the most common or economical but it does offer significant advantages. These include rapid, sensitive analysis, information-rich spectra, minimal or no sampling [32]. Handheld Raman spectrometers now allow the measurement to be taken to samples allowing analysis at the point of receipt and not just in a

QC laboratory. However GMP constraints on sampling and potential for cross contamination may not make this analysis route desirable.

Using Raman spectroscopy for API identification offers significant advantages over more traditional approaches such as FT-IR and HPLC. These advantages include greater specificity and sensitivity; automation, limited or no sample preparation and manipulation, which ensures that no chemical or physical changes occur in the sample, i.e. polymorph conversions. In addition health and safety issues are negated, as contact with the sample by the operator is not required. Finally, Raman spectroscopy selection rules dictate that functional groups with high symmetry produce strong vibrational, whereas functional groups with strong dipoles such as water are weak. Therefore wet or aqueous samples of API can be analysed with ease by Raman which is notoriously difficult with FT-IR.

There are occasions, for example, prior to the release of clinical supplies, when an identification of the API and a formulation label check (i.e. tablet strength) are required. This is often performed by HPLC or UV spectroscopy, both of which require time-consuming sample preparation and analysis. To speed up the analysis time, this test can be performed by single reflection attenuated total reflectance (e.g. Golden Gate^{TM}) FT-IR. However, as API and excipients have similar absorbance properties, low concentration API may not be detected in the bulk of the tablet excipients. Raman spectroscopy offers an added level of sensitivity to this type of analysis as APIs are generally stronger Raman scatterers than excipients making detection of low-level API attainable [48]. This is clearly seen in Fig. 9.7 where the three tablet strengths (placebo, 1 mg and 5 mg) of the same formulation have been analysed by FT-IR and FT-Raman. Discrimination between the three strengths is difficult, if not impossible, by FT-IR, but is obvious by FT-Raman allowing rapid identification of the API and confirmation of the product's label strength.

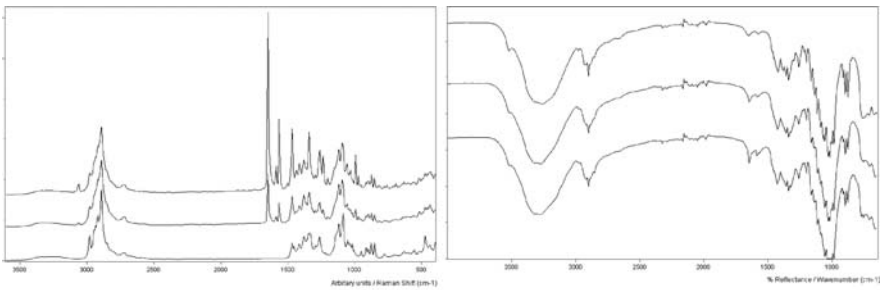

(a) (b)

Fig. 9.7. (a) FT-Raman spectra: *top* to *bottom*: 5 mg active tablet, 1 mg active tablet, placebo. **(b)** ATR FT-IR spectra: *top* to *bottom*: placebo, 1 mg active tablet, 5 mg active tablet

Finally the Raman spectroscopy approach for API identification is not widely used in regulatory documentation. As previously detailed a major reason is that interpretation of Raman spectra is not as advanced as FT-IR. Additionally, Raman spectrometers are relatively more expensive than FT-IR spectrometers, so are more likely to be found in R&D labs rather than QC facilities. However, moving forward the benefits of using a Raman spectroscopy approach will ensure that its usage will become more common and may be adopted into regulatory packages.

9.8 Overall Summary

The use of Raman spectroscopy in pharmaceutical R&D is varied and provides valuable information on API, excipients and formulations alike. It provides methods to analyse solid state materials, some of which produce unique information. Despite its many advantages over other analytical techniques, economic and educational factors currently prevent Raman spectroscopy from becoming a main stream technology. PAT may give the technology a higher profile in the future, but currently it is relegated to niche or supporting activities. It is therefore for practising Raman spectroscopists to promote and implement this versatile spectroscopy in pharmaceutical R&D.

Acknowledgement

Thanks to Shawn Mehrens (Pfizer, Groton, CT, USA) for helpful comments during the preparation of this chapter.

References

1. C.A. Lipinski, F. Lombardo, B.W. Dominy, P.J. Feeney, Adv. Drug. Deliv. Rev. **23**, 3–25. doi:10.1016/S0169-409X(00)00129-0
2. P. Hendra, C. Jones, G. Warnes, *Fourier Transform Raman Spectroscopy Instrumentation and Chemical Applications* (Ellis Horwood, Chichester, 1991), pp. 156–162
3. L.A. Nafie, Annu. Rev. Phys. Chem. **48**, 357–386 (1997)
4. X. Qu, E. Lee, G.-S. Yu, T.B. Freedman, L.A. Naffie, Appl. Spectrosc. **50**(5), 649–657 (1996)
5. R.K. Dukor, Protein conformational studies using vibrational spectroscopy: Comparison of techniques. Paper presented at 232nd ACS national meeting, biophysical and biomolecular symposium: New and emerging techniques for protein characterization, Hilton, San Francisco, 10–14 September 2006
6. K.M. Spencer, R.B. Edmonds, R.D. Rauh, Appl. Spectrosc. **50**(5), 681–685 (1996)
7. D.E. Pivonka, I. Noda, in *Applications of Vibrational Spectroscopy in Pharmaceutical Research and Development*, ed. by D.E. Pivonka, J.M. Chalmers, P.R. Griffiths (Wiley, Chichester, 2007), pp. 109–127

8. D. Pivonka, Appl. Spectrosc. **58**, 323 (2004)
9. D. Pivonka, in *Proceedings of the XXIst International Conference on Raman Spectroscopy*, ed. by R. Withnall, B.Z. Chowdry (IM Publications, Chichester, 2008), pp. 26–29
10. *Pharmaceutical Preformulation and Formulation: A Practical Guide from Candidate Drug Selection to Commercial Dosage Form*, ed. by M. Gibson (Informa Health Care, London), 2001
11. C. Anderton, Am. Pharm. Rev. **10**(3), 34–40 (2007)
12. T. Kojima, S. Onoue, N. Murase, F. Katoh, T. Mano, Y. Matsuda, Pharm. Res. **23**(4), 806–812 (2006)
13. D. Clark, Am. Pharm. Rev. **7**(4), 76–81 (2004)
14. M. Wall, J. Hodkiewicz, P. Henson, Application note 50873; Thermo Electron Corporation, Madison, WI, USA
15. http://www.chem.gla.ac.uk/snap/
16. M. Maiwald, Am. Pharm. Rev. **9**(4), 95–99 (2004)
17. F. Tian, J.A. Zeitler, C.J. Strachan, D.J. Saville, K.C. Gordon, T. Rades, J. Pharm. Biomed. Anal. **40**, 271–280 (2006)
18. F. LaPlant, X. Zhang, Am. Pharm. Rev. **8**, 88–95 (2005)
19. S. Ward, M. Perkins, J. Zhang, C.J. Roberts, C.E. Madden, S.Y. Luk, N. Patel, S.J. Ebbens, Pharm. Res. **22**(7), 1195–1202 (2005). doi:10.1007/s11095-005-6027-4
20. G. Fini, J. Raman Spectrosc. **35**, 335–337 (2004)
21. D.E. Bugay, Proc. SPIE-Int. Soc. Opt. Eng. **3608**, 56–63 (1999)
22. A. O'Grady, A.C. Dennis, D. Denvir, J.J. McGarvey, S.E.J. Bell, Anal. Chem. **73**(9), 2058–2065 (2001)
23. J. Johansson, S. Petterson, S. Folestad, J. Pharm. Biomed. Anal. **39**, 510–516 (2005)
24. J. Johansson, S. Petterson, L.S. Taylor, J. Pharm. Biomed. Anal. **30**, 1223–1231 (2002)
25. D. Pratiwi, J.P. Fawcett, K.C. Gordon, T. Rades, Eur. J. Pharm. Biopharm. **54**(3), 337–341 (2002)
26. A.T.G. De Paepe, J.M. Dyke, P.J. Hendra, F.W. Langkilde, Spectrochim. Acta A **53**, 2261–2266 (1997)
27. F.W. Langkilde, J. Sjoblom, L. Tekenbergs-Hjelte, J. Mrak, J. Pharm. Biomed. Anal. **15**, 687–696 (1997)
28. S.C. Brown, M. Claybourn, V. Fawcett, C. Rodger; Am. Pharm. Rev. **10**(6), 58–67 (2007)
29. M. Sohn, D.S. Himmelsbach, F.E. Barton, Cereal Chem. **81**, 429–433 (2004)
30. R.N. Feudale, Y. Liu, N.A. Woody, H. Tan, S.D. Brown. J. Chemometr. **19**, 55–63 (2005)
31. M.A. Coimbra, A.S. Barros, E. Coelho, F. Goncalves, S.M. Rocha, I. Delgadillo, Carbohydr. Polym. **61**, 434–440 (2005)
32. F.C. Thorley, K.J. Baldwin, D.C. Lee, D.N. Batchelder, J. Raman Spectrosc. **37**, 335–341 (2006)
33. B. Herman, M.J. Parry-Hill, I.D. Johnson, M.W. Davidson, Molecular Expressions Microscopy Primer – Photobleaching – Interactive Java Tutorials (2006)
34. M.-W Pan, R.E. Benner, L.M. Smith, in *Handbook of Vibrational Spectroscopy,* vol. 2, ed. by J.M. Chalmers, P.R. Griffiths (Wiley, Chichester, 2002), p. 490
35. M.J. Pelletier, Appl. Spectrosc. **57**, 20A–42A (2003)

36. A.C. Schmidt, V. Niederwanger, U.J. Griesser, J. Therm. Anal. Calorim. **77**, 639–652 (2004)
37. M. Szelagiewicz, C. Marcolli, S. Cianferani, A.P. Hard, A. Vit, A. Burkhard, M. Von Raumer, U. Ch. Hofmeier, A. Zilian, E. Francotte, R. Schenker, J. Therm. Anal. Calorim. **57**, 23–43 (1999)
38. S.M. Mehrens, U.J. Kale, X. Qu, J. Pharm. Sci. **94**(6), 1354–1367 (2005)
39. K.L.A. Chan, O.S. Fleming, S.G. Kazarian, D. Vassou, G.D. Chryssikos, V. Gionis, J. Raman Spectrosc. **35**, 353–359 (2004). doi:10.1002/jrs.1139
40. D. Clark, A. Pysik, in *Applications of Vibrational Spectroscopy in Pharmaceutical Research and Development*, ed. by D.E. Pivonka, J.M. Chalmers, P.R. Griffiths (Wiley, Chichester, 2007), pp. 213–239
41. H.R.H. Ali, H.G.M. Edwards, M.D. Hargreaves, T. Munshi, I.J. Scowen, R.J. Telford, Anal. Chim. Acta, **602**, 103–112 (2008)
42. B. Allieri, in *Proceedings of the XXIst International Conference on Raman Spectroscopy*, ed. by R. Withnall, B.Z. Chowdry (IM Publications, Chichester, 2008), pp. 139–141
43. J.F. Kauffman, L. Batykefer, D. Tuschel, J. Pharm. Biomed. Anal. (2008) 48(5), 1310–1315. doi:10.1016/j.jpba.2008.09.008
44. L.E. O'Brien, P. Timmins, A.C. Williams, P. York, J. Pharm. Biomed. Anal. **36**, 335–340 (2004)
45. D. Jayawickrama, A.E. Hagrasy, S.-Y. Chang, Am. Pharm. Rev. **9**(7), 10–17 (2006)
46. A. El Hagrasy, S.-Y. Chang, D. Desai, S. Kang, Am. Pharm. Rev. **9**(1), 40–45 (2006)
47. S. Webster, K.J. Baldwin, Pharm. Technol. Eur. **17**(8), 30–35 (2005)
48. C.J. Strachan, T. Rades, K.C. Gordon, J. Rantanen, J. Pharm. Pharmacol. **59**, 179–192 (2007)
49. V. Busignies, B. Leclerc, P. Porion, P. Evesque, G. Couarraze, P. Tchoreloff, Eur. J. Pharm. Biopharm. **64**(1), 38–50 (2006)
50. D. Clark, M. Henson, F. LaPlant, S. Šašić, L. Zhang, in *Applications of Vibrational Spectroscopy in Pharmaceutical Research and Development*, ed. by D.E. Pivonka, J.M. Chalmers, P.R. Griffiths (Wiley, Chichester, 2007), pp. 309–335
51. S. Šašić (ed.), *Pharmaceutical Applications of Raman Spectroscopy* (Wiley, Hoboken, 2007)
52. J. Breitenbach, W. Schrof, J. Neumann, Pharm. Res. **16**(7), 1109–1113 (1999)
53. N.J. Everall, Appl. Spectrosc. **54**(10), 1515–1520 (2000)
54. N.J. Everall, Appl. Spectrosc. **62**(6), 591–598 (2008)
55. D. Clark, in *Proceedings of the XXIst International Conference on Raman Spectroscopy*, ed. by R. Withnall, B.Z. Chowdry (IM Publications, Chichester, 2008), pp. 132–133
56. E. Kang, J. Robinson, K. Park, J.-X. Cheng, J. Control. Release **122**, 261–268 (2007). doi:10.1016/j.conrel.2007.05.007
57. E. Lee, in *Next Generation Spectroscopic Technologies*, ed. by C.D. Brown, M.A. Druy, J.P. Coates, Proc. SPIE **6765**, 67650E-1–67650E-8, (2007). doi:10.1117/12.735006
58. S. Šašić, D.A. Clark, J.C. Mitchell, M.J. Snowden, Analyst **130**, 1530–1536 (2005)
59. A. Belu, C. Mahoney, K. Wormuth, J. Control. Release **126**, 111–121 (2008). doi:10.1016/j.conrel.2007.11.015

60. A. Docoslis, K.L. Huszarik, G.Z. Pappageorgiou, A. Stergiou, E. Georgarakis, AAPSJ **9**(3), E361–E369 (2007), http://www.aapsj.org
61. S. Šašić, Pharm. Res. **24**(1), 58–65 (2007). doi:10.1007/s11095-006-9118-y
62. M.J. Henson, L. Zhang, Appl. Spectrosc. **60**(11), 1247–1255 (2006)
63. S.E. Bell, J.R. Beattie, J.J. McGarvey, K. Laota Peters, N.M.S. Sirimuthu, S.J. Spears, J. Raman Spectrosc. **35**, 409–417 (2004)
64. S. Šašić, M. Whitlock, Appl. Spectrosc. **62**(8), 916–921 (2008)
65. D.F. Steele, P.M. Young, R. Price, T. Smith, S Edge, D. Lewis, AAPSJ **6**(4), 1–4 article number 32 (2004)
66. A. Theophilius, A. Moore, D. Prime, S. Rossomanno, B. Whitcher, H. Chrystyn, Int. J. Pharm. **313**, 14–22 (2006)
67. W.H. Doub, W.P. Adams, J.A. Spencer, L.F. Buhse, M.P. Nelson, P.J. Treado, Pharm. Res. **24**(5), 934–945 (2007). doi:10.1007/s11095-006-9211-2
68. http: //www.wipo.int/pctdb/en/wo.jsp?wo=2003082816

10

Raman Spectroscopy: A Strategic Tool in the Process Analytical Technology Toolbox

Jonas Johansson, Mike Claybourn, and Staffan Folestad

Abstract An overview of the role and use of Raman spectroscopy for advanced process measurements is presented. Special emphasis is given to the potential of Raman spectroscopy as a tool for assessment, monitoring and advanced control of chemical content and crystallinity/polymorphism during pharmaceutical processing. As a Process Analytical Technology (PAT) tool, Raman spectroscopy can add value to both product/process development and to manufacturing processing. The wide range of PAT examples that are reviewed in this chapter emanates from emerging applications in primary and secondary manufacturing processing and in bioprocessing. In addition, strategies and the special requirements on Raman instrumentation for PAT are discussed.

10.1 PAT – An Emerging Revolution in Processing Industry

Assessing quality of materials and processes in real time is, in the pharmaceutical industry, referred to as PAT.[1,2] In broader terms, this is founded on a holistic approach to manufacturing science and has resulted in PAT emerging as a strategic area of new technology. PAT already has had, and will in the future have, a major impact on the way in which the processing industries operates. For the pharma industries, PAT is also leading to major changes in

[1] Guidance for Industry, PAT: A Framework for Innovative Pharmaceutical Development, Manufacturing, and Quality Assurance; U.S. Department of Health and Human Services, Food and Drug Administration, Center for Drug Evaluation and Research (CDER), Center for Veterinary, Medicine (CVM), Office of Regulatory Affairs (ORA), Pharmaceutical CGMPs, September 2004. URL: http://www.fda.gov/cder/guidance/6419fnl.htm. and U.S. Food and Drug Administration (FDA) PAT web site: http://www.fda.gov/cder/OPS/PAT.htm

[2] European Medicines Agency (EMEA) PAT web site: http://www.emea.eu.int/Inspections/PAThome.html

regulation of drug product quality and process validation[3] [1]. The 'mantra' here is process understanding, design, analysis and control, all conducted in a systems approach to Processing and Quality. In addition to new technology, the fundamental guiding principle that PAT rests on is **'quality cannot be tested in, rather it must be designed or built in'**. Here, scientific design and advanced assessment of materials and processes, with respect to intended product quality, yield an in-depth understanding of the product and associated process. Such a structured approach is referred to as quality by design (QbD) for which PAT is a key means. In addition, QbD and PAT provide new routes for control of quality and process output. In Fig. 10.1 the conceptual framework for PAT-based control is depicted. The systems approach goes beyond operating processes solely based on the use of traditional process parameters, such as flows, temperatures. These are mainly indicative of the process conditions whereas complementary information from PAT-based sensors is indicative of the apparent transformation of the material during processing. In all, this constitutes new opportunities for direct prediction of process output and product quality. In technical and scientific terms this translates into advanced means for a holistic control of both process and quality. In summary,

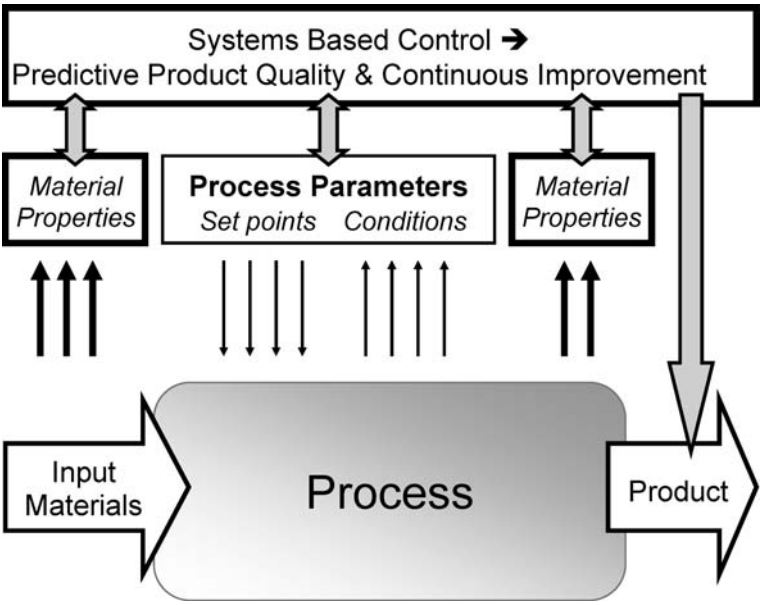

Fig. 10.1. PAT-based control

[3] ICH Q8A Pharmaceutical Development, ICH guidance for industry, May 2006, and ICH Q9A Quality Risk Management, ICH guidance for industry, June 2006, and, ICH Q10 Quality Systems, ICH draft guidance for industry, May 2007, and FDA Guidance for Industry, Process Validation: General Principles and Practices, Nov 2008. All are accessible at FDA web site: http://www.fda.gov/cder/guidance/

PAT-based control provides the basis for a more efficient design, establishment and operation of manufacturing processing where predictive product quality and continuous improvement are two cornerstones of the operational strategy.

Although PAT has gained increased interest since 2004 after publication of the FDA Guidance, the scientific basis of PAT is, however, not new. Rather, it builds on a framework laid out in the mid-1980s by Kowalski and others, when this concept was referred to as Process Analytical Chemistry (PAC) [2]. For more details on the background of PAT (PAC) the reader is referred to the recent reviews by Workman et al. [3–5]. The references therein are also a valuable source of demonstrated PAT applications as well as give a thorough overview of the broad range of different PAT tools. In practice PAT comprises opportunities for measurements in direct connection with manufacturing processes (at-line/online analysis) or even inside chemical and physical processes (in-line analysis). This progress has been enabled by the rapid development within fields such as optronics, computer technology and not least, development of methods for extracting information from complex data matrices (chemometrics). Still, to enable a successful implementation of PAT in the Processing Industries, availability of appropriate and reliable tools for non-invasive and non-destructive measurements of physicochemical properties of materials in situ during chemical and physical processing is a key prerequisite.

Among several techniques possible to design process measurement tools, those based on spectroscopic techniques such as near-infrared (NIR), infrared (IR), Raman, terahertz (THz), fluorescence and UV–Vis absorption offer obvious advantages for PAT owing to their speed, compactness and versatility. Spectroscopic assessment yields chemical information such as content of active pharmaceutical ingredient (API) or of the relative concentration of different ingredients in a suspension, a blend, a composite preparation/formulation. However, physical information may also be obtained that is directly or indirectly related to, for example, particle size, porosity and density. Physical information is particularly valuable in characterisation of manufacturing processes and for reliable prediction of finished product properties.

In the PAT context, Raman spectroscopy is a particularly powerful alternative for advanced process measurements because it can provide high analytical selectivity and sensitivity. Moreover, Raman spectroscopy enables non-invasive and non-destructive measurements in situ. Raman scattering emanates from changes in the polarisability of a molecule where the associated vibrational and rotational energy changes result in a spectrum that in qualitative terms resemble IR spectra. The very high selectivity offered by Raman spectroscopy allows the information on the molecular properties of the measured sample to be interpreted in a straightforward way, directly from the spectral bands. In addition to these qualitative features, Raman also enables accurate quantitative assessment of concentration of compounds in various types of samples: liquids, solids and multiphase samples. Surprisingly, the use of Raman spectroscopy for process analysis in the pharmaceutical industry is so far quite limited compared to the use of NIR. In particularly, since Raman spectroscopy is less sensitive to variations in physical parameters than

NIR, Raman would be expected to offer advantages such as ease of use for quantitative analysis. The reason for less widespread use of process Raman spectroscopy is due in part to more expensive equipment, relative to NIR. A broader implementation of process Raman spectroscopy in the pharmaceutical industry has previously also been hampered by inherent weaknesses in sampling in remote measurements on solids. This is discussed further in Section 10.3.

10.2 Strategic Role of Raman Spectroscopy for PAT

Raman spectroscopy for PAT measurements holds some interesting features such as non-destructive analysis of solids, semi-solids and solid-state transformations. In addition, sampling times as short as down to hundreds of milliseconds offer possibilities for high throughput analysis, which are key in process monitoring and control applications. Ultimately this allows for process intervention if needed. An additional feature is that many common packaging materials (e.g. plastics) are transparent when conducting Raman spectroscopy in the NIR wavelength range, which makes direct inspection of packaged materials possible. As has been discussed above, Raman spectroscopy has the capability to distinguish chemical materials that differ only in physical state. This can be taken advantage of both in spectroscopic and in imaging applications, e.g. allowing for determination of spatial distributions of different ingredients in composite samples such as tablets, capsules and granules. Furthermore, this opens new opportunities for monitoring changes in the physical state of a chemical as an effect of processing, e.g. changes in the polymorphic form of the active pharmaceutical ingredient.

An adequate strategy for when and where to apply Raman spectroscopy-based measurements in manufacturing processing applications is outlined in Figs. 10.2 and 10.3. The strategic role of Raman in process monitoring and control of chemical content and homogeneity is outlined in Fig. 10.2 for primary and secondary manufacturing processing and for bioprocessing, respectively. Analogously, the strategic role of Raman in process monitoring and control of crystallinity and polymorphism is outlined in Fig. 10.3. The underpinning science for this strategy emanates both from the intrinsic features of Raman spectroscopy, as briefly discussed above, and from the review of recent PAT examples demonstrated in the scientific literature. These examples are further discussed in the Section 10.4, where technical details for the various applications are given.

The dashed boxes in Figs. 10.2 and 10.3 represent typical unit operations that are more strategic to monitoring and control through use of Raman spectroscopy, depending on what materials are processed. For example, in primary manufacturing of active pharmaceutical ingredients, the strategic unit operations where application of Raman spectroscopy adds value, typically concerns the synthesis and crystallisation process steps. Notably, demonstrated appli-

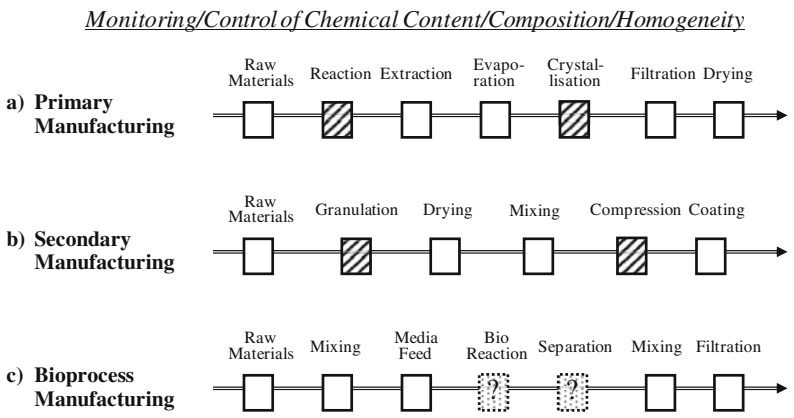

Fig. 10.2. Strategic role of Raman in process monitoring and control of chemical content and homogeneity

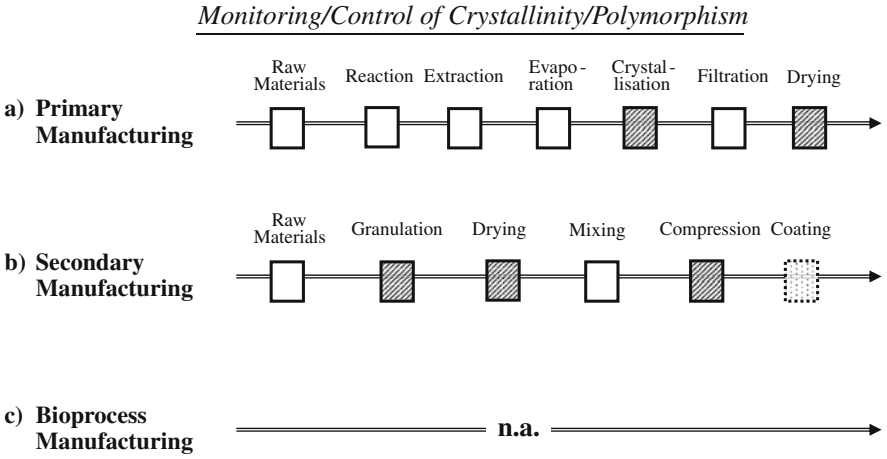

Fig. 10.3. Strategic role of Raman in process monitoring and control of crystallinity and polymorphism

cations so far comprise both at-line measurements, i.e. on samples withdrawn from the process vessel and in-line/online measurements, i.e. measurements conducted in situ in process vessels or in the associated process piping. Also note that the respective series of unit operations described in Figs. 10.2 and 10.3 are not complete. Alternative routes exist, e.g. in secondary manufacturing processing such as in the manufacturing of a tablet product. Powders can be compressed to a tablet after dry mixing or powders can be granulated and thereafter compressed into tablets. The latter route is described in Figs. 10.2 and 10.3. Here, the key dry and wet mixing is conducted during the granulation process step where Raman spectroscopy is an attractive means for

monitoring and control of homogeneity and crystallinity/polymorphism. In addition, Raman spectroscopy is a powerful means to verify the chemical content downstream during the tablet compression process step. Finally, in the area of bioprocessing the role of Raman spectroscopy for monitoring and control is still in an exploratory stage. The few applications demonstrated so far are mainly related to bioreactor and separation process steps as is discussed in Section 10.3.

10.3 In-Process Measurement Equipment

In the manufacturing process environment there are a wealth of process conditions and materials' physical states and chemistry that drive the type of measurement and equipment needed. Typical process monitoring and control applications using Raman spectroscopy will probe specific characteristics and can be used for evaluating key attributes of a material or process, be they static or dynamic. Optimisation of the instrument design and measurement configuration is critical to the success of a process application. Generally, the conventional approach for an in-process Raman measurement is based around a probe that provides both light delivery and Raman scatter collection; this is clearly a backscatter collection geometry. The probe is optically connected to a spectrometer via fibre optics. One of the key advantages of this design is sampling flexibility and relative ease of integration into a manufacturing process. The design of the process measurement then drives the design of the probe based on process requirements such as immersion vs remote or non-contacting probe, working distance, dimensions of sampling, speed of sampling.

There are many types of probes that are designed for specific types of measurement. The important criteria are efficient delivery of the excitation light to the sample, efficient collection of the Raman scattered radiation and removal of background responses. Cooney et al. [6, 7] have compared probe designs for throughput and collection efficiency and have modelled sensitivity and sampling volume. These models are based on transparent samples. In general, pharmaceutical materials and processes are opaque and highly scattering and therefore, the solution is partly driven by an empirical approach and is sample dependent.

A simple probe design for backreflection measurements might be a single light delivery fibre surrounded by an array of collection fibres, so delivery and collection are effectively on the same optical axis. The probe may have a window or lens at the end to improve light delivery and collection and to protect the integrity of the probe. A problem with the use of a fibre-optic-based design is that a Raman signal can be generated in the delivery fibre by interaction with the fused silica matrix [8]. This signal can be intense and degrade the Raman response of the sample. In addition, Fresnel reflected and elastically scattered light from the sample can be captured by the collection fibre, generate a Raman response in the fibre and further degrade the signal. Elimination

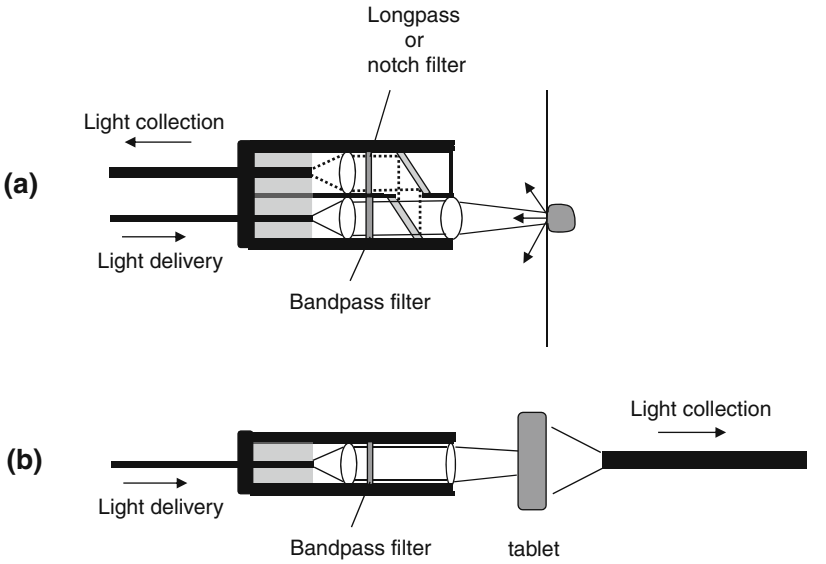

Fig. 10.4. Raman probing principles based on backscatter (**a**) and transmission (**b**) geometry

of the background response from fibre-optic Raman measurements has been described by Myrick and Angel [9]. Most fibre probes are designed around the principles described in this chapter. Figure 10.4a shows a typical probe design that filters background responses. A bandpass filter is positioned at the front of the delivery fibre to remove unwanted Raman from the fibre. A longpass or notch filter is placed in front of the collection fibre(s) to remove the intense light at the laser wavelength propagating through the collection fibre to the analyser.

A typical fibre probe will illuminate the sample with a laser spot whose dimensions are dependent on the launch optics and the position of the sample relative to the probe end. For a static sample, the volume interrogated will depend on the Raman scattering properties, working distance and the acceptance angle of the fibre collection optics. For a sample moving in the laser beam, the sampled volume is also dependent on the time taken for signal averaging and the velocity of the sample.

Non-contact measurements with the probe head sited remotely from the process are well established. Tumuluri et al. [10] have described a probe-based process measurement for monitoring the drug content in an extruded film. A commercially available probe head with a working distance of around 5 cm gave excellent results for quantitative monitoring of the process in real time. Appropriate working distance can be up to tens of centimetres depending on the application. However, for many pharmaceutical processes that involve

particulates such as crystals and powders, light scattering losses can be high and therefore, a closer working distance can be more beneficial.

Immersion probes are in close proximity to the process materials. In order to protect the internal optics of the probe, the housing, including the window material, needs to be chemically resistant or withstand the abrasive nature of moving particles. Immersion probes are typically used for monitoring the reaction chemistry and drug crystallisation in the primary manufacturing processing of the drug molecule. Barnes et al. have used an immersion-based system to monitor the morphological state of a crystalline drug to show the impact of manufacture hold time, post-crystallisation [11]. The probe was a short-focus immersion optic to maximise the signal response for the material to give the sensitivity needed. Immersion probes have also been used for monitoring powder processes including blending [12] and drying [13, 14] and homogenisation of aqueous-based pharmaceutical process [15].

One of the disadvantages of Raman measurements in backreflection mode is sub-sampling because the laser and Raman collection spots are relatively small. An example is Raman measurements on tablet formulations where multipoint measurements or an excitation beam cross-section of the order of a few millimetres is used to get around this problem [16]. A more elegant approach for formulated products is transmission Raman [17] whereby the light is delivered to one side of the sample and collected on the other. A possible arrangement for this is shown in Fig. 10.4b. Matousek and Parker [18] and Johansson et al. [19] have demonstrated this as an effective quantitative approach for bulk properties of pharmaceutical formulations. The light incident on the sample is internally scattered, generating Raman from the bulk of the material. A process instrument designed for transmission Raman gives us significant opportunities for rapid measurements on tablets in a production environment.

The technical development is still very rapid and addresses the growing need within process monitoring. The current trend includes further improvement of instrument design for smaller and more rugged equipment, integration into automated analytical systems and miniaturisation for multiple installations and portability.

10.4 Raman in Manufacturing Application

There is a fast growing number of Raman applications in the pharmaceutical industry reported in the literature. Still, the vast majority of these reports are on lab-based measurements for determination of physical form changes and fairly little is reported about the use of Raman in pharmaceutical manufacturing. In particular, the use of Raman in secondary manufacturing is quite uncommon. In this review we focus on papers published after year 2000.

Folestad et al. reviewed the role of Raman spectroscopy in secondary manufacturing and discussed a strategy for implementing Raman spectroscopy in

pharmaceutical manufacturing. Potential applications were outlined in terms of pharmaceutical unit operations [20]. The use of Raman spectroscopy for in-process analytical applications was further reviewed recently by Rantanen [21]. This review discussed the applications ranging from synthesis of API to stability monitoring of finished product. He also discusses the future challenges for Raman spectroscopy. In another recent review paper the broad use of spectroscopy in the process environment was presented by Ciurczak [22]. The role of Raman spectroscopy was discussed in relation to other spectroscopic techniques and the merits of them were summarised in terms of different process applications. Fini [23] summarised to applications of Raman spectroscopy to pharmacy in a special issue of the *Journal of Raman Spectroscopy*. Strachan et al. [24] reviewed the use of Raman spectroscopy for quantitative analysis of solid pharmaceuticals. They reviewed different applications and discussed remaining issues of quantitative analysis of solids, in particular representative sampling and data evaluation.

In the following, applications of Raman spectroscopy in the pharmaceutical industry with special emphasis on process applications is reviewed. The applications are divided into three processing areas discussed in the strategy section above (Figs. 10.2 and 10.3): primary manufacturing, secondary manufacturing and bioprocessing. The ambition is not to present a full coverage of the literature but to highlight some recent and relevant contributions.

10.4.1 Primary Manufacturing

The application of Raman spectroscopy in primary manufacturing was reviewed by Fevotte [25] who put a special emphasis on crystallisation monitoring. It includes tables of typical applications in crystallisation monitoring and other transient processes, respectively. The author concludes that several open questions such as better calibration procedures, dependence on size distribution and sampling techniques need to be addressed before we will see a wider use of Raman spectroscopy in pharmaceutical manufacturing applications. Yu et al. [26] presented a broader review of crystallisation control including in-line Raman for polymorph monitoring. The authors discuss future developments needed for the respective techniques and point out the potential of Raman spectroscopy for in-line polymorph detection.

Schwartz et al. evaluated the use of fibre-optic probe dispersive Raman and PLS calibration to study crystallisation in a hanging drop experiment. They could show that the lysosome concentration could be monitored during the experiment through the concentration phase, nucleation and crystal growth [27]. In later experiments, they were able to utilise in-line Raman data to control the concentration of lysozyme to affect the crystallisation path and thereby obtaining the desired large single crystals [28]. The same setup was used for crystallisation of apoprotein. Also in this case the Raman data were used to control the evaporation and thus the supersaturation for optimised crystal size [29].

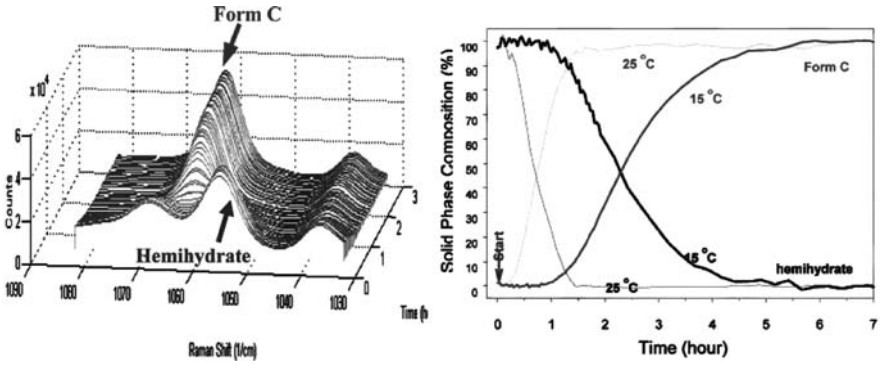

Fig. 10.5. In situ reaction kinetics of polymorphic transition from hemihydrate to form C in a MK-A reaction, Starbuck et al. [30]. Copyright by American Chemical Society

Several authors have addressed the very important aspect of control of solid-state form in primary manufacturing. In complicated reactions where several polymorphic forms as well as solvates compete, in-line monitoring of reaction rates and concentrations is a need in order to optimise the reaction to achieve the desired end result. Starbuck et al. used in-line dispersive Raman spectroscopy to monitor polymorph concentrations of forms A, B, C and D and the concentration of dihydrate, hemihydrate and *N*-methyl pyrrolidinone solvate forms [30]. In Fig. 10.5, a 3D plot shows the time development of the reaction as well as the evaluated formation of form C. Raman spectroscopy was concluded to be most useful for determining reaction rates and turnover pathways. They were able to show that a temperature of 65°C was optimal to achieve maximum turnover from form C to form A. Agrawal et al. studied the influence of different polymeric additives on calcium carbonate crystallisation [31]. Acusol and polyacrylic acid were used as examples of polymers that were used to optimise the precipitation of calcium carbonate. The polymorph content was compared for in-line Raman spectroscopy and XRD showing agreement of about 2%. Ono et al. used in-line Raman to monitor polymorph content of L-glutamic acid during batch cooling crystallisation and the subsequent solvent-mediated transformation of α-form to β-form [32]. By increased temperature the desired α-form yield was optimised.

Falcon et al. explored the benefit of using principal component analysis (PCA) for extracting more information out of crystallisation monitoring [33]. They used a fibre-optic Raman system for in-line probing of antisolvent addition crystallisation of progesterone and concluded that with the aid of PCA subtle changes in the spectra could be used as a warning of the onset of crystallisation. Hu et al. used in-line Raman to monitor both the solid-state formation and solute concentration during crystallisation of an enantiotropic polymorphic system of flufenamic acid [34]. They followed polymorphic com-

position as a function of temperature using an immersion probe Raman spectrometer. In addition, a comparison with particle size monitoring using focused beam reflectance measurement (FBRM) showed a good correlation of the kinetics measured by the two techniques. Kobayashi [35] compared in-line and at-line Raman spectroscopy, NIR spectroscopy and FBRM particle size monitoring on a solid-state transition of taltirelin and timepidium bromide in slurries. It was concluded that Raman spectroscopy is the most suitable of the techniques for these systems although FBRM is useful for establishing indirect correlation to polymorphic transition. Qu et al. studied a carbamazepine system in ethanol–water mixtures using in-line Raman spectroscopy to establish transition mechanism of anhydrous to dihydrated carbamazepine [36]. The reaction kinetics was concluded to be a two-step process of dissolution of anhydrous material and crystallisation of the dihydrated form. Schöll et al. reported on modelling and monitoring of polymorphic transitions of L-glutamic acid [37]. The authors combined Raman spectroscopy, NIR spectroscopy, FBRM and particle vision to study polymorph conversion from α-form to β-form. Caillet et al. developed a calibration model based on relative peak intensities for both concentration and polymorph ratio of anhydrous and monohydrate citric acid in water [38]. Reliable models were reported that were mainly insensitive to both solid concentration and scaling up of the reactor volume. It was commented that the potential issues of sensitivity to particle size distribution and temperature remain to be studied. Ferrari et al. studied polymorphic transitions of α-form to β-form L-glutamic acid [39]. They reported that the transition rate was dependent on scale of operation of the experiment.

O'Sullivan discussed the influence of particle size on quantitative Raman monitoring in slurries [40]. A system of β-form D-mannitol in toluene in the presence of sucrose was studied. It was found that although keeping the number and size of mannitol crystals constant the measured Raman signal varied with different particle size of the sucrose. These results show that particle size must always be taken into consideration in quantitative measurements and a linear relationship can not be taken for granted.

Savolainen et al. investigated the role of Raman spectroscopy for monitoring amorphous content and compared the performance with that of NIR spectroscopy [41]. Partial least squares (PLS) models in combination with several data pre-processing methods were employed. The prediction error for an independent test set was in the range of 2–3% for both NIR and Raman spectroscopy for amorphous and crystalline α-lactose monohydrate. The authors concluded that both techniques are useful for quantifying amorphous content; however, the performance depends on process unit operation. Rantanen et al. performed a similar study of anhydrate/hydrate powder mixtures of nitrofurantoin, theophyllin, caffeine and carbamazepine [42]. They found that both NIR and Raman performed well and that multivariate evaluation not always improves the evaluation in the case of Raman data. Santesson et al. demonstrated in situ Raman monitoring of crystallisation in acoustically levitated nanolitre drops [43]. Indomethazine and benzamide were used as model

systems. The authors also demonstrated SERS in a benzoic acid/Ag colloid system in the same instrumental setup.

Several authors report Raman spectroscopy for use in reaction monitoring. Svensson et al. used an immersion probe in an ethanol/acetic acid/ethyl acetate system and evaluated the use of multivariate approaches and found a similar performance for univariate and multivariate PLS evaluations [44]. McGill et al. compared in-line NIR, Raman and UV spectroscopy and at-line NMR in an esterification reaction of 2-butyl crotonate [45]. The performance of Raman spectroscopy was not as good as for NIR spectroscopy in this study. Ehly et al. studied the effect of scale-up on an esterification of 1-butanol [46]. Both NIR and Raman spectroscopy were used for in-line monitoring. Second-order kinetics was applied to the data and a good agreement was found between the actual and calculated concentration. Reis et al. reported on monitoring in dispersed media using NIR and Raman spectroscopy [47]. The authors discussed the role of elastic light scattering in emulsion and suspension polymerisations and found that it lowered the detected Raman intensity and suggested that this effect could be used to estimate particle size.

10.4.2 Secondary Manufacturing

In the review of Raman applications in primary manufacturing a fairly large number of contributions were found. In secondary manufacturing, on the other hand, reports on Raman monitoring are more unusual, in particular related to in-line monitoring. This may reflect the added complexity of secondary manufacturing and the challenges associated with in-line Raman monitoring in turbid media.

One of the basic unit operations is dry mixing that is used in most manufacturing schemes. In Fig. 10.6, an example of the use of Raman monitoring for blend control is shown. In this case the blending procedure is very fast and the mixture is well blended within the 5 min used. De Beer et al. used an in situ Raman immersion probe setup to study an ibuprofen–xanthan gum

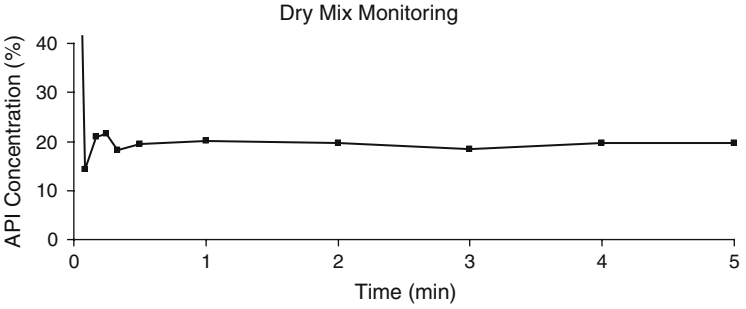

Fig. 10.6. Raman monitoring of dry mixing of propranolol and excipients in a Turbula blender

homogenisation process [15]. Process parameters mixing speed and high concentrations were varied according to an experimental design and a principal component regression model was developed for API concentration. Real-time monitoring of API concentration and endpoint determination was reported successful and the prospect of improved process efficiency and understanding was pointed out. Jayawickrama et al. reported on four different in-line Raman applications [48]. They demonstrated non-contact monitoring of granule blend homogeneity, non-contact monitoring of polymorph transformation of API during high-shear wet granulation, non-contact monitoring of API distribution as a solid suspension in a molten excipient solution and immersion probe monitoring of API solubilisation in a molten excipient. Wikström et al. reported on the use of in situ Raman spectroscopy for high-shear wet granulation monitoring of the transition of anhydrous to monohydrate theophylline using an immersion probe setup [49]. In Fig. 10.7, the transition from anhydrous to monohydrate theophylline is shown. Later, they compared three different probe designs including a large spot probe instrument [50]. They determined effective sampling volumes and could show the significant benefit of going from a point focus to an extended large spot focus. Hausman et al. demonstrated the use of in-line Raman spectroscopy for monitoring of drug hydration state during fluid bed drying [14]. The relation of risedronate sodium hydration state and physical parameters of the tablets was investigated and the final granulation moisture was identified as a critical parameter. Walker

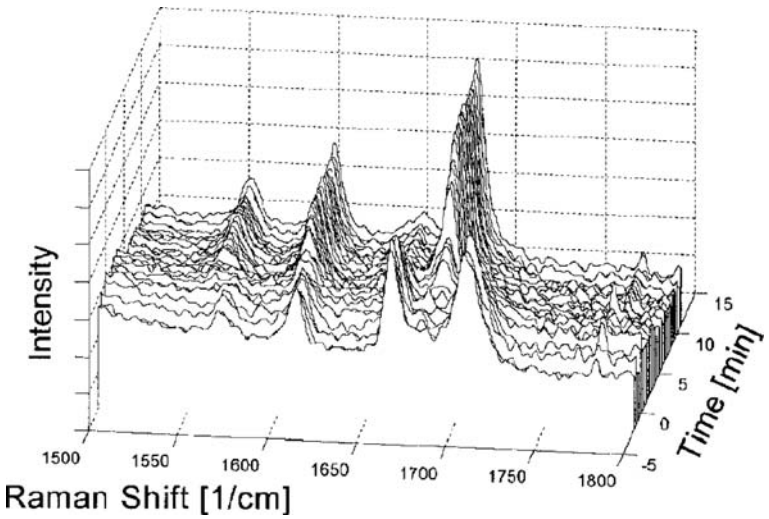

Fig. 10.7. Three-dimensional plot of wet granulation theophylline process. The plot shows transformation from anhydrous to monohydrate form [49]. Copyright by Wiley Liss Inc. and the American Pharmacists Association

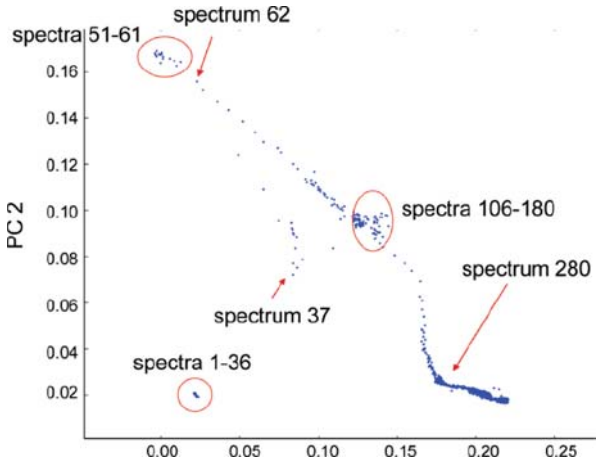

Fig. 10.8. PCA scores plot from a freeze-drying process of mannitol, a solution monitored by in-line Raman spectroscopy [52]. Copyright by American Chemical Society

et al. performed 3D Raman mapping in a fluidised bed to study the distribution of a poloxamer glass bead mixture [51]. The authors also discuss the potential of solid-state determination using Raman to obtain physical information in 3D within a fluidised bed. Tumuluri et al. used Raman spectroscopy to investigate hot-melt extruded films [10]. Quantitative in-line measurements of the content of clotrimazole and ketoprofen in films were reported. In addition, off-line determination of solid-state form of ketoprofen indicated a transition from the API during the hot-melt extrusion procedure. De Beer et al. [52] and Romero-Torres et al. [53] demonstrated the use of in-line Raman spectroscopy for monitoring of freeze-drying of mannitol solutions. Both groups could show the potential for Raman monitoring of physical state changes during the freeze-drying process. Figure 10.8 shows mannitol crystallisation during freeze-drying as measured with Raman spectroscopy [52]. Wikström et al. reported on online monitoring of content uniformity of acetaminophen tablets and discussed sampling statistics of batch characterisation [54].

In addition to the small number of in-line applications reported in the literature, many off-line applications of Raman spectroscopy reported show the potential for in-line use of Raman spectroscopy in a manufacturing environment. Folestad et al. reviewed the role a Raman spectroscopy in secondary manufacturing and discussed potential applications in terms of pharmaceutical unit operations [20]. Results were shown for content uniformity of a tabletting process, Fig. 10.9. Williams et al. used FT-Raman spectroscopy to gain understanding of granulation, tabletting and storage processes and to assess crystalline hydrochloride form versus amorphous free base of the

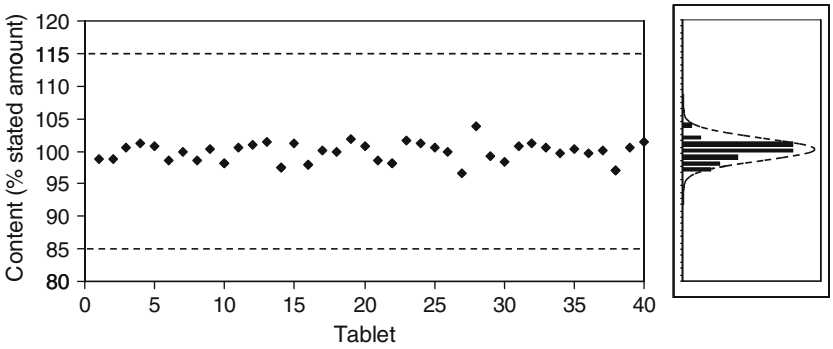

Fig. 10.9. Raman monitoring of tablet content uniformity during tablet manufacturing

API [55]. Romero-Torres et al. used a revolving-focus Raman probe for whole area sampling to characterise coating variations [56]. The authors discuss the role of Raman versus NIR for coating applications and suggest the use of Raman for coating concentration, sample weight increment and tablet disintegration times. Kauffman et al. evaluated different multivariate approaches for determining coating thickness in acetaminophen tablets [57] and found target factor analysis to be a viable method. Several authors have addressed the problem of sub-sampling in tablets. Jedvert et al. [58] and Johansson et al. [16] used and investigated rotating tablet holders for extending the probed surface. Kim et al. described the use of a wide area illumination probe for a similar purpose for process applications [59]. Matousek et al. described the concept Raman sampling in a transmission geometry for further enhanced sampling volume [17] and Johansson et al. [19] presented quantitative aspects and modelling of transmission Raman spectra of tablets and capsules. Transmission Raman is the latest development for improved sampling volumes but is presented in a separate chapter of this book (Chap. 3 by Matousek et al.). Kim et al. described the use of Raman spectroscopy for monitoring the content ambroxol in intact capsules [60]. Kim et al. presented measurements of povidone in solution through plastic bottles [61]. Recently, chemical imaging has been proposed to present PAT opportunities [62].

10.4.3 Bioprocessing

Biopharmaceutics is a fast growing area with many new opportunities for the pharmaceutical industry. Raman process monitoring has some great potential in this field due to its compatibility with water, in contrast to, e.g. IR or THz spectroscopy, although very little has been demonstrated so far. There are also challenges to be considered such as significant fluorescence background

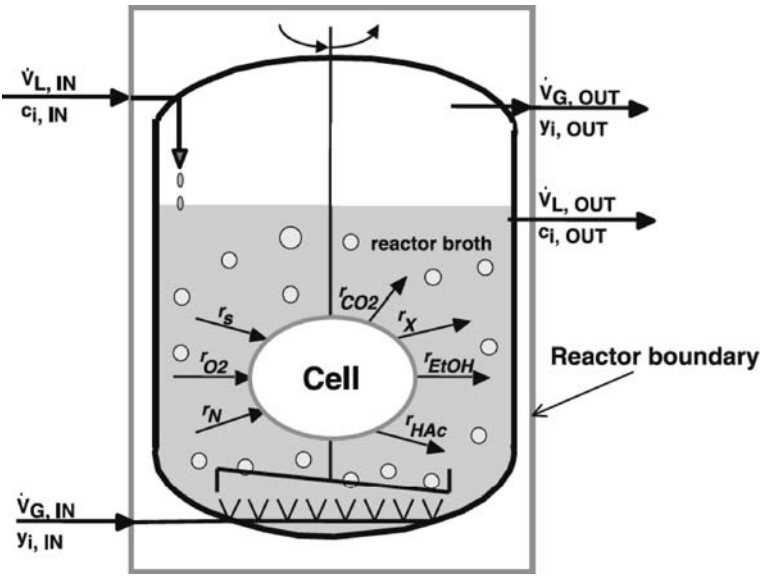

Fig. 10.10. An example of bioprocess reactor chemistry [63]. Copyright by Elsevier Inc.

from these systems. In case of bioprocessing the reaction kinetics can be very complicated. Figure 10.10 shows an example of a bioprocess reactor and in the related paper von Stockar et al. [63] presents a broad review of the field discussing the 'know-how and know-why'. Becker et al. [64] reviewed the large array of bioprocess monitoring possibilities. Ulber et al. [65] and Pons et al. [66] reviewed the large variety of optical sensors with applicability in bioprocess monitoring including Raman spectroscopy. McGovern et al. compared Raman spectroscopy, FT-IR spectroscopy and mass spectrometry to monitor metabolite concentrations in a gibberellic acid process [67]. Different data evaluation schemes were tested including PLS regression and artificial neural networks for improved process understanding. The authors found Raman spectroscopy highly suitable for bioprocess monitoring and discussed the in-line capability of the technique. Lee et al. reported in situ Raman monitoring of glucose, acetate, formate, lactate and phenylalanine in an *Escherichia coli* bioreaction [68]. The Raman spectra were reported to be strongly affected by light scattering by air bubbles, an effect that was corrected for using normalisation against the water Raman signal. Clarke et al. compared Raman spectroscopy with SERS to study fermentation broths from a reaction containing five different penicillins [69]. The authors showed a much improved detection limit with SERS compared with Raman spectroscopy, as shown in Fig. 10.11, but pointed out the difficulties of using the technique as an in-line modality.

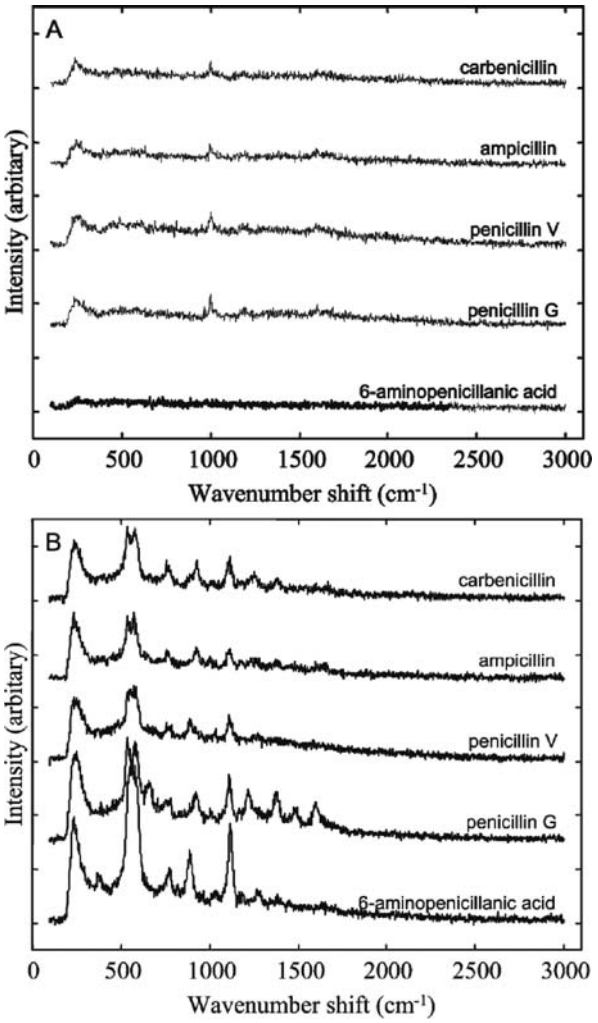

Fig. 10.11. Raman (**A**) and SERS (**B**) spectra of different penicillin samples in fermentation broths [69]. Copyright by the Royal Society of Chemistry

10.5 Future Opportunities and Challenges

Raman spectroscopy has its main strength in the combination of a fairly high chemical selectivity and a true remote sensing capability. In comparison, NIR has been used extensively in the manufacturing industry due to its ruggedness and simplicity with respect to interfacing of probes to process vessels. However, due to fairly poor spectral selectivity it has to be paired with multivariate data evaluation and is thus sometimes considered as a 'black box' technique. Mid-IR, on the other hand, offers a high selectivity and is also well established

in chemical manufacturing. Here, limitations include a poor remote sensing capability in particular regarding solids manufacturing processes such as dry mixing, granulation and tabletting, high water absorption and very poor light penetration in solid samples. Thus, Raman spectroscopy presents very interesting opportunities in pharmaceutical manufacturing processing with its unique features. Further development is, however, needed in some areas for Raman spectroscopy to take the final step and be a widespread tool in pharmaceutical manufacturing.

The influence of particle size has been discussed by, e.g. De Beer et al. [70]. The authors developed a polynomial model for amount of salicylic acid in vaseline ointments and pointed out the necessity of controlling the particle size for quantitative assessment. This is related to the more general problem of quantitative assessment in turbid media in which the optical path length changes with elastic light scattering probability. This effect was studied in greater detail by Abrahamsson et al. for NIR spectroscopy who showed the benefit of simultaneous measurement of light absorption and scattering for solid samples of highly varying morphology [71]. This issue is less of a problem for Raman spectroscopy of solid formulations such as tablets or capsules, for which several authors have shown satisfactory calibrations of content API as discussed above, e.g. [16]. One reason why it appeared to be difficult for crystallisation monitoring [38, 70] may be that in these examples a single Raman scatterer was monitored whose intensity was measured on an absolute scale rather than evaluated against a calibration based on spectral shape including several components.

Fluorescence from excipients is another factor that limits the applicability of Raman spectroscopy. Excipients such as microcrystalline cellulose (MCC) and lactose exhibit very strong fluorescence upon excitation at 785 nm and shorter. This has the effect of filling up the dynamic range of the detector and also introducing the inherent noise associated with the fluorescence increase. This limits the sensitivity of detecting much weaker Raman bands. In order to deal with the fluorescence problem, bleaching by prolonged laser irradiation has been demonstrated [57]. By irradiating a sample for a few minutes the fluorescence background can be substantially lowered. This is, however, not a very attractive solution for process applications where the acceptable sampling time is very short, typically on the order of a sample per second. An alternative approach may be to go to longer excitation wavelengths for which fluorescence excitation efficiency decreases significantly. FT-Raman instruments, for instance, employ Nd:YAG lasers that emit at 1064 nm and result in very low fluorescence but these are not very well suited for process applications. Another possibility is to use dispersive systems at a fairly longer excitation wavelength in the range of 800–900 nm. For excitation at 830 nm much of the Raman emission will still fall within the sensitivity of a silicon-based CCD detector, which has a cut-off at 1050–1100 nm. For excitation wavelengths above 900–1000 nm, another option is dispersive spectrometers employing InGaAs detector elements for better sensitivity in the NIR region.

These are now commercially available although the performance is still inferior to Si-based CCDs. Quite clearly, substantial additional development is needed in this area to achieve the ideal process Raman spectrometer.

Critical to successful spectroscopy in a process environment is to have a thorough understanding of the scale of scrutiny in relation to different process unit operations. Obviously, light penetration in pharmaceutical material is limited typically to a few millimetres due to a high absorption and an even higher elastic light scattering. Although optical path lengths of individual photons are on the order of tens of centimetres [71], the high scattering coefficient will result in quite small sampling volumes. The effect of sampling volume on quantitative assessment has been reported by Johansson et al. [16] for different laser excitation areas and geometries in tablet assessment and by Wikström et al. [50] for different probe types in granulation monitoring. Both studies show the benefit of utilising larger laser spot sizes and thus larger sampling volumes. The important aspect of this is that the sampling volume has to be put into relation to the heterogeneity of the sample, whether it is single tablets or a powder mixture in a granulation vessel and to design the probe in order to attain representative sampling. A further complication for in-line Raman monitoring is that samples often move with a velocity that is high in relation to the required sampling times. As a result the spectral information may change during the acquisition time of a single measurement and will cause a smearing of spectral signatures. This effect has not been studied in detail for Raman spectroscopy; however, similar studies have been carried out for NIR spectroscopy [72] comparing scanning and FT spectrometers. Although data acquisition times are different for Raman spectroscopy, these studies suggest that CCD-based spectrometers are likely to be more suitable for process monitoring in a wider context.

Raman spectroscopy has developed rapidly in the past few years and there are very interesting prospects for future process applications. By building on the fact that Raman spectroscopy is fast, selective, informative and can be remotely coupled to process vessels, it is very likely that we will see Raman spectrometers much more widely used in pharmaceutical manufacturing. Several challenges are still hampering future success in some areas as discussed above. In particular, more efforts on interfacing the Raman spectrometer to different secondary process unit operations are needed before we will see the robust use of the technique.

References

1. C. Potter, S. Folestad, R. Beerbohm, G. Muirhead, S. Roenninger, A. Coupe, A. Swanson, F. Erni, G. Fischer, A guide to EFPIA's mock P.2 document. Pharm. Technol. Int. **18**(12), 39–44 (2006)
2. J.B. Callis, D.L. Illman, B.R. Kowalski, Process analytical chemistry. Anal. Chem. **59**, 624A–637A (1987)

3. J. Workman, M. Koch, D.J. Veltkamp, Anal. Chem. **75**, 2859–2876 (2003)
4. J. Workman, M. Koch, D.J. Veltkamp, Anal. Chem. **77**, 3789–3806 (2005)
5. J. Workman, M. Koch, D.J. Veltkamp, Anal. Chem. **79**, 4345–4364 (2007)
6. T.F. Cooney, H.T. Skinner, S.M. Angel, Appl. Spectrosc. **50**, 836–848 (1996)
7. T.F. Cooney, H.T. Skinner, S.M. Angel, Appl. Spectrosc. **50**, 849–860 (1996)
8. G.E. Walrafen, J. Stone, Appl. Spectrosc. **29**, 337–344 (1975)
9. M.L. Myrick, S.M. Angel, Appl. Spectrosc. **44**, 565–570 (1990)
10. V.S. Tumuluri, M.S. Kemper, I.R. Lewis, S. Prodduturi, S. Majumdar, B.A. Avery, M.A. Repka, Int. J. Pharm. **357**, 77–84 (2008)
11. S. Barnes, J. Gillian, D. Burton, D. Ertl, Am. Pharm. Rev. **11**, 80–85 (2008)
12. T.R.M. De Beer, C. Bodson, B. Dejaegher, B. Walczak, P. Vercruysse, A. Burggraeve, A. Lemos, L. Delattre, Y.V. Heyden, J.P. Remon, C. Vervaet, W.R.G. Baeyens, J. Pharm. Biomed. Anal. **48**, 772–779 (2008)
13. G.M. Walker, S.E.J. Bell, K. Greene, D.S. Jones, G.P. Andrews, Chem. Eng. Sci. **64**, 91–98 (2009)
14. D.S. Hausman, R.T. Cambron, A. Sakr, Int. J. Pharm. **299**, 19–33 (2005)
15. T.R.M. De Beer, W.R.G. Baeyens, J. Ouyang, C. Vervaet, J.P. Remon, Analyst **131**, 1137–1144 (2006)
16. J. Johansson, S. Pettersson, S. Folestad, J. Pharm. Biomed. Anal. **39**, 510–516 (2005)
17. P. Matousek, A.W Parker, Appl. Spectrosc. **60**, 1353–1357 (2006)
18. P. Matousek, A.W Parker, J. Raman Spectrosc. **38**, 563–567 (2007)
19. J. Johansson, A. Sparén, O. Svensson, S. Folestad, M. Claybourn, Appl. Spectrosc. **61**, 1211–1218 (2007)
20. S. Folestad, J. Johansson, Eur. Pharm. Rev. **8**, 36–42 (2003)
21. J. Rantanen, J. Pharm. Pharmacol. **59**, 171–177 (2007)
22. E.W. Ciurczak, Pharm. Manuf. July/August 18–26 (2008)
23. G. Fini, J. Raman Spectrosc. **35**, 335–337 (2004)
24. C.J. Strachan, T. Rades, K.C. Gordon, J. Rantanen, J. Pharm. Pharmacol. **59**, 179–192 (2007)
25. G. Fevotte, Chem. Eng. Res. Des. **85**, 906–920 (2007)
26. Z.Q. Yu, J.W. Chew, P.S. Chow, R.B. Tan, Eng. Res. Des. **85**, 893–905 (2007)
27. A.M. Schwartz, K.A. Berglund, J. Cryst. Growth **203**, 599–603 (1999)
28. A.M. Schwartz, K.A. Berglund, J. Cryst. Growth **210**, 753–760 (2000)
29. R.E. Tamagawa, E.A. Miranda, K.A. Berglund, Cryst. Growth Des. **2**, 263–267 (2002)
30. C. Starbuck, A. Spartalis, L. Wai, J. Wang, P. Fernandez, C.M. Lindeman, G.X. Zhou, Z. Ge, Cryst. Growth Des. **2**, 515–522 (2002)
31. P. Agrawal, K.A. Berglund, Cryst. Growth Des. **3**, 941–946 (2003)
32. T. Ono, J.H. ter Horst, P.J. Jansens, Cryst. Growth Des. **4**, 465–469 (2004)
33. J.A. Falcon, K.A. Berglund, Cryst. Growth Des. **4**, 457–463 (2004)
34. Y. Hu, J.K. Liang, A.S. Myerson, L.S. Taylor, Ind. Eng. Chem. Res. **44**, 1233–1240 (2005)
35. R. Kobayashi, Y. Fujimaki, T. Ukita, Y. Hiyama, Org. Process Res. Dev. **10**, 1219–1226 (2006)
36. H. Qu, M. Louhi-Kultanen, J. Rantanen, J. Kallas, Cryst. Growth Des. **6**, 2053–2060 (2006)
37. J. Schöll, D. Bonalumi, L. Vicum, M. Mazzotti, M. Müller, Cryst. Growth Des. **6**, 881–891 (2006)

38. A. Caillet, F. Puel, G. Fevotte, Int. J. Pharm. **307**, 201–208 (2006)
39. E.S. Ferrari, R.J. Davey, Cryst. Growth Des. **4**, 1061–1068 (2004)
40. B. O'Sullivan, P. Barret, G. Hsiao, A. Carr, B. Glennon, Org. Process Res. Dev. **7**, 977–982 (2003)
41. M. Savolainen, K. Jouppila, O. Pajamo, L. Christiansen, C. Strachan, M. Karjalainen, J. Rantanen, J. Pharm. Pharmacol. **59**, 161–170 (2007)
42. J. Rantanen, H. Wikström, F.E. Rhea, L.S. Taylor, Appl. Spectrosc. **59**, 942–951 (2005)
43. S. Santesson, J. Johansson, L.S. Taylor, I. Levander, S. Fox, M. Sepaniak, S. Nilsson, Anal. Chem. **75**, 2177–2180 (2003)
44. O. Svensson, M. Josefson, F.W. Langkilde, Chemometr. Intell. Lab. Syst. **49**, 49–66 (1999)
45. C.A. McGill, A. Nordon, D. Littlejohn, Analyst **127**, 287–292 (2002)
46. M. Ehly, P.J. Gemperline, A. Nordon, D. Littlejohn, J.K. Basford, M. DeCecco, Anal. Chim. Acta **595**, 80–88 (2007)
47. M.M. Reis, P.H.H. Araújo, C. Sayer, R. Giudici, Anal. Chim. Acta **595**, 257–265 (2007)
48. D. Jayawickrama, A. El Hagrasy, S.-Y. Chang, Am. Pharm. Rev. **9**, 10–17 (2006)
49. H. Wikström, P.J. Marsac, L.S. Taylor, J. Pharm. Sci. **94**, 209–219 (2005)
50. H. Wikström, I.R. Lewis, L.S. Taylor, Appl. Spectrosc. **59**, 934–941 (2005)
51. G. Walker, S.E.J. Bell, M. Vann, D.S. Jones, G. Andrews, Chem. Eng. Sci. **62**, 3832–3838 (2007)
52. T.R.M. De Beer, M. Allesø, F. Goethals, A. Coppens, Y. Vander Heyden, H. Lopez De Diego, J. Rantanen, F. Verport, C. Vervaet, J.P. Remon, W.R.G. Baeyens, Anal. Chem. **79**, 7992–8003 (2007)
53. S. Romero-Torres, H. Wikström, E.R. Grant, L.S. Taylor, J. Pharm. Sci. Technol. **61**, 131–145 (2007)
54. H. Wikström, S. Romero-Torres, S. Wongweragiat, J.A. SuartWilliams, E.R. Grant, L.S. Taylor, Appl. Spectrosc. **60**, 672–681 (2006)
55. A.C. Williams, V.B. Cooper, L. Thomas, L.J. Griffith, C.R. Petts, S.W. Booth, Int. J. Pharm. **275**, 29–39 (2004)
56. S. Romero-Torres, J.D. Pérez-Ramos, K.R. Morris, E.R. Grant, J. Pharm. Biomed. Anal. **38**, 270–274 (2005)
57. J.F. Kauffman, M.D. Dellibovi, C.R. Cunningham, J. Pharm. Biomed. Anal. **43**, 39–48 (2007)
58. I. Jedvert, M. Josefson, F. Langkilde, J. Near Infrared Spectrosc. **6**, 279–289 (1998)
59. M. Kim, H. Chung, Y. Woo, M. Kemper, Anal. Chim. Acta **579**, 209–216 (2006)
60. J. Kim, J. Noh, H. Chung, Y.A. Woo, M. Kemper, Y. Lee, Anal. Chim. Acta **598**, 280–285 (2007)
61. M. Kim, H. Chung, Y. Woo, M.S. Kemper, Anal. Chim. Acta **587**, 200–207 (2007)
62. A.A. Gowen, C.P. O'Donnell, P.J. Cullen, S.E.J. Bell, Eur. J. Pharm. Biopharm. **69**, 10–22 (2008)
63. U. von Stockar, S. Valentinotti, I. Marison, C. Cannizzaro, C. Herwig, Biotechnol. Adv. **21**, 417–430 (2003)
64. T. Becker, B. Hitzmann, K. Muffler, R. Pörtner, K.F. Reardon, F. Stahl, R. Ulber, Adv. Biochem. Eng. Biotechnol. **105**, 249–293 (2007)
65. R. Ulber, J.-G. Frerichs, S. Beutel, Anal. Bioanal. Chem. **376**, 342–348 (2003)

66. M.-N. Pons, S. Le Bonté, O. Potier, J. Biotechnol. **113**, 211–230 (2004)
67. A.C. McGovern, D. Broadhurst, J. Taylor, N. Kaderbhai, M.K. Winson, D.A. Small, J.J. Rowland, D.B. Kell, R. Goodacre, Biotechnol. Bioeng. **78**, 527–538 (2002)
68. H.L.T. Lee, P. Boccazzi, N. Gorret, R.J. Ram, A.J. Sinskey, Vib. Spectrosc. **35**, 131–137 (2004)
69. S.J. Clarke, R.E. Littleford, W.E. Smith, R. Goodacre, Analyst **130**, 1019–1026 (2005)
70. T.R.M. De Beer, W.R.G. Baeyens, Y. Vander Heyden, J.P. Remon, C. Vervaet, F. Verport, Eur. J. Pharm. Sci. **30**, 229–235 (2007)
71. C. Abrahamsson, A. Löwgren, B. Strömdahl, T. Svensson, S. Andersson-Engels, J. Johansson, S. Folestad, Suppl. Spectr. **59**, 1381–1387 (2005)
72. O. Berntsson, L.-G. Danielsson, S. Folestad, Anal. Chim. Acta **431**, 125–131 (2001) and 91–98 (2009)

11

Emerging Dental Applications of Raman Spectroscopy

Lin-P'ing Choo-Smith, Mark Hewko, and Michael G. Sowa

Abstract Until recently, the application of Raman spectroscopy to investigate dental tissues has primarily focused on using microspectroscopy to characterize dentin and enamel structures as well as to understand the adhesive interface of various resin and bonding agents used in restorative procedures. With the advent of improved laser, imaging/mapping and fibre optic technologies, the applications have expanded to investigate various biomedical problems ranging from oral cancer, bacterial identification and early dental caries detection. The overall aim of these applications is to develop Raman spectroscopy into a tool for use in the dental clinic. This chapter presents the recent dental applications of Raman spectroscopy as well as discusses the potential, strengths and limitations of the technology in comparison with alternative techniques. In addition, a discussion and rationale about combining Raman spectroscopy with other optical techniques will be included.

Key words: dental, oral cavity, cancer, microorganisms, materials characterization, enamel, caries, polarized Raman spectroscopy, optical coherence tomography, clinic, fibre optics

Abbreviations: PRS – polarized Raman spectroscopy, OCT – optical coherence tomography

Symbols: $\rho-$ Raman depolarization ratio, r – correlation coefficient

11.1 Introduction

The evolution of lasers and detectors has enabled Raman spectra of high signal-to-noise ratio to be acquired in shorter time frames with lower laser powers, thus opening up new possibilities for Raman spectroscopic analysis of biological samples. Some applications have evolved to the point that it is no longer necessary to excise out the sample and bring it to the spectrometer for analysis. Rather, with fibre-optic probe technology, it is now possible

to leave the sample in situ or in vivo for examination [1–4]. These key advancements have allowed in vivo measurements using Raman spectroscopy to further understand problems of relevance to human health. For non-invasive or minimally invasive Raman measurements of human tissues, accessibility is still a key criterion. Unless there is an invasive surgical incision by which a Raman probe can gain access to the tissue of interest, the technology is initially limited to accessible tissues such as skin and superficial layers of underlying tissues. Another means of gaining access to internal organs without surgery is via natural openings and orifices of the body. One such access point is the oral cavity. Through the oral cavity various established endoscopic procedures already exist whereby clinicians gain access to respiratory and gastrointestinal organs for further examination. However, the oral cavity itself has clinical significance and this chapter will review some of the emerging applications of Raman spectroscopy in the field of dentistry which deals with the diagnosis and treatment of human diseases of the oral cavity. The oral cavity is a natural starting point for the development of in vivo Raman applications due to its relatively accessible state. Not only is the oral cavity a portal for access to internal organs, in recent years, it is believed there is a connection between the oral cavity and systemic health. It is thought that the oral cavity can serve as a window to provide clues and manifestations of systemic diseases that are not yet detected but are underlying within the human body. Similarly oral infections could be linked to systemic diseases [5–7].

11.2 Dental Applications of Raman Spectroscopy

The diseases of the oral cavity can be divided into three main regions. Those that affect (a) the soft tissues, (b) the hard tissues and finally, those involving (c) microorganisms of the oral cavity. Despite the wealth of disorders and conditions involving the oral cavity, early dental applications of Raman spectroscopy have primarily focused on using (micro)spectroscopy to characterize dentin and enamel structures as well as to understand the adhesive interface of various resin and bonding agents used in restorative procedures [8–10]. Thus, the key interest has been largely from those involved with biomaterials characterization and the development of appropriate and improved components for restorative dentistry applications. With the advent of improved lasers, imaging/mapping capabilities and fibre-optic technologies, the applications have expanded to investigate various biomedical problems ranging from oral cancer, bacterial identification and early dental caries detection. The overall aim of these applications is to develop Raman spectroscopy into a tool for use in the dental clinic.

11.3 Oral Soft Tissue Pathology by Raman Spectroscopy

Much of the research in this area has focused on examining oral lesions and oral cancers. Oral cancers are among the top 10 cancers globally and are the leading form of cancers in developing countries such as India and South Asian countries [11]. As there is already a chapter that focuses on the application of Raman spectroscopy for early cancer detection and diagnosis (see Chapt. 13 by Stone et al.), a comprehensive review in this area will not be repeated here. Interested readers are directed to recent studies by Oliveira et al. that include the use of FT-Raman spectroscopy with 1064 nm laser excitation to investigate healthy, dysplastic and squamous cell carcinomal tissues of the oral cavity. Spectral changes between normal and malignant tissue are attributed to compositional, conformation and structural changes of proteins with a possible increase in protein content in malignant epithelia [12]. Using principal component analysis, the sensitivity and specificity were 91% and 69%, respectively, in the training set, with 100% sensitivity and 55% specificity using a prospective test set. In addition, Malini et al. have used NIR laser excitation to examine samples from healthy, inflammatory, pre-malignant and malignant tissues [11]. The spectra of healthy control tissue are dominated by lipid bands likely due to the bilayer membrane of the squamous epithelial surface. On the other hand, inflammatory, pre-malignant and malignant tissues have spectra that are dominated by protein bands due to the increased amounts of surface proteins such as receptor proteins, enzymes, antigens and antibodies as a result of the disease. Using PCA analysis, it was possible to differentiate healthy from diseased tissue but the discrimination between the three pathological states was poor. When coupling PCA with multiparameter limit tests, correct classification of the four tissue types was obtained. The group of de Veld et al. used autofluorescence and Raman spectroscopy to investigate oral mucosal tissue sections [13]. Autofluorescence images had contributions derived from keratin and connective tissue fluorophores (e.g. elastin and collagen) but cluster analysis did not reveal any obvious clustering by lesion type or cell layer. Cluster analyses of Raman spectra enabled classification of the spectra according to cell layers although only non-significant differences between spectra of various lesion types could be identified. Other earlier Raman spectroscopic studies related to oral cancer can be found in the following references [14, 15]. For the most part, the various studies above involve ex vivo tissue samples. To date, the only in vivo Raman spectroscopic study of oral lesions was reported by Bakker Schut et al. where dysplasia in the epithelium of the palate of a rat was used as a model of early cancer [16]. With specialized in-the-tip filtered Raman fibre-optic probes and laser excitation at 830 nm, Raman spectra were acquired for 100s and used to train a tissue classification model. Using multivariate statistical analyses and an independent test set of spectra acquired for 10s, the model was developed to classify healthy from

low-grade and high-grade dysplasia (i.e. carcinoma in situ). The sensitivity and specificity values for distinguishing healthy from high-grade dysplastic tissue was 1.0 and 1.0, respectively, with values of 0.93 (specificity) and 0.78 (sensitivity) for distinguishing healthy from low-grade dysplasia.

11.4 Raman Spectroscopy for Identifying Oral Pathogens

Human oral microorganisms found above the gum line that are of clinical relevance are those from the *Streptococci* group, with *Streptococcus mutans* of particular interest as it can accumulate within dental plaque found on tooth surfaces. High levels of *S.mutans* are correlated with high dental caries risk, i.e. tooth decay. There have only been a few studies by the group of Berger et al. that involve the use of near-infrared Raman spectroscopy to study oral bacteria [17–19]. In an initial study, it was shown that Raman spectroscopy followed by cluster analysis was able to identify and separate out spectra derived from pure cultures of *S. mutans*, *S. sanguis*, *S. intermedius* and *S. oralis* on agar plates, with 93.7% success rate. In a follow-up study, using partial least-squares analysis, it was possible to discriminate and quantify Raman spectra of bacteria obtained directly in a solid mixture of *S. mutans* and *S. sanguis*. The root mean square error was $< 5\%$. More recently, Raman spectra of bacterial mixtures of *S. mutans*, *S. sanguis* and *S. gordonii* could be quantified with relative fractions of each species predicted with a root mean square error of 0.07. Overall therefore, Raman spectroscopy has potential as a tool for the quantification of microbial mixtures such as those found in oral plaque.

11.5 Characterizing Dental Materials with Raman Spectroscopy

Classically, Raman spectroscopy has been a valuable tool in understanding various properties of dental biomaterials. This has been the emphasis and continues to be a large emphasis of the dental application of Raman spectroscopy. This is a vast field that predominantly focuses on understanding the mechanical, physical and chemical properties of various agents and their interaction with human enamel and/or dentin. In addition, the majority of these studies involve Raman microspectroscopy where the microscope interface is the primary means of focusing the laser excitation light and collecting the backscattered Raman signal. The overall aims of these studies are to understand the nature of these interactions whereby stronger and/or more effective agents or materials are used in vivo for various restorative or prosthodontic dentistry applications. In so doing, there is less tendency for the restorative materials to crack, break or fail which would precipitate pain and discomfort

for the patient and a need for a return visit to fix the failed restorative component. Some recent topics in the literature include the effects of cosmetic treatments such as bleaching agents on tooth structure [20]. These studies have examined the tooth surfaces pre- and post-treatment and found that there can be adverse effects on the mineral and organic components. Other studies have used Raman spectroscopy to investigate the curing of dental polymers [21], to examine the adhesive–dentin interface [22] as well as investigate the adhesive bond strength [23]. Furthermore, other reports include investigating the biocompatibility of dental materials [24] and examining the coatings (e.g. hydroxyapatite, titanium) of dental implants in order to develop better materials of improved strength and performance for prosthodontic applications [25, 26]. Many of these studies are correlated with biomechanical tests to validate the biochemical understanding obtained with Raman spectroscopy. As this chapter will focus on emerging dental applications aimed at developing new tools and techniques for human disease understanding and detection, a comprehensive review of the topic of dental materials characterization is beyond the scope of this chapter. Interested readers are directed to recent papers by the groups of Spencer and Wang [22, 27], Marshall [28], Martin [21, 24] and various recent abstracts from conference meetings of the International Association for Dental Research.

11.6 Raman Spectroscopy of Oral Hard Tissues

11.6.1 Biochemical Composition and Raman Spectra of Teeth

The dominant hard tissue in the oral cavity is the teeth. Teeth play the critical role of chewing, breaking and grinding up food thereby facilitating digestion and absorption of nutrients within the gastrointestinal tract. The cutting, grinding and mixing function requires that teeth must withstand a significant amount of wear and tear forces. Therefore, nature has designed that the hardest structure of the human body is the enamel crown which covers the exposed portion of the tooth (Fig. 11.1). The enamel is a highly mineralized acellular tissue composed of 80–90% by volume of crystals of carbonated calcium hydroxyapatite ($Ca_{10}(PO_4)_6(OH)_2$ where PO_4^{3-} can be substituted by CO_3^{2-}), with the remaining 10–20% being fluid and organic (mainly collagen protein) material [29]. In enamel, the carbonated apatite crystals are arranged into bundles to form rods or prisms with intercrystalline spaces between rods, i.e. crystalline lattices of hydroxyapatite. Underlying the enamel crown is the dentin which is composed of 75% inorganic material, 20% organic material (primarily collagen) with the remaining 5% made up by water and other materials. It is, therefore, less mineralized and softer than enamel [30]. Traces of other minerals such as magnesium, sodium, potassium, fluoride (e.g. in enamel) and chloride are also found in enamel and dentin. Dentin is the dominant component of the tooth which extends the entire tooth down to

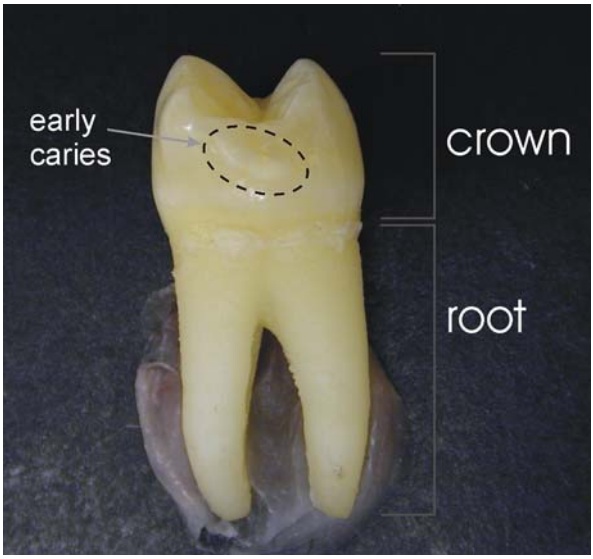

Fig. 11.1. Photograph of the distal surface of an extracted permanent human premolar containing an early carious lesion (*white* spot)

the root tips. Though enamel is the hardest substance of the human body, it is a brittle rigid structure with high elastic modulus and low tensile strength [30]. Relative to enamel, dentin is comparatively flexible allowing it to support the non-resilient enamel. Both enamel and dentin have very similar biochemical composition to bones where the dominant component is also carbonated hydroxyapatite. Chapter 14 by Michael Morris focuses on various Raman spectroscopic studies of bones and diseases related to bone. With all these mineralized tissues (enamel, dentin, bone), adverse changes in the biochemical composition lead to weakening of the tissue structural integrity thus resulting in disease.

Since carbonated hydroxyapatite is the dominant component of dental tissues, it is not surprising to find that the fingerprint region of Raman spectra acquired of healthy enamel and dentin are dominated by peaks arising from phosphate groups of apatite (Fig. 11.2). Several spectral peak assignments of enamel and dentin are summarized in Table 11.1. The prominent peak is the symmetric stretching ν_1 mode of phosphate (PO_4^{3-}) at 959 cm^{-1}. The peak position is characteristic of type B carbonated biological apatite (where CO_3^{2-} substitutes PO_4^{3-} versus type A carbonated apatite where CO_3^{2-} substitutes OH^-). This is in contrast to synthetic hydroxyapatite where the peak maximum is typically at ∼962–964 cm^{-1} [31, 32]. The higher peak position of the synthetic variant indicates that it has a higher mineral crystallinity compared to the carbonated-substituted hydroxyapatite where the crystal packing is less tight and therefore crystallinity is lower. The various other PO_4^{3-} vibrations observed are the ν_2 symmetric bending mode, the ν_3

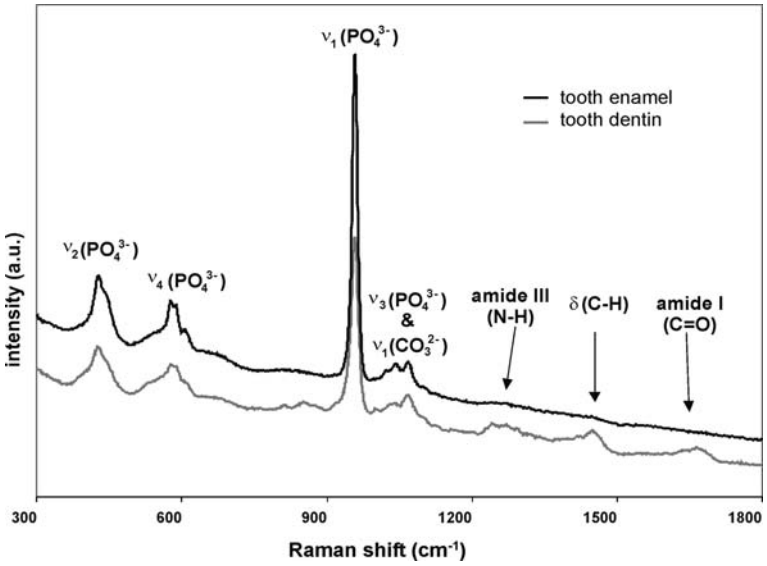

Fig. 11.2. Representative Raman spectra in the fingerprint region of human tooth enamel and dentin. Peak assignments are marked

Table 11.1. Raman spectral peak assignments of human tooth enamel and dentin

Peak (cm^{-1})	Assignment
959	ν_1 symmetric stretching mode of PO_4
431, 446	ν_2 symmetric bending mode of PO_4
1023, 1043, 1052, 1069	ν_3 asymmetric stretching mode of PO_4
579, 590, 608, 614	ν_4 asymmetric bending mode of PO_4
1104	ν_1 symmetric stretching mode of type A CO_3
1069	ν_1 symmetric stretching mode of type B CO_3
∼1242	Amide III (N–H)
∼1450	C–H bending mode
∼1665	Amide I (C=O)

asymmetric stretching mode and the ν_4 asymmetric bending vibrations (see Table 11.1 for peak positions). Mixed in with the ν_2 mode is the ν_1 symmetric stretching mode of type B CO_3^{2-}. The enamel spectrum does not show significant peaks from other moieties aside from apatite. The spectrum of dentin on the other hand, along with peaks from carbonated hydroxyapatite, contains several additional bands that can be assigned to be characteristic of the protein collagen. These spectra correlate well with the different biochemical compositions of these tissue types, suggesting that Raman spectroscopy is well suited for studying dental hard tissues.

11.6.2 Raman Spectroscopy of Dental Caries

Clinical Problem

Caries is the clinical term for tooth decay and most people are familiar with the term cavities. Cavities are actually advanced clinical endpoints of tooth decay whereby regions of tooth structure and integrity have deteriorated to the point that the structure collapses to form a hole or cavity. Dental caries results from the destruction of tooth structure due to acid leaching of calcium and phosphate ions from minerals of the tooth (i.e. a process known as demineralization) resulting in a porous weak structure. The acid is secreted from bacteria that harbour in dental plaque biofilm formed on tooth surfaces. Dental caries is a chronic infectious disease that is experienced by most individuals at some point in their life [33]. Caries is the most common chronic disease in childhood. Despite the decline in the incidence of caries in the western world due to improved prevention methods such as water fluoridation and fluoride in toothpastes and mouth rinses, there are still large segments of the population who suffer from this disease. With appropriate oral health hygiene, caries is deemed a preventable disease. However, where prevention is not possible, it is still feasible to repair the early uncavitated caries lesion through conservative non-surgical treatment strategies such as fluoride for remineralization, sealants and anti-microbials. Unfortunately, when cavitation occurs, the only treatment option is surgical intervention involving drilling and placing of fillings. Current diagnostic clinical methods involving visual inspection and tactile examination with the dental explorer rely on subjective clinical criteria such as colour, softness and resistance to removal. Furthermore, carious lesions that are visible on conventional dental radiographs have already 30–40% mineral loss before they are detected radiographically and thus are already more advanced lesions [34].

Early dental caries (incipient lesions) are non-cavitated and limited to the outer enamel surface. Clinically, these lesions are identified as visible "white spots" when the tooth is air-dried (Fig. 11.1). The incipient lesion is known as a subsurface lesion since the surface appears intact. However, histological investigations have shown that below the surface, there are zones that vary in porosity (voids from mineral loss) as well as biochemical composition (e.g. fluoride, water and carbonate content) [29]. The enamel caries can vary from a depth of ∼100–250 μm (for incipient caries) to entirely through the enamel (∼1.5 mm deep), at which point the cavitated lesion has extended into the underlying dentin [35]. The diagnostic challenge remains early caries detection and the focus has been on caries lesions that form on the tooth crown affecting the enamel. The remainder of the discussion will therefore concentrate on enamel caries.

Conventional Raman Spectroscopy of Dental Caries

The application of Raman spectroscopy for studying dental caries began about a decade ago. At that time, the team of Hill and Petrou used Raman

spectroscopy with 1064 nm laser excitation to characterize dental caries [36, 37]. In these studies, the spectral difference observed between sound and advanced carious regions was based on the broadband fluorescence background of unknown origin. Spectra of early lesions very closely resembled sound enamel. In a subsequent study, this same group used 785 nm laser excitation and a fibre-optic probe to acquire intra-oral Raman spectra. Similar findings were obtained largely based on the spectral background feature. These initial studies demonstrate that intra-oral Raman spectroscopic analysis of carious lesions is feasible. Since then, various research groups have further examined the utility of Raman spectroscopy for caries characterization [38–41]. For example, using Raman microspectroscopy to examine human tooth samples that have been sectioned, Kinoshita et al. observed decrease intensity of the 960 cm^{-1} phosphate peak at regions of pit and fissure caries (i.e. those formed on pits at chewing surfaces) and attributed to demineralization. In these regions, the amide I intensity was increased and reported to be derived from organic component as the region was visibly blackened in the more advanced pit and fissure caries. Bulatov et al. reported decreasing intensity of the 960, 1070 and 590 cm^{-1} peaks in going from sound enamel to moderate fissures and advanced caries. Many of these studies reported on more advanced caries which are already discoloured brown or black. Methods such as Hill and Petrou mainly focused on the difference in the fluorescence/luminescence between sound and carious regions of the tooth. As outlined in other sections of this book, in biological tissues, the confounding background fluorescence is typically the enemy of Raman spectroscopy as it obscures Raman spectral peaks of interest such as sharp Raman peaks derived from the apatite's phosphate groups. The fluorescence background can be plagued with the same confounding sources of variation (e.g. calculus, stains and organic matter) as other fluorescence-based methods of caries detection.

Our group at the National Research Council Canada's Institute for Biodiagnostics has been focusing on early caries lesions (white spots). For the most part, these early lesions are not discoloured. Furthermore, by using a slightly longer laser excitation wavelength of 830 nm, fluorescence background interference can be further minimized. In our initial Raman spectroscopic studies, we used a Raman microspectrometer to examine intact (i.e. unsectioned) teeth [42]. The tooth samples were positioned with the surfaces to be studied oriented approximately orthogonal (i.e. 90°) to the laser beam in a backscattering sampling geometry. This sampling geometry is known as the normal excitation/detection sampling mode as described by Tsuda and Arends [31]. Healthy sound enamel and early carious enamel did not show obvious dramatic changes in the phosphate 959 cm^{-1} peak intensity (Fig. 11.3). Similar to some of the findings of Bulatov et al., changes were observed in the relative intensities of the various other PO_4^{3-} peaks pairs: 431 and 466 cm^{-1}; 579 and 590 cm^{-1}. The 431, 590 and 1043 cm^{-1} peaks were consistently higher in spectra from carious enamel. These changes, though characteristic of caries, are based on weak peaks requiring long measurement times to have sufficiently high signal-to-noise ratio to reliably determine relative peak intensities. The

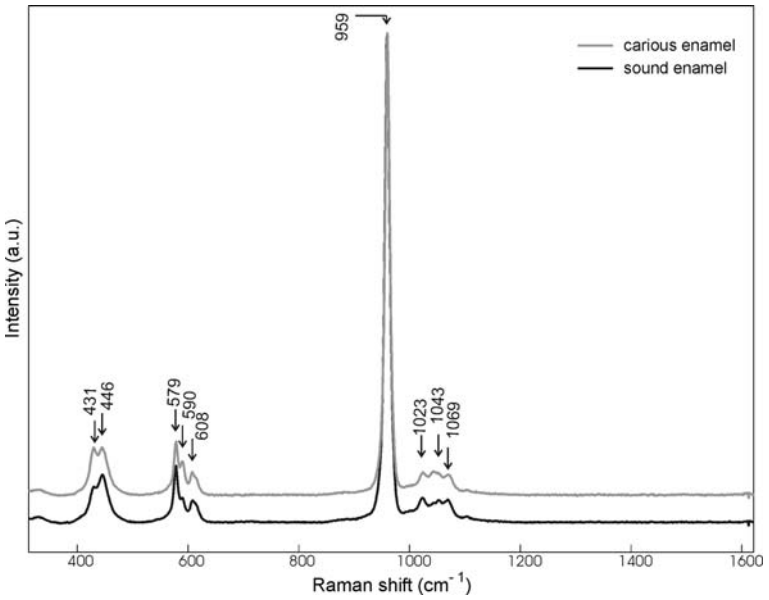

Fig. 11.3. Representative Raman spectra of sound and carious enamel acquired using conventional non-polarized Raman spectroscopy

clinical utility of this approach using such peaks for in vivo patient use is therefore limited.

Like Kinoshita et al., we also demonstrated that Raman microspectroscopic mapping of sectioned samples exhibited decreased phosphate intensity of the 959 cm^{-1} peak at carious regions thus indicative of demineralization (Fig. 11.4) [43]. The intensity was heterogeneous throughout the subsurface lesion but overall was lower than surrounding sound enamel. Studies based on the spectra acquired from the cut surface of longitudinally sectioned healthy sound tooth samples, i.e. using a transverse excitation/detection sampling mode, revealed that the same three bands (431, 590 and 1043 cm^{-1}) that changed intensities in carious lesions also demonstrated large intensity variations depending on measurement geometry. The differences are attributed to the relative orientation of enamel rods to the laser beam direction. In sound enamel, most of the enamel rods are highly ordered where their *c*-axis (i.e. long axis) is oriented orthogonal to the tooth surface. The spectroscopic changes observed with intact carious enamel suggest that orientational changes of enamel crystallites are possibly responsible for the alterations.

A Polarized Raman Spectroscopic Approach to Examining Caries

To examine the concept of orientational changes of enamel rods, our follow-up studies report the use of polarized Raman spectroscopy (PRS) [44]. PRS

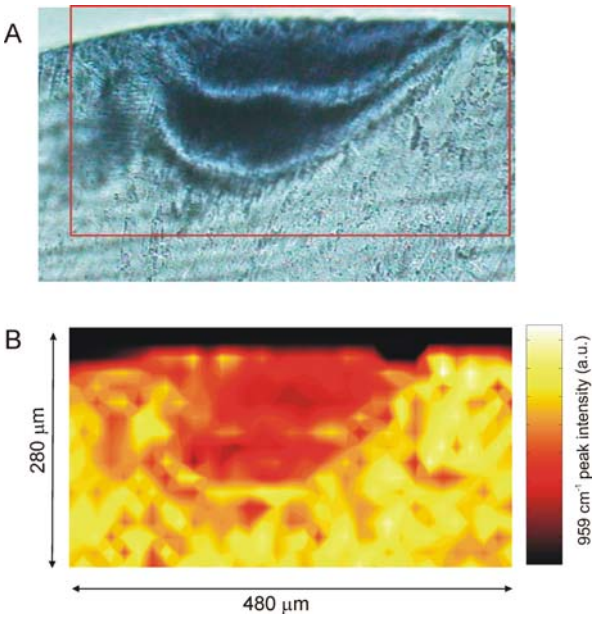

Fig. 11.4. A Photomicrograph of a histological tooth section (∼100 µm) in the region of sound and carious enamel. Area mapped is outlined by the *rectangle*. **B** The corresponding Raman map of the 959 cm^{-1} phosphate peak intensity

has been used previously to study molecular structure such as to examine the orientation of molecules within polymers as well as protein structures [45, 46]. Polarization techniques exploit properties of anisotropy to provide information about the structure and composition of materials. The ordered structure of the enamel should therefore be sensitive to polarized light with this property changing upon enamel demineralization in caries development. Other studies in the literature have used PRS to examine the fundamental structural characteristics of enamel crystallites and the orientation of enamel rods from sound enamel. These studies reported differences as a result of the crystal orientation [31, 47]. Using linearly polarized laser excitation and placing a polarizer analyzer in the collection path, we measured the parallel-polarized and cross-polarized Raman signal, relative to the initial laser polarization direction. Figure 11.5 shows representative parallel-polarized and cross-polarized spectra acquired from sound and carious enamel. Again we observed subtle peak intensity changes at 590, 608, 959, 1069 and 1104 cm^{-1} between the two polarization states. More interestingly, we observed that the ν_1 959 cm^{-1} hydroxyapatite phosphate peak intensity is markedly reduced in the cross-polarized spectra. The reduction is more pronounced for sound enamel compared to carious enamel. Based on these findings, the depolarization ratio (ρ) or polarization anisotropy (A) of this Raman band can be derived using

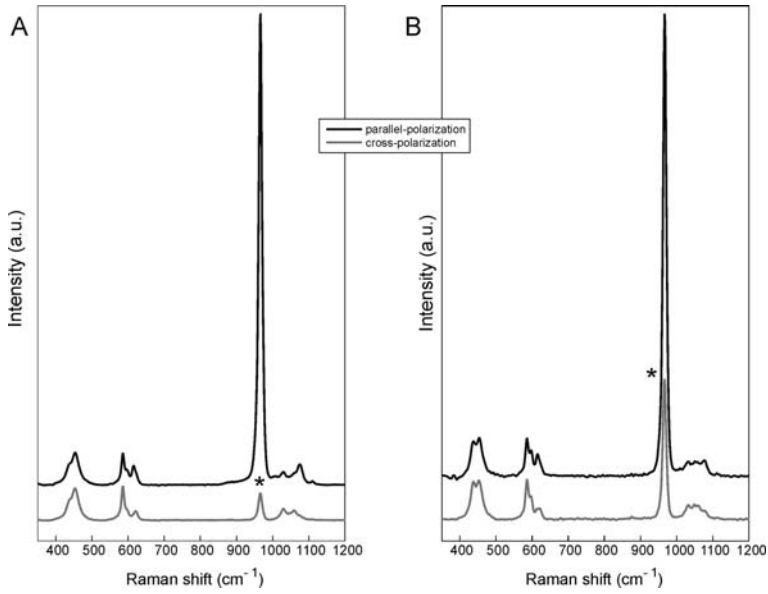

Fig. 11.5. Representative parallel-polarized (*black* lines) and cross-polarized (*grey* lines) Raman spectra of (**A**) sound and (**B**) carious enamel

$$\rho_{959} = I_{959(\perp)}/I_{959(\|)} \qquad \underline{\text{or}} \tag{11.1}$$

$$A_{959} = \left(I_{959(\|)} - I_{959(\perp)}\right) / \left(I_{959(\|)} + 2I_{959(\perp)}\right) \tag{11.2}$$

where $I_{959(\perp)}$ and $I_{959(\|)}$ are the integrated peak intensities of the 959 cm^{-1} peak detected with the polarization analyzer oriented perpendicular to ($\perp$) and parallel to ($\|$) the polarization direction of the incident linearly polarized laser light, respectively. Using this approach, the depolarization ratio is a parameter that can discriminate sound enamel from incipient caries with the depolarization ratio being higher for carious enamel compared to sound enamel (Fig. 11.6). In a study comparing the Raman depolarization ratio from sound (n=47 measurements) and carious (n=27 measurements) sites from 23 extracted human teeth, the mean depolarization ratio was statistically significantly different at $p<0.001$ (Student's t-test) [48, 49].

The spectral change demonstrated using polarized Raman spectroscopy indicates that biochemical and structural changes in the enamel occur due to demineralization. The structural changes could arise from changes in the orientation or scrambling of the previously ordered enamel rods from acid dissolution. Furthermore, as caries present with a more porous structure, there is also increased light scattering within the lesion that scrambles the polarization state of the Raman-scattered photons leading to increased depolarization of the Raman signal in caries. Thus a combination of increased scattering, structural/orientational changes and/or biochemical alterations of the

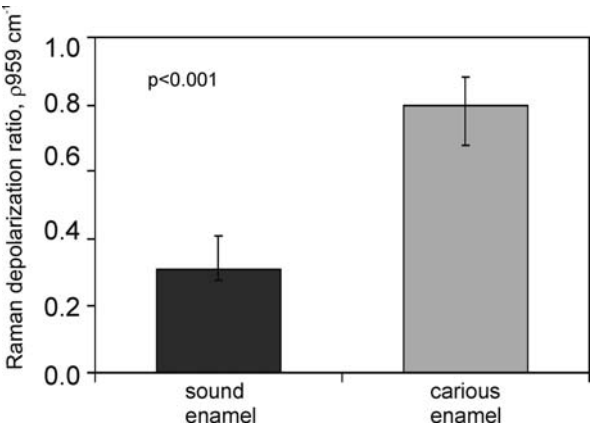

Fig. 11.6. Bar graphs of the mean Raman depolarization ratio calculated from the parallel- and cross-polarized intensities of the 959 cm^{-1} PO_4^{3-} peak. Data were obtained from 47 (sound) and 27 (caries) PRS measurements on 23 extracted teeth. Student's *t*-test analysis reveal $p < 0.001$. Error bars show standard deviation

carbonated hydroxyapatite enamel crystals from demineralization is responsible for the spectral changes observed with PRS. The intensity changes observed suggests that the depolarization ratio could be a clinically useful parameter for in vivo measurements.

11.7 Towards Clinical Utility and Clinical Validation

The initial studies described above were conducted on Raman microspectrometers on extracted human teeth. In order to translate this research from the laboratory bench to the dental chair side, the next step it is to develop dedicated systems for clinical use. A key element to this development is the use of fibre-optic probes to allow measurements in vivo. We recently reported a study in which optical fibres were used for PRS measurements [48]. Although not yet fully realized into a dental probe, this study demonstrated the design and feasibility of acquiring parallel- and cross-polarized Raman spectra via a bifurcated optical fibre whose distal terminal has the two fibres aligned vertically for simultaneously collecting spectra from the two polarization channels on a 2D CCD array. Simultaneous data acquisition will allow for more rapid measurement times in vivo.

To examine the clinical utility of our method, we have conducted various preliminary studies in which we have shown using artificial caries models of demineralization and remineralization that the ρ_{959} depolarization ratio of PRS measurements enables us to not only follow the progression and extent/severity of early caries development, but also to monitor the repair process involving fluoride treatment [49, 50]. In addition, other initial studies have

focused on the effects of possible confounding factors such as staining, calculus and hypocalcification on the sensitivity and specificity of the method for caries assessment [51–53]. Future studies are aimed at validating the clinical utility of this method on a much larger sampling set (over 100 teeth) as well as at various tooth surfaces beyond the interproximal region between teeth which has been the focus to date.

11.7.1 Comparing PRS with Other Emerging Methods for Caries Detection

In recent years, various new methods have emerged for early caries detection. These include direct digital radiography, digital imaging fibre-optic transillumination, electroconductivity measurements, electrochemical impedance spectroscopy, quantitative light-induced fluorescence (QLF) and laser fluorescence, photothermal radiometric with modulated luminescence methods, ultrasound, optical coherence tomography (OCT), near-infrared illumination, terahertz imaging and Raman spectroscopy. Several of these methods have been extensively reviewed in recent papers and interested readers are directed to these references [54–56].

Some of the strengths of the PRS method over these other methods is the use of non-ionizing radiation and thus is safe for use on children, pregnant mothers and frequent use with repeat visits for monitoring purposes. PRS is well suited for examining enamel caries due to the strong Raman scattering signals from hydroxyapatite, the predominant component of this type of tissue. Furthermore, the PRS technique measures the tooth mineral composition and structure that are directly affected by the development of caries. In contrast, some of the fluorescence-based methods (e.g. DIAGNOdent device or QLF device) are indirect approaches relying on the presence of bacterial porphyrins secreted into regions of caries or the natural fluorescence of teeth when excited with blue light. These methods can be prone to false-positive readings due to the presence of stains or trapped food particles in the region of interest. False positives (i.e. low specificity) will lead to overtreatment with unnecessary strategies. In addition, with several other emerging detection methods, high inter- and intra-examiner variability remains problematic [57–60]. Despite the potential of these various methods, few studies have shown the necessary high sensitivity and high specificity for widespread clinical adoption of these new methods.

11.7.2 Combining OCT and PRS for Caries Assessment

One of the limitations of the PRS method is that it is not trivial to determine the incipient lesion depth. This parameter is clinically relevant as it can guide the clinician in the treatment decision-making process. Furthermore, one additional challenge facing the use of the depolarization ratio of the ν_1 PO_4^{-3} mode as a marker for early caries formation is the speed required to complete a full

clinical assessment using Raman spectroscopy. A dental examination needs to be carried out within a reasonably short period of time (10 min) which precludes painstaking point-by-point measurements of the Raman scattered light from surfaces of teeth. A multimodal strategy that employs a rapid screening tool to guide the Raman measurements has been advocated [42]. One such approach relies on optical coherence tomography (OCT) to rapidly image the surface of the tooth to search for areas of demineralization. An in-depth discussion of the principles and operation of OCT is outside the scope of this chapter and interested readers are directed to several articles on the topic [61, 62]. In brief, OCT is a non-invasive technique that provides high-resolution depth imaging of near-surface tissue structures. This technique is based on the coherent cross-correlation detection of the interference fringe intensity of backscattered light. Similar to ultrasound in operation but offering an order of magnitude greater spatial resolution, OCT provides morphological images with 10–20 μm resolution to depths of ∼2–4 mm [61]. This technology has been applied to image retinal tissue of glaucoma patients [63, 64] and is being developed for cancer detection [65, 66] and vulnerable atherosclerotic plaque assessment [67]. OCT imaging is sensitive to refractive index changes within the sample. Light scattered from boundaries or interfaces with differing refractive indices is detected in the OCT setup. The technique is capable of making thousands of measurements in a second, particularly when using a swept-source OCT configuration [68]. Thus the method is capable of scanning a tooth with reasonably high resolution in a few seconds.

Figure 11.7 displays representative OCT images acquired at 1310 nm from a region of sound enamel and compared to a region at the site of a carious lesion. From these depth images, we observe that OCT imaging nondestructively provides morphological information of the tooth with regions of the crown and root well delineated. The OCT backscattered light signal is intense at the air–enamel interface and dies out rapidly with depth within healthy sound enamel (Fig. 11.7B). In contrast, there is subsurface light backscattering within carious enamel sites (Fig. 11.7C). The porous carious enamel allows for increased scattering which is detected by the OCT system. A comparison of the OCT image with light photomicrographs generated from destructive sectioning methods indicate that the shape of the underlying lesions match those observed with OCT imaging (Fig. 11.7C inset). From OCT imaging, it is possible to obtain information regarding the lesion depth. Preliminary studies examining a group (n=15) of OCT images at 850 nm matched with light photomicrographs indicate that there is a linear correlation between the lesion depths obtained from these two methods with r=0.91 [69]. In addition, we have derived a parameter, the optical attenuation coefficient, that fits the decaying A-scan signal of the OCT backscattered intensity and found that it is a useful parameter for distinguishing sound enamel from carious enamel [70, 71]. Our initial findings based on more than 500 measurements from 21 teeth indicate that the attenuation of the OCT signal is more pronounced in sound enamel than in carious lesions. OCT attenuation coefficient at 850 nm

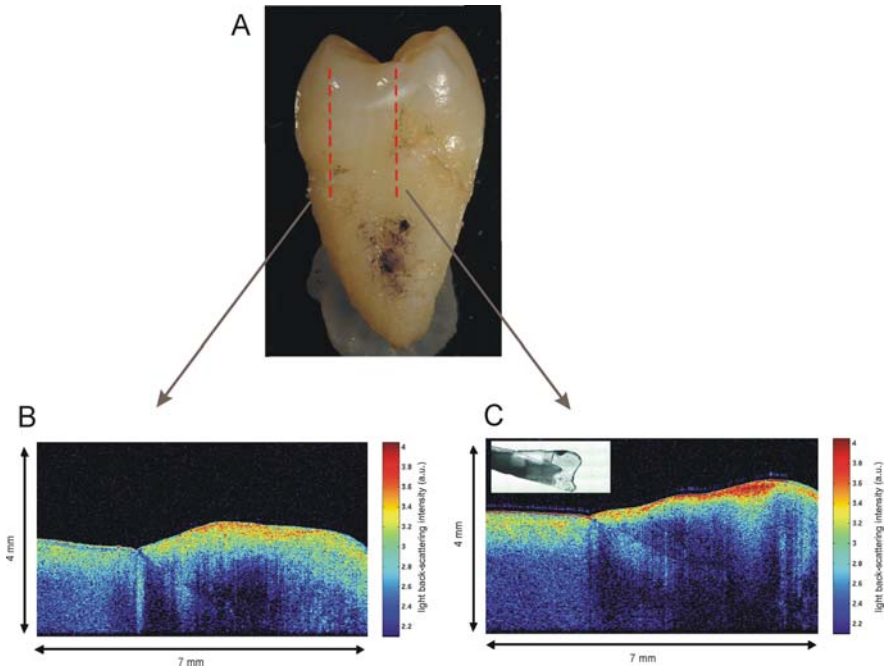

Fig. 11.7. A Mesial surface of an extracted human premolar containing an early carious lesion. *Dashed lines* mark the regions scanned to produce the OCT images in (**B**) and (**C**). **B** OCT depth image from a region of sound enamel. **C** OCT depth image from a region of the carious lesion. Inset: photomicrograph of a thin tooth section revealing the subsurface lesion.

was found to range from 0.7 to 2.14 mm^{-1} for sound enamel while the attenuation values at carious regions were in the range between 0.47 and 1.89 mm^{-1}. Using the measured OCT attenuation as a screen for early caries holds considerable promise. The receiver operating characteristic (ROC) curve demonstrates the trade-off between the sensitivity (the ability to correctly detect a caries lesion) and specificity (ability to correctly determine healthy enamel) of the 850 nm OCT attenuation coefficient. The area under the ROC curve, AUC, is often used to assess the discriminatory performance of a test. The ROC curve for a random test, represented by the dashed line in Fig. 11.8, runs through the diagonal from the origin of the plot and has an AUC=0.5. The more shifted the curve is towards the upper left and top of the plot, the better the discriminatory performance. The perfect test has an AUC=1 while the 850 nm OCT attenuation coefficient has an AUC=0.94 for distinguishing between caries and normal enamel. The ROC curve is useful for setting the decision threshold for a diagnostic test. For example, setting an OCT attenuation of 0.9 mm^{-1} as the threshold between caries and normal would provide a test that was nearly 80% sensitivity but with very high

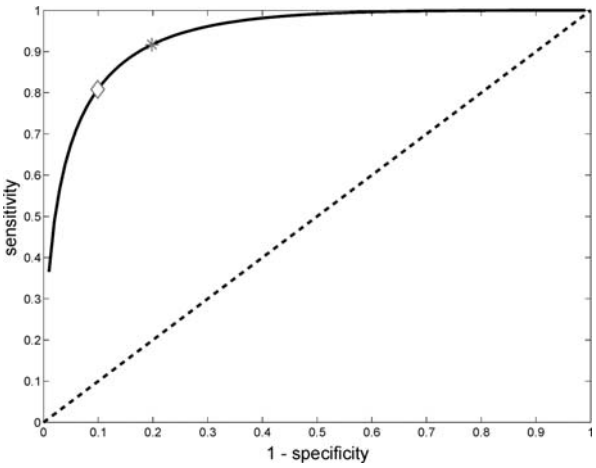

Fig. 11.8. A binormal receiver operating characteristic (ROC) curve (*solid line*) plotting the sensitivity versus 1–specificity using the 850 nm OCT attenuation coefficient to distinguish between early caries and healthy enamel. The *dashed line* represents the ROC curve for a nondiscriminatory test. The markers on the curve represent setting an OCT attenuation coefficient threshold between caries and healthy enamel at 0.9 mm^{-1} (*diamond*) and at 1.08 mm^{-1} (*star*)

specificity, 96.9% (see diamond in Fig. 11.8). A second threshold, marked on Fig. 11.8 with a star, corresponding to an attenuation of 1.08 mm^{-1} provides high sensitivity, 91%, but rather low specificity, 80%. In the setting of screening for early caries lesions, the threshold should be set to provide maximum sensitivity while controlling for false positives. The strategy of raising the threshold in order not to miss potential lesions (sensitivity) can only be carried to the point where the false positives stay within an acceptable rate.

While the application of OCT for caries characterization is not new, its combination with PRS is novel. In a sequential OCT–PRS approach, a high false-positive rate would necessitate a large number of confirmatory Raman measurements which in turn would slow the total time required to examine the oral cavity. Using an OCT 850 nm attenuation coefficient between 0.95 and 1.1 mm^{-1} as the threshold provides a suitable compromise between sensitivity (>85%) and specificity (>85%). OCT measurements lying above the selected attenuation threshold would be flagged as normal or healthy enamel not requiring further examination, while sites with an attenuation below the threshold would be subject to a confirmatory Raman measurement of the depolarization ratio of the ν_1 $PO_4{}^{-3}$ stretching vibration. Preliminary studies have shown that regions of high backscattering due to genetic defects in enamel formation such as hypocalcification can be misinterpreted as regions of OCT lesions. Setting the threshold for the OCT attenuation coefficient at 1.0 mm^{-1} to flag possible regions of caries and following up those

regions flagged with a measurement of the ρ_{959} depolarization ratio (threshold ρ>0.2) leads to a test with 90.5% sensitivity and 97% specificity for detecting and distinguishing caries from healthy enamel. This tandem approach utilizes the speed of OCT to survey large areas to identify suspicious areas of the tooth with the diagnostic biochemical capacity of Raman spectroscopy to detect demineralization. Using the depolarization of the ν_1 PO_4^{-3} peak as a marker of demineralization means that the final device will not need to be a fully functional Raman spectrometer but a more simplified filter-based instrument that interrogates both polarization states of the 959 cm^{-1} stretching vibration. The overall aim of this approach is to develop the technique into a simple device that can be deployed in dental clinics for early caries detection.

11.8 Concluding Remarks

Raman spectroscopy is a powerful tool for investigating various tissues and microorganisms of the oral cavity. Several highlights of the emerging dental applications of Raman spectroscopy include its use to characterize oral carcinoma, to identify pathogenic oral microbes, for developing improved (bio) materials for restorative and prosthodontic purposes and finally, the development of in vivo clinical tools involving polarized Raman spectroscopy and optical coherence tomography for early dental caries detection and longitudinal monitoring of tooth mineralization.

Raman spectroscopy is well suited for examining calcified tissues such as bones and teeth owing to its ability to probe both the inorganic and organic constituents of the tissue. The frequency and band shape of the symmetric and asymmetric phosphate stretching vibrations provide critical information on the crystallinity and orientation of the hydroxyapatite matrix. The analysis of a Raman spectrum of dental enamel provides features that are highly characteristic of the health and integrity of the tissue.

Demineralization is associated with early caries development and loss of mineral density and crystallinity of the hydroxyapatite matrix are important early indicators of demineralization. Bacterial action penetrating below the surface layer of the enamel can begin to disrupt the structural integrity of the enamel by attacking the hydroxyapatite matrix. Left unchecked this action will eventually degrade the enamel surface resulting in a cavity that requires filling. A number of treatments are available to intervene in this process before the enamel becomes cavitated and these treatments are intended to restore the structural integrity of the hydroxyapatite matrix. However, to effectively employ these treatments, the areas requiring repair need to be identified. Raman spectroscopy has the potential to detect early caries lesions by identifying spots where the order of the hydroxyapatite matrix is disrupted. A simple Raman scattering-based method that examines the depolarization ratio of the ν_1 symmetric stretch of the phosphate ion at 959 cm^{-1} has been developed

as a means of detecting early carious lesions [42]. An ordered hydroxyapatite matrix shows a strongly polarization dependent ν_1 PO_4^{-3} stretch while the ν_1 PO_4^{-3} stretch shows a reduced polarization dependence when the ordered matrix is disrupted. Early caries formation disrupts the structure of the hydroxyapatite matrix which in turn increases the depolarization ratio of the ν_1 mode of the PO_4^{-3} peak.

Though a sensitive marker, polarized Raman spectroscopy on its own has limited clinical utility due to the point-by-point nature of measurement. To overcome this limitation, we have coupled PRS with optical coherence tomography which will serve as an initial screening tool that provides morphological images that the dental clinician can readily relate to as well as provide clinically relevant parameters such as lesion shape, depth and extent. As with all diagnostic methods, this light backscattering approach too can suffer from false-positive readings such as in the presence of hypocalcification. Where OCT flags regions of suspicious carious activity, PRS is used to provide biochemical confirmation of the presence of a carious lesion. In so doing the OCT–PRS method will provide high sensitivity and high specificity for early caries detection and monitoring. Both OCT and PRS are readily adapted for fibre-optic measurements thus allowing its use in vivo. Research is underway to develop a combined OCT–PRS intra-oral probe for use in the dental clinic. In so doing, research that began as classical laboratory bench studies can be translated into use at the dental clinic chair side. The multi-modal approach involving OCT and PRS provides pieces of evidence that the clinician can use in formulating a diagnostic assessment for improved and effective patient oral health care.

Acknowledgements

Research funding has been derived in part from past and current grants from the Manitoba Medical Service Foundation, Canadian Institutes of Health Research – Institute of Musculoskeletal Health and Arthritis, and the US National Institutes of Health – National Institute of Dental and Craniofacial Research (#R01DE017889). We thank our clinical collaborators, Dr. Cecilia Dong (Faculty of Dentistry, U. Manitoba) and Dr. Blaine Cleghorn (Faculty of Dentistry, Dalhousie U.) for insightful discussions and clinical assessments. We also thank the staff and students of the Dental Clinics at U. Manitoba and at Dalhousie U. for assistance with tooth collection.

References

1. P.J. Caspers, G.W. Lucassen, E.A. Carter, H.A. Bruining, G.J. Puppels, J. Invest. Dermatol. **116**, 434 (2001)
2. M.A. Short, S. Lam, A. McWilliams, J.H. Zhao, H. Lui, H.S. Zeng, Opt. Lett. **33**, 711 (2008)

3. A.H. Chau, J.T. Motz, J.A. Gardecki, S. Waxman, B.E. Bouma, G.J. Tearney, J. Biomed. Opt. **13**, 040501 (2008)
4. G.J. Puppels, T.C. Bakker Schut, P.J. Caspers, R. Wolthuis, M. van Aken, A. van der Laarse, H.A. Bruining, H.P.J. Buschman, M.G. Shim, B.C. Wilson, *Handbook of Raman Spectroscopy* (Marcel Dekker, New York, 2001), p. 549.
5. X. Li, K.M. Kolltveit, L. Tronstad, I. Olsen, Clin. Microbiol. Rev. **13**, 547 (2000)
6. R. Rautemaa, A. Lauhio, M.P. Cullinan, G.J. Seymour, Clin. Microbiol. Infect. **13**, 1041 (2007)
7. A.M. Iacopino, J. Can. Dent. Assoc. **74**, 418 (2008)
8. R.M. Lemor, M.B. Kruger, D.M. Wieliczka, J.R. Swafford, P. Spencer, J. Biomed. Opt. **4**, 22 (1999)
9. H. Tsuda, J. Arends, Adv. Dent. Res. **11**, 539 (1997)
10. Y. Wang, P. Spencer, J. Biomed. Mater. Res. **59**, 46 (2002)
11. R. Malini, K. Venkatakrishna, J. Kurien, K.M. Pai, L. Rao, V.B. Kartha, C.M. Krishna, Biopolymers **81**, 179 (2006)
12. A.P. Oliveira, R.A. Bitar, L. Silveira, R.A. Zangaro, A.A. Martin, Photomed. Laser Surg. **24**, 348 (2006)
13. D.C.G. de Veld, T.C. Bakker Schut, M. Skurichina, M.J.H. Witjes, J.E. Van der Wal, J.L.N. Roodenburg, H. Sterenborg, Lasers Med. Sci. **19**, 203 (2005)
14. K. Venkatakrishna, J. Kurien, K.M. Pai, M. Valiathan, N.N. Kumar, C.M. Krishna, G. Ullas, V.B. Kartha, Curr. Sci. **80**, 665 (2001)
15. C.M. Krishna, G.D. Sockalingum, J. Kurien, L. Rao, L. Venteo, M. Pluot, M. Manfait, V.B. Kartha, Appl. Spectrosc. **58**, 1128 (2004)
16. T.C. Bakker Schut, M.J.H. Witjes, H. Sterenborg, O.C. Speelman, J.L.N. Roodenburg, E.T. Marple, H.A. Bruining, G.J. Puppels, Anal. Chem. **72**, 6010 (2000)
17. A.J. Berger, Q.Y. Zhu, J. Mod. Opt. **50**, 2375 (2003)
18. Q.Y. Zhu, R.G. Quivey, A.J. Berger, J. Biomed. Opt. **9**, 1182 (2004)
19. Q.Y. Zhu, R.G. Quivey, A.J. Berger, Appl. Spectrosc. **61**, 1233 (2007)
20. T. Jiang, X. Ma, Y.N. Wang, H. Tong, X.Y. Shen, Y.G. Hu, J.M. Hu, J. Biomed. Opt. **13**, 014019 (2008)
21. L.E.S. Soares, P.C.S. Liporoni, A.A. Martin, Oper. Dent. **32**, 160 (2007)
22. R. Parthasarathy, G. Thiagarajan, X. Yao, Y.P. Wang, P. Spencer, Y. Wang, J. Biomed. Opt. **13**, 014020 (2008)
23. M.A. Latta, J. Adhes. Dent. **9**(S2), 245 (2007)
24. L.E.S. Soares, A.A. Martin, A.L.B. Pinheiro, M.T.T. Pacheco, J. Biomed. Opt. **9**, 601 (2004)
25. J.L. Katz, A. Misra, P. Spencer, Y. Wang, S. Bumrerraj, T. Nomura, S.J. Eppell, M. Tabib Azar, Mater. Sci. Eng. C Biomim. Supramol. Syst. **27**(S3), 450 (2007)
26. M.A. Lopez Heredia, J. Sohier, C. Gaillard, S. Quillard, M. Dorget, P. Layrolle, Biomaterials **29**, 2608 (2008)
27. Y. Wang, P. Spencer, M.P. Walker, J. Biomed. Mater. Res. A **81A**, 279 (2007)
28. K.A. Schulze, M. Balooch, G. Balooch, G.W. Marshall, S.J. Marshall, J. Biomed. Mater. Res. A **69A**, 286 (2004)
29. C. Robinson, R.C. Shore, S.J. Brookes, S. Strafford, S.R. Wood, J. Kirkham, Crit. Rev. Oral. Biol. Med. **11**, 481 (2000)
30. T.M. Roberson, H. Heymann, E.J. Swift, C.M. Sturdevant, *Sturdevant's Art & Science of Operative Dentistry* (Mosby, St. Louis, 2002), p. 947
31. H. Tsuda, J. Arends, J. Dent. Res. **73**, 1703 (1994)
32. G. Penel, G. Leroy, C. Rey, E. Bres, Calcif. Tissue Int. **63**, 475 (1998)

33. National Institutes of Health Consensus Development Conference Statement, J. Dent. Educ. **65**, 1162 (2001)
34. S.C. White, M.J. Pharoah, *Oral Radiology: Principles and Interpretation* (Mosby, Toronto, 2004), p. 297
35. D.J. White, Adv. Dent. Res. **9**, 175 (1995)
36. W. Hill, V. Petrou, Appl. Spectrosc. **51**, 1265 (1997)
37. W. Hill, V. Petrou, Appl. Spectrosc. **54**, 795 (2000)
38. T. Izawa, M. Wakaki, Prog. Biomed. Opt. Imaging Proc. SPIE **5687**, 1 (2005)
39. M. Mukhin, A. Sklyarov, V.B. Dhuru, V.V. Yakovlev, Prog. Biomed. Opt. Imaging Proc. SPIE **5687**, 9 (2005)
40. H. Kinoshita, N. Miyoshi, Y. Fukunaga, T. Ogawa, T. Ogasawara, K. Sano, J. Raman Spectrosc. **39**, 655 (2008)
41. V. Bulatov, L. Feller, Y. Yasman, I. Schechter, Instr. Sci. Tech. **36**, 235 (2008)
42. A.C.-T. Ko, L.-P. Choo-Smith, M. Hewko, L. Leonardi, M.G. Sowa, C.C.S. Dong, P. Williams, B. Cleghorn, J. Biomed. Opt. **10**, 031118 (2005)
43. L.-P. Choo-Smith, A.C.-T. Ko, M.D. Hewko, C.C.S. Dong, B.M. Cleghorn, M.G. Sowa, Lasers Dent. XII Proc. SPIE **6137**, 613706 (2006)
44. A.C.-T. Ko, L.-P. Choo-Smith, M. Hewko, M.G. Sowa, C.C.S. Dong, B. Cleghorn, Opt. Express **14**, 203 (2006)
45. S. Frisk, R.M. Ikeda, D.B. Chase, J.F. Rabolt, Appl. Spectrosc. **58**, 279 (2004)
46. M. Tsuboi, J.M. Benevides, P. Bondre, G.J. Thomas, Biochemistry **44**, 4861 (2005)
47. G. Leroy, G. Penel, N. Leroy, E. Bres, Appl. Spectrosc. **56**, 1030 (2002)
48. A.C.-T. Ko, M. Hewko, M.G. Sowa, C.C.S. Dong, B. Cleghorn, L.-P. Choo-Smith, Opt. Express **16**, 6274 (2008)
49. L.-P. Choo-Smith, C.C.S. Dong, B. Cleghorn, M. Hewko, J. Can. Dent. Assoc. **74**, 913 (2008)
50. L.-P. Choo-Smith, K. Gibrayel, C.C.S. Dong, D. Popescu, M.G. Sowa, B. Cleghorn, Caries Res. **41**, 326 (2007)
51. A. Huminicki, C.C.S. Dong, B. Cleghorn, L.-P. Choo-Smith, J. Dent. Res. **87**(Spec. Iss. B), 521 (2008)
52. C.C.S. Dong, A. Huminicki, M.G. Sowa, B. Cleghorn, L.-P. Choo-Smith, Caries Res. **42**, 213 (2008)
53. L.-P. Choo-Smith, A. Huminicki, C.C.S. Dong, M. Hewko, B. Cleghorn, M.G. Sowa, Caries Res. **42**, 214 (2008)
54. A. Hall, J.M. Girkin, J. Dent. Res. **83**(Spec. Iss. C), 89 (2004)
55. I.A. Pretty, J. Dent. **34**, 727 (2006)
56. A.F. Zandona, D.T. Zero, J. Am. Dent. Assoc. **137**, 1675 (2006)
57. C.A. Murdoch-Kinch, J. Calif. Dent. Assoc. **27**, 773 (1999)
58. X.Q. Shi, U. Welander, B. Angmar-Mansson, Caries Res. **34**, 151 (2000)
59. A. Lussi, S. Imwinkelried, N. Pitts, C. Longbottom, E. Reich, Caries Res. **33**, 261 (1999)
60. J.D. Bader, D.A. Shugars, A.J. Bonito, J. Public Health Dent. **62**, 201 (2002)
61. F.I. Feldchtein, G.V. Gelikonov, V.M. Gelikonov, R.R. Iksanov, R.V. Kuranov, A.M. Sergeev, N.D. Gladkova, M.N. Ourutina, J.A. Warren Jr., D.H. Reitze, Opt. Express **3**, 239 (1998)
62. X.J. Wang, T.E. Milner, J.F. de Boer, Y. Zhang, D.H. Pashley, J.S. Nelson, Appl. Opt. **38**, 2092 (1999)

63. W. Drexler, C.K. Hitzenberger, H. Sattmann, A.F. Fercher, Opt. Eng. **34**, 701 (1995)
64. J.S. Schuman, M.R. Hee, A.V. Arya, T. Pedut-Kloizman, C.A. Puliafito, J.G. Fujimoto, E.A. Swanson, Curr. Opin. Ophthalmol. **6**, 89 (1995)
65. X.D. Li, S.A. Boppart, J. Van Dam, H. Mashimo, M. Mutinga, W. Drexler, M. Klein, C. Pitris, M.L. Krinsky, M.E. Brezinski, J.G. Fujimoto, Endoscopy **32**, 921 (2000)
66. M. Tsuboi, A. Hayashi, N. Ikeda, H. Honda, Y. Kato, S. Ichinose, H. Kato, Lung Cancer **49**, 387 (2005)
67. I.K. Jang, G.J. Tearney, B. MacNeill, M. Takano, F. Moselewski, N. Iftima, M. Shishkov, S. Houser, H.T. Aretz, E.F. Halpern, B.E. Bouma, Circulation **111**, 1551 (2005)
68. D.C. Adler, Y. Chen, R. Huber, J. Schmitt, J. Connolly, J.G. Fujimoto, Nat. Photonics **1**, 709 (2007)
69. L.-P. Choo-Smith, P. Qiu, D. Popescu, M. Hewko, C.C.S. Dong, B.M. Cleghorn, M.G. Sowa, J. Dent. Res. **87**(Spec. Iss. B), 2838 (2008)
70. D.P. Popescu, M.G. Sowa, M.D. Hewko, L.-P. Choo-Smith, J. Biomed. Opt. **13**, 054053 (2008)
71. M.G. Sowa, D.P. Popescu, J. Werner, M. Hewko, A.C.-T. Ko, J. Payette, C.C.S. Dong, B. Cleghorn, L.-P. Choo-Smith, Anal. Bioanal. Chem. **387**, 1613 (2007)

12

Raman Spectroscopy of Ocular Tissue

Igor V. Ermakov, Mohsen Sharifzadeh, and Warner Gellermann

Abstract The optically transparent nature of the human eye has motivated numerous Raman studies aimed at the non-invasive optical probing of ocular tissue components critical to healthy vision. Investigations include the qualitative and quantitative detection of tissue-specific molecular constituents, compositional changes occurring with development of ocular pathology, and the detection and tracking of ocular drugs and nutritional supplements. Motivated by a better understanding of the molecular mechanisms leading to cataract formation in the aging human lens, a great deal of work has centered on the Raman detection of proteins and water content in the lens. Several protein groups and the hydroxyl response are readily detectable. Changes of protein compositions can be studied in excised non-cataractous tissue versus aged tissue preparations as well as in tissue samples with artificially induced cataracts. Most of these studies are carried out in vitro using suitable animal models and conventional Raman techniques. Tissue water content plays an important role in optimum light transmission of the outermost transparent ocular structure, the cornea. Using confocal Raman spectroscopy techniques, it has been possible to non-invasively measure the water to protein ratio as a measure of hydration status and to track drug-induced changes of the hydration levels in the rabbit cornea at various depths. The aqueous humor, normally supplying nutrients to cornea and lens, has an advantageous anterior location for Raman studies. Increasing efforts are pursued to non-invasively detect the presence of glucose and therapeutic concentrations of antibiotic drugs in this medium. In retinal tissue, Raman spectroscopy proves to be an important tool for research into the causes of macular degeneration, the leading cause of irreversible vision disorders and blindness in the elderly. It has been possible to detect the spectral features of advanced glycation and advanced lipooxydation end products in excised tissue samples and synthetic preparations and thus to identify potential biomarkers for the onset of this disease. Using resonance Raman detection techniques, the concentration and spatial distribution of macular pigment, a protective compound, can be detected in the living human retina Useable in clinical settings for patient screening, the technology is suitable to investigate correlations between pigment concentration levels and risk for macular degeneration and to monitor increases in pigment levels occurring as a result of dietary intervention strategies.

12.1 Introduction

Healthy vision is arguably one of the most important concerns of human health. Therefore it makes good sense to apply non-invasive Raman spectroscopy techniques also to investigations of ocular tissue components. The visual process is enabled by the light-sensitive retina, which is positioned as a hemispherical tissue layer system in the back of the eye (Fig. 12.1). The retina is light sensitive, depending on age, over approximately the 400–750 nm wavelength range, with highest sensitivity at green wavelengths. To reach the photoreceptor layer of the retina, the light has to traverse an optical path length of ∼2 cm through all anterior ocular tissue structures. Apertured by the iris, the light has to propagate through the cornea, the aqueous humor, the lens, the vitreous humor, and also through part of the anterior retinal layer structure, the nerve fiber layer. While nature has designed all these ocular tissues for high transmission in the visible wavelength region, any tissue degeneration effects can easily attenuate the propagating light via induced absorption and scattering processes. To view an object with high visual acuity, humans have to move their eyes such that the object light falls into the small central region of the retina, the macula, where the color-sensitive cone photoreceptor cells are located. Outside the macula, the retina is mainly used for peripheral vision, enabled by the rod photoreceptor cells. All interior ocular tissue structures are protected by the surrounding thick, white sclera, a tough tissue layer consisting of non-transparent collagen and elastin, which is partially visible on the outside of the eye.

Due to the transparent nature of all ocular tissue components anterior to the retina, Raman spectroscopy holds potential as a non-invasive optical probe of the internal tissue components. It offers the possibility to identify molecular tissue constituents with high chemical specificity, to quantify their

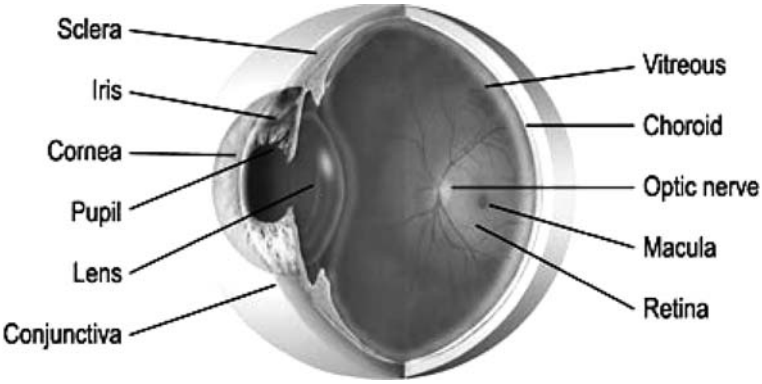

Fig. 12.1. Schematics of the human eye with main anatomical components. Raman probing of any ocular tissue component in the living eye requires light delivery and collection through the preceding ocular media

concentrations, and to track changes occurring with developing tissue pathologies. The tissue components could include internal structural compounds such as proteins and lipids, molecules such as glucose, external compounds such as drugs, and also molecular biomarkers for health or disease, such as macular pigment or glycation products. Also, the Raman method is capable, in principle, of generating all spectral information from very small tissue volumes. It is therefore useable for spatially resolved detection of bio-medically interesting tissue compounds as well as for their spatially integrated detection. Spatially resolved detection could be achieved in high-resolution imaging configurations.

Since Raman scattering is a relatively weak optical effect, high excitation light levels and/or exposure times are usually required to obtain spectra with good signal-to-noise ratios. This poses a strong challenge for applications to the living human eye, since the retina is highly light sensitive, and therefore can be easily and irreversibly damaged. Raman measurements of anterior ocular media can employ light excitation and detection geometries that avoid excessive retinal exposure, such as excitation light paths that are perpendicular to the optical axis. Probing of inner ocular structures such as the lens, however, necessitates some degree of a collinear detection scheme, and exposure of the retina with high light levels can be expected to be problematic.

In this chapter, we describe selected examples of Raman work carried out in ocular tissue research, with emphasis on recent in vivo applications where possible. For earlier, more comprehensive reviews, including Raman studies of visual pigments, we refer the reader to the literature [1, 2].

12.2 Protein Structure Investigations of the Lens

The lens is positioned between the aqueous humor and the vitreous humor and provides about 30% of the eye's refractive power. It consists of a highly viscous, gel-like crystalline protein structure and is able to change its curvature and, correspondingly, its refractive power. Combined with the fixed refractive power of the cornea, precise focusing of object rays is achieved in healthy eyes onto the photoreceptor cells of the retina. The lens contains about 34% protein and 66% water, with the protein content being the highest among human tissues. Protein content is highest in the central regions of the lens (nucleus) and decreases slightly toward outer regions (cortex). Lens proteins are synthesized by a monolayer of epithelial cells on the anterior surface of the lens. In this process, the epithelial cells at the equator of the lens elongate to form fiber cells that lose their intracellular organelles. The youngest fiber cells, the cortical fibers, occupy the outer two-thirds of the lens. With age, the cortical fibers are compressed toward the central nuclear region.

Since there is virtually no turnover of proteins in the lens with aging, it can be expected that aging and environmental stress factors lead to changes in protein structure and water content of the lens, and that these changes

could play a key role in the development of opacities or cataracts, which are widespread visual impairments affecting the elderly population. Motivated by these questions, Yu and East [3] and Schachar and Solin [4] applied Raman spectroscopy to ocular protein research for the first time in the 1970s. Working with excised bovine eyes, Yu and East [3] first generated isolated protein fractions from a gel filtration chromatography column. Based on the order in which the lens proteins eluted from the column, they could distinguish several protein fractions with high molecular weight (α-, β-, and γ-crystallins), and also a fraction consisting of lower molecular weight materials (peptides, amino acids, etc.). For all fractions they could detect distinct Raman responses, and subsequently were able to assign them to the Raman features they observed for intact lenses.

An example of a lens Raman spectrum for a young, non-cataractous, excised human eye lens, which is nearly identical to the bovine lens in all its Raman features, is shown in Fig. 12.2, which is reproduced from Bertoluzza et al. [5]. Based on the earlier assignment results [3] the spectrum is characterized by broad and strong scattering responses from water OH stretching modes near 3390 cm^{-1}, strong aliphatic CH and CH_2 stretching modes of protein components near 2900 cm^{-1}, weaker modes of sulfhydryl (S–H) protein subgroups in the 2500–2800 cm^{-1} region, and a large number of distinct protein component modes in the 500–1700 cm^{-1} region.

The latter include the amide I and amide III bands near 1672 and 1240 cm^{-1}, respectively, which are characteristic for the peptide CONH groups (the 1672 cm^{-1} line originates from the C=O stretch vibration and the lines in the 1240 cm^{-1} region from C–N stretching and N–H in-plane bending modes). Furthermore, there are well-resolved lines from the aromatic amino acids phenylalanine (Phe) at 1004 cm^{-1}, tryptophan (Try) at 760 cm^{-1}, and tyrosine (Tyr), the latter having several modes in the 600–900 cm^{-1} region. The spectral region between 1800 and 2500 cm^{-1} does not reveal any appreciable Raman response.

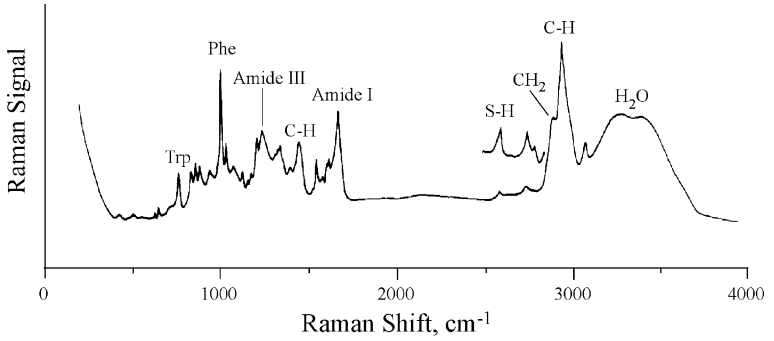

Fig. 12.2. In vitro Raman spectrum of the nucleus of a 23-year-old human intact lens, showing Raman responses from protein components and water in the 500–4000 cm^{-1} region. Adapted from [5]

The frequency of the amide I peak observed in the lens is sensitive to protein secondary structure. From its absolute position at $1672\,\mathrm{cm}^{-1}$, which is indicative for an antiparallel pleated β-sheet structure, and the absence of lines in the $1630–1654\,\mathrm{cm}^{-1}$ region, which would be indicative of parallel β-sheet and α-helix structures, the authors could conclude that the lens proteins are all organized in an antiparallel, pleated β-sheet structure [3]. Schachar and Solin [4] reached the same conclusion for the protein structure by measuring the amide I band depolarization ratios of lens crystallins in excised bovine lenses. Later, the Raman-deduced protein structure findings of these two groups were confirmed by x-ray crystallography.

Further results from these Raman studies showed that the lens nucleus and cortex had somewhat different amino acid compositions. It could be concluded that the nuclear portion has highest concentration of γ-crystallin, and that the content of α-crystallin increases significantly from the nucleus to the cortex. Furthermore, it was found that sulfhydryl groups and β-conformation are unaffected in the conversion from a transparent to totally opaque lens by heat denaturation. This indicates that the opacification of the lens does not necessarily involve the oxidation of sulfhydryl groups or conformational changes [3].

Using laser excitation with visible wavelengths, cataracteous lens regions are typically generating large, overwhelming fluorescence contributions to the Raman spectra due to fluorescing protein aggregates with high molecular weight. This limits Raman experiments usually to the cortical lens regions, where the cataracts and corresponding fluorescence intensities are diminished relative to the nuclear region of the lens. The fluorescence can be reduced to some degree by choosing laser excitation in the red wavelength region [6]. While it was possible to extend lens Raman studies to the living rabbit eye [7], use with living human eye lenses has not yet been possible due to the required high light levels (∼15 mW at cornea) and rather long exposure times (∼2 min).

Duindam et al. [8] investigated sharply localized, small opaque areas in the human lens, termed as focal opacities, which are progressing slowly over a lifetime, and which may be precursors to mature cataracts. Working with human donor eyes, the authors were able to detect changes in proteins, phospholipids, and cholesterol in these opacities, employing a combination of high-resolution techniques, including Raman microspectroscopy, cytochemistry, and transmission electron microscopy. With electron microscopy they could identify normal and opaque lens regions, and then compare these areas with their Raman responses. The difference *Raman spectrum, obtained from spectra within the opacity and from spectra of normal tissue areas, is reproduced in Fig. 12.3. Compared with normal tissue regions, it shows that opacities contain unchanged protein content, but significantly increased aliphatic CH and CH_2 chains and reduced aromatic amino acid content. Also, the opacities contained elevated levels of cholesterol, and there was evidence for the formation of disulfide (S–S) bridges [8].

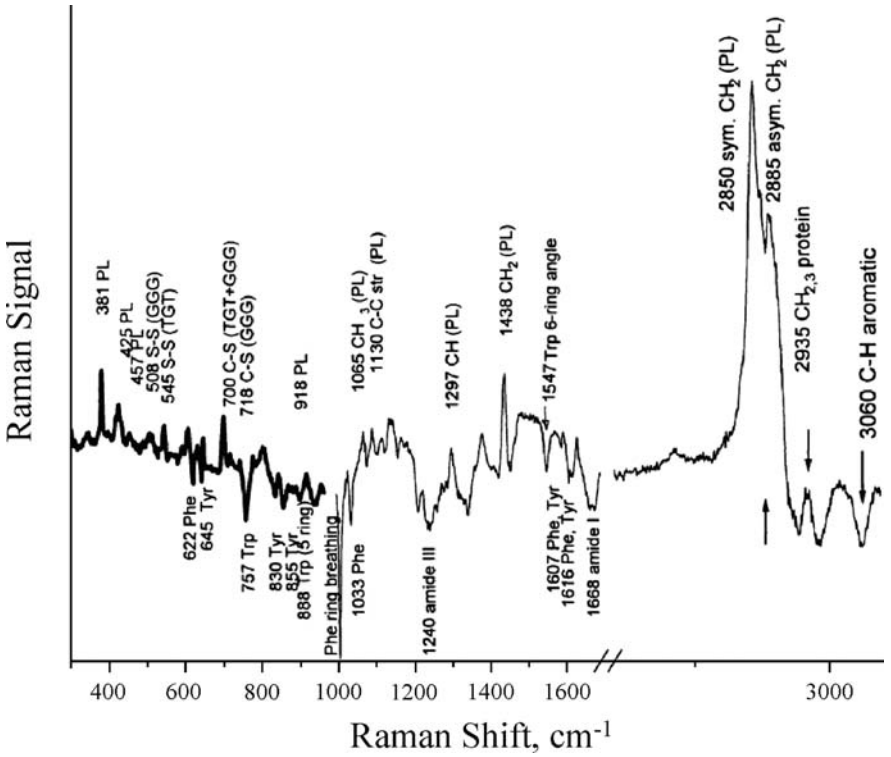

Fig. 12.3. Comparison of average Raman spectra measured in vitro for normal and cataractous human lens tissue. Adapted from [8]

To investigate age-related changes in the composition of lipid membranes in human lens tissue, as well as regional differences between the lens cortex and nucleus, Borchman et al. [9] employed Fourier transform (FT) infrared absorption and FT near-IR Raman methods. They measured the CH_2 stretching mode of lens lipids and discovered an increase of frequency with increasing age. This effect occurred in lipid samples from all regions of the lens. The frequency was used to estimate lipid hydrocarbon order. Lipid order was found to increase with age, and this correlated with changes of the Raman-active skeletal C–C stretch bands of the hydrocarbon chains. The obtained results suggest an important role of lipids in human lens clarity and cataract formation.

Combined elastic and confocal Raman microspectrometry experiments were carried out by Yaroslavsky et al. [10] to investigate the spatially resolved scattering behavior along the visual axis of human donor lenses ranging in age from 20 to 68 years. They explored the relation between local protein content and local intensity of elastically scattered light, and compared their results with protein scattering behavior from a model that assumes

short-range liquid-like order of the crystallin proteins. As a measure for protein content, they used the ratio between the Raman intensity of the aliphatic CH stretch mode of proteins at 2935 cm^{-1} and the water OH stretch mode at 3390 cm^{-1} [11]. The authors were able to establish that changes in the amount of light scattering along the visual axis of the lens are not explainable with protein concentration effects. Rather, these effects need to be attributed to local changes in protein conformation, such as polydispersity, aggregation, and non-sphericity of the crystallins. These changes vary among and within human lenses and change with age, leading to significant age-related and local variations in light scattering.

The prospects of influencing the structural changes of lens protein with vitamin E effects were investigated by Shih et al. [12] in lenses of tilapia. Using FT-Raman spectroscopy they explored potential structural changes of lens proteins occurring as an effect of dietary vitamin E supplementation. The authors found that while the protein secondary structure remained unaltered, significant changes occurred in the microenvironment of the lens constituents tyrosine, tryptophan, and thiol compounds. The changes were more pronounced in the cortex than the nucleus. The authors detected a close connection between vitamin E intake and a Raman band at 1090 cm^{-1}, attributed to the lens membrane. Potentially, the strength of this band could be used to investigate the role of vitamin E in the protection of lens membranes against external stresses.

12.3 Hydration Studies of the Cornea

The cornea accounts for about 70% of the refractive power of the unaccommodated human eye, and therefore plays an important role in maintaining optimal vision. Apart from water, the cornea consists of ∼15% collagen proteins, which are mostly comprised of glycine, an aliphatic amino acid, and proline, the only cyclic amino acid. Areas where Raman spectroscopy can contribute include investigations of collagen proteins, corneal hydration status, and the pharmacokinetics of topically applied ocular hydration drugs.

High-quality Raman spectra of corneal collagen proteins with conventional Raman spectroscopy had been difficult to obtain due to strong interferences from interior autofluorescence responses, and due to excessively high laser excitation levels. However, some progress in this area occurred after the development of Fourier-based IR and Raman spectroscopy techniques. These techniques avoid the influence of fluorescence on the spectra and also feature higher sensitivity. As a result, good-quality Raman spectra could be obtained from excised animal corneas, as shown in Fig. 12.4 as an example for a rabbit cornea [13]. Comparing the animal Raman spectra with those of pure type I collagen and other connective tissue components, such as proteoglycans, hyaluronic acids, chondroitin sulfates, and keratin sulfates, it was possible to assign the observed amide I and III responses of the animal spectra to

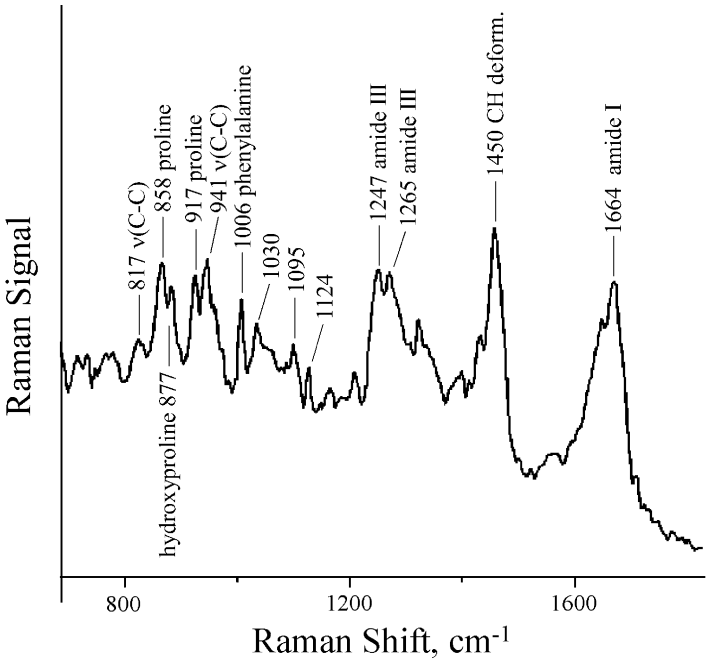

Fig. 12.4. Raman spectra of excised rabbit cornea. Adapted from [13]

type I collagen fibers. Furthermore, it was found that corneal collagen has a relatively large amount of phenylalanine amino acid content.

Bauer et al. [14] and Erckens et al. [15] used confocal Raman spectroscopy to investigate the corneal hydration status and drug-induced changes of the living rabbit cornea. Their confocality approach allowed them to monitor changes along the axis of the cornea. To determine the corneal hydration status, they determined the ratios of the Raman intensities of the water OH stretch mode at $3390\,\mathrm{cm}^{-1}$ and the protein CH stretch mode at $2945\,\mathrm{cm}^{-1}$, respectively. The studies demonstrated an increased gradient of corneal water content from the anterior to the posterior region [14].

Manipulations of the hydration are possible with a topically applied dehydrating agent, such as Muro 128®, an ointment usually used to treat corneal edema [15]. Representative results of this study are shown in Fig. 12.5, which displays a series of average Raman spectra obtained for successive axial locations of normal rabbit corneas and the same corneas after treatment with the drug. A comparison shows a decrease of about 30% of the OH/CH ratio between the untreated and treated cases. As future applications of their method the authors [14] envision the monitoring of healing processes following photorefractive keratectomy, the monitoring of corneal grafts, and studies of the effects of contact lenses on the cornea. Regarding pharmacokinetic applications, it may be possible in the future to study open questions such as the

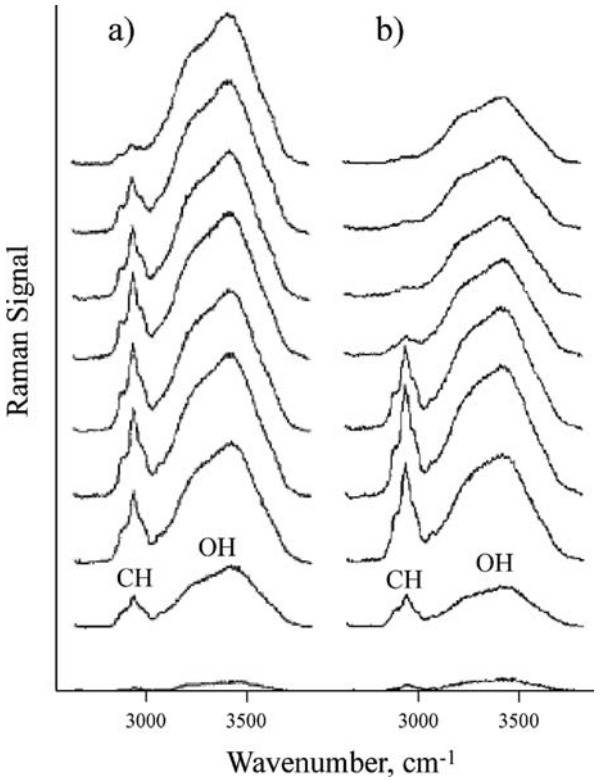

Fig. 12.5. Series of Raman spectra of normal cornea (*left*) and drug-treated cornea (*right*) in the CH and OH stretch frequency region, obtained as function of probing depth into the cornea. Relative CH and OH Raman band strengths reveal local changes in corneal hydration. Adapted from [15]

adherence of drugs to the corneal epithelium, their ability to penetrate into the different cornea layers, and the hydration status of these layers.

While Raman-based corneal hydration measurements on healthy living human eyes are not yet possible due to the excessive laser excitation light levels required by the method, corneal hydration status has been successfully measured in legally blind patients [16].

12.4 Detection of Physiological Compounds and Drugs in Aqueous and Vitreous Humors

Raman spectroscopy could potentially be used for the non-invasive detection of intrinsic compounds and ocular drugs in the aqueous and vitreous humors. Intrinsic compounds of interest are glutamate and glucose. If Raman were able to measure the concentrations of these compounds in a quantitative way, the

technique could serve as non-invasive, indirect way of measuring blood sugar levels, and it could be used as a biomarker for risk of diabetic retinopathy, glaucoma, and cataract formation.

Glutamate plays an important role in the healthy central nervous system, including the retina, as a neurotransmitter. Injury or death of a nerve cell leads to discharge of its physiological glutamate levels into the surrounding tissue. This can cause excessive concentration levels, leading to overstimulation and subsequent destruction of adjacent nerve cells. This glutamate-mediated neurotoxicity process has been shown to play a role in widespread ocular diseases such as age-related macular degeneration (AMD), glaucoma, diabetic retinopathy, and retinal detachment. Elevated levels of glutamate would not only exist in the retinal nerve cells but would also diffuse into neighboring anterior tissues such as the vitreous and the lens. To investigate the possibility of detecting glutamate in these anterior ocular media with Raman methods, Katz et al. [17] used excised porcine eyes and a semi-confocal excitation–detection scheme. Combining this with near-infrared (785 nm) wavelength excitation, the authors minimized the strong confounding spectral signals originating from lens and other native proteins. Monosodium glutamate was injected near the back of the eye to simulate disease conditions. Glutamate-specific Raman responses could be successfully detected at 1369 and 1422 cm^{-1} through all anterior eye structures, using light excitation levels that would comply with safety standards for living human eyes. However, the measurements still required rather long exposure times, and the authors note that concentrations required for Raman detection were still much higher than physiological concentrations. Future work is needed in this area that develops more sensitive detection approaches.

Diabetes is known to alter the basement membranes and other connective tissues in all organs of the human body. Sebag et al. [18] investigated the molecular effects of diabetes on human vitreous. They used near-IR excited FT Raman spectroscopy to measure responses from vitreous specimen obtained at surgery from patients with diabetic retinopathy. Comparing the spectra with controls, they could identify two prominent Raman peaks at 1604 and 3057 cm^{-1}, which were more pronounced in patients with diabetic retinopathy than in patients without pathology. The Raman signatures were tentatively assigned to the characteristic stretch frequency of carbon–carbon double (C=C) and CH bonds, respectively, and their origin was attributed to π-conjugated aromatic molecules formed as a result of a glycation process in the diabetic tissues.

Ocular drugs can be delivered intravitreally by direct injection into the eye or via drug-releasing implants that could be surgically implanted in the vitreous. For the development of effective drugs it would be desirable to know their precise dose as well as their diffusion and elimination rate inside the tissue. An example for Raman detection of ocular drugs is the detection of amphotericin B, a widely used polyene anti-fungal drug. The chemical structure of amphotericin B, shown in Fig. 12.6a, features a conjugated long carbon backbone,

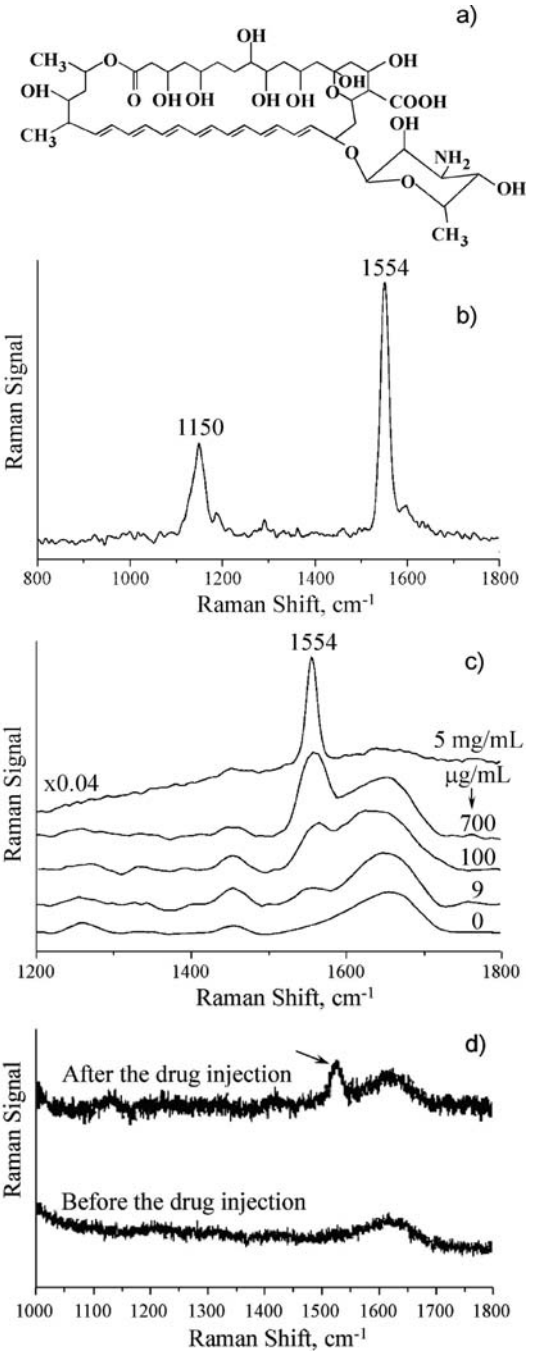

Fig. 12.6. Raman detection of ocular drugs in the anterior chamber. *Top panel* **a** molecular structure; **b** Raman spectrum of aqueous solution of antibiotic drug amphotericin B (adapted from [19]; **c** Raman spectra from aqueous humor of excised porcine eye obtained for decreasing levels of injected drug, adapted from [19]; **d** in vivo Raman spectra of vitreous humor of rabbit eye measured through all anterior optical media before and after injection with drug, adapted from [20]

consisting of alternating single and double carbon bonds. This structure generates a Raman response in an aqueous solution of this drug that is similar to the resonance Raman spectrum of carotenoids (see detailed discussion below). As shown in Fig. 12.6b, this drug features two prominent Stokes lines at 1150 and 1554 cm^{-1}, corresponding to the stretch frequencies of C–C and C=C groups of the drug. Sideroudi et al. [19] were able to obtain Raman responses of the drug when injected into the aqueous chamber of intact ex vivo porcine eyes. They used a non-collinear excitation and detection geometry, with a 514.5 nm laser excitation light path traversing the anterior chamber almost perpendicularly with respect to the optical axis of the eye. The image of the light channel inside the aqueous humor could be efficiently relayed to the entrance slit of a spectrograph entrance slit. The realized scattering geometry is optimal for safety considerations and detection sensitivity. The tested amphotericin B concentrations varied from several μg/mL up to 5 mg/mL. Corresponding Raman spectra, reproduced in Fig. 12.6c, demonstrate a lowest measurable concentration of about 9 μg/mL, which is promising since it is within the minimum inhibitory concentration range for this drug (0.5–16 μg/mL).

Several years earlier, Hosseini et al. [20] were able to detect amphotericin B Raman scattering in vivo from the aqueous chamber of a rabbit eye. Measurements from the vitreous require light delivery and collection through all anterior components of the intact eye, resulting basically in a confocal excitation–detection geometry, and an associated unavoidable degree of retinal illumination. The Raman spectra from the rabbit vitreous obtained before and after injection of a dose of 1 mg amphotericin B into the vitreous through the sclera are shown in Fig 12.6d. A drug-specific C=C Stokes Raman line is clearly resolved at 1550 cm^{-1}. The detection limit was about 30 μg, corresponding to a drug concentration of about 120 μg/mL in the rabbit eye. The minimum detectable drug concentration in the living vitreous is therefore higher than in the aqueous humor of excised eyes, which is to be expected. Similar Raman ocular drug experiments have been carried out with the antibiotic drug ciproflaxin [21]. As test sites, the authors [19] used artificial anterior chambers [21] and the aqueous humor of an excised porcine eye. Also, the antiviral drug ganciclovir was tested in the aqueous humor of a rabbit eye [22].

Glucose has distinct Raman features in the ∼400–1500 cm^{-1} region [23]. Several groups have set out to detect glucose with Raman methods, but due to the required high light excitation levels, experiments have been limited so far to artificial anterior chambers. Nevertheless, progress is made in this area by the development of various statistically methods which may be able to push the glucose detection limit to physiologically relevant concentrations [24–27].

Currently, all attempts to detect ocular drugs and physiological compounds in vitreous and aqueous humors via Raman scattering are still rather insensitive. The goal of using the method on living human eyes to probe pharmacokinetics, to track the release of drugs from intravitreal implants, and thus to monitor intra-ocular and systemic diseases thus remain a challenge.

12.5 Collagen Identification of the Sclera

Recently, Dehring et al. [28] used Raman microscopy to study changes in collagen secondary structure with aging and defective type II collagen in the sclera of eye tissue from wild-type mice and transgenic mice having genetic modifications to the type II collagen gene that result in truncated collagen fiber. They expected that abnormal type II collagen would be expressed in ocular tissue, and indeed observed an increased collagen disorder, as evidenced by changes in amide III band properties. The increase in disorder in the collagen fiber was found in the genetically altered mouse as well as in the aged wild-type mouse. This demonstrates that Raman can identify collagen changes occurring as a result of normal aging. The method may become useful as diagnostic tool for ocular collagen damage due to acquired or genetic defects, inflammatory disorders, or the natural aging process.

12.6 Confocal Microscopy of Advanced Glycation End Products in the Retina

A well-established phenomenon of aging is the modification of proteins by non-enzymatic glycation, leading to an accumulation of advanced glycation end products (AGEs) in the retinal pigment epithelium (RPE). Particularly the AGEs affect Bruch's membrane, the thin retinal layer that separates the choroid from the RPE (Fig. 12.8). Elevated levels of AGEs are known to exist in drusen, fatty deposits that start to form in the sub-RPE layer of the retina with starting pathology. Accompanied by the formation of lipofuscin granules in the RPE, thickening of Bruch's membrane, AGE-induced cross-linking of proteins, these and other processes can lead to geographic atrophy of retinal cells and/or choroidal neovascularization, both causing irreversible damage of the photoreceptors and eventually leading to the dry or wet form of age-related macular degeneration (AMD). AMD is the leading cause of blindness and affects about 30% of the population at age 70 in the western world. Currently there is no cure, and the disease provides major challenges for treatment.

The causes of AMD are an intensive research topic, and any modifications of Bruch's membrane can be considered important factors in the understanding of the microscopic pathways leading to AMD. The accumulation of AGEs in Bruch's membrane and/or oxidative cell damage is a likely pathogenic factor since the membrane is continually exposed to high light levels, and since due to high metabolic demand, this layer is also supplied by the underlying choroid with high concentrations of oxygen and glucose. Light-induced singlet oxygen formation would lead to oxidative cell damage, and in combination with AGE accumulation this could result in modifications of the membrane such as reduced permeability, changes in hydraulic conductivity, enhanced rigidity, and thickening.

A comprehensive confocal Raman microscopy study was carried out by Glenn et al. [29] to identify and quantify AGEs in Bruch's membrane in a non-destructive, analytical fashion. The authors dissected Bruch's membrane and the innermost retinal layers of the underlying choroid from 56 postmortem eye-cups, placed the samples onto microscope slides, and recorded Raman spectra with a confocal microscope. In parallel, they analyzed homogenized tissue samples with standard chemical analytical techniques including reverse-phase high-performance liquid chromatography (HPLC), mass spectrometry, and immunohistochemistry. One of their main Raman results for a spectral analysis of Bruch's membrane is shown in Fig. 12.7. Using a range of statistical approaches, the authors were able to deconvolute the Raman spectra into component spectra characteristic for heme, collagen, and AGE contributions, all shown, respectively, in Fig. 12.7a–c. Importantly, three AGE-specific Stokes lines could be identified at 880, 980, and 1080–1090 cm^{-1} [29].

The Raman data set for the AGEs provided quantitative data that compared well with the conventional analytical results, and as an advantage they offered the possibility to investigate AGEs with high spatial resolution. Using the Raman spectral fingerprint of AGEs, the authors were able to predict chronological age of the tissue samples and to confirm a gender-specific difference in AGE concentration, with higher levels found in females. The ability to accurately predict chronological age in Bruch's membrane from Raman spectra is a significant finding, showing that AGEs in long-lived proteins correlate

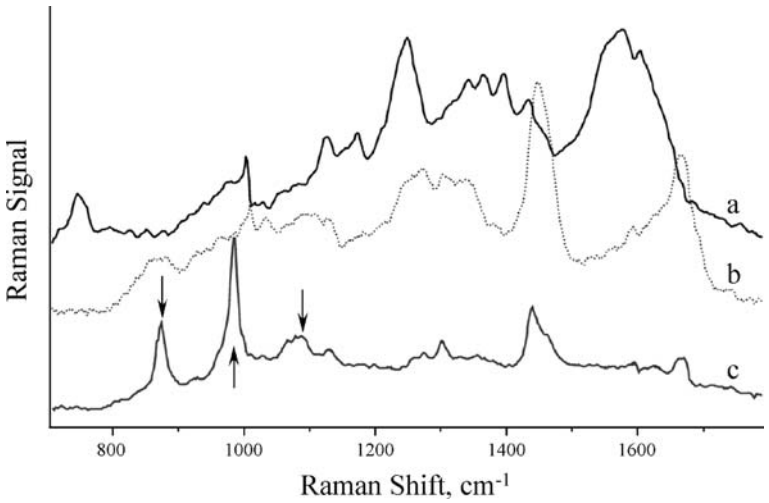

Fig. 12.7. Analysis of Raman spectra obtained in vitro for Bruch's membrane, showing component spectra **(a)** and **(b)** for heme and collagen, respectively, and a residual spectrum **(c)** assigned to Raman responses of age-related glycation end products and proteins. Adapted from [29]

with aging in humans and animals. Also, the identification of a gender difference is interesting since it correlates with the higher AMD rates of females.

The use of Raman spectroscopy to evaluate the extent of aging in Bruch's membrane as well as the pathogenicity of corresponding protein modifications is an important step toward non-invasive evaluation of the retina. It could serve as a powerful tool for the investigation of the effects of therapeutic drugs designed to prevent or even break established AGE–protein adducts in the aging processes of the human retina [30].

12.7 Detection of Macular Pigments in the Living Human Retina

The macular region of the retina contains the highest concentration of carotenoids in the human body. Of about ten carotenoid species found in human serum, two of them, lutein and zeaxanthin, are selectively taken up at this tissue site. Their concentrations can be as high as several 10 ng/g of tissue in the healthy human retina. Due to their strong absorption in the blue-green spectral range, the macular carotenoids, also termed macular pigment, MP, impart a yellow coloration to the macula. When viewed in cross section, MP is located anterior to the photoreceptor outer segments and the retinal pigment epithelium (Fig. 12.8). It is very likely, therefore, that MP shields the underlying photoreceptors from light-induced oxidative damage by blocking the phototoxic blue and near-UV components of ambient light. Also, MP may directly protect the cells in this area, since lutein and zeaxanthin are efficient antioxidants and scavengers of reactive oxygen species.

There is increasing evidence that MP may play a role in protecting the retina against visual loss from age-related macular degeneration, AMD, the leading cause of irreversible blindness affecting a large portion of the elderly population [31, 32]. Since lutein and zeaxanthin are taken up through the diet, there is a chance that early age screening of MP concentrations can be used to identify individuals with low levels of MP. Dietary interventions such as nutritional supplementation could then be recommended, with the prospects of helping to prevent or delay the onset of the disease. Motivated by these applications, our own group investigated Raman methods for the non-invasive optical detection of carotenoids/MP in the living human retina.

Carotenoids are π-electron-conjugated carbon chain molecules and are similar to polyenes with regard to their structure and optical properties. Distinguishing features are the number of conjugated C=C bonds, the number of attached methyl side groups, and the presence and composition of attached end groups. The molecular structures of the macular pigments lutein and zeaxanthin are shown as an example in Fig. 12.9a, along with a typical absorption spectrum and a configuration coordinate diagram for the

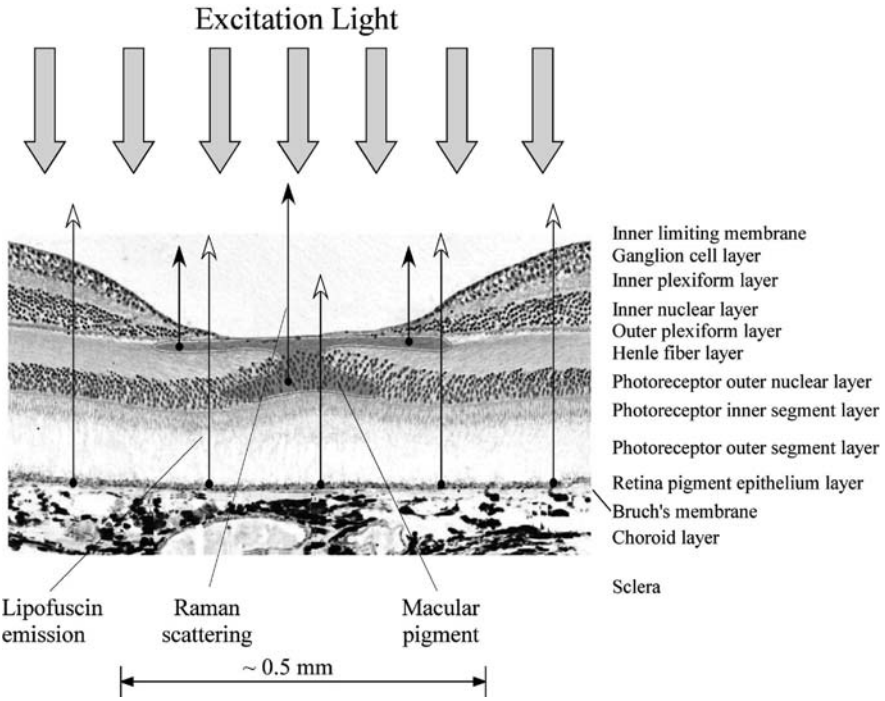

Fig. 12.8. Layer structure of the central retina, with indication of light paths used to measure macular pigment

three lowest lying energy states. Absorption, fluorescence, and Raman transitions occur at fixed nuclear positions of the molecule's atoms (fixed configuration coordinate) as vertical transitions. A characteristic strong, electric dipole allowed absorption transition occurs between the molecule's delocalized π-orbital from the $1\ ^1A_g$ singlet ground state to the $1\ ^1B_u$ singlet excited state,

Fig. 12.9. **a** Molecular structure of lutein and zeaxanthin, which both feature a linear, conjugated, carbon backbone with alternating carbon single (C–C) and double bonds (C=C). Resonance Raman spectroscopy detects the vibrational stretch frequencies of the carbon bonds; **b** absorption spectrum of a lutein solution corresponding to the molecule's $1\ ^1A_g \rightarrow 1\ ^1B_u$ transition, showing the characteristic broad absorption with vibronic substructure in the blue-green spectral range; **c** configuration coordinate diagram for three lowest lying energy levels of carotenoids, with indication of optical and non-radiative transitions between all levels. Luminescence transitions are very weak due to the existence of a low-lying excited even parity state that has the same parity as the ground state, which allows one to detect the relatively weak resonance Raman responses of the molecule without an otherwise overwhelming intrinsic luminescence background

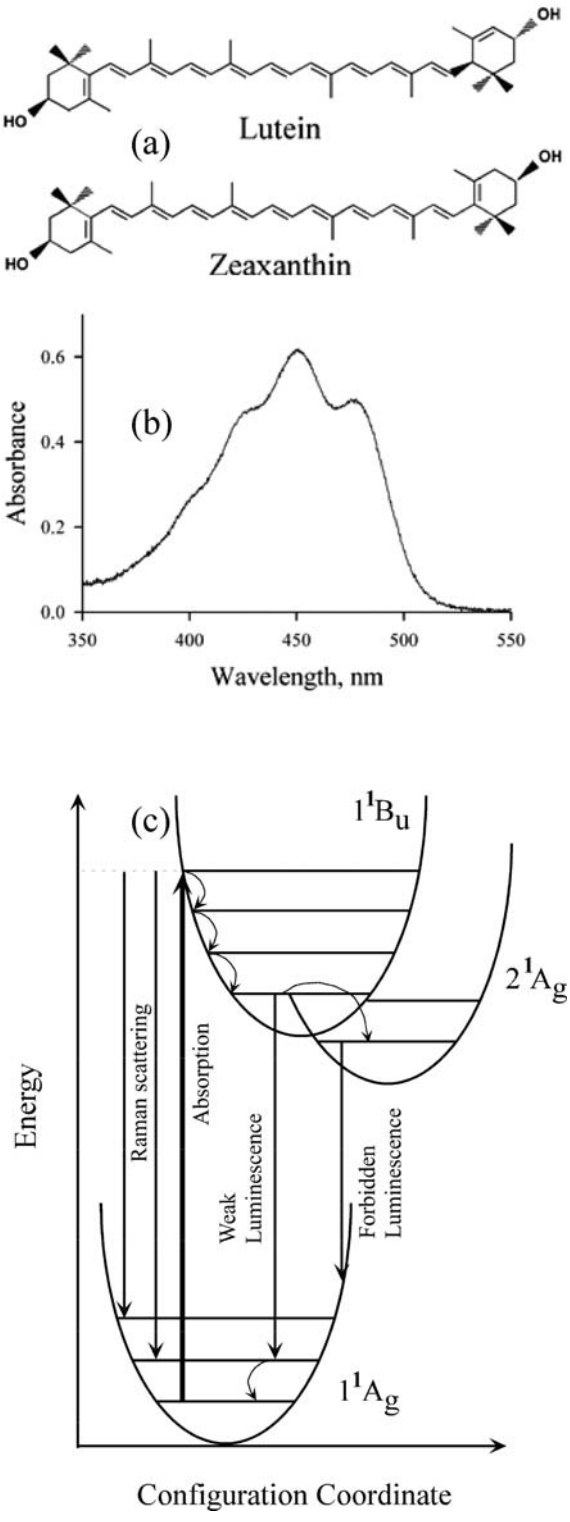

Fig. 12.9. (continued)

giving rise to a broad absorption band (∼100 nm width) in the blue-green spectral region, with peak at ∼460 nm and clearly resolved vibronic substructures with a spacing of ∼1400 cm^{-1}, as illustrated in Fig. 12.9b. Following excitation of the 1 ^1B_u state, the carotenoid molecule relaxes very rapidly, via non-radiative transitions, to the lower lying 2 ^1A_g excited state, from which electronic emission to the ground state is parity forbidden (Fig. 12.9c). As a consequence, the luminescence transitions from the 1 ^1B_u and 2 ^1A_g states to the ground states are very weak (10^{-5}–10^{-4} efficiency). This allows one to use resonance Raman spectroscopy (RRS) methods for carotenoid detection. Compared to non-resonant Raman scattering of carotenoids the RRS cross section is about five orders of magnitude larger [33]. It becomes possible, therefore, to explore this method not only for the identification of carotenoids in their tissue environments but also, through the intensity of the RRS response, for the measurement of their tissue concentrations.

The development of Raman-based carotenoid detection for ocular applications can benefit from already completed previous applications of the method to human skin [34]. Human skin contains about half a dozen carotenoid species thought to play a protective role in this largest organ of the human body, with β-carotene and lycopene having the highest carotenoid concentrations, and lutein and zeaxanthin playing only a minor role. Since carotenoids are a good biomarker for fruit and vegetable intake, Raman measurements of skin carotenoid levels can be used as an indirect rapid, optical method to assess fruit and vegetable consumption in large populations. These results are of interest in improving dietary data collected in epidemiological studies, which in turn are used in developing public health guidelines that promote healthier diets. The protective effects of diets rich in fruits and vegetables have been observed for many disease outcomes, including various cancers [35, 36] and cardiovascular disease [37]. Based on these health benefits, Raman-based skin carotenoid detection has found large-scale commercial use in the nutritional supplement industry, where thousands of instruments are in use to monitor skin uptake of carotenoid-containing multi-vitamin supplements.

Skin carotenoid levels, however, do not correlate with ocular levels of lutein and zeaxanthin which are likely to be concentrated in the macula by specific binding proteins. Therefore it is necessary to develop separate detection technology for the macular pigment measurements.

12.7.1 Spatially Integrated Macular Pigment Measurements

In vivo RRS spectroscopy of the macula can take advantage of favorable anatomical features of the tissue structures encountered in the excitation and light scattering pathways. The major site of macular carotenoid deposition is the Henle fiber layer, which has a thickness of only about 100 μm, and to a lesser extent the plexiform layer (Fig. 12.8). Considering that the optical density of MP in the peak of the absorption band is typically quite a bit smaller than 1, as determined from direct absorption measurements of MP in excised

eye cups, these tissue properties provide essentially an optically thin film with minimal self-absorption for both the excitation and Raman scattered light, if properly excited in the long-wavelength shoulder of the absorption. Second, since Raman scattering uses only the backscattered, single-path Raman response from the lutein- and zeaxanthin-containing MP layers, as indicated in Fig 12.8, and since these layers are located anteriorly in the optical pathway through the retina, absorption and fluorescence effects originating from other chromophores, such as rhodopsin in the photoreceptor layer, and melanin and lipofuscin in the retinal pigment epithelial layer, RPE, respectively, can be ignored or subtracted from the Raman spectra.

Initial "proof of principle" studies of ocular carotenoid RRS employed a laboratory-grade high-resolution Raman spectrometer and flat-mounted human cadaver retinas and eyecups. In Fig. 12.10, typical Raman spectra are shown for an excised eyecup, in which the excitation laser was aimed at the center of the macula, the fovea, and at two locations with increased eccentricities. In all cases, RRS spectra are obtained that display the

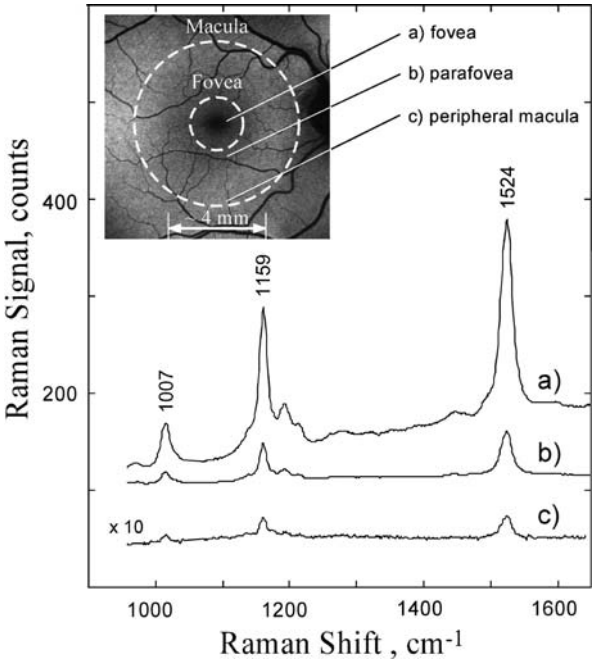

Fig. 12.10. Raman spectra of excised human eyecup, obtained from tissue locations in the central fovea (*trace a*), the parafovea (*trace b*), and the peripheral macula (*trace c*). Macular pigment carotenoid peaks are obtained at 1159 and 1524 cm^{-1} with good signal-to-noise ratio, and decreasing strengths (factor of ∼30) when the excitation beam is moved from the center of the macula (*trace a*) toward the peripheral retina (*trace c*)

characteristic carotenoid Stokes lines at ∼1524 cm^{-1} (C=C stretch), 1159 cm^{-1} (C–C stretch), and 1007 cm^{-1} (C–CH_3 rocking motions) [33]. Spatial resolution was about 100 μm. The intensities of the Raman responses were seen to decrease when probing macular locations of increasing eccentricity, in agreement with the known general spatial concentration profile of the macular pigments. The linearity of the Raman response with concentration could be verified by extracting and analyzing tissue carotenoids by high-pressure liquid chromatography, HPLC, after completion of the Raman measurements [38].

For in vivo experiments and clinical use, several Raman instruments with lower spectral resolution but highly improved light throughput were developed [39–41]. A version that is combined with a retinal camera, which permits independent operator targeting of the subject's macula, is shown in Fig. 12.11a [42]. The instrument's Raman module, containing a 488 nm laser excitation source, a spectrograph, and a CCD array detector, is optically connected with the fundus camera using a beam splitter that is mounted between the front-end optics of the fundus camera and the eye of the subject. Once alignment is established, an approximately 1 mm diameter, 1.0 mW, light excitation disk is projected onto the subject's macula for 0.25 s through the pharmacologically dilated pupil, and the backscattered light is routed to the Raman module for detection. Retinal light exposure levels of the instrument are in compliance with ANSI safety regulations since ocular exposure levels are a factor of 19 below the thermal limit, and a factor of 480 below the photochemical limit for retinal injury [42].

Typical RRS spectra measured from the macula of a healthy human volunteer through a dilated pupil are displayed, in near real time, on the instrument's computer monitor, as shown in Fig. 12.11b. The left panel shows the raw spectrum obtained from a single measurement, and clearly reveals the three characteristic carotenoid Raman signals, which are superimposed on a steep, spectrally broad fluorescence background. The background is caused partially by the weak intrinsic fluorescence of lutein and zeaxanthin, and partially by the short-wavelength emission tail of lipofuscin, which is present in the retinal pigment epithelial layer, and which is excited by the portion of the excitation light that is transmitted through the MP-containing Henle fiber and plexiform layers (Fig. 12.8). The ratio between the intensities of the carotenoid C=C Raman response and the fluorescence background is usually high enough (∼0.25) that it is easily possible to quantify the amplitudes of the C=C peak after digital background subtraction. This step is automatically accomplished by the instrument's data processing software, which approximates the background with a fourth-order polynomial, subtracts the background from the raw spectrum, and displays the final result as processed, scaled, spectrum in the right panel of the computer monitor, as shown in Fig 12.11b. MP carotenoid RRS spectra measured for the living human macula were indistinguishable from corresponding spectra of pure lutein or zeaxanthin solutions, measured with the same instrument.

Developed as a portable instrument, the Raman method is currently used in eye clinics to investigate the role of MP levels in the development of retinal

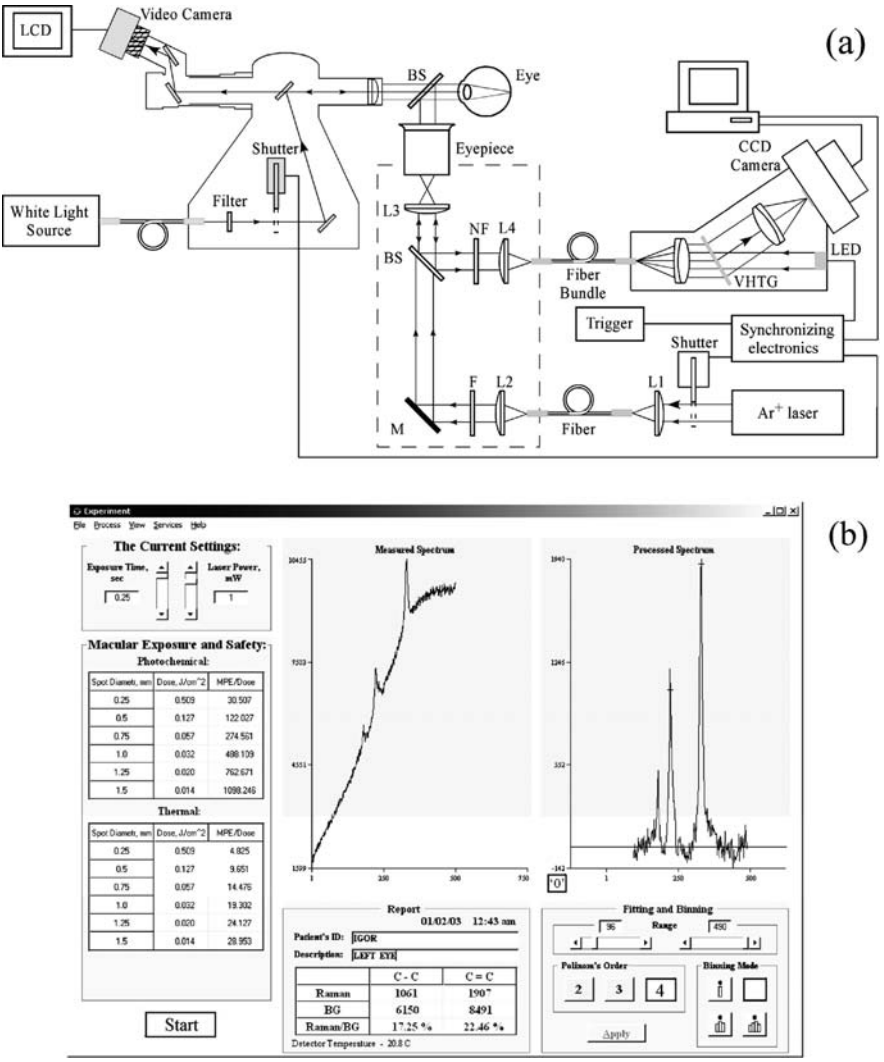

Fig. 12.11. a Schematics of fundus camera-interfaced RRS instrument for measurement of integral MP concentrations in human clinical studies; **b** computer monitor display showing raw Raman spectrum obtained after single measurement (*left panel*) and processed, scaled, spectrum obtained after subtraction of fluorescence background (*right panel*)

pathology. In Fig. 12.12, MP levels are shown as an example for ∼100 healthy volunteer subjects, ranging in age from ∼20 to 50 years. Each circle represents an MP concentration of a subject's retina, as determined by the Raman intensity of the MP carotenoid response. As seen in Fig. 12.12, the MP concentration can vary strongly between subjects at any age. Low MP levels of subjects are likely to correlate with their risk for vision problems later in life.

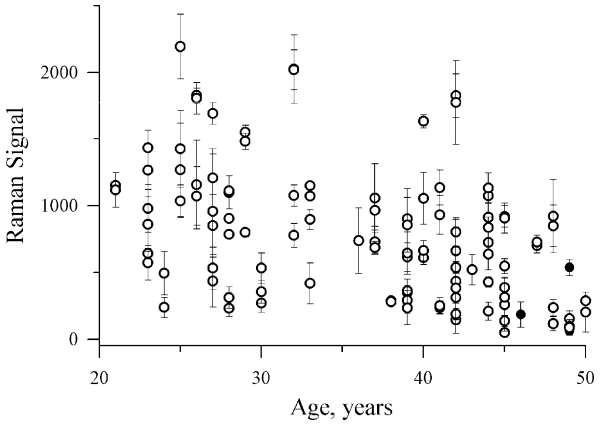

Fig. 12.12. Macular pigment levels measured with spatially integrated Raman detection in about 100 volunteer subjects ranging in age between 20 and 50 years. Each *circle* represents a subject's MP concentration. MP levels can vary strongly between subjects

12.7.2 Spatially Resolved Imaging of Macular Pigment

MP distributions are often assumed to have strict rotational symmetry, high central pigment levels, and a monotonous decline with increasing eccentricity. However, initial resonance Raman imaging, RRI, results obtained with excised human eyecups demonstrated intriguing deviations, clearly revealing the existence of strong significant rotational asymmetries, distribution patterns with central depletions, patterns with widely differing widths between samples, and patterns with fragmented concentration levels [43].

To confirm these "new" distribution features in the living human retina, the Raman method was developed for in vivo imaging applications [44]. The experimental setup for this purpose is shown in Fig. 12.13a. Once the subject achieves head alignment with the help of a red fixation target, as can be seen in Fig. 12.13b, blue light from a solid state 488 nm laser is projected onto the macula as a ∼3.5 mm diameter excitation disk, and two images are recorded with a CCD camera. In the first image, "Raman plus fluorescence image," the light returned from the retina under 488 nm excitation is filtered to transmit only 527 nm light, which is the spectral position of the resonance Raman response of the 1525 cm^{-1} carbon–carbon double bond stretch frequency of the MP carotenoids. Each pixel of this image contains the Raman response of MP as well as the fluorescence components overlapping the Raman response at this wavelength. In the second image, "fluorescence image," the light returned from the retina is filtered to only transmit fluorescence components slightly above the Raman wavelength. The contribution of the broad fluorescence at the Raman wavelength is approximately the same as at the slightly offset longer wavelength position, and the RRI image of an MP distribution can thus be derived with a digital image subtraction routine.

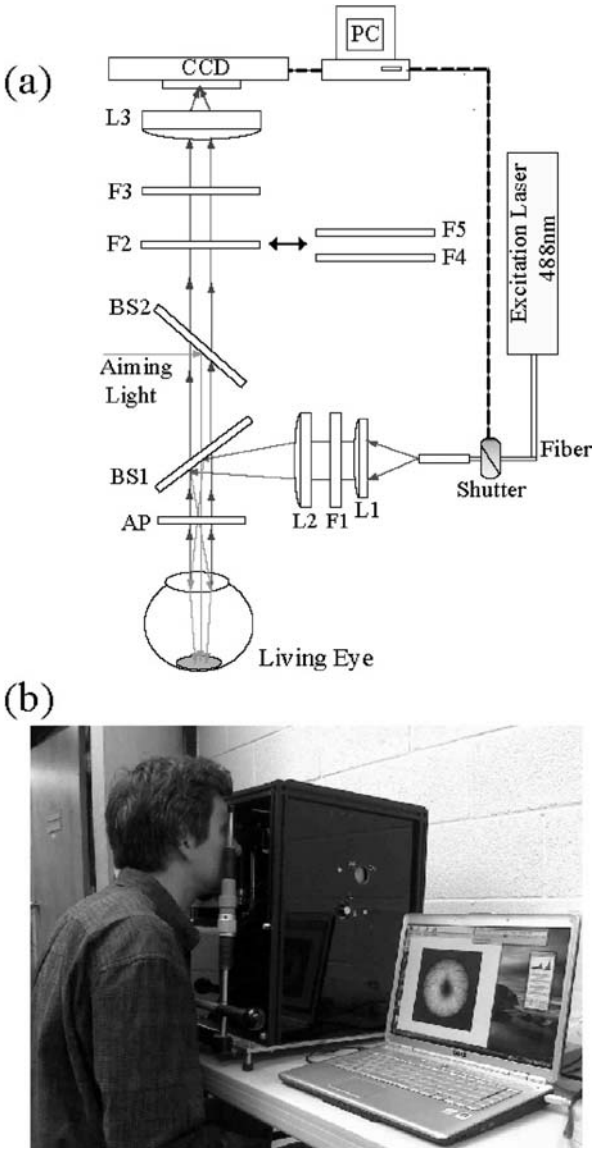

Fig. 12.13. a Schematics of experimental setup used for in vivo resonance Raman imaging, RRI, of macular pigment distributions in the human retina. Light from a blue laser source is projected onto the macula as a large-diameter excitation disk, and the backscattered is imaged onto a CCD camera array. Two sets of filters are used sequentially to selectively image light at the macular pigment molecules' C=C Raman wavelength (Raman image) and at a slightly longer wavelength (offset image). Afterward, the images are digitally subtracted and displayed as topographic or three-dimensional pseudocolor images of the spatial concentrations of macular pigment. **b** Photograph of subject measured with portable instrument developed for use in eye clinics

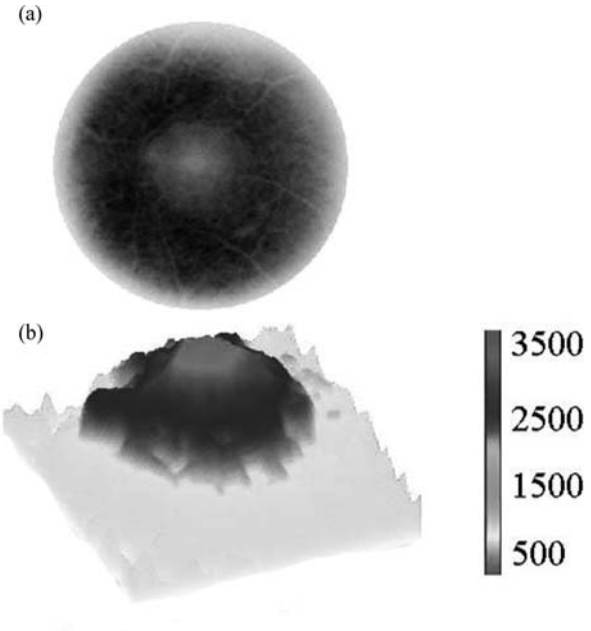

Fig. 12.14. Resonance Raman imaging results for the macular pigment distribution in the retina of a volunteer subject. **a** Typical gray-scale image obtained after subtraction of fluorescence background from pixel intensity map containing Raman response and superimposed fluorescence background. **b** Gray-scaled, three-dimensional representation of gray-scale image

A typical RRI result for a healthy volunteer subject is shown in Fig. 12.14. Figure 12.14a shows a gray-scaled MP distribution obtained after subtraction of the fluorescence background. Figure 12.14b shows the same result as a three-dimensional representation. The MP distribution in this subject features a wide, axially slightly asymmetric distribution, with relatively high central MP levels and a monotonous decline of MP levels toward the peripheral retina. The spatial resolution obtainable with the instrument is $\sim$ sub-50 μm, as can be determined from the size of small blood vessels discernable in the gray-scale images.

When evaluating MP distributions in different subjects, distinctly different patterns are apparent. Figure 12.15 shows as examples two ring-like MP distributions. The first one, obtained again from a healthy subject, consists of a central narrow MP peak and a surrounding, strong, ring-like distribution. The second one, obtained from a patient with a mild form of dry AMD, features a narrow central MP peak and a fragmented distribution at all peripheral locations. Line plots of pigment concentrations along the nasal–temporal (solid line) and inferior–superior meridians (dotted line) can be derived from the images to further highlight the significant inter-subject variations in MP levels, symmetries, and spatial extent.

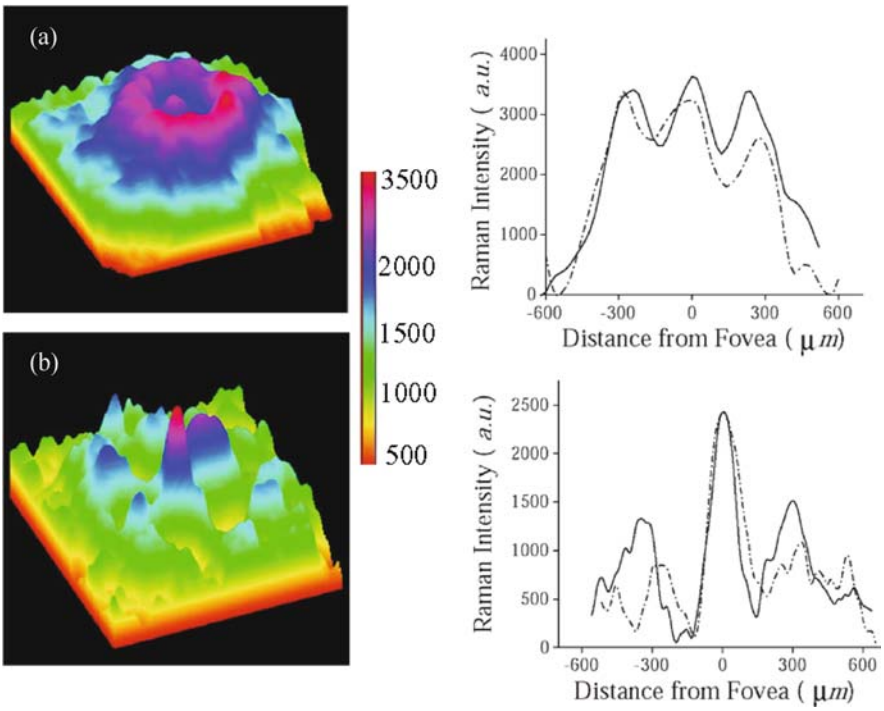

Fig. 12.15. Pseudocolor-scaled, three-dimensional macular pigment resonance Raman images of two volunteer subjects, along with related line plot profiles, derived for each distribution along nasal–temporal (*solid line*) and inferior–superior meridians (*dashed line*), both running through the center of the macula. Distribution (**a**) features a narrow-diameter central peak surrounded by a ring-like distribution component. Varying in relative strengths of central and ring components, this "ring-like" pattern is encountered in about 30% of the measured population. Distribution (**b**) is an example for a fragmented distribution with narrow central peak and broken-up ring structure measured in a subject with a mild form of dry macular degeneration. All images are color coded with the same intensity scale

Both integral and spatially resolved MP Raman methods use the backscattered, single-path, Raman response from lutein and zeaxanthin in the MP-containing retinal layer and largely avoid light traversal through the deeper retinal layers (Fig. 12.8). This is an advantage since optical effects in the deeper layers do not need to be taken into account. Therefore, overlapping fluorescence signals from the anterior optical media can be simply subtracted from the overall light response. On the other hand, since the Raman measurements are an absolute measure of MP concentration levels, potential attenuation effects of the anterior optical media are fully effective and have to be avoided. Fortunately, optical losses from the lens can be neglected in longitudinal studies provided these are carried out over a time span in which lens absorptions can be considered to stay constant (1–2 years), or in any other

studies involving subjects with lens implants. Therefore, the Raman method would be well suited, for example, in important nutritional supplementation trials, studies in which significant increases in individual MP levels have been demonstrated to be achievable in a time span of about 12 months [45].

While the resonance Raman methods are rapid, non-invasive, and highly specific for the non-invasive measurements of MP, the Raman response is still relatively weak. To compensate for this, dilated pupils with 6 mm diameter or larger have to be used. Although common practice in eye examination, this requirement is inconvenient for rapid measurements of large populations. This drawback can be avoided in the recently developed, non-mydriatic version of the lipofuscin fluorescence imaging (autofluorescence imaging) method [46], and potentially also in reflection-based imaging methods which are currently under development [47]. Both methods benefit from the lower excitation light levels required in fluorescence and reflectance detection schemes.

Autofluorescence imaging, AFI, detects the light emitted from lipofuscin in the retinal pigment epithelium and derives the concentration of MP only indirectly via fluorescence excitation spectroscopy [48–50]. The method takes advantage of the fact that both lipofuscin and MP have overlapping absorption bands in the blue wavelength region, and that light excitation with blue wavelengths leads to a strong lipofuscin emission band in the red/near-IR wavelength region. Furthermore, it uses the fact that lipofuscin is relatively evenly distributed throughout the retina, while MP is concentrated only in the macula.

Using blue light illumination of the retina with a large-diameter disk centered on the macula and extending to peripheral regions, the AFI method compares the lipofuscin fluorescence intensities outside and inside the macula. Outside the macula, the fluorescence is not attenuated, since the excitation light can stimulate the lipofuscin fluorescence without any attenuation. Inside the macular region, however, MP located in the anterior layers can attenuate the excitation light. This results in a corresponding reduced lipofuscin fluorescence response. MP optical density levels can then be determined from the logarithm of the ratio of lipofuscin fluorescence levels inside and outside the macula.

AFI has an additional advantage over the Raman approach since the peripheral reference location allows one to eliminate, in first order, any potentially confounding attenuation effects arising from anterior optical media. Also, AFI-derived MP results can be obtained with one image only. On the other hand, this method is not as specific, however, compared to Raman, and care has to be taken to avoid potentially confounding fluorescence effects from anterior ocular media such as the lens.

In Fig. 12.16 the main results are compared for MP distributions and concentrations obtained with both the RRI and AFI methods for an identical subgroup of subjects. Compared to the RRI image, the AFI image is nearly identical, with the exception of a smoother appearance of the distribution. For a group of 16 subjects, MP levels obtained with both methods were spatially

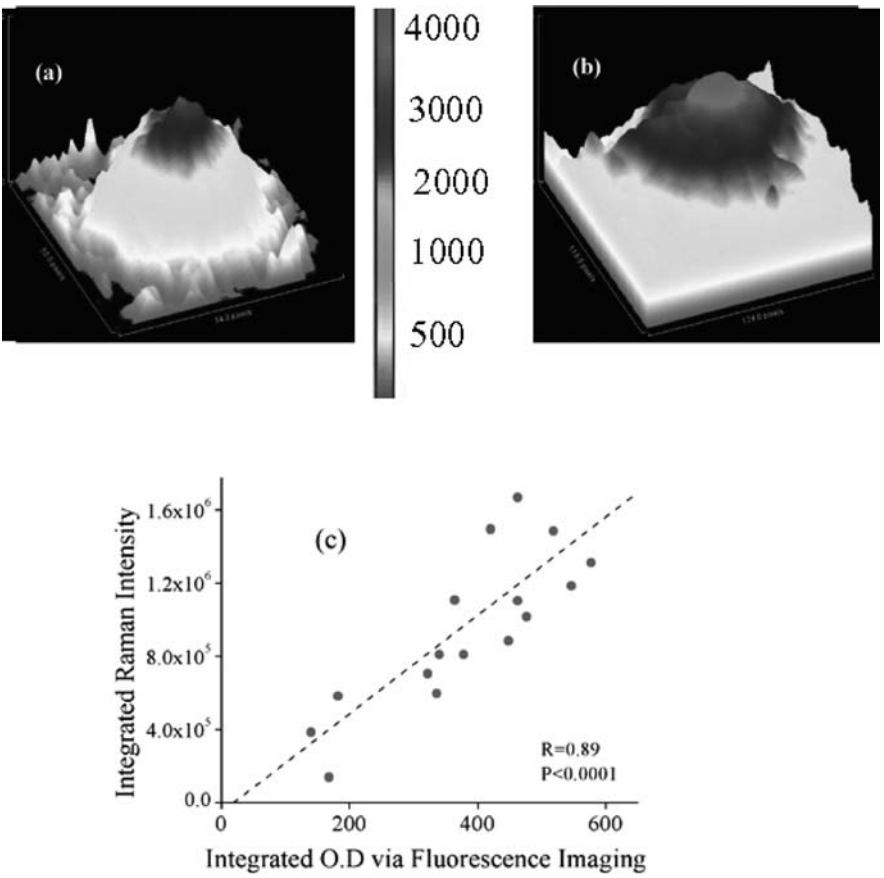

Fig. 12.16. Resonance Raman images of macular pigment distributions obtained for the same subject with the Raman method (**a**) and with a fluorescence-based imaging method (**b**); (**c**) comparison of integrated pigment densities obtained for 16 volunteer subjects with both imaging methods. A high correlation coefficient of R=0.89 is obtained for the correlation between both methods

integrated and compared. Using a best fit that is not forced through zero, a high correlation coefficient of R=0.89 was obtained between both methods. The high correlation is remarkable in view of the completely different optical beam paths and derivation methods used to calculate MP densities in both methods.

Both methods can therefore quickly and objectively assess the composite lutein and zeaxanthin concentrations of MP using spatially averaged "integral" measurements or images that quantify and map the complete MP distribution with high spatial resolution. Imaging reveals the existence of spatially complex MP distribution patterns throughout the subject population. The distributions vary strongly regarding widths, axial and rotational

asymmetries, locally depleted areas, and integrated concentration levels and are more complicated in human subjects than previously thought.

These findings should stimulate future clinical studies aiming to correlate the MP patterns and MP levels with genetics, protein-binding effects, and risk for retinal pathology. Importantly, these non-invasive methods should be attractive for early-age screening of large populations for adequate MP levels, allowing one to track MP levels and distributions over time and detect changes occurring in them upon dietary modifications or supplementation.

12.8 Conclusion

Raman spectroscopy is very appealing for the characterization of biological tissue since it combines a non-invasive optical detection approach with exquisite molecular specificity. The Raman effect is very weak, however, and the detection of useful tissue Raman responses usually requires high light intensities and/or long exposure times. This poses strong challenges for the application to living ocular tissue since the retina is highly light sensitive and therefore very vulnerable to irreversible tissue damage.

Nevertheless, it has been possible to take advantage of Raman spectroscopy in studies of almost all ocular tissue structures in vitro. The obtained results have already provided valuable insight into protein conformations, collagen properties, identification of physiological and pathogenic tissue compounds, and pathways to ocular tissue pathology. The Raman method can become useful for in vivo ocular measurement if the Raman responses are resonantly enhanced. This has been demonstrated for macular pigments, which can be detected non-invasively in living human subjects with spatially integrated or spatially resolved resonance Raman methods. Suitable for use in clinical and field settings, these measurements are expected to contribute to age-related macular degeneration research and to screen large populations for retinal health. Another area that appears on the threshold to in vivo applications is the Raman detection of ocular drugs featuring conjugated molecular subcomponents with enhanced Raman responses.

References

1. R.J. Erckens, F.H.M. Jongsma, J.P. Wickstedt, F. Hendrikse, W.F. March, M. Motamedi, Lasers Med. Sci. **16**, 236 (2001)
2. I. Nabier, I. Chourpa, M. Manfeit, J. Raman Spectrosc. **25**, 13 (1994)
3. N.-T. Yu, E.J. East, J. Biol. Chem. **250**, 2196 (1975)
4. R.A. Schachar, S.A. Solin, Invest. Ophthalmol. Vis. Sci. **14**, 380 (1975)
5. A. Bertoluzza, C. Fagnano, P. Monti, R. Caramazza, M. Cellini, J. Raman Spectrosc. **17**, 133 (1986)
6. N.-T. Yu, M. Bando, J.F.R. Kuck, Invest. Ophthalmol. Vis. Sci. **26**, 97 (1985)
7. N.-T. Yu, J.F.R. Kuck, C.C. Askren, Curr. Eye Res. **1**, 615 (1982)

8. J.J. Duindam, G.F.J.M. Vrensen, C. Otto, J. Greve, Invest. Ophthalmol. Vis. Sci. **39**, 94 (1998)
9. D. Borchman, Y. Ozaki, O.P. Lamba, W.C. Byrdwell, M.C. Yappert, Biospectroscopy **2**, 113 (1996)
10. I.V. Yaroslavsky, A.N. Yarovslavsky, C. Otto, G.J. Puppels, G.F.J.M. Vrensen, H. Duindam, J. Greve, Exp. Eye Res. **59**, 393 (1994)
11. A. Huizenga, A.C.C. Bot, F.F.M. De Mul, G.F.J.M. Vrensen, J. Greve, Exp. Eye Res. **48**, 487 (1989)
12. S. Shih, Y.M. Weng, S. Chen, S.L. Huang, C.H. Huang, W. Chen, Arch. Biochem. Biophys. **420**, 79 (2003)
13. A. Mizuno, M. Tsuji, K. Fujii, K. Kawauchi, Y. Ozaki, Jpn. J. Ophthalmol. **38**, 44 (1994)
14. N.J. Bauer, J.P. Wickstedt, F.H.M. Jongsma, W.F. March, F. Hendrikse, M. Motamedi, Invest. Ophthalmol. Vis. Sci. **39**, 831 (1998)
15. R.J. Erckens, F.H.M. Jongsma, J.P. Wicksted, F. Hendrikse, W.F. March, M. Motamedi, J. Raman Spectrosc. **32**, 733 (2001)
16. N.J.C. Bauer, F. Hendrikse, W.F. March, Cornea **18**, 483 (1999)
17. A. Katz, E.F. Kruger, G. Minko, C.H. Liu, R.B. Rosen, R.R. Alfano, J. Biomed. Opt. **8**, 167 (2003)
18. J. Sebag, S. Nie, K. Reiser, M.A. Charles, N.T. Yu, Invest. Ophthalmol. Vis. Sci. **35**, 2976 (1994)
19. T.I. Sideroudi, N.M. Pharmakakis, G.N. Papatheodorou, G.A. Voyiatzis, Lasers Surg. Med. **38**, 695 (2006)
20. K. Hosseini, F.H.M. Jongsma, F. Hendrikse, M. Motamedi, Lasers Surg. Med. **32**, 265 (2003)
21. Th. Sideroudi, N. Pharmakakis, A. Tyrovolas, G. Papatheodorou, G.D. Chryssikos, G.A. Voyiatzis, J. Biomed. Opt. **12**, 034005-1 (2007)
22. K. Hosseini, W. March, F.H.M. Jongsma, F. Hendrikse, M. Motamedi, J. Ocular Pharmacol. Ther. **18**, 277 (2002)
23. J. Qu, B. Wilson, D. Suria, Appl. Opt. **38**, 5491 (1999)
24. M.J. Goetz et al., IEEE Trans. Biomed. Eng. **42**, 728 (1995)
25. R.J. Erckens, M. Motamedi, W. March, J.P. Wickstedt, J. Raman Spectrosc. **28**, 293 (1997)
26. J. Berger et al., Appl. Opt. **38**, 2916 (1999)
27. J.L. Lambert, J.M. Morookian, S.J. Sirk, M. Borchert, J. Raman Spectrosc. **33**, 524 (2002)
28. K. Dehring, A.S. Smukler, B.J. Roessler, M. Morris, Appl. Spectrosc. **60**, 366 (2006)
29. J.V. Glenn, J.R. Beattie, L. Barrett, N. Frizzell, S.R. Thorpe, M.E. Boulton, J.J. McGarvey, A.W. Stitt, FASEB J. **21**, 3542 (2007)
30. B.H. Wolfenbuttel, C.M. Boulanger, F.R. Crijns, M.S. Huijberts, P. Poitevin, G.N. Swennen, S. Vasan, J.J. Egan, P. Ulrich, A. Cerami, B.I. Levy, Proc. Natl. Acad. Sci. U S A **95**, 4630 (1998)
31. Age-Related Eye Disease Study Research Group, AREDS Report No. 22, Arch. Ophthalmol. **125**, 1225 (2007)
32. A.J. Whitehead, J.A. Mares, R.P. Danis, Arch. Ophthalmol. **124**, 1038 (2006)
33. Y. Koyama, Resonance Raman spectroscopy, in *Carotenoids*, *Vol 1B, Spectroscopy*, ed. by G. Britton, S. Liaaen-Jensen, H. Pfander (Birkhäuser, Basel, 1995), pp. 135–146

34. I.V. Ermakov, M. Sharifzadeh, M.R. Ermakova, W. Gellermann, J. Biomed. Opt. **10**(6), 064028-1–064028-18 (2005)
35. D.S. Michaud, D.D. Feskanich, E.B. Rimm, et al., Am. J. Clin. Nutr. **92**, 990–997 (2000)
36. L.N. Kolonel, J.H. Hankin, A.S. Whittemore, et al., Cancer Epidemiol. Biomarkers Prev. **9**, 795–804 (2000)
37. S. Liu, J.E. Manson, I.M. Lee, et al., Fruit and vegetable intake and risk of cardiovascular disease: The women's health study, Am. J. Clin. Nutr. **72**, 922–928 (2000)
38. P.S.B. Bernstein, M.D. Yoshida, N.B. Katz, R.W. McClane, W. Gellermann, Invest. Ophthalmol. Vis. Sci. **39**, 2003 (1998)
39. I.V. Ermakov, R.W. McClane, W. Gellermann, P.S. Bernstein, Opt. Lett. **26**, 202 (2001)
40. W. Gellermann, I.V. Ermakov, M.R. Ermakova, R.W. McClane, D.Y. Zhao, P.S. Bernstein, J. Opt. Soc. Am. A **19**, 1172 (2002)
41. I.V. Ermakov, M.R. Ermakova, W. Gellermann, Appl. Spectrosc. **59**, 861 (2005)
42. I.V. Ermakov, M.R. Ermakova, P.S. Bernstein, W. Gellermann, J. Biomed. Opt. **9**, 139 (2004)
43. W. Gellermann, I.V. Ermakov, R.W. McClane, P.S. Bernstein, Opt. Lett. **27**, 833 (2002)
44. M. Sharifzadeh, D.-Y. Zhao, P.S. Bernstein, W. Gellermann, J. Opt. Soc. Am. A **25**, 947 (2008)
45. S. Richer, W. Stiles, L. Statkute, J. Pulido, J. Frankowski, D. Rudy, K. Pei, M. Tsipursky, J. Nyland, Optometry **75**, 216 (2004)
46. M. Sharifzadeh, P.S. Bernstein, W. Gellermann, J. Opt. Soc. Am. A **23**, 2373 (2006)
47. T.T.J.M. Berendschot, D. van Norren, Invest. Ophthalmol. Vis. Sci. **47**, 709 (2006)
48. A.G. Robson, J.D. Moreland, D. Pauleikoff, T. Morrissey, G.E. Holder, F.W. Fitzke, A.D. Bird, F.J.G.M.D. van Kuijk, Vision Res. **43**, 1765 (2003)
49. M. Trieschmann, G. Spittal, A. Lommartzsch, E. van Kuijk, F. Fitzke, A.C. Bird, D. Pauleikoff, Graefe's Arch. Clin. Exp. Ophthalmol. **241**, 1006 (2003)
50. F.C. Delori, Arch. Biochem. Biophys. **430**, 156 (2004)

13

Raman Spectroscopy for Early Cancer Detection, Diagnosis and Elucidation of Disease-Specific Biochemical Changes

Nicholas Stone and Catherine A. Kendall

Abstract Raman spectroscopy can provide a wealth of diagnostic information to the clinician, with potential *in vivo* application at endoscopy, outpatient clinic or in surgery, and unstained molecular histopathology in the laboratory. In this chapter we explore the potential of Raman spectroscopy for the detection and diagnosis of two important cancers, breast and oesophageal. These are used to illustrate the differing requirements for disease diagnostics in solid and hollow organs.

13.1 Introduction

Overall, it is estimated that more than one in three people will develop some form of cancer during their lifetime [1]. Traditional methods of cancer diagnosis involve surveillance of at-risk populations or investigation of suspicious symptoms. Unfortunately, often by the time a patient is symptomatic it is too late to facilitate a full cure. However, most cancers need not be killers if they can be exposed to the wide range of improving treatments at an early stage. The primary requirement for the successful treatment of any malignancy is early accurate detection.

There is great interest in developing optical techniques to perform in vivo pathology and detailed morphological assessment, with the prospect of progressing to optical molecular diagnostics of biomarkers. Raman spectroscopy is an optical technique which can interrogate biological tissues, probing the changes in molecular structure that occur with disease, measuring in effect a characteristic tissue fingerprint. Raman spectroscopy can provide rapid, non-invasive, near patient, measurement of tissue biochemistry. This would allow specific targeting of potential abnormalities and early degeneration that can then be ablated using minimally invasive techniques. It has demonstrated potential in addressing the significant challenge of improved diagnosis in several areas of clinical need in the field of oncology as illustrated in Fig. 13.1.

Since the 1990s several groups have used Raman spectroscopy to distinguish between normal and neoplastic tissue. The first studies looked at differentiating between normal tissue and advanced cancers in the breast [2] and

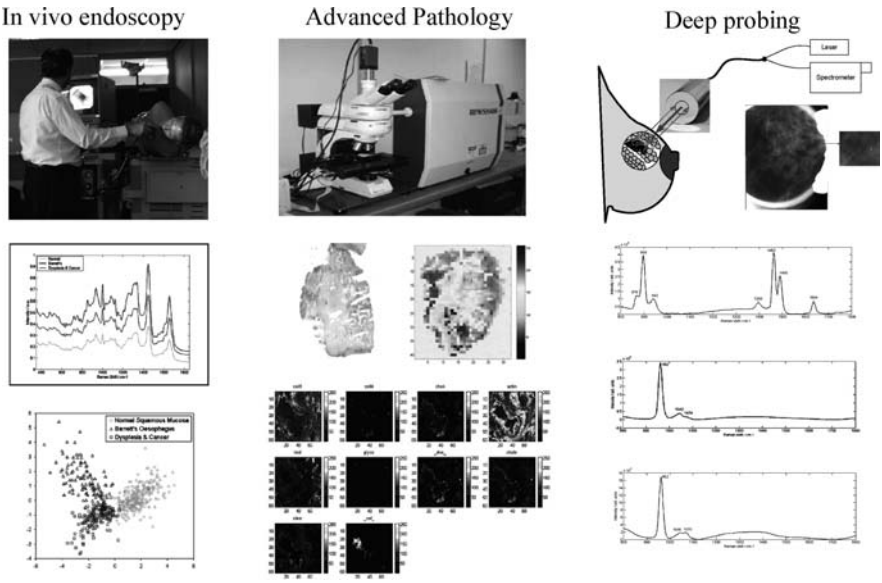

Fig. 13.1. Raman spectroscopy for cancer diagnosis – a multipronged approach: (**a**) in vivo endoscopy, (**b**) advanced pathology (unstained molecular imaging) and (**c**) deep probing

gynaecological cancers [3, 4]. Studies have been performed to differentiate between different pathologies in a number of tissues including colon [5], oesophagus [6–8], skin [9–11], larynx [12], breast [13, 14], cervix [15–17], bladder [18, 19], prostate gland [20, 21] and lymph nodes [22–24].

13.1.1 Competing Technologies

Several other optical techniques that rely on various mechanisms by which light interacts with matter, including absorption, reflection, elastic scattering and autofluorescence, are also being developed for cancer diagnostics. This section will discuss these optical biopsy techniques.

Infrared Spectroscopy

Extensive research has been undertaken using infrared (IR) spectroscopy and imaging to provide rapid mapping of unstained thin tissue biochemistry giving information on disease state with potential for automated differentiation of tissues for cancer and non-cancer diagnostics. The diagnosis of many cancers has been investigated with IR spectroscopy including breast [25, 26], cervix [27], prostate [28–30], colon [31, 32] and lymph nodes [22, 23, 33]. Interrogation of biological tissues in real time using infrared spectroscopy has largely been a challenging proposition because of the strong absorption of mid-infrared light

in water-filled tissues. To enable sampling of tissues they must be sectioned and dried, which has time and resource implications. FTIR of touch imprint cytology has provided detailed spectra which can be used to differentiate various tissue pathologies, circumventing sample processing problems [34]. FTIR spectroscopic imaging with multivariate clustering techniques has been investigated as a tool to detect the changes in cellular composition that may reflect the onset of a disease [35].

Infrared spectroscopy has been shown to spectrally discriminate normal and malignant tissues in conjunction with statistical analysis methods, many of these mathematical methods are applicable to Raman spectral analysis.

Elastic Scattering (Reflectance) Spectroscopy

Elastic scatter is light scattered with the same wavelength as the incident light. Elastic scattering spectroscopy (ESS) includes light scattering spectroscopy (LSS) and diffuse reflectance spectroscopy (DRS) which utilise single and multiple scattering, respectively, to indirectly obtain morphological information about a tissue sample. Only 2–5% of the total reflectance signal can be attributed to singly scattered photons. Despite this, the LSS signal can still be extracted using mathematical models or polarisation since the multiple scattered light becomes depolarised [36].

Elastic scattering probe systems suitable for endoscopic use are simple and cheap to manufacture. They utilise a white light source and the backscattered signal is strong and easy to detect. The technique has been shown to be capable of detecting precancerous degeneration including changes in the nuclear size and degree of pleomorphism (cellular atypia) [37]. Dysplastic changes characterised by nuclear crowding and an increase in nuclear size have been detected using single point acquisitions of less than 1 s [38]. Furthermore, LSS is reported to reliably distinguish between low and high grade dysplasia in patients with Barrett's oesophagus, although this was a limited study with only 4–5 patients in each category [39]. A recent more substantial and important clinical study has used ESS measurements at endoscopy to differentiate non-dysplastic and low grade dysplasia from high grade dysplasia and cancer. Overall 81 patients (181 biopsies) were examined. Elastic scattering spectroscopy detected high grade dysplasia/cancer with 92% sensitivity and 60% specificity and separated these pathologies from inflammation with a sensitivity and specificity of 79% [40]. One major disadvantage is that ESS only probes the morphology of the tissue and not the biochemical changes. Importantly, the technology is simple and inexpensive, making it a possible tool for in vivo diagnosis or multimodal techniques.

Optical Coherence Tomography (OCT)

OCT is an imaging technology based on low-coherence interferometry [41]. OCT is often compared with ultrasound by its virtue of probing for the

intensity of backscattered light ('echo') from within a sample. Agreeing with this association, the classic OCT scanning protocol consists of adjacent one-dimensional A-Scans, which are joined to form a two-dimensional image or three-dimensional volumetric data. In contrast to ultrasound, the 'echo' of the incident light cannot be detected directly. The incident light beam is characterised by short 'pulses' of coherent light, which are crucial for detection. Interference of this coherent part with a reference beam allows the path length to be quantified and hence the location of the scattering can be found with high precision.

Typical OCT systems provide a axial resolution of around 10 μm, 'ultra-high' resolution is of the order of 1 μm. OCT systems typically use near infrared light with penetration depths in soft tissue of the order of a few millimetres. The mode of contrast in OCT is based on boundaries between zone of differences in refractive index within a specimen; specifically, layers of different types of tissue can show up prominently on OCT images. Since the mid-1990s OCT has been suggested to be promising for real-time optical biopsy [42, 43]. State-of-the-art probe systems have dimensions of a few millimetres and can be readily used at endoscopy.

The feasibility of distinguishing dysplasia in Barrett's epithelium in the upper GI tract has been demonstrated by several groups, showing sensitivities of 68–69% and specificities of 71–82% [44, 45]. More recently, intramucosal carcinoma and high grade dysplasia have been distinguished from low grade dysplasia and intestinal metaplasia with a sensitivity and specificity of 83% and 75%, respectively [46]. Hsiung et al. [47] have been able to show crypts on high-resolution volumetric data. The OCT classification relies upon operator interpretation of images and remains somewhat subjective. However methods of, less subjective, automated analysis and processing are under investigation [48] and large trials are awaited.

Autofluorescence

Tissue fluoresces strongly when it is illuminated with ultraviolet or short wavelength visible light. This is called autofluorescence (from endogenous fluorophores) and is generally emitted at a longer wavelength. The concentration of natural fluorophores varies in different layers of tissue and also with increased metabolic activity associated with malignant transformation, which makes it potentially useful for diagnostic purposes. Fluorescence can either be used to obtain real-time images which can be used in conjunction with white light endoscopy, or alternatively point spectral measurements can be made, from which diagnostic algorithms can be developed. The first use of fluorescence point spectroscopy in the oesophagus appeared promising, but has been hindered by false positives from inflammation [49, 50]. Fluorescence imaging is also hindered by false positives, but it has the benefit of being carried out in conjunction with white light endoscopy. There are several commercial systems available with fluorescence imaging capabilities [51].

Administration of Fluorescence Agents

Fluorescence can be enhanced using exogenously administered photosensitisers such as those used in photodynamic therapy. The benefit here is that the operator is looking for a relatively sharp positive fluorescence signal, rather than a reduction in a broad fluorescence signal. Photodiagnosis predominantly uses 5-aminolevulinic acid (5-ALA) which can be administered either locally to the oesophagus or systemically [50]. Others report that 5-ALA can achieve high sensitivity in detecting dysplasia, but lacks the appropriate selectivity, again due to the presence of inflammatory cells which induce a high fluorescence [52].

Multimodal Optical Diagnosis

Several groups have applied a multimodal approach to optical diagnosis. Intrinsic fluorescence, diffuse reflectance and light scattering spectroscopic (LSS) techniques have been assessed alone and in combination for the detection of cervical squamous intraepithelial lesions [53]. In the upper gastrointestinal tract, near infrared (NIR) autofluorescence and LSS were combined to identify dysplastic oesophageal lesions on biopsy samples from 20 patients [54]. In this study, a classification model was developed to discriminate between low risk (Barrett's mucosa without dysplasia and other benign samples) and high risk (dysplasia, squamous cell carcinoma and adenocarcinoma) with a sensitivity and specificity of 86 and 96%, respectively. The most effective diagnostic algorithms are seen to be those developed using a combination of Raman and autofluorescence spectroscopy [55, 56].

13.1.2 Potential Raman techniques

In Vivo Endoscopy

Many technical problems must be solved to enable routine use of Raman spectroscopy as an in vivo clinical tool. The employment of Raman spectroscopy in situ for the study of most tissues necessitates the use of fibre optics to deliver and return the signal from the tissue site. There have been a number of fibre probe designs considered and this is an active area of research [57–60, 10]. Clinical applications to date include GI tract [61], urology [62], lung [63], stomach [64] and cervix [65].

The major problem associated with Raman probes is that Raman signals are generated by the fibres themselves. The signal is proportional to the length of the fibre and to the excitation light intensity. It can have magnitudes equal to and often greater than that of the sample under study [66]. The development of fibre optic Raman probes for biomedical and pharmaceutical applications is discussed further in Chap. 2.

Advanced Pathology

Raman spectroscopy as an adjunct to current diagnostic tools offers many benefits to the histopathologist in evaluating excised tissue samples. Histopathology observes changes in tissue morphology through the disease process. However, it is likely that these architectural changes are driven by early biochemical changes within tissue. The qualitative analysis of such variations provides important clues in the search for a specific diagnosis [67], and the quantitative analysis of biochemical abnormalities is important in measuring the extent of the disease process, designing therapy and evaluating the efficacy of treatment. Raman spectroscopy probes the biochemistry of the tissue sample, and therefore can potentially detect pre-malignant changes within the tissue before morphological changes are evident in histopathological sections, enabling an earlier diagnosis and improved prognosis. Indeed there is scope for Raman to provide prognostic information identifying which patients are more likely to develop cancer. Raman mapping (see also Chap. 5) can rapidly provide biochemical information across an unstained tissue section. Raman provides the additional benefit of an objective diagnosis in comparison to the subjectivity of histopathology, where low levels of inter-observer agreement [6, 68] characterise some critical decisions, for example, whether to perform treatments involving radical surgical excision, radiotherapy, or chemotherapy, which carry risks of mortality and substantial complications [69]. Current significant technological improvements leading to rapid sample scanning are making unstained molecular imaging a real prospect as a histopathological tool [70].

Deep Probing

Until very recently Raman spectroscopy was a technique applied to the surface of the specimen of interest, thus limiting the molecular specific probe for disease to the near surface of outer or hollow inner organs. One of the main problems with the use of Raman spectroscopy for in vivo measurements of biological tissue is that the collected Raman signal decreases when probing at greater tissue depth, causing the surface Raman signal and fluorescence to be significantly stronger than the sub-surface Raman signal. Use of confocal Raman microspectrometry has enabled specific volumetric sampling up to a maximum of 100–200 μm in turbid media such as human tissues. However a number of significant cancers originate in organs deep within the body, for example, breast and prostate cancer and lymph node metastatic involvement. Breast cancer is now the most common cancer in the UK and incidence rates have increased by more than 50% over the last 25 years. The accurate and safe diagnosis of breast cancer is a significant issue in the UK, with annual incidence of 44,000 women and around 300 men. Early diagnosis of the disease allows more conservative treatments and better patient outcomes.

Mammographic screening has demonstrated itself to be effective at identifying lesions within older women. However, there are difficulties in that mammography can only be used on older less dense female breasts and that the identification of a suspect lesion does not provide the clinician with its benign or (pre-)malignant status. In the UK 1,749,185 women were screened in 2004/2005. Approximately 4.9% (85,710) of women screened were referred for further assessment and only 0.8% (13,993) of those women screened were found to have malignancies present [71, 72]. This demonstrates that in the UK alone, 71,717 women in 2004/2005 had further investigations including excisional biopsy, with all the associated risks, costs and anxiety involved, when they had no malignancies present.

The ability to probe tissue biochemistry deep within the body using Raman spectroscopy to identify which calcifications may indicate malignancy has potentially huge benefits. A series of collaborative technological developments at the Rutherford Appleton Laboratory (UK) and elsewhere have advanced this field and have brought Raman spectral probing of gradually increasing depths within tissue closer to a clinical reality. Examples of clinical applications and progress are outlined below and have been discussed further in Chap. 3.

Surface-Enhanced Raman Spectroscopy

A further exciting possibility for advanced cancer diagnostics involves the use of surface-enhanced Raman spectroscopy (SERS). Further discussion is beyond the scope of this chapter but, in conjunction with specific biomarker tags for DNA mutations or protein expression, may provide much stronger disease-specific signals than normal Raman. The technology can also be more easily multiplexed than fluorescence techniques. Potential for microscopy and in vivo diagnostics is being demonstrated [73–77]. Further detail is provided in Chap. 4.

13.2 In Vivo Raman Spectroscopy

Many cancers develop in epithelial tissues that line hollow organs in the body, which are exposed to numerous assaults from chemical and pathogenic carcinogens over a lifetime. Although the carcinogenesis process is often poorly understood, some cancers are known to develop through a pre-malignant condition. For example, Barrett's oesophagus (BO) is associated with an increased risk of oesophageal adenocarcinoma [78, 79]. Progression of BO to adenocarcinoma is thought to be via a multistep process recognised phenotypically as the histological sequence of metaplasia, low grade dysplasia, high grade dysplasia and adenocarcinoma, a transformation that takes several years [80, 81]. The potential benefits of removing an oesophagus exhibiting dysplasia must be weighed against the relatively high mortality associated with oesophagectomy

(5–15%) and the poor outcome in patients who present with invasive adenocarcinoma of the oesophagus (30% survival at 1 year and 8% survival at 5 years for men in England and Wales diagnosed in 2000–2001) [82]. Currently there is a dramatic rise in the incidence of adenocarcinoma centred on the UK [83, 84]. In 2005 in the UK 2% of all cancers diagnosed were oesophageal (7,823) but (in 2006) 5% of all cancer deaths were from oesophageal cancer (7,405) [85].

13.2.1 The Current Gold Standard

Patients with pre-malignant conditions are routinely identified through endoscopic surveillance programmes, during which blind biopsies are taken and examined at a cellular level by a histopathologist; the 'gold standard' for the diagnosis and detection of malignancies and pre-malignancies. Histopathology relies upon sectioning tissue to less than one cell thick ($< 10\,\mu m$) and staining with haematoxylin and eosin (H&E). This provides some general functional information in addition to the morphologic arrangement of the tissue that can be viewed under a conventional light microscope. The principle of histology has changed little since its conception in the 19th century [86]. One problem associated with the gold standard involves the targeting of biopsy samples from microscopic abnormal lesions. Generally a random tissue selection procedure must be employed in the detection of early lesions, which can lead to a high probability of missing abnormal tissue [87]. Biopsy also has inherent risks, including perforation and bleeding. In vivo optical biopsy using Raman spectroscopy has many clinical benefits, including obviating the need for the excisional tissue biopsy, reducing trauma to the patient and the clinicians' workload, especially that of the pathologist. Further, an in vivo Raman biopsy could eliminate the need for many secondary procedures, by enabling treatment to take place directly following diagnosis or by ensuring resection margins are accurately defined. This is likely to improve patient outcomes and decrease waiting times by reducing the number of costly procedures required.

13.2.2 Development of Oesophageal Raman Spectroscopy

A myriad of studies have been undertaken to explore the use of Raman spectroscopy to discriminate diseased from healthy tissues. The early studies generally involved only normal and cancerous tissues, but as researchers have improved their understanding of the clinical processes involved they have realised the need to include as many pathology groups as are likely to be found in the organ of interest. The carcinogenesis process in epithelial tissues follows a complex biochemical pathway and Raman spectroscopy is able to measure aspects of these molecular changes, but they are often very subtle and may require good signal to noise spectra and multivariate analysis techniques for reliable discrimination.

Our group and others have explored the use of Raman spectroscopy for discrimination between numerous pathology groups, leading to the possibility of providing a histopathological tool providing molecular information to support decision-making processes. Furthermore, a fibre probe-based approach can be used to provide detailed molecular information in real time during endoscopic procedures. The following section summarises the findings from a study that was undertaken to evaluate the robustness and explore the architecture of a spectral linear discriminant analysis (LDA) model constructed for classification of oesophageal biopsy samples. The objective was to scope the strength of the model and the required instrumental characteristics for Raman analysis and prediction of pathology within the oesophagus.

A relatively small optimised model has been used as the basis for this work. Perturbations to the spectra in this model, representing likely instrument-to-instrument variations, have been made to evaluate the effects of these on the prediction performance.

Spectral Library Build and Analysis

Here we explore an optimised biopsy targeting model in which all specimens were sent for histopathological analysis by three expert pathologists, who were blinded to patient history and each other's results. Samples were histopathologically graded following the procedures defined by the panel of pathologists in advance, following current international guidelines for pre-malignant/malignant diagnosis in these tissues [88]. Those samples demonstrating mixed pathologies (non-homogeneous) or any histopathological disagreement were rejected to increase the certainty of the pathology of the spectra measured. The importance of gaining a consensus histopathological opinion on all specimens used cannot be overstated. It has been shown by Kendall et al. [6] that using specimens with only a majority of opinion from two out of the three expert pathologists seriously downgrades the performance of the model. This is especially the case for pathology groups where there is greater inter-observer variability.

Specimens from eight pathology groups were included and combined into three key groups for likely biopsy targeting (1) normal squamous, (2) Barrett's, (3) dysplasia and cancers. An 830 nm diode laser was used for illumination with a customised Renishaw System 1000 used to collect the spectra. More detail is provided elsewhere [6, 7]. At least 10 spectra were acquired from the mucosal surface of each sample, which when defrosted from a −80°C freezer were placed on UV grade calcium fluoride slides (Crystran, UK). Spectra were corrected for energy sensitivity of the spectrometer using a National Physical Laboratory (NPL) calibrated lamp source [89]. Table 13.1 details the data included in the study and the mean spectra from the three groups are shown in Fig. 13.2.

Table 13.1. Details of spectra included in the biopsy targeting model. Each of the pathology groups is made up of a combination of others (e.g. Barrett's includes samples of fundic, cardiac and intestinal metaplasia)

Histopathology	Number of patients	Number of spectra
Normal squamous	25	310
Barrett's oesophagus	11	145
Dysplasia and cancers	12	162

Initially an optimised model was constructed using the data collected as outlined above by constructing a principal component (PC)-fed linear discriminant analysis (LDA) model (described elsewhere) [7, 89]. The linear discriminant function was calculated for maximal group separation and each individual spectral measurement was projected onto the model (using leave-one-out cross-validation) to obtain a score. The scores for each individual spectrum projected onto the model and colour coded for consensus pathology are shown in Fig. 13.3. The simulation experiments used this optimised model as a baseline to compare performance of models with spectral perturbations applied to them. The optimised model training performance achieved 93% accuracy overall for the three groups.

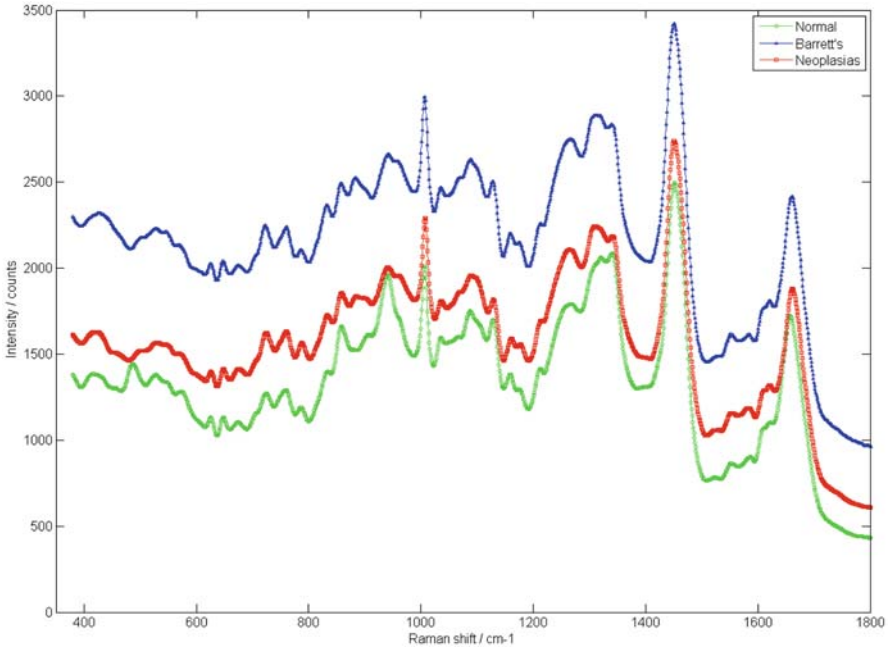

Fig. 13.2. Mean oesophageal Raman spectra from the three pathology groups in the biopsy targeting model

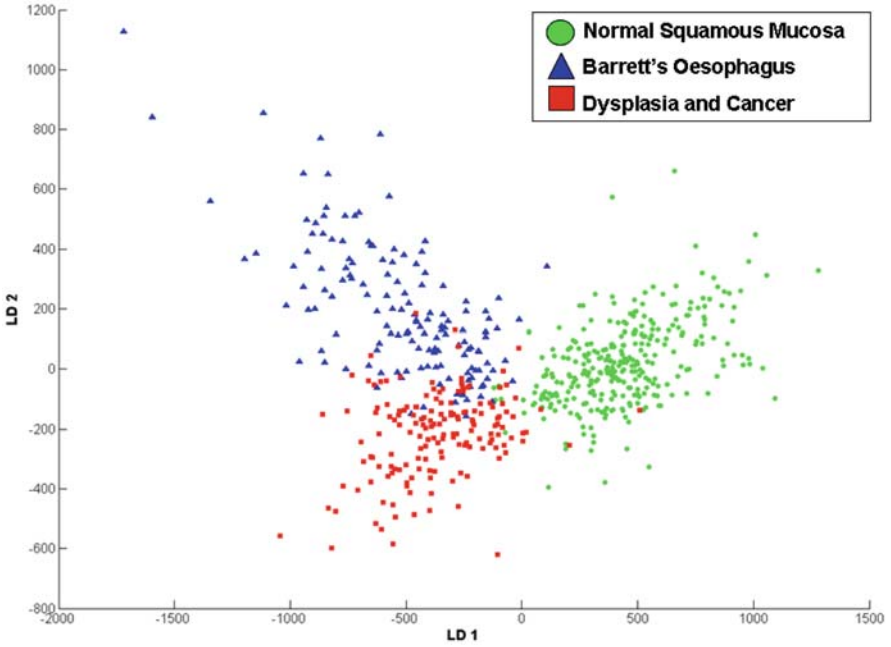

Fig. 13.3. Scatter plot of linear discriminant scores for each spectrum in the biopsy targeting model when tested against all the others, colour coded for consensus pathology

Study of Model Architecture

Initially a study of the architecture of the PC-fed LDA model was made. The three-group model used in this study was constructed from the first 25 principal components of the spectral data set. Each sequential principal component describes a decreasing level of variance from the mean of the spectral data set. Therefore the later PCs will tend to describe more subtle spectral changes across the data set. The balance must be achieved between excluding subtle potentially diagnostic information and including too much noise from the higher level PCs.

The principal component contributions to the model have been studied. In this model the first 25 PCs were included. Figure 13.4 shows the mean PC scores for each of the three pathology groups (top). This enables visualisation of the most significant variations between the groups. The ANOVA F-value is plotted next (middle) to indicate the PCs with the most statistically significant differences between the groups. The bottom plot is the weight of each PC used to construct the LD functions. It can be seen that the first 10–12 PCs are the most significant (middle). However if the LD weights are studied in isolation, it appears that higher PCs are given more weight in the model. This misconception is overcome by studying Fig. 13.5, which shows

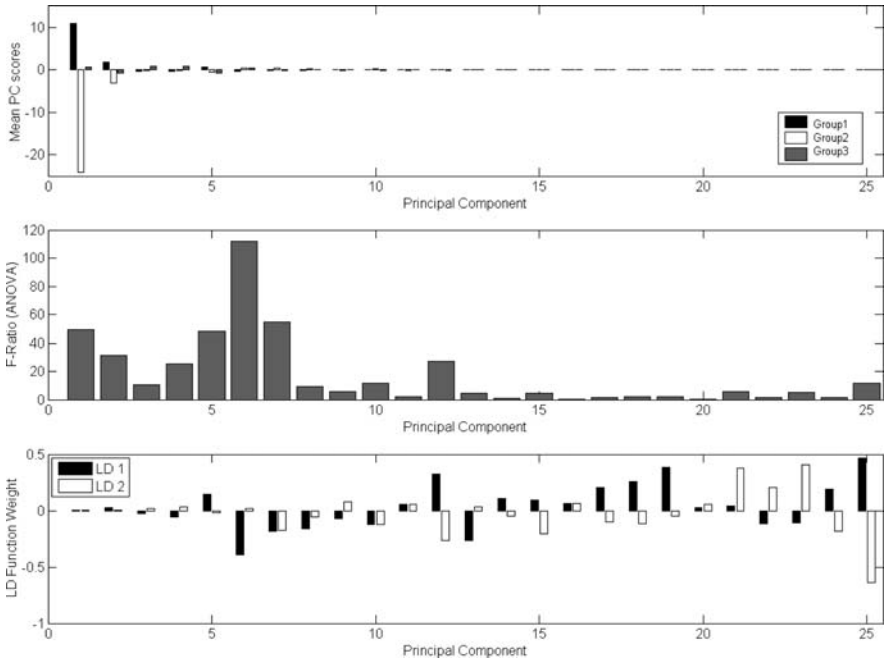

Fig. 13.4. (*Top*) Mean PC scores for each of the three pathology groups. (*Middle*) The ANOVA F-value is plotted to indicate the PCs with the most significant differences between the groups. (*Bottom*) The weight of each PC used to construct the LD functions

the combined contribution of LD weights and PC scores that make up the mean scores for each group in the model. It can be seen that the most significant contributions come from those PCs with high F-values in Fig. 13.4 (middle).

Perturbation of Spectra to Evaluate Effect on Predictive Power of Model

The baseline model outlined above was used to evaluate the effect of simulated perturbations of the spectra on the predictive ability of the model. These perturbations were selected to represent spectral changes that would be caused by likely system variations, such as calibration changes, misalignments, optical aberrations and temperature change, in addition to changes in spectrometer design. For simplicity only a single perturbation has been applied for each test; however, in reality it is likely that there will be a combination of these instrumental effects. The pathology of the perturbed spectra have been predicted by the baseline model and the effect investigated. Numerous spectral model simulations have been performed. These include the following perturbations: number of PCs, linear wave number x-shift, signal-to-noise

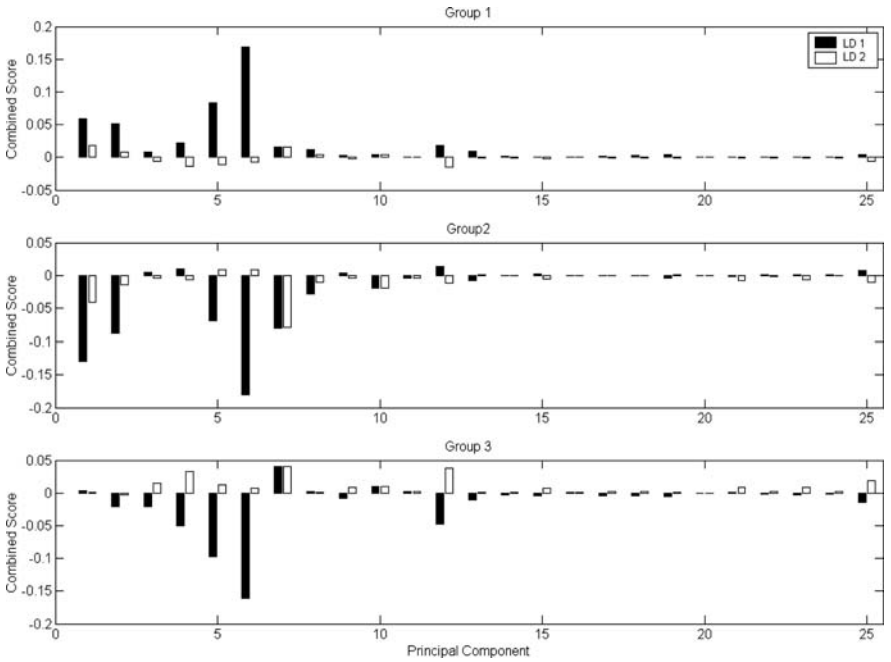

Fig. 13.5. A display of overall contribution of each PC to the power of the discriminant model. This is achieved by multiplying the score of each PC by the LD function weights (Fig. 13.4 (*top*) and (*bottom*))

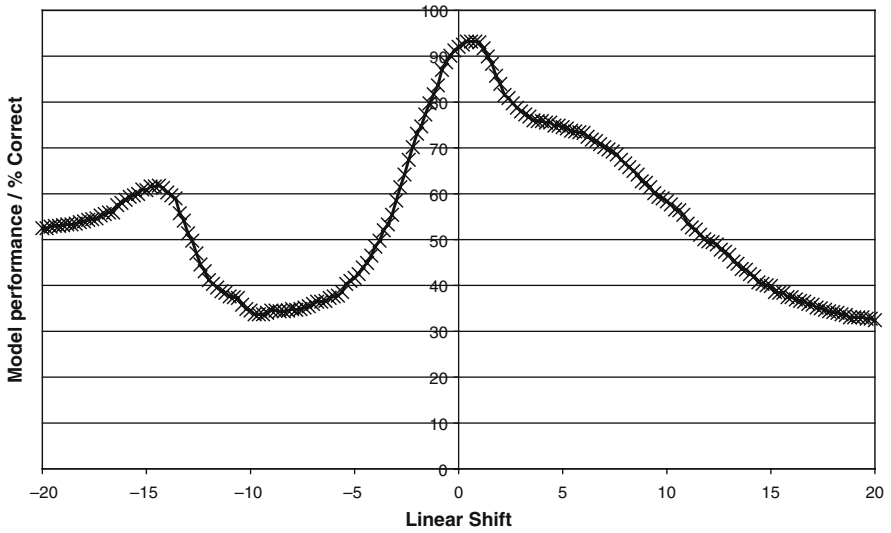

Fig. 13.6. The effect of a linear shift on the spectra between –20 and +20 cm^{-1} in steps of 0.2 cm^{-1}

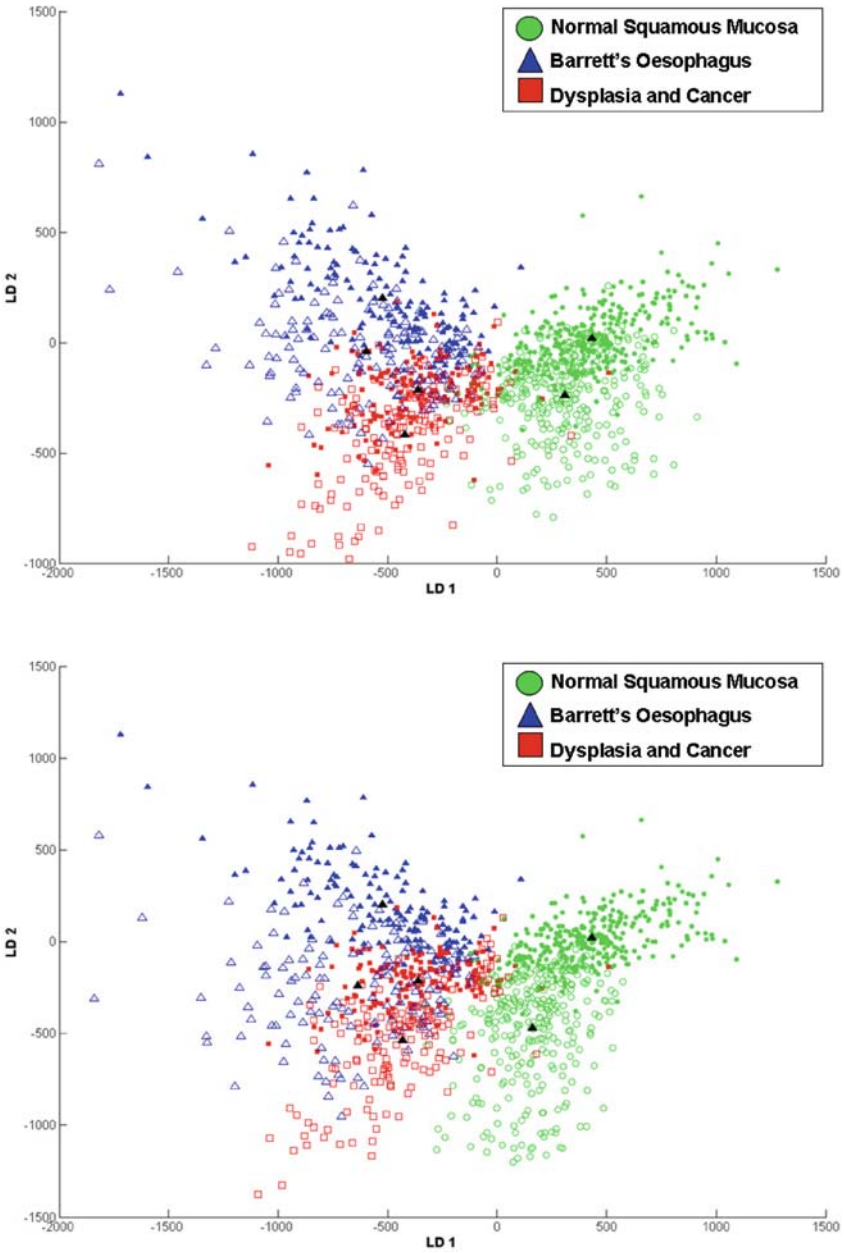

Fig. 13.7. Scatter plots of linear x-shifted spectra superimposed over original model. *Top* x-shift $2\,\mathrm{cm}^{-1}$, *bottom* x-shift $5\,\mathrm{cm}^{-1}$. *Solid* markers are original model and hollow markers are the shifted data. *Black* triangles are group centroids

ratio, spectral resolution, spectral range, non-linear x-shift, constant-, linear-, polynomial y-shift. The biggest impact on the prediction performance of the PCA-fed LDA model was shown to be a linear shift in the predicted spectra. This is demonstrated here.

The effect of a linear wave number shift on the spectra was investigated by shifting spectra between –20 and $+20\,\mathrm{cm}^{-1}$ in steps of $0.2\,\mathrm{cm}^{-1}$. The accuracy of the model in predicting these spectra is displayed in Fig. 13.6. It can be seen that even small x-shifts of one or two wave numbers can have a marked effect on the outcome. The mechanism that causes such a significant reduction in prediction can be seen in Fig. 13.7, which shows scatter plots of linear x-shifted spectra superimposed over the original model. The movement of the group clouds is large even for a $2\,\mathrm{cm}^{-1}$ shift (top); however for $5\,\mathrm{cm}^{-1}$ (bottom) the model has very little overlap with the original data. We have shown (unpublished) that changes of a few degrees Centigrade in ambient temperature can induce spectral shifts of sufficient levels to cause problems with model prediction performance. In addition, an energy sensitivity correction protocol using a broadband lamp source or fluorescent glass has been shown to significantly improve system transferability [90].

13.3 Application of Raman Spectroscopy to Breast Cancer

Vibrational spectroscopy has a number of clinically important applications for breast cancer diagnostics alone: detection and identification of abnormal lesions in vivo; a histopathological classification tool; a surgical tool for tumour margin and metastatic lymph node identification; and even a possible measure of prognostic biochemical changes. A variety of groups have studied the discrimination between breast tissue pathologies using Raman spectroscopy [2, 13, 14, 89, 91]. Early studies demonstrated differences between malignant and normal breast tissue. The key differences appeared to be increases in collagen relative to the high lipid content in normal tissues. This has since proved to be a more complex picture. Disease-specific changes in the breast follow a complex pathway associated with subtle vibrational spectral changes. The empirical peak analysis approach may identify advanced disease, but would be unlikely to be successful for identification of early cancerous changes.

13.3.1 Ductal Carcinoma In Situ

There have been major advances in the detection of carcinoma of the breast in the past several decades. The increased use of mammography for screening and early detection has resulted in a significant increase in the diagnosis of early breast cancer and specifically ductal carcinoma in situ (DCIS) [92]. The number of patients found to have this lesion has grown 10-fold (from 2 to 20%) in the last decades. In the UK national health screening programme

[92], DCIS now forms some 20% of all breast cancers diagnosed by screening. Approximately 80% of DCIS is picked up due to microcalcifications (see later in chapter). Once the radiologist has identified suspicious calcifications, these are biopsied, so that architectural and cytological information can be obtained.

Ductal carcinoma in situ (DCIS) is an intraepithelial proliferation with features of malignancy localised predominantly within ducts. Studies suggest up to 50% of patients with microscopic foci of DCIS develop invasive carcinoma [93]. The invasive lesion occurs in the same area as the original lesion indicating a likely precursor process [94]. A series of cases in which DCIS was not excised has been reviewed and these indicate that progression to invasion is related to the subtype of DCIS: comedo disease progresses into invasive carcinoma both more often and more rapidly than low grade DCIS [95]. Several histopathological systems for subdividing DCIS have been attempted and there is no clear consensus of opinion between the pathologists [96]. This causes great concern in the management of these cases [97].

Raman of DCIS

The Raman spectroscopic studies on the breast (outlined above) have demonstrated discrimination between pathology groups of interest in the breast, but they have not to date demonstrated a sub-classification of ductal carcinoma in situ, over which most clinically important decisions are made for early diagnosis. Here we outline the use of Raman spectroscopic mapping and discrimination for the characterisation and classification of DCIS of the breast.

Breast samples were collected and snap frozen in liquid nitrogen, following informed written consent during routine breast surgery. The National Coordination Group for Breast Screening Pathology in the UK recommend a system derived from the work of Holland and colleagues, which classify DCIS as high, low, intermediate grade based on cytonuclear features [98]. This study utilised this system to identify specific ducts of interest for Raman mapping. For each sample following cryosectioning, an area which corresponded to a marked duct on the adjacent haematoxylin and eosin (H&E) stained section was selected for Raman mapping. Figure 13.8 shows an example of an H&E of DCIS and an image of an unstained duct area for Raman mapping.

A customised Raman microspectrometer [7] was used for this study to enable the acquisition of tissue spectra. Laser light at 830 nm was focused on the tissue section using an Olympus x80 MIRPLAN ultra long working distance objective to provide 35 mW into a spot of about $3 \times 10\,\mu m$ in diameter. The sample was mounted on a Leica DML light microscope, which was equipped with a motorised, computer-controlled sample stage, which enabled automatic scanning of the sample. The area to be scanned and the scanning step size were programmable. Raman maps were acquired using a step size of $10\,\mu m$ and a signal collection time for each pixel of 30 s. The selected area varied from $0.4\,mm^2$ (400 spectra) to $4\,mm^2$ (40,000 spectra) depending on the size of the ducts imaged.

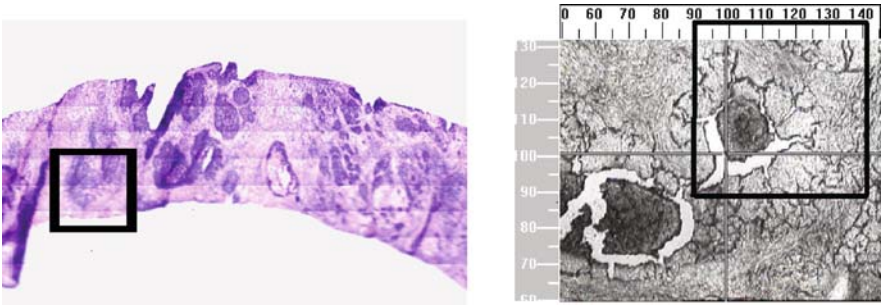

Fig. 13.8. *Left* shows an example of a core biopsy specimen (H&E stained) with high grade DCIS (marked by a consultant histopathologist) and *right* a white light image of the selected duct as imaged on Raman microspectrometer

Wave number calibration, cosmic ray removal and system energy sensitivity correction were performed following spectral acquisition. Each spectrum acquired in the Raman map can be represented by a pixel in an image using principal components to construct pseudocolour score images. Figure 13.9 shows an example duct PC score image and associated mean spectra calculated from the regions of interest selected on the score image.

Further analysis was achieved by utilising the spectra selected from the specific regions of each duct. These spectra were averaged according to their pathological classification to enable visualisation of the mean spectral differences (Fig. 13.10). The individual spectra were then entered into a principal component-fed linear discriminant classification model (as described earlier). This used a total of 5,661 spectra, which were acquired from 22 selected breast ducts covering the four DCIS groups as defined by the Holland classification outlined above. There were four low grade, four intermediate grade, seven high grade non-comedo and seven high grade comedo necrosis.

The classification model was cross-validated using leave one spectrum out to test the robustness of the model. By doing so the individual spectrum is

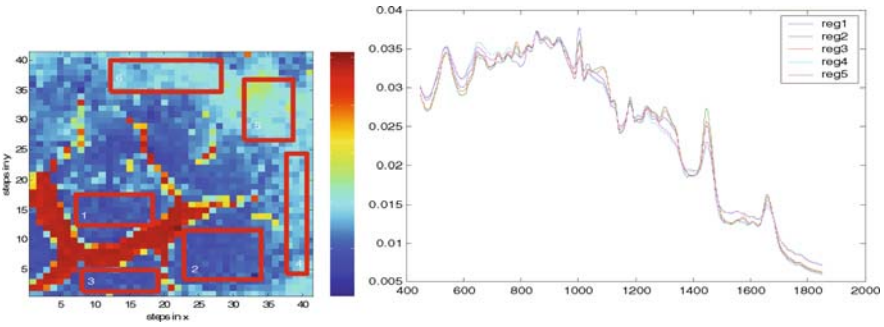

Fig. 13.9. Pseudocolour map and selection of regions of the duct and their corresponding spectra

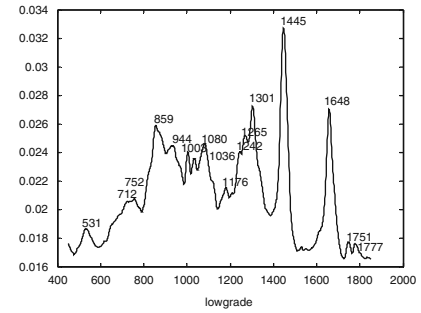

(a) Mean spectrum low-grade DCIS (b) Mean spectrum intermediate DCIS

(c) Mean spectrum high grade non-comedo (d) Mean spectrum high grade comedo

Fig. 13.10. Mean Raman spectra of each duct type

held out of the model and the rest of the spectra are reassigned to the model. Leave one duct out cross-validation was not available prospect as the sample size was too small. The spectral model showed 83% (4,656/5,661) correct prediction of the spectra belonging to the histopathological group assigned. Table 13.2 shows the breakdown by sub-DCIS grouping when the spectra were reassigned to the ducts and compared to the gold standard histopathology. This of course requires more detailed study and validation, but certainly shows some promise.

Table 13.2. Performance of PC-fed LDA model for DCIS sub-group classification

DCIS sub-group	Number of ducts correctly classified	Percentage of ducts correctly classified
Low grade	4	100
Intermediate grade	3	75
High grade, non-comedo	6	86
High grade, comedo	6	86

These Raman breast studies have demonstrated the potential of the technique for sampling and identifying disease processes on excised tissue sections. Although this would be a helpful tool it is yet to be realised for clinical decision making. If the performance of the DCIS model can be carried forward to more extensive population-based diagnostic models then the use of an automated Raman DCIS classification tool would allow histopathologists to reliably utilise the DCIS pathology to provide a prediction of likely carcinoma development, and therefore drive critical clinical decision making [99].

The biochemical changes that occur during carcinogenesis are thought to be a gradual continuum from normal to malignant; therefore, a means of detecting pre-malignancies within these tissues could be achieved by detecting the biochemical changes that are associated with disease progression before the actual progression has occurred. To date direct analysis of the biochemical information in the spectra has been rarely exploited. This has been performed in breast [100] using tissue-derived constituents or urological and oesophageal tissues [21, 67] using pure chemical standards.

Even though there is great potential for future molecular diagnostics and potential prognostication; the greatest early breakthrough for clinical detection and diagnosis is likely to come from a tool which can be used during screening to minimise false results and identify disease-specific tissue composition changes. This is proving to be feasible as an adjunct to mammography possible by using the novel developments in deep Raman techniques. An overview of progress to date is provided below.

13.4 Deep Raman for Diagnostics in Solid Organs

There is great difficulty in accurate diagnosis and detection of malignancies in solid organs such as the breast and prostate. Screening programmes by their nature often result in a high false-positive rate for detection of any 'abnormality'. This leads to a high negative biopsy rate from targeting these 'abnormalities'. There are many negative aspects for the patient of a false-positive diagnosis, from anxiety to risk of infection and the costs to the health community are huge.

A significant problem for those interested in the use of Raman spectroscopy for in vivo measurements of biological tissue is that the collected Raman signal decreases when probing at greater tissue depth. This causes the surface Raman signal and any accompanying fluorescence to be significantly stronger than the sub-surface Raman signal. A series of early collaborative technological developments at the Rutherford Appleton Laboratory in the UK have made Raman spectral probing of gradually increasing depths within tissue become a reality [101–103]. This field is rapidly developing and further details regarding the evolution of deep probing Raman techniques are outlined in Chap. 3.

This section will outline the developments of deep Raman spectroscopy from the use of time gating to spatially offset Raman spectroscopy to transmission Raman; a sequence of increasing practical probing depth as advances have been made. This is counterbalanced by a reduction in depth selectivity with each new technique. An exploration of the potential use of deep Raman for breast cancer diagnostics will be used to illustrate the potential here.

13.4.1 Deep Raman for Breast Cancer Diagnostics

The presence of calcifications on mammography is a feature of particular diagnostic significance because this may be the only marker indicating the possible presence of a malignant breast lesion. While mammography can detect small masses, areas of distortion, ill-defined densities and microcalcifications not detectable by physical examination, it relies only on the morphology of the specimen. This limitation means it gives no definitive criteria for classifying benign and malignant calcifications. This contributes to the fact that only 10–25% of mammographically detected lesions are found to be malignant upon needle biopsy [104, 105].

Microcalcifications can be divided into two types of deposits: type I, which consist of calcium oxalate dihydrate, and type II, which are composed of calcium phosphates, mainly calcium hydroxyapatite. The type of deposit has been correlated with disease [106]. Calcium oxalate crystals are mainly found in benign ductal cysts and rarely found in carcinoma [107], whereas calcium hydroxyapatite deposits are present in proliferative lesions, which can include lesions of both benign and malignant pathology [106]. It has been shown [106] that benign proliferative lesions have calcifications with higher levels of carbonate than the more pure calcium hydroxyapatites found in malignant lesions. At present, there is no reliable way to distinguish between these calcification types by mammography. There are differences in the chemical makeup between the two types of calcification and therefore it is realistic to propose that Raman spectroscopy should be capable of distinguishing between them. Indeed, Haka et al. [106] demonstrated this in a well-designed early study. However, to be truly effective any technique should be able to be utilised transcutaneously in vivo so as to enable a quick and simplistic diagnosis of breast lesions minimising the patient trauma, time delay and high medical costs of biopsies. We develop all these concepts here using Raman spectroscopy.

Specimens

Throughout the following studies the specimens involved human and animal tissues doped with differing levels of powders representing breast

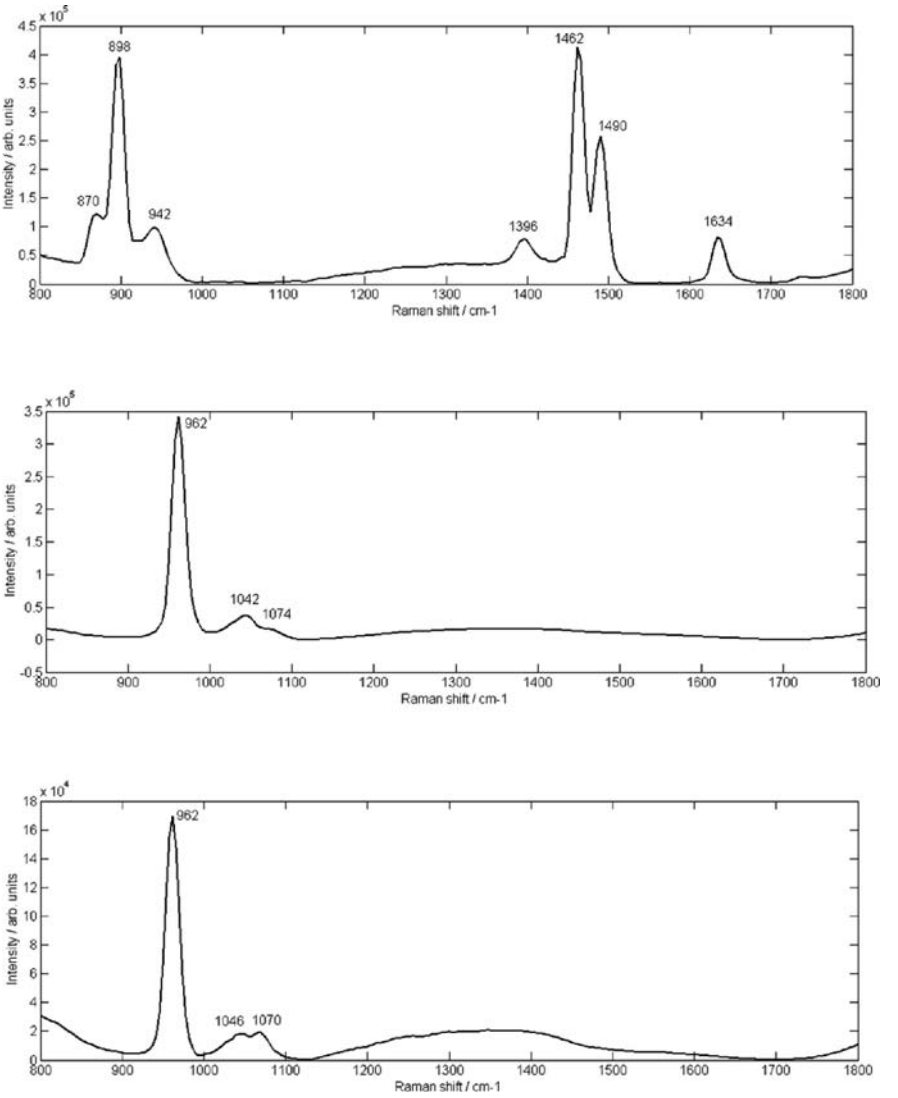

Fig. 13.11. Raman spectra of (**a**) type I calcium oxalate, (**b**) type II calcium hyroxyapatite and (**c**) type II carbonate-substituted calcium hydroxyapatite

calcifications. Polycrystalline standards were purchased of 'pure' calcium hydroxyapatite (HAP), calcium oxalate monohydrate (COM) and a 3.5% carbonate-substituted hydroxyapatite (COHAP). These represented the chemical composition of type I and type II calcifications, respectively. Figure 13.11 shows Raman spectra at 830 nm of these pure calcification standards.

Depth Probing with Kerr-Gated Raman Spectroscopy

Raman signal from deep within tissues tends to be diminished by elastic scattering and therefore the surface signal is usually significantly stronger. A possible way to overcome this is by temporal-gating techniques such as picosecond Kerr gating. The Kerr-gating technique uses excitation with a picosecond pulsed laser, in combination with a fast temporal gating of the Raman scattered light. The scattered light is collected at various time delays following the laser pulse.

In this way Raman photons originating from differing depths within the tissue will emerge at different times thereby making their separation in the temporal domain [108]. It is therefore possible to detect underlying structures through overlying tissue by the rejection of early photons. There have been studies utilising the Kerr-gating technique to improve upon Raman spectra obtained from bone interiors [103, 109] as well as test experiments demonstrating the depth resolving power of the Raman–Kerr-gating concept on artificially prepared samples.

We performed a study using Kerr-gated surface signal suppression for deep probing of tissue calcifications in the breast [110] The Kerr-gated experimental setup is described elsewhere [108]. Experiments were performed to obtain Raman spectra that could distinguish between type I (COD) and type II (HAP/COHAP) calcifications. The samples were placed into quartz cuvettes (windows 300 μm thick) and measured alone (for 10 s with five acquisitions and three cycles) and through sections of chicken breast and fatty tissue; and through normal and cancerous human breast tissue (20 s with 10 acquisitions and three cycles) to demonstrate the ability to obtain Raman spectra from tissue layers. The recovered spectrum was found to be comparable to the spectrum from pure hydroxyapatite [110]. There was some mixing of cancerous breast tissue and HAP signals; however, this was not a problem for discrimination between buried calcium oxalate and HAP.

Spatially Offset Raman Spectroscopy (SORS) for Deep Probing of Calcifications

SORS follows a much simpler approach than Kerr-gated RS. It uses continuous wave laser light and relies on moving the area of collection of the scattered light away from the laser illuminated zone. Apart from being substantially less complex in terms of instrumentation, it is also compatible with the use of lower power continuous wave laser beams and is therefore less likely to induce any laser radiation-induced changes in the tissue. The technique is based on the collection of Raman spectra from regions spatially offset, by different amounts, from the point of incidence of the probe laser beam on the surface of a diffusely scattering sample. Crucially, such an array of spectra contains different relative Raman contributions from the surface and sub-surface layers. Chapter 3 contains more explanation of this approach.

HAP, COHAP and COD were measured through slabs of varying thickness from 2 to 10.2 mm of normal chicken breast tissue, and chicken breast with chicken skin on the surface. Chicken breast and skin tissue were used in the model due to their spectrally homogenous nature. Normal fresh chicken breast was obtained and a small section cut varying thicknesses between 2 and 10.2 mm (2.0, 3.1, 5.0, 5.9, 8.7, 10.2 mm) with other dimensions approximately 20×20 mm. A small section of skin tissue was also cut (to 1.1 mm thick). The samples were stored in a refrigerator and warmed to room temperature before use.

The SORS experimental setup is described in detail elsewhere [111] (Fig. 3.3, Chap. 3 shows a schematic). In brief, 60 mW of laser light at 827 nm was incident on the sample surface into a 0.6 mm spot. The spectra collected from the outer ring of fibres of the SORS fibre probe [111], i.e. at 3 mm spatial offset, were used throughout the data analysis for this study. All spectra were background subtracted and pre-processed with a seven-point Savitzky–Golay smooth. At each depth measured, the calcification spectra were recovered by obtaining the difference between the spectra obtained from the slab of tissue over a calcification standard and the spectrum from the slab of tissue without. Discrimination between spectra of different calcification types with SORS at 8.7 mm depth was demonstrated to be trivial leading to the possibility of performing this study with lower calcification concentrations or through another few millimetres of tissue [112].

Reverse SORS

Further recent advances by both Matousek [113] and Morris [114] have demonstrated significant advantages to using SORS in the reverse configuration, whereby the illumination is made in a ring offset from the central collection point. Flexible depth selection can be achieved with adjustable spatial offsets using an axicon lens. Furthermore, significantly greater powers of illumination can be used safely. For example, with a central spot illumination, 60 mW in a 0.6 mm spot (as we have used) gives a power density of 18 $\mathrm{mW mm^{-2}}$, whereas illumination into a 200 µm thick ring at 8 mm spatial offset at similar power density would require 1 W of laser power. It can be seen from this that provided the tissue can manage to dissipate any total heat buildup, then signals can be significantly increased in this configuration. This illumination could theoretically rise to 2 W into a 15 mm offset ring and 3 W into a 22 mm offset ring.

13.5 Transmission Raman Spectroscopy (TransRaman) for Deep Probing of Calcifications

In the transmission Raman approach, the laser beam is incident upon one side of the probed object and the Raman light is collected from the opposite side.

This geometry is ideally suited for breast mounts used in conventional mammography where the breast is inserted between two plates which are slightly compressed against each other diminishing its thickness to several centimetres. Previous work adopting a transmission geometry, with Raman spectroscopy, has demonstrated that for non-absorbing or weakly absorbing diffusely scattering samples, the bias of traditional backscattering geometries to the surface layers of the sample can be practically eliminated. This has enabled detailed spectroscopic information relating to the interior of the sample to be obtained [115].

TransRaman is largely insensitive to the depth from which signal is collected for a given thickness of the probed medium. This leads to a relative suppression of interference from signals emanating from surface layers of the sample, such as melanin-induced fluorescence from skin and the depth insensitivity permits the monitoring of the presence of lesions irrespective of their depth, e.g. whether in the middle or at the opposite side of the sample, in all the cases yielding a similar level of the Raman signal with respect to the surrounding tissue.

Unlike SORS, the transmission geometry concept in its basic form does not offer the ability to separate layers into individual components but instead it yields, in a simple way, average-volume sample information superseding that obtainable with conventional approaches [115]. Consequently, it cannot yield the depth of the probed object. Nevertheless this information is readily available from mammography or can be obtained using ultrasound or the abovementioned SORS approach.

This experiment utilised the transmission Raman geometry to evaluate its possible use as a mammographic adjunct. Polycrystalline standards were used and placed into 2 mm thick vials with 300 μm UV grade quartz windows. Initially chicken breast and skin tissues were used in this experimental model due to their homogenous nature. This was followed up by a more accurate representation of the human breast using a pork phantom. Normal fresh tissue was obtained from the abattoir and cut to the desired thickness. The samples were stored in a refrigerator and warmed to room temperature before use. The Raman spectra in this work were obtained using a modified SORS Raman apparatus developed for non-invasive spectroscopy of bones described earlier [111]. Figure 3.3, Chap. 3 shows a schematic diagram of the setup used for this study. The probe beam was generated using a temperature stabilised diode laser for Raman spectroscopy and operating at 827 nm (Micro Laser Systems, Inc., L4 830S-115-TE). The laser power at the sample was about 60 mW and the laser spot diameter before the sample was ∼4 mm.

Initial results enabled a simple discrimination between calcification types (buried at 16 mm in chicken breast tissue) using a difference spectrum method of analysis. Furthermore, signal could be obtained from a thin (100–300 μm) powder layer placed with the tissue. This gave a relative volume of calcifications to tissue of between 0.625 and 1.875%. This compares with an approximate physiological level of around 0.05–0.14% [116].

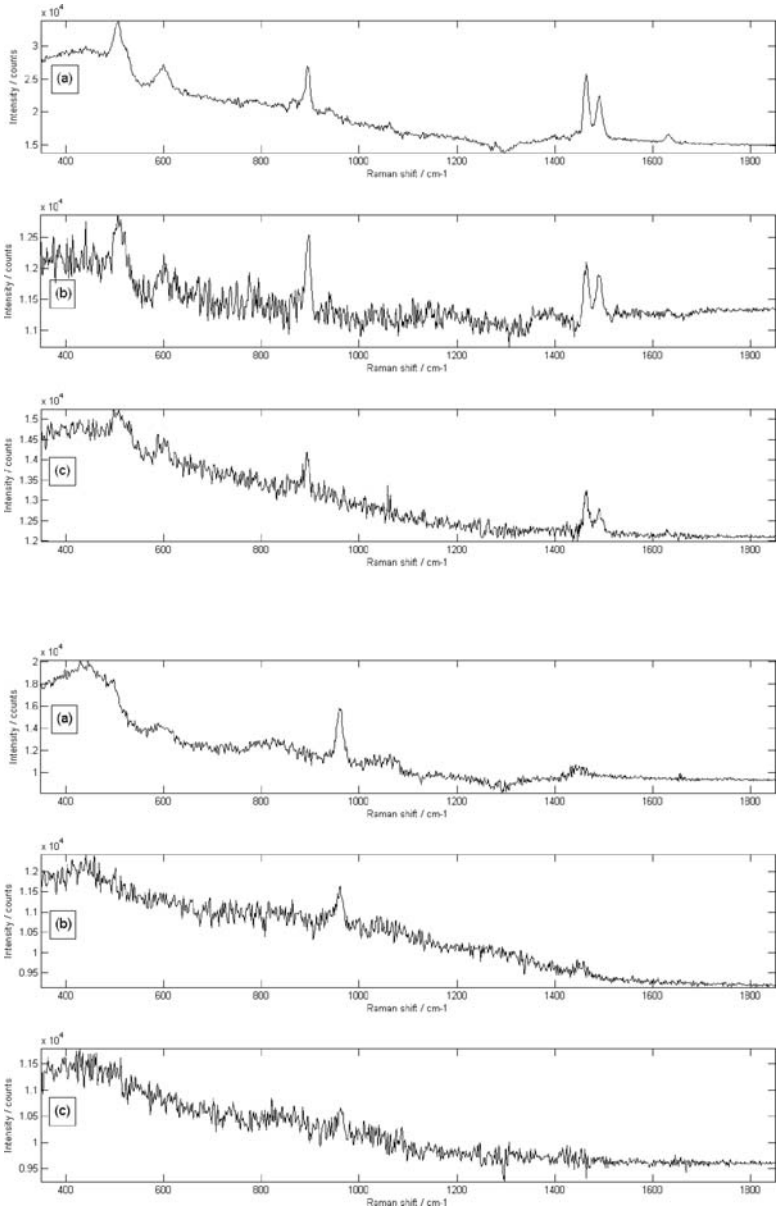

Fig. 13.12. Recovered signals from type I (upper) and type II (lower) calcifications through varying thicknesses and compositions of porcine breast model tissue. (**a**) 17 mm skin/fat/muscle, (**b**) 27 mm muscle and (**c**) 26 mm skin/fat/muscle

Further advances in transmission Raman spectroscopy have enabled signal recovery and calcification identification at clinically useful depths of 27 mm and at calcification volume densities within physiological levels [117]. Collection efficiency has been improved utilising a dielectric bandpass filter at the surface of the tissue to force photons emitted on the illumination surface to re-enter the tissue [118]. This can add 10–20% to the signal in these tissues. Further development of multivariate analysis approaches has led to significant improvements in signal levels recovered (not shown here) [117]. Figure 13.12 shows the recovered signals from type I and type II calcifications through varying thicknesses and compositions of porcine breast model tissue. Finally, this experiment demonstrated that physiologically relevant calcification levels could be detected, through 20 mm of porcine tissue, at a sufficient signal level to spectrally discriminate pathology-specific composition [117].

A programme of work has been outlined that is establishing the possibility of using novel advances in Raman spectroscopy to probe the composition of materials buried within tissues, with an eye on the possibility of using the technique for non-invasive diagnostics. To date this has been performed on human, mammalian and avian tissues from 0.31 to 27 mm. For a summary of progress to date on the use of deep Raman for probing pathological-specific tissue composition, see Table 13.3.

Table 13.3. Summary of progression towards potential in vivo calcification probing with deep Raman spectroscopy

Technique	Wavelength	Depth achieved	Samples
Kerr-gate	488/532 nm	0.3–2.0 mm	Urea/prostate HAP-COM/breast
SORS	830 nm	2.0–10.2 mm	HAP-COM/ chicken breast
TransRaman	830 nm	16–27 mm	HAP-COM/chicken breast/porcine breast phantom

13.6 Conclusions

Here we have explored a number of potential applications of Raman spectroscopy for early cancer diagnostics. In the last 10 years there have been dramatic breakthroughs in technological developments and understanding of what can be achieved with them. These advances are beginning to grab the attention of both scientific and medical communities, as advances are made and more teams move into this promising field.

Raman spectroscopy has been shown to identify disease-specific compositional changes in numerous cancers and pre-cancerous steps, and in the future these changes will be critical to potentially revolutionising clinical diagnostics and detection methodologies.

Acknowledgements

This chapter has been written utilising data from ongoing work within the Biophotonics Research Group at Gloucestershire Hospitals, UK. Work involving Becky Baker, Krishnan Subramanian, Joanne Hutchings, Neil Shepherd, Jonathan Christie Brown, Charlie Chan and Hugh Barr has been outlined here. Dr. Catherine Kendall is a Royal Society Dorothy Hodgkin Fellow and Prof. Nicholas Stone holds a National Institute of Health Research Career Scientist Fellowship.

The deep Raman section has involved a collaborative programme of work with Prof. Pavel Matousek at the Rutherford Appleton Laboratory, UK.

References

1. Office for National Statistics: Cancer Research UK Incidence and Mortality Statistics (2005), http://info.cancerresearchuk.org/cancerstats/mortality/?a=5441. Accessed 14 Oct 2008
2. R. Alfano, C.H. Liu, W.L. Sha, H.R. Zhu, D.L. Akins, J. Cleary, R. Prudente, E. Cellmer, Lasers Life Sci. **4**(1), 23 (1991)
3. C. Liu, B.B. Das, W.I. Sha Glassmen, G.C. Tang, K.M. Yoo, H.R. Zhu, D.L. Akins, S.S. Lubicz, J. Cleary, R. Prudente, E. Cellmer, A. Caron, R.R. Alfano, J. Photochem. Photobiol. B, Biol. **16**, 187 (1992)
4. A. Mahadevan-Jansen, R. Richards-Kortum, J. Biomed. Opt. **1**, 31 (1996)
5. M. Shim, L.M. Song, N.E. Marcon, B.C. Wilson, J. Photochem. Photobiol. **72**, 146 (2000)
6. C. Kendall, N. Stone, N. Shepherd, K. Geboes, B. Warren, R. Bennett, H. Barr, J. Pathol. **200**, 602 (2003)
7. N. Stone, C. Kendall, N. Shepherd, P. Crow, H. Barr, J. Raman Spectrosc. **33**(7), 564 (2002)
8. T.C. Bakker Schut, M.J.H. Witjes, H.J.C.M. Sterenborg, O.C. Speelman, J.L.N. Roodenburg, E.T. Marple, H.A. Bruining, G.J. Puppels, Anal. Chem. **72**, 6010–6018 (2000)
9. S. Sigurdsson, P.A. Philipsen, L.K. Hansen, J. Larsen, M. Gniadecka, H.C. Wulf, IEEE Trans. Biomed. Eng. **51**(10), 1784–1793 (2004)
10. C.A. Lieber, S.K. Majunder, D.L. Ellis, D.D. Billheimer, A. Mahadevan-Jansen, Laser Surg. Med. **40**, 461–467 (2008)
11. A. Nijssen, T.C.B. Schut, F. Heule, P.J. Caspers, D.P. Hayes, M.H.A. Neumann, G.J. Puppels, Invest. Dermatol. **119**(1), 64–69 (2002)
12. N. Stone, P. Stravroulaki, C. Kendall, M. Birchall, H. Barr, Laryngoscope **110**, 1756 (2000)

13. R.E. Kast, G.K. Serhatkulu, A. Cao, A.K. Pandya, H. Dai, J.S. Thakur, V.M. Naik, R. Rabah, Biopolymers **89**(3), 235–241 (2008)
14. J.S. Thakur, H. Dai, G.K. Serhatkulu, R. Naik, V.M. Naik, A. Cao, A. Pandya, C. Freeman, J. Raman Spectrosc. **38**(2), 127–134 (2007)
15. A. Mahadevan-Jansen, W.F. Mitchell, N. Ramanujam, U. Utzinger, R. Richards-Kortum, Photochem. Photobiol. **68**(3), 427–431 (1998)
16. F.M. Lyng, E.Ó. Faoláin, J. Conroy, A.D. Meade, P. Knief, B. Duffy, M.B. Hunter, J.M. Byrne, P. Kelehan, H.J. Byrne, Exp. Mol. Pathol. **82**(2), 121–129 (2007)
17. C.M. Krishna, N.B. Prathima, R. Malini, B.M. Vadhiraja, R.A. Bhatt, D.J. Fernandes, P. Kushtagi, M.S. Vidyasagar, V.B. Kartha, Vib. Spectrosc. **41**(1), 136–141 (2006)
18. M.C. Hart Prieto, P. Crow, C. Kendall, J. Uff, M. Wright, A.W. Ritchie, N. Stone, SPIE **5321**, 57 (2004)
19. P. Crow, J.S. Uff, J.A. Farmer, M.P. Wright, N. Stone BJU **93**, 1232–1236 (2004)
20. P. Crow, N. Stone, C.A. Kendall, J.S. Uff, J.A. Farmer, H. Barr, M.P. Wright, Br. J. Cancer **89**(1), 106 (2003)
21. N. Stone, M.C. Hart Prieto, P. Crow, J. Uff, A.W. Ritchie, Anal. Bioanal. Chem. **387**(5), 1657–1668 (2007)
22. M. Isabelle, N. Stone, H. Barr, M. Vipond, N. Shepherd, K. Rogers, Spectroscopy **22**(2–3), 97–104 (2008)
23. W.E. Katzin, J.A. Centeno, L.-J. Feng, M. Kiley, F.G. Mullick, Am. J. Surg. Pathol. **29**(4), 506–511 (2005)
24. J. Smith, C. Kendall, A. Sammon, J. Christie-Brown, N. Stone, Tech. Cancer Res. Treat. **2**(4), 327–331 (2003)
25. H. Fabian, N.A.N. Thi, M. Eiden, P. Lasch, J. Schmitt, D. Naumann, Biochim. Biophys. Acta Biomembr. **1758**, 874–882 (2006)
26. L. Zhang, G.W. Small, A.S. Haka, L.H. Kidder, E.N. Lewis, Appl. Spectrosc. **57**, 14–22 (2003)
27. K.R. Bambery, B.R. Wood, M.A. Quinn, D. McNaughton, Aust. J. Chem. **57**, 1139–1143 (2004)
28. D.C. Fernandez, R. Bhargava, S.M. Hewitt, I.W. Levin, Nat. Biotech. **23**, 469–474 (2005)
29. E. Gazi, J. Dwyer, N.P. Lockyer, J. Miyan, P. Gardner, C. Hart, M. Brown, N.W. Clarke, Biopolymers **77**, 18–30 (2005)
30. J.J. Aning, M. Isabelle, J. Uff, A.W.S. Ritchie, H.W. Gilbert, N. Stone, SPIE **6628**, 66280F (2007). doi:10.1117/12.727855
31. P. Lasch, D. Naumann, Cell. Mol. Biol. **44**, 189–202 (1998)
32. T. Richter, G. Steiner, M.H. Abu-Id, R. Salzer, R. Bergmann, H. Rodig, B. Johannsen, Vib. Spectrosc. **28**, 103–110 (2002)
33. B. Bird, M. Miljkovic, M.J. Romeo, J. Smith, N. Stone, M.W. George, M. Diem, BMC Clin. Pathol. **8**, 8 (2008)
34. K. Das, C. Kendall, M. Isabelle, C. Fowler, J. Christie-Brown, N. Stone, J. Photochem. Photobiol. B, Biol. **92**(3), 160–164 (2008)
35. X.-Y. Wang, J.M. Garibaldi, B. Bird, M.W. George, Appl. Intell. **27**(3), 237–248 (2007)
36. L.M. Wong Kee Song, B. Wilson, Tech. Gastrointest. Endosc. **7**, 78–85 (2005)

37. R.S. DaCosta, B.C. Wilson, N.E. Marcon, Best Pract. Res. Clin. Gastroenterol. **20**, 41–57 (2006)
38. V. Backman, M.B. Wallace, L.T. Perelman, J.T. Arcndt, R. Gujar, M.G. Muller, Q. Zhang, G. Zonios, E. Kline, T. McGillican, S. Shapshay, T. Valdez, K. Badizadegan, J.M. Crawford, M. Fitzmaurice, S. Kabani, H.S. Levin, M. Sciler, R.R. Dasari, I. Itzkan, J. Van Dam, M.S. Feld, Nature 406, 35–36 (2000)
39. M.B. Wallace, L.T. Perelman, V. Backman, J.M. Crawford, M. Fitzmaurice, M. Seiler, K. Badizadegan, S.J. Shields, I. Itzkan, R.R. Dasari, J. Van Dam, M.S. Feld, Gastroenterology **119**, 677–682 (2000)
40. L.B. Lovat, K. Johnson, G.D. Mackenzie, B.R. Clark, M.R. Novelli, S. Davies, M. O'Donovan, C. Selvasekar, S.M. Thorpe, D. Pickard, R. Fitzgerald, T. Fearn, I. Bigio, S.G. Bown, Gut **55**, 1078–1083 (2006)
41. D. Huang, E.A. Swanson, C.P. Lin, J.S. Schuman, W.G. Stinson, W. Chang, M.R. Hee, T. Flotte, K. Gregory, K.A. Puliafitio, Science **254**, 1178–1181 (1991)
42. G.J. Tearney, M.E. Brezinski, B.E. Bouma, S.A. Boppart, C. Pitris, J.F. Southern, J.G. Fujimoto, Science **276**, 2037–2039 (1997)
43. P.H. Tomlins, R.K. Wang, J. Phys. D Appl. Phys. **38**, 2519–2535 (2005). doi:10.1088/0022-3727/38/15/00
44. L.-M. Wong Kee Song, K.K. Wang, Technol. Cancer Res. Treat. **2**, 289–302 (2003)
45. G. Isenberg, M. Sivak Jr, A. Chak, R. Wong, J. Willis, B. Wolf, D. Rowland, A. Das, A. Rollins, Gastrointest. Endosc. **62**, 825–831 (2005)
46. J.A. Evans, J.M. Poneros, B.E. Bouma, J. Bressner, E.F. IIalpern, M. Shishkov, G.Y. Lauwers, M. Mino-Kenudson, N.S. Nishioka, G.J. Teamey, Clin. Gastroenterol. Hepatol. **4**, 38–43 (2006)
47. P. Hsiung, L. Pantanowitz, A. Aguirre, Y. Chen, D. Phatak, T. Ko, S. Bourquin, S. Schnitt, S. Raza, J. Connolly, Gastrointest. Endosc. **62**, 561–574 (2005)
48. F. Bazant-Hegemark, N. Stone, J. Biomed. Opt. **13**(3), 034002 (2008)
49. M. Panjehpour, B.F. Overholt, J.L. Schmidhammer, C. Farris, F.P. Buckley, T. Vo-Dinh, Gastrointest. Endosc. **41**, 577–581 (1995)
50. E. Endlicher, R. Knuechel, T. Hauser, R.-M. Szeimies, J. Schölmerich, H. Messmann, Gut **48**, 314–319 (2001)
51. Y. Kusunoki, F. Imamura, H. Uda, M. Mano, T. Horai, Chest **118**, 1776–1782 (2000)
52. I.A. Boere, T.C. Bakker Schut, J. Van den Boogert, RWF. de Brain, G.J. Puppels, Vib. Spectrosc. **32**, 47–55 (2003)
53. I. Georgakoudi, E. Sheets, M. Muller, V. Backman, C. Crum, K. Badizadegan, R. Dasari, M. Feld, Am. J. Obstet. Gynecol. **186**, 374–382 (2002)
54. C.A. Lieber, S. Uratama, N. Rahim, Opt. Express **14**, 2211–2219 (2006)
55. Z. Huang, H. Lui, Photochem. Photobiol. **81**, 1219–1225 (2005)
56. M.G.M. Grimbergen, C.F.P. van Swol, R.J.A. van Moorselaar, A. Mahadevan-Jansen, J. Uff, N. Stone, J. Photochem. Photobiol. B, Biol. **95**, 170–176 (2009)
57. U. Utzinger, D.L. Heintzelman, A. Mahadevan-Jansen, A. Malpica, M. Follen, R. Richards-Kortum, Appl. Spectrosc. **55**, 955–959 (2001)
58. Z. Huang, H. Zeng, I. Hamzavi, D.I. McLean, H. Lui. Opt. Lett. **26**, 1782–1784 (2001)

59. M.G. Shim, B.C. Wilson, E. Marple, M. Wach, Appl. Spectrosc. **53**, 619–627 (1999)
60. Y. Komachi, H. Sato, K. Aizawa, H. Tashiro, Appl. Opt. **44**(22), 4722–4732 (2005)
61. A. Molckovsky, L.-M. Wong Kee Song, M.G. Shim, N.E. Marcon, B.C. Wilson, Gastrointest. Endosc. **57**, 396–402 (2003)
62. P. Crow, A. Molckovsky, N. Stone, J. Uff, B. Wilson, L.-M. Wong Kee Song, Urology **65**, 1126–1130 (2005)
63. M.A. Short, S. Lam, A. McWilliams, J. Zhao, H. Lui, H. Zeng, Opt. Lett. **33**, 711–713 (2008)
64. S.K. Teh, W. Zheng, K.Y. Ho, M. Teh, K.G. Yeoh, Z. Huang, Br. J. Cancer **98**, 457–465 (2008)
65. A. Robichaux-Viehoever, E. Kanter, H. Shappell, D. Billheimer, H. Jones III, A. Mahadevan-Jansen, Appl. Spectrosc. **61**(9), 986–993 (2007)
66. M.L. Myrick, S.M. Angel, Appl. Spectrosc. **44**, 565–570 (1990)
67. G. Shetty, C. Kendall, N. Shepherd, H. Barr, N. Stone. Br. J. Cancer **94**(10), 1460–1464 (2006)
68. E. Montgomery, M.P. Bronner, J.R. Goldblum, J.K. Greenson, M.M. Haber, J. Hart, L.W. Lamps, G.Y. Lauwers, A.J. Lazenby, D.N. Lewin, M.E. Robert, A.Y. Toledanao, K. Washington, Hum. Pathol. **32**, 268–378 (2001)
69. D. Alderson, Gut **51**, 620–621 (2002)
70. J. Hutchings, C. Kendall, B. Smith, N. Shepherd, H. Barr, N. Stone, J. Biophotonics **2**, 91–103 (2009)
71. DH Breast Screening Results from the NHSBSP (England, Wales, Scotland & Northern Ireland, 2004/2005), http://www.cancerscreening.nhs.uk/breastscreen/nhsbsp-results-2004-2005.pdf
72. A.J. Evans, A.R. Wilson, H.C. Burrell, I.O. Ellis, S.E. Pinder, Mammographic features of ductal carcinoma in situ (DCIS) present on previous mammography, Clin. Radiol. **54**(10), 644–646 (1999)
73. S. Keren, C. Zavaleta, Z. Cheng, A. de la Zerda, O. Gheysens, S.S. Gambhir, PNAS **105**(15), 5844–4849 (2008)
74. B. Lutz, C. Dentinger, L. Sun, L. Nguyen, J. Zhang, A.J. Chmura, A. Allen, S. Chan, B. Knudsen, J. Histochem. Cytochem. **56**(4), 371–379 (2008)
75. R.J. Dijkstra, W.J.J.M. Scheenen, N. Dam, E.W. Roubos, J.J. ter Meulen, J. Neurosci. Methods **159**(1), 43–50 (2007)
76. L. Sun, K.-B. Sung, C. Dentinger, B. Lutz, L. Nguyen, J. Zhang, H. Qin, M. Yamakawa, M. Cao, Y. Lu, A.J. Chmura, J. Zhu, X. Su, A.A. Berlin, S. Chan, B. Knudsen, Nano Lett. **7**(2), 351–356 (2007)
77. R.J. Stokes, A. Macaskill, P.J. Lundahl, W.E. Smith, K. Faulds, D. Graham, Small **3**(9), 1593–1601 (2007)
78. A.P. Naef, M. Savary, L. Ozzelo, J. Thorac. Cardiovasc. Surg. **70**, 826–835 (1975)
79. M.M. Berenson, R.H. Riddell, D.B. Skinner, J.W. Freston, Cancer **41**, 554–561 (1978)
80. J.A. Jankowski, N.A. Wright, S.J. Meltzer, G. Triadafilopoulos, K. Geboes, A.G. Casson, D. Kerr, L.S. Young. Am. J. Pathol. **154**(4), 965–973 (1999)
81. A. Woodman, J.A. Jankowski, N.A. Shepherd, in *Barrett's Esophagus*, ed. by H.W. Tilanus, S.E.A. Attwood (Kluwer, Amsterdam, 2001), p. 167–180

82. Office for National Statistics: Oesophageal cancer survival statistics (2008), http://info.cancerresearchuk.org/cancerstats/types/oesophagus/survival/#source1. Accessed 14 Oct 2008
83. H.B. El Serag. Gastrointest Endosc. Clin. North Am. **31**, 21–44 (2002)
84. W.J. Blot, S.S. Devesa, J.F. Fraumeni, JAMA **270**, 1320 (1993)
85. Office for National Statistics: Oesophageal cancer survival statistics (2008), http://publications.cancerresearchuk.org/WebRoot/crukstoredb/CRUK_PDFs/mortality/IncidenceMortalitySummary.pdf. Accessed 14 Oct 2008
86. R. Virchow, *Cellular Pathology as Based upon Physiological and Pathological Histology* 7th American Ed., Frank Chance (Translator) New York (1860)
87. J.W. Van Sandick, J.J. van Lanshot, B.W. Kuiken, G.N. Tytgat, G.J. Offenhaus, H. Obertop, Gut **43**, 216–222 (1998)
88. R.J. Schlemper, R.H. Riddell, Y. Kato, F. Borchard, H.S. Cooper, S.M. Dawsey, M.F. Dixon, C.M. Fenoglio Preiser, J.-F. Flejou, K. Geboes, T. Hattori, T. Hirota, M. Itabashi, M. Iwafuchi, A. Iwashita, Y.I. Kim, T. Kirchner, M. Klimpfinger, M. Koike, G.Y. Lauwers, K.J. Lewin, G. Oberhuber, F. Offner, A.B. Price, C.A. Rubio, M. Shimizu, T. Shimoda, P. Sipponen, E. Solcia, M. Stolte, H. Watanabe, H. Yamabe, Gut **47**, 251–255 (2000)
89. N. Stone, C. Kendall, J. Smith, P. Crow, H. Barr, Faraday Discuss Pap. **126**, 141–157 (2003)
90. N. Stone, C. Kendall, H. Barr, in *Vibrational Spectroscopy for Medical Diagnosis*, ed. by M. Diem, P.R. Griffiths, J.M. Chalmers (Wiley, New York, 2008), p. 203
91. D.C.B. Redd, Z.C. Feng, K.T. Yue, T.S. Gansler. Appl. Spectrosc. **47**(6), 787–791 (1993)
92. Office for National Statistics: Registrations. Registration of cancer diagnosed in 2000. England. Series MBI no31. London National Statistics (2003), http:/www.statstics.gov.uk
93. D.L. Page, W.D. Dupont, L.W. Rogers, M. Landenberger, Cancer **49**, 751–758 (1982)
94. D.L. Page, W.D. Dupont, L.W. Rogers, M.S. Rados, Cancer **55**,2698–2708 (1985)
95. A. Ketcham, F. Muffat, Cancer **65**, 387–393 (1990)
96. J.P. Sloane, R. Ellman, T. Anderson, Eur. J. Cancer **30A**, 1414–1419 (1994)
97. K.A. Skinner, M.J. Silverstein, Endocr. Relat. Cancer **8**, 33–45 (2001)
98. P.A. Holland, A. Gandhi, W.F. Knox, M. Wilson, A.D. Baildam, N.J. Bundred, Br. J. Cancer **77**, 110–114 (1998)
99. M.J. Silverstein, M.D. Lagios, P.H. Craig, J.R. Waisman, B.S. Lewinsky, W.J. Colburn, D.N. Poller, Cancer **77**, 2267–2274 (1996)
100. K.E. Shafer-Peltier, A.S. Haka, M. Fitzmaurice, J. Crowe, J. Myles, R.R. Dasari, M.S. Feld, JRS **33**(7), 552–563 (2002)
101. P. Matousek, M. Towrie, A. Stanley, A.W. Parker, Appl. Spectrosc. **53**, 1485–1489 (1999)
102. N. Everall, T. Hahn, P. Matousek, A.W. Parker, M. Towrie, Appl. Spectrosc. **55**, 1701–1708 (2001)
103. M.D. Morris, A.E. Goodship, E.R.C. Draper, P. Matousek, M. Towrie, A.W. Parker, SPIE **5321**, 164–169 (2004)
104. Y. Sun, X.R. Zeng, L. Wenger, H.S. Cheung, Biochem. Biophys. Res. Commun. **312**, 1053–1059 (2003)

105. A.S. Haka, K.E. Shafer-Peltier, M. Fitzmaurice, J. Crowe, R.R. Dasari, M.S. Feld, Proc. Natl. Acad. Sci. U S A **102**, 12371–12376 (2005)
106. A.S. Haka, K.E. Shafer-Peltier, M. Fitzmaurice, J. Crowe, R.R. Dasari, M.S. Feld, Cancer Res. **62**, 5375–5380 (2002)
107. R.E. Lenkinski, M. Ahmed, A. Zaheer, J.V. Frangioni, S.N. Goldberg, Acad. Radiol. **10**, 1159–1164 (2003)
108. P. Matousek, N. Everall, M. Towrie, A.W. Parker, Appl. Spectrosc. **59**, 200–205 (2005)
109. E.R.C. Draper, M.D. Morris, N.P. Camacho, P. Matousek, M. Towrie, A.W. Parker, A.E. Goodship, J. Bone Miner. Res. **20**, 1968–1972 (2005)
110. R. Baker, P. Matousek, K.L. Ronayne, A.W. Parker, K. Rogers, N. Stone, Analyst **132**, 48–53 (2007)
111. P. Matousek, I.P. Clark, E.R.C. Draper, M.D. Morris, A.E. Goodship, N. Everall, M. Towrie, W.F. Finney, A.W. Parker, Appl. Spectrosc. **59**, 393–400 (2005)
112. N. Stone, R. Baker, K.D. Rogers, A.W. Parker, P. Matousek, Future possibilities in the diagnosis of breast cancer by subsurface probing of calcifications with spatially offset Raman spectroscopy (SORS). Analyst **132**, 899–905 (2007)
113. P. Matousek, Appl. Spectrosc. **60**, 1341 (2006)
114. M.V. Schulmerich, K.A. Dooley, M.D. Morris, T.M. Vanasse, S.A. Goldstein, J. Biomed. Opt. **11**, 060502 (2006)
115. P. Matousek, A.W. Parker, Appl. Spectrosc. **60**, 1353 (2006)
116. P. Matousek, N. Stone, J. Biomed. Opt. **12**(2), 024008 (2007)
117. N. Stone, P. Matousek, Cancer Res. **68**, 4424–4430 (2008)
118. C. Eliasson, P. Matousek, J. Raman Spectrosc. **39**(5), 633–637 (2008)

14

Raman Spectroscopy of Bone and Cartilage

Michael D. Morris

Abstract This chapter will reviews the Raman spectroscopy of the subject tissues. After a brief introduction to the structure, biology, and function of these tissues, we will describe the spectra and band assignments of the tissues and then summarize applications to studies of tissue development, mechanical function and competence, and pathology. Both metabolic diseases and genetic disorders will be covered.

14.1 Raman Spectroscopy of Bone

Chemical composition is an important contributor to bone quality, a term that encompasses the effects of architecture, composition, and remodeling dynamics. These are usually measured as band height or band area ratios and in some cases as band widths. FTIR spectroscopy of both bone and cartilage was extensively developed in the 1980s and 1990s, preceding the intense interest in Raman spectroscopy that began in the middle and the late 1990s. Interpretation of Raman spectra of bone and cartilage has relied extensively on this body of knowledge, but with use of bands that are strong in the Raman spectra rather than those that are strong in the infrared. The differences are greatest in the mineral components of the spectra, which are primarily vibrations of phosphate and carbonate, which have intense totally symmetric X–O stretches. Applications, on the other hand, have exploited the generally recognized strengths of Raman spectroscopy. These include the ability to obtain spectra of hydrated specimens and of thick specimens, the superior spatial resolution of Raman microscopy, and compatibility with silica core optical fiber. The latter has enabled the emerging field of in vivo Raman spectroscopy.

A typical Raman spectrum of bone tissue [1] is shown in Fig. 14.1. The major bands are identified in the figure. A more complete tabulation of bands in the Raman spectrum can be found in [2].

The mineral/matrix ratio is a measure of the mineral content and is calculated from the infrared spectrum as the ratio of the integrated phosphate ν_1, ν_3 envelope (ca. 900–1200 cm^{-1}) to the collagen amide I envelope

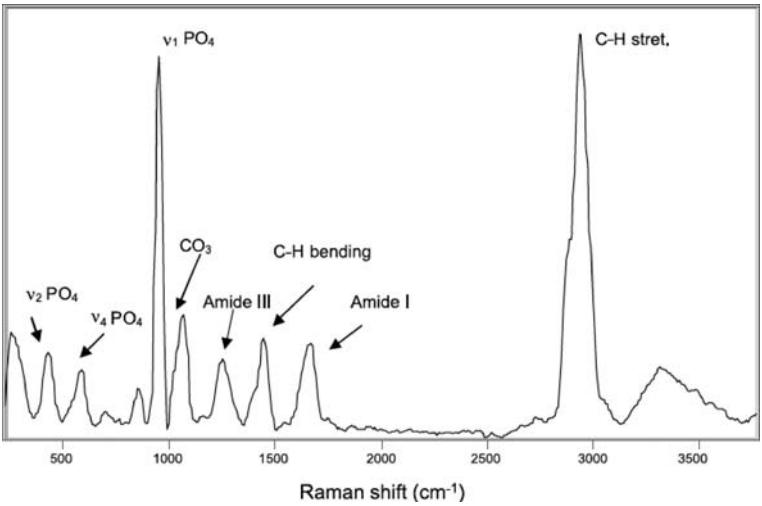

Fig. 14.1. Raman spectrum of osteonal bone tissue. Major band assignments are marked. Reprinted with permission from [1]

(ca. 1600–1700 cm^{-1}) [3, 4]. Much early, Raman spectroscopy also used the height or area ratio of the phosphate ν_1 envelope to the amide I envelope. It should be noted that the amide envelope is sensitive to the state of collagen cross-linking [5] or to anything else causing changes in the hydrogen bonding in collagen fibrils. While the methylene deformation mode at ca. 1445 cm^{-1} has occasionally been proposed as a measure of matrix content, it overlaps the lipid methylene band and must be used with caution. For these reasons, our laboratory now prefers to use bands at 853 and 876 cm^{-1} as measures of collagen content [6, 7]. These bands are predominantly due to hydroxyproline and are relatively insensitive to changes in the collagen secondary structure. An emerging consensus favors their use.

Crystallinity is a metric related to mineral maturity and is a measure of mineral crystallite size, mineral maturity, and the amount of substitution into the apatitic lattice. Crystallinity increases when crystals are larger and more perfect (i.e. less substitution). It is directly proportional to the inverse width of the 002 reflection (*c*-axis reflection) in the powder x-ray diffraction pattern of bone mineral. Several features in the infrared spectra of bone correlate with mineral crystallinity, most of which are components of the phosphate ν_1, ν_3 envelope [8]. Any of these correlations should be usable in the Raman spectrum provided there are no other overlapping Raman peaks. However, there has been less emphasis on crystallinity in the bone Raman literature and only the inverse width of the phosphate ν_1 band has been used as a measure of crystallinity [9–12].

The carbonate/phosphate ratio in the infrared spectrum is calculated from the area of the $CO_3^{-2}\nu_2$ components at 866 cm^{-1} (labile carbonate), 871 cm^{-1}

(B-type carbonate), and 878 cm^{-1} (A-type carbonate) and the area of the $PO_4{}^{-3}\nu_1, \nu_3$ envelope. These correlations use earlier carbonate band assignments [13, 14].

Carbonate band assignment has been more difficult in Raman spectra than in the infrared [15] because of near overlap of the major carbonate ν_1 mode at 1070 cm^{-1} with a component of phosphate ν_3 at 1076 cm^{-1} in carbonated apatites [16]. These bands have earlier been reported as coincident [17] or have been assumed to be a single broad carbonate band [18]. Most investigators have used the ratio of the carbonate ν_1 band/phosphate ν_1 band as a measure of the carbonate/phosphate ratio. It is likely that in many cases this error is small, but for lightly carbonated mineral, typically freshly precipitated mineral, the error may be important. Remeasurement or reinterpretation of some Raman spectroscopic data may be needed.

Collagen cross-linking is measured as changes in the amide I envelope, as first described in the FTIR literature [5]. Biochemical analysis of collagen model peptides showed that pyridinoline (Pyr) cross-links resulted in a band at ca. 1660 cm^{-1} and dehydrodihydroxylysinonorleucine (de-DHLNL) cross-links resulted in a band at ca. 1690 cm^{-1}. It is known that the content of de-DHLNL cross-links decreases with bone collagen maturity, while Pyr cross-link content increases [19], probably because the former matures into the latter [20]. Thus the 1660 cm^{-1}/1690 cm^{-1} ratio is an indicator of matrix maturity. This metric was developed for IR spectroscopy and has been used successfully in Raman spectroscopy [21, 22]. The same ratio has been used to indicate abnormal matrix cross-linking [23] and to infer rupture of cross-links under mechanical load [21]. Changes in the amide I envelope report changes in collagen secondary structure and are only indirect measures of cross-linking. Amide I or amide III envelope analysis should be used with caution.

14.2 Raman Mapping and Imaging of Bone

The development, aging, pathology, microstructure, and compositional basis of mechanical functioning of musculoskeletal tissue are major application areas for vibrational spectroscopic imaging [18, 24]. The chemical composition and organization of bone components determine the function of musculoskeletal tissue. But bone is not homogeneous. So a Raman spectrum measured at a single point offers limited information. Raman imaging provide chemical composition information at a micron spatial scale, thus providing insight into the distribution of both mineral and organic matrix components. This information provides a more complete characterization of bone development, microstructure, and aging because chemical spatial variations contribute greatly to the structural integrity and ultimate biological function of bone. Similar information is obtainable from FTIR imaging, although with reduced spatial resolution. Because of the greater availability of FTIR imaging systems, FTIR has been the preferred imaging mode.

As described above, a common approach to spectroscopic imaging of musculoskeletal tissue is to use band height or area ratios after background subtraction. Sources of background may include autofluorescence and fluorescence of polymethyl methacrylate (PMMA) and epoxies if specimens are fixed and embedded. Histological stains may also contribute. Unless very heavy staining is used, absorption by common histological stains does not result in thermal damage. In Raman imaging stain fluorescence is not observed because the deep red and NIR excitation often lie well to the red of the absorption spectra of almost all stains. Crane and coworkers [25] have shown that the bands of hematoxylin and eosin, the most common stains, are not visible in Raman images.

There has extensive use of self-modeling curve resolution (SMCR) in Raman imaging, beginning with the work of Timlin [26] who showed that factor score images rather than band intensity or intensity ratio images could be used. Although the phenylalanine ring-breathing mode was misidentified as a HPO4-2 band that is found at nearly the same wave number, the ability of SMCR to extract and image spatially varying components was demonstrated.

Our laboratory now routinely employs band target entropy minimization (BTEM) [27] to extract Raman spectra and generate score image contrast [28]. The technique allows extraction of even minor components, provided that a band target, a region of the spectrum that uniquely identifies the component, can be identified either from the underlying spectra or from features in the first few eigenvectors of the spectra that comprise the image data set. Other laboratories prefer other methods, and there is not yet any consensus on the best multivariate techniques for this or other tissue Raman imaging.

An important caution is that any data reduction procedure that begins with extraction of principal components is based on the assumption that the data set consists of a small number of constituents that contribute to the measured spectrum at any point in proportion to their composition at that point. These methods cannot be used if that assumption is not correct. For example, mechanical loading of bone tissue causes wave number and intensity shifts in both mineral and matrix bands. While the shifts are not always linear with Appl. load, they do vary continuously.

14.3 Applications of Bone Raman Imaging

Because bone is a heterogeneous material, single point spectroscopic measurements can be misleading. Bone tissue of different ages is found in both osteonal and cancellous bone as a function of the remodeling process. Within an osteon ($\sim$200–250 μm in diameter), the youngest tissue is found at the center and the most mature is found at the edges. For cancellous bone, the youngest tissue is found at the edges of individual trabeculae while the more mature tissue is found at the center.

The consensus from the more developed FTIR imaging is that mineral/matrix ratio and crystallinity increase from the center to the edge of an individual osteon [15] and from the periosteal region to endosteal region of cortical bone [29–31]. The collagen cross-link ratio follows the same trends as mineral/matrix ratio and crystallinity [32], while the carbonate/phosphate ratio and acid phosphate content are found to decrease away from the center of an osteon, with the most marked changes in acid phosphate occurring within 30 µm of the osteon [15, 31]. Raman imaging of bone began with the work of Timlin [26], who imaged trabecular bone at moderately high definition (100 × 100 and 100 × 200 pixels) and moderately high resolution (1.4 µm × 1.4 µm) pixels (Fig. 14.2).

In interstitial tissue, SMCR has been used to generate Raman images of bone [33]. Two mineral factors were observed, one corresponding to normal mineral and the other containing a peak at 952 cm^{-1}, interpreted as arising from amorphous calcium phosphate (ACP). Images of this factor showed that ACP was located away from the edge of the osteon. The authors suggested that ACP might be found in regions susceptible to damage or that perhaps ACP was a result of prior damage.

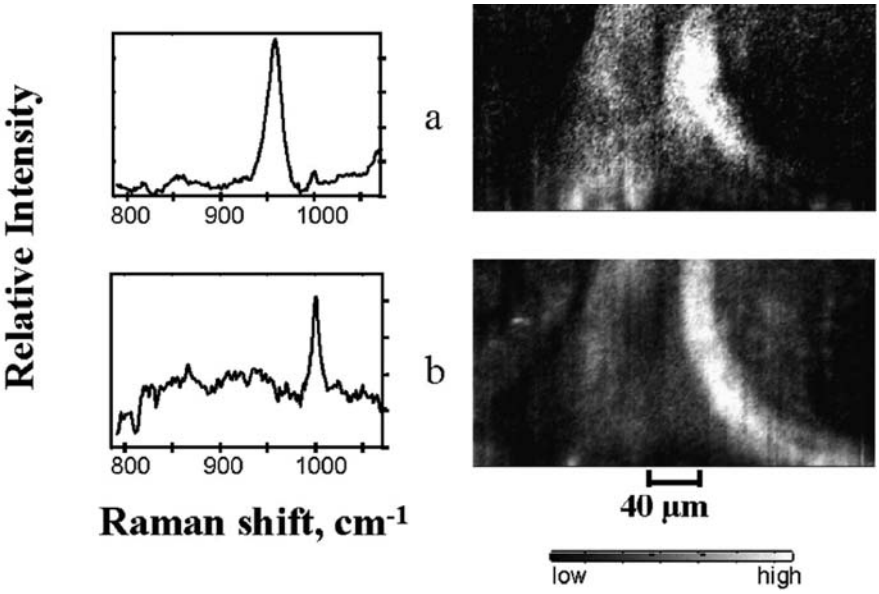

Fig. 14.2. Factors and score images of a 275 µm × 140 µm region of mature canine trabecular bone strut. **(a)** $PO_4^{-}3$ and **(b)** phenylalanine. Each pixel is 1.4 µm × 1.4 µm. Reprinted with permission from [26]

14.4 Polarized Raman Spectroscopy and Imaging

The use of polarized light to generate contrast between bone components provides information on the spatial distribution of bone components and their orientation. Kazanci et al. used polarized Raman imaging to examine the distribution of mineral and matrix constituents around osteons and showed that the $PO_4^{-3}\nu_1$ and amide I bands are highly orientation dependent, whereas the amide III and $PO_4^{-3}\nu_2$ and ν_4 are less orientation dependent [34]. Importantly, $PO_4^{-3}\nu_1$ is polarized along the long axis (*c*-axis) of mineral crystallites. Crystallites have their long axis oriented along the collagen fibril axis. Collagen amide I, however, is polarized perpendicular to the fibril axis because the amide carbonyls are perpendicular to collagen chain direction. Orientation effects are illustrated in Fig. 14.3 [35]. The $PO_4^{-3}\nu_1$/amide I ratio coincides with the orientation of the lamellae. The same lamellae have different contrast depending on the polarization of the excitation light and the orientation of the specimen.

Prior to the work of Kazanski et al. there was almost no mention of polarization effects in the bone Raman literature, although the polarized Raman spectrum of dental enamel was reported as early as 1994 [36]. The reason may well be that most Raman spectra of cortical bone have been obtained by

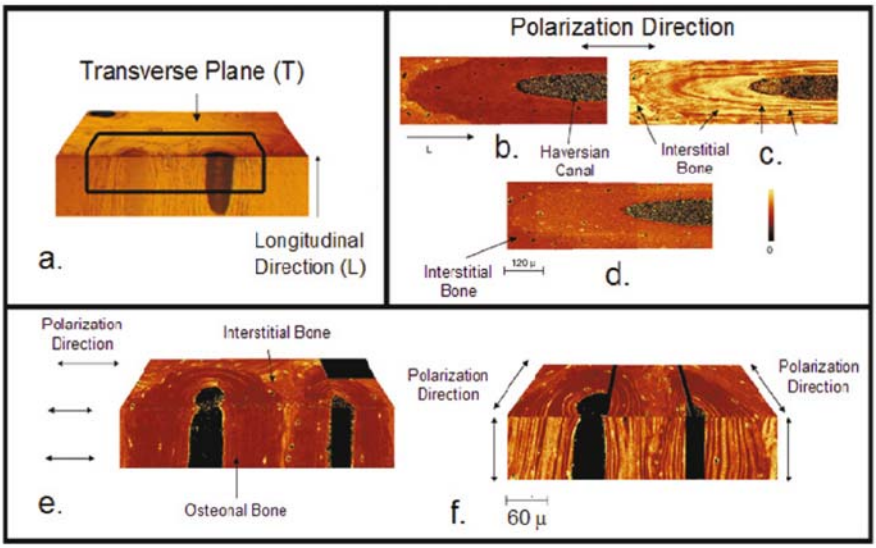

Fig. 14.3. (**a**) Bone section under polarized light, *black line* outlines where Raman images were acquired. Polarized Raman images of (**b**) phosphate ν_2/amide III, (**c**) phosphate ν_1/amide I, and (**d**) carbonate/phosphate ν_2 band ratios at the interface between osteon and interstitial bone. (**e** and **f**) Three-dimensional view of phosphate ν_1/amide I ratio for different polarization directions. Reprinted with permission from [1]

focusing light onto the periosteal surface using microprobes fitted with low numerical aperture objectives. In this case, the laser light would penetrate through several lamellae. The lamellae themselves have staggered orientation [37]. This property, together with depolarization by light scattering, makes it difficult or impossible to observe polarization effects under these experimental conditions.

14.5 Genetic Defects and Genetic Modifications

Morris and coworkers have investigated early mineralization in mouse calvaria subjected to periodic loading to model craniosynostosis, a birth defect in which the calvarial sutures fuse prematurely. Raman imaging was used to study the composition, relative amounts, and locations of mineral and matrix components in murine fetal calvarial sections [38]. The results are summarized in Fig. 14.4. The same mineral composition was found in the control- and force-induced tissue. Addition of fibroblast growth factor-2 (fgf2) was found to increase the rate of mineralization without causing a change in mineral composition [6, 39, 40]. However, accelerating mineralization did result in a less ordered mineral structure.

In a subsequent study mineralization in cultured fetal murine calvarial sections was followed for up to 72 h [7]. Transient octacalcium phosphate (OCP) or OCP-like intermediates were observed and converted to CA over periods of a few hours. Increased levels of OCP were found in sutures undergoing fgf2-induced accelerated mineralization. These results supported the transient precursor mineralization mechanism, which had been hypothesized but not previously observed [41, 42].

Kozloff and coworkers reported changes in mineralization for the Brtl mouse, a model of Sillence type IV osteogenesis imperfecta in which glycine-349 is replaced by cysteine in one or both α_1 chains of matrix collagen [43]. They found no differences in crystallinity (inverse band width of phosphate ν_1 between wild type and the heterozygous brtl mouse). Mineral/matrix ratios were different.

14.6 Biomechanical Studies

The first studies relating damage to bone chemistry focused on mineral changes that occurred near sites of mechanical deformation. While these changes were initially interpreted as phase changes[21, 44–46], other workers have interpreted similar changes as increases or decreases in mineral lattice strain as the applied load is change [47, 48]. This interpretation is consistent with Raman studies of bone powder at high (up to 4 GPa) hydrostatic loading [49]. In this case band shifts are completely reversible when the tissue is unloaded (Fig. 14.4).

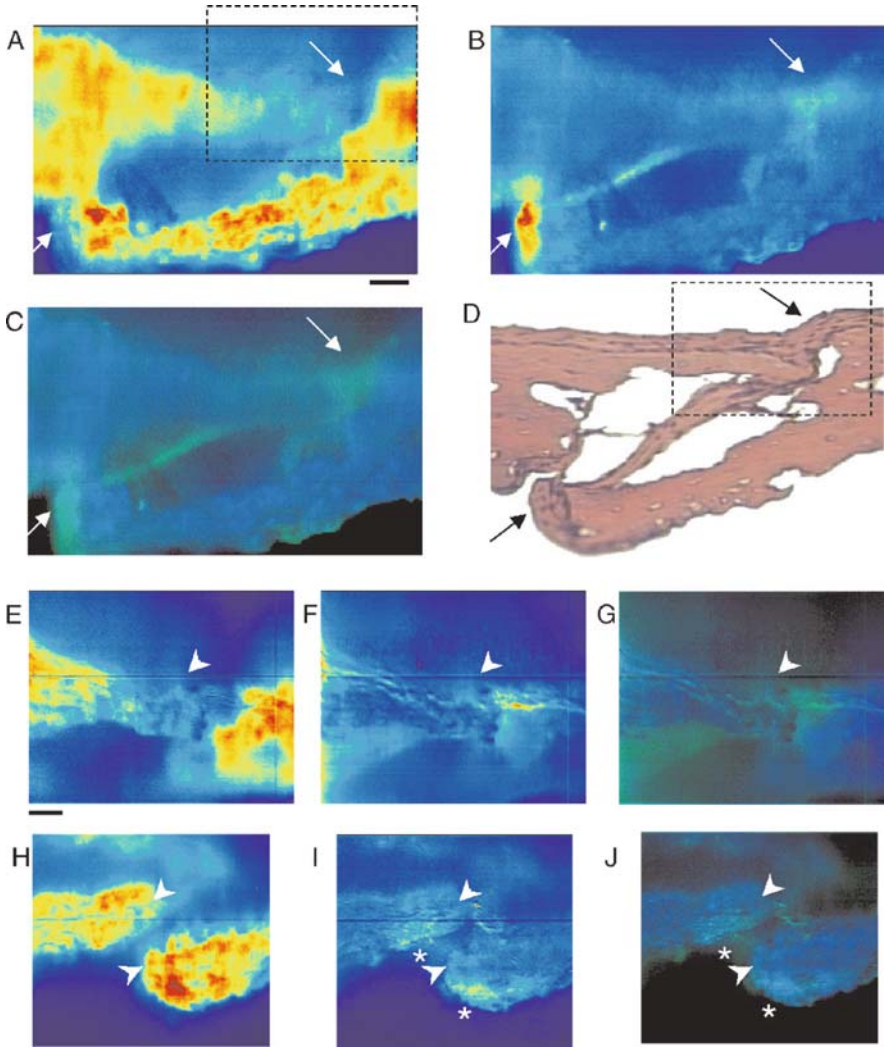

Fig. 14.4. Decreased mineral content is seen at osteogenic fronts (OFs) of the loaded specimen and increased matrix production extends beyond the OFs. Increased matrix is present on the endocranial side of the tissue of both loaded and unloaded specimens. Raman score images and RGB images for 4-day loaded and unloaded specimens. The endocranial surfaces of the calvaria are at the bottom of the images. (**A**–**G**) Loaded specimen. (**H**–**I**) Unloaded specimen. (**A**, **E**, and **H**) Mineral score image. (**B**, **F**, and **I**) Matrix score image. Scale for Raman score images: *red*, high intensity; *blue*, low intensity. (**C**, **G**, and **J**) RGB contrast-enhanced images (*blue* areas indicate mineral presence; *green* areas indicate matrix presence; *light blue-green* areas indicate the presence of mineral and matrix). (**D**) Reference hematoxylin and eosin-stained section from the same specimen imaged in **A**–**G**. The boxed area of the specimen shown in **A**–**D** was reimaged to show the OF on a smaller intensity scale and show more detail; the Raman score images are shown in **E**–**G**. The loaded

Lattice strain changes have been seen in areas where microdamage and deformation/fracture are present [21, 44–46]. Timlin et al. used Raman imaging to investigate the relationship between bone mineral composition and microdamage in bovine bone [46]. Where no visible microdamage was present, only one mineral factor with a phosphate band at $959\,\mathrm{cm}^{-1}$ was found. In areas of visible microcracks, two mineral factors were observed, one representing unperturbed apatitic mineral and the other containing a high-frequency phosphate band at $963\,\mathrm{cm}^{-1}$. Images of each factor showed differences in their distribution at the crack tip. In regions of diffuse damage, an unperturbed mineral factor was found, in addition to one factor that contained a phosphate band at $961\,\mathrm{cm}^{-1}$, a frequency slightly higher than normal bone, but not as high as bone regions near a visible microcrack. The score image of this factor showed a random distribution and also that diffuse damage was associated with smaller changes than microcracking.

Subsequent studies confirmed that the abnormal mineral signature present in microdamaged bone was, in fact, a result of the damage and not a cause of it [21, 44]. Morris et al. used Raman imaging to investigate the effect of macroscopic fracture using femora from young and aged mice [44]. In undamaged 4-month-old control tissue only one "normal" mineral factor was observed. After fracture two mineral factors were found. One was similar to that observed prior to fracture and another that contained a high-frequency phosphate band at $965\,\mathrm{cm}^{-1}$ but no carbonate. These results are similar to those seen in the microdamage study and are possibly consistent with phase transformations, a process that occurs in other crystalline materials like ceramics as a way to adapt to an applied mechanical load. Score images showed significant overlap between the two factors. However, in an 18-month-old mouse, only one mineral factor was observed after fracture, possibly because the damage did not propagate far enough from the fracture boundary to be observed.

In mechanically indented bovine bone, Raman imaging showed additional mineral factors in the indented areas where compression had occurred, but not at the edge of the indent or in control areas [21]. The additional mineral factor was consistent with earlier results; however, the factor in the nanoindentation studies usually contained a lower frequency phosphate component

Fig. 14.4. (continued) mineral score image shows a decreased amount of mineral at the OF (**A** and **E**), whereas the unloaded mineral score image (**H**) shows that the mineral is evenly dispersed throughout the unloaded calvaria. (**B** and **F**) Increased matrix is present beyond the mineral at the OFs in the loaded specimens. *Arrows* in **B**–**D** indicate areas of increased collagen production and cell proliferation in the loaded specimens [observed as increased intensity in the Raman matrix score image (**B**) and heavy *purple* staining in the stained section (**D**)]. (**I** and **J**) Increased protein presence is seen along the surfaces of the unloaded calvaria and especially along the endocranial surface. Image sizes: **A**–**D**, $180\,\mu\mathrm{m} \times 325\,\mu\mathrm{m}$; **E**–**G**, $180\,\mu\mathrm{m} \times 230\,\mu\mathrm{m}$; **H**–**J**, $180\,\mu\mathrm{m} \times 200\,\mu\mathrm{m}$. Scale bars $25\,\mu\mathrm{m}$. Reprinted by permission from [38]

rather than the higher frequency component found in the fracture study, a result that is explainable by an increase rather than a decrease in lattice strain. The addition of either a higher or lower frequency component is consistent with high-pressure studies on calcium hydroxyapatite, where the frequency of the phosphate ν_1 band initially increases and then decreases with greater pressure [21]. Importantly, in both the indent and control areas, only one matrix factor was found. A second matrix factor was found at the edge of the indent where shear forces were great. The spectral features of this factor were characteristic of the absence or at least reduced number of mature Pyr cross-links [5] and were interpreted as rupture of these cross-links. This conclusion was strengthened by the scanning electron microscopy, which showed shear bands at the edges of the indents. No collagen damage was spectroscopically observable in the center of indents, consistent with the known weakness of bone in shear mode, relative to compression.

Other studies have produced apparently conflicting results on the relationship between local composition and microcrack formation [50, 51]. In 2005, Akkus and coworkers used Raman microspectroscopy and human male femurs to examine mineralization in the vicinity of microdamage. Mineralization was evaluated by calculating the intensity ratio of the phosphate ν_1 band to the CH_2-scissoring band ($\sim$1450 cm^{-1}). Raman maps of this mineral/matrix ratio showed that the mineralization near microcracks was greater than elsewhere, and that the mineralization was uniform in regions of microcracks and did not vary with distance from the crack. Statistical analysis showed average mineralization of areas near microcracks was consistently and significantly greater than overall mineralization, suggesting that the formation of some microcracks may be composition dependent.

Pezzotti and coworkers monitored the spectral shift of Raman bands with mechanical loading to examine the in situ response of femoral and cortical bone to external stress [47, 48]. It has been proposed that collagen operates by a crack-bridging mechanism during fracture initiation and propagation [52]. Tensile microstresses were quantitatively assessed for the first time by constructing microscopic stress maps from shifts of the phosphate ν_1 band. Figure 14.5 shows the stress maps in bovine femoral bone near a fracture. An area of high stress exists ahead of the crack tip, and subsequent micrographs showed that microcracks were present in this area of high stress [47]. Consistent with the crack-bridging mechanism, the stress field contained areas of stress relaxation and stress intensification, seen as the striped pattern in the maps.

A follow-up study showed the relation between the composition and the redistribution of stress [47]. Cortical bone was loaded with external compression and tension, and the stress stored within the apatite crystals was assessed via the shift in phosphate ν_1 band in two regions: a collagen-rich area and an apatite-rich area. In the collagen-rich areas, stress was released under external tension, but localized stress intensification occurred under external. In apatite-rich areas, both tensile and compressive stresses were observed.

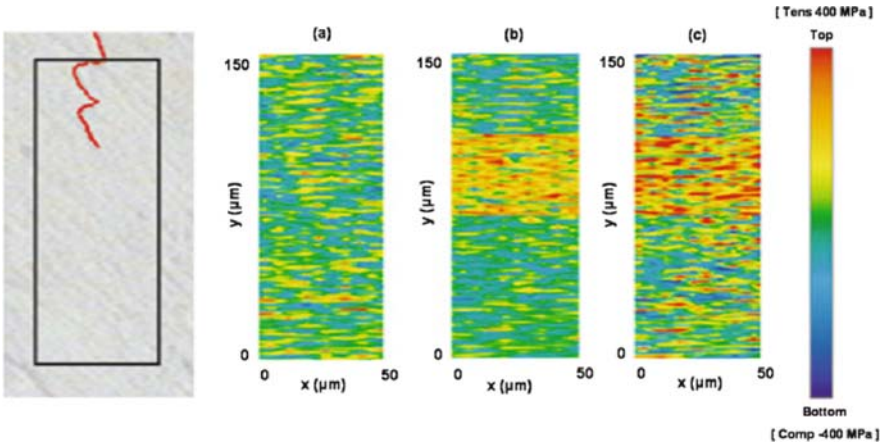

Fig. 14.5. An optical micrograph and stress maps in bovine femoral bone near a fracture. The map in (**a**) was acquired at zero applied stress and in (**b**) at critical stress for crack propagation. The net stress field was obtained by subtracting (**a**) from (**b**) and is shown in (**c**). Reprinted with permission from [48]

Tensile stresses were intensified even under weak external compression, and a crisscross-like pattern was observed, suggesting a particular organization of the collagen fibrils.

14.7 Osteoporosis

Most vibrational spectroscopic studies of osteoporotic tissue have been performed in the infrared. For example, FTIR imaging of specimens from human iliac crest biopsies showed that mineralization in untreated osteoporotic trabecular bone samples were decreased by ∼40% from the normal and the mineral/matrix ratio was lower in the center of trabeculae (more mature tissue) than for controls [53]. The crystallinity ratio also increased in osteoporotic specimens. Differences between the trabecular bone matrix of osteoporotic and normal bone have also been demonstrated [54]. The spatial variation of cross-links at bone-forming trabecular surfaces (within 50 µm) in patients with osteoporotic or multiple spontaneous fractures was significantly different than in normal bone and the collagen cross-link ratio was higher. It has been hypothesized that the matrix produced in osteoporosis might mature more quickly or undergo post-translational modifications for a longer time than normal bone matrix.

However, signatures of susceptibility to osteoporotic fracture have been identified in osteoporotic tissue matched for bone volume fraction. Fracture is associated with more carbonated mineral [55], which is in turn associated with

higher crystallinity. While further work in this area is warranted, the results are significant because both crystallinity and mineral/matrix ratio may be measurable non-invasively, as discussed below.

14.8 Subsurface Raman Spectroscopy and Imaging

Prior to true subsurface bone spectroscopy, Penel and coworkers obtained bone Raman spectra using a titanium chamber with a fused silica window placed in the calvaria of New Zealand rabbits [2]. With this apparatus they were able to study both bone tissue and implanted hydroxyapatite and β-tricalcium phosphate over a 8-month period. In addition to bone spectra, hemoglobin spectra were obtained close to blood vessels.

The first subsurface bone tissue Raman spectroscopic measurements were performed using picosecond time-resolved Raman spectroscopy on excised equine cortical bone [56, 57]. In these experiments it was shown that a polystyrene backing could be detected through 0.3 mm of bone. The same picosecond technology was used to perform the first transcutaneous Raman spectroscopic measurements of bone tissue [58]. In this study, the cortical bone mineral/matrix ratios of excised limbs of wild type and transgenic (oim/oim) mice were compared and the differences demonstrated.

Transcutaneous Raman spectroscopic measurements using spatially offset optical fibers were reported less than a year later [59, 60]. The test systems were chicken tibiae and the humeri of human cadavers. The use of cadaveric and ex vivo specimens allowed validation of the measurements by comparison to exposed bone tissue. In these measurements a depth of 3–4 mm below the skin was reached. In vivo measurements began with a report of the Raman spectrum of a phalange of a human volunteer [61]. The periosteal surface was probably 1–2 mm below the skin and the mineral phosphate ν_1 was accurately reproduced, although incomplete separation of mineral and matrix spectra introduced errors in other bands.

Using a ring-disk probe (also called inverse SORS) in backscattered geometry we have been able to reach bone about 6 mm below the skin [60]. Mineral/matrix ratios are accurately (<4% relative error) reproduced if a protocol for optimizing the ring/disk spacing is followed [62].

Very recently, ex vivo diffuse Raman tomography of canine bone tissue has been reported [63]. Importantly, signal was collected even through tissue thicknesses of 40 mm (Fig. 14.6). This encouraging result suggests that non-invasive in vivo bone Raman spectroscopy at clinically significant depths may be feasible. In diffuse optical tomography an image is constructed from the data obtained with excitation and collection fibers placed at different points on a specimen. The reconstruction is an ill-posed inverse problem and best results are obtained if the shape of the object is known independently. In an extension of that work, it has been shown that high contrast can be obtained

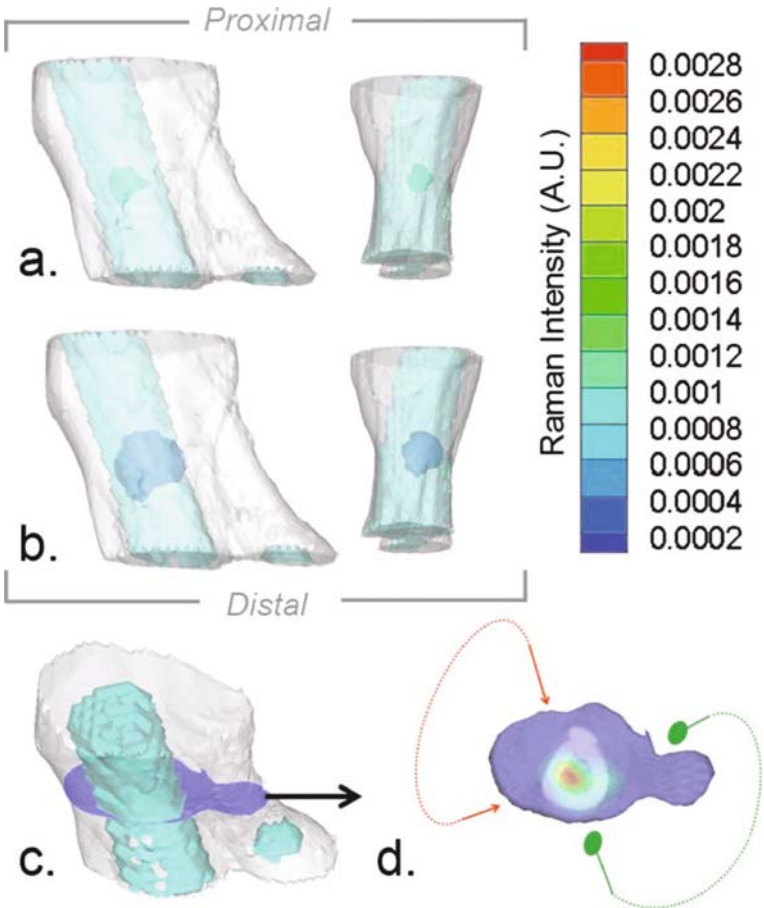

Fig. 14.6. Raman tomographic images of canine bone tissue. (**a**) Medial and anterior views of soft tissue mesh (*white*) and bone surface mesh of tibia and calcaneus (*turquoise*) overlaid with 50% contrast isosurface of the reconstructed three-dimensional Raman image of bone (*green*). (**b**) Same view as panel (**a**) overlaid with 10% contrast isosurface of the reconstructed Raman image of bone (*blue*). (**c**) Three-dimensional mesh of limb section (*white*), including bone (*turquoise*), illustrating location of the cross section (*blue*) containing the highest Raman scatter intensity. (**d**) Intensity at cross section in panel (**c**) in pseudo-color overlaid on the micro-CT image of the bone, showing range of illumination (*red arrows*) and collection (*green dots*) positions. Reprinted with permission from [63]

by image-guided spectroscopy [64]. The measured spectroscopic data is used to generate contrast, here the recovered bone factor, which is then used to color the shape of the specimen. As in diffuse Raman tomography, better results were obtained if the shape is known independently.

14.9 Raman Spectroscopy of Cartilage

Cartilage tissue plays a significant role in the musculoskeletal system because of its proximity to bone, its role in long bone formation, and in diseases such as osteoarthritis. There are three main types of cartilage: hyaline, elastic, and fibrocartilage. Hyaline cartilage has been the focus of most vibrational spectroscopic studies because it is the cartilage type that covers the ends of bones at joints (as articular cartilage), and it comprises epiphyseal plates where bones grow by endochondrial ossification [65]. Articular cartilage is an avascular tissue located at the intersection of two bones, within the synovial joint. For example, a thin layer of cartilage is attached to the joint surface of the patella, femur, and tibia, and the cavity between and around the joint is filled with synovial fluid [66]. The primary function of articular cartilage is to minimize friction between bones during movement of the joints and provide resistance to compression.

Cartilage contains mostly chondrocytes, proteoglycans, and type II collagen. Water is also a major component of cartilage, comprising between 60–80% of its total weight. Aggrecan is the most abundant proteoglycan in cartilage. Proteoglycans consist of a hyaluronic acid (HA) backbone with core protein side chains that attach to sulfated glycosaminoglycans (GAGs), chondroitin sulfate, and keratin sulfate. At physiological pH, GAGs are negatively charged and highly hydrated.

The collagen fiber orientation, as well as the overall composition of articular cartilage, is heterogeneous in the axial direction and thus contribute to the distinction of three zones of articular cartilage. The superficial zone contains the highest density of chondrocytes, and type II collagen fibers are oriented parallel to the joint surface. In the tangential or mid zone, collagen fibers are not preferentially oriented. In the deep zone, type II collagen is ubiquitous and is oriented perpendicular to the cartilage surface. Articular cartilage is unmineralized in surface layers, but contains a layer of calcified tissue adjacent to subchondral bone.

Many vibrational spectroscopic studies of macromolecular components of cartilage have been performed. Glycosaminoglycans, sodium hyaluronate, chondroitin 6-sulfate, and chondroitin 4-sulfate have been examined using IR and Raman spectroscopy [67–72]. Hyaluronic acid and chondroitin sulfate have been studied by FTIR [73–76], and the dichroic properties of HA functional groups have been investigated by polarized IR spectroscopy [70, 71, 77]. Enzymatically digested HA was also examined by NMR, IR, Raman, and visible spectroscopies [78]. While vibrational spectroscopic examination of type I collagen has been more extensive than type II collagen [79–84], the same methods can be used to examine type II collagen structure in tissue, identify pathologic tissue, and monitor fiber tension [85–92].

Studies like those discussed above provide a framework for assessing pathological changes in cartilage tissue. For example, infrared examination of proteoglycans and GAGs present in a case of Langer-Saldino achondrogenesis

revealed low sulfation of proteoglycan and the amount of chondroitin 4-sulfate was decreased relative to chondroitin 6-sulfate [93].

The role of subchondral bone has been examined in current models of osteoarthritis because a common indication of osteoarthritis is thickening of the subchondral bone plate. Radiography and imaging studies have shown alterations in bone architecture and chemistry in addition to plate thickening [94–97]. However, it is still unclear if subchondral bone damage occurs before cartilage damage or if bone tissue is altered to compensate for cartilage damage. Pathological mineralization of subchondral bone, cartilage matrix vesicles, and cartilage have been examined using Raman and synchrotron infrared spectroscopy. Infrared microscopy of subchondral bone was first reported in 1998 by Miller et al. [98]. Effects of age and defective type II collagen formation on murine subchondral bone were reported by Dehring et al. [99]. In this study, subchondral bone specimens from normal mice and Del 1 (+/−) transgenic mice, a mouse model for early-onset osteoarthritis, were examined using Raman spectroscopy.

14.10 Conclusions

In the past decade Raman spectroscopy has assumed an important role in musculoskeletal tissue studies, especially in bone tissue studies. Applications to a wide range of problems in basic biology, biomechanics, and medicine have appeared in the journal literature. Most workers have used cell cultures or excised bone tissue, including human biopsy and cadaveric tissue. We expect that Raman spectroscopy will become increasingly important in such studies, as more life scientists and engineers learn how to employ it. Just as importantly, recent reports of non-invasive spectroscopy suggest that Raman spectroscopy may have a role in human subjects studies of bone development, function, and disease.

References

1. M. Kazanci, P. Roschger, E.P. Paschalis, K. Klaushofer, P. Fratzl, J. Struct. Biol. **156**, 489 (2006)
2. G. Penel, C. Delfosse, M. Descamps, G. Leroy, Bone **36**, 893 (2005)
3. E.P. Paschalis, F. Betts, E. DiCarlo, R. Mendelsohn, A.L. Boskey, Calcif. Tissue Int. **61**, 480 (1997)
4. C.P. Tarnowski, M.A. Ignelzi Jr., M.D. Morris, J. Bone Miner. Res. **17**, 1118 (2002)
5. E.P. Paschalis, K. Verdelis, S.B. Doty, A.L. Boskey, R. Mendelsohn, M. Yamauchi, J. Bone Miner. Res. **16**, 1821 (2001)
6. N.J. Crane, M.D. Morris, M.A. Ignelzi Jr., G.G. Yu, J. Biomed. Opt. **10**, 031119 (2005)

7. N.J. Crane, V. Popescu, M.D. Morris, P. Steenhuis, J.M.A. Ignelzi, Bone **39**, 434 (2006)
8. N. Pleshko, A. Boskey, R. Mendelsohn, Biophys. J. **80**, 786 (1991)
9. O. Akkus, F. Adar, M.B. Schaffler, Bone **34**, 443 (2004)
10. J.G. Ramasamya, O. Akkus, J. Biomech. **40**, 910 (2007)
11. J.S. Yerramshetty, O. Akkus, Bone **42**, 476 (2008)
12. J.S. Yerramshetty, C. Lind, O. Akkus, Bone **39**, 1236 (2006)
13. C. Rey, V. Renugopalakrishnan, B. Collins, M.J. Glimcher, Calcif. Tissue Int. **49**, 251 (1991)
14. H. El Feki, C. Rey, M. Vignoles, Calcif. Tissue Int. **49**, 269 (1991)
15. E.P. Paschalis, E. DiCarlo, F. Betts, P. Sherman, R. Mendelsohn, A.L. Boskey, Calcif. Tissue Int. **59**, 480 (1996)
16. A. Awonusi, M. Morris, M. Tecklenburg, Calcif. Tissue Int. **81**, 46 (2007)
17. G. Penel, G. Leroy, C. Rey, E. Bres, Calcif. Tissue Int. **63**, 475 (1998)
18. A. Carden, M.D. Morris, J. Biomed. Opt. **5**, 259 (2000)
19. K. Otsubo, E.P. Katz, G.L. Mechanic, M. Yamauchi, Biochemistry **31**, 396 (1992)
20. D.R. Eyre, M.A. Paz, P.M. Gallop, Annu. Rev. Biochem. **53**, 717 (1984)
21. A. Carden, R.M. Rajachar, M.D. Morris, D.H. Kohn, Calcif. Tissue Int. **72**, 166 (2003)
22. M.D. Morris, W.F. Finney, Spectroscopy **18**, 155 (2004)
23. R.D. Blank, T.H. Baldini, M. Kaufman, S. Bailey, R. Gupta, Y. Yershov, A.L. Boskey, S.N. Coppersmith, P. Demant, E.P. Paschalis, Connect. Tissue Res. **44**, 134 (2003)
24. A.L. Boskey, R. Mendelsohn, Vib. Spectrosc. **38**, 107 (2005)
25. N.J. Crane, L.E. Gomez, M.A. Ignelzi Jr., M.D. Morris, Calcif. Tissue Int. **74**, 86 (2004)
26. J. Timlin, A. Carden, M.D. Morris, J.F. Bonadio, C.E. Hoffler II, K.M. Kozloff, S.A. Goldstein, J. Biomed. Opt. **4**, 28 (1999)
27. C. Wee, E. Widjaja, M. Garland, Organometallics **21**, 1982 (2002)
28. E. Widjaja, N. Crane, T. Chen, M.D. Morris, M.A. Ignelzi Jr., B. McCreadie, Appl. Spectrosc. **57**, 1353 (2003)
29. R. Mendelsohn, E. Paschalis, A.L. Boskey, J. Biomed. Opt. **4**, 14 (1999)
30. H. Ou-Yang, E.P. Paschalis, A.L. Boskey, R. Mendelsohn, Appl. Spectrosc. **56**, 419 (2002)
31. L.M. Miller, V. Vairavamurthy, M.R. Chance, R. Mendelsohn, E.P. Paschalis, F. Betts, A.L. Boskey, Biochim. Biophys. Acta **1527**, 11 (2001)
32. H. Ou-Yang, E.P. Paschalis, W.E. Mayo, A.L. Boskey, R. Mendelsohn, J. Bone Miner. Res. **16**, 893 (2001)
33. A. Carden, J.A. Timlin, C.M. Edwards, M.D. Morris, C.E. Hoffler, K. Kozloff, S.A. Goldstein, Biomed. Appl. Raman Spectrosc. **3608**, 132 (1999)
34. M. Kazanci, P. Roschger, E.P. Paschalis, K. Klaushofer, P. Fratzl, J. Struct. Biol. **156**, 489 (2006)
35. M. Kazanci, H.D. Wagner, N.I. Manjubala, H.S. Gupta, E. Paschalis, P. Roschger, P. Fratzl, Bone **41**, 456 (2007)
36. H. Tsuda, J. Arends, J. Dent. Res. **73**, 1703 (1994)
37. S. Weiner, W. Traub, H.D. Wagner, J. Struct. Biol. **126**, 241 (1999)
38. C.P. Tarnowski, M.A. Ignelzi Jr., W. Wang, J.M. Taboas, S.A. Goldstein, M.D. Morris, J. Bone Miner. Res. **19**, 64 (2004)

39. N.J. Crane, W. Wang, M.A. Ignelzi, M.D. Morris, Proc. SPIE **4959**, 111 (2003)
40. N.J. Crane, G.G. Yu, M.A. Ignelzi Jr., M.D. Morris, Proc. SPIE **5321**, 242 (2004)
41. M.D. Grynpas, S. Omelon, Bone **41**, 162 (2007)
42. S. Weiner, H.D. Wagner, Annu. Rev. Mater. Sci. **28**, 271 (1998)
43. K.M. Kozloff, A. Carden, C. Bergwitz, A. Forlino, T.E. Uveges, M.D. Morris, J.C. Marini, S.A. Goldstein, J. Bone Miner. Res. **19**, 614 (2004)
44. M.D. Morris, A. Carden, R.M. Rajachar, D.H. Kohn, Proc. SPIE **4614**, 47 (2002)
45. K. Golcuk, G.S. Mandair, A.F. Callender, N. Sahar, D.H. Kohn, M.D. Morris, Biochim. Biophys. Acta **1758**, 868 (2006)
46. J. Timlin, A. Carden, M.D. Morris, R.M. Rajachar, D.H. Kohn, Anal. Chem. **72**, 2229 (2000)
47. G. Pezzotti, Anal. Bioanal. Chem. **381**, 577 (2005)
48. G. Pezzotti, S. Sakakura, J. Biomed. Mater. Res. **65A**, 229 (2003)
49. O. de Carmejane, M.D. Morris, M.K. Davis, L. Stixrude, M. Tecklenburg, R.M. Rajachar, Kohn, David H., Calcif. Tissue Int. **76**, 207 (2005)
50. N.N. Wasserman, J.J. Yerramshetty, O.O. Akkus, Eur. J. Morphol. **42**, 43 (2005)
51. M.E. Ruppel, D.B. Burr, L.M. Miller, Bone **39**, 318 (2006)
52. R.K. Nalla, J.H. Kinney, R.O. Ritchie, Nat. Mater. **2**, 164 (2003)
53. E.P. Paschalis, E. Shane, G. Lyritis, G. Skarantavos, R. Mendelsohn, A.L. Boskey, J. Bone Miner. Res. **19**, 2000 (2004)
54. R. Mendelsohn, E.P. Paschalis, P.J. Sherman, A.L. Boskey, Appl. Spectrosc. **54**, 1183 (2000)
55. B.R. McCreadie, M.D. Morris, T.C. Chen, D. Sudhaker Rao, W.F. Finney, E. Widjaja, S.A. Goldstein, Bone **39**, 1190 (2006)
56. M.D. Morris, A.E. Goodship, E.R.C. Draper, P. Matousek, M. Towrie, A.W. Parker, Proc. SPIE **5321**, 164 (2004)
57. M.D. Morris, P. Matousek, M. Towrie, A.W. Parker, A.E. Goodship, E.R.C. Draper, J. Biomed. Opt. **10**, 014014 (2005)
58. E.R.C. Draper, M.D. Morris, N.P. Camacho, P. Matousek, M. Towrie, A.W. Parker, A.E. Goodship, J. Bone Miner. Res. **20**, 1968 (2005)
59. M.V. Schulmerich, W.F. Finney, R.A. Fredericks, M.D. Morris, Appl. Spectrosc. **60**, 109 (2006)
60. M.V. Schulmerich, W.F. Finney, V. Popescu, M.D. Morris, T.M. Vanasse, S.A. Goldstein, Proc. SPIE **6093**, 60930O (2006)
61. P. Matousek, E.R.C. Draper, A.E. Goodship, I.P. Clark, K.L. Ronayne, A.W. Parker, Appl. Spectrosc. **60**, 758 (2006)
62. M.V. Schulmerich, K.A. Dooley, T.M. Vanasse, S.A. Goldstein, M.D. Morris, Appl. Spectrosc. **61**, 671 (2007)
63. M.V. Schulmerich, S. Srinivasan, J.H. Cole, J. Kreider, K.A. Dooley, S.A. Goldstein, B.W. Pogue, M.D. Morris, J. Biomed. Opt. **13**, 020506 (2008)
64. S. Srinivasan, M. Schulmerich, J.H. Cole, K.A. Dooley, J.M. Kreider, B.W. Pogue, M.D. Morris, S.A. Goldstein, Opt. Express **16**, 12190 (2008)
65. E.N. Marieb, *Human Anatomy and Physiology* (Benjamin/Cummings Science Publishers, Menlo Park, 1998)
66. N.P. Cohen, R.J. Foster, V.C. Mow, J. Orthop. Sports Phys. Ther. **28**, 203 (1998)
67. R. Bansil, I.V. Yannas, H.E. Stanley, Biochim. Biophys. Acta **541**, 535 (1978)

68. T.W. Barrett, W.L. Peticolas, J. Raman Spectrosc. **8**, 35 (1979)
69. F. Cabassi, B. Casu, A.S. Perlin, Carbohydr. Res. **63**, 1 (1978)
70. J.J. Cael, D.H. Isaac, J. Blackwell, J.L. Koenig, E.D.T. Atkins, J.K. Sheehan, Carbohydr. Res. **50**, 169 (1976)
71. J.J. Cael, J.L. Koenig, J. Blackwell, Carbohydr. Res. **32**, 79 (1974)
72. R. Gilli, M. Kacurakova, M. Mathlouthi, L. Navarini, S. Paoletti, Carbohydr. Res. **263**, 315 (1994)
73. R. Servaty, J. Schiller, H. Binder, K. Arnold, Int. J. Biol. Macromol. **28**, 121 (2001)
74. K. Haxaire, Y. Maréchal, M. Milas, M. Rinaudo, Biopolymers **72**, 10 (2003)
75. K. Haxaire, Y. Maréchal, M. Milas, M. Rinaudo, Biopolymers **72**, 149 (2003)
76. Y. Maréchal, M. Milas, M. Rinaudo, Biopolymers **72**, 162 (2003)
77. F.R. Quinn, F.A. Bettelheim, Biochim. Biophys. Acta **69**, 544 (1963)
78. J.A. Alkrad, Y. Mrestani, D. Stroehl, S. Wartewig, R. Neubert, J. Pharm. Biomed. Anal. **31**, 545 (2003)
79. H.G.M. Edwards, E.A. Carter, *Biological Applications of Raman Spectroscopy*, vol. 24 (Marcel Dekker, New York, 2001)
80. J.T. Pelton, L.R. McLean, Anal. Biochem. **277**, 167 (2000)
81. S. Leikin, V.A. Parsegian, W.H. Yang, G.E. Walrafen, Proc. Natl. Acad. Sci. **94**, 11312 (1997)
82. G.E. Walrafen, Y.C. Chu, Chem. Phys. **258**, 427 (2000)
83. B.G. Frushour, J.L. Koenig, Biopolymers **14**, 379 (1975)
84. M. Khajehpour, J.L. Dashnau, J.M. Vanderkooi, Anal. Biochem. **348**, 40 (2006)
85. S.C. Goheen, L.J. Lis, J.W. Kauffman, Biochim. Biophys. Acta **536**, 197 (1978)
86. A. Mizuno, M. Tsuji, K. Fujii, K. Kawauchi, Y. Ozaki, Jpn. J. Ophthalmol. **38**, 44 (1994)
87. K.A. Dehring, A.R. Smukler, B.J. Roessler, M.D. Morris, Appl. Spectrosc. **60**, 366 (2006)
88. M. Jackson, L.P. Choo, P.H. Watson, W.C. Halliday, H.H. Mantsch, Biochim. Biophys. Acta **1270**, 1 (1995)
89. C.J. Frank, R.L. McCreery, D.C.B. Redd, Anal. Chem. **67**, 777 (1995)
90. S. Koljenovic, T.C.B. Schut, J.P. van Meerbeeck, A.P.W.M. Maat, S.A. Burgers, P.E. Zondervan, J.M. Kros, G.J. Puppels, J. Biomed. Opt. **9**, 1187 (2004)
91. C. Krafft, S.B. Sobottka, G. Schackert, R. Salzer, J. Raman Spectrosc. **37**, 367 (2006)
92. Y.N. Wang, C. Galiotis, D.L. Bader, J. Biomech. **33**, 483 (2000)
93. S.P. Feshchenko, I.A. Rebrin, V.P. Sokolnik, B.M. Sher, B.P. Sokolov, V.N. Kalinin, G.I. Lazjuk, Hum. Genet. **82**, 49 (1989)
94. H. Matsui, M. Shimizu, H. Tsuji, Microsc. Res. Tech. **37**, 333 (1997)
95. T.R. Oegema, R.J. Carpenter, F. Hofmeister, R.C. Thompson, Microsc. Res. Tech. **37**, 324 (1997)
96. D.B. Burr, M.B. Schaffler, Microsc. Res. Tech. **37**, 343 (1997)
97. C.E. Tye, K.R. Rattray, K.J. Warner, J.A.R. Gordon, J. Sodek, G.K. Hunter, H.A. Goldberg, J. Biol. Chem. **278**, 7949 (2003)
98. L.M. Miller, C.S. Carlson, G.L. Carr, M.R. Chance, Cell. Mol. Biol. **44**, 117 (1998)
99. K.A. Dehring, N.J. Crane, A.R. Smukler, J.B. McHugh, B.J. Roessler, M.D. Morris, Appl. Spectrosc. **60**, 1134 (2006)

15

Raman Microscopy and Imaging: Applications to Skin Pharmacology and Wound Healing

Carol R. Flach, Guojin Zhang, and Richard Mendelsohn

Abstract The utility of confocal Raman microscopy to study biological events in skin is demonstrated with three examples. (i) monitoring the spatial and structural differences between native and cultured skin, (ii) tracking the permeation and biochemical transformation in skin of a Vitamin E derivative and (iii) tracking the spatial distribution of three major skin proteins (keratin, collagen, and elastin) during wound healing in an explant skin model.

15.1 Introduction

Vibrational microspectroscopy provides a unique means for molecular level structure characterization of a variety of biological processes associated with skin. For the past several years, this laboratory has utilized Raman and IR spectroscopy, microscopy, and imaging to monitor the biophysics of the skin barrier, mechanisms of drug permeation and metabolism in intact tissue, and, more recently, the complex events that transpire during wound healing in an ex vivo skin model [1–6].

This chapter is organized as follows: We initially provide a brief overview of the basic elements of skin structure. Next, a validation of confocal Raman measurements to monitor skin processes and structure is given. Finally, we demonstrate the utility of the approach with three examples taken from our own work: (i) monitoring the spatial and structural differences between native and cultured skin; (ii) tracking the permeation and biochemical transformation in skin of a vitamin E derivative; and (iii) tracking the spatial distribution of three major skin proteins (keratin, collagen, and elastin) during wound healing. Our approach tends to emphasize the molecular structure information inherent in the spectra, obviously a unique advantage of the technology. Although the primary focus of this chapter is to introduce the technology and to highlight efforts from this laboratory, we of course recognize the efforts of other groups around the world. We refer to and comment on pertinent aspects of their work and apologize at the outset for any oversights.

15.2 Preliminaries

15.2.1 Skin Microanatomy

Figure 15.1 presents a photomicrograph of a human skin section. The heterogeneity of the tissue is immediately evident. The main barrier to permeability resides in the highly specialized outermost layer of the epidermis, the stratum corneum (SC). A major function of this layer is to maintain water homeostasis, although many other SC functions have been described [7]. This 10–20 μm thick layer consists of anucleated keratin-rich corneocytes embedded in a highly ordered lamellar layer comprised of fatty acids, ceramides, and cholesterol derivatives. The standard "bricks and mortar" representation of SC structure in which the lipids act as the "mortar" holding the corneocyte "bricks" in the appropriate geometric array is depicted in Fig. 15.2a. Several other models exist in the dermatology literature. In particular the detailed "domain mosaic" model of Forslind [8] has gained popularity. As shown in the atomic force micrograph in Fig. 15.2b, corneocytes are highly asymmetric cells, ∼0.5 μm thick along the "z"-direction (perpendicular to the plane of the skin) and ∼50 μm in the other two dimensions. The lipid constituents organize themselves into non-covalent supramolecular membranous sheets which constitute the primary barrier to permeability. Some possible packing motifs available to the lipids, namely orthorhombic, hexagonal, and liquid crystalline, are schematically depicted in two ways in Fig. 15.2c. The top figure depicts standard bilayer structures which become thinner with looser

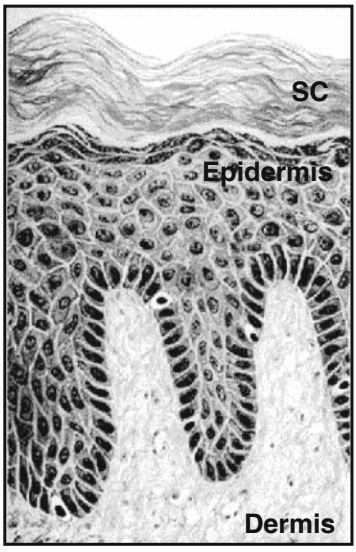

Fig. 15.1. Photomicrograph of a human skin section. The thickness of the stratum corneum (SC) shown ranges from about 15 to 20 μm. Scale bar = 20 μm

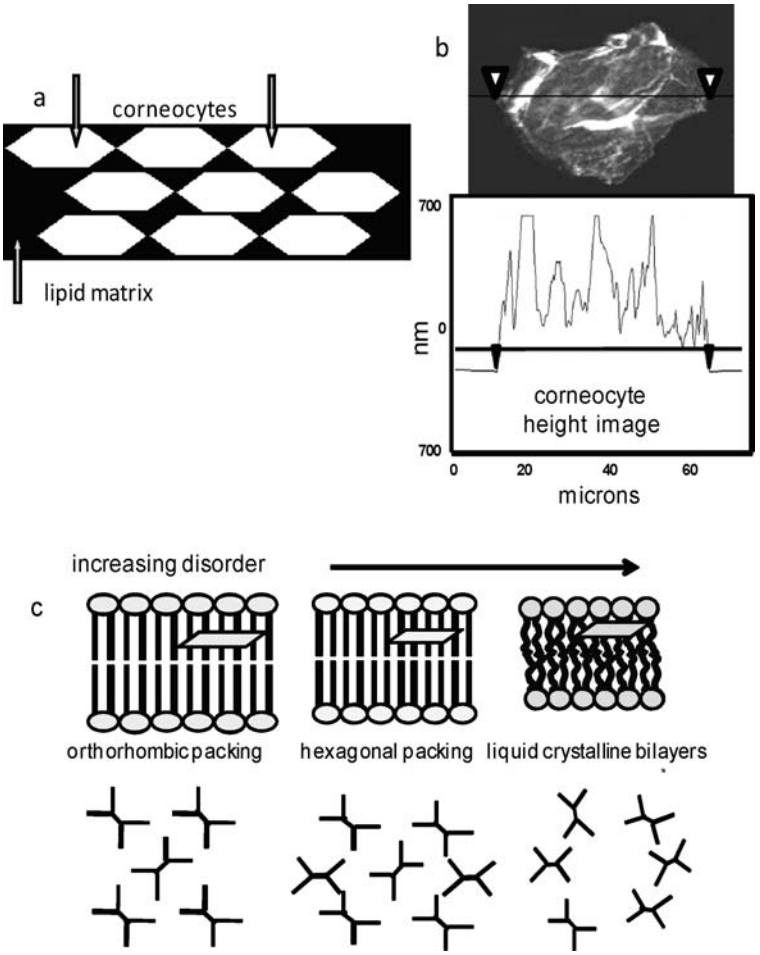

Fig. 15.2. a Schematic of the "bricks and mortar" stratum corneum model. The corneocytes, depicted as hexagons, are embedded in a lipid matrix background. Scale bar = 10 µm. **b** AFM micrograph of a corneocyte. The corneocyte is a flattened cell with x, y, dimensions of ∼50 µm and irregular thickness ranging to 700 µm. **c** Packing motifs and chain conformations of lipid bilayers. The orthorhombic phase and hexagonal phase chains are both conformationally highly ordered, while the liquid crystalline phase contains conformationally disordered chains. The liquid crystalline state occurs rarely if at all in the SC. The bottom half of the figure attempts to diagram the progressive loosening of chain packing in going from orthorhombic to hexagonal to liquid crystalline phases. C–C bonds are shown (in projection) as viewed through planes drawn parallel to the bilayer plane in the region of the lipid chains in the top half of the figure

chain packing and/or increasing chain conformational disorder. The bottom half of the figure attempts to diagram the progressive loosening of chain packing in going from orthorhombic to hexagonal to liquid crystalline bilayers.

Underlying the SC is the viable epidermis (see Fig. 15.1). The thickness of this layer ranges from ∼40 μm (eyelids) to >1 mm (palms). A major overall function of the epidermis is to generate the SC. The principal cell in this region is the keratinocyte, which differentiates upon migration toward the SC. The epidermis is highly stratified, starting from the basal layer, in which proliferation followed by differentiation of the cells takes place. The layer directly beneath the SC is the stratum granulosum and is the region where keratinocytes are morphologically transformed from a rounded to a flattened shape.

The underlying layer of the skin, the dermis, ranges in thickness from 600 μm to 4 mm. This region consists of connective tissue and specialized structures (including blood vessels) with collagen comprising 75% of the dry weight. Once a substance reaches the dermis, it is generally assumed to have access to the systemic circulation.

15.2.2 Experimental Considerations – Confocal Raman Microscopy for the Study of Skin

Early studies by Puppels, Caspers, and their co-workers demonstrated the utility of Raman microscopy for the study of skin [9, 10]. The major advantage of the approach is that spectra may be collected in a confocal manner, thus permitting acquisition of both molecular composition and structural information as a function of depth from full thickness samples. Caspers et al. acquired in vitro spectra from 6 μm thick skin sections as well as in vivo spectra with laser excitation wavelengths of 850 and 730 nm focused ∼85 μm below the skin surface. From their initial experiments, a commercial instrument has resulted in which in vivo depth profiles of water [11, 12] or pharmacological agents (e.g., retinol) [13] can be readily generated. In addition, the Puppels group and several other groups [14–20] have produced a variety of studies applying multivariate statistics for diagnosis of pathological states of skin from Raman spectra.

Technically, the heterogeneity of skin and the presence of refractive index gradients likely impose some constraints to the accurate determination of imaging parameters. However, uncertainties in the determination of spatial resolution and axial location in transparent samples from which spectra are extracted, such as those described by Everall [21–23] and others [24, 25], are probably not important for highly opaque skin samples. We estimate the axial resolution to be 2–3 μm with the 785 nm excitation wavelength used in the current measurements. A study from this lab has suggested that errors in depth measurements are less than ∼15% which is probably adequate for most current purposes.

The weakness of Raman scattering imposes constraints on the size of the Raman images that may be conveniently collected. We typically acquire two-dimensional confocal image planes from an $80 \times 60\,\mu m$ spatial region, with $\sim 4\,\mu m$ intervals between acquisition points (357 spectra). It typically requires 2 min to obtain a decent quality spectrum, thus ~ 12 h are needed to generate an image plane under the conditions described above. Although this duration is too long for certain classes of experiments (e.g., studies of in vivo permeation), it is noted that recent instrumentation advances may permit acquisition of adequate quality spectra at least 10–100× faster than noted above. It thus appears that the technical ability to rapidly (seconds or minutes) acquire large three-dimensional Raman images is imminent.

15.2.3 Data Reduction – A Comment About Factor Analysis

As noted above, Raman images of skin are usually derived from hundreds to thousands of spectra. Examination of each individual spectrum is evidently impractical. Multivariate approaches are required to condense the information into a small set of components with a minimum loss of spectral information. We have found initial evaluation by principal component analysis (PCA) followed by factor analysis to be useful for this purpose.

Factor analysis transforms PCA loadings to factor loadings that resemble Raman spectra with scattering intensities of particular components linear in concentration (all other optical factors being equal, which rarely occurs). Compared to PCA, factor analysis offers a major advantage in that the loadings resemble real spectra, although they are generally not spectra of pure components. Thus, since the origin of peaks within the loading (and therefore in the spectra) is usually available and since spectra structure correlations are occasionally known, molecular structure information from within the tissue may be acquired. The benefit of the approach to characterize the molecular structure of skin constituents is demonstrated in some examples below. However, when comparing factors with spectra it is important to remember that factors are generated from all sources of variance in the data. For example, baseline distortions may appear as "features" in the factor loadings which are unrelated to vibrational modes in the sample. To validate the applicability of factor analysis for a given set of experiments, we routinely compare factors with appropriately selected spectra, e.g., those from spatial regions where scores for a particular factor are high. The similarity between spectra and factor loadings is generally very strong, thereby justifying our approach.

15.2.4 Delineation of Skin Regions and Accuracy in their Dimensions from Factor Analysis

As noted above, the thickness of the layered structure of skin is variable across the tissue, so that no absolute standard is available for estimating uncertainties in Raman-generated measurements of thickness. For the measurements

described below and in Zhang et al. [4], Raman spectra were acquired from an untreated piece of skin from a Yucatan hairless pig, a standard pharmacological model. Data were acquired in steps of 2.5 µm in the z (axial) direction and 5 µm in the lateral direction. The area of the image plane constructed was 75 × 40 µm. The nature of the measurement precludes the acquisition of a meaningful optical micrograph from the same sample used to generate Raman spectra, so that validation of the approach required comparison of factor analysis of Raman spectra with optical images generated from a microtomed parallel section. The results are shown in Fig. 15.3.

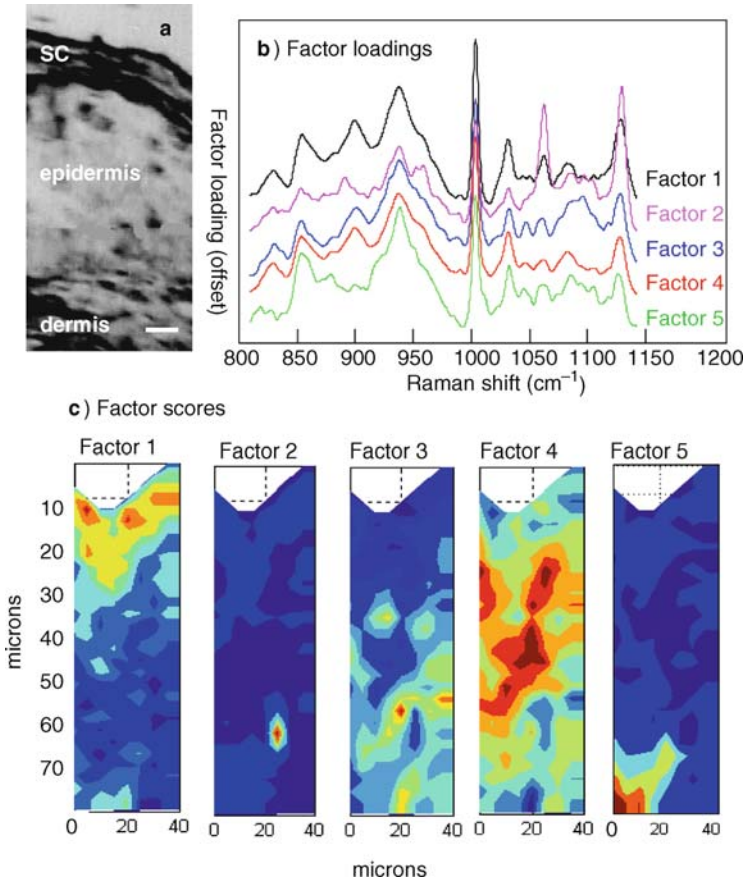

Fig. 15.3. **a** Optical micrograph of a microtomed 5 µm thick pigskin section. **b** The results of factor analysis in the 800–1150 cm^{-1} region conducted on a confocal Raman map acquired from a section parallel to that pictured in (**a**). The five distinct factor loadings generated by the "ISys" score segregation algorithm are offset and labeled factors 1–5. **c** The spatial distribution of factor scores are shown for each of the loadings as marked. *Dark blue* indicates the lowest score with *green*, *yellow*, *orange*, and *red* indicative of progressively higher scores. Factor loading and score images have been assigned to different skin regions as described in the text

The optical image is shown in Fig. 15.3a. Five significant factors whose loadings in the 800–1140 cm^{-1} spectral region are shown in Fig. 15.3b were extracted. Score images for each factor are given in Fig. 15.3c. Three of the score images and their corresponding loadings are easily correlated with known spatial regions of skin. Thus, factor 1 corresponds to the SC, factor 4 to the viable epidermis, and factor 5 to the dermis. The skin thickness of the SC determined from factor score images is consistent with the known properties of pigskin as seen in the optical image.

The two remaining factor score images (factors 2 and 3) highlight particular features within the viable epidermis not generally evident in optical micrographs and demonstrate a major advantage of the Raman approach, namely the ability to extract molecular structure/composition information from data generated at particular tissue sites. The process of assigning the chemical origin of a particular image feature is demonstrated for factor 2 (Fig. 15.3c) in Fig. 15.4a–c. An average spectrum of the stratum corneum as labeled (top spectrum in each of Fig. 15.4a–c) is compared with an average spectrum localized to the small spectral region highlighted in Fig. 15.3c (labeled factor 2). Both spectra display strong bands near 1058, 1130, 1296, 2880, and 2850 cm^{-1} (Fig. 15.4b and c). These bands are assigned [26, 27] to lipid C–C stretching (1058, 1130 cm^{-1}) and CH_2 stretching modes (2850 and 2880 cm^{-1}) of conformationally ordered (all-*trans*) chains, and lipid CH_2 twisting $(1296\,cm^{-1})$. In addition, the bands observed at 605 and 700 cm^{-1} (Fig. 15.4a) arise from

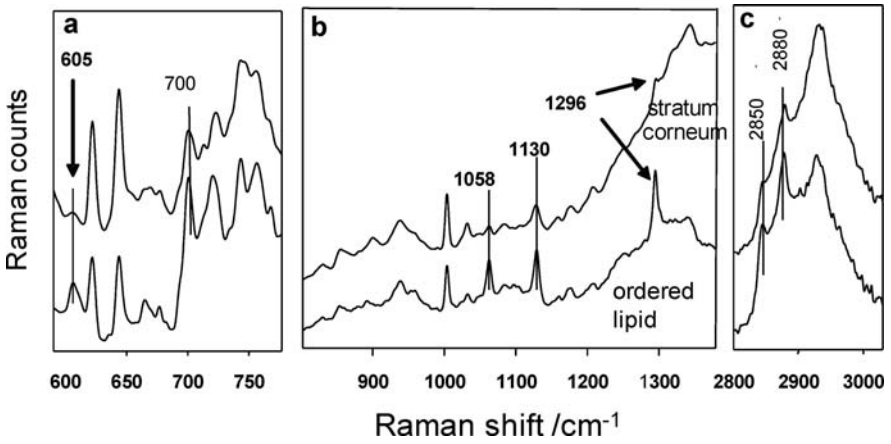

Fig. 15.4. Averaged Raman spectra from within the SC (*top*) and lipid (*bottom*) regions as noted in Fig. 15.3b and c as factors 1 and 2, respectively. **a** The 590–780 cm^{-1} region with bands at 605 and 700 cm^{-1} assigned to cholesterol as marked. **b** The 800–1380 cm^{-1} region displays three major bands (1058, 1130, and 1296 cm^{-1}) characteristic for ordered (all-*trans*) lipid chains. **c** The C–H stretching $(2800–3000\,cm^{-1})$ region with symmetric $(2850\,cm^{-1})$ and asymmetric $(2880\,cm^{-1})$ methylene stretching modes noted. The frequencies of the bands are consistent conformationally ordered chains

cholesterol [28]. In all cases, this set of bands is more intense in spectra from the region depicted in the score image of factor 2 (Fig. 15.3c). Thus, this small pocket likely consists of an ordered lipid phase in which cholesterol and ordered long chain molecules co-exist, possibly from lamellar bodies or from "lipid rafts." The observation that the same bands arise from the ordered lipid chains known to occur in the SC (Fig. 15.4a–c) strengthens the above assignment. As noted above, highly ordered lipid phases consisting of ceramides, fatty acids, and cholesterol comprise the inter-corneocyte matrix of the SC. We have observed [29] a temperature-induced orthorhombic → hexagonal packing change in the IR spectrum of isolated stratum corneum.

Finally, a similar approach was undertaken to evaluate the origin of factor 3 in Fig. 15.3c whose score image reveals several small-localized pockets in the epidermis. The loading from factor 3 (Fig. 15.3b) depicts one broad feature at $\sim$1090 cm^{-1} not present in the other factor loadings. Based on both the position of this particular band and the spatial distribution of the factor score, the band probably arises from a phosphodiester mode of DNA [30, 31] present in the nuclei of keratinocytes or other cells. An additional feature at 780 cm^{-1} in both spectra and factors (not shown) arises from cytosine in DNA [32] and is consistent with this interpretation.

The point of the above experiments is to demonstrate that in addition to reporting with reasonable accuracy the spatial dimensions of the various skin phases, the molecular structure information inherent in the spectra provides additional important characterization of the skin.

15.3 Applications of Confocal Raman Microscopy to Skin Pharmacology and Wound Healing

15.3.1 Comparison of Spatial and Molecular Properties of Human and Cultured Skin

This study compares tissue properties in human skin with a cultured skin model. Such experiments will take on increasing importance in the near future for two reasons. First, the acquisition and availability of either human skin or animal models for studies of drug permeation or other aspects of skin pharmacology are becoming increasingly limited by government regulation and/or by ethical considerations. Thus, significant attention is now given to the use of cultured skin as a substitute. Second, as noted by Tfayli et al. [33], the type of studies reported here may be of general importance due to a new European Union chemicals policy termed REACH (Registration, Evaluation and Authorization of Chemicals). Under this policy, the European Commission proposes to evaluate toxicity profiles of 30,000 chemicals within a period of 15 years. Raman microscopy of drug permeation into artificial skin offers unique possibilities in this area.

In their initial studies, Tfayli et al. [33] acquired spectra from an Episkin model. This model is comprised of human adult keratinocytes which produce stratified epidermis following a 13 h culture period. Raman spectra from this model were compared with normal human skin. Significant differences were noted, particularly in spectral features arising from the 850/830 tyr Fermi doublet (which is sensitive to the H-bonding state of the –OH group [34]) and in the protein amide III region. Usable spectra were acquired to a depth of 15–20 µm.

We have been successful in acquiring useful Raman data from a similar model. The particular version we have used, EpiDerm^{TM} (full thickness-EFT 200) from MatTEK Corp., also contains epidermal layers and is mitotically and metabolically active. Raman image planes, 60 µm (z-direction) ×30 µm (x-direction), were constructed from spectra acquired with a step size of 5 µm in each direction. The results of factor analysis in the C–H stretching region are shown in Fig. 15.5a–c. Two factors with significant scores from the SC of human and cultured skin are presented in Fig. 15.5. The loadings are shown in Fig. 15.5a, while score images are presented in Fig. 15.5b and c. Two issues of

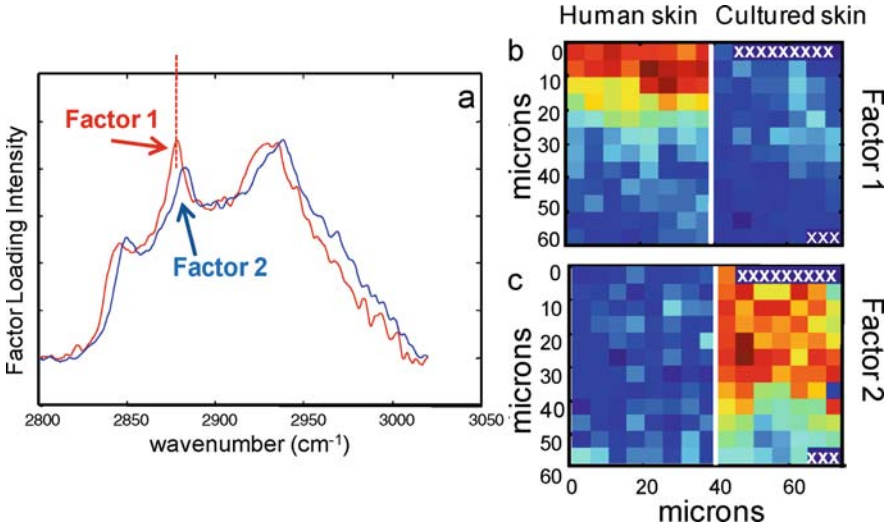

Fig. 15.5. Factor analysis results for the C–H stretching region (2800–3050 cm^{-1} region) in human skin and in cultured skin model (Epiderm^{TM}). Data from human skin (8 × 12 pixels) and cultured skin (7 × 12 pixels) have been concatenated. Pixels marked with x's were excluded from the analysis. **a** Factor loadings for the methylene stretching region. The *dashed vertical line* marks 2876 cm^{-1} and emphasizes the shift in frequency between factors 1 and 2. **b** Score plots for factor 1 are depicted for human skin in the left set of 8 × 12 pixels and for cultured skin in the right set of 7 × 12 pixels. **c** Score plots for factor 2 are depicted for human skin in the left set of 8 × 12 pixels and for cultured skin in the right set of 7 × 12 pixels

significance are evident. First, the CH_2 stretching frequencies in the loadings of the asymmetric stretching modes in the high score region of human SC (Fig. 15.5a) are significantly lower $\left(2876\,\mathrm{cm}^{-1}\right)$ than in the factor that maps to cultured skin $\left(2882\,\mathrm{cm}^{-1}\right)$, indicating that the lipid chains in the human barrier are conformationally much more ordered than in the cultured skin model. This is consistent with a stronger barrier in the native material. Second, the SC barrier thickness deduced from the score images is much greater in artificial skin ($\sim$35 µm, Fig. 15.5c) than in human SC ($\sim$15 µm, Fig. 15.5b). These differences in the physical barrier properties between human and cultured skin presumably produce profound differences in permeability and other functional measurements.

Another striking difference between normal and cultured skin is shown in Fig. 15.6. As discussed above (see Fig. 15.3c, factor 2), cholesterol-rich pockets containing highly ordered lipid chains are occasionally detected in human skin and are characterized by a Raman-active mode of cholesterol near $\sim 700\,\mathrm{cm}^{-1}$ and an intense lipid C–C stretch near $1130\,\mathrm{cm}^{-1}$ in Fig. 15.4a and b, respectively. The intensity of the cholesterol mode is normalized to a Phe vibration near $620\,\mathrm{cm}^{-1}$ and imaged in Fig. 15.6b. As is evident there are many such pockets in the cultured skin model, in contrast to human skin where they are only rarely observed (Fig. 15.3c, factor 2), and usually in the viable epidermis rather than in the SC (as in the cultured skin). These measurements illustrate the power of confocal Raman microscopy for combining spatial measurements with molecular structure characterization.

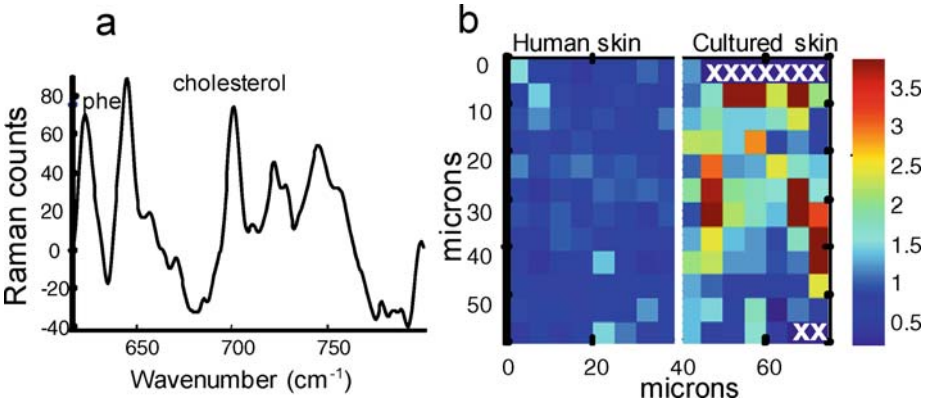

Fig. 15.6. Results of factor analysis in the 600–800 cm^{-1} region in human skin and a cultured skin model (Epiderm$^{\mathrm{TM}}$). Data from human skin (8×12 pixels) and cultured skin (7×12 pixels) have been concatenated. Pixels marked with x's were excluded from the analysis. **a** The cholesterol $\left(700\,\mathrm{cm}^{-1}\right)$ and Phe vibrations $\left(620\,\mathrm{cm}^{-1}\right)$ are marked. **b** An image of the 700/620 cm^{-1} band intensity ratios

15.3.2 Vitamin E Acetate Delivery and Metabolism in Skin by Confocal Raman Microscopy

Introduction

Human skin is frequently exposed to oxidative stress. The resulting damage is likely an important factor in pathogenesis of skin cancer and photoaging. Vitamin E (α-TH, structure in Fig. 15.7a), well known for its free radical scavenging activity, protects biomembranes of cells from peroxidation and prevents ultraviolet-induced skin damage.

Due to the relative ease of oxidation of the parent compound, common delivery forms in cosmetic formulations and clinical trials are vitamin E acetate (α-TAc, structure in Fig. 15.7a) and vitamin E phosphate. These forms are expected to permeate and to regenerate free active α-TH through enzyme-catalyzed hydrolysis activities in skin. Although α-TAc is readily hydrolyzed by esterase action to vitamin E upon oral ingestion, no consensus as to the extent of bioconversion of topically applied α-TAc has been reached. Two published studies demonstrate bioconversion up to 10–15% in the viable epidermis [35] including the basal layer [36]. These and other studies show no detectable metabolism of α-TAc in stratum corneum [37].

The traditional methods for evaluation of the delivery and metabolism of exogenous materials in skin involve the use of diffusion cells and/or tape stripping followed by HPLC and mass spectrometry. These methods involve modification of the skin, provide no spatial information, and may alter skin transport properties. In this section, both the permeation and metabolism of α-TAc are monitored inside skin with confocal Raman microscopy.

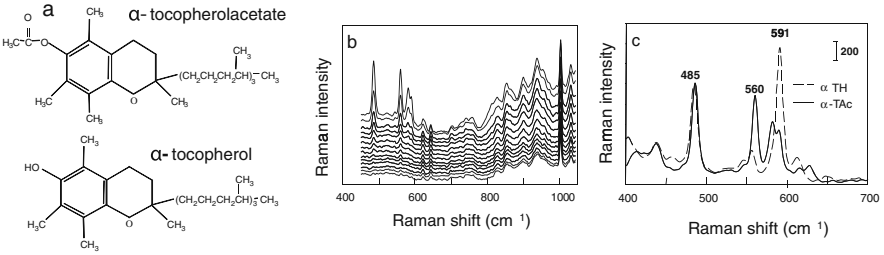

Fig. 15.7. **a** Chemical structures of vitamin E (α-TH) and vitamin E acetate (α-TAc) as indicated. **b** Confocal Raman spectra of skin after topical application of 60% α-TAc in octanol were acquired every 2 µm to an overall depth of 60 µm. The first 15 spectra of skin in the 450–1050 cm^{-1} range are shown. **c** Raman spectra of the 400–700 cm^{-1} region for pure vitamin E (α-TH) and pure vitamin E acetate (α-TAc) as marked

Results

Confocal Raman spectra of skin following topical application of 60% α-TAc in octanol were acquired every 2 μm to an overall depth of 60 μm. The first 15 spectra of skin in the 450–1100 cm^{-1} range are shown in Fig. 15.7b. The spectral region selected for the current work, 450–600 cm^{-1}, is free from octanol bands. Both α-TAc and α-TH exhibit (Fig. 15.7c) a strong feature at 485 cm^{-1} whose presence permits us to track the penetration of α-TAc or α-TH, although the relative proportions of the two cannot be deduced from this single common spectral feature. The integrated area ratio, $I(485)/I(1004)$ cm^{-1}, thus tracks the relative α-TAc and/or α-TH concentration in skin; the 1004 cm^{-1} band is a Phe ring mode from skin proteins whose intensity corrects for the depth dependence of the scattering, as discussed elsewhere [3].

Confocal Raman images were acquired from 50 μm (axial) ×20 μm (lateral) areas with step sizes of 2 μm in the axial direction and 4 μm in the lateral direction. The map of the integrated area ratio 485 cm^{-1}/1004 cm^{-1} is plotted in Fig. 15.8. Most of the exogenous α-TAc permeated ∼15 μm into skin with a more-or-less monotonic diminishing gradient at depths between 15 and 30 μm. Small pockets of material are observed at depths of ∼30–35 μm.

To distinguish the SC from the underlying epidermis and hence to define the site within the skin to which the α-TAc had permeated, a confocal Raman image was acquired from an untreated section taken from the same piece of skin whose spatial distribution of factor scores is depicted in Fig. 15.3c. A comparison of Fig. 15.3c (factors 1 (SC) and 4 (epidermis)) with the map of α-TAc permeation (Fig. 15.8) clearly reveals that α-TAc remains localized mostly in the stratum corneum, with little reaching the viable epidermis. The

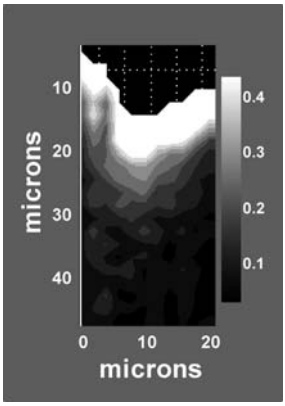

Fig. 15.8. Integrated area ratio map (485 cm^{-1}/1004 cm^{-1}) calculated from Raman spectra acquired from 50 μm × 20 μm areas with step sizes of 4 μm in the x (parallel to skin surface) direction and 2 μm in the z (axial) direction

lipophilicity of the acetate presumably permits intercalation within the well-ordered region of the SC.

Tracking the formation of the bioactive material (α-TH in this case) from its acetate pre-cursor is an important demonstration of the power of confocal Raman microscopy. To develop an analytical approach to track the in situ hydrolysis, we observe (Fig. 15.7c) that α-TAc has a strong feature at 560 cm^{-1} and weaker bands at 582 and 591 cm^{-1}, while α-TH exhibits a strong feature at 590 cm^{-1} and a weaker feature at ∼558 cm^{-1}. Thus the area ratio $I(590)/I(560)$, with the denominator metric including both the 558 (α-TH) and 560 (α-TAc) bands, provides a useful measure of the hydrolysis. The area ratio of the high-frequency half of the 590 cm^{-1} to the band at 558/560 cm^{-1} was used to track hydrolysis. This procedure reduces interference from the 582 cm^{-1} feature of α-TAc.

A calibration curve tracking mixtures comprised of the two pure components mixed in various proportions is shown in Fig. 15.9a. A ratio map of the same parameter from a skin sample to which α-TAc has been added is imaged in Fig. 15.9b. As is evident from a comparison of the image with the calibration curve, most of the α-TAc remains un-hydrolyzed. Values of the ratio range mostly from 0.12 to 0.25 and reveal (from the calibration plot in Fig. 15.9a) little or no hydrolysis. In a few regions of the viable epidermis, the ratios are slightly elevated (∼0.25–0.30). It is noted that the Raman marker bands deep in skin are weak, possibly leading to significant errors in the estimate of the extent of hydrolysis. Data from deeper regions (>30 μm) in the sample have therefore been removed from the image. In addition, the scattering coefficients of the two species may differ in skin compared with the mixtures used for calibration. Nevertheless, the ability to estimate (at least semiquantitatively) the extent of hydrolysis in different spatial regions is a potentially useful advance.

15.3.3 Wound Healing

Introduction

The response of the human body to wounding leads to rapid sealing of the site, prevention of infection, and organization of a complex spatially and temporally coordinated response to initiate healing of the injured tissue. For recent reviews, see Gurtner et al. [38] and Coulombe [39]. Cutaneous wounds lead to disruption of the epidermis and dermis resulting in the loss and damage of epithelial cells and connective tissue. Wound closure involves two main cellular mechanisms, re-epithelialization and contraction of connective tissue. Re-epithelialization of skin wounds begins within a few hours following injury [40]. At the edge of the wound, keratinocytes become activated, start to proliferate, and migrate to cover the site. The migration becomes significant within the first 2 days and is carried out by a layer of epidermal cells known as the migrating epithelial tongue [41]. The process is essentially complete

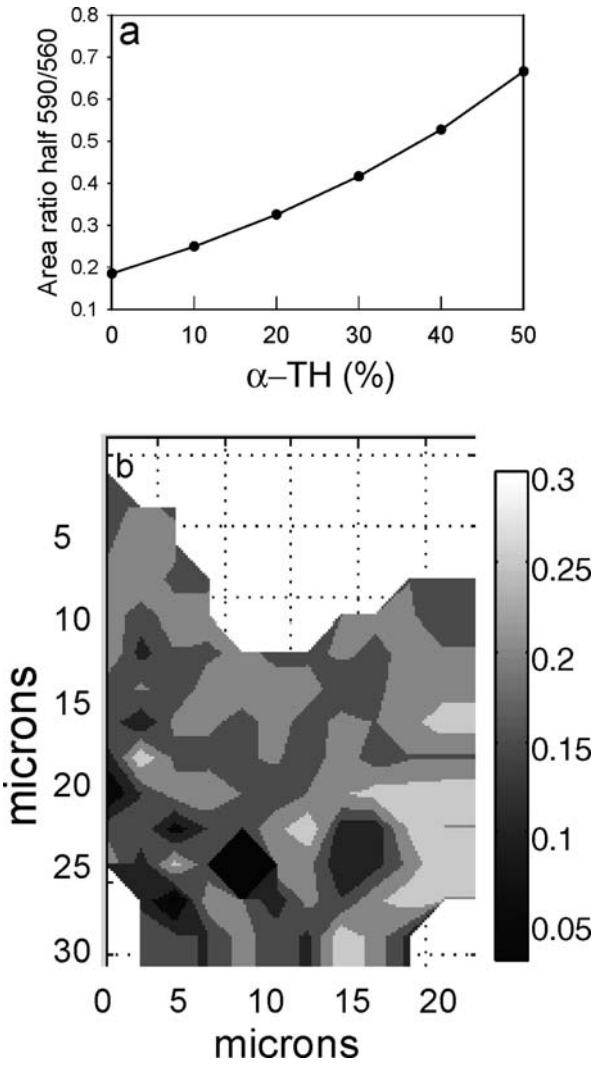

Fig. 15.9. a Calibration curve for tracking the composition of mixtures of vitamin E (α-TH) and vitamin E acetate (α-TAc). The origin of the ordinate scale is discussed in the text. **b** A Raman image of the spatial distribution of the ordinate scale parameter in Fig. 15.9a measured in a skin sample to which α-TAc has been added. The image tracks the spatial distribution and extent of hydrolysis of α-TAc

(∼7–9 days following the injury) when the wound bed is covered by a layer of keratinocytes. This process is followed by the re-establishment of the stratified epidermal layer.

To date, these major organizational changes during healing have been substantially studied with molecular biology and immunofluorescence-based approaches [42, 43]. Although the spatial distribution of gene products may be mapped with the latter technique, destruction of the sample is usually required, and separate (microtomed) sections are needed for each protein whose spatial distribution is of interest. The development of vibrational microscopy approaches, which permit the simultaneous determination of the spatial distribution of several protein species, as well as non-protein species, would be beneficial. The current experiments [6] demonstrate the feasibility of tracking changes in the spatial distribution of the major skin proteins within the first several days after wounding in an organ culture wound healing model and correlate these changes with data obtained using microarray analysis.

Human Organ Culture Wound Healing Model

Human skin specimens were obtained from reduction abdominoplasty (tummy tuck) and used to generate acute wounds as described elsewhere [42]. A 3 mm biopsy punch was used to create an acute wound. Skin specimens were maintained at the air–liquid interface at 37°C, 5% CO_2, and 95% relative humidity for 6–7 days.

Validation of Vibrational Imaging Protocols with IR Microscopic Imaging

The generic procedure for collecting either confocal Raman micrographs or IR images from a healing wound is shown in Fig. 15.10a. The wound is generated with a punch biopsy and the residual tissue is retained for spectroscopic examination.

For IR imaging, flash frozen samples were microtomed (5 µm thick sections) perpendicular to the SC. The sections were placed on BaF_2 windows and mapped with a Perkin–Elmer "Spotlight" system. Typical image sizes are 300×750 µm and are sampled with ∼6000 spectra. The visible image of a skin section acquired 4 days following wounding (Fig. 15.10b) reveals a clear MET, indicating the persistence of biological events in the explants. Factor loadings (Fig. 15.10c) in the 1475–1750 cm^{-1} region clearly identify collagen (factor 1) and keratin (factor 2). The score images of these factors, as shown in Fig. 15.10d and e, depict the collagen-rich epidermis and the keratin-rich dermis, respectively.

Confocal Raman Microspectroscopy of a Healing Wound

Raman spectra were collected from an image plane encompassing both wounded and non-wounded areas. In a typical experiment, a confocal Raman image was

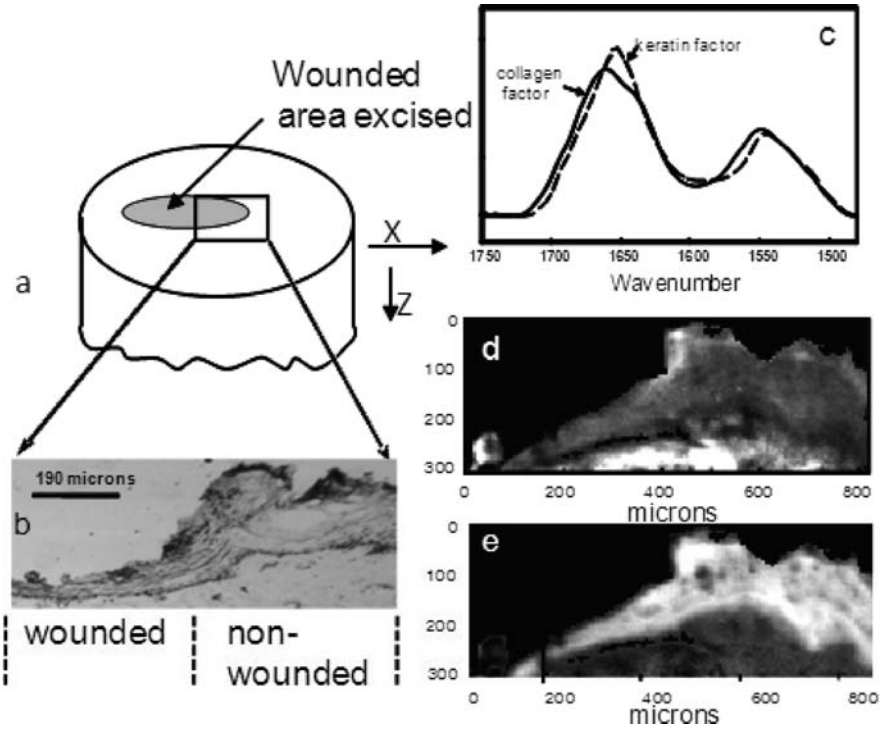

Fig. 15.10. Schematic and IR validation of the wound healing experiment **a** Schematic of the wound healing experiment. Both wounded and non-wounded areas were examined in each Raman and IR measurement. **b** Visible image of a typical wound 4 days following wounding. The migrating epithelial tongue (MET) indicates the persistence of healing in the explants. **c** Factor loadings of the IR data in the amide I and II spectral regions. The loadings in the 1475–1750 cm^{-1} region clearly identify collagen (factor 1, *solid line*) and keratin (factor 2, *dashed line*). **d** Factor score image of the collagen-rich factor 1. A *brighter shade* indicates the greater contribution of the factor loading (and therefore collagen) to the pixel. **e** Factor score image of the keratin-rich factor 2. A *brighter shade* indicates the greater contribution of the factor loading (and therefore keratin) to the pixel

collected starting at ~60–80 µm from the left edge of a wound into the non-wounded area and scanning 170 µm into the wounded area with a depth of ~60 µm. This resulted in a measurement area ~250 µm wide and 60 µm deep. Spectra were acquired ~12 h post-wounding. The spatial distribution of components in this region is initially investigated using factor analysis conducted over the 1140–1690 cm^{-1} region. Factor loadings specific to the wounded area 12 h post-wounding are shown in Fig. 15.11a, and corresponding score images are presented in Fig. 15.11b. In the loading plots (Fig. 15.11a), the amide I and III contours of factors 1 and 2 are characteristic of collagen and keratin, respectively. The score images reveal that collagen in the wounded area is pressed up from the dermis, while the keratin in non-wounded area arises

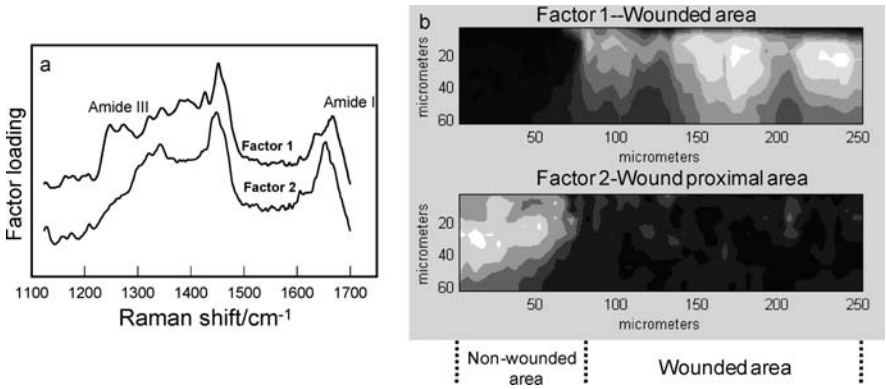

Fig. 15.11. a Factor loadings constructed from Raman spectra specific to the general area of the wound. The amide I and III contours of factors 1 and 2 are characteristic of high collagen and high keratin levels, respectively. **b** Factor score images reveal that collagen (factor 1) in the wounded area is pressed up from the dermis, while the keratin (factor 2) in the non-wounded area arises from the SC and from the viable epidermis

from both the SC and from the viable epidermis. The spatial distribution of components in the wounded area of skin is best investigated with factor analysis conducted over the 700–1010 cm^{-1} region. Factor loadings specific to the wounded area are shown in Fig. 15.12a and corresponding score images are presented in Fig. 15.12c. In the loading plots (Fig. 15.12a), the doublet of doublets between 830 and 960 cm^{-1} in all three traces is characteristic of collagen; these bands have been assigned to vibrations of Pro and Hyp amino acids and the C–C stretch of the protein backbone [44]. Factors 2 and 3, whose loadings are quite similar throughout the spectral range, have score plots (Fig. 15.12c, middle and bottom) in the wounded area that generally complement each other spatially. The molecular structure differences producing the slightly altered loadings are currently under investigation, and may be related to altered collagen hydration levels. Factor 1 in Fig. 15.12a is distinguished from the others by the presence of the band at 906 cm^{-1} and a relatively stronger Phe band at 1004 cm^{-1}. To explore the origin of this factor, the average spectrum of pixels having low scores in the area surrounding the higher scoring regions (in Fig. 15.12c, top image) was subtracted from the average spectrum of pixels with high scores for f1. The resulting difference spectrum (shown in Fig. 15.12b) reveals that f1 contains the elastin component in the wound bed. The spectrum is essentially identical to a published spectrum of bovine elastin [44, 45]. It is likely that the elastin component was not identified as a separate factor due to the small diameter of the elastin fiber bundles ($\sim$0.25–1.0 µm) in the dermis compared to the spot size of the excitation laser. Thus, factor 1 (Fig. 15.12a) contains features of both elastin and collagen.

Overall, confocal Raman microscopy demonstrates the ability to track changes in the spatial distribution of two major skin proteins (collagen and

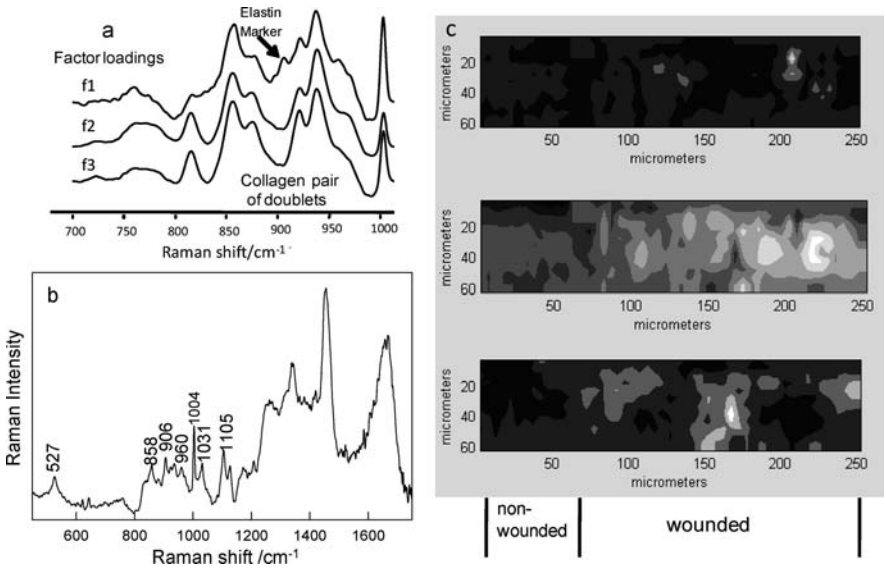

Fig. 15.12. Factor analysis conducted over the 700–1010 cm^{-1} region in a spatial area containing non-wounded and wounded regions. **a** Factor loadings specific to the wounded area. **b** Difference spectrum of average pixels with a high score of f1 in (**a**), from which the average spectrum of pixels having low scores of f1 in the area surrounding the higher scoring regions has been subtracted. The spectrum strongly resembles that of elastin. **c** Factor scores for f1 (*top*), f2 (*middle*), and f3 (*bottom*). The top factor arises from elastin-containing regions while the score images of f2 and f3 are from two forms or types of collagen

elastin) during wound healing. Along similar lines, we have also used IR microscopy to track the spatial dependence of several types of keratin. The vibrational spectroscopy methods complement microarray analysis and immunofluorescent staining. Further developments in the spectral analysis of additional wound healing samples and purified materials under controlled environmental conditions will provide us with the opportunity to probe the full realm of molecular information inherent in the data and in complementary IR data. This in turn may begin to provide a basis for understanding changes in the observed spatial distributions of particular proteins during therapeutic interventions for wound healing.

References

1. C. Xiao, D.J. Moore, M.E. Rerek, C.R. Flach, R. Mendelsohn, J. Invest. Dermatol. **124**, 622 (2005)
2. G. Zhang, D.J. Moore, R. Mendelsohn, C.R. Flach, J. Invest. Dermatol. **126**, 1088 (2006)

3. G. Zhang, D.J. Moore, K.B. Sloan, C.R. Flach, R. Mendelsohn, J. Invest. Dermatol. **127**, 1205 (2007)
4. G. Zhang, D.J. Moore, C.R. Flach, R. Mendelsohn, Anal. Bioanal. Chem. **387**, 1591 (2007)
5. G. Zhang, C.R. Flach, R. Mendelsohn, J. Control. Release **123**, 141 (2007)
6. K.L.A. Chan, G. Zhang, M. Tomic-Canic, O. Stojadinovic, B. Lee, C.R. Flach, R. Mendelsohn, J. Cell. Mol. Med. **12**, 2145 (2008)
7. P.M. Elias, J. Control Release **15**, 199 (1991)
8. B. Forslind, Acta Derm. Venerol. **74**, 1 (1994)
9. P.J. Caspers, G.W. Lucassen, R. Wolthuis, H.A. Bruining, G.J. Puppels, Biospectroscopy **4**, S31 (1998)
10. P.J. Caspers, A.C. Williams, E.A. Carter, H.G. Edwards, B.W. Barry, H.A. Bruining, G.J. Puppels, Pharm. Res. **19**, 1577 (2002)
11. P.J. Caspers, G.W. Lucassen, H.A. Bruining, G.J. Puppels, J. Raman Spectrosc. **31**, 813 (2000)
12. P.J. Caspers, G.W. Lucassen, E.A. Carter, H.A. Bruining, G.J. Puppels, J. Invest. Dermatol. **116**, 434 (2001)
13. P.D.A. Pudney, M. Mélot, P.J. Caspers, A. Van Der Pol, G.J. Puppels, Appl. Spectrosc. **61**, 804 (2007)
14. A. Nijssen, T.C. Bakker Schut, F. Heule, P.J. Caspers, D.P. Hayes, M. Neumann, G.J. Puppels, J. Invest. Dermatol. **119**, 64 (2002)
15. J. Wohlrab, A. Vollmann, S. Wartewig, W.C. Marsch, R. Neubert, Biopolymers **62**, 141 (2001)
16. J. Choi, J. Choo, H. Chung, D.-G. Gweon, J. Park, H.J. Kim, S. Park, C.-H. Oh, Biopolymers **77**, 264 (2005)
17. M. Gniadecka, P.A. Philipsen, S. Sigurdsson, S. Wessel, O.F. Nielsen, D.H. Christensen, J. Hercogova, K. Rossen, H.K. Thomsen, R. Gniadecki, L.K. Hansen, H.C. Wulf, J. Invest. Dermatol. **122**, 443 (2004)
18. A. Nijssen, K. Maquelin, L.F. Santos, P.J. Caspers, T.C. Bakker Schut, J.C. den Hollander, M.H.A. Neumann, G.J. Puppels, J. Biomed. Opt. **12**, 034004 (2007)
19. E. Ly, O. Piot, A. Durlach, P. Bernard, M. Manfait, Appl. Spectrosc. **62**, 1088 (2008)
20. N.S. Eikje, K. Aizawa, Y. Ozaki, in *Biotechnology Annual Review*, vol. 11, ed. by M.R. El-Gewely (Elsevier, Amsterdam, 2005), p. 191
21. N.J. Everall, Appl. Spectrosc. **54**, 1515 (2000)
22. N.J. Everall, Appl. Spectrosc. **54**, 773 (2000)
23. N. Everall, Appl. Spectrosc. **62**, 591 (2008)
24. T.E. Bridges, M.P. Houlne, J.M. Harris, Anal. Chem. **76**, 576 (2004)
25. A.M. Macdonald, A.S. Vaughan, P.J. Wyeth, J. Raman Spectrosc. **36**, 185 (2005)
26. B.W. Barry, H.G.M. Edwards, A.C. Williams, J. Raman Spectrosc. **23**, 641 (1992)
27. J.L. Lippert, W.L. Peticolas, Proc. Natl. Acad. Sci. U S A **68**, 1572 (1971)
28. J.J. Baraga, M.S. Feld, R.P. Rava, Proc. Natl. Acad. Sci. U S A **89**, 3473 (1992)
29. R.D. Pensack, B.B. Michniak, D.J. Moore, R. Mendelsohn, Appl. Spectrosc. **60**, 1399 (2006)
30. H. Deng, V.A. Bloomfield, J.M. Benevides, G.J. Thomas, Biopolymers **50**, 656 (1999)

31. W.L. Peticolas, W.L. Kubasek, G.A. Thomas, M. Tsuboi, in *Biological Applications of Raman Spectroscopy*, vol. 1, ed. by T.G. Spiro (Wiley, New York, 1987), p. 81
32. R.C. Lord, G.J. Thomas, Spectrochim. Acta A **23**, 2551 (1967)
33. A. Tfayli, O. Piot, F. Draux, F. Pitre, M. Manfait, Biopolymers **87**, 261 (2007)
34. M.N. Siamwiza, R.C. Lord, M.C. Chen, T. Takamatsu, I. Harada, H. Matsuura, T. Shimanouchi, Biochemistry **14**, 4870 (1975)
35. M. Rangarajan, J.L. Zatz, J. Cosmet. Sci. **52**, 225 (2001)
36. W. Baschong, C. Artmann, D. Hueglin, J. Roeding, J. Cosmet. Sci. **52**, 155 (2001)
37. A. Mavon, V. Raufast, D. Redoulès, J. Control. Release **100**, 221 (2004)
38. G.C. Gurtner, S. Werner, Y. Barrandon, M.T. Longaker, Nature **453**, 314 (2008)
39. P.A. Coulombe, J. Invest. Dermatol. **121**, 219 (2003)
40. I.M. Freedberg, M. Tomic-Canic, M. Komine, M. Blumenberg, J. Invest. Dermatol. **116**, 633 (2001)
41. A.J. Singer, R.A.F. Clark, N. Engl. J. Med. **341**, 738 (1999)
42. M. Tomic-Canic, S.W. Mamber, O. Stojadinovic, B. Lee, N. Radoja, J. McMichael, Wound Repair Regen. **15**, 71 (2007)
43. H. Brem, O. Stojadinovic, R.F. Diegelmann, H. Entero, B. Lee, I. Pastar, M. Golinko, H. Rosenberg, M. Tomic-Canic, Mol. Med. **13**, 30 (2007)
44. B.G. Frushour, J.L. Koenig, Biopolymers **14**, 379 (1975)
45. L. Debelle, A.J.P. Alix, M.-P. Jacob, J.-P. Huvenne, M. Berjot, B. Sombret, P. Legrand, J. Biol. Chem. **270**, 26099 (1995)

16

Raman Spectroscopy of Blood and Urine Specimens

Andrew J. Berger

Abstract Blood and urine are frequently analyzed for their chemical content. Raman spectroscopy, with its high specificity, can provide chemical information in a non-contact and potentially non-invasive manner. In this chapter, key experimental and analytical techniques for converting Raman spectra into quantitative chemical concentration measurements are presented, along with a survey of the current status of the field.

16.1 Overview

This chapter discusses the use of Raman spectroscopy for analysis of biofluids, specifically blood and urine. After a brief overview of the clinical motivations for analyzing biofluids, the benefits of optical approaches in general and Raman spectroscopy in particular are presented. The core of the chapter is a survey of equipment, data-processing, and calibration options for extracting concentration values from Raman spectra of biofluids or, in the in vivo cases, volumes that include biofluids. The chapter finishes with a discussion of fundamental limits on how accurately concentrations can be determined from Raman measurements and how closely current experiments approach that limit.

16.2 Clinical Motivation

16.2.1 General Goals

Chemical testing of biofluids such as blood and urine plays a significant role in society, primarily in health care. Analyzing blood or urine at even a single time point can provide essential, wide-ranging baseline information about a person's state of health, for example as part of a routine annual physical exam or upon admission to a hospital. People with diabetes or high cholesterol levels

use regularly spaced blood analysis to monitor their condition and to make choices that minimize acute events. During surgery or in the intensive care unit, repeated blood analysis can monitor levels of both native chemicals and externally delivered medications to prevent acute situations from developing. Detection of other types of foreign substances, such as illegal drugs, is another important purpose for blood and urine analysis in society.

Typical analysis of blood and urine is based upon chemical reactions, one per chemical species (or "analyte") of interest. Low-accuracy, single-analyte tests such as for blood glucose can be performed using at-home kits; comprehensive blood tests at hospitals are performed using dedicated analyzers that suck in a sample and pump portions of it to various sensor modules. The purpose of this chapter is to explore the possibility of using Raman spectroscopy to replace conventional present tests in certain circumstances.

16.2.2 Blood

Detailed chemical analysis of blood (for example, in hospital analyzers) is usually performed upon blood serum, the clear or yellowish liquid in which the red and white blood cells reside. (One obvious and important exception for which whole blood is required is the measurement of hematocrit, or fraction of blood volume occupied by red blood cells.) Removing the cells makes the tests more straightforward experimentally, both by reducing chemical interferents and by making colorimetric reactions easier to detect optically. Further filtering to remove large proteins can improve detection of minor constituents still more.

A typical "full workup" of major components of blood serum on a hospital analyzer reports about 20 concentrations, among them protein (both the total amount and some major subcategories such as albumin), cholesterol and several related quantities (triglycerides, high- and low-density lipoproteins), glucose, bilirubin, and several ions. Many of these, as will be discussed below, have sufficiently strong Raman signatures that they can be detected in a Raman spectrum acquired on the scale of a minute.

16.2.3 Urine

In the case of most chemicals, urine analysis provides less precise information than blood serum analysis about the donor's instantaneous state of health. This is because the chemicals build up over time as filtered by the kidney and are diluted by variable amounts of water in the bladder depending upon the donor's hydration state. However, the easy availability of urine, compared with blood, means that repeated urinalysis can monitor a person's state of health with little pain or disruption. As noted above, another major use of urine analysis is the detection of breakdown products from medications or illegal drugs.

16.3 Motivation for Raman Spectroscopy

Multiwavelength spectroscopy of biofluids provides several advantages over chemical assays that are not particular to Raman spectroscopy. First, all measurements are performed on the same sample volume, since multiple chemicals' concentrations can be computed from a single spectrum. There is typically just one optical "sensor unit" or cartridge required. In multi-chemical assays, the sample must be separated into subvolumes that are sent to different single-chemical sensor units. This increases the volume of sample needed, the complexity of the sample's path through the analyzer, and the number of sensor units needed.

Another general advantage is that optical sensing requires no physical or chemical contact with the sample. After a spectroscopic measurement is performed, the sample can be sent on to other diagnostic instruments, recycled into the body (e.g., dialysis), or archived for future analysis. Such options do not exist when chemical tests are used. The non-contact nature of optical spectroscopy also eliminates the need for reagents and reduces the number of components that need to be cleaned (for a multi-use instrument).

Raman spectroscopy has some particular advantages for biofluid analysis as well. The sharpness of fundamental vibrational peaks enables dense packing of information into a spectral interval, much more so than for the broader peaks typical of fluorescence or visible/NIR absorption. These extra degrees of spectral freedom are important when it comes to measuring the concentration of minor contributors above the various noise sources.

Mid-IR absorption spectroscopy probes the same energy regime of fundamental vibrations and provides comparable quantitative accuracy (to be discussed below). However, a Raman advantage for biofluids is that water is a weak Raman scatterer but a strong mid-IR absorber. Thus, mid-IR absorption requires samples to be dried prior to analysis, which requires extra preparation steps and time, and does not permit the sample to be saved or passed along in its original liquid state. Another advantage is that Raman spectroscopy can be performed in a backscattering direction, thereby permitting analysis of thick and/or turbid samples (including in vivo applications), whereas absorption spectroscopy is intrinsically a transmissive approach.

16.4 Experimental Setups and Data Processing

16.4.1 Equipment and Geometries

Overwhelmingly, the published research on Raman-based biofluid analysis uses excitation in the near-infrared regime in order to reduce fluorescence. Standard linewidth-narrowed diode lasers at 785 or 830 nm are most common. As noted in Chap. 1, several hundred milliwatts of multiple-spatial mode light can routinely be obtained from diode lasers, making them economical choices

for in vitro biofluid applications, where diffraction-limited focusing is rarely needed. Spectra are recorded using conventional spectrographs and CCD arrays as described in Chap. 1.

The possible optical geometries for ex vivo biofluid measurements fall into many categories. One standard approach is to perform epi-Raman (backscattering) measurements using the same lens for excitation and collection, as depicted in Fig. 16.1. This common-path geometry is appropriate for all working distances, making it useful both for confocal Raman microscopy and for more remote inspection of bulk specimens. The automatic overlap of excitation and collection volumes is particularly effective when using optics with large focal depths (i.e., high f-number) on non-turbid, low-absorption samples such as urine and blood serum.

Several other geometries do not use the same optical paths for excitation and collection. For instance, Cassegrain-style reflective objectives [1] or paraboloidal mirrors [2] can be used for collection, with a laser-steering prism occupying a central obscuration as shown in Fig. 16.2. The excitation and collection volumes do not fully overlap, although the geometry is still backscattering. These all-reflective approaches reduce the spectral background contribution from refractive lens elements, and can also utilize non-imaging optics to increase light-gathering efficiency [2]. With clear samples, another option

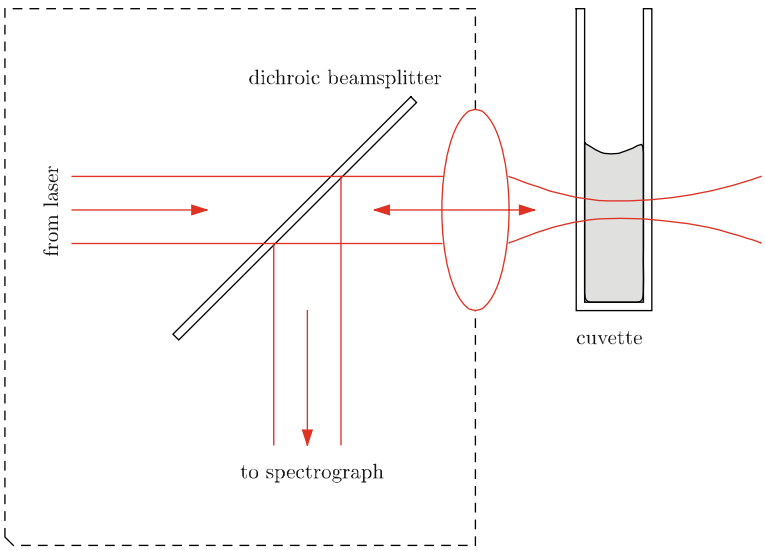

Fig. 16.1. Typical geometry for common-path epi-scattering Raman measurements of biofluids, in vitro. The common path ensures that the excitation and collection volumes overlap (aside from slight changes in refractive index between the laser and Stokes-shifted wavelengths). A dichroic beamsplitter is required; as drawn here, it is reflective at the Stokes-shifted wavelengths, but more commonly it is reflective at the laser wavelength

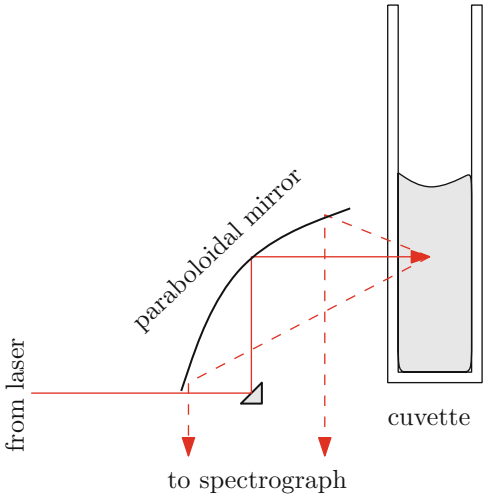

Fig. 16.2. An example of an all-reflective, non-common-path geometry. Light is delivered by a weakly focused beam, and large-angle scattering is gathered and collimated by the paraboloidal reflector; see [2] for an application and further references

is to collect the scattering at 90° from excitation. At low numerical aperture, the excitation in this case looks like an extended line or cylinder, which can be imaged onto a spectrograph slit or captured by an array of optical fibers.

In the published work on Raman spectroscopy of biofluids, there are no present examples of placing optical fibers themselves directly within, or adjacent to, a biofluid; there is always a free-space region immediately adjacent to the sample. As such, although the field of fiber-based biomedical Raman probes is certainly an active area (see, for example, Motz et al. [3]) as noted in Chap. 2, the studies on biofluids cited in this chapter used optical fibers only for convenient piping of light from source to sample to spectrograph.

16.4.2 Liquid Containers

Ex Vivo

For ex vivo applications, the fluid sample can reside in any sort of container into which light can penetrate. The simplest, if there is at least a sizeable fraction of a milliliter of sample, is probably a 1–10 mm pathlength cuvette, irradiated from the side as depicted in Fig 16.1. Plastic cuvettes, while least expensive, give rise to much stronger Raman bands than glass or quartz and are therefore avoided in the epi-collection mode unless there is a compelling reason (e.g., high-volume cost).

The liquid nature of blood and urine samples lends itself to flow-in or flow-through containers. One approach, used by Qu, is to suck the sample into a capillary tube, insert an excitation optical fiber at one end of the tube, and

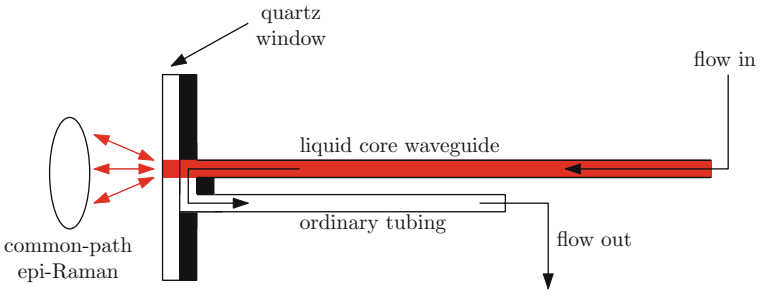

Fig. 16.3. Schematic of a flow-through Raman-based biofluid analysis system. A waveguiding tube delivers the fluid near a quartz window, through which laser light is coupled into the waveguide to perform the spectroscopy [5]. The liquid then flows through a groove to another piece of tubing that carries it away. The waveguiding nature of the delivery tube creates a long optical sampling region, thereby enhancing the Raman signal

collect Raman emission through the tube walls with abutting fiber arrays. The technique exploits the index mismatch at the quartz/air interface to achieve waveguiding conditions, confining the light to travel down the tube, and excite the whole sample efficiently [4]. Another waveguiding-tube approach, used by Qi et al. and depicted in Fig. 16.3, is to use a common-path geometry, both delivering and collecting light from one entrance to the tube. In this case, the waveguiding not only steers excitation light down the tube but also funnels some of the Raman emission back to the entrance aperture, thereby enhancing the collection efficiency. By placing an optical window near the entrance to the tube and allowing the liquid to enter via a right-angle bend, this approach is compatible with a sealed-off liquid flow-through process [5].

In Vivo

The most intriguing "container" for biofluids is, of course, the body itself. While in vivo measurements of urine hold no appeal because it is regularly and painlessly excreted, blood measurements are obviously attractive. There have been three main approaches for transcutaneous Raman spectroscopy of blood, all sketched in Fig. 16.4.

The first is to acquire a "pure blood" spectrum by volume localization. Confocal microscopy can routinely interrogate regions more than 100 µm below the tissue surface, which is deep enough to reach blood capillaries. Because light from out-of-focus regions is strongly rejected, the method makes it possible to gather a more or less "pure blood" spectrum without an interference signal from surrounding tissue structures (Fig. 16.4a).

Another tactic is to compute a "difference spectrum" contrasting two measurements of a tissue region taken before and after some change in the blood content, as sketched in Fig. 16.4b. This provides a spectrum that is nominally

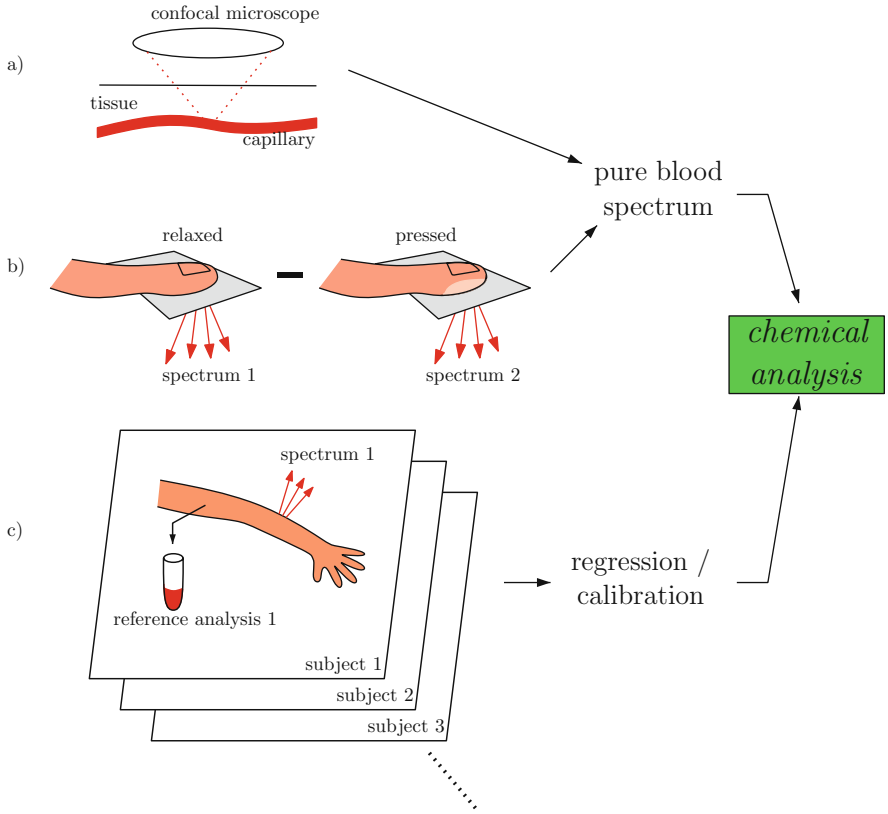

Fig. 16.4. Three methods of obtaining Raman-based estimates of biofluid concentrations in vivo. **a** Confocal isolation of a subsurface volume occupied by a blood vessel, enabling direct measurement of a blood spectrum. **b** Difference measurement between tissue in two states, one with more blood in the sampling volume (in this case, due to pressure modulation by the subject [6]). Computing the difference removes the bulk tissue contributions to the spectral measurement and emphasizes the contribution from blood. **c** Statistical correlation approach of measuring many volunteers' tissue in a region where sufficient blood is present (e.g., the forearm as shown here) and obtaining a correlated reference value from a blood sample drawn at the same time. Multivariate calibration is then used to find correlations between the reference value and the spectral data vector. Unlike the previous two methods, this does not intrinsically isolate the blood chemicals' Raman signatures from those of the surrounding tissue volume

of "pure blood" as well. This technique is most famously exploited in pulse oximetry, a widespread absorption-based technique, in which tissue measurements (usually on the finger or toe) are compared at different time points during the heartbeat cycle. In the case of Raman spectroscopy, where many seconds of integration are typically required, the changes can be induced by

the application of pressure; the "whitening" of a pressed fingertip is an example. Differences in fingertip spectra before and after the application of gentle pressure have been shown to exhibit blood-like spectral features [6].

Finally, one can abandon the goal of extracting a "pure blood" spectrum from that of the surrounding tissue, and instead search for correlations between a bulk-tissue Raman spectrum and the one or more blood analytes whose concentrations are ultimately desired to be known. For example, as depicted in Fig. 16.4c, a study could obtain Raman spectra from volunteers' arms and simultaneously obtain blood samples whose chemical levels are analyzed on a traditional chemical analyzer. Correlation analysis is then performed in an attempt to predict a chemical's concentration based upon the corresponding Raman data. In principle, if the calibration proves to be accurate and robust, it does not matter whether the spectral signature of the chemical actually arises from the blood, as opposed to the surrounding tissue (e.g., interstitial fluid) or some weighted combination of the two. It could even be possible that the target chemical contributes no Raman signal at all but is correlated in concentration with another chemical that does. Details of the calibration process are sketched in the following section.

16.4.3 Extracting Chemical Concentrations

This chapter focuses on extracting quantitative chemical concentrations. Presumably, those values are ultimately used to make a binary decision (classification), such as whether to take clinical action. In principle and often in practice, one can go straight from Raman spectra to classification, bypassing the step of interpreting chemical contributions. Here, however, we will confine ourselves to converting the Raman signal into concentration predictions of one or more chemicals present in the sample.

Assumption of Linearity

To convert an optical signal into a concentration prediction, a linear relationship between the raw signal and the concentration is not necessary. Beer's law for absorption spectroscopy, for instance, models transmitted light as a decaying exponential function of concentration. In the case of Raman spectroscopy of biofluids, however, the measured signal often obeys two convenient linearity conditions without any need for preprocessing. The first condition is that any measured spectrum S of a sample from a certain population (say, of blood samples from a hospital) is a linear superposition of a finite number of pure basis spectra P_i that characterize that population. One of these basis spectra is presumably the pure spectrum P_A of the chemical of interest, A. The second linearity assumption is that the amount of P_A present in the net spectrum S is linearly proportional to the concentration c_A of that chemical. In formulaic terms, the assumptions take the mathematical form

$$S = c_A P_A + \sum_i c_i P_i \tag{16.1}$$

where c_i are weighting coefficients for the other basis spectra. The contribution of the target chemical is thus doubly linear: it scales linearly with concentration, and it linearly superposes upon the rest of the spectrum. It is not necessary to assume that the other c_i values physically correspond to concentrations that scale linearly.

Equation (16.1) is an approximation; it assumes that the measured spectral contribution from P_A is independent of the overall composition of the sample. In reality, the bulk absorption and scattering properties of different samples will cause variations in how much Raman signal is collected. In the case of urine and blood serum specimens, the variation is often negligible. For whole blood and turbid tissue specimens, the influence of bulk optical properties is more important. Methods of correcting for their effects and returning to the simple linearity assumptions of (16.1) are mentioned briefly in the next section.

As in most biomedical applications, the Raman spectra of biofluids typically are superimposed upon a broad emission background that is 10–100 times more intense and not consistent from sample to sample, i.e., it consists of one or more basis spectra B_i with various weights c_i. As such, $S = R + \sum_i c_i B_i$, where R is the Raman spectrum to be extracted. Because of how strong the background signal is, it is wise to minimize its influence prior to training a concentration prediction algorithm. By far the most common approach is to approximate the background by a low-order polynomial (typically fifth order) over the entire spectral range; such a shape cannot fit the sharp Raman peaks. The simplest tactic is to perform a linear least-squares polynomial fit to the spectrum. In situations where the broad background is truly well modeled by polynomials, this linear approach has the merit of outputting a consistent spectrum (i.e., a least-squares fit to the Raman spectrum) regardless of the particular background. More recently, various groups have proposed iterative, nonlinear algorithms for polynomial fitting that do a better job of "ignoring" the Raman peaks, thereby fitting the true background more closely and providing Raman spectra with baselines that do not dip below zero [7]. While such algorithms produce better estimates of the true spectrum R (which may be the final goal in other applications), the nonlinearity means that the outputted spectrum is now influenced by the particularities of the background. A recent study calculated the influence of various Raman baseline removal techniques upon the resulting concentration prediction accuracy [8]; no strong recommendation emerged in favor of this modified polynomial removal method as opposed to derivative-based methods of background suppression. Further comparisons of background removal techniques for Raman spectroscopy are desirable, as the broader literature on spectroscopic background removal in general is vast [9].

Methods of Extracting Concentrations

Ideally, a target analyte would exhibit an identifiable Raman scattering peak in a sufficiently uncluttered region of the overall spectrum from the sample.

Such a peak could either ride solely on the non-Raman background or be sharp enough to distinguish easily from other Raman peaks that overlap it. In either case, the analyte could be associated with a univariate peak, i.e., one whose variations in height were caused uniquely by the target analyte. The peak's height at that pixel (or equivalently, the integrated area under the peak over a few pixels) would directly predict the concentration of that analyte, just as in simple absorption spectrophotometry.

In most applications involving biofluids, there is too much spectral overlap of the many constituents to allow direct analysis of univariate peaks. Concentration measurements can still be extracted, however, using multivariate techniques. The essential model is still the same as in (16.1), namely that the measured spectrum S is a linear superposition of contributions from individual pure components with spectra P_i: $S = \sum_i c_i P_i$. The generic goal is to invert this relationship, modeling the target analyte's concentration c as a correspondingly linear function of the measured spectral values: $c = \sum_\lambda S_\lambda b_\lambda$, where the coefficients b_λ are the weighting factors to be derived. In cases where the mixtures are well understood and simple, it may be possible to measure the pure spectra (by isolating each pure component and taking its spectrum), in which case the coefficients b_λ can be calculated in matrix notation as $b = P^{\mathrm{t}} \left(PP^{\mathrm{t}}\right)^{-1}$, where P now represents the full matrix of pure component spectra (one spectrum occupying each row). When direct measurement of P is not feasible (e.g., it is difficult to isolate some of the pure components or their spectra may be different when in the mixture), it may instead be possible to estimate P by running a set of chemical tests to measure the complete concentration matrix C for a set of so-called *training samples*. If N is the number of pure components, then at least N training samples must be measured; a rule of thumb is to use at least two or three times N samples for robustness against noise. Once C is known, the above equation for S can be solved for an estimate of the pure spectra P, and then one is able to solve for the b_λ coefficients as before. These approaches are called "explicit" modeling because the $S = \sum_i c_i P_i$ relationship is used directly.

Explicit models require comprehensive input in the calibration phase: either the actual spectrum of each pure component or the full chemical breakdown for many training samples. The success of these methods is greatly compromised if the calibration information is incomplete or inaccurate. For samples with many components, such as most whole blood, blood serum, and urine specimens, explicit modeling is an inefficient approach when only one or a subset of the full number of chemicals is of interest.

Practical Raman-based analysis of biofluids is instead usually performed using "implicit" or chemometric approaches, such as principal component analysis and partial least squares, as discussed in Chap. 8. In contrast to explicit models, the required inputs for implicit modeling are matched efficiently to the desired output. If the goal is to predict the concentration of a single target analyte, then the training set need only provide that analyte's concentration for each sample. Generally, this is a win–win situation: it is easier to perform the calibration and the implicit modeling can handle un-

characterized system properties (e.g., a Raman scatterer whose presence in the system was not known) that would doom an explicit calibration.

For the past two decades, the workhorse of implicit linear modeling has been partial least squares (PLS) (see Haaland and Thomas [10] and Chap. 8). PLS uses only training spectra and a target analyte's concentration to perform its calibration. If the Raman spectrum of the target is also available, this can be folded into the calibration process. Various methods of utilizing this information have been explored, including making a better model of the interference spectra [11] and requiring the regression vector to share the target's main spectral features [12]. These methods usually provide only incremental advantages over standard PLS in most circumstances, but they are an important part of the calibrator's toolbox when the information is available.

Three metrics characterizing chemometric concentration predictions are commonly reported: the number of basis spectra in the optimal model (or the "rank"), the root-mean-squared error of prediction (RMSEP), and the correlation between the predicted and reference values (usually given as an r^2 value). For a training set of N samples, a model of rank less than $N/2$ or $N/3$ is generally regarded as unreliable, as mentioned above. When N is not large enough to build independent training and validation sets of sufficient size, often a cross-validation is performed, where one or more samples are rotated out of the training set in sequence, until each sample's concentration has been predicted. In this case, one should report a root-mean-squared error of cross-validation (RMSECV), which is likely to be slightly lower than an RMSEP value. The distinction is often not crucial, particularly in exploratory work; the general term "error" will be used in the discussions below to apply to both RMSEP and RMSECV unless noted otherwise.

For applications in which bulk optical properties vary from sample to sample, the linearity assumptions mentioned above can be strongly violated. This is an issue, for example, in in vivo tissue measurements on a cohort of human subjects. In this case, it is important to decouple the Raman spectral signature from the modifications imparted by the turbidity. A recent pair of publications has reported a way of extracting the so-called "intrinsic Raman signal" from turbid media [13, 14]. The general method requires an independent measurement of the mean free scattering pathlength in the turbid medium; the authors advertise, however, a future publication concering limiting cases that can bypass this constraint.

16.5 Published Results

16.5.1 Best-Case Limits of Detection

Raman spectra of biological fluids always include a broad background component, and usually this background is much stronger than the signal of the analyte of interest. Although pure biofluids do not tend to autofluoresce as

strongly as tissue specimens, they still exhibit a substantial fluorescence component, even when excited in the near-infrared to limit absorption by fluorescent species. Even when physical methods of fluorescence rejection are employed (e.g., time-gating), the water itself contributes a broad non-fluorescent background spectrum (from excitations of the hydrogen bonding network). While water interference is far more troublesome when vibrations are probed in absorption mode in the mid-IR (requiring specimens to be dried or studied with very short pathlengths), the Raman signal from water is still an order of magnitude or more stronger than signals from analytes present at millimolar (mM) concentrations or less.

Shot noise from this background limits the accuracy with which analytes' concentrations can be calculated. If the concentration is too low, the number of Raman-scattered photons measured from the analyte simply does not exceed the random fluctuations in the number of background counts arriving over that same spectral range. Such a concentration becomes fundamentally indistinguishable from zero. The only remaining ways to improve the signal-to-noise ratio, and thus the concentration prediction accuracy, are to increase the overall signal strength by increasing the laser power, improving the collection geometry, or integrating for a longer time.

A straightforward experimental estimate of best-case prediction limits can be made by inspecting the spectrum of an analyte dissolved in water with no other spectral interferents present. Figure 16.5 shows Raman spectra of water and dissolved glucose in water, both obtained in 60 s in a cuvette-based epi-Raman setup with $\sim$ 435 mW of 830 nm excitation power. In both cases, an

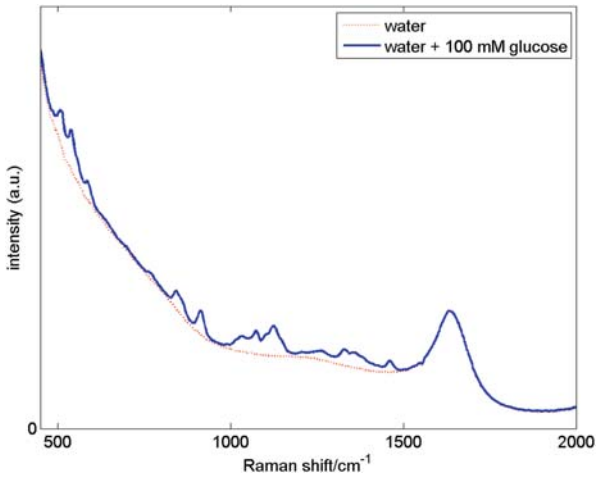

Fig. 16.5. Comparison of Raman spectra of pure water (*dotted line*) and water with dissolved glucose at a high concentration of 100 mM (*solid line*). This shows that even in a best-case scenario (i.e., no fluorescence), the majority of the shot noise in a dissolved analyte spectrum comes from the host environment rather than the targeted analyte itself

appropriate background spectrum was subtracted to isolate the signal of interest, and the glucose spectrum has been scaled to correspond to a concentration of 100 mM. Even at this physiologically large value, glucose's Raman bands are smaller than the amount of signal coming from water. If we call the integrated area under the Raman peaks the "true glucose signal" corresponding to 100 mM concentration, we can inspect the water spectrum and estimate how much its shot noise will cause the "glucose signal" to fluctuate from measurement to measurement. For this particular laser wavelength, excitation power, collection geometry, and choice of analyte (glucose), that standard deviation in signal corresponds to approximately 1.2 mg/dL, or equivalently 0.07 mM concentration of glucose. This is thus the best-case estimate of the prediction error obtained from aqueous Raman-based measurements under these conditions.

This best-case order-of-magnitude estimate of about 0.1 mM error in predicting a single analyte aligns with experimental results that have come from studies of dissolved biological analytes in prepared aqueous mixtures containing no significant fluorophores. In the mid-1990s, in work that laid the foundation for Raman analysis of blood and urine, Goetz et al. took Raman spectra of mixtures of three biological analytes (glucose, lactic acid, urea) in deionized, distilled water at various concentrations. A side-scattering geometry was used; they passed a 10 mW beam of 514.5 nm laser light through a capillary tube and viewed the side-emitted Raman emission through the wall of the tube. PLS calibration and prediction were used. Prediction error in the 1 mM regime was achieved for glucose and lactic acid, with urea error at 3 mM [15]. Three-analyte studies in phosphate-buffered saline published by a different group the following year obtained similar 1.2 mM prediction errors for glucose and creatinine and 1.3 mM errors for lactic acid, with a comparable measurement time of 100 s, longer wavelength of 830 nm, and higher power of 200 mW at the sample [16]. In a more recent study, Sćepanović et al. acquired Raman spectra of aqueous 3-analyte mixtures (glucose, creatinine, urea) and analyzed them using explicit fits to spectra of the individual components. About 217 mW of 830 nm light were used for a total integration time of 60 s. Prediction errors were 0.49, 0.27, and 0.32 mM for the three analytes. Moreover, a rigorous error analysis confirmed that the errors obtained nearly reached the fundamental measurement-noise limit [17].

The recurring message from these basic studies is that spontaneous Raman spectroscopy cannot do much better than about 0.2 mM accuracy on these analytes in about 100 s of integration. The shot noise from the spectral background, which cannot be eliminated because it comes from the host medium's constituents (e.g., water), imposes a fundamental constraint. In all three mixture studies, the error levels were very consistent among the analytes studied. This is unsurprising, as all of the analytes happened to have similar molecular weights (around 100) and, in a rough sense, would therefore be expected to have similar Raman scattering cross sections per molecule. Converting the 0.2 mM accuracy limit to a mass density for this size range, the equivalent error limit is 2 mg/dL.

This barrier of about 0.2 mM in 100 s can be overcome in limited ways. If the target analyte has a substantially larger cross section than those mentioned above, it will be correspondingly easier to detect with more accuracy. Occasionally, the molecule simply happens to have an unusually large cross section for its molecular weight. In this case, this is a true advantage over glucose and the other analytes mentioned above. Larger molecules with many subunits, such as proteins and DNA, tend to have correspondingly larger cross sections per molecule as well. In such cases, while the minimum error in millimolar can drop well below 0.2 mM, the error in milligram per deciliter remains relatively unchanged. In terms of parameters the experimenter can control, most simplistically, one can increase the laser power on the sample, as long as damage is not done. More elegantly, one can revise the collection geometry to increase efficiency. In either case, the benefit in sensitivity only grows as the square root of the increase in signal, as the Raman peak and the spectral background will grow in tandem.

If an application calls for the quantification of a single analyte rather than a broad panel, then another possibility can be resonance Raman spectroscopy. In resonance Raman, the laser is tuned to an electronic absorption band of the target species, greatly increasing the species' Raman scattering cross section while leaving other chemicals largely unaffected. Typically, this is performed with UV lasers, although unusual level structure in carotenoids and hemoglobin make resonance Raman practical in the visible for these important molecules. To date, no major applications of resonance Raman to biofluid analysis have been reported to the author's knowledge.

16.5.2 Blood Serum

Representative spectra of blood serum samples, processed as described above to remove broad fluorescent background via a polynomial, are shown in Fig. 16.6, along with similar samples of urine (data from Qi and Berger [5]). Serum spectra contain many more visible Raman peaks than urine, whose spectrum is dominated by a single urea peak.

The first major reports of analyte quantification in blood serum samples came out in 1999. (As noted above, most conventional blood analysis is performed upon blood serum, not whole blood.) Berger et al. [1] and Qu et al. [18] used similar near-infrared laser wavelengths (830 and 785 nm), powers (250 and 300 mW), spectral integration times (1–5 min), total number of patients' samples (60–70), and multivariate calibration methods (PLS). Both experiments analyzed samples in cuvettes using non-equivalent excitation and collection volumes, one employing a Cassegrain collecting lens to view through the cuvette wall, the other 90° scattering from a collimated beam passing up through the cuvette's floor. In both cases, significant correlations between reference concentrations and PLS predictions were obtained for multiple analytes in blood serum, including total protein, albumin, triglyceride, cholesterol, blood urea nitrogen (BUN), and glucose. In Qu's study, spectra were

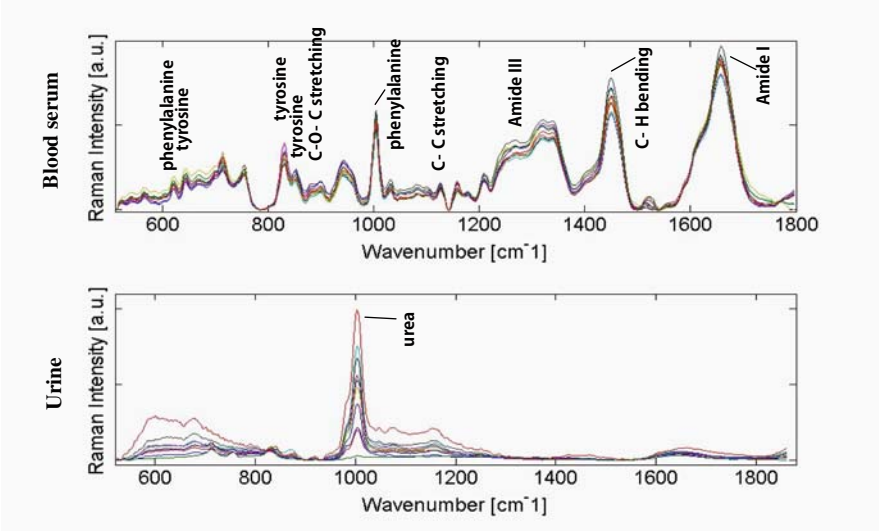

Fig. 16.6. Representative Raman spectra, after background subtraction, of blood serum (*above*) and urine (*below*). Spectra from multiple subjects are shown (data replotted from [5]). The spectrum of blood serum contains many chemical signatures at comparable amplitudes, whereas that of urine is dominated by a urea peak

acquired both before and after a filtration step that removed large molecules (such as proteins). They showed that this strongly reduced the background fluorescence and improved the accuracy with which lighter molecular species, such as glucose, were predicted.

In the decade since these first reports, various advances in blood serum Raman spectroscopy have been reported. As mentioned above, Qu developed a system with a waveguiding sample-filled capillary tube and two linear arrays of abutting fibers, with 100 mW sample illumination at 745 nm. On synthetic mixtures that simulated human serum, they obtained prediction errors for glucose and urea of 0.5 and 0.4 mM, respectively [4].

The most extensive test to date was performed by Rohleder et al. [19, 20] using 400 mW of 785 nm excitation (200 mW at sample), a quartz cuvette, epi-detection, 5 min of spectral integration, and PLS calibration. The number of blood donors was 247, much higher than previous studies. Concentrations of glucose, urea, uric acid, cholesterol, triglycerides, and both high-density and low-density lipoprotein (HDL and LDL) were predicted with significant correlations. For the smaller molecules, ultrafiltration significantly improved the prediction accuracy. Concentration errors for glucose and urea were 0.95 and 0.73 mM, respectively, when predicted in native serum; these values improved to 0.38 and 0.35 mM with ultrafiltration.

Recently, Qi et al. made measurements on approximately 70 serum samples using an epi-illuminated waveguiding sample chamber, 160 mW of 830 nm excitation, up to 150 s of spectral integration, and PLS leave-one-out

cross-validation [5]. The waveguiding geometry increased the collected Raman signal strength compared to epi-illumination of a cuvette by the same lens. The analytes successfully predicted again included glucose, triglyceride, HDL, LDL, blood urea nitrogen, cholesterol, and total protein, and additionally included total bilirubin and CO_2 (in mEq/L). Glucose was predicted with 0.66 mM error in 20 s of spectral integration, with a reduction to 0.49 mM when 150 s were used. The corresponding values for urea were 0.37 (9 s) and 0.25 mM.

Consistently, the blood serum prediction accuracies in the above-mentioned studies are near the ~ 0.1 mM limit for smaller molecules that was suggested by fundamental and empirical results for simpler ensembles. Indeed, Rohleder et al. made this observation about vibrational spectroscopy approaches (both Raman and mid-IR absorption) in general, based upon their comprehensive literature review: "Considering the molar weights of the analytes investigated, vibrational-spectroscopy based quantification appears to be limited to accuracies in the 0.1 mmol/L range, regardless of the particular choice of the spectroscopic technique [20]."

It is worth noting that the optimal number of PLS loading vectors employed to predict various analytes in these papers is also consistent, ranging almost exclusively from 10 to 17, even for the largest of calibration sets. For integration times of a few minutes or less, it appears that any spectrum one acquires can be modeled (fit) to within the shot noise using no more than 20 independent spectral lineshapes. This then places a fundamental limit on the number of independent analyte concentrations that can be calculated from such data.

These two empirically observed limits, on minimum achievable concentration error and maximum number of independent spectral components, could well be related. Fundamentally, as discussed above, improving the signal to noise (by collecting more photons) should always reduce the minimum achievable error, bringing more analytes within the range of detectability. By the same token, improved signal to noise should reveal additional features in the spectra, increasing their information content (i.e., the number of independent lineshapes required to fit them). Since all of the above-referenced blood serum experiments were carried out using fairly similar parameters, the consistency in the empirical limits is unsurprising. However, there is no reason to think that either limit transcends the particular signal-to-noise range that these experiments consistently explored.

16.5.3 Whole Blood

In vitro measurements of native chemical concentrations in whole blood were first reported for a 69-sample data set by Berger et al. using the same Cassegrain-based reflective geometry that was designed originally for serum [1]. Enejder et al. subsequently optimized the collection optics for whole blood

samples using Monte Carlo simulations of light propagation in whole blood and an off-axis paraboloidal mirror [2]. Their study used 31 samples and PLS leave-one-out cross-validation. They obtained strong correlations in their predictions of glucose, urea, total protein, albumin, triglycerides, hematocrit, and hemoglobin. The glucose error was 1.2 mM, moderately higher than the current best results for blood serum, which is unsurprising for two reasons. First, the number of samples was 31, which is significantly smaller than most of the blood serum work and larger than the typical number of loading vectors by only a factor of 2, usually not considered a large enough set to be comprehensive. More importantly, the natural variations in bulk optical properties of the different blood samples (due, for instance, to different levels of red blood cell concentration) distort the strength of the remitted signal, disrupting the presumed linear relationship between analyte concentration and measured Raman peak signals. As noted earlier, calibration methods that can extract the "intrinsic Raman signal" by correcting for these variations have recently been demonstrated [14], but to date have not been applied to whole blood data sets in the literature.

There have been a few publications to date regarding in vivo Raman spectroscopy of blood, all of them preliminary. Using reflectance confocal microscopy for guidance, Caspers et al. demonstrated the ability to acquire a confocal Raman spectrum of a subsurface blood vessel in the arm (cf. Fig. 16.4a) that matched up well with an in vitro sample [21]. Further development of this technique for noninvasive blood analysis has not since been reported. In a glucose detection application, Chaiken et al. developed a transcutaneous fingertip-based Raman system using the pressure on/off technique of Fig. 16.4b. Integrating the Raman counts above the baseline over a chosen spectral range $\left(375\text{–}686\,\mathrm{cm}^{-1}\right)$, they reported statistically significant correlations between this integrated signal and blood glucose concentration as measured by blood draws [6]. A mean glucose prediction error of 1.2 mM was obtained, though several outlier spectra had to be rejected. Why the integral should be insensitive to Raman signatures from other analytes was not explained. Again on the theme of glucose, Enejder et al. reported Raman-based predictions of blood glucose concentration from transcutaneous forearm measurements [22]. Glucose prediction accuracy was reported not in terms of absolute concentration but rather in mean absolute error (MAE) of a cross-validation, where "absolute error" for each prediction was defined as the absolute difference between predicted and reference concentration, divided by the reference concentration. Values ranged from 7.7% for single-volunteer calibrations to 16.9% when all the data from 17 volunteers were pooled. These initial results are encouraging, and the presence of glucose-like features in their PLS calibration weightings offset some of the fear of spurious calibrations due to temporal correlations in glucose concentration between adjacent time points.

16.5.4 Urine

As noted above, concentrations of native urine chemicals hold less clinical importance than those from blood, and there has been correspondingly less research devoted to this area. Early papers testing the feasibility of measuring certain chemicals in urine were published by Premasiri et al. [23] and Dou et al. [24], though validated predictions of concentrations at native levels in actual urine specimens were not carried out. Improving upon preliminary work by McMurdy that used a Cassegrainian sampling geometry [25], Qi et al. used the same LCOF system as in their blood serum work to analyze 69 in vitro urine specimens [5]. They obtained strong PLS-based correlations for creatinine and urea content, limited by the accuracy of the reference chemistry in both cases. The creatinine error was 0.38 mM, empirically in line with the sorts of results found in blood serum, although unlike those cases this was a limit imposed by the reference chemistry, not the Raman methodology.

Some particular applications of Raman-based urine analysis have recently been reported. Park et al. explored the ability of Raman spectroscopy to detect abnormally high levels of glucose in diluted urine, with the goal of installing such technology on toilet bowls to monitor diabetic users [26, 27]. Using a linear discrimination technique, they reported an ability to discriminate between spectra of pure water and water with 0.28 mM glucose. They claimed that if they could reproduce these results in urine and at somewhat lower concentration, then they would be able to distinguish between normal and elevated levels in urine that has been diluted, presumably by the toilet bowl water. The possibility of modifying the toilet bowl to enable capture and analysis of undiluted urine was not mentioned. Meanwhile, Guimaraes et al. doped the drug ephedrine into urine specimens and also obtained the urine of an ephedrine-injected rat. By simple calculation of a peak area for a band at 1002 cm^{-1} corresponding to the drug, they report an ability to detect drug concentrations as low as 0.03 mM [28], which is plausible from first principles (especially since the drug probably has a stronger Raman cross section than most natively occurring chemical species). Their regression line does not extrapolate to zero Raman signal for zero drug concentration, probably because the urea Raman band at 1005 cm^{-1} is not perfectly removed, so the lower detection limit claimed is slightly suspect.

16.6 Conclusion

Spontaneous Raman spectroscopy has the ability to provide clinically relevant chemical concentration measurements of multiple analytes in biofluids. Blood serum, whole blood, and urine have all been studied. The detection limit (assuming a few hundred seconds of spectral acquisition) appears, based upon fundamental noise considerations, to be around 0.1 mM for most biochemicals; this places several important analytes within reach but certainly precludes

detection of many lower concentration species of interest. Multiple research groups have performed in vitro Raman-based measurements approaching this level of accuracy, suggesting that further improvements in experimental design (e.g., more accurate reference concentrations against which to regress) may pay only diminishing returns. In vivo measurements of blood chemical concentrations, while still in the preliminary stages and faced with a higher noise floor due to the greater background fluorescence signal emitted from tissue, have begun to yield promising results as well.

References

1. A.J. Berger, T.-W. Koo, I. Itzkan, G.L. Horowitz, M.S. Feld, Appl. Opt. **38**(13), 2916 (1999)
2. A.M.K. Enejder, T.-W. Koo, J. Oh, M. Hunter, S. Sasic, M.S. Feld, Opt. Lett. **27**(22), 2004 (2002)
3. J.T. Motz, M. Hunter, L.H. Galindo, J.A. Gardecki, J.R. Kramer, R.R. Dasari, M.S. Feld, Appl. Opt. **43**(3), 542 (2004)
4. J.Y. Qu, L. Shao, Rev. Sci. Inst. **72**(6), 2717 (2001)
5. D. Qi, A.J. Berger, Appl. Opt. **46**(10), 1726 (2007)
6. J. Chaiken, W. Finney, P.E. Knudson, R.S. Weinstock, M. Khan, R.J. Bussjager, D. Hagrman, P. Hagrman, Y. Zhao, C.M. Peterson, K. Peterson, J. Biomed. Opt. **10**(3), 031111 (2005)
7. C.A. Lieber, A. Mahadevan-Jansen, Appl. Spectrosc. **57**(11), 1363–1367 (2003)
8. N.K. Afseth, V.H. Segtnan, J.P. Wold, Appl. Spectrosc. **60**(2), 1358 (2006)
9. G. Schulze, A. Jirasek, M.M.L. Yu, A. Lim, R.F.B. Turner, M.W. Blades, Appl. Spectrosc. **59**(5), 545 (2005)
10. D.M. Haaland, E.V. Thomas, Anal. Chem. **60**, 1193 (1988)
11. A.J. Berger, T.-W. Koo, I. Itzkan, M.S. Feld, Anal. Chem. **70**, 623 (1998)
12. W.-C. Shih, K.L. Bechtel, M.S. Feld, Anal. Chem. **79**, 234 (2007)
13. W.-C. Shih, K.L. Bechtel, M.S. Feld, Opt. Express **16**(17), 12726 (2008)
14. K.L. Bechtel, W.-C. Shih, M.S. Feld, Opt. Express **16**(17), 12737 (2008)
15. M.J. Goetz Jr., G.L. Coté, R. Erckens, W. March, M. Motamedi, IEEE Trans. Biomed. Eng. **42**(7), 728 (1995)
16. A.J. Berger, Y. Wang, M.S. Feld, Appl. Opt. **35**(1), 209 (1996)
17. O.R. Sćepanović, K.L. Bechtel, A.S. Haka, W.-C. Shih, T.-W. Koo, A.J. Berger, M.S. Feld, J. Biomed. Opt. **12**(6), 064012 (2007)
18. J.Y. Qu, B.C. Wilson, D. Suria, Appl. Opt. **38**(25), 5491 (1999)
19. D. Rohleder, W. Kiefer, W. Petrich, Analyst **129**, 906 (2004)
20. D. Rohleder, G. Kocherscheidt, K. Gerber, W. Kiefer, W. Kohler, J. Mocks, W. Petrich, J. Biomed. Opt. **10**(3), 031108 (2005)
21. P.J. Caspers, G.W. Lucassen, G.J. Puppels, Biophys. J. **85**, 572 (2003)
22. A.M.K. Enejder, T.G. Scecina, J. Oh, M. Hunter, W.-Ch. Shih, S. Sasic, G.L. Horowitz, M.S. Feld, J. Biomed. Opt. **10**(3), 031114 (2005)
23. W.R. Premasiri, R.H. Clarke, M.E. Womble, Lasers Surg. Med. **28**, 330 (2001)
24. X. Dou, Y. Yamaguchi, H. Yamamoto, S. Doi, Y. Ozaki, Biospectroscopy **3**(2), 113 (1998)
25. J.W. McMurdy III, A.J. Berger, Appl. Spectrosc. **57**(3), 522 (2003)

26. C.S. Park. J.M. Choi, K.S. Park, in *Proc. IEEE Eng. Med. Biol. 27th Annual Conference*, Shanghai, China, Septr 2005, p. 1991
27. C. Park, K. Kim, J. Choi, K. Park, Physiol. Meas. **28**, 583 (2007)
28. A.E. Guimaraes, M.T.T. Pacheco, L. Silveira Jr., D. Barsottini, J. Duarte, A.B. Villaverde, R.A. Zangaro, Spectroscopy **20**, 185 (2006)

17

Quantitative Raman Spectroscopy of Biomaterials for Arthroplastic Applications

Giuseppe Pezzotti

Abstract Raman microprobe spectroscopy has considerable potential as an analytical tool in orthopedic science for its capability of non-destructively assessing the physical, chemical and mechanical characteristics of load-bearing parts in arthroplastic components (i.e., artificial joints). In comparison to other assessment techniques, Raman spectroscopy offers high spatial resolution in the characterization of oxidation states, phase transformations, crystallographic textures and residual stress/strain fields as developed at load-bearing surfaces of arthroplastic components, when embedded in biological envi-ronment. Furthermore, confocal probes can be used for non-destructively determining highly graded properties along the material subsurface. We show in this chapter a quantitative visualization of biomaterial mesostructures and, through such information, how the surfaces of orthopedic prostheses react to load bearing in biological environment.

17.1 Introduction

A significant contribution of Raman spectroscopy to the analytical characterization of biomedical issues has been made in the area of biomaterials, especially in the identification of biodegradation and deterioration [1, 2]. The general impact of Raman spectroscopy on the study of biomaterials has been described by this author in three recent review articles [3–5]. In this chapter, the topic of Raman characterization of biomaterials is revisited with particular emphasis placed on those biomaterials widely employed for load-bearing surfaces in artificial joints. Important recent case studies are presented to illustrate the power of the Raman technique to answer key questions of broad medical, scientific, and technological interest. The analytical and physical science lying behind the Raman effect is shown to contribute to the accumulation of a wealth of fundamental information about the medical and technical achievements of prosthesis makers.

17.2 Raman Microspectrometer and Related Equipments

In modern Raman equipments, maps of oxidation state, phase fractions, and stress/strain in synthetic biomaterials can be collected by impinging on the biomaterial a laser beam with suitable excitation frequencies of blue and green at 488 and 514 nm, respectively, as emitted by an Ar-ion laser. Such a suitable excitation sources for synthetic biomaterials, besides proving the least intrusive (i.e., minimizing damage to or alteration of the biomaterial surface), also allow maximizing the signal-to-noise ratio for most materials of technological interest in the orthopedic field. Some benefits may be introduced using confocal optics: a better discrimination of Raman signals originating from different depths inside the sample; an improved detection of subsurface species showing very weak Raman spectra; and the rejection of non-specific sample fluorescence. Distribution gradients of molecular species, stress/strain fields, and phase transformation patterns, together with their distribution maps, can be easily detected and this new arrangement enables one to finalize research projects, especially in terms of both spectral and spatial resolution, which were not feasible before. The confocal configuration of the probe adopted in the experiments allows shifting the focal plane below the material surface in order to collect maps of selected spectral features non-destructively in the

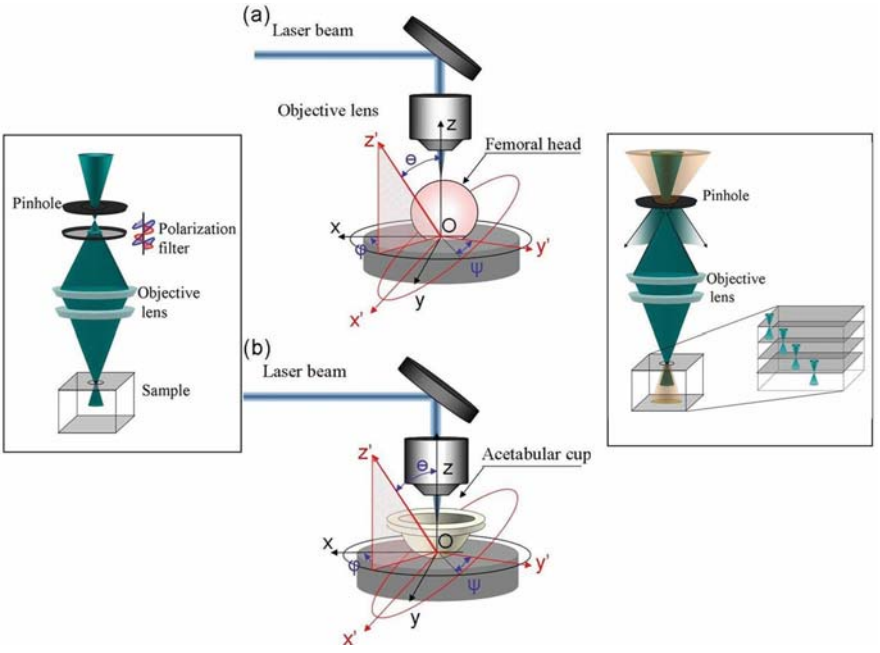

Fig. 17.1. Drafts of two distinct protocols for performing Raman spectroscopic analyses using rotating jigs on **(a)** femoral heads and **(b)** acetabular cups. In inset, illustrative schemes of measurements using polarization filters and confocal probe

material sub-surface. It is not within the scope of this chapter to describe in detail the confocal microprobe spectroscopy technique, the procedure is reported somewhere else [6–10]. Throughout our studies, we needed to employ polarization filters in order to both separate contributions from different vibrational modes and to clarify, through analyses of Raman tensors, the crystallographic orientation of the investigated materials. An explanatory draft of a confocal Raman analysis performed on a femoral head and on an acetabular cup is shown in Fig. 17.1a and b, respectively.

17.3 Quantitative Raman Spectroscopy of Synthetic Biomaterials

Stress assessments in a Raman spectroscope can be made by exploiting the so-called piezo-spectroscopic (PS) effect, which can be simply defined as the shift in frequency of a spectroscopic transition in response to an applied strain or stress. The definition of the PS effect has been stated independent of spectrum arising from luminescence [11], or Raman scattering [12], and it can be represented with a linear relationship between the second-rank stress tensor and the observed Raman shift [11, 13, 14]. In the experimental practice, the various components of the PS tensor need to be directly measured. In addition, various kinds of quantitative information can be achieved by Raman inspection: the extent of surface changes in terms of phase transformation; the associated residual strain stored within different phases; and the amount of oxidation and other chemistry-related alterations of the bearing surfaces. Clear correlations can be found between the degree of phase transformation, the residual strain magnitude, and the oxidative phenomena, which are in turn related to the complex, environmentally assisted wear interactions in artificial joints, for example, between the femoral head and its bearing counterpart acetabular cup.

The interpretation of Raman spectra in the presence of overlapping phases might be not straightforward; however, it has been shown [15] that an assessment of the surface Raman response of relevant zirconia bands is possible with the aid of confocal spectroscopy. Phase transformation fractions in the early nucleation stage of the monoclinic phase on the surface of ZrO_2 femoral heads can be characterized. The monoclinic phase content can be quantitatively evaluated from the relative intensities of Raman bands arising from different polymorphs: the tetragonal and the monoclinic phases. The formula, which was first proposed by Katagiri et al. [16], can be used for such structural assessments and the technique is accurate to about ± 0.1 vol%. Intensification of surface stress fields are expected on the surface of zirconia hip joints and they may be rather severe owing to the overlapping of several factors, including pre-existing defects, phase transformation, and machining effects. Residual stress components arising from phase transformation are expected to be tensile in the tetragonal phase and compressive in the monoclinic

phase, due to the phenomenon of volume expansion occurring during phase transformation.

Raman spectroscopy characterizations are also important for polyethylene and, in particular, for ultrahigh molecular weight polyethylene (UHMWPE), which is a material of wide usage in arthroplasty. Gamma (γ) radiation is commonly used for the sterilization of medical devices. Cobalt 60 gamma sterilization has become the industry's method of choice because of its reliability in sterilizing thoroughly throughout the entire sample, the absence of chemical residues after sterilization, its flexibility, and its cost-effectiveness. Although numerous studies have considered the effects of sterilization on the surface structure and properties of polyethylene components for joint implants, no fully conclusive verdict has been reached about the optimum radiation dose. All studies agree on the mechanism that produces the change in mechanical properties but do not necessarily agree on how these changes affect the success or failure rates of the joint implants [17, 18]. The method of sterilization, therefore, becomes a primary concern with regard to total joint replacements. In this context, the goal of Raman spectroscopic experiments is to verify the actual structural changes that occur during γ-radiation sterilization in UHMWPE, specifically with regard to its wear properties, and to evaluate the extent to which such structural changes influence the lifetime of the joint. It should be noted that two types of mechanism contribute to joint degradation, creep deformation, and oxidation [19]. We shall show in this chapter that Raman spectroscopy can enable one to make quantitative assessments of UHMWPE internal structure and residual strain.

17.4 Applications of Raman Spectroscopy to Artificial Joint Prostheses: Case Studies

17.4.1 Phase Transformation and Fracture of Zirconia Femoral Heads

In a recent review paper, Clarke et al. [20] pointed out how, since their inception 18 years ago, the performance of zirconia ceramic femoral heads has been both confusing and controversial. Grouping all zirconia materials as the same product, in the absence of a rigorous scientific classification of their individual chemical and physical properties, has led to confusion and to misleading generalizations. The degree of metastability of zirconia materials as well as the involved probability of fracture strongly depends on the microstructural characteristics of the individual material, and thus strongly on the manufacturing process. For example, the clinical history of yttria-stabilized zirconia ceramic has been quite controversial. In vivo, a combination of hydrothermal and mechanical exposure may selectively trigger detrimental changes on the surface of femoral heads that have inferior phase stability. Local transformation from the tetragonal to the monoclinic phase may be influenced on

the material surface by the effect of body fluid and load impingement conditions. Hydrothermal processes are most salient to material stability, thus making the implant sensitive to the adopted lubrication mode; for example, for zirconia ceramic-on-ceramic bearing systems tested in a hip simulator, early catastrophic failure is found when run in water but implants survive up to 20 million cycles when run with calf serum lubrication. This may suggest that tribological conditions under the cup are the trigger for a metastable behavior. However, some femoral heads were found to be completely stable and untransformed, showing that yet little is understood of how the hydrothermal conditions actually affect the kinetics of hip joints in vivo. Raman spectroscopic analysis can be very useful to clarify the effect of surface aging and of localized stress-related phenomena in zirconia materials.

The effect of highly localized loading on the surface of yttria-stabilized zirconia ceramic was investigated by polarized Raman microprobe spectroscopy. Figure 17.2a–d shows a micrograph of an indentation print, a map of

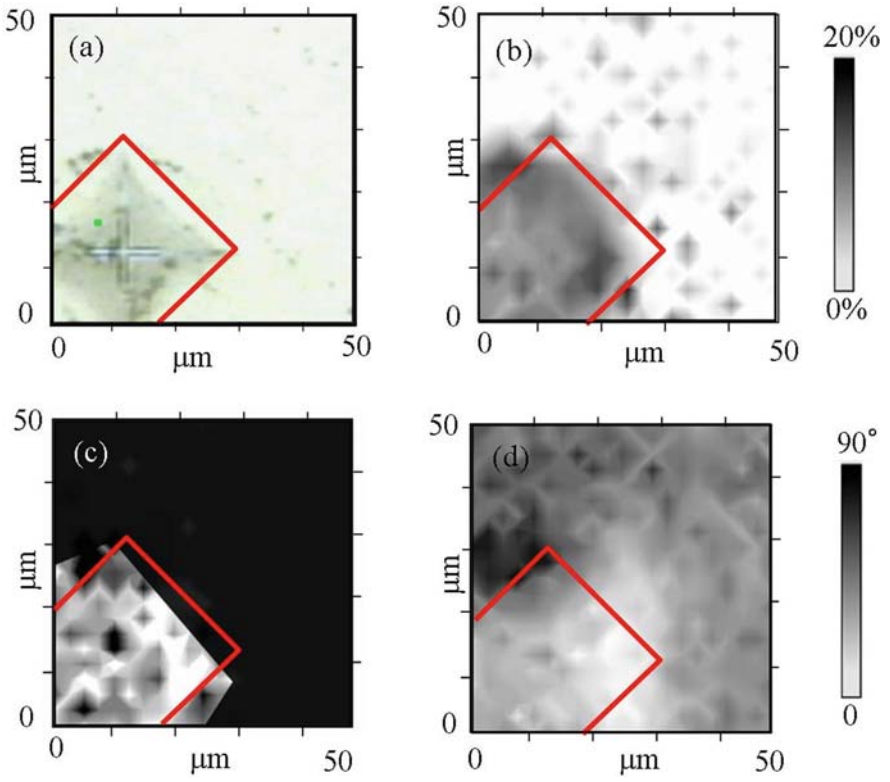

Fig. 17.2. Results of polarized Raman spectroscopic analyses on the surface of yttria-stabilized zirconia in the presence of an indentation print: **(a)** optical micrograph of the indentation print, **(b)** map of transformed monoclinic fraction, **(c)** map of *b*-axis orientation of the monoclinic phase, and **(d)** map of the angle of *c*-axis orientation of the residual tetragonal phase. In both **(c)** and **(d)**, the represented angle gives the inclination of the respective axes with respect to the sampling plane

transformed monoclinic fraction, a map of the angle of *c*-axis orientation of the residual tetragonal phase, and a map of *b*-axis orientation of the monoclinic phase, respectively. The maps in b–d reveal a strong preferential orientation of the crystalline structures of both transformed and residual untransformed polymorphs. This phenomenon may have a large impact on the development of surface roughness, especially when local scratching occurs during in vivo loading under the condition of third-body wear between the bearing surfaces.

Intensification of surface stress fields on the surface of zirconia hip joints may arise from residual stresses associated with the tetragonal-to-monoclinic phase transformation. The presence in the material of "islands" of very high tensile stress makes the implant prone to catastrophic fracture. Figure 17.3 shows the largest of three pieces of a fractured femoral head retrieved at Loma Linda Medical Center from a 45-year-old male patient after 5-year implantation. The femoral head, which was impinging on a UHMWPE cup and mounted on a Ti64 femoral stem, "snapped" getting out of bed in the morning. Typical Raman spectra collected in selected areas of the fractured piece are also shown in Fig. 17.3. As seen, no transformation was noticed in the internal part of the head, but relatively high fractions of monoclinic phase were systematically found in contact areas, namely on both internal and external surfaces (cf. fractions and depths indicated in Fig. 17.3). Given the complicated morphology of the fractured piece, the determination of a single location as fracture origin is difficult. However, the machined corner region where the Ti64 taper-cone impinges on the ball likely represents a high-probability failure origin area in this case. This is indeed confirmed by a scanning electron microscopy analysis of such a corner area (Fig. 17.3a) and by the confocal Raman analysis, as shown in the maps of Fig. 17.3b and c with respect to residual stress in the residual tetragonal phase and to monoclinic transformation fraction measured from the same area of the micrograph in Fig. 17.3a. Raman spectra also revealed that the taper-edge area underwent severe phase transformation with a maximum of about 30% monoclinic volume fraction. The material surface also underwent severe phase transformation due to environmentally assisted friction phenomena, while the overall equilibrium stress on the head surface was compressive in nature (cf. Fig. 17.3c and d for equilibrium stress and phase transformation maps, respectively). The Raman microprobe characterization suggests that, despite the partly transformed material surface was stable under a state of compressive residual stress, fracture may have easily found its propagation path due to stress intensification at internal corner whose untransformed tetragonal regions were highly stressed in tension.

17.4.2 Oxidation, Strain, and Molecular Orientation Patterns in Polyethylene Acetabular Cups

Two retrieved cross-linked UHMWPE acetabular cups were preliminary investigated by Raman microprobe spectroscopy with respect to their oxidation

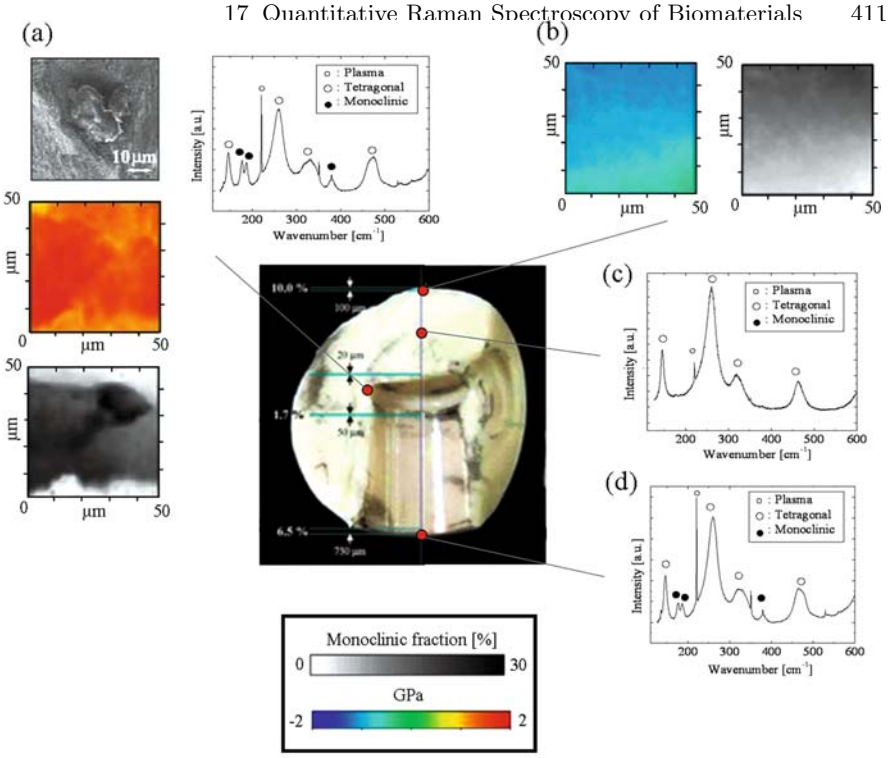

Fig. 17.3. Raman spectroscopy analysis on a zirconia femoral head retrieved after being fractured in the human body. The center photograph represents the largest piece of the fractured head. In **(a)**–**(c)**, a scanning electron micrograph, a stress map in the residual tetragonal phase, and a map of transformed monoclinic fraction are given, respectively, as collected at the fracture origin (cf. upper corner of the conical cavity). Typical Raman spectra are shown at various locations, which quantitatively reveal the monoclinic contents at different locations, as indicated on the photograph. In the spectra, the band labeled "plasma" is intrinsic to the laser and was used as an internal calibration of the Raman instrument. **(d)** and **(e)** An equilibrium stress map and a monoclinic volume fraction map as collected on the bearing surface of the femoral head. In this context, the term equilibrium stress refers to an average stress magnitude weighted by the volume fraction of the two constituent phases [3]

state. Two retrieved acetabular cups, both sterilized by EtO, were obtained at the time of the respective hip arthroplasty revision surgeries. The acetabular components (manufactured by Kyocera Co.) were both employed in female patients in cemented total hip arthroplasty and retrieved due to aseptic loosening. One of the retrieved acetabular cup belonged to a 49-year-old female patient for which the follow-up period was 25 years 3 months. In the remainder of this chapter, this cup will be referred to as "cup A." The other retrieval also belonged to a female patient (52 years old). For this latter cup, the follow-up period was 17 years 9 months. This acetabular cup is referred to as "cup B."

The two retrievals were both from left hip joints, thus showing a main wear zone on the cup surface between the superior and the posterior poles. The non-wear zone of the cups could also be found on the surface portion between the interior and the anterior poles of the cups. Both acetabular cups were employed against CoCr femoral heads of the same type. Figure 17.4 shows maps of near-surface oxidation (in both non-wear and main wear zone) and strain (only in the main wear zone), which were measured as a function of in-depth abscissa for the UHMWPE acetabular cups A and B (in Fig. 17.4a and b, respectively). Data were obtained from shifting the confocal probe along the sub-surface of the material and calculated after deconvolution of the obtained profiles according to in-depth analysis [9, 18]. It should be noted that both the revised implants were used in successful surgeries from the viewpoint of the rather long-term implantation time. From a comparison among the oxidation profiles shown in Fig. 17.4, it is suggested that in this kind of acetabular cup the overall amount of oxidation abruptly increases after exposure times longer than about 18 years. In addition, the maximum of the oxidation index in cup A was observed in the sub-surface profile of the retrieved cup, which represents a puzzling observation for in vivo exposed UHMWPE components. As far as profiles of strain are concerned, interestingly, in the case of EtO-sterilized cups, enhanced features in the strain profile were found on the material surface. On the other hand, γ-ray-sterilized cups were found to follow a different trend. In order to analyze the relationship between oxidation state and creep deformation of UHMWPE acetabular cups, strain and oxidation profiles were retrieved down to a millimeter-size depth by confocal Raman spectroscopy and the results compared among five acetabular cups. Figure 17.5 shows a comparison between creep and oxidation profiles

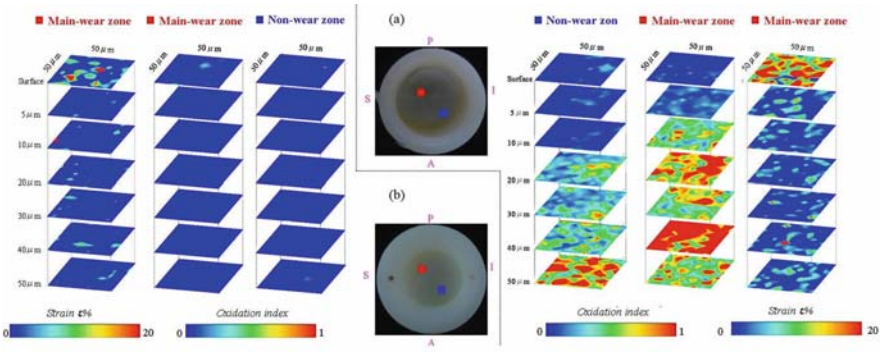

Fig. 17.4. Typical near-surface oxidation maps as measured in the non-wear and main wear zones, and strain maps as measured in the wear zone of UHMWPE-retrieved acetabular cups: (**a**) 25 years and 3 months exposure in vivo and (**b**) 17 years and 9 months exposure in vivo. The linear dimensions of the map and the collection depth of the focal plane in confocal probe configuration are also explicitly shown

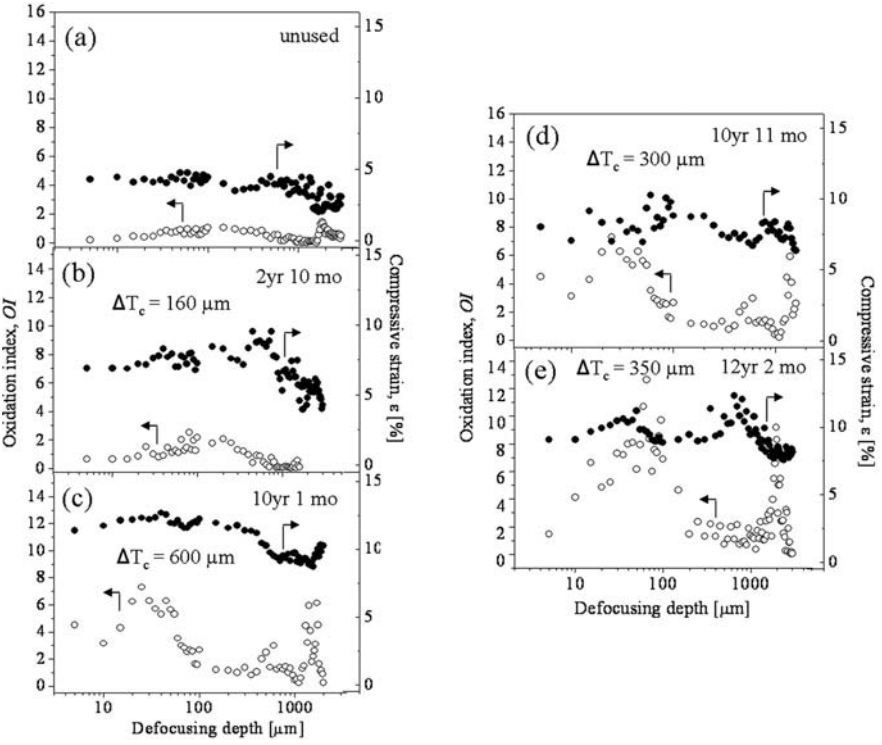

Fig. 17.5. Comparison between oxidation profiles and compressive strain profiles for a series of four retrieved and one unused UHMWPE cups (details in the inset of each plot)

for a series of five retrieved UHMWPE cups whose details are shown in the inset of each plot in the figure. The most relevant outcome of the present experiments is that, in γ-ray-sterilized cups, there is a clear correspondence between oxidation and creep profiles. From a more general viewpoint, the present data show that the confocal Raman spectroscopic approach may enable one to directly measure the creep displacement along the liner thickness, and thus to discriminate, within the loading history of the liner, between the amounts of penetration arising from creep deformation and that due to wear. Using the strain profiles shown in Fig. 17.5, we were able to calculate the respective thickness reductions due to creep deformation, which are shown as linear shrinkages from the initial thickness in inset to each figure. Raman experiments also show that, in γ-ray-sterilized cups, creep deformation is already preponderant in short-term exposed liners, while oxidation in the main wear zone yet experiences a low profile. In other words, although sub-surface maxima of creep strain and oxidation ultimately occur at the same locations in depths, the PE structure creeps first and then oxidizes, and not vice versa.

Additional source of information for UHMWPE acetabular cups arises from the quantitative analysis of polarized Raman spectra. Figure 17.6 shows photographs and the outcome of such analysis for two acetabular cups, which were retrieved after substantially different in vivo lifetimes. The retrieved acetabular cups were both belonging to male patients and sterilized by γ-rays, but produced by different processes. One acetabular component (manufactured in 2002 by Biomet Inc.) was prepared by isostatic compression molding and sterilized before implantation by a dose of 33 kGy of γ-rays. It was retrieved due to infection after 2 years 5 months. This cup will be referred to as the "short-term" retrieval. The other retrieval (manufactured in 1995 by Zimmer Inc.) was prepared by Ram-extruded molding and sterilized in air by a dose of 25–37 kGy of γ-rays. For this latter cup, the follow-up pe-

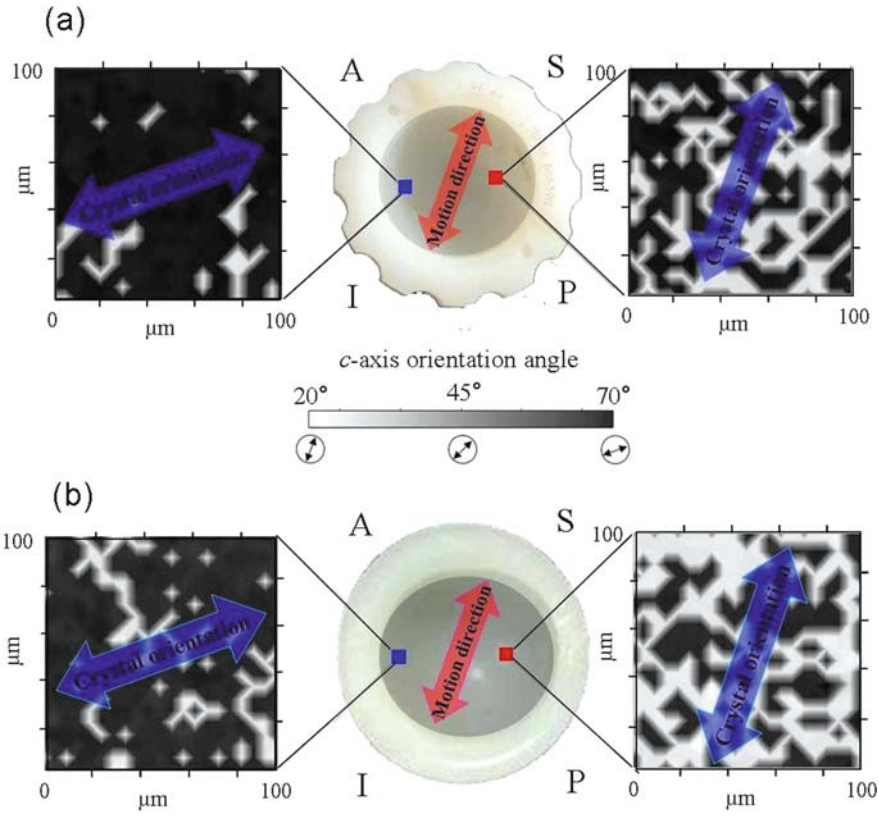

Fig. 17.6. Maps of in-plane crystallographic orientation of the orthorhombic cell in the crystalline part of the polyethylene structure: **(a)** short-term and **(b)** long-term implanted acetabular cups (cf. the central photographs). Compare the average direction of *c*-axis orientation and the motion direction shown on the respective maps and on the photographs of the acetabular cups, respectively

riod was 10 years 4 months, and we shall henceforth refer it as the "long-term" retrieval. The two investigated retrievals were both from left hip joints. Polarized Raman spectra enabled us to visualize the crystallographic orientation of the orthorhombic cell in the crystalline part of the polyethylene structure, as shown in Fig. 17.6a and b for the short-term and long-term implanted acetabular cups, respectively. Orientation maps in both wear and non-wear zones are shown, which clarify how the crystalline *c*-axis in the lamellar structure of polyethylene tends to align itself with the motion direction during sliding of the bearing surfaces (cf. also the average crystal orientation angles in the respective figures). Independent of exposure time in vivo, the degree of crystal orientation was higher in the wear zone compared to the non-wear zone of each acetabular cup; on the other hand, the degree of alignment increased with increasing exposure time in vivo. These results clearly show that the salient features of the reciprocal sliding motion between bearing surfaces of the joint remain recorded in the alignment of the crystalline structure of polyethylene, thus providing a unique tool for analyzing the internal kinetics of hip joints.

17.4.3 Residual Stress Patterns on Retrieved Alumina Load-Bearing Surfaces

Standard tribological studies of ceramic-on-ceramic load-bearing surfaces usually only rely on phenomenological parameters for describing the wear effects. Spectroscopic Raman analyses can be useful to clarify the mechanisms behind the wear behavior of ceramics, which typically occur on the sub-micrometer range. These considerations are particularly relevant to ceramic-on-ceramic bearings, which are recently considered as the main protagonists in the new generation of materials for arthroplastic applications.

In ceramic-made artificial hip joints, distinct wear tracks might be observed on the femoral heads in retrievals, suggesting that different types of activity can be responsible for wear scars. During walking, the upper rim of the socket presses against the anteromedial zone of the femoral head. When rising from a seated position, the maximum contact stress is between the lower rim of the socket on the posterolateral zone of the head, attributable to the action of the gluteus muscles [21]. Walter et al. [22] analyzed a large number of alumina ceramic-on-ceramic retrievals and, among them, reported about a significant fraction of implants with stripe wear. It was noted that all stripes in stable implants were posteriorly inclined with an average tilt of 20° and latitude of 47°. The phenomenon of stripe wear may lead to ball-rim contact and have serious consequences for the ceramic wear performance. The stripe wear, which has been identified to appear as early as 6 months, arises from rim-wear during 90° flexion activities such as rising from a chair. Such early generation of ceramic-on-ceramic femoral heads indeed generally reveals extensive stripe wear on their surface, as indeed do the respective liners on their rim areas. Microscopic analyses of the bearing surface are usually carried out

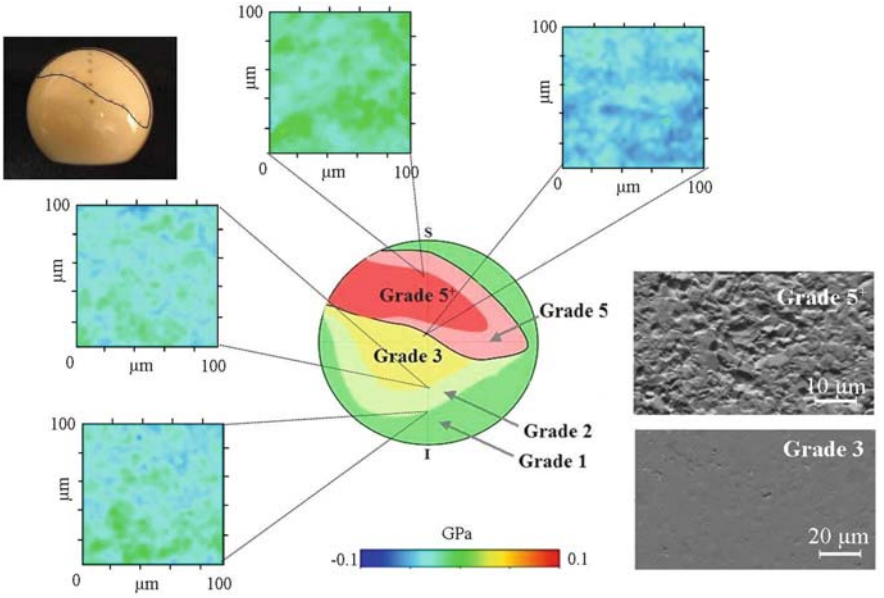

Fig. 17.7. Photograph of an alumina femoral head in **(a)**, on which we have drawn the surface stripe wear zone. In the center of the figure, a schematic draft is given of the different degrees of wear observed on the femoral head surface. Maps of residual stress collected on the sample surface by Raman piezo-spectroscopy are also given for zones affected by different amounts of wear fatigue. In **(b)** and **(c)**, two scanning electron micrographs are shown, which give the surface morphology of the femoral head surface worn to grade 3 and grade 5^+ wear

using scanning electron microscopy, which merely visualize the morphology of the surface. On the other hand, Raman microprobe maps reveal the presence of microscopic residual stresses that remain stored onto the material surface due to severe impingement and microseparation promoted by the bulky implant design. In other words, the micromechanics of wear can be traced back by analyzing hyperspectral residual stress images collected by Raman microprobe spectroscopy on the surface of joint retrievals. Raman analysis was performed in a highly confocal probe configuration on a retrieved alumina femoral head, which was donated from Professor Sedel's series in Paris (Ceraver-Osteal, Roissy CDG, France). Although the confocal configuration was selected in order to single out the residual stress field on the very surface of the material, thus minimizing the influence of the sub-surface, the need to screen large areas necessarily imposed a limitation on the lateral resolution achievable by the Raman probe (i.e., a 20× optical lens was selected). Such a lack in resolution might reflect in the detection of a lower value of the absolute magnitude of residual stress. At revision, the head, which was employed against an alumina liner, has been marked for orientation. The implantation time in vivo was as

long as 19 years. Figure 17.7a shows a photograph of the head, a draft of the wear conditions on its surface is given in the central part of the figure, and the outcome of Raman spectroscopy analyses are reported for selected zones (as shown on the draft), which were affected by different amounts of wear (grade 1 to grade 5^+ for increasing wear damage, according to Manaka et al. [23]). Scanning electron micrographs are shown in Fig. 17.7b and c for zones that underwent grade 5^+ and grade 3 wear damages, respectively. The studied femoral head retrieval revealed one wear stripe on the superoposterior area (cf. grade 5 and grade 5^+ zones in the draft in Fig. 17.7). From a purely morphological point of view, wear patterns of medium-high depth (labeled grade 3 in Fig. 17.7) were found on the main wear region, while high-level damages (labeled up to grade 5^+ in Fig. 17.7) were revealed on the stripe wear (cf. also electron micrographs in Fig. 17.7b). As a general feature, the Raman spectroscopic analysis revealed compressive residual stresses stored on the load-bearing surface, which arose from long-term pressure of the socket against the anteromedial zone of the femoral head. The residual stress intensity increased with increasing the degree of wear; however, in the grade 5^+ zone, namely the most exposed to localized pressure, the residual stress was almost released. The reason for such a stress release resides in the fact that, above a threshold stress level, the grain boundaries fractured and pieces of material detached from the surface, thus releasing the stress. The grain pull-out mechanism was indeed confirmed by scanning electron microscopy, as shown in Fig. 17.7b. In an effort to visualize the microstructural situation and, thus, to estimate the actual stress magnitude at the threshold for grain pull-out, additional stress maps were collected with the highest lateral resolution achievable by the Raman microprobe (i.e., $\approx 1\,\mu m$) in areas of grade 5 wear.

17.5 Conclusion

In conclusion, this chapter has attempted to provide a description of how the fundamental theory of Raman spectroscopy can be fully developed and used to obtain quantitative physical, mechanical, and chemical information on a wide family of biomaterials employed in arthroplasty. Direct methods for quantitatively and non-destructively assessing in-depth residual stress/strain fields, phase transformations, and oxidation states in femoral and acetabular components have been put forward and some peculiar aspects clarified in the in vivo time dependence during the development of such features, with particular emphasis placed on phenomena occurring in vivo on load-bearing surfaces. The possibility to non-destructively and quantitatively measure parameters like stress, strain, phase fractions, and oxidation index from confocal/polarized Raman spectra in biomaterials for arthroplastic applications definitely offers a chance to surgeons to fully understand the actual performance of selected biomaterials, thus rationally addressing their own choice on the most advanced ones. The large body of information retrieved from Raman spectroscopy should also be helpful to material scientists and technologists in

order to promptly put forward advanced guidelines for the development of new materials with improved resistance to fracture, oxidation, and wear.

References

1. P. Taddei, A. Tinti, G. Fini, J. Raman Spectrosc. **32**, 619 (2001)
2. D.W. Hahn, D.L. Wolfarth, N.L. Parks, J. Biomed. Mater. Res. **31**, 355 (1996)
3. G. Pezzotti, Expert Rev. Med. Dev. **4**, 165 (2007)
4. G. Pezzotti, in *Hip Replacement: Approaches, Complications and Effectiveness*, ed. by F. Columbus (Nova Publisher, New York, 2009)
5. G. Pezzotti, Anal. Bioanal. Chem. **381**, 577 (2005)
6. G. Pezzotti, T. Tateiwa, W. Zhu, T. Kumakura, K. Yamada, K. Yamamoto, J. Biomed. Opt. **11**, 024009 (2006)
7. K.S. Wan, W. Zhu, G. Pezzotti, J. Appl. Phys. **98**, 113101 (2005)
8. D.M. Lipkin, D.R. Clarke, J. Appl. Phys. **77**, 1855 (1995)
9. G. Pezzotti, T. Kumakura, K. Yamada, T. Tateiwa, L. Puppulin, W. Zhu, K. Yamamoto, J. Biomed. Opt. **12**, 014011 (2007)
10. W. Zhu, G. Pezzotti, Appl. Spectrosc. **59**, 1042 (2005)
    F. A. Cotton, *Chemical Applications of Group Theory* (Interscience Publishers, New York, 1963)
11. L. Grabner, J. Appl. Phys. **49**, 580 (1978)
12. A. Atkinson, S.C. Jain, J. Raman Spectrosc. **30**, 885 (1999)
13. G. Pezzotti, W.H. Mueller, Continuum Mech. Therm. **14**, 113 (2002)
14. Q. Ma, D.R. Clarke, J. Am. Ceram. Soc. **76**, 1433 (1993)
15. G. Pezzotti, A.A. Porporati, J. Biomed. Opt. **9**, 372 (2004)
16. G. Katagiri, H. Ishida, A. Ishitani, T. Masaki, Adv. Ceram. **24**, 537 (1988)
17. L.S. Bargmann, B.C. Bargmann, J.P. Collier, B.H. Currier, M.B. Mayor, Clin. Orthop. **369**, 49 (1999)
18. H.H. Trieu, R. Avent, Effect of sterilization on shelf-aged UHMWPE tibial inserts, in *Transactions of the 21st Annual Meeting of the Society for Biomaterials*, San Francisco, 1995, p. 109
19. T. Kumakura, K. Yamamoto, L. Puppulin, Y. Takahashi, G. Pezzotti, J. Biomater. Sci. Polym. Ed. **20**(12), 1809 (2009) (in press)
20. I.C. Clarke, M. Manaka, D.D. Green, P. Williams, G. Pezzotti, Y.H. Kim, M. Ries, N. Sugano, L. Sedel, C. Delauney, B. Ben Nissan, T. Donaldson, G.A. Gustafson, J. Bone Joint Surg. Am. **85-A**, 73 (2003)
21. J. Dorlot, Clin. Orthop. Relat. Res. **282**, 47 (1992)
22. W.L. Walter, G.M. Insley, W.K. Walter, M.A. Tuke, J. Arthroplasty **19**, 402 (2004)
23. M. Manaka, I.C. Clarke, K. Yamamoto, T. Shishido, A. Gustafson, A. Imakiire, J. Biomed. Mater. Res. **69B**, 149 (2004)

18

Raman Spectroscopy: A Tool for Tissue Engineering

Gavin Jell, Robin Swain, and Molly M. Stevens

Abstract Raman spectroscopy can potentially offer a non-invasive, information rich biochemical "snap-shot" of living human cells, tissues or material-cell tissue constructs rapidly (seconds-minutes), without the need of labels or contrast enhancers. This chapter details the exciting potential and challenges associated with the use of this analytical technique in tissue engineering (TE). The use of Raman spectroscopy in three intricately linked areas of TE will be considered; (1) the characterisation of the various scaffolds and "smart" materials, (2) the biochemical analysis of cellular behaviour important in TE (e.g. differentiation) and (3) the use of Raman spectroscopy for the analysis of tissue/extra-cellular matrix (ECM) formation in vitro or possibly in vivo.

18.1 Introduction

18.1.1 Introduction to Tissue Engineering

TE involves the complex interplay of materials science and cell biology to develop tissues that restore, maintain or enhance tissue function (Fig. 18.1). Cells are inherently sensitive to physical and chemical stimuli from their surroundings [1]. In vivo, cells are surrounded by a biological matrix comprising tissue-specific combinations of proteins and glycosaminoglycans (plus inorganic crystals in bone) that are collectively referred to as the extracellular matrix (ECM). The hierarchical diversity of tissue arises through combinations of specific spatial molecular interactions between cells and the ECM constituents. The ECM provides not only the physical architecture and mechanical properties of the tissue but also a reservoir of biological signalling agents which provide a cell-specific "niche". This "niche" determines cell phenotype and changes to the local cell environment (e.g. a drop in oxygen pressure due to damaged vasculature, increased chemokine/cytokines concentration and/or varying mechanical stress) results in an altered cell phenotype. This adaptive

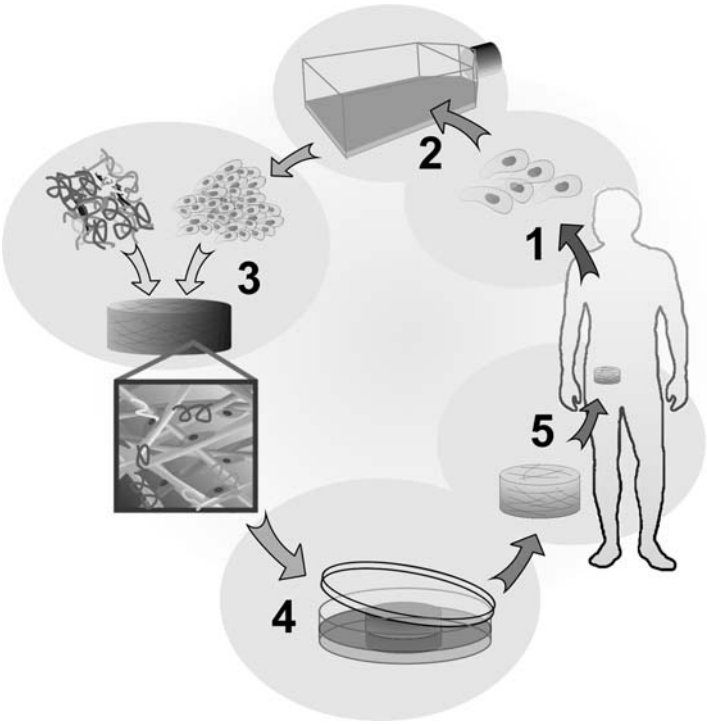

Fig. 18.1. Tissue engineering (TE) involves the complex interplay of materials and cells to develop tissues that restore, maintain or enhance tissue function. Typically cells are (1) removed from the body, (2) expanded and differentiated in culture, (3) seeded onto a biomaterial scaffold (possessing appropriate mechanical properties, surface chemistry and architecture), (4) cultured with suitable growth factors and (5) implantation into the damaged tissue site. Many alternative TE strategies exist, including implanting a suitable scaffold (3) directly into damaged tissue site (5), without pre-seeding, whereby the scaffold will release specific biologically active factors to induce in vivo cell recruitment and tissue regeneration. *Picture courtesy of Julian George, Stevens group, Imperial College* London

response is vital for homeostasis and enables the body to react to different situations, e.g. to grow, heal and regenerate.

Tissue scaffolds and "smart materials" are therefore designed to mimic aspects of the natural healthy in vivo cell environment and/or activate natural healing responses to provide cues that guide cell behaviour and initiate tissue regeneration [2]. Designing materials with specific physicochemical properties and biofunctionality (e.g. micromechanical properties, micro/nanoscale architecture, surface chemistry, topography and spatial arrangement of ligands) enables a degree of control over the type and rate of protein adsorption, the functionality of the adsorbed proteins and subsequently cell attachment and behaviour. Establishing which environmental signals are important in guiding

cell behaviour and whether the novel materials developed are having their desired effect on cell behaviour (and subsequent formation of functional tissue) are, however, complex questions to which Raman spectroscopy may offer some answers.

18.1.2 Advantages of Raman Spectroscopy

Raman spectroscopy can offer a number of advantages over traditional cell or tissue analysis techniques used in the field of TE (Table 18.1). Commonly used analytical techniques in TE include the determination of a specific enzyme activity (e.g. lactate dehydrogenase, alkaline phosphatase), the expression of genes (e.g. real-time reverse transcriptase polymerase chain reaction) or proteins (e.g. immunohistochemistry, immunocytochemistry, flow cytometry) relevant to cell behaviour and tissue formation. These techniques require invasive processing steps (enzyme treatment, chemical fixation and/or the use of colorimetric or fluorescent labels) which consequently render these techniques unsuitable for studying live cell culture systems in vitro. Raman spectroscopy can, however, be performed directly on cells/tissue constructs without labels, contrast agents or other sample preparation techniques.

The Raman spectra of a biological cell (Fig. 18.2 [3]) or tissue construct contain a complex array of peaks which provide molecular-level information about all the cellular and extracellular biopolymers (nucleic acids, proteins, lipids and carbohydrates). Thus the Raman spectrum of a cellular component, single cell or tissue construct, provides a unique biochemical spectral "fingerprint", which provides a "snapshot" of all the biomolecular components of the spectral sample area. Raman imaging also provides information on the spatial distribution of one or more chemical species within a heterogeneous sample. Raman spectroscopy of a cell/TE construct thereby provides a more detailed "global" information bundle than that obtained by traditional cell biological techniques, whereby the expression of individual genes or proteins is studied. However, the very information-rich nature of this biochemical technique leads to extremely complex spectra, which requires careful interpretation and analysis to extract valid and quantitative data [4].

The effect of laser irradiation on cells during Raman spectral analysis is contested and is certainly dependent upon laser wavelength, power and the use of enhancement molecules (e.g. SERS particles) [5]. It is generally accepted, however, that NIR excitation (∼700–1064 mm) is preferred for non-invasive analysis of biological samples, as visible wavelength excitation of live samples is plagued by fluorescence interference, and UV excitation-associated biological damage by photo-degradation.

Fluorescent labelling of protein/RNA or DNA combined with optical or confocal microscopy imaging is a powerful widely used imaging technique that can (like Raman spectroscopy) also be applied to live cells or tissues. This technique, however, is limited by the number of fluorescent molecular

Table 18.1. Analytical techniques commonly used in tissue engineering

Technique		Description	Advantages/disadvantages	Invasive?
Proteomic	Fluorescence microscopy	In situ visualisation of cellular/ECM protein with fluorescence-labelled antibody	Multiplexing capability (typically 3 fluorophores). Extra- and intracellular antigen location on opaque biomaterials. Issues with bleaching and autofluorescence.	Yes/no
	Colorimetric microscopy	As above but using colorimetic chromogens	Limited multiplexing (typically 1–2 chromogens). Permanent staining. Requires transmitted light for high-resolution images	Yes
	ELISA	Quantifiable detection of antibody/antigen from lysed cells, serum or culture media	Inexpensive equipment, relatively quick and very sensitive	Yes
	Western blotting	Sensitive, specific and semi-quantifiable (band intensity)	Unable to localise antigen expression	Yes
	Protein arrays	Detection of a range of proteins from a lysed tissue/cell population	Multiplexing of vast amounts of proteins at once – semi-quantitative	Yes
	Flow cytometry	Allows the quantification of the proportion of cells expressing a certain antigen/s	Multiplexing capability. Cells must be detached from material prior to analysis	Yes
Genomic	Total DNA	Commonly used to determine cell number	No genotype or phenotype information	Yes
	In situ hybridisation	Localizes specific genes within cells with nucleic acid-labelled probes	Sensitivity and specificity dependent upon tissue and probe quality	Yes
	Real-time RT-PCR	Determines expression of a particular gene of interest (mRNA) in a cell population	Simple, sensitive, quick, specific and quantitative. Lysed cells required	Yes
	Gene micro-array	Measures the expression levels of a large numbers of genes simultaneously	Requires large amount of RNA from lysed cells. Vast amount of information obtained	Yes
Electron microscopy		Enables high-resolution imaging of cellular–material interaction	Morphological/ topographical information but subjective interpretation of images	Yes

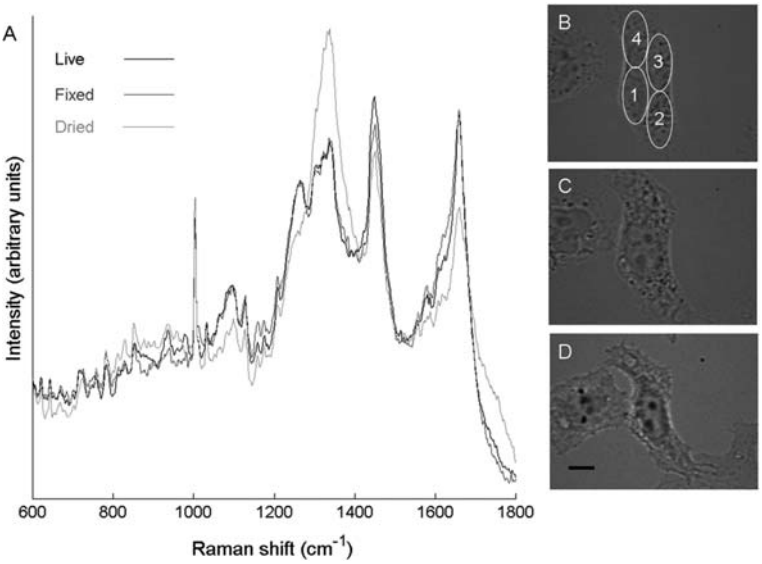

Fig. 18.2. Raman spectroscopy of live, fixed and dried cells. Raman spectrum of a single cell construct provides a unique biochemical "fingerprint", which provides a "snap shot" of the entire biomolecular components. The mean Raman spectra (4 separate measurements) of a single live, fixed and desiccated epithelial cell are compared (**a**). Fixation and desiccation influence cellular biochemistry. Desiccation distorts Raman bands describing all cellular biopolymers, especially proteins. Distinct biochemical changes in the secondary structure of proteins in the fixed cell can also be detected. Similar results were obtained in several other cells when analysed under similar conditions. Light microscope pictures of the cells in live cell culture (**b**), and after fixation (**c**) and desiccation (**d**) are shown. Scalebar = 10 μm. [3]

imaging agents available in the near-infrared (NIR) window, which together with the large spectral overlap between them restricts the number of targets it is possible to investigate simultaneously (multiplexing) [6]. Background autofluorescence emanating from superficial tissue layers or material/tissue scaffold can also restrict the sensitivity and the depth to which fluorescence imaging can be used. Furthermore, labelling a target biomolecule with (often large) fluorescent probes may, both prior to and post-laser excitation, alter the target's molecular properties and thereby cause undesirable effects on cell behaviour [5]. Rapid photobleaching of fluorescent molecules also limits their useful lifetime, thus preventing long-term studies. Moreover, while a vibrational resonance signal is specific to the resonant frequency of the molecular bond, fluorophores are sensitive to their surrounding environment which may affect the fluorescent signal.

FTIR spectroscopy is a class of vibrational spectroscopy similar to Raman spectroscopy which provides molecular-level information based on the absorption of electromagnetic radiation, rather than inelastic scattering in Raman.

FTIR has also been used for cell [7], tissue [8, 9] and biomaterial characterisation [10]. Since FTIR spectroscopy and imaging is also derived from the intrinsic molecular vibrational energy levels of a sample, like Raman spectroscopy, no external markers, dyes or labels are required for sample characterisation. However, the ∼10–20 μm spatial resolution provided by broadband IR beams used in FTIR spectroscopy is significantly inferior to that offered by diffraction-limited confocal Raman microspectroscopy (∼1 μm). Furthermore, while the weak Raman scattering of water enables spectral analysis of hydrated biological samples (thereby allowing live, in situ measurements), the strong absorbance of water throughout the infrared region in FTIR spectroscopy requires either fixation and/or dehydration of samples, or omission of distorted spectral regions, both of which have the potential to induce artefacts (Fig. 18.2). Transmission FTIR measurements also require very thin samples, which necessitates invasive processing (e.g. sectioning) of biological samples. Alternatively, attenuated total reflectance (ATR) FTIR can be used to analyse sample surface properties. This technique, however, requires contact with an ATR crystal, which can physically damage delicate biological samples.

18.1.3 Raman Spectroscopy Applied to Tissue Engineering

The recent boom in bioanalytical applications of Raman spectroscopy has unsurprisingly coincided with technological developments in laser sources, key spectrometer components (e.g. holographic notch filters), charged coupled device detectors and optimisation of collection geometries. These technological advances have somewhat overcome the strong fluorescent interferences from biological samples and the inherently weak magnitude of the Raman effect. Furthermore, the development of enhanced and non-linear Raman techniques, such as resonance Raman scattering (RRS), surface-enhanced Raman scattering (SERS), surface-enhanced resonance Raman spectroscopy (SERRS), coherent anti-Stokes Raman scattering (CARS) and FT-Raman spectroscopy, offers exciting new opportunities in molecular imaging of biological samples by reducing fluorescence and/or increasing the Raman scattering, resolution and sensitivity [6, 11, 12].

In TE, non-resonant spontaneous Raman spectroscopy has, however, some advantages over the enhancement techniques listed above, including the use of relatively inexpensive excitation lasers, instrument compactness, robustness, mobility, lower technical complexity and broadband ability (as all vibrational modes are excited simultaneously). Furthermore, enhanced RRS and SERS techniques require culture on a metal substrate or cellular uptake/membrane attachment of enhancement molecules, which may influence cell behaviour thereby inhibiting the non-invasive nature of spontaneous Raman spectroscopy. Moreover, while CARS produces a directed laser-like signal beam that is many times stronger than spontaneous Raman scattering and avoids fluorescence interference (which occurs exclusively with Stokes signal), a technically complex spectrometer is required and multiplexed chemical spectral resolution is limited. FT-Raman systems with noisy InGaAs detectors,

meanwhile, generally require long data collection times to obtain sufficient signal-to-noise ratios, thereby limiting their suitability in the analysis of live cell culture systems (for further details refer to the following reviews, FT-Raman [13], RRS [14], SERS [15], CARS [16]).

18.2 Material Characterisation

18.2.1 Materials in Tissue Engineering

Numerous materials have been used in TE and a tremendous variety of techniques have been used to modify the surface properties of these materials to promote biocompatibility and induce tissue formation. Material surface properties can be modified by physicochemical modification, topographical surface structuring and biofunctionalisation, to promote specific protein and desirable cellular responses. Cell behaviour, for example, has been known to be influenced by micro- and nanoscale surface topographical features [17] and the geometric/spatial arrangement of chemical moieties [18]. Raman spectroscopic characterisation of biomaterial surfaces is a well-established technique for a variety of TE materials, including bioactive glasses, ceramic materials, carbon fibres/carbon nanotubes, polymers, hydrogels and bioresorbable composites [19–21].

18.2.2 Biofunctionalisation of Materials

Biofunctionalisation of materials is a common strategy in TE to promote selective protein and cell adhesion (in vitro or following implantation in vivo). Specific bioactive molecules such as enzymes, peptides and cell receptor ligands (often ECM elements) are immobilised onto material surfaces and/or integrated within the materials for their controlled exposure. These biomolecules can be simply adsorbed on the material's surface or covalently linked via chemical groups previously created on the surface. The biological response to the material-bound biomolecules depends upon many parameters including their spatial distribution, density, steric hindrance, co-localisation with synergistic ligands and structural conformation to maintain the exposure of cell-binding domains [2]. Raman spectroscopy could offer some much-needed insight in the characterisation of these parameters.

Raman spectroscopy has been successfully used to detect nanomolar concentrations of biologically relevant molecules, to distinguish between structurally similar peptides (e.g. $\alpha V\beta 3$ and $\alpha 5\beta 1$ integrins [22]) and also to detect peptide S-nitrosylation and phosphorylation [23, 24]. Raman spectroscopy has been used to determine the functionalisation of carbon nanotubes and other particles with bioactive peptides (e.g. RGD), whereby their biofunctionalisation has enabled their accumulation at specific sites (e.g. tumours) within small animal models [25]. Furthermore, the in vivo distribution and

excretion/clearance of these biofunctionalised particles could be assessed non-invasively using Raman spectroscopy [26]. However, despite the potential of Raman spectroscopy to detect the presence, density and conformation of biomolecules on biomaterial surfaces, the use of Raman spectroscopy to determine tissue scaffold biofunctionalisation is currently limited. Caution should also be extended when determining peptide structure with SERS particles, as protein–particle interactions and laser irradiation may cause structural changes to proteins.

18.2.3 Apatite Formation on Materials

For bone TE applications, a variety of materials which promote spontaneous in situ apatite formation have been developed (a hydroxylated carbonated calcium phosphate mineral which forms the inorganic component of bone). These materials promote apatite formation through the controlled release of specific ions (e.g. calcium and phosphate) and by supplying crystallisation nucleation sites. Typically apatite formation on the materials is characterised by a variety of techniques, including vibrational spectroscopy. Raman spectroscopy permits the real-time determination of apatite formation, the spatial distribution of the apatite formation on the material (e.g. to compare scaffold features, such as pores, with apatite-forming ability) and apatite characterisation. The amount of hydroxycarbonated apatite (HCA) on a sample surface can be estimated using the relative area and/or peak height of the strong P–O symmetric stretch peak at 960 cm^{-1}. The phosphate ν_1 symmetric stretch band is a prominent marker of mineral content, describing both the degree of mineralisation and crystallinity of the mineral species. The additional phosphate and carbonate modes are indicators of change in mineral composition and microenvironment (e.g. carbonate substitution within the apatitic lattice has previously been used as an indicator of bone maturity). A detailed literature review on the application of vibrational spectroscopy to study mineralised tissues and comparison to native bone tissue has been reported [27] (refer to chapter 14).

18.2.4 Scaffold Degradation

Another important issue in TE, for which Raman spectroscopy has proved a useful analytical tool, is to understand the degradation kinetics of tissue scaffolds and the impact of these degradation products on cell behaviour. Raman spectroscopy has been used to monitor the dynamic in vitro and in vivo remodelling of degradable silk fibroin-based biomaterials [28] and biodegradable polymers in histological sections [29]. Moreover, van Apeldoorn et al. (2004) used confocal Raman microscopy to obtain chemical information about polymer and hydrogel microsphere degradation inside macrophages [30]. Confocal Raman microscopy revealed the degradation rate of these microspheres within macrophages and that prolonged internalisation of both types of microspheres caused macrophage conversion to lipid-laden foam cells (an inflammatory response) [30].

18.3 Determination of Cell Behaviour

18.3.1 Raman Spectroscopy Applied to Cell Biology

Raman spectroscopy of cells is of rapidly growing importance in biological science and becoming an important tool in TE. Raman spectroscopy can further our understanding of primary cellular process vital for developing functional tissue constructs, such as differentiation and maintenance of cell phenotype, in addition to non-invasively monitoring the cellular response to tissue scaffolds. Raman spectroscopy has been successfully demonstrated to be capable of characterising cellular events important in TE, such as cell death [31], toxicity [32, 33], proliferation [34], cell cycle [35, 36], differentiation [12, 37–39], mineralisation [40], ECM production [41] and phagocytosis [30]. Furthermore Raman spectroscopy has been shown to be able to distinguish between cells grown on substrates coated with different ECM proteins [7] and between cancerous and non-cancerous phenotypes [42, 43]. Raman spectral monitoring of cellular responses to scaffold materials is an extremely promising step towards development of functional TE constructs. While Raman spectroscopy provides a biochemical "global snapshot" of the biomolecular composition, verification of results with established cell analysis techniques is vital to understand how these spectral changes relate to cell genotype and phenotype.

18.3.2 Cell Cycle

Raman spectroscopy has been shown to be capable of distinguishing between live exponentially growing and (contact inhibited) confluent cells [31], cell suspensions [34], high-resolution fixed cells at different stages of mitosis [35] and in single live cells chemically inhibited at various stages of the cell cycle [36]. An undoubtedly important application of monitoring cell cycle dynamics is in cancer research, where identifying and understanding uncontrolled cell growth is of paramount importance. Monitoring changes in cell cycle is also important in TE research. Non-invasively monitoring changes in cell cycle dynamics induced by tissue scaffold/biomaterial interactions may indicate material biocompatibility, cellular proliferation and to some degree differentiation status [38].

18.3.3 Cell Differentiation

In the last decade stem cell research has justifiably gained one of the highest scientific profiles both within the medical community and the general public. The ability of stem cells to undergo both self-renewal and differentiation into more functionally specialised mature cells offers tremendous promise in TE. The isolation, expansion and directed differentiation of human stem cells in vitro, however, demand improved understanding of the interplay between the

cell and its surrounding microenvironment. Cell "stemness" is currently determined by the expression of specific surface markers (e.g. CD34 for haematopoietic stem cells). While identification of surface markers is of undoubted benefit, Raman spectroscopy can offer a more global perspective. Raman spectroscopy could be used to identify spectral biochemical signatures of "stemness" (i.e. cell plasticity) and thereby offer both a rapid non-invasive screening method of cell "stemness" and help understand fundamental biochemical changes occurring during differentiation and cultivation.

The differentiation of mouse embryonic stem cells in culture has been characterised using spontaneous Raman spectroscopy [37] and more recently CARS spectroscopy [12]. In these studies, Raman bands assigned to DNA and RNA backbone vibrations 788 and 811 cm^{-1} (as well as several protein bands) were identified as spectral markers of mESC differentiation. Furthermore, a study by our group employing spontaneous Raman spectroscopy demonstrated that the dissolution products of a commercially available biomaterial (45S5 Bioglass® (BG)) accelerated the differentiation of foetal osteoblasts (FOBs) (Fig. 18.3) [38]. The identification of unique biochemical Raman spectral signatures of cells during important cellular events, such as differentiation,

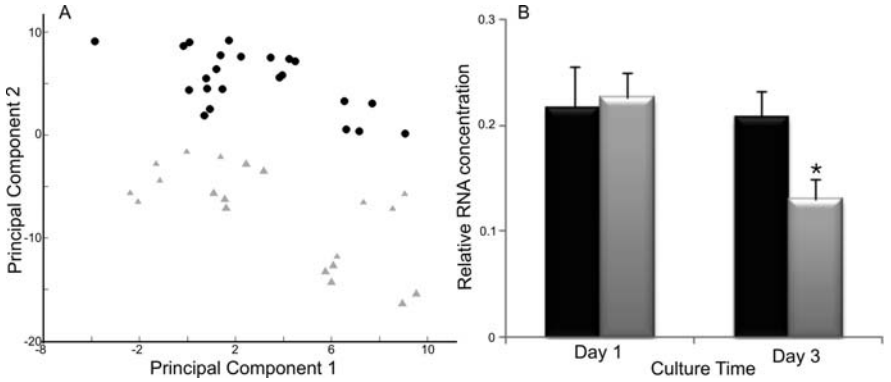

Fig. 18.3. Raman spectral analysis of foetal osteoblast (FOB) differentiation. Unsupervised PCA of FOB cells cultured for 3 days in bioactive glass (BG) conditioned media (*triangle*) or control media (*circle*) (**a**). BG-treated cells formed a distinct cluster separate from control cells after 3 days culture. Least square (LS) analysis (which decomposes the cell spectra into the linear combination of Raman spectra obtained from the pure chemical constituents of the cell, e.g. nucleic acid, proteins, lipids, phospholipids and carbohydrates) of the relative RNA concentration of FOBs cultured for 1, 3 and 14 days in culture media (*black*) or BG condition media (*grey*), revealed a significantly reduced relative RNA concentration in FOBs culture in BG-conditioned media (**b**). FOBs cultured in BG-conditioned media appeared to accelerate FOB differentiation into mature adult osteoblast phenotypes (parallel gene and protein expression experiments confirmed this). *Significant difference to control ($p < 0.05$) [38]

has the potential to offer rapid "live" screening of cellular interactions with novel biomaterials.

Raman spectroscopy has also been recently used by our group to detect the spontaneous differentiation of live primary lung cells [39]. The unique pulmonary alveoli environment is established and maintained by two highly specialised epithelial cell types, alveolar type I (ATI) and type II (ATII) cells. Primary alveoli type II cells spontaneously lose their distinctive phenotype and express phenotypic features characteristic of ATI cells when cultured in vitro. Considerable lung regenerative medicine research is thereby focused on methods of maintaining or inducing ATII phenotype. Raman spectra from undifferentiated ATII cells contained strong phospholipid vibrations, arising from alveolar surfactant stored within cytoplasmic lamellar bodies. Differentiated ATI-like cells, however, yielded Raman spectra with significantly less lipid content. Factor analysis revealed a phospholipid-dominated spectral component as the main discriminator between the ATII and ATI-like phenotypes, while spectral modelling of the data revealed a significant decrease in the spectral contribution of cellular lipids (phosphatidyl choline). These observations were consistent with the clearance of surfactant from lamellar bodies as ATII cells differentiate [39].

18.4 Tissue Formation and Characterisation

18.4.1 Scope of Raman Spectroscopy in Tissue Engineering

Numerous tissues have been analysed with Raman spectroscopy, including skin [44, 45], brain [46], lung [47, 48], spleen [49], spinal tissue [50], cartilage

Table 18.2. Applications of Raman spectroscopy in tissue engineering

TE field	Application examples	References
Material	Hydrogel degradation	[21]
	Apatite formation	[27]
	Bioactive glass structure	[20]
Cell behaviour	Viability	[31]
	Cell cycle	[35, 36]
	Differentiation	[12, 37, 38]
	Phagocytosis	[30]
Tissue characterisation	Bone	[27, 52, 53]
	Cartilage	[51]
	Skin	[44, 45]
	Brain	[46]
	Spleen	[49]
	Lung	[47, 48]

[51] and bone [27, 52, 53] (Table 18.2). The majority of these studies have, to date, been designed to detect biochemical signatures of abnormality (in cell behaviour and/or ECM constituents) for cancer or other disease diagnostic purposes (e.g. osteogenesis imperfecta or osteoporosis). The use of Raman spectroscopy for (non-invasive) disease diagnosis and understanding the biochemical consequence of disease is undeniably important (either at the site of the suspected disease, biopsy or at distal sites such as finger nails, hair or saliva which may show biochemical markers of "deep-tissue" disease [54]) and is discussed in Chap. 13. Raman spectroscopy can also, however, reveal biomolecular insights into how tissues develop, respond to injury and regenerate. Furthering our understanding of these fundamental processes is crucial for the development of successful tissue-engineered constructs. Indeed Chaps. 14 and 15 detail the analysis of skin, bone and cartilage tissue by Raman spectroscopy and this knowledge will invariably assist in the development of successful TE constructs for these tissues.

Raman spectroscopy can also directly benefit TE analysis by non-invasively monitoring the growth and development of ECM by different cells on a multitude of scaffold materials exposed to various stimuli (e.g. growth factors, mechanical forces and/or oxygen pressures). Indeed the non-invasive nature of Raman spectroscopy enables the determination of the rate of ECM formation and the biochemical constituents of the ECM formed. Univariate (peak area, peak ratios, etc.) and multivariate analytical techniques (e.g. principal component analysis (PCA)) can be used to determine if there are any significant differences between the ECM formed on various scaffolds and/or cultured with different environmental parameters, and what these biochemical differences are. Least square (LS) modelling, for example, could allow the quantification of the relative components of the ECM formed (Fig. 18.3) [4, 38].

Determining how similar artificially engineered tissue is to native tissue is a vitally important step in generating successful TE constructs. Raman spectroscopy may be a particularly powerful comparison tool by providing a complete biochemical "snapshot" of tissue composition. The information-rich nature of the Raman spectra thereby offers distinct advantages over the expression of single or multiple genes or proteins (techniques commonly used to investigate the composition of TE constructs). For example, in cartilage engineering the identification of collagen type(s) (by immunochemical techniques) is typically performed to validate correct ECM/tissue formation. However, the heterogeneity observed between different cartilagenous tissues (hyaline, elastic and fibrocartilage cartilage) and the structural/architectural organisation within cartilage at a specific site is due to concentration-dependent combinations of numerous proteins. This hierarchical organisation would not be revealed by techniques with limited multiplexing capability. Furthermore the expression of one tissue-specific protein (e.g. collagen type II) does not preclude the expression of non-tissue-specific proteins, which may be of particular importance in TE constructs derived from stem

cells. Raman spectroscopy therefore offers tissue engineers a highly sensitive tool for the spatial and temporal comparison of engineered tissue to native tissue [9].

Raman spectral mapping of TE constructs, may also, when combined with optical imaging techniques (e.g. scanning electron microscopy (SEM)) [55] reveal if the heterogeneity or homogeneity of ECM formed is associated with particular scaffold features. Furthermore, Raman spectroscopic monitoring of the variation between tissue constructs (developed using the same TE manufacturing processes) may be important for obtaining the necessary regulatory approval for clinical studies. Similarly, non-invasive Raman spectral analysis could potentially be used to "batch test" or "screen" TE constructs prior to implantation, to both validate the correct ECM formation and detect rogue spectral signatures, such as undifferentiated stem cells (which could lead to tumour formation).

18.4.2 Current Examples of Raman Spectroscopy as a Tool for Tissue Engineering

Raman spectroscopy can be used for live, in situ, temporal studies on the development of bone-like mineral (bone nodules) in vitro in response to a variety of biomaterials/scaffolds, growth factors, hormones, environmental conditions (e.g. oxygen pressure, substrate stiffness) and from a variety of cell sources (e.g. stem cells, FOBs or adult osteoblasts). Furthermore, Raman spectroscopy enables a detailed biochemical comparison between the TE bone-like nodules formed and native bone tissue. Bone formation by osteoblasts (OB) is a dynamic process, involving the differentiation of progenitor cells, ECM production, mineralisation and subsequent tissue remodelling.

Considerable spectral similarities between the Raman spectra of TE bone nodules and native bone nodules exist ($R = 0.99$ for mean spectrum of MOBs compared to mean bone spectrum), including prominent mineral vibrations and matrix peaks characteristic of collagenous proteins (Fig. 18.4). However, despite these similar biomolecular signatures, univariate and multivariate spectral analyses revealed distinct biochemical differences in both the mineral and matrix environments. Biochemical differences between TE bone and native bone may be of particular importance as small changes in the mineral environment in humans have been linked to diseases such as osteoporosis [56]. Spectral mapping of the developing bone nodules also enables spatial imaging of biochemicals (e.g. PO_4^{3-}) and/or biochemical ratios (e.g. mineral (PO_4^{3-}) to matrix (amide I)) in bone nodules (Fig. 18.4 [57]). Spectral mapping thereby allows insights into bone nodule structure during development and can reveal biochemical heterogeneities (Fig. 18.4).

The direct accessibility of the skin, the critical clinical need for effective skin regeneration technologies and the huge commercial interest in cosmetic skin products has stimulated a number of skin-based Raman spectroscopic

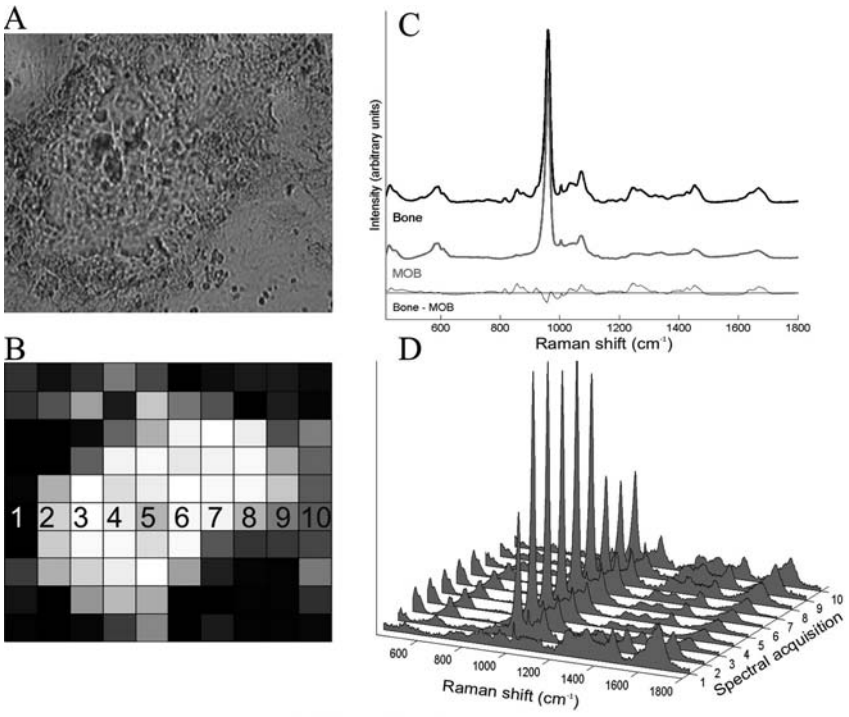

Fig. 18.4. Raman spectral imaging of a tissue-engineered bone nodule. **(a)** An optical image and (**b)** greyscale spectral map of a mineralised bone-like nodule formed in vitro (after 28 days culture) by MOBs a mouse osteoblast (MOB). (**c)** The mean native mouse bone spectra compared to the mean spectra from a mineralised bone nodule, the spectral difference is also shown (note the increase in the spectral regions associated with protein/matrix in native bone). The greyscale map (**b)** describes the mineral:matrix ratio at different positions within each nodule (normalised to the maximum mineral:matrix ratio obtained for the combined set of spectra). The spectra obtained in a cross section of the bone nodule (1–10 (**d**)) [3]

studies (see Chap. 15) [44, 45]. A number of engineered skin models are therefore being created to both replace/regenerate damaged skin and to test various pharmaceuticals or cosmetic products. A recent study compared a commercially available tissue-engineered epidermis (Episkin®) to native tissue and associated molecular and structural differences between the two [45]. Furthermore the authors demonstrated the feasibility of using Raman spectroscopy to track the absorption of unlabelled drug absorption (metronidazole in the organic solvent transcutol) into the reconstructed skin model. TE constructs that capture both the hierarchical organisation and multicellular complexity of the target tissues, such as skin, could thereby provide powerful tools for screening the effects of pharmaceuticals.

18.5 Challenges and Limitations

18.5.1 Sample Imaging, Spectral Acquisition Time and Laser Damage

Many 3D scaffolds used for TE are light impenetrable, thereby making the selection of (suitable) sample sites, laser focussing and the interpretation of scaffold features with spectral signatures somewhat problematic. SEM combined with Raman offers a high-resolution solution to this problem but requires fixed or frozen samples. In terms of Raman spectroscopic analysis of live cell culture systems, a trade-off between spectral acquisition time and spectral resolution occurs. This is a particularly pertinent issue for live cell or tissue spectral analysis, where without an adequate sterile environmental chamber (37°C, 5% CO_2) cells will respond to the environmental changes which will cause phenotypic changes (e.g. cold shock) and artificial spectral signatures. Furthermore, depending upon laser wavelength and power, increasing spectral acquisition time will eventually cause laser damage to the biological system.

18.5.2 Scaffold Substrate

A further issue for Raman spectroscopy in TE is substrate/scaffold spectral interference, whereby the Raman signal from the scaffold (e.g. polymer) overwhelms the much weaker Raman scattering from cellular and/or ECM biopolymers. For this reason most Raman cell studies use substrates (e.g. CaF_2, MgF_2 and fused silica) which have low Raman signals in the biochemical spectral regions of interest. Where multiple cell and protein layers exist, substrate interference is somewhat diminished depending upon laser spot size, substrate, depth of biopolymer layer and Raman set-up. Certainly a reduced laser spot size, a confocal Raman spectroscopy set-up and spatially offset Raman spectroscopy (SORS), allow both depth profiling and reduced substrate spectral interference [44]. Reduced laser spot sizes will, however, invariably increase spectral acquisition time, which may again cause issues for live construct/cell analysis.

18.5.3 Total Tissue Construct or Surface Characterisation

Raman spectroscopic imaging of tissue-engineered constructs (using standard instrument set-ups) is largely restricted to surface or near-surface biochemical imaging. For example, for live cell or engineered tissue analysis our group (and others) use a spontaneous Raman system with a 785 nm, 100 mW excitation laser whereby the depth of imaging is approximately 40 µm. While Raman spectroscopic surface characterisation remains a valuable technique in the field

of TE (e.g. for biomaterial characterisation, determining cell behaviour and real-time analysis of ECM formation), understanding the processes occurring beneath the construct surface would greatly enhance our ability to understand the development of the 3D hierarchical constructs and consequently design new scaffolds. For example, is the ECM uniformly formed throughout the construct or do gaseous and/or nutrient diffusion effects cause biochemical changes in ECM formed?

These questions are particularly imperative with the creation of more sophisticated scaffolds which may (in a similar manner to native tissue) comprise various levels of biofunctionalisation, degradation rates and mechanical properties within the same scaffold. Furthermore, deep-tissue biochemical Raman spectral imaging of TE constructs in vivo would enable insights into implant integration, tissue regeneration and/or reasons for failure. Currently the ability for Raman spectral imaging of whole TE constructs or deep-tissue in vivo spectral analysis is restricted due to the inherently weak magnitude of the Raman scattering and by the limited NIR light penetration of tissues.

Increased tissue penetration could be achieved with confocal Raman setups, SORS and by increasing the magnitude of the Raman scattering with RRS or SERS. Indeed SERS-active nanoparticles were recently used for deep-tissue biomolecular Raman imaging in small living animals [25], whereby their biofunctionalisation enabled their accumulation and imaging at specific sites within the live animal model. Similar techniques could be applied for 3D Raman spectral imaging of TE constructs in vitro or to monitor scaffold degradation in vivo. The Raman enhancement effects are, however, limited to a very short distance from the enhancement particle and the spectra obtained are thereby dominated by the peptide used for biofunctionalisation, and little biochemical information can be obtained from the targeted cell or tissues. Furthermore, the cellular response to attached or internalised Raman enhancement particles (before or following laser excitation) may induce cellular behavioural changes, thereby thwarting the non-invasive advantage of this technique.

18.6 Conclusions

Raman spectroscopy currently offers considerable promise as a tool for the development of viable tissue-engineered constructs. The identification of unique biochemical Raman spectral signatures of cells during important cellular events (e.g. differentiation) and during ECM formation has the potential to offer rapid "live" screening of cellular interactions with novel biomaterials. Future technological developments, combined with greater understanding and interpretation of the complex biological spectra (which will be achieved through increased inter-disciplinary interaction) would further enhance the scope, application and use of Raman spectroscopy in TE.

Acknowledgements

The authors would like to thank the Rothermere Foundation and the Leverhulme Trust for their financial support.

References

1. M.M. Stevens, J.H. George, Science **310**, 1135 (2005)
2. H. Shin, S. Jo, A.G. Mikos, Biomaterials **24**, 4353 (2003)
3. R.J. Swain, Non-invasive biochemical analysis of cells, tissues and tissue constructs with Raman spectroscopy. PhD Thesis, Imperial College, London, 2008
4. I. Notingher, G. Jell, P.L. Notingher, I. Bisson, O. Tsigkou, J.M. Polak, M.M. Stevens, L.L. Hench, J. Mol. Struct. **744–747**, 179 (2005)
5. J.W. Dobrucki, D. Feret, A. Noatynska, Biophys. J. **93**, 1778 (2007)
6. K. Faulds, R.P. Barbagallo, J.T. Keer, W.E. Smith, D. Graham, Analyst **129**, 567 (2004)
7. A.D. Meade, F.M. Lyng, P. Knief, H.J. Byrne, Anal. Bioanal. Chem. **387**, 1717 (2007)
8. C. Krafft, D. Codrich, G. Pelizzo, V. Sergo, Analyst **133**, 361 (2008)
9. A. Boskey, C.N. Pleshko, Biomaterials **28**, 2465 (2007)
10. C. Delogne, P.V. Lawford, S.M. Habesch, V.A. Carolan, J. Microsc. **228**, 62 (2007)
11. H.J. van Manen, Y.M. Kraan, D. Roos, C. Otto, J. Phys. Chem. B **108**, 18762 (2004)
12. S.O. Konorov, C.H. Glover, J.M. Piret, J. Bryan, H.G. Schulze, M.W. Blades, R.F. Turner, Anal. Chem. **79**, 7221 (2007)
13. D. Naumann, in *Infrared and Raman Spectroscopy of Biological Materials*, ed. by H.-U. Gremlich, B. Yan (Marcel Dekker, New York, 2001), p. 323
14. P.R. Carey, Q. Rev. Biophys. **11**, 309 (1978)
15. A.G. Ryder, Curr. Opin. Chem. Biol. **9**, 489 (2005)
16. L.G. Rodriguez, S.J. Lockett, G.R. Holtom, Cytometry A **69**, 779 (2006)
17. A.S. Curtis, M. Varde, J. Natl. Cancer Inst. **33**, 15 (1964)
18. M.J. Dalby, N. Gadegaard, R. Tare, A. Andar, M.O. Riehle, P. Herzyk, C.D. Wilkinson, R.O. Oreffo, Nat. Mater. **6**, 997 (2007)
19. A. Bertoluzza, C. Fagnano, P. Monti, R. Simoni, A. Tinti, M.R. Tosi, R. Caramazza, Clin. Mater. **9**, 49 (1992)
20. J.J. Blaker, J.E. Gough, V. Maquet, I. Notingher, A.R. Boccaccini, J. Biomed. Mater. Res. A **67**, 1401 (2003)
21. T. Van Sr., A. Mens, C.F. van Nostrum, W.E. Hennink, Biomacromolecules **9**, 158 (2008)
22. M.H. Chowdhury, V.A. Gant, A. Trache, A. Baldwin, G.A. Meininger, G.L. Cote, J. Biomed. Opt. **11**, 024004 (2006)
23. R.M. Jarvis, E.W. Blanch, A.P. Golovanov, J. Screen, R. Goodacre, Analyst **132**, 1053 (2007)
24. G.M. Walsh, D. Leane, N. Moran, T.E. Keyes, R.J. Forster, D. Kenny, S. O'Neill, Biochemistry **46**, 6429 (2007)
25. S. Keren, C. Zavaleta, Z. Cheng, Z.A. de la, O. Gheysens, S.S. Gambhir, Proc. Natl. Acad. Sci. U S A **105**, 5844 (2008)

26. Z. Liu, C. Davis, W. Cai, L. He, X. Chen, H. Dai, Proc. Natl. Acad. Sci. U S A **105**, 1410 (2008)
27. A. Carden, M.D. Morris, J. Biomed. Opt. **5**, 259 (2000)
28. W.L. Rice, S. Firdous, S. Gupta, M. Hunter, C.W. Foo, Y. Wang, H.J. Kim, D.L. Kaplan, I. Georgakoudi, Biomaterials **29**, 2015 (2008)
29. S.T. Nandagawali, J.S. Yerramshetty, O. Akkus, J. Biomed. Mater. Res. A **82**, 611 (2007)
30. A.A. van Apeldoorn, H.J. van Manen, J.M. Bezemer, J.D. de Bruijn, C.A. van Blitterswijk, C. Otto, J. Am. Chem. Soc. **126**, 13226 (2004)
31. I. Notingher, S. Verrier, S. Haque, J.M. Polak, L.L. Hench, Biopolymers **72**, 230 (2003)
32. I. Notingher, C. Green, C. Dyer, E. Perkins, N. Hopkins, C. Lindsay, L.L. Hench, J. R. Soc. Interface **1**, 79 (2004)
33. C.A. Owen, J. Selvakumaran, I. Notingher, G. Jell, L.L. Hench, M.M. Stevens, J. Cell Biochem. **99**, 178 (2006)
34. K.W. Short, S. Carpenter, J.P. Freyer, J.R. Mourant, Biophys. J. **88**, 4274 (2005)
35. C. Matthäus, S. Boydston-White, M. Miljkovic, M. Romeo, M. Diem, Appl. Spectrosc. **60**, 1 (2006)
36. R.J. Swain, G. Jell, M.M. Stevens, J. Cell Biochem. **104**, 1427 (2008)
37. I. Notingher, I. Bisson, A.E. Bishop, W.L. Randle, J.M. Polak, L.L. Hench, Anal. Chem. **76**, 3185 (2004)
38. G. Jell, I. Notingher, O. Tsigkou, P. Notingher, J.M. Polak, L.L. Hench, M.M. Stevens, J. Biomed. Mater. Res. A **86**, 31 (2008)
39. R.J. Swain, S.J. Kemp, P. Goldstraw, T.D. Tetley, M.M. Stevens, Biophys. J. **95**, 5978–5987 (2008)
40. J.E. Gough, I. Notingher, L.L. Hench, J. Biomed. Mater. Res. A **68**, 640 (2004)
41. J.R. Jones, A. Vats, I. Notingher, J.E. Gough, N.S. Tolley, J.M. Polak, L.L. Hench, Key Eng. Mater. **623** 284–286, (2005)
42. I. Notingher, G. Jell, U. Lohbauer, V. Salih, L.L. Hench, J. Cell Biochem. **92**, 1180 (2004)
43. P. Crow, B. Barrass, C. Kendall, M. Hart-Prieto, M. Wright, R. Persad, N. Stone, Br. J. Cancer **92**, 2166 (2005)
44. P.J. Caspers, G.W. Lucassen, G.J. Puppels, Biophys. J. **85**, 572 (2003)
45. A. Tfayli, O. Piot, F. Draux, F. Pitre, M. Manfait, Biopolymers **87**, 261 (2007)
46. C. Krafft, S.B. Sobottka, G. Schackert, R. Salzer, Analyst **130**, 1070 (2005)
47. S. Koljenovic, T.C. Bakker Schut, J.P. van Meerbeeck, A.P. Maat, S.A. Burgers, P.E. Zondervan, J.M. Kros, G.J. Puppels, J. Biomed. Opt. **9**, 1187 (2004)
48. M.A. Short, S. Lam, A. McWilliams, J. Zhao, H. Lui, H. Zeng, Opt. Lett. **33**, 711 (2008)
49. C. Krafft, R. Salzer, G. Soff, M. Meyer-Hermann, Cytometry A **64**, 53 (2005)
50. H. Wang, Y. Fu, P. Zickmund, R. Shi, J.X. Cheng, Biophys. J. **89**, 581 (2005)
51. M. Heger, S. Mordon, G. Leroy, L. Fleurisse, C. Creusy, J. Biomed. Opt. **11**, 024003 (2006)
52. E.R. Draper, M.D. Morris, N.P. Camacho, P. Matousek, M. Towrie, A.W. Parker, A.E. Goodship, J. Bone Miner. Res. **20**, 1968 (2005)
53. M.V. Schulmerich, J.H. Cole, K.A. Dooley, M.D. Morris, J.M. Kreider, S.A. Goldstein, S. Srinivasan, B.W. Pogue, J. Biomed. Opt. **13**, 020506 (2008)

54. M.R. Towler, A. Wren, N. Rushe, J. Saunders, N.M. Cummins, P.M. Jakeman, J. Mater. Sci. Mater. Med. **18**, 759 (2007)
55. A.A. van Apeldoorn, Y. Aksenov, M. Stigter, I. Hofland, J.D. de Bruijn, H.K. Koerten, C. Otto, J. Greve, C.A. van Blitterswijk, J. R. Soc. Interface. **2**, 39 (2005)
56. B.R. McCreadie, M.D. Morris, T.C. Chen, R.D. Sudhaker, W.F. Finney, E.Widjaja, S.A. Goldstein, Bone **39**, 1190 (2006)
57. E. Gentleman, R.J. Swain, N.D. Evans, S. Boonrungsiman S, G. Jell, M.D. Ball, T.A. Shean, M.L. Oyen, A. Porter, M.M. Stevens, Nat. Mater. **8**(9), 763 (2009).

19

Applications of Raman Spectroscopy to Virology and Microbial Analysis

Michaela Harz, Stephan Stöckel, Valerian Ciobotă, Dana Cialla, Petra Rösch, and Jürgen Popp

Abstract This chapter reports from the utilization of Raman spectroscopic techniques like Raman microscopy, Raman optical activity (ROA), UV-resonance Raman (UVRR)-spectroscopy, surface enhanced Raman spectroscopy (SERS), and tip-enhanced Raman spectroscopy (TERS) for the investigation of viruses and microorganisms, especially bacteria and yeasts for medical and pharmaceutical applications. The application of these Raman techniques allows for the analysis of chemical components of cells and subcellular regions, as well as the monitoring of chemical differences occurring as a result of the growth of microorganisms. In addition, the interaction of microorganisms with active pharmaceutical agents can be investigated. In combination with chemometric methods Raman spectroscopy can also be applied to identify microorganisms both in micro colonies and even on single cells.

19.1 Introduction

The prevention of the occurrences and the real-time diagnosis of diseases, and the enabling of a sensible treatment without side-effects is the aim of biomedical diagnosis and therapy. In the last years several vibrational spectroscopic techniques, in particular IR absorption spectroscopy and Raman spectroscopy, have led to major breakthroughs in biological, pharmaceutical, and clinical research [1–3].

Especially Raman spectroscopy is a promising clinical tool for the real-time diagnosis of diseases and in situ or in vivo evaluation of living healthy and cancerous tissue, cells and their subcellular compounds and structures, as well as to track the mode of action of drugs on a molecular level. This allows for the derivation of dysfunctions and an *online* monitoring of etiopathologies since Raman spectroscopy provides detailed non-destructive information on the structures and dynamic processes of molecules and intra- and intermolecular interactions [4, 5]. Due to its high sensitivity and selectivity Raman spectroscopy requires only a small sample volume and minimal preparation efforts. A further advantage of Raman investigations of biological systems is the possibility, unlike IR absorption spectroscopy, to study aqueous samples.

Since water as a solvent or environmental matrix offers only negligible Raman signals it does not interfere with signals of biomolecules such as DNA/RNA, proteins, lipids, and/or carbohydrates.

For a quantitative analysis or classification of biological or medical problems by means of Raman spectroscopy the application of multivariate spectral analysis methods is required. These multivariate methods allow one to extract diagnostic, chemical, and morphological relevant information out of the complex Raman spectrum and must be applied due to the high amount of similar spectral features.

With the help of a micro-Raman setup the laser spot can be focused down to about 1 µm in diameter. This allows for the differentiation of single bacterial cells or a biochemical analysis of subcellular components within bacterial (diameter approx. 1 µm) or yeast cells (diameter approx. 5–10 µm). A confocal Raman setup achieves an even better spatial resolution [6, 7]. This possibility enables Raman *mapping* or *imaging* experiments with spatially resolved information of the whole sample in axial and lateral directions.

Cellular and biomolecular analysis with Raman excitation wavelengths in the visible or near-infrared spectral range is often hampered by fluorescence emission bands. By applying excitation wavelengths in the deep UV region fluorescence-free Raman spectra can be attained since fluorescence bands are mostly located in the visible range. If UV light with wavelengths between 200 and 260 nm is chosen, specific biomolecules with absorption maxima in this region, like aromatic amino acids as well as purine and pyrimidine bases, exhibit high Raman intensities. With this resonance effect by means of the so-called UV-resonance Raman spectroscopy (UVRR) an intensity increase of up to 10^6 compared to the normal Raman scattering can be achieved for a vibration coupled to this electronic transition. Hence, such biomolecules can be detected selectively and sensitively in a complex biological environment even if they are only present in low concentrations. However, by applying UV light irradiation high laser intensities have to be avoided due to an inherently possible photochemical sample damage. Further Raman signal-enhancing methods such as surface-enhanced Raman scattering (SERS) can be applied with enhancement factors of 10^4–10^{15} demonstrating the potential of single molecule detection [8]. Hereby, the enhancement effect results from molecules adsorbed on rough noble metal surfaces. These substrates increase the electromagnetic field at the metal surface when the incident laser wavelength is close to a resonance of surface plasmon oscillations. Tip-enhanced Raman spectroscopy (TERS), a combination of SERS with atomic force microscopy or scanning tunneling microscopy, even yields a spatial resolution in the nanometer scale [9]. In addition to SERS and UVRR further experimental techniques such as optical activity spectroscopy can be used in combination with Raman spectroscopy to gain further molecular information. The so-called Raman optical activity (ROA) measures the sensitivity toward chiral elements within biomolecular structures. ROA provides new insights in molecular structure, folding, and function due to small

differences of the Raman intensity scattered from chiral molecules using right- and left-circularly polarized incident laser light [10].

In this contribution we present the unique potential of the above-mentioned Raman spectroscopic techniques for viral and microbial studies in biomedical and pharmaceutical applications.

19.2 Viruses

Viruses are sub-microscopic non-cellular parasites without their own metabolisms and therefore unable to grow or reproduce outside a host cell. Each viral particle or virion consists of a nucleic acid molecule, single- or double-stranded DNA, or single-stranded RNA. The nucleic acid molecule is encapsulated with a protective protein coating, the so-called capsid, with a variety of different shapes. The study of its geometry on a molecular level is of major importance since it serves as a basis for morphological and antigenic distinction and therefore for a structure-guided antiviral drug design [11].

19.2.1 Conventional Raman Spectroscopy

Conventional virus detection is based on a wide range of microbiological methods, like the detection of virus antigens, the analysis of antibodies as an immune response (immunoblot, ELISA, or immunofluorescence), or the amplification and detection of nucleic acid (polymerase chain reaction – PCR, in situ hybridization). Recently X-ray crystallography and high-resolution nuclear magnetic resonance (NMR) spectroscopy are also used for the analysis of the molecular structure of viruses and biomolecules as well as their environment and molecular interactions [12]. But these methods are often hampered due to practical difficulties [13]. Resent studies demonstrated that Raman spectroscopy is more widely applicable than these high-resolution methods since there is no size limit or requirement for diffracting crystals [14]. It became evident that Raman spectroscopy is a promising method for a three-dimensional structural analysis of viruses since Raman spectra of virus assemblies consist of numerous Raman bands representing sensitive and selective molecular fingerprints [15]. Raman investigations to elucidate virus assembly pathways, to study the nucleic acid conformation and protein geometry of a wide variety of viruses, RNA viruses, and single- and double-stranded DNA viruses as bacteriophages have been addressed. Tuma et al. studied conformational changes in the coat protein subunit accompanied during the assembly of the procapsid shell to a mature capsid of the bacteriophage P22, which is a prototype of the morphogenesis of many double-stranded DNA viruses [16]. Another prototype member of virulent bacteriophages is PRD1 consisting of an icosahedral capsid that encloses a membrane-packaged double-stranded DNA genome. Other Raman investigations focused on the characterization of changes in the P3 subunit structure and organization during shell capsid assembly of bacteriophage PRD1 [17].

Raman difference spectroscopy has also been used to understand the molecular mechanism of viral core assemblies yielding information on viral subunits from precursor and mature states. Benevides et al. employed Raman difference spectroscopy to investigate conformational changes of the protein building blocks of the icosahedral core of a double-stranded RNA φ6 virus during viral procapsid and capsid assembly [18].

Novel experimental approaches increased the analytical power of Raman spectroscopy. Lambert showed the great potential of the combination of Raman spectroscopy with optical tweezers for viral investigations. The sample can be manipulated without physical contact, hence enabling the molecular investigation of samples closer to their native state [19].

19.2.2 UV-Resonance Raman Spectroscopy

The application of ultraviolet-resonance Raman spectroscopy (UVRR) has attracted great interest to probe selectively DNA and protein residues in complex biological systems since the UV laser excitation wavelength matches the UV absorption of the nucleic acid bases from DNA/RNA as well as aromatic amino acids from protein subunits. For structural studies of viruses by means of UVRR, accurate band assignments, intensity measurements, and quantitative determination of UVRR band intensities are essential [15, 20]. A wide variety of filamentous viruses were investigated by means of UVRR spectroscopy applying several excitation wavelengths ranging from 229 to 257 nm. Wen et al. performed UVRR investigations to study the structure and interactions of single-stranded DNA filamentous viruses Pf1, Pf3, and fd. In doing so, Raman excitation at 257 nm yields rich Raman bands originating mostly from the single-stranded DNA genome. Using 229 nm as UVRR excitation wavelength the spectra are dominated by tyrosine and tryptophan residues of the coat subunits of the single-stranded DNA viruses from filamentous bacteriophages Pf1 and fd [21]. Overman et al. unraveled the effect of virion concentration and solution salt concentration on the alignment and aggregative properties of filamentous phages probed by UVRR [22].

19.2.3 Raman Optical Activity

In the last years the application of vibrational optical activity (VOA), i.e., vibrational circular dichroism (VCD) and Raman optical activity (ROA), led to major progress in biospectroscopy. The effect of VOA and especially ROA refers to slight differences in the Raman spectra of chiral molecules excited with right- and left-circularly polarized light [10]. Hence, ROA provides valuable insights for a deeper understanding of the structure, folding, and behavior of chiral molecules, making it an attractive probe for the investigation of viruses, viral assemblies, and precursors. Raman optical activity allows for a simultaneous investigation and determination of the three-dimensional structure and conformation of major coat proteins and nucleic acid core components of different structural types of intact viruses in

aqueous solution [13, 23, 24]. Protein ROA spectra yield information on secondary and tertiary structures of polypeptide backbones and therefore reflect their conformation [25]. In addition protein ROA bands carry information about backbone hydration and side chain conformations as well as of structural elements in the unfolded state [25]. The exact analysis of these structure-sensitive protein bands via multivariate analysis such as principal component analysis (PCA) or nonlinear mapping (NLM) allows one to derive relationships between different proteins and structural classes [24]. Nucleic acid ROA spectra provide information about the sugar ring conformation, base stacking arrangement, as well as the orientation of sugar and bases around the C–N glycosidic linkage [25].

The combination of Raman spectroscopy and Raman optical activity provides spectral signatures to assess valuable information on RNA structural motifs in the encephalomyocarditis virus (EMCV). Raman and ROA spectra were collected for RNA oligonucleotides to investigate contributions of helix, tetraloop, mismatch base pairs, and asymmetric bulge structures of the RNA [14].

Blanch et al. investigated several viruses, including single-stranded RNA helical rod-shaped plant viruses: tobacco rattle (TRV) and tobacco mosaic viruses (TMV) [26], as well as single-stranded RNA helical filamentous plant viruses like the potato virus X (PVX) and the narcissus mosaic virus (NMV) [27] by means of ROA leading to new information about structure and conformation of coat protein subunits and packing arrangements within the virus. The ROA spectra are dominated by protein signatures revealing large amounts of α-helix. RNA ROA bands are absent or much weaker due to the low RNA contents in the range of 5–6% of the total particle mass for each case. A comparative ROA study of several virus types like the filamentous bacteriophage fd, the tobacco mosaic virus (TMV), and the satellite tobacco mosaic virus (STMV), the empty protein capsid of bacteriophage MS2 and the cowpea mosaic virus (CPMV) showed the ability of ROA to discriminate between different structure types [13]. Raman spectroscopy is an extremely capable method to distinguish between taxonomically similar viruses leading to an increasing potential in medical diagnostics [19].

19.2.4 Surface-Enhanced Raman Spectroscopy on Viruses

Since most biomolecules normally exhibit medium or low Raman cross sections, an enhancement of the signal intensity for the ability to characterize even low concentrations would be preferable. Besides the application of resonance Raman spectroscopy, surface-enhanced Raman spectroscopy (SERS) is a promising alternative. In doing so the vicinity of molecules to rough noble metal surfaces leads to Raman enhancement factors of 10^6–10^8 and even up to 10^{14} leading to a single molecule detection limit [9].

For the detection of viruses different SERS approaches are reported. One possibility is the direct detection of the DNA or the protein shell. Additionally, the presence of the DNA can also be detected indirectly via marker molecules. The third possibility is the detection via antibodies [28].

Reyes-Goddard et al. detected herpes simplex viruses directly in synthetic tears on gold and silver island films. For a discrimination between synthetic tears with and without viruses a linear discriminant analysis was performed [29]. Commercially available solid SERS substrates were used for the direct detection of different taxonomically similar Poxviridae viridons by their species-specific components. Here, two models for the identification and quantitative estimation of both bovine popular stomatitis virus and pseudocowpox virus in the presence of Yaba monkey tumor virus and abiotic particles by means of PLS2 were performed [30]. In addition, solid silver nanorod substrates, made with oblique angle deposition, were used for the direct detection of respiratory viruses. It could be shown that various virus types and even strains can be differentiated via these SERS substrates. With this setup a minimal concentration of approximately 10^3 pfu/ml (plaque forming units) for the detection from cell lysates was evaluated [31]. In addition, analyzing the SERS spectra with different chemometric approaches allows for the identification of the strains [32].

For an indirect detection of viral DNA the capture DNA is labeled with either a marker molecule and/or a SERS-active substrate. One approach is the use of a DNA hairpin. Here, the capture DNA is attached at one side to a SERS substrate and at the other side to a dye. The single-stranded DNA forms a loop bringing both the SERS substrate and the marker dye into close contact leading to an intense SERS signal. The presence of the complementary DNA opens the DNA loop and the SERS signal is suppressed [33, 34].

Another approach for an indirect DNA detection uses a three-component sandwich assay. Here, a SERS-active particle is labeled both with a marker dye and a specific oligonucleotide and monitors the presence of a target DNA strand. On a chip surface the representative capture DNA is spotted. A SERS signal at the corresponding spot can be detected for the right DNA combination. For signal enhancement the gold particle can be enlarged by a silver layer resulting in a more efficient SERS substrate [35]. This approach can be modified with magnetic beads instead of the solid biochip surface as immobilization tool [36].

The third method does not detect the viral DNA or protein components but the antigens. In this immunoassay the antibodies are both localized on a biochip surface and on a SERS-active particle, which is in addition also marked with a SERS label. The antibodies can then either bind to the viral particles [37] or the isolated antigens [38]. For both variations the presence of viral particles or antigens leads to a SERS signal at the corresponding spot on the biochip.

Since conventional virus detection methods are not suitable for the detection and identification of single virus particles, one method allowing the anal-

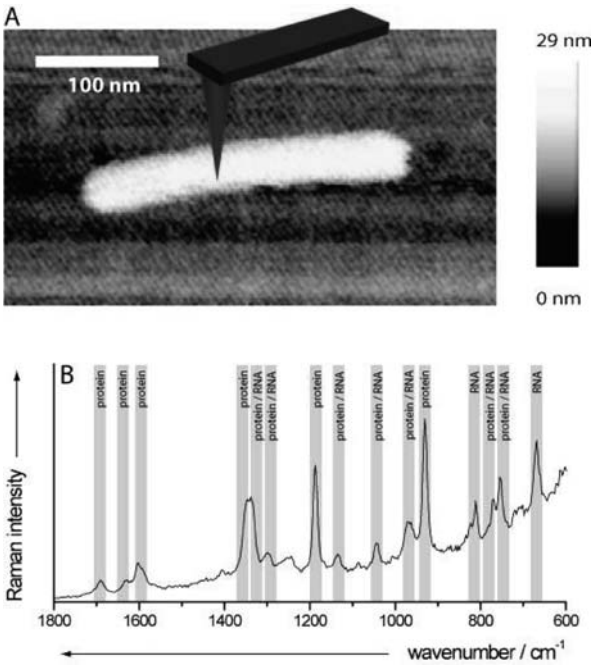

Fig. 19.1. Tip-enhanced Raman (TERS) spectroscopic analysis of a single tobacco mosaic virus (TMV) particle: (**A**) AFM image of the single virus and (**B**) TERS spectrum of the virus particle with an excitation wavelength of 568.2 nm showing contributions of protein and DNA

ysis of single viruses is tip-enhanced Raman spectroscopy, combining atomic force microscopy (AFM) or scanning tunneling microscopy (STM) with Raman spectroscopy. Thereby the spatial resolution can be improved to be less than 50 nm to characterize single viruses at a molecular level.

In Fig 19.1A a typical AFM image of a single tobacco mosaic virus (TMV) is depicted. The measured height of this virus corresponds well with given values from the literature to be around 20 nm in diameter and around 300 nm in length. In order to detect a molecular fingerprint of a single TMV a silver-coated AFM tip is placed directly on the virus particle. TERS spectra with a good signal-to-noise ratio were detected. One of the recorded spectra is depicted in Fig 19.1B. All TERS bands can be assigned as both protein and RNA contributions since these are the components of TMV [39].

19.3 Prokaryotes

Beside viruses also prokaryotes need to be identified in order to find the origin of contaminations or infections. Prokaryotes like archaea and bacteria are

cellular life forms without a nucleus. Since the nucleus is missing, the DNA can be found in the cytoplasm of the cell. In addition, also other cell organelles like mitochondria which are present in most eukaryotes cannot be found in these cells.

19.3.1 Conventional Raman Spectroscopy for Bulk Investigations

An alternative to classical routine microbiological identification based on nutritional and biochemical tests is the use of micro-Raman spectroscopy. Since only microcolonies are necessary for the identification, the time required for microbial identification decreases from 24 to 6 h by means of Raman bulk measurements. Maquelin et al. measured bacteria directly from microcolonies on solid culture media to reduce the sample preparation as much as possible [40]. Since the biochemical composition alters with respect to different growth parameters, the influence of culture media on the microorganisms' Raman spectra was investigated. In addition, the heterogeneity of microcolonies has a large effect on the identification results. After 6 h of incubation, a *Staphylococcus* microcolony is relatively homogeneous. Detectable changes in chemical composition of different colony layers only occur for microorganisms older than 12 h. For this case, a higher concentration of glycogen was identified in the surface layer, the deeper layers contained higher amounts of nucleic acids. For *Staphylococcus aureus*, a pigmented bacterium, the amount of carotenoid is higher within the upper layers, revealing that this substance plays an important role in bacterial resistance against photodecomposition [41]. In addition, the Raman signals from different carotenoids can also be used to differentiate between various colored microorganisms [42].

In principle the chemical composition of the bacterial cells is influenced by the growth conditions, since bacteria have the possibility to easily adapt to environmental changes. These biochemical changes influence the Raman spectra and therefore have a strong impact on the recognition rate in case of bacterial identification. A few studies were dedicated to the influence of cultivation conditions on three *Bacillus* species [43] or various *Staphylococcus* species [44]. Since for Raman bulk measurements a cultivation time of at least 6 h is required, a standardization of the method is possible [45]. With standardized cultivation conditions, Maquelin et al. investigated various bacterial and fungal pathogens from blood cultures and obtained a recognition rate of 92% [46]. On the other side, Kirschner et al. showed the potential usefulness of Raman spectroscopy for the differentiation between various species of enterococci [47].

Due to the fact that Raman spectroscopy is a very sensitive technique, even identification on the strain level becomes possible. Various studies were performed distinguishing different strains of *Acinetobacter baumannii* [48], *Staph. cohnii*, and *Staph. epidermidis* strains [44], as well as various *Bacillus* strains [45]. Goeller et al. applied Raman spectroscopy not only to discriminate

between bacteria but also between bacteriophages [49]. In addition, closely related *Bacillus* species [50] as well as various strains of tuberculosis and non-tuberculosis mycobacteria [51] could be distinguished.

Beside identification, also a molecular characterization of bacteria by means of Raman spectroscopy was performed. Escoriza et al. reported about variations in bacterial Raman spectra in different metabolic states [52]. Here, the intensity of nucleic acid signals showed a maximum at the beginning of the exponential phase and then slowly decreased with time, the other bands remaining relatively constant.

Raman spectroscopy can also be used to investigate the changes in chemical composition induced by various chemical and physical inactivation methods [51]. A clear differentiation between normal and deactivated cells was possible based on the Raman spectra.

The correlation between chemical composition of microorganisms and their susceptibility to sakacin P, a bacteriocin produced by some lactic acid bacteria, was carried out by Oust et al. [53]. It could be shown that at least some of the variations in the susceptibility to sakacin P in *Listeria monocytogenes* can be correlated to alterations in the chemical composition of the bacterial cell wall.

Berger et al. used Raman spectroscopy for oral bacteria identification of *Streptococcus* species [54]. Furthermore, it was possible to determine the relative concentrations of different *Streptococcus* species in a polymicrobial mixture [55]. De Gelder et al. used the Raman signal to monitor the amount of PHB in bacterial cells [56]. In addition, the amount of bacteria in drinking water was quantified by Escoriza et al. [57].

Foodborne microorganisms were analyzed directly on the food surface by means of FT-Raman spectroscopy [58]. These results indicate that FT-Raman has the ability to discriminate between pathogenic and non-pathogenic bacteria.

19.3.2 Single Cell Identification of Bacteria by Means of Micro-Raman Spectroscopy

By using high numerical aperture illumination and light gathering optics, micro-Raman setups allow for Raman studies on a single organism level, thus making the time-consuming cultivation step to generate enough biomass for bulk measurements unnecessary. The combination of an optical microscope and a common Raman setup leads to a lateral spatial resolution of approximately 1 µm. The application of a confocal detection regime, i.e., by integrating a pinhole at the image point of the focused laser spot, leads to an even higher spatial resolution. By doing so, the scattering signals emerging from material outside the measuring volume are removed. However, the application of a confocal pinhole is attended by a loss of signal, depending on the pinholes and the objects' size. But if the latter has the dimension of the laser beam focus only suppression of the background signal will occur. Therefore, the study

of bacteria and other microorganisms, e.g., archaea, exhibiting dimensions in the micrometer range are favorable targets for micro-Raman spectroscopy. The obtained Raman signatures reflect the overall composition of the cell, in case that single prokaryotes exhibit a spatial homogeneity, which is generally true [45].

However, it has to be kept in mind that only very small sample volumes $(0.5–2.5\,\mu m^3)$ are analyzed [45], so a lower signal-to-noise ratio and additional signals due to the substrate might appear in contrast to the aforementioned bulk measurements.

Like already mentioned for the bulk studies presented above different culturing environments lead to changes in the biochemical composition of a microbial cell and could therefore affect the ability to discriminate and identify the investigated species [43]. It is also a striking feature of Raman spectra of single cells that the spectra are strongly affected by the cells' individual physiological states [44, 59]. This is certainly also true for bulk Raman spectra, but to a lesser extent since the spectra are an average over several bacterial cells [41, 43, 57].

This results in a dilemma: which information in Raman spectra are representative for the whole ensemble of the bacterial community and which emerge from the specific individualities of the single cell? This information has to be extracted out of the vast amount of multidimensional data obtained by measuring a number of single cells making a chemometrical analysis of the data necessary. In doing so, only a handful of multivariate methods, unsupervised and supervised, are applied in every work dealing with chemotaxonomic identification of single cells by micro-Raman spectroscopy. Frequently, a data reduction step is performed using the principal component analysis (PCA), which is a well-known method for reducing the dimensionality in a data set. Also well established in this context is the unsupervised hierarchical cluster analysis (HCA), mainly useful as preliminary analysis step. Finally as supervised classification method the so-called support vector machine (SVM) provided hugely satisfying results in combination with micro-Raman analysis. However, like all classification methods an SVM model is only as good as the database backing it up is comprehensive. A valid signature library has to be customized to the objective: If, for example, *Bacillus* spores isolated out of soil need to be identified the library must comprise spectra of several *Bacillus* strains of different species, of genetic near neighbors, and also of typical soil material.

The basis of phenotypic discrimination of closely related species via Raman spectroscopy lies in its sensitivity to the intracellular molecular components including extrachromosomally encoded phenotypes, such as the *Bacillus anthracis* or *B. thuringiensis* toxins or polyglutamic acid capsules. Other prominent examples are cell storage materials like the polyhydroxy butyric acid (PHB), carotenoid-based pigments like sarcinaxanthin, hemoproteins like cytochrome or calcium dipicolinate (CaDPA). Raman spectra of single bacteria, in which the latter four intracellular substances occur, are shown in

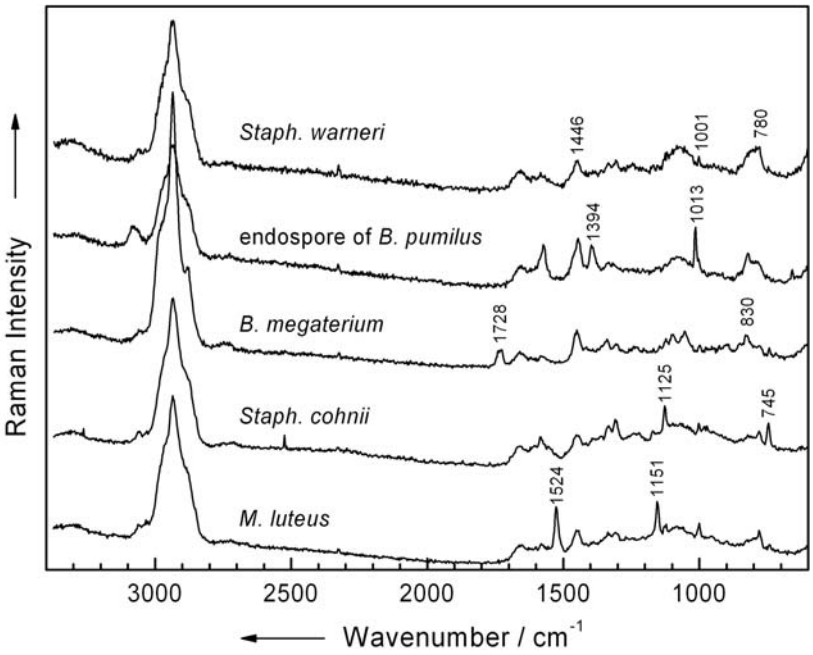

Fig. 19.2. Micro-Raman spectra of different single bacterial cells: normal bacterial Raman spectrum of *Staph. warneri* compared to Raman spectra with enhanced amounts of subcellular components: calcium dipicolinate for a spore of *B. pumilus* polyhydroxy butyric acid (PHB) in *B. megaterium* cytochrome in *Staph. cohnii* and sarcina xanthin in *M. luteus*

Fig 19.2. The Raman spectrum of *Staph. warneri* is prototypical for bacterial vegetative cells, showing signals emerging from main macromolecular building blocks within biological cells, e.g., at 780 cm^{-1} (DNA/RNA) or 1001 cm^{-1} and 1446 cm^{-1} (proteins). The endospore spectrum exhibits these bands, too, but is mainly characterized by prominent signals of CaDPA, e.g., at 1013 and 1394 cm^{-1}. This is also the case for the spectra of *B. megaterium* and *Staph. cohnii*, where the dominant features are caused by PHB (830 and 1728 cm^{-1}) and cytochrome (745 and 1125 cm^{-1}), respectively. Finally, the signals at 1151 and 1524 cm^{-1} of the pigment sarcinaxanthin are striking in the spectrum of *M. luteus*. All Raman spectra are dominated by bands of the respective components, which are strong Raman scatterers, resonantly enhanced and/or just abundantly present within the cells. While on the one hand these substances deliver recognizable marker bands to sort out microorganisms for which these substances are characteristic, they are unsuitable for discriminating between them on species or even strain level. To accomplish this, bands of the main biological building blocks (nucleic acids, proteins, carbohydrates, lipids) need to be assessed.

Though especially the cultural parameters of the studied cells have a huge impact on their signature variability it seems that – a decent Raman signature library provided – the majority of cultivation differences can be accommodated and thus no extreme standardization of culturing conditions is required for identification via this method. But for the sake of taxonomic resolution care has to be taken in finding appropriate culturing conditions to affect the implementation possibilities of Raman spectroscopy in microbial analysis positively [43].

An alternative approach is to bring the cells to uptake a specific substrate provided in the growth media and afterward to monitor this substrate within single cells on the basis of the substrate's specific Raman signature. Huang et al. [60] incorporated ^{13}C-marked glucose into bacteria cells and monitored its distribution concentration correlated. Bearing that in mind it is, for example, imaginable to follow up the uptake of a specifically labeled drug within the human body by in vivo micro-Raman spectroscopy.

The interactions of drugs with bacterial cells were also analyzed by means of micro-Raman spectroscopy [61, 62]. Whole-cell changes inside the Gram-positive bacterium *Staph. epidermidis*, which occur as a result of the presence of the drug moxifloxacin, led to spectral changes mainly of bands assigned to protein constituents and DNA moieties.

The vast identification potential of micro-Raman spectroscopy combined with the aforementioned sophisticated chemometric analysis methods is corroborated within various works: In one study a total of 2257 Raman spectra of single cells were used to differentiate among 20 strains belonging to 9 different species. Here, a recognition rate of 89.2% for strains using the SVM technique could be achieved, albeit these bacteria were grown under different conditions (cultivation time medium, and temperature). [45]

Another example with a higher practical relevance demonstrates Fig. 19.3 and Table 19.1. Here more than 6500 micro-Raman spectra of single microorganisms belonging to 10 bacteria species were analyzed by SVM. Although their representative micro-Raman spectra do not display unique features except for the yellow-colored *M. luteus* an excellent differentiation of the species was possible. The classification results are summarized in Table 19.1 indicating an average recognition rate of 92% on species level. These results form the analytical basis for a real-time identification of, e.g., bacterial contaminants in clean room environment on single cell level.

Also bacterial endospores were targets of profound analysis by micro-Raman spectroscopy. Under environmental stress these tough, dormant, and non-reproducing structures are produced by a few Gram-positive bacteria mainly of the genera *Bacillus* and *Clostridium*. Some of them demonstrate several pathogenic effects: The acute fatal disease anthrax can be caused by *B. anthracis*, which therefore is a potential biological weapon due to its high toxicity [63]. *B. thuringiensis* on the other hand is toxic to a great number of insect larvae due to its intracellular produced protein crystals [64], whereas

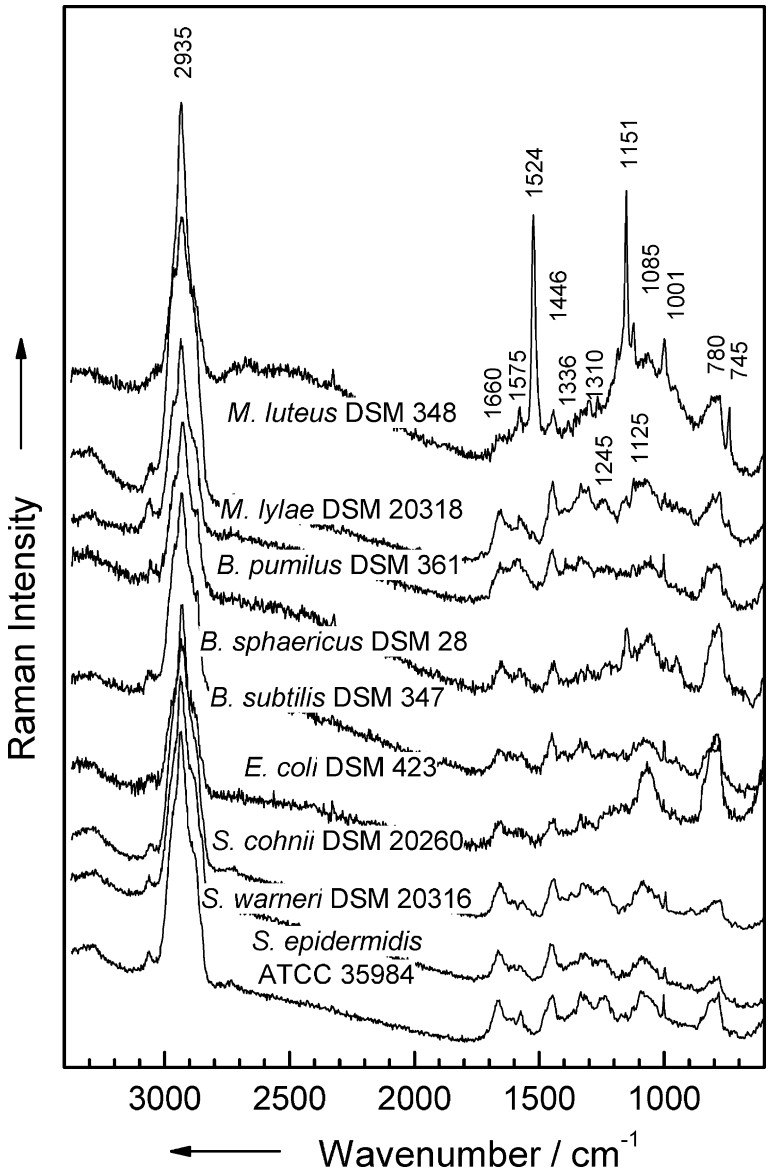

Fig. 19.3. Representative micro-Raman spectra of single bacterial cells belonging to different species and strains that are predominantly present in pharmaceutical production in case of microbial contamination

Table 19.1. Average recognition rate for single bacterial cell identification by means of a support vector machine

	Number of strains	Number of spectra	Recognition rate for species (%)
B. pumilus	7	594	93.2
B. megaterium	1	94	87.3
B. sphaericus	3	275	77.0
B. subtilis	7	924	91.6
E. coli	7	641	98.4
M. luteus	7	1259	93.0
M. lylae	2	186	94.1
Staph. cohnii	6	665	96.9
Staph. epidermidis	8	1885	89.0
Staph. warneri	2	245	99.2
	$\sum$ **50**	$\sum$ **6768**	**92.0**

B. cereus is an ubiquitous soil bacterium and an opportunistic pathogen which commonly causes food poisoning [65].

Calcium dipicolinate (CaDPA), which is the calcium chelate of dipicolinic acid (2,6-pyridinedicarboxylic acid), is a major chemical component in the endospores, accounting for 5–15% of its molecular weight. The Raman scattering of this mineral, found in the core and cortex of endospores, dominates their Raman spectra (s. endospores of *B. pumilus*, Fig 19.2). Nevertheless, the Raman spectra of endospores exhibit sufficient species-related spectral characteristics to allow for an investigation of spore-to-spore variability and differences in spores attributable to environmental variation. For example De Gelder et al. monitored the sporulation of single *B. licheniformis* endospores and correlated it to the CaDPA content [66]. Also a classification of endospores of five different species has been achieved according to inherent strain differences and culturing conditions.

Beside the identification of single bacterial cell or spores by means of Raman spectroscopy, the localization of these cells inside partly complex matrices has to be performed. One approach is the combination of Raman spectroscopy, fluorescence spectroscopy, and digital imaging techniques. This method was applied to detect traces of endospores and other biothreat organisms even in the presence of complex environmental matrices like bioaerosolic background, nasal mucin [67], or tap water [68]. Another fully automated device was built to analyze bioaerosols in clean room environments, where prior to the Raman identification method a particle preselection took place [69].

The differentiation in abiotic and biotic particles before the actual Raman measurement allows a higher sample throughput. Here, especially morphological features can be evaluated by bright light or glancing light illumina-

tion referring to size or shape. Endospores, for example, exhibit characteristic birefringence clearly visible under phase contrast conditions. Also fluorescence characteristics among single cells are exploited, either by utilizing the intrinsic autofluorescence to differentiate between biotic/abiotic particles [69] or by implementing active fluorescence staining methods to perform a live/dead assessment [70, 71] or to find bacteria co-localized within amorphous background [72].

A clever way to minimize the unwanted background from the cover plate or the environment is combining laser tweezers and confocal Raman spectroscopy (LTRS) [73, 74]. While the single cells are levitated well off the surface and held in the focus of the laser beam the Raman spectral patterns of these cells are recorded with high sensitivity. Another appealing fact is the usage of one laser for both Raman excitation and optical trapping to keep the instrumental efforts as low as possible. Additionally the trapped cells can also be micromanipulated and moved from one place to another, e.g., from the native matrix to a clean collection chamber.

With this technique the CaDPA content inside single *Bacillus* endospores could be determined [75] to $> 800\,\mathrm{mM}$ per single endospore, way above the CaDPA solubility. Using LTRS also bacteria in spoiled milk samples were localized, among other food particles and thereafter manipulated to a new position [76]. Also the discrimination of bacteria according to their species, various growing conditions or growth phases [74] and preliminary heat treatments [77] were studied with LTRS.

19.3.3 UV-Resonance Raman Spectroscopy of Bacteria

Non-resonant Raman spectroscopy has been applied with success to bacterial characterization and identification. However, the drawback of this technique is the low probability of Raman scattering. A solution for this problem is to use a Raman signal-enhancing method, e.g., SERS, TERS, or UVRR. As already mentioned above an additional advantage of using deep UVRR spectroscopy is the avoidance of a strong fluorescence background of most biological samples. Furthermore resonance Raman spectroscopy allows one to selectively monitor certain chromophoric groups present in macromolecules and depends greatly on the Raman excitation wavelength applied [78]. Raman spectra excited at 218–231 nm reflect aromatic acid contributions, while spectra excited at 242–257 nm are dominated by bands from nucleic acids [79]. Figure 19.4 compares bacterial Raman spectra recorded for different excitation wavelengths in the UV and visible regions. The non-resonant Raman spectrum (532 nm) displays Raman bands originating from all cell components while the UVRR spectrum (257 nm) is dominated by bands from nucleic acids. Here, the signals at $1330\,\mathrm{cm}^{-1}$ can be assigned to adenine, whereas the bands at 1480 and $1575\,\mathrm{cm}^{-1}$ are due to adenine and guanine. Although these bands can also be seen in the non-resonant Raman spectrum, their intensities are much lower. In the UVRR spectrum, the proteins are represented only

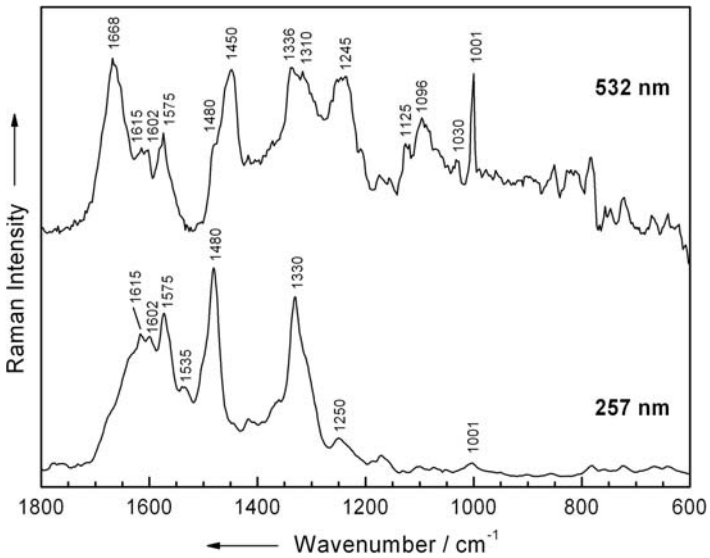

Fig. 19.4. UVRR spectrum of a bacterial bulk layer with genotypic information due to enhanced DNA and protein signals compared with a micro-Raman spectrum of a bacterial cell for phenotypic characterization since all subcellular components DNA, protein, carbohydrates, and lipids contribute to the Raman spectrum

by phenylalanine $\left(1001\,\mathrm{cm}^{-1}\right)$, tryptophan $\left(1602\,\mathrm{cm}^{-1}\right)$, and tryptophan and tyrosine $\left(1615\,\mathrm{cm}^{-1}\right)$. The Raman signals from amide I $\left(1650\text{–}1680\,\mathrm{cm}^{-1}\right)$ and amide III $\left(1230\text{–}1295\,\mathrm{cm}^{-1}\right)$ are only present in the non-resonant Raman spectrum. Moreover, the Raman signals from carbohydrates located in the $1030\text{–}1130\,\mathrm{cm}^{-1}$ region are missing in the UVRR spectrum.

In biological studies, 244 nm is one of the most commonly applied excitation wavelengths in the ultra-violet region yielding Raman spectra exhibiting signals from nucleic acids and from aromatic amino acids. Javis et al. used 244 nm and showed the capability to distinguish between various urinary tract bacteria [78]. Lopez-Diez and Goodacre analyzed different *Bacillus* species and compared these results with those obtained by 16S rDNA gene sequencing. Here, a good agreement between both Raman identification and 16S rDNA sequencing was noticed [80]. The influence of cultivation conditions on the identification of different lactic acid bacteria was investigated by Gaus et al. [81]. The results indicate that the variation of cultivation conditions does not influence the identification results for UVRR measurements. Grun et al. employed a new approach for bacterial identification, measuring two-dimensional resonant Raman spectra [82]. In this approach, the Raman spectra are recorded for 30 excitation wavelengths between 210 and 280 nm. The wavelength-dependent changes are found to be characteristic for the different species.

UV-resonance Raman spectroscopy is not only used for bacterial identification but also to study the influence of antibiotics on bacterial cells. The mode of action of amikacin on *Pseudomonas aeruginosa* cells was studied by Lopez-Diez et al. [83]. Neugebauer et al. monitored the effect of ciprofloxacin and moxifloxacin on the chemical composition of *B. pumilus* and *Staphylococcus epidermidis* [62, 84].

19.3.4 Surface-Enhanced Raman Spectroscopy of Bacteria

The first SERS spectra of bacterial bulk samples were published in 1998 by Efrima and Bronk [85]. In this study silver colloids were selectively grown on or inside *E. coli* cells, depending on the reaction conditions. The method of silver-coating bacteria was then extended to several other species [86] and alternatively silver or gold colloids were used to coat bacteria [87]. In addition, it was possible to identify different cell components like FAD (flavin adenine dinucleotide) [88]. The SERS spectra can also be used to differentiate between several genera like *E. coli* and *L. monocytogenes* [89]. Laucks et al. investigated mesophilic terrestrial or aquatic bacteria [90]. In this study the content of unsaturated fatty acids in the bacterial cell wall of *E. coli* and *P. aeruginosa* compared to arctic psychro-active marine bacteria isolated from ice core samples was investigated. Applying silver colloids the detection limit for the characterization of *E. coli* was defined to be approximately 10^3 cfu/ml [91]. To minimize the limit of detection Senguputa et al. analyzed bioaerosols by means of an aerosol sampling system allowing for the identification of bacteria [92]. The application of gold colloids made the discrimination of *E. coli* and two bacteriophages possible [93].

Jarvis et al. distinguished between five different bacterial species from clinical isolates. Here, the silver colloids placed on bacterial layers exhibit SERS spectra which could mainly be assigned to the bacterial cell wall component *N*-acetyl-D-glucosamine [94]. In addition, the combination of a SEM setup with micro-Raman spectroscopy allows for an identification of SERS-active spots from silver nanoparticles adsorbed on bacterial layers. With this method it was possible to enhance the quality of the SERS spectra and to discriminate between *E. coli* and *B. subtilis* [95]. Due to the different SERS signals of their cell walls Gram-negative and Gram-positive bacteria as well as different *Bacillus* isolates could be distinguished [96].

The marker substance for *Bacillus* endospores is calcium dipicolinate (CaDPA). One approach is the isolation of CaDPA from a minimal amount of spores and its subsequent identification by SERS spectroscopy [97]. The detection of CaDPA in endospores was used for the detection of minimal amount of spores [98] even in automated mail sorting systems [99]. The detection of CaDPA does not give any information about the *Bacillus* species present. The investigation of the components in the outmost layers of the endospores, the outer sporecoat, or the exosporium will lead to more precise information,

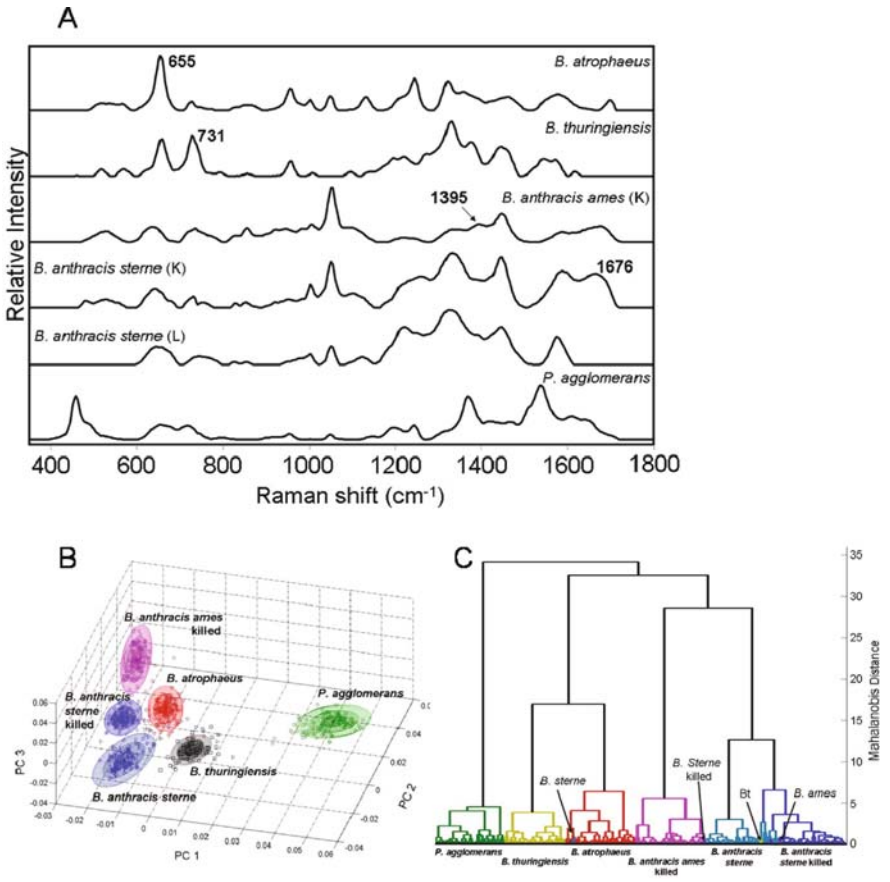

Fig. 19.5. (**A**) Representative SER spectra of three Gram-positive live (L) and two formalin-killed (K) *Bacillus* spore samples and the Gram-negative *Pantoea agglomerans*; (**B**) PCA plot showing discrimination; and (**C**) dendrogam showing classification between the samples (reprinted with permission from [100]. Copyright (2008) The Society for Applied Spectroscopy)

since SERS spectra are devoid of CaDPA information [100]. Representative SERS spectra of three Gram-positive live and two formalin-killed *Bacillus* endospore samples together with one of the Gram-negative *Pantoea agglomerans* are depicted in Fig 19.5A. The results of the subsequent chemometrical analysis are shown in Fig 19.5B and C. The PCA plot in Fig 19.5B shows a clear discrimination between the Gram-positive endospores and the Gram-negative vegetative cells of *P. agglomerans* and even indicates a differentiation of several *Bacillus* species. Also a satisfactory classification between these biological threat simulants was achieved as can be seen on the dendrogam of a hierarchical cluster analysis in Fig. 19.5C [100].

Since the SERS spectra of bacteria are highly variable [87] obtaining a reproducible SERS spectra for single bacteria is difficult. Grow et al. used

SERS spectroscopy in combination with biochips to detect the antibody signal of microbes [101]. Premasiri et al. established the first SERS classification of single bacteria for six different species under defined cultivation conditions [102].

TERS experiments were performed to study the bacterial cell surface. Biju et al. combined silver island films on glass coverslips with an AFM to investigate the effect of electron-acceptor limitation on the outer cell membrane of *Shewanella oneidensis* [103].

Neugebauer et al. performed the first TERS spectra on bacteria [104]. *Staph. epidermidis* cells exhibit TERS signals of cell wall components which showed a time-dependent behavior [61, 105].

19.4 Eukaryotes

Besides the development of novel approaches for a fast bacterial detection and identification, many efforts have also been made for the analysis of yeast cells. For clinical purposes rapid methodologies for the diagnosis of invasive yeast infections, e.g., by *Candida* species, have yet emerged to advise antifungal drugs or to adjust empirical therapy when resistant species are isolated.

Conventional microbiological identification of isolates from patients can normally be obtained with a total turnaround time of 48–96 h. Ibelings et al. [106] and Maquelin et al. [46] developed alternatively a Raman spectroscopic approach for the identification of clinically relevant *Candida* species from smears and microcolonies in peritonitis patients taking at least overnight (smears) or about 6 h (microcolonies). Hereby, a prediction accuracy of 90% was obtained for Raman spectroscopy in combination with multivariate statistical data analysis.

Raman spectroscopy appears to offer an accurate and non-invasive monitoring technique of the microbial fermentation progress when combined with the appropriate chemometric method. The online monitoring of carotenoid synthesis [107] as well as the online detection of alcoholic fermentation in living yeast cells for ethanol production from glucose was investigated by in situ Raman measurements. Furthermore, the influence of the activity of several enzymes of the glycolytic pathway in dependency of different hydrostatic pressures can be monitored [108]. Since cell wall structure and the metabolic state of the cell depend on substrate composition, the growth in different media influences the uptake of special substances. Dostalek et al. investigated the influence of specific growth conditions on the biosorption capacity and selectivity for several heavy metals for *Saccharomyces cerevisiae* [109].

For single yeast cell investigations it is not sufficient to characterize a yeast cell by means of a single Raman spectrum equivalently to the bacterial analysis described above. Yeast cells as eukaryotes exhibit in contrast to

bacteria (prokaryotes) organelles such as a nucleus, endoplasmatic reticulum, or mitochondria which are delimited from the cell plasma. Since yeast cells are approx. 10 times larger greater in size than the spatial resolution of a micro-Raman setup ($<1\,\mu m$) and due to the compartimentation and therefore spatial heterogeneity within a single yeast cell, a single point spectrum is not representative for the whole cell [110]. Consequently, Raman *mapping* or *imaging* experiments are appropriate approaches to catch the whole-cell information by recording several Raman spectra.

By calculating an average Raman spectrum from a line scan over the long axis of yeast cells a differentiation of single yeast cells on a species and strain level can be performed [110, 111]. The application of Raman spectroscopy in combination with a supervised classification method allows for the identification of single yeast cells in a large data set [69].

With Raman *mapping* experiments different cell components can be detected and monitored in a living yeast cell during yeast mitosis by means of time- and space-resolved confocal Raman spectroscopy [112]. In addition, the Raman signature of a yeast cell alters significantly by poisoning the cell with potassium cyanide [113]. Furthermore, Huang et al. studied mitochondria in a single living fission yeast cell under different nutrient, stress, and atmospheric conditions by means of time- and space-resolved in vivo Raman spectroscopy. The results show that the Raman band located at $1602\,cm^{-1}$ is sensitive to environmental changes to monitor the metabolic activity in living cells in real time. Hereby, this band decreases when oxidative stress is applied to the yeast cells [114].

The combination of optical tweezers with Raman spectroscopy offers new possibilities in the cellular in vivo analysis for manipulation and identification of single biological cells [115]. With optical trapping a single living cell can be immobilized in a physiological solution or an organelle can be kept within a living cell. Consequently, its Raman spectrum can be measured and changes of the cell state reflected in its Raman spectrum can be monitored in real time. This technique allows for the study of dynamic processes, e.g., of heat denaturation and in addition this system is appropriate for a rapid reagentless identification of microbes in a fluid [116].

19.5 Conclusions

Because of minimal sample preparation and minimally invasive approaches Raman spectroscopy has the potential to gain new insights into viral and microbial biochemistry as well as a rapid identification of pathogenic microorganisms. In this chapter the unique potential of several Raman spectroscopic techniques for medical and pharmaceutical issues is discussed, which focus on the analysis of viruses as well as on microbial detection

and identification of yeast and bacterial cells for bulk environment and single cell analysis. Recent improvements in Raman spectroscopic instrumentation and special experimental approaches increase its analytical power. Different instrumentation (e.g., micro-Raman or UVRR spectroscopy) and combinations with other techniques (e.g., optical tweezers, SERS/TERS, ROA) are applied for the elucidation of a specific biomolecular information value.

References

1. B. Schrader, *Infrared and Raman Spectroscopy – Methods and Applications* (Wiley-VCH, New York, 1995), p. 786
2. H.-U. Gremlich, B. Yan (eds.), *Infrared and Raman Spectroscopy of Biological Materials* (Marcel Dekker, New York, 2001), p. 581
3. S. Wartewig, R.H.H. Neubert, Adv. Drug Del. Rev. **57**, 1144–1170 (2005)
4. J.R. Baena, B. Lendl, Curr. Opin. Chem. Biol. **8**, 534–539 (2004)
5. J. Popp, P. Rösch, M. Harz, M. Schmitt, K.D. Peschke, O. Ronneberger, H. Burkhardt, Proc. SPIE-Int. Soc. Opt. Eng. **6180**, 6180/6241–6180/6249 (2006)
6. L. Baia, K. Gigant, U. Posset, G. Schottner, W. Kiefer, J. Popp, Appl. Spectrosc. **56**, 536–540 (2002)
7. L. Baia, K. Gigant, U. Posset, R. Petry, G. Schottner, W. Kiefer, J. Popp, Vib. Spectrosc. **29**, 245–249 (2002)
8. S. Nie, S.R. Emory, Science **275**, 1102–1106 (1997)
9. K. Hering, D. Cialla, K. Ackermann, T. Dörfer, R. Möller, H. Schneideweind, R. Mattheis, W. Fritzsche, P. Rösch, J. Popp, Anal. Bioanal. Chem. **390**, 113–124 (2008)
10. L.A. Nafie, Annu. Rev. Phys. Chem. **48**, 357–386 (1997)
11. C. Mathe, G. Gosselin, Antivir. Res. **71**, 276–281 (2006)
12. S.B. Larson, A. McPherson, Curr. Opin. Struct. Biol. **11**, 59–65 (2001)
13. E.W. Blanch, L. Hecht, C.D. Syme, V. Volpetti, G.P. Lomonossoff, K. Nielsen, L.D. Barron, J. Gen. Virol. **83**, 2593–2600 (2002)
14. A.J. Hobro, M. Rouhi, E.W. Blanch, G.L. Conn, Nucleic Acids Res. **35**, 1169–1177 (2007)
15. G.J. Thomas Jr., Annu. Rev. Biophys. Biomol. Struct. **28**, 1–27 (1999)
16. R. Tuma, H. Tsuruta, J.M. Benevides, P.E. Prevelige Jr., G.J. Thomas Jr., Biochemistry **40**, 665–674 (2001)
17. R. Tuma, J.H.K. Bamford, D.H. Bambord, M.P. Russell, G.J. Thomas Jr., J. Mol. Biol. **257**, 87–101 (1996)
18. J.M. Benevides, J.T. Juuti, R. Tuma, D.H. Bamford, G.J. Thomas Jr., Biochemistry **41**, 11946–11953 (2002)
19. P.J. Lambert, A.G. Whitman, O.F. Dyson, S.M. Akula, Virol. J. **3**, 51 (2006)
20. Z.Q. Wen, G.J. Thomas Jr., Biopolymers **45**, 247–256 (1998)
21. Z.Q. Wen, S.A. Overman, G.J. Thomas Jr., Biochemistry **36**, 7810–7820 (1997)
22. S.A. Overman, D.M. Kristensen, P. Bondre, B. Hewitt, G.J. Thomas Jr., Biochemistry **43**, 13129–13136 (2004)

23. L.D. Barron, L. Hecht, E.W. Blanch, A.F. Bell, Prog. Biophys. Mol. Biol. **73**, 1–49 (2000)
24. L.D. Barron, F. Zhu, L. Hecht, G.E. Tranter, N.W. Isaacs, J. Mol. Struct. **834–836**, 7–16 (2007)
25. E.W. Blanch, L. Hecht, L.D. Barron, Methods **29**, 196–209 (2003).
26. E.W. Blanch, D.J. Robinson, L. Hecht, L.D. Barron, J. Gen. Virol. **82**, 1499–1502 (2002)
27. E.W. Blanch, D.J. Robinson, L. Hecht, C.D. Syme, K. Nielsen, L.D. Barron, J. Gen. Virol. **83**, 241–246 (2002)
28. R.A. Tripp, R.A. Dluhy, Y. Zhao, Nano Today **3**, 31–37 (2008)
29. J.M. Reyes-Goddard, H. Barr, N. Stone, Photodiagn. Photodyn. Ther. **5**, 42–49 (2008)
30. T.A. Alexander, Anal. Chem. **80**, 2817–2825 (2008)
31. S. Shanmukh, L. Jones, J. Driskell, Y. Zhao, R. Dluhy, R.A. Tripp, Nano Lett. **6**, 2630–2636 (2006)
32. S. Shanmukh, L. Jones, Y.P. Zhao, J.D. Driskell, R.A. Tripp, R.A. Dluhy, Anal. Bioanal. Chem. **390**, 1551–1555 (2008)
33. M.B. Wabuyele, T. Vo-Dinh, Anal. Chem. **77**, 7810–7815 (2005)
34. M.Y. Sha, S. Penn, G. Freeman, W.E. Doering, Nanobiotechnology **3**, 23–30 (2007)
35. Y.C. Cao, R. Jin, C.A. Mirkin, Science **297**, 1536–1540 (2002)
36. Y. Liang, J.-L. Gong, Y. Huang, Y. Zheng, J.-H. Jiang, G.-L. Shen, R.-Q. Yu, Talanta **72**, 443–449 (2007)
37. J.D. Driskell, K.M. Kwarta, R.J. Lipert, M.D. Porter, J.D. Neill, J.F. Ridpath, Anal. Chem. **77**, 6147–6154 (2005)
38. W. Xu, S. Xu, X. Ji, B. Song, H. Yuan, L. Ma, Y. Bai, Colloids Surf. B Biointerfaces **40**, 169–172 (2005)
39. D. Cialla, T. Deckert-Gaudig, C. Budich, M. Laue, R. Möller, D. Naumann, V. Deckert, J. Popp, J. Raman Spectrosc. **40**, 240–243 (2008)
40. K. Maquelin, L.-P.I. Choo-Smith, T. Van Vreeswijk, H.P. Endtz, B. Smith, R. Bennett, H.A. Bruining, G.J. Puppels, Anal. Chem. **72**, 12–19 (2000)
41. L.P. Choo-Smith, K. Maquelin, T. Van Vreeswijk, H.A. Bruining, G.J. Puppels, N.A.N. Thi, C. Kirschner, D. Naumann, D. Ami, A.M. Villa, F. Orsini, S.M. Doglia, H. Lamfarraj, G.D. Sockalingum, M. Manfait, P. Allouch, H.P. Endtz, Appl. Environ. Microbiol. **67**, 1461–1469 (2001)
42. P. Rösch, M. Schmitt, W. Kiefer, J. Popp, J. Mol. Struct. **661–662**, 363–369 (2003)
43. D. Hutsebaut, K. Maquelin, P. De Vos, P. Vandenabeele, L. Moens, G.J. Puppels, Anal. Chem. **76**, 6274–6281 (2004)
44. M. Harz, P. Rösch, K.-D. Peschke, O. Ronneberger, H. Burkhardt, J. Popp, Analyst **130**, 1543–1550 (2005)
45. P. Rösch, M. Harz, M. Schmitt, K.-D. Peschke, O. Ronneberger, H. Burkhardt, H.-W. Motzkus, M. Lankers, S. Hofer, H. Thiele, J. Popp, Appl. Environ. Microbiol. **71**, 1626–1637 (2005)
46. K. Maquelin, C. Kirschner, L.P. Choo-Smith, N.A. Ngo-Thi, T. van Vreeswijk, M. Stammler, H.P. Endtz, H.A. Bruining, D. Naumann, G.J. Puppels, J. Clin. Microbiol. **41**, 324–329 (2003)

47. C. Kirschner, K. Maquelin, P. Pina, N.A.N. Thi, L.P. Choo-Smith, G.D. Sockalingum, C. Sandt, D. Ami, F. Orsini, S.M. Doglia, P. Allouch, M. Mainfait, G.J. Puppels, D. Naumann, J. Clin. Microbiol. **39**, 1763–1770 (2001)
48. K. Maquelin, L. Dijkshoorn, J.K. van der Reijden Tanny, J. Puppels Gerwin, J. Microbiol. Methods **64**, 126–131 (2006)
49. L.J. Goeller, M.R. Riley, Appl. Spectrosc. **61**, 679–685 (2007)
50. D. Hutsebaut, J. Vandroemme, J. Heyrman, P. Dawyndt, P. Vandenabeele, L. Moens, P. de Vos, Syst. Appl. Microbiol. **29**, 650–660 (2006)
51. P.C.A.M. Buijtels, H.F.M. Willemse-Erix, P.L.C. Petit, H.P. Endtz, G.J. Puppels, H.A. Verbrugh, A. van Belkum, D. van Soolingen, K. Maquelin, J. Clin. Microbiol. **46**, 961–965 (2008)
52. M.F. Escoriza, J.M. Vanbriesen, S. Stewart, J. Maier, Appl. Spectrosc. **60**, 971–976 (2006)
53. A. Oust, T. Moeretroe, K. Naterstad, G.D. Sockalingum, I. Adt, M. Manfait, A. Kohler, Appl. Environ. Microbiol. **72**, 228–232 (2006)
54. A.J. Berger, Q. Zhu, J. Mod. Opt. **50**, 2375–2380 (2003)
55. Q. Zhu, R.G. Quivey Jr., A.J. Berger, Appl. Spectrosc. **61**, 1233–1237 (2007)
56. J. De Gelder, D. Willemse-Erix, M.J. Scholtes, J.I. Sanchez, K. Maquelin, P. Vandenabeele, P. De Boever, G.J. Puppels, L. Moens, P. De Vos, Anal. Chem. **80**, 2155–2160 (2008)
57. M.F. Escoriza, J.M. VanBriesen, S. Stewart, J. Maier, P.J. Treado, J. Microbiol. Methods **66**, 63–72 (2006)
58. H. Yang, J. Irudayaraj, J. Mol. Struct. **646**, 35–43 (2003)
59. K.C. Schuster, E. Urlaub, J.R. Gapes, J. Microbiol. Methods **42**, 29–38 (2000)
60. W.E. Huang, R.I. Griffiths, I.P. Thompson, M.J. Bailey, A.S. Whiteley, Anal. Chem. **76**, 4452–4458 (2004)
61. U. Neugebauer, U. Schmid, K. Baumann, W. Ziebuhr, S. Kozitskaya, V. Deckert, M. Schmitt, J. Popp, ChemPhysChem. **8**, 124–137 (2007)
62. U. Neugebauer, U. Schmid, K. Baumann, W. Ziebuhr, S. Kozitskaya, U. Holzgrabe, M. Schmitt, J. Popp, J. Phys. Chem. A **111**, 2898–2906 (2007)
63. M. Mock, A. Fouet, Annu. Rev. Microbiol. **55**, 647–671 (2001)
64. W.L. Nicholson, Cell. Mol. Life Sci. **59**, 410–416 (2002)
65. M.-J. Lee, D.-H. Bae, D.-H. Lee, K.-H. Jang, D.-H. Oh, S.-D. Ha, J. Microbiol. Biotechnol. **16**, 639–642 (2006)
66. J. De Gelder, P. Scheldeman, K. Leus, M. Heyndrickx, P. Vandenabeele, L. Moens, P. De Vos, Anal. Bioanal. Chem. **389**, 2143–2151 (2007)
67. K.S. Kalasinsky, T. Hadfield, A.A. Shea, V.F. Kalasinsky, M.P. Nelson, J. Neiss, A.J. Drauch, G.S. Vanni, P.J. Treado, Anal. Chem. **79**, 2658–2673 (2007)
68. A. Tripathi, R.E. Jabbour, P.J. Treado, J.H. Neiss, M.P. Nelson, J.L. Jensen, A.P. Snyder, Appl. Spectrosc. **62**, 1–9 (2008)
69. P. Rösch, M. Harz, K.-D. Peschke, O. Ronneberger, H. Burkhardt, A. Schuele, G. Schmauz, M. Lankers, S. Hofer, H. Thiele, H.-W. Motzkus, J. Popp, Anal. Chem. **78**, 2163–2170 (2006)
70. M. Krause, B. Radt, P. Rösch, J. Popp, J. Raman Spectrosc. **38**, 369–372 (2007)
71. M. Krause, P. Rösch, B. Radt, J. Popp, Anal. Chem. **80**, 8568–8575 (2008)
72. M. Krause, B. Beyer, C. Pietsch, B. Radt, M. Harz, P. Rösch, J. Popp, Proc. SPIE **6991**, 69910E/69911–69910E/69918 (2008)
73. J.W. Chan, A.P. Esposito, C.E. Talley, C.W. Hollars, S.M. Lane, T. Huser, Anal. Chem. **76**, 599–603 (2004)

Future Outlook and Wrap Up

We hope the book has conveyed a compelling picture of the vast potential of Raman spectroscopy which recent applications and instrumentation advances have unlocked. Many areas within these specialist biomedical and pharmaceutical fields are rapidly progressing from academic research environments to implementation as solutions to practical problems. In the pharmaceutical industry this process is well advanced. The march into the biomedical area is underway and further penetration into clinical applications appears imminent.

In pharmaceutical sciences Raman spectroscopy is presently poised to make significant advances in process control environment. Future applications unlocked include real-time process control using Raman spectroscopy to monitor and adjust process parameters during the manufacture in contrast to present mere quality check – a trend in line with US Food and Drug Administration Process Analytical Technology (PAT) initiative. Raman spectroscopy is also expected to play a significant role in the coming move from batch to continuous manufacturing processes in production environments due to its non-destructive and non-invasive character and speed. Future areas promising rapid advances are bioprocess control where compatibility of Raman spectroscopy with aqueous samples will be of particular advantage.

Further advances in miniaturisation and reduction of power consumption are envisaged that could lead to more effective handheld instruments that outperform the existing ones and approach the performance of current larger instruments. The wider applications and lower cost of the new devices will be expected to further drive the emergence of new application areas across many disciplines including those covered in this book.

Further developments are also expected in imaging applications with faster imaging methods with higher spatial resolution becoming available (e.g. sub-diffraction-limited spatial resolution). Advanced non-linear techniques such as CARS and specialist methods such as ROA will broaden their respective application areas, as instruments become more compact and more systems become commercially available.

We look forward to the next exciting analytical developments. It is apparent that Raman spectroscopy will have much more to say to the world in the coming years!

PM and MDM

Index

74. C. Xie, J. Mace, M.A. Dinno, Y.Q. Li, W. Tang, R.J. Newton, P.J. Gemperline, Anal. Chem. **77**, 4390–4397 (2005)
75. S.-S. Huang, D. Chen, P.L. Pelczar, V.R. Vepachedu, P. Setlow, Y.-Q. Li, J. Bacteriol. **189**, 4681–4687 (2007)
76. C.G. Xie, D. Chen, Y.Q. Li, Opt. Lett. **30**, 1800–1802 (2005)
77. C. Xie, Y.-Q. Li, J. Appl. Phys. **93**, 2982–2986 (2003)
78. R.M. Jarvis, R. Goodacre, FEMS Microbiol. Lett. **232**, 127–132 (2004)
79. W.H. Nelson, R. Dasari, M. Feld, J.F. Sperry, Appl. Spectrosc. **58**, 1408–1412 (2004)
80. E.C. Lopez-Diez, R. Goodacre, Anal. Chem. **76**, 585–591 (2004)
81. K. Gaus, P. Rösch, R. Petry, K.-D. Peschke, O. Ronneberger, H. Burkhardt, K. Baumann, J. Popp, Biopolymers **82**, 286–290 (2006)
82. J. Grun, C.K. Manka, S. Nikitin, D. Zabetakis, G. Comanescu, D. Gillis, J. Bowles, Anal. Chem. **79**, 5489–5493 (2007)
83. E.C. Lopez-Diez, C.L. Winder, L. Ashton, F. Currie, R. Goodacre, Anal. Chem. **77**, 2901–2906 (2005)
84. U. Neugebauer, U. Schmid, K. Baumann, U. Holzgrabe, W. Ziebuhr, S. Kozitskaya, W. Kiefer, M. Schmitt, J. Popp, Biopolymers **82**, 306–311 (2006)
85. S. Efrima, B.V. Bronk, J. Phys. Chem. B **102**, 5947–5950 (1998)
86. L. Zeiri, B.V. Bronk, Y. Shabtai, J. Czege, S. Efrima, Colloid Surf. A Physicochem. Eng. Asp. **208**, 357–362 (2002)
87. L. Zeiri, S. Efrima, J. Raman Spectrosc. **36**, 667–675 (2005)
88. L. Zeiri, B.V. Bronk, Y. Shabtai, J. Eichler, S. Efrima, Appl. Spectrosc. **58**, 33–40 (2004)
89. Y. Liu, Y.-R. Chen, X. Nou, K. Chao, Appl. Spectrosc. **61**, 824–831 (2007)
90. M.L. Laucks, A. Sengupta, K. Junge, E.J. Davis, B.D. Swanson, Appl. Spectrosc. **59**, 1222–1228 (2005)
91. A. Sengupta, M. Mujacic, E.J. Davis, Anal. Bioanal. Chem. **386**, 1379–1386 (2006)
92. A. Sengupta, N. Brar, E.J. Davis, J. Colloid Interface Sci. **309**, 36–43 (2007)
93. L.J. Goeller, M.R. Riley, Appl. Spectrosc. **61**, 679–685 (2007)
94. R.M. Jarvis, R. Goodacre, Anal. Chem. **76**, 40–47 (2004)
95. R.M. Jarvis, A. Brooker, R. Goodacre, Anal. Chem. **76**, 5198–5202 (2004)
96. R.M. Jarvis, A. Brooker, R. Goodacre, Faraday Discuss. **132**, 281–292 (2006)
97. S. Farquharson, A.D. Gift, P. Maksymiuk, F.E. Inscore, Appl. Spectrosc. **58**, 351–354 (2004)
98. X. Zhang, M.A. Young, O. Lyandres, R.P. Van Duyne, J. Am. Chem. Soc. **127**, 4484–4489 (2005)
99. S. Farquharson, L. Grigely, V. Khitrov, W. Smith, J.F. Sperry, G. Fenerty, J. Raman Spectrosc. **35**, 82–86 (2004)
100. J. Guicheteau, L. Argue, D. Emge, A. Hyre, M. Jacobson, S. Christesen, Appl. Spectrosc. **62**, 267–272 (2008)
101. A.E. Grow, L.L. Wood, J.L. Claycomb, P.A. Thompson, J. Microbiol. Methods **53**, 221–233 (2003)
102. W.R. Premasiri, D.T. Moir, M.S. Klempner, N. Krieger, G. Jones, II, L.D. Ziegler, J. Phys. Chem. B **109**, 312–320 (2005).
103. V. Biju, D. Pan, Y.A. Gorby, J. Fredrickson, J. McLean, D. Saffarini, H.P. Lu, Langmuir **23**, 1333–1338 (2007)

104. U. Neugebauer, P. Rösch, M. Schmitt, J. Popp, C. Julien, A. Rasmussen, C. Budich, V. Deckert, ChemPhysChem. **7**, 1428–1430 (2006)
105. C. Budich, U. Neugebauer, J. Popp, V. Deckert, J. Microsc. **229**, 533–539 (2008)
106. M.S. Ibelings, K. Maquelin, H.P. Endtz, H.A. Bruining, G.J. Puppels, Clin. Microbiol. Infect. **11**, 353–358 (2005)
107. C. Cannizzaro, M. Rhiel, I. Marison, U. von Stockar, Biotechnol. Bioeng. **83**, 668–680 (2003)
108. A. Picard, I. Daniel, G. Montagnac, P. Oger, Extremophiles **11**, 445–452 (2007)
109. P. Dostalek, M. Patzak, P. Matejka, Int. Biodeterior. Biodegr. **54**, 203–207 (2004)
110. P. Rösch, M. Harz, M. Schmitt, J. Popp, J. Raman Spectrosc. **36**, 377–379 (2005)
111. P. Rösch, M. Harz, K.D. Peschke, O. Ronneberger, H. Burkhardt, J. Popp, Biopolymers **82**, 312–316 (2006)
112. Y.-S. Huang, T. Karashima, M. Yamamoto, H.-O. Hamaguchi, Biochemistry **44**, 10009–10019 (2005)
113. Y.-S. Huang, T. Karashima, M. Yamamoto, T. Ogura, H. Hamaguchi, J. Raman Spectrosc. **35**, 525–526 (2004)
114. Y.-S. Huang, T. Nakatsuka, H.-O. Hamaguchi, Appl. Spectrosc. **61**, 1290–1294 (2007)
115. R. Gessner, C. Winter, P. Rösch, M. Schmitt, R. Petry, W. Kiefer, M. Lankers, J. Popp, ChemPhysChem. **5**, 1159–1170 (2004)
116. C. Xie, Y.-Q. Li, W. Tang, R.J. Newton, J. Appl. Phys. **94**, 6138–6142 (2003)